12th INTERNATIONAL CONFERENCE ON HIGH-POWER PARTICLE BEAMS

BEAMS'98

HAIFA, ISRAEL, JUNE 7-12, 1998

PROCEEDINGS - VOLUME II

EDITED BY:
MEIR MARKOVITS
AND
JOSEPH SHILOH

IEEE

RAFAEL

REPORT DOCUMENTATION PAGE

Form Approved OMB No. 0704-0188

1. AGENCY USE ONLY (Leave blank)	2. REPORT DATE 1998	3. REPORT TYPE AND DATES COVERED 7-12 June 1998 Final Report

4. TITLE AND SUBTITLE

International Conference on High-Power Particle Beams (12th) (BEAMS'98). Held in Haifa, Israel on June 7-12, 1998. Proceedings, Volume 2.

5. FUNDING NUMBERS

6. AUTHOR(S)

Meir Markovits and Joseph Shiloh, Editors

7. PERFORMING ORGANIZATION NAME(S) AND ADDRESS(ES)

8. PERFORMING ORGANIZATION REPORT NUMBER

ISBN 0-7803-4287-9

9. SPONSORING/MONITORING AGENCY NAME(S) AND ADDRESS(ES)

Office of Naval Research,
European Office
PSC 802 Box 39
FPO AE 09499-0039

10. SPONSORING/MONITORING AGENCY REPORT NUMBER

11. SUPPLEMENTARY NOTES

See also Volume 1. This work relates to Department of the Navy Grant issued by the Office of Naval Research International Field Office. The United States has a royalty free license throughout the world in all copyrightable material contained herein.

12a. DISTRIBUTION/AVAILABILITY STATEMENT

Approved for Public Release; Distribution Unlimited.
U.S. Government Rights License. All other rights reserved by the copyright holder.

12b. DISTRIBUTION CODE

A

12. ABSTRACT (Maximum 200 words)

This is volume 2 of 2 of the Proceedings of the 12th International Conference on High-Power Particle Beams (BEAMS'98) held in Haifa, Israel on June 7-12, 1998.

The conference covered all topics relevant to the physics and technology of intense beams of charge particles and included sessions devoted to pulsed power and accelerator technology, ion beams and diodes, ICF, electron beams generation and propagation, radiation sources, HPM, beam-matter sources, z-pinches and explosive generations. Special emphasis was given to newly emerging fields and industrial application.

13. SUBJECT TERMS

ONR, Foreign reports, Conferences, High-power particle beams

15. NUMBER OF PAGES

16. PRICE CODE

17. SECURITY CLASSIFICATION OF REPORT	18. SECURITY CLASSIFICATION OF THIS PAGE	19. SECURITY CLASSIFICATION OF ABSTRACT	20. LIMITATION OF ABSTRACT
UNCLASSIFIED	UNCLASSIFIED	UNCLASSIFIED	UL

NSN 7540-01-280-5500

Standard Form 298 (Rev. 2-89)
Prescribed by ANSI Std. 239-18
298-102

BEAMS'98

The Organizing Committee thanks the
following organizations
for their support of BEAMS'98:

SPONSORS

Naval Research Laboratory, **USA**

Office of Naval Research, **USA**

European Office of Naval Research, **USA**

Sandia National Laboratories, **USA**

Los Alamos National Laboratory, **USA**

Primex Physics International, **USA**

Maxwell Technologies, **USA**

Nichicon Corporation, **Japan**

Nissin Electric Corporation, **Japan**

Nissin High Voltage Corporation, **Japan**

ESC Medical Systems, **Israel**

Ministry of Defense, **Israel**

Rafael, **Israel**

Haifa Municipality

TECHNICAL CO-SPONSORS

IEEE

IEEE Electron Devices Society, USA

American Physical Society, USA

HOSTED BY

RAFAEL

BEAMS'98

PROCEEDINGS OF THE
12th INTERNATIONAL CONFERENCE ON HIGH-POWER PARTICLE BEAMS

VOLUME II

Edited By:
Meir Markovits
and Joseph Shiloh
Rafael, Haifa

20011203 214

AQ F02-02-0278

BEAMS'98

TABLE OF CONTENTS

BEAMS'98

12th INTERNATIONAL CONFERENCE ON HIGH-POWER PARTICLE BEAMS

Vol. II

LIST OF PROCEEDINGS

VOLUME 1
ORALS

PULSED POWER AND ACCELERATOR TECHNOLOGY

ELECTRON BEAM GENERATION AND PROPAGATION

DIAGNOSTICS AND EXPERIMENTAL METHODS

RADIATION SOURCES, HPM

X-RAY SOURCES, Z-PINCHES AND EXPLOSIVE GENERATORS

MODELS AND SIMULATIONS

ION BEAMS AND DIODES, ICF

X-RAY SOURCES, Z PINCHES AND EXPLOSIVE GENERATORS

POSTERS

PULSED POWER AND ACCELERATOR TECHNOLOGY

ELECTRON BEAM GENERATION AND PROPAGATION

DIAGNOSTICS AND EXPERIMENTAL METHODS

MODELS AND SIMULATIONS

VOLUME II

POSTERS continued

X-RAY SOURCES, Z PINCHES AND EXPLOSIVE GENERATORS

ION BEAMS AND DIODES, ICF

BEAM-MATTER INTERACTION AND INDUSTRIAL APPLICATIONS

BEAMS'98

12th INTERNATIONAL CONFERENCE ON HIGH-POWER PARTICLE BEAMS

POSTERS

X-Ray Sources, Z Pinches and Explosive Generators

Vol. II

2D DYNAMICS OF DOUBLE LINER
IMPLODED BY HIGH CURRENT PULSE

R. Benattar,
Laboratoire de Physique des Milieux Ionisés (LPMI)
Ecole Polytechnique, 91128, Palaiseau, Cedex, France
S.V. Zakharov,
LPMI, France
TRINITI, Russia
A.F. Nikiforov, V.G. Novikov,
KIAM, Russia
V.A. Gasilov, A. Yu. Krukovski
IMM, Russia

Modeling of implosion of nested tungsten wire arrays on the Z generator by two-dimensional magnetohydrodynamic code ZETA including radiation transport with non-LTE - LTE approximation is performed in order to reproduce experimental results. It is shown that it is possible to fit the experimental results if 10% level of initial mass perturbation of the tungsten wire arrays is imposed. Dynamics of implosion, the Rayleigh-Taylor instability developing are discussed. Plasma of the z-pinch is in nonLTE regime.

INTRODUCTION

A liner implosion in high current pulsed power generators permits to obtain dense multicharged ion plasma z-pinches of improved quality and produce high intensity thermal radiation. High power radiation experimental results were obtained on the generator Z of Sandia National Laboratory with tungsten multiwire liners [1]. Pulses of soft X-ray radiation of a power level greater than 200 TW were reached. Powerful flashes of radiation were obtained as a result of magnetic compression induced by currents of the order of 20 MA. One half of the soft X-ray radiation was due to kinetic energy of the accelerated plasma of wires, the other half was due to ohmic heating of the plasma pinch when reaching rather small cross section ($\sim 1 \mathrm{mm}^2$).

In order to increase the radiating power of the z-pinch plasma on Z they began to implode nested wire arrays. One can explain this increase in the power by the lowering of the level of instabilities at the collision of the two shells observed earlier in double liner experiments on

Angara-5-1 generator [2]. So, at the end of the compression all the parts of the plasma reach the center close in time and the major part of the radiated energy is emitted in a shorter time and consequently the radiating power increases.

In this configuration on Z facility a radiation power close to 280TW was obtained. Two nested multiwire liners of tungsten are imploded. The outer shell has a mass of 3.6 mg put at a radius of 2cm, the inner shell a mass of .91 mg of tungsten put at a radius of 1cm. The total height of the load is 2cm. The number of wires of the outer and inner liners are 240 and 120 respectively.

The heating and explosion of wires is accompanied by well known heat instability due to decreasing of wire conductivity vs temperature at metallic and phase transition stages. This instability produces plasma mass perturbations for consequent instabilities.

One of the main processes defining a radiation power of the pinch is MHD plasma instabilities of the Rayleigh-Taylor type which develops mostly as axial and is suppressed in azimuthal direction by magnetic line strength forces. Therefore it is reasonable in two-dimensional simulations of nested wire arrays to prefer r-z geometry and distribute a plasma density randomly inhomogeneously as a cylindrical double liner.

The goal of this paper is to study the implosion dynamics of the double liner and examine the influence of different levels of initial perturbations onto the z-pinch quality and X-ray production by means of 2-D numerical simulations on examples of nested wire array experiments on Z generator.

ZETA SIMULATIONS

The ZETA-code [3] was used for the complete simulation of 2-D multicharged ion plasma magnetohydrodynamics.

The mathematical model is based on a fully conservative, implicit difference scheme in Euler-Lagrange variables with different algorithms for a grid reconstruction. At every time step calculations run in three stages: first - Lagrange stage of substance movement together with radiation transport and magnetic field, second - grid reconstruction if it is necessary to avoid a grid crossing on the next step, third - Euler stage of the recalculation of values for the new grid.

The physical model includes the quasi neutral plasma magnetohydrodynamics with self-consistent electromagnetic field, energy exchange between "electron" plasma component and the "heavy" one (i.e., ions and neutrals), finite conductivity, heat conduction and radiation transport. A special attention in ZETA is paid for the radiation transport simulation which is calculated in a multigroup semianalytical self-consistent model both in LTE and in non-LTE regimes.

To perform simulations for wire array the tables of EOS, atomic constants, spectral opacities, emissivities and kinetic plasma coefficients for tungsten plasma in a wide range of temperatures and densities were calculated first by ZETA code pre-processor THERMOS in LTE and nonLTE limits.

The initial geometry and liner masses were taken from experimental data of nested liners. Large amount of wires should provide almost uniform cylindrical plasma liners after explosion of metal wires due to Joule heating and their plasma merger. The merger of plasmas of wires occurs earlier than its implosion by collective magnetic field if the distance between

neighboring wires $d = \dfrac{2\pi R}{N}$ is less than the skin depth $\Delta \approx \sqrt{\dfrac{c^2 t}{2\pi\sigma}}$ (R - radius of the wire

array, N - the number of wires in it, σ - characteristic conductivity of the wire plasma during expansion, t - time of its expansion), i.e. $d \ll \Delta$. This condition is satisfied in those Z experiments unlike of previous ones [4] where wire arrays imploded as separate plasma streams. So at initial time outer and inner liner masses were distributed as cylindrical shells with thickness 1mm both on the respective radii with initial temperature more than the tungsten sublimation temperature assuming that the explosion of the wires and the cylindrical shell formation take relatively short time (estimations show several tens nanoseconds on a pre-pulse stage yet). The density of the liners were randomly disturbed with different levels (5%, 10%) or undisturbed.

The simulation of the liner implosion was in a pure eulerian mode.

A coupling of the z-pinch with the pulsed power generator was modeled by an electrical circuit with a given electromagnetic wave (voltage pulse maximum 2U=5.4 MV), resistance, inductance and variable load (z-pinch) similar to the Z output parameters. During the double liner implosion the total current reached 18-19 MA depending on the load.

For comparison we present here results of 3 tasks including radiation transport with nested wire arrays. The sizes of the loads are the same in the 3 cases: inner shell 1cm radius, outer shell 2cm radius height 2cm:

(i) inner mass 0.93mg, outer mass 3.6mg, 10% level of perturbation distributed randomly along the z-axis, i.e. the mass density varies randomly along z between ρ and ρ+10%.

(ii) inner mass 0.93mg, outer mass 3.6mg, no perturbation on the inner shell, 5% perturbation on the outer shell.

(iii) inner mass 2.8mg, outer mass 2.8mg, no perturbation on the inner shell, 5% perturbation on the outer shell.

As a result of the calculations, we plot on the same graph the currents and the radiating powers function of time for the 3 configurations. The time is taken from the beginning of the voltage pulse.

Figure 1 shows the result on a wide time range in order to see at what time inside the current pulse the x-ray emission occurs. The x-ray power is maximum at the final compression
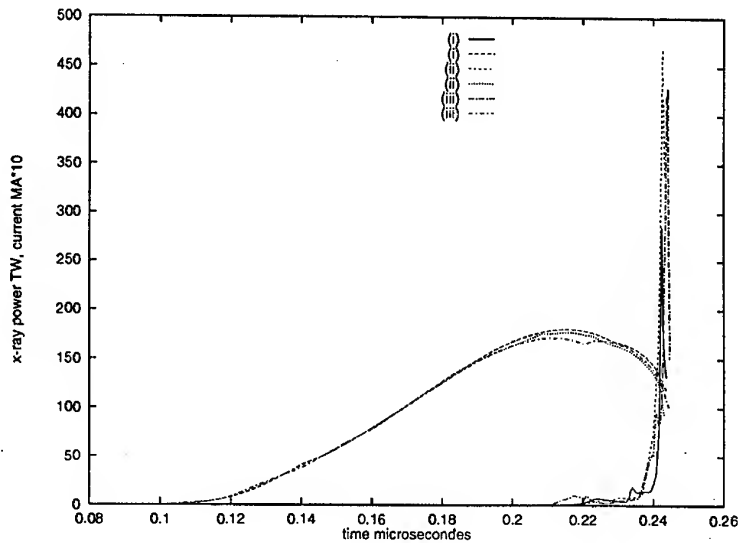
Figure 1. X-ray power and current pulse for the 3 tasks presented
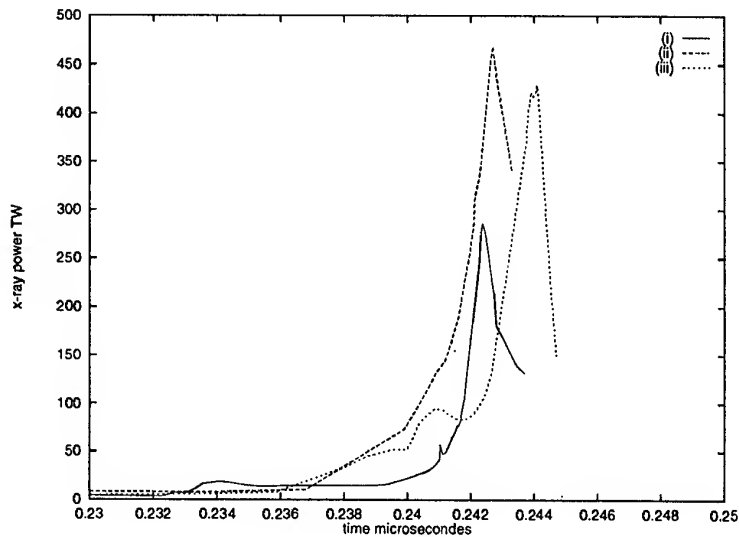
Figure 2. Radiation pulses on a reduced time scale to see more details.

of the plasma about 140ns after the start of the current. On figure 2 the radiative pulses are represented in details.

Curve (i) gives the peak power (286TW). The level of perturbation in this case is 10% so the compression is unstable and at the pinch the different parts of the plasma do not reach the center at the same time. This is shown of figure 3 where are represented the spatial distributions of mass density at different time moments: a - before strike, b - after strike and c - at z-pinch peak power emission. The external surface of the outer liner is unstable, its internal surface is closely stable before strike, during strike the effective thickness of merged liners decreases, but after closer to the axis perturbations of the inner surface as of the outer one increases .

The dense plasma of a z-pinch is concentrated in several high density points, but the surrounding plasma is dense enough to reabsorb a part of radiation and as a result an electron plasma temperature distribution on the z-direction of the pinch is more homogeneous than

a   b

c   d
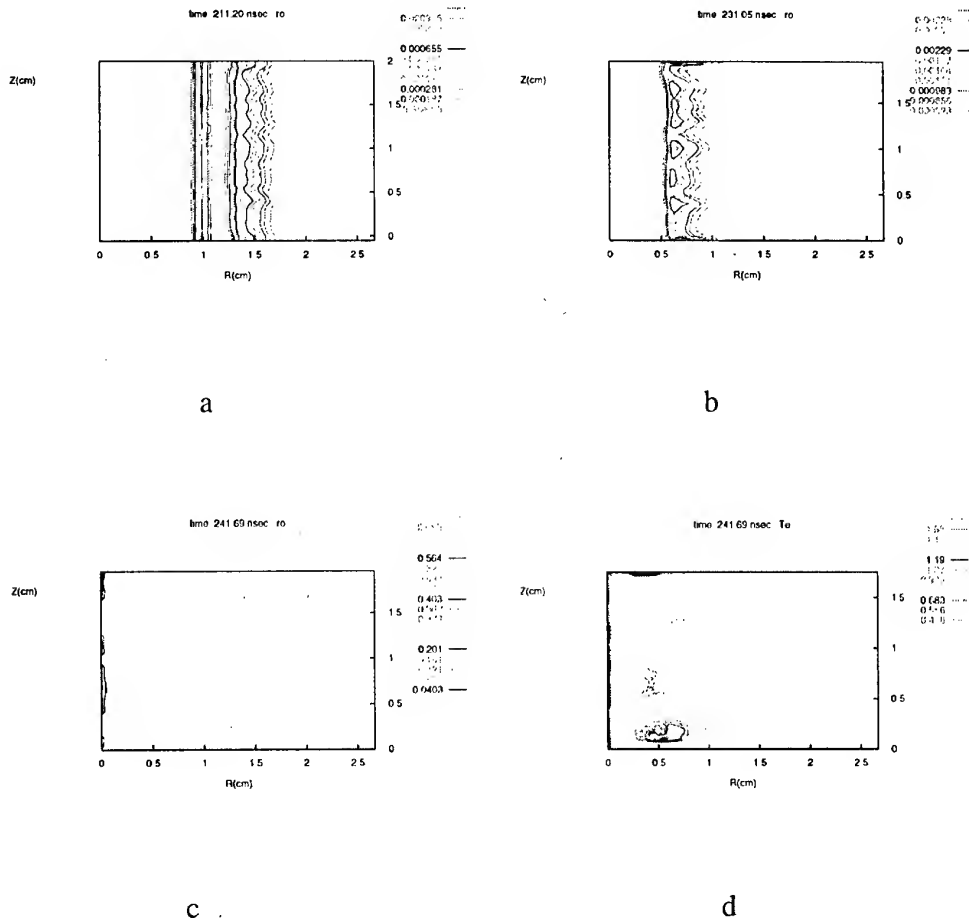
Figure 3. The history of implosion for the simulation (i): : a - the density before strike of the liners, b - after strike, c - at z-pinch peak power emission and d - the electron temperature at this moment. The box has 2.67 cm along R axis and 2 cm along Z axis. The initial positions of two liners are marked at R=1cm and R=2cm

density, this is shown on the figure 3 d. The plasma of the pinch at the moment of radiation power peak is in non-LTE regime (the effective nonequilibrium degree $\xi = \dfrac{U}{U_{Pl}}$ - ratio of the real radiation energy density to the planckian one is not more than 0.03). Such value of ξ is sufficiently large to make difference from transparent nonLTE case on one side and LTE on the other side, for example average ion charge for transparent nonLTE plasma for the typical z-pinch parameters $Te=300eV$, $\rho=0.06g/c.c.$ is $z=17.76$, for LTE $z=42.15$ but for $\xi=0.03$ $z=27.03$. Large differences are in spectral properties of z-pinch plasma. On the figure 4 the calculated spectral power of the pinch is shown.

Curve(ii) gives the greatest peak power. Curve (iii) has an intermediate value for the peak power. Curves (ii) and (iii) have the same level of initial perturbation. Density distributions of z-pinches are very smooth in z-direction in these two cases. So due to this low level of instability at the final pinch, the main part of the plasma reaches the center very close in time. The radiative pulse is less spread in time and consequently the power is higher. Continuing to compare (ii) and (iii), we can say that when the mass of the outer shell is four times the inner one (curve (ii)) the power is greater. This is due to a greater kinetic energy of plasma after collision of the two shells.
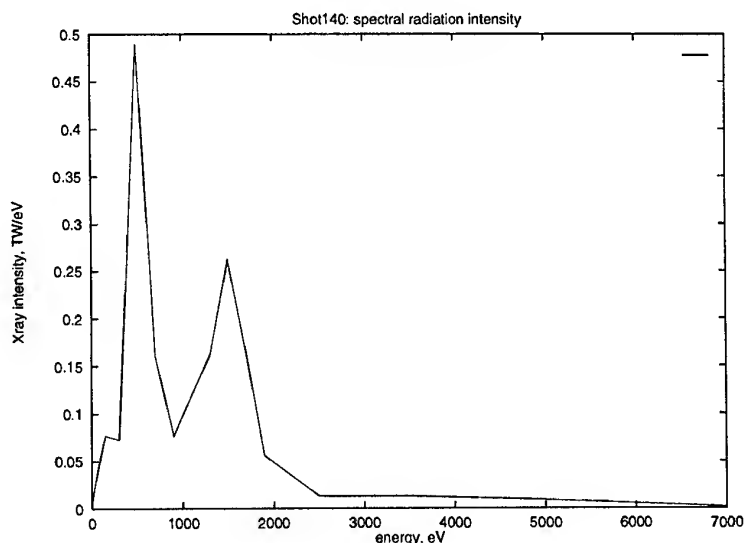
Figure 4. The z-pinch radiation spectral power at the power peak in a multigroup representation for the simulation (i):

CONCLUSION

In conclusion we have been able to model with the code ZETA experiments on the Z generator and to recover the amount of radiating power obtained and the time of final compression accepting some amount of instability during the time evolution of the liner.
The presented results of 2-D double liner modeling of nested wire array implosion show that the best fit with the experimental data on the Z facility is for 10% random level of perturbations on initial density. Consequently, the level of instability during the compression is pretty high and this lowers the peak radiation power comparatively to a smooth compression close to 1D evolution of the liners. The plasma of the z-pinch is in a nonLTE regime and thermal radiation reabsorption is significant.

This work has been performed with the support of D.G.A. - Centre d'Etude de Gramat.

REFERENCES

[1] Spielman R.B., Deeney C., Chandler G.A., Douglas M.R., Fehl D.L., Matzen M.K., McDaniel D. H., Nash T.J., Porter J.L., Sanford T.W.L., Seamen J.F., Stygar W.A., Struve K.W., Breeze S.P., McGurn J.S., Torres J.A., Zagar D.M., Gilliland T.L., Jobe D.O., McKenney J.L., Mock R.C., Vargas M., Wagoner T., Peterson D.L. Physics of Plasmas, 5, 2105 (1998).
[2] Zakharov S.V., Smirnov V.P., Grabovskii E.V. et al. Proc. of the I.A.E.A Technical Commitee Meeting on Drivers for Inertial Confinement Fusion. Paris, France Nov. 14-18,1994. 395 (1995).
[3] Benattar R., Ney P., Nikitin A., Zakharov S.V., Starostin A.N., Stepanov A.E., Rerich V.K., Nikiforov A.F., Novikov V.G., Solomyannaya A.D., Gasilov V.A., Krukovskii A.Yu., 4th International Conference on Dense Z-Pinches Vancouver Canada 1997, AIP Conference Proceedings 409, 211.
[4] Behtev M.B., Zakharov S.V., Smirnov V.P. et al. Plasma dynamics of imploding multiwire array liners. Sov. Phys. JETP, 68, 955 (1989).

Cauchios spectrograph application for investigation of bremsstrahlung and line spectra, emitted by plasma focus discharge

E.O.Baronova, V.A.Rantsev-Kartinov and M.M.Stepanenko
Nuclear Fusion Institute, RRC Kurchatov Institute,
123182 Moscow, Russia

Abstract. Paper presents the results of bremsstrahlung spectra investigation at the range of 20-200 keV. Spectra emitted by plasma focus device (U=14 kV, I=360 kA) were registered by transmission spectrograph. Analysis has shown the maximum of intensity corresponds to 150 keV, anode surface was determined as emitting bremsstrahlung and characteristics spectra due to the bombardment by electron beam with energy about 200 keV.

Introduction

Creation of pulsed radiation source with energy more than 10 keV, and elucidation of interaction of such emission with different materials are of great interest. Among probable sources of such radiation z-pinch devices may be characterized as enough simple in operation and relatively cheap for manufacturing.

The goal of this paper is to investigate bremsstrahlung and x-ray line emission at the range 20-200 keV, radiated from plasma focus discharge.

X-ray emission of these energy range is nontrivial for registration and especially for correct interpretation of data obtained. The point is that interaction of 20-200 keV x-rays with different materials (detectors) is strongly depend on energy, what may be stated for such the effects as luminosity, thermoluminosity, phosforescence, photoconductivity, photo chemical processes. Therefore x-ray measurements of this spectral range, made without spectral resolution, might lead to essential mistakes, because as a rule to interpret such the results one needs to assume some spectral distribution apriore.

So spectral resolution and knowledge of spectral characteristics of detectors are highly recommended. Ross filter approach [1] provides spectral resolution, but the difficulties are that quite compensated pairs of filters are expensive, and measurements can be performed for limited number of values of energy.

We used transmission x-ray spectrograph, supplied with pair film-luminophor LaOBr to measure mentioned spectra range. This type of device are successfully applied to line spectra registration [2], present paper describes in more detail another effective ability of transmission x-ray instruments, namely bremsstrahlung spectra measurements.

Experimental set up and diagnostics

Experimental facility [3] is schematically shown in Fig.1. Discharge chamber was supplied with metal liner 1000mm in diameter, Cu anode, 700 mm in diameter with special insertion (D=50 mm). Ta, Mo, Wo were used as insertion materials. Camera was filled with Ar at pressure P~30 Pa, experiments were done at U=14 kV and I=360 kA. Z-pinch diagnostics, situated at the upper flange of the chamber were:
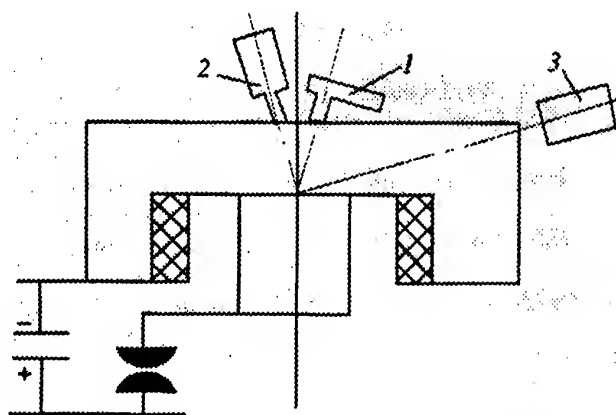
Fig. 1. Diagnostics accomodation. 1-pinhole camera, 2-mica spectrograph, 3-Cauchios device.

1. Pinhole-camera to obtain image in x-rays, with a hole diameter about 100 μm; 320 mm plasma to pinhole distance and magnification, equal to 1:8.

2. X-ray spectrograph with convex mica crystal [4] for registering line spectra at the range 1-19 A, plasma - crystal distance L about 490 mm,

3. Time integrated bremsstrahlung and line spectra at the range of 20-200 keV, transmitted through 150 μm Be filter, was registered with Cauchois device, in which using of six different transmission crystals is a possibility.

Crystal unit can be aligned with regard to detector part in order to obtain high quality spectra. Central part of crystal unit is supplied by camera obscure, needed for alignment of the device.

The dispersive elements comprised three quartz crystals used simultaneously with the following working cuts: 1010 (2d=8,5 A), 1120 (2d=4,9 A), 1340 (2d= 2,36 A) geometrical sizes of each crystals is 6X80 mm2, radius of curvature R=600 mm. Pumping of the device was not necessary due to high penetration of studied x-rays.

Fig.2 shows Cu k-alpha emission, registered in the first order of reflection with quartz crystal 1340 (2d=2,36A), in the first, second and third orders of reflection, registered with crystal 1010, and spectra in the first order of reflection, registered with 1120 quartz crystal.
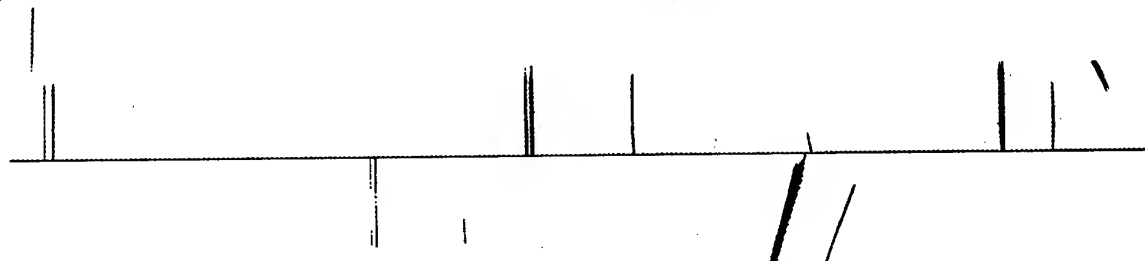
Fig. 2. Cu K-alpha, registered in the first order of reflection from crystal 1340 (upper spectra), in the first, second and third orders of reflection from the crystal1010 (middle spectra), in the first order of reflection, from crystal 1120 (lower spectra).

Reflection coefficient of quartz 1340 in the first order of reflection is more than ten times larger, than those of the other orders, reflected by this crystal, therefore we analyzed the data from 1340 crystal only, where there is no orders overlapp.

The pair of RM-K film and luminophour LaOBr with density 40 mg/cm^2 was used as a detector. The same pair is well studed and widely used in radiology, this region of medical science has more than 50 years expirience in minimizing x-ray exposition just at the range 50-150 keV. Luminescence spectra of LaOBr contains four lines (3800-4800A), what corresponds to maximal sensitivity region of RM-K film.

Absolute calibration of this pair was made with X-ray tube (U=75kV, I=10 mA) and ionization chamber as a detector. Aluminum filter of 7 mm thickness was used for selection of necessary spectra range in bremsstrahlung spectra. Fig.3 shows the results of this calibration for RM-K film. Jamma coefficient is equal to 2,15, maximal and minimal film density are 3,0 and 0,2 correspondingly. Radiation dose equal to 0,001 roentgen provides film density D=1.
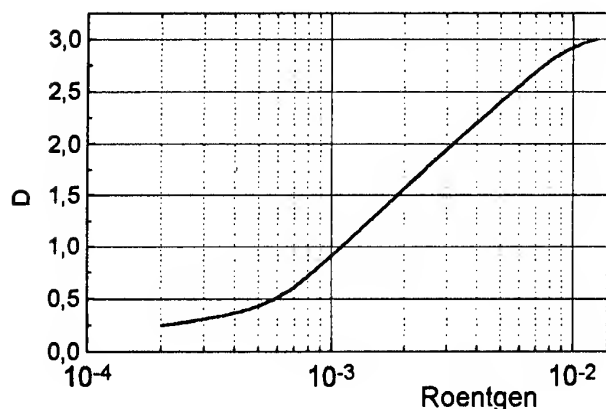
Fig. 3. Calibration curve of RM-K and LaOBr.

It was experimentally shown, that within investigated energy range the pair of RM-K film and LaOBr luminophor is at least ten times more effective than single film. Application of this pair permitted us to obtain bremsstrahlung spectra from one shot. Simple relation was used to determine the position of x-rays with energy E on the film: X=2rθ,

where 2r-radius of the crystal, θ-reflection angle. Bragg,s law was used in the following suitable form:

$$\sinθ=5,25/E,$$

where E-energy of x-rays in keV, θ-reflection angle, which were within 1,5-30 degrees.

Results and discussion.

Densitogramm of the spectrograph film exposured in one shot of plasma focus machine, supplied with flat Mo insertion, is represented on Fig.4. Maximum film density corresponds to the energy about 80-100 keV. Film density at the energies less than 20 keV is practically equal to background density 0,2. Analysis of such the densitogramm permits one to obtain intensity on energy distribution of spectra emitted from plasma after the account of:
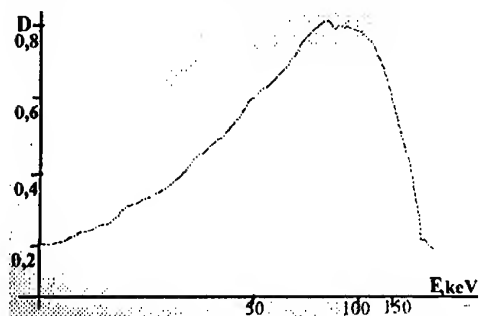
Fig.4.Densitogramm of bremsstrahlung spectra, obtained in one shot.

1) luminophor efficiency G(E) vs energy,

2) reflection coefficient of quartz crystal K(E) vs energy,

3) transmission coefficient of quartz crystal T(E) vs energy,

4) transmission coefficient Kb(E) of Be filter

5) dispersive curve of the device .

Actually, intensity of visible light Ix, emitted by luminophor, radiated with x-rays of energy Ex (position on the film with coordinate X=2rθ, where θ corresponds to the energy Ex) may be expressed as follows:

Ix~G(Ex)*Nx*Ex*(dEx/dx)*Kb(Ex)*T(Ex)*K(Ex)

where Nx-number of x-ray photons with energy Ex per 1 cm^2, dEx/dx~1/E^2. Flat crystal has complicated reflection coefficient on energy dependence, but for bent quartz (1340) crystal it is known that K(E)~1/E^2, and K(E)=3*10^{-5} rad. for E=50 keV [5]. We assume that transmission coefficient of film for 20-200 keV x-rays is 1, also Kb~1, T(E)~1. G(Ex) were calculated, using table data, are given on Fig5.

Referring to [6], experimental data for different luminophors are in close agreement with calculated one, therefore we made absolute calibration of pair film-luminophor for one energy E=50 keV.

Relative intensity I~Nx*Ex on energy dependence is shown on Fig.6. Maximum of intensity is near 150 keV.

We assume this spectra is emitted by anode surface, bombarded with electron beam, generated in plasma, which is transparent for 20-200 kev (obscure shows 5 mm in diameter plasma region, localized in close vicinity to the anode surface). Relative intensities of Mo K-alpha, K beta lines, registered with Cauchios device, are similar to that, known for x-ray tube, so one can assume these lines emitted from the anode surface.

Bremsstralung spectra obtained is different with spectra, presented in [7]. Authors, using the detectors, covered by different filters, received the more soft x-ray emission with maximum near 50 keV, registered in the direction, perpendicular to that, described in this paper.

Fig. 5. LaOBr effectivity.

Fig. 6. Relative intensity of bremsstrahlung spectra , emitted from plasma focus discharge in direction, perpendicular to z-axis.

Remembering the distribution of bremsstrahlung emission from x-ray tube, we find quite reasonable the direction of observation of Cauchious device, described here, to be enriched with hard x-rays in comparison with direction, analyzed in [7].

Total energy per centimeter at the range 20-200 keV, emitted from plasma and anode surface in the investigated direction is about 10^{-4} J/cm^2, total x-ray yield at 20-200 keV is not more than 5J for one shot. Maximal electron beam energy is estimated not more than 200 keV, maximal electron beam current is 10 kA. This experimantal results are in close agreement with electron beam theory, suggested in [8].

Summary

1. Bremsstruhlung spectra at the range 20-200 keV , emitted from plasma focus with Mo anode insertion could be registered from one shot.

2. K-alpha lines of Mo were also registered, relative intensities of these group of line testifies the anode being the source of these lines.

3.Bremsstrahlung spectra of above mentioned range is emitted from the anode surface, bombarded by electron beam, generated in plasma. Energy of electron beam in our experiment is not more than 200 keV, electron beam current 10 kA.. Energy per cm^2 at the range of 20-200 keV in the direction of investigation was 10^{-4}...J/cm^2, total x-ray yield is not more than 5 J.

4. Small Cauchious devices (with crystal radius less than 1m) might be succesfully used for investigation of both line and continious spectra, emitted from z-pinch apparatus.

In conclusion authors express their gratitude to Prof. N.Filippov for scientific interest and help in experiment and colleagues from his laboratory for technical assistance.

References.
1. V.N.Suvorov, N.A.Tulin, B.A.Potiha, PTE, no 2, 1979, 264.
2. V.A.Boiko, A.V.Vinigradov,S.A.Pikuz, X-ray spectroscopy of laser produced plasma, ser.Radiotecnique, v.27,1980, 263.
3. Filippov N.V., Agafonov V.I., Beliaeva I.F.,etc. Plasma Physics and Controlled Nucler Fusion research IAEA, Vienna, 1971, v1,p573.
4. N.J.Peacock, R.J.Speer,M.J.Hobby, J.Phys.B, ser2,v2,p798.
5. .Symbaev
6. A.M.Gurvich, X-ray luninophors and x-ray screens.,Moscow, Atom press, 1976,150.
7. N.V.Filippov, T.I.Filippova, M.A.Karakin,etc, EEE Trans. Of Plasma Sci. V24, n4, 1996, 1215.
8. V.V.Vikhrev, E.O.Baronova, present conference.

INVESTIGATION OF NeIX AND NeX LINE EMISSION FROM A GAS-PUFF Z-PINCH PLASMA USING ROSS FILTER SYSTEMS

I.N. Bogatu[*], L. Gregorian, E. Klodzh, E. Kroupp, Y. Maron, Yu.V. Ralchenko

Weizmann Institute of Science, Rehovot 76100, Israel
[*]*Permanent address: Plasma Physics and Nuclear Fusion Laboratory,*
National Institute for Lasers, Plasma, and Radiation Physics, Bucharest-Magurele 76900,
Romania

1. INTRODUCTION

Semiconductor detectors can provide measurements of the X-ray emission spectra from z-pinch plasmas with spectral, time and spatial resolution simultaneously. PIN detectors working in the current regime (up to 1 A), fast enough (1 nsec rise time), and small enough (1 to 3 mm^2 active area) are suitable, provided the X-ray spectral resolution is achieved by some element external to the detector before the X-ray flux is reaching its sensitive area. Ross (or balanced) filters [1] are especially useful for this X-ray filtration system. A Ross filter system was designed and built for the investigation of the NeIX and NeX line emission [2].

The experiments were carried out on the moderate density and temperature Ne plasma (14 mm length and approximately <1 mm final diameter) produced in a 1.2 μs, 300 kA gas-puff z-pinch device. The current is measured by an absolutely calibrated one turn B-dot coil located at 8 cm distance from the z-axis. We are reporting the first results of the NeIX and NeX ion line emission measurements using the recently built Ross filter diagnostic.

2. EXPERIMENTAL SETUP

A basic Ross filter system consists of two identical detectors placed behind two X-ray absorbing foils (or layers) that are looking at the same plasma volume. This pair of foils (or layers) is made of elements or compounds with adjacent or nearly adjacent atomic numbers Z. The foil thickness is adjusted to achieve matched transmission curves over the entire energy range except within the narrow region between their absorption edges (L_{III} or K). The difference of the energies of the absorption edges (L_{III} or K) of the foils thus defines the energy pass band of the Ross filter. The adjusted thickness makes the transmitted spectra to be identical for all the energies except those lying within this energy pass band. Since the transmission characteristics of the foils above and below their absorption edges (L_{III} or K) are the same, any difference in the two detected signals is proportional to the total X-ray power detected between these two edges. The off-line calculated signal difference is thus directly related to the total incident X-ray power within the Ross filter energy pass band.

The theory and principles of the Ross filters were applied to the computer modeling (using the collisional radiative code that is taking into account the opacity) for the design of a three channel spectrometer for investigating NeIX (E=0.99202 keV) and NeX (E=1.0215 keV and E=1.02195 keV) lines simultaneously providing spectral, time (nsec. rise time), and spatial (2 mm active surface diameter) resolution. For electron temperature within the range 100 eV to 1000 eV NeIX and NeX are the only line emitting ions (Fig.1).
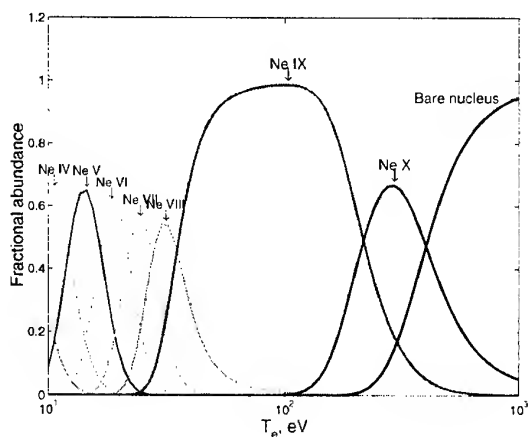
Fig.1 Fractional abundance of the Ne ions as a function of T_e for $n_e=10^{20}$ cm^{-3} (collisional radiative code results).

Fig.2 Linear absorption coefficient of Ni, Cu, Zn, and Ga showing the L_{III} edges and the experimental and modeled NeIX and NeX line spectra.

The spectrometer is composed of six Quantrad 003-PIN-035-UM X-ray diodes (3 mm^2 sensitive area, 0.7 μm Si entrance window, and 35 μm Si sensitive depth) and three L_{III}-edge Ross filters placed 88 cm from the pinch axis. The Ross filters are micron and sub-micron single, double, and triple-coating layers of Ni, Cu, Zn, and Ga$_2$O$_3$ on a soft X-ray transparent support. The filter set was carefully designed based on a previously observed spectrum (obtained using a convex Mica crystal and an X-ray film). The L_{III} absorption edges [3] are strategically chosen so that to fall in between the NeIX and NeX ions lines (Fig.2) and the transmissions outside the energy pass bands are identical (Fig.3). The Zn filter (L_{III}-edge at E=1.0218 keV) discriminates the 1/2-1/2 (E=1.0215 keV) and 1/2-3/2 (E=1.02195 keV) fine structure components of the 1s-2p NeX Ly$_\alpha$ line.

The first experiments were performed with four channels looking at the plasma from the radial direction and using the Ross filters (1) and (2). The axial spatial resolution was 2 mm achieved by means of a lead collimator and the temporal resolution was defined by the 1 ns rise time of the detector and the digital oscilloscope used, which had a 2Gs/s sampling rate with a 500 MHz bandwidth.

Fig.3 Composition and transmission of the Ross filters for NeIX and NeX lines.

The identical behavior of the channels for NeIX and NeX lines was checked by recording the signals from X-rays passing through both a 15 μm Be filter and, to avoid saturation of the signal, a 1.1 μm Cu filter which covered all four of the detectors. The difference of the corresponding pairs of signals gave the zero line within the noise level as it is needed (Fig.4).

Shot no. 2
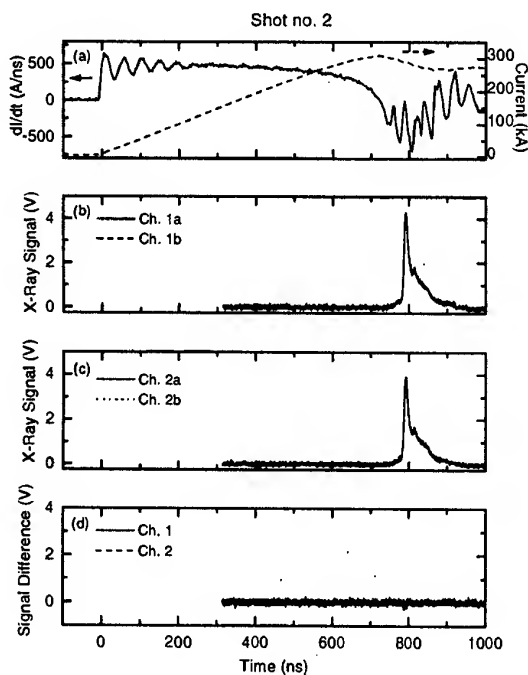
Fig. 4 Channel balance check. (a) Traces of dI/dt (solid line) and the current I (dashed line) measured by the B-dot probe; (b)-(c) The four X-ray signals measured through the same 15 μm Be and 1.1 μm Cu Ross filter; (d) The difference of the X-ray signals showing an identical response by giving the zero level.

3. RESULTS

The NeIX and NeX line evolution was recorded in a series of shots, some of them presenting a multiple pinch structure (Fig.5).

An example of line power evolution and calculated total energy of the NeIX and NeX lines is presented in Fig. 6. The NeIX line emission is starting well before NeX line and is still existing long after the NeX line has disappeared. Interesting fast time-scale phenomena can be observed throughout the emission process such as the early "pedestal" (flat signal of the NeIX and very small NeX powers) which is related to a poor compression of the plasma column as indicated by the low amplitude of the B-dot signal at the maximum compression time. The different time-resolved power signals (peaked for

the NeX line) can be analyzed by relating them to collisional radiative code results.

Shot no. 33
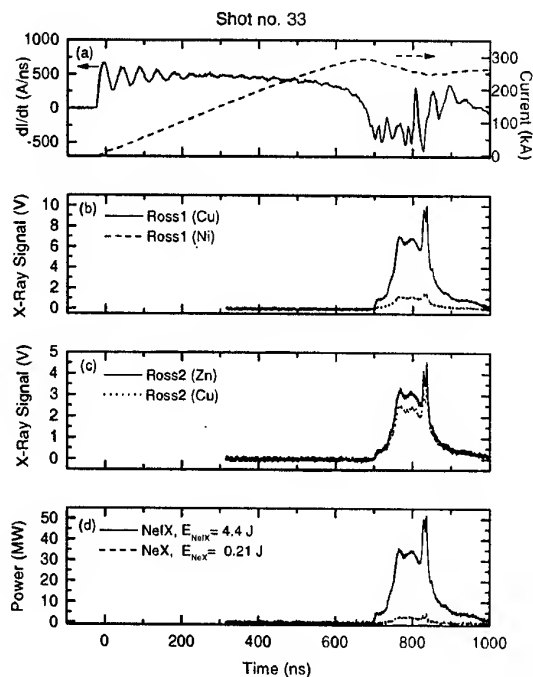
Fig. 5 NeIX and NeX line evolution in a multiple-pinch structure shot. (a) Traces of dI/dt (solid line) and the current I (dashed line); (b) Time-resolved (Cu, Ni) Ross filter-PIN diode X-ray signal; (c) Time-resolved (Zn, Cu) Ross filter-PIN diode X-ray signal; (d) X-ray NeIX and NeX line power measured by the Ross filter system and determined from the difference in the respective detector signals.

Shot no. 33
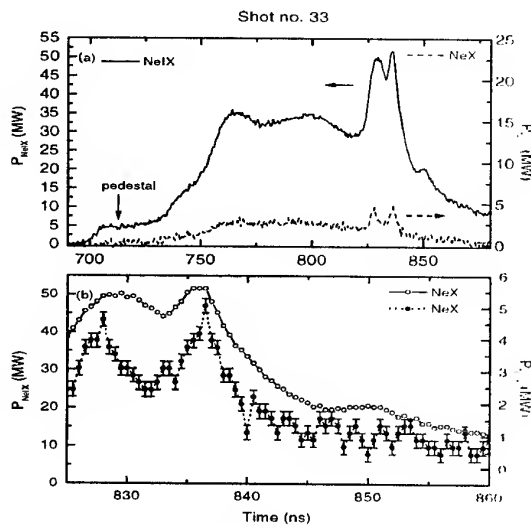
Fig. 6 Detailed line evolution of the NeIX and NeX as measured by the Ross filters.

The typical shots with good pinch compression produced enough X-ray signal to saturate at least one channel (Fig. 7).

Shot no. 36
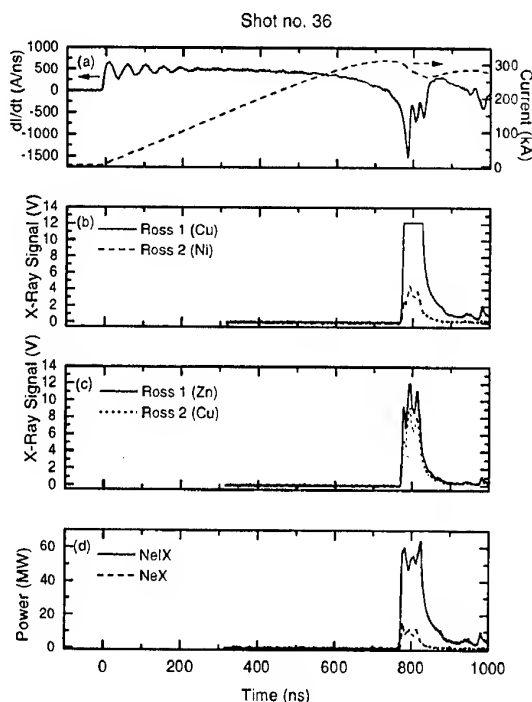
Fig. 7 NeIX and NeX line evolution in a shot with saturated X-ray signals.

Fig. 8 Comparison between the two shots showing the absence of the pedestal (pre-pinch) for higher X-ray power emission.

Despite the apparent drawback of the impossibility of following the signal evolution within the saturation period, these data showed us that narrowing the slit for achieving a better spatial resolution will still provide large enough signals.

In the case of high X-ray power emission the absence of the "pedestal" is noted, as well as a fast rise time and a smaller full width half maximum of the signal (Fig. 8).

SUMMARY

Using the L_{III} absorption edges of Ni, Cu, and Zn filters the time evolution of the NeIX line and the low energy Ly_α component of the NeX 1s-2p line were investigated with a 500 MHz bandwidth, 2 Gs/s time resolution for a region of 2 mm in length along the axial direction of the z-pinch. The first results look very promising and the data obtained will be further analyzed and additional experiments will be performed.

ACKNOWLEDGMENTS

REFERENCES

[1] P.A. Ross, Phys. Rev. 28, 425 (1926); P.A. Ross, J. Opt. Soc. Am. and Rev. Sci. Inst. 16, 433 (1928).
[2] I.N. Bogatu, et al., paper pThpP4.15, presented at the APS Division of Plasma Physics Annual Meeting, Pittsburgh, November 17 to 21, 1997.
[3] B.L. Henke et al., ADNDT, 54, 2 (1993) 181.

GENERATION OF POWERFUL BREMSSTRAHLUNG
IN A HEAVY GAS TARGET

V. V. Chorny, O. I. Frolov, V. M. Dubina, V. T. Kolisnyk, G. V. Tsepilov, V. S. Solovjov

Kharkov State University
(Svoboda Sq.,4. 310077 Kharkov Ukraine. E-mail: chorny@pht.univer.kharkov.ua.)

The results of experimental researches of Bremsstrahlung gas converters are reported in the paper. The idea to use some heavy gas for Bremsstrahlung generation was offered in [1]. To increase the radiation loss density of electrons in gas the electron gradient drift in azimuthal magnetic field produced by line current is used.

The gas converter experiments have been performed on «Nadezshda» nanosecond electron accelerator at about 1 MeV accelerating voltage and 7 Ohm output impedance of the double forming line (DFL).

As we have noted earlier [2] the efficiency of energy transfer from the accelerator diode into gas depends much upon the conditions upon which the electron beam is injected from the diode into the regular drift region. Therefore, a special attention in our experiments was given to avoiding the beam loss in the transition region between the accelerator diode and the region (regular along the interaction chamber axis) of the magnetic field.
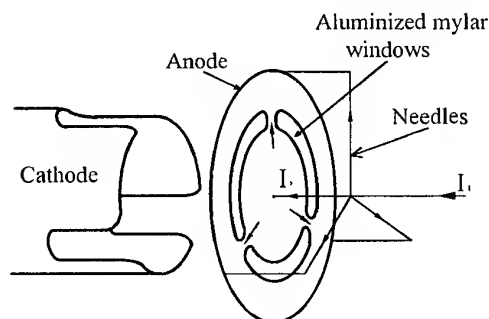
Fig.1

Schematically the diode and transient region are shown in Fig.1. To avoid the electron loss in the anode and in the current leading needles, that are placed behind the anode, the beam output window is made of three segments covered with thin aluminized mylar film. The cathode construction ensures the electron emission exactly in the output window region. To support the possibility of regulating the gradient magnetic field behind the anode three needles were used that allowed to choose the optimal I_r/I_i current ratio. *Xe* was used as a working gas. The diode functioning was studied in two operative conditions: in the first case it was a high-resistance diode at about 30 Ohm impedance which was used to eliminate the beam pinching at the anode center. Since the beam divergence was great and its energy was partially lost outside the output windows because of big anode-cathode gap, the other version of the diode has been performed to operate at 6.5-7.0 Ohm impedance. A portion of this diode back current flew inside the cathode and shorted to the outside current lead through the cathode transition isolated by the own magnetic field. This diode enabled the injection of the practically entire electron current into the space above the anode.

THE EXPERIMENTAL RESULTS

Fig. 2 presents the photographs made in visible 1 and in X-rays 2, 3 of the gas converter for a high-resistance diode, operating at different electron beam parameters, azimuthal magnetic field strength and gas density.
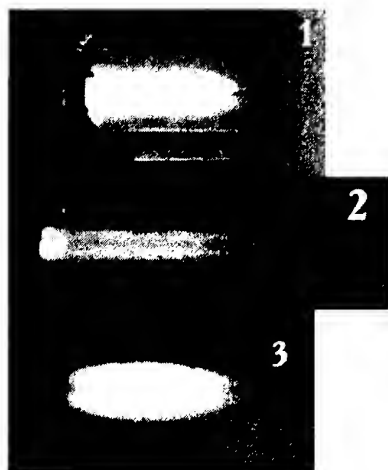
Fig. 2
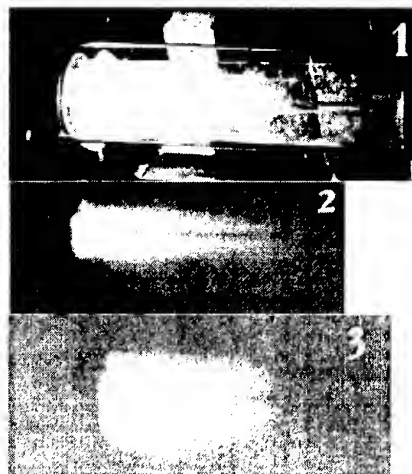
Fig. 3

Fig.3 presents the photographs of analogous converter for a convalutive diode. From these photographs one can see that by varying the gas density and the azimuthal magnetic field strength (owing to varying the magnitude of the conductor current at the drift chamber axis) one can vary the radiation source dimensions thereby providing the entire beam energy to be absorbed in the gas space. Due to small mass thickness of the target in its radial direction the effective output of low-energy X-ray photons is achieved. The X-rays absorption by the output windows and by the medium filling the space between the output window and the irradiated object determines the low-energy boundary of the radiative spectrum.

In Fig. 4 an example of the spectrum on cylindrical chamber surface for the accelerator pulse whose typical traces are shown in Fig.5 is presented. The chamber is made of plexiglass, its diameter - 130 mm and wall thickness - 1mm.
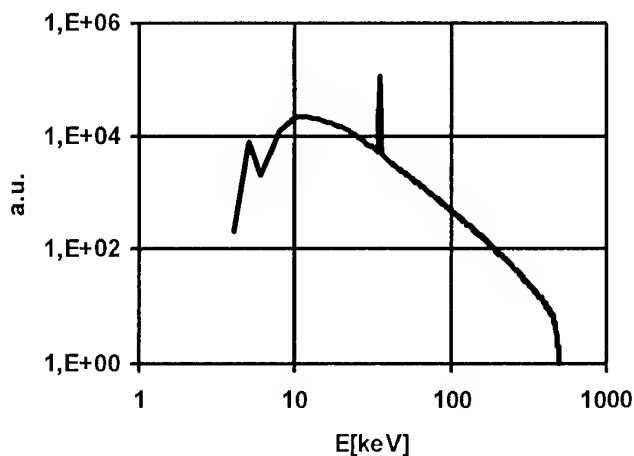
Fig. 4
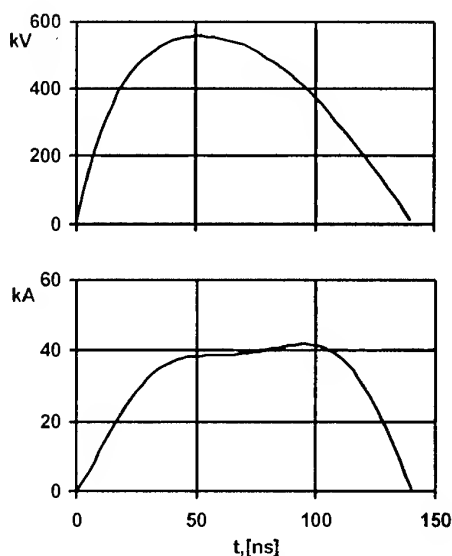
Fig. 5

Figs. 6 and 7 show the dependencies of distribution of the radiation emerging along its radius upon the distance to the anode for different types of diodes.
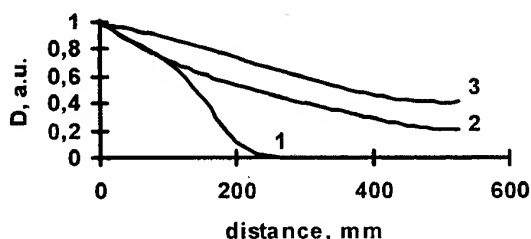
Fig. 6. Dose profiles along the gas target for the high-resistance diode. Diode voltage - 650kV; conductor current - 35 kA; *Xe* pressure in the chamber: 1-0.5 at, 2-0.25 at, 3-0.1 at.
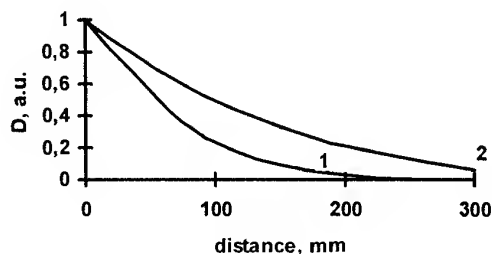
Fig. 7. Dose profiles along the gas target for the convalutive diode. Diode voltage - 500kV; axial conductor current - 20 kA; *Xe* pressure in the chamber: 1-0.3at, 2-0.2at.

Fig. 8 shows the influence of the magnetic field strength on the length of the electron beam energy deposition in gas.
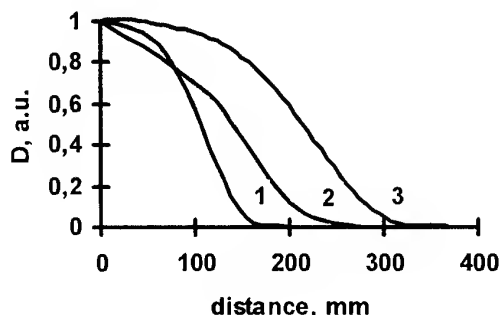
Fig. 8. Dependence of dose profiles along the gas target upon the magnitude of the axial conductor current. 1- 44 kA; 2-36 kA; 3-26 kA. The diode voltage - 650 kV; *Xe* pressure in the chamber - 0.5 at.

Fig. 9. Beam transport to the gas target. The photograph is made in X-rays.

Increasing the azimuthal magnetic field strength or the gas density along with increasing the distance to the anode one can improve the radiation uniformity along the chamber axis. Figure 9 presents the case where a thin-wall rubber balloon with *Xe* was housed at the end of the drift chamber. The beam was transported to the balloon in the air at some Hg mm pressure which provides the optimal conditions for the beam transport.

Table 1

I conductor [kA]	I beams [kA]	Pressure [Torr]	Beam energy [kJ]	Bremsstrahlung energy output [J/kJ]	Average absorbed energy [rad(Si)] R = 16 cm, S = 6000 cm²
40	40	78	1.225	11.87	165

The results of radiation dose measurements for one of the pulses whose typical traces are shown in Fig. 5 are summarized in Table 1. Comparisons of Bremsstrahlung output for gas targets with the measurement results for *Ta* targets showed that in terms of the Bremsstrahlung generation efficiency a gas target is in no way inferior to a metal one.

So, the Bremsstrahlung gas converter can be used to best advantage when it is necessary to ensure great values of $D \times S$.

REFERENCES

1. Morgun O.N., Cherny V.V., Dunaevsky A.V. IREB Interaction with Dense Gas // Proc. 8th Int.Conf. on High Power Particle Beams (BEAMS'90). - Novosibirsk, 1990. - P.689-694.
2. Chorny V.V., Dubina V.M., Dunaevsky O.V., Lomako A.O., Frolov O.I. Generation of Powerful Pulses of X-Radiation in IREB-Dense Gas System //Final Program and Abstr., 11th Int. Pulsed Power Conf., June 29-July 2, 1997. - Baltimore, 1997. - P.226. (The paper to be published in 11th Int. Pulsed Power Conf. Proceedings).

MHD-nozzle Device as a Thermonuclear Target in MAGO/MTF Concept.

Demin A.N., Chernyshev V.K., Korchagin V,P., Mokhov V.N., Ivanov V.A.,Pak S.V.,
Yakubov V.B., Garanin S.F., Mamyshev V.I., Kuznetsov S.D., Subbotin A.N.,
Burencov O.M., Dolin Y.N., Dudin V.I., Morozov I.V., Volkov A.A., Trusilo S.V.,
Usenko P.L., Skobelev A.N., Shpagin V.I.

Russian Federal Nuclear Center - All-Russian
Scientific Research Institute of Experimental Physics
607190, Sarov, Nizhni Novgorod region, Russia.

At present one of the most acute tasks that the world community faces is to master the controllable thermonuclear fusion and to solve on this basis the energy problems of mankind. The main areas of research and development that have got general recognition are the following two:

- magnetic confinement (tokomaks, stellarators, etc.) - MCF
- inertial confinement (lasers, electron and ion beams, etc.) - ICF.

These are two principally different approaches that have the only common requirement, which is to obtain a high temperature of plasma ~ 100000000°K (10 keV).

Characteristic plasma parameters for these approaches are:

a) MCF:
- plasma density $n \sim 10^{14}$ $1/cm^3$;
- plasma lifetime $\tau \geq 1$ sec;
- energy expenditures for reaction ignition $E_o \sim 10$ GJ.

b) ICF:
- plasma density $n \sim 10^{24}$ $1/cm^3$;
- plasma lifetime $\tau \leq 1$ nsec;
- energy expenditures for reaction ignition $E_o \geq 10$ GJ.

In the 80[ies] in Russia and in the US a new approach to controllable thermonuclear fusion was independently formulated. It was significantly different from the above-mentioned and got the name of MAGO/MTF.* This approach occupies an intermediate position in comparison with the above-described from the view-point of plasma parameters:

- plasma density $n \sim 10^{18}$ $1/cm^3$;
- plasma lifetime $\tau \sim 1$ μs;
- energy expenditures for reaction ignition $E_o \sim 500$ MJ.

The peculiarity of this approach is that it can be realized with the help of the existing pulsed power technologies [1,2]. This can be achieved by means of the unique Pulsed Power sources – the explosive magnetic generators (EMGs), which provide power and energy levels that can't be achieved by any other methods at present. The EMG working principle, proposed in Russia in 1952 by A.D.Sakharov, consists in conversation of the high explosives (HE) energy into electromagnetic energy. The EMG with a stored energy up to 500MJ (due to use HE) has the dimensions people got used to (~2-3m), while the stationary sources of pulsed power, considerable with EMGs in energy but not in power, occupy the buildings of several hectares areas. The EMG developed in VNIIEF are at present the most

---

- MAGO -an abbriviation from Russian MAGnitnoe Obzhatie.

MTF -an abbriviation from English Magnetized Target Fusion
powerful laboratory sources of energy in the world. In case of MAGO/MTF the thermonuclear reaction ignition has two stages:
1) heated magnetized plasma formation;
2) adiabatic compression of the obtained plasma and the achievement of thermonuclear reaction burning conditions.

The formation of plasma with definite temperature and lifetime is carried out by means of plasma acceleration up to ultrahigh velocities in the MGD Laval nozzle under the influence of quick-increasing magnetic field pressure and by means of the further plasma thermalisation . Some results of the MHD-nozzle device calculations are presented in Fig.1, in which one can see the character of plasma motion and the dynamics of its heating.

MAGO CHAMBER OPERATION

density
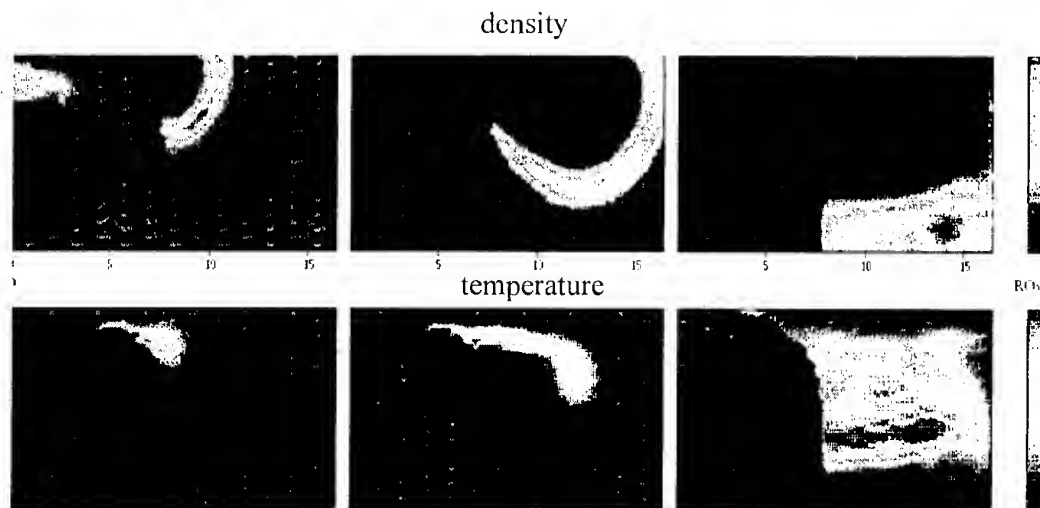
temperature

Fig.1

Plasma heating is of volumetric character and the maximum temperatures reach the values of several kiloelectronvolts. This has also been confirmed in the experiments [3,4]: the yield of DT neutrons exceeds $5*10^{13}$ neutrons per pulse and the plasma image, obtained by means of neutron pinhole camera (Fig.2), testifies to the volumetric character of neutrons radiation.

Neutron image   X-ray image
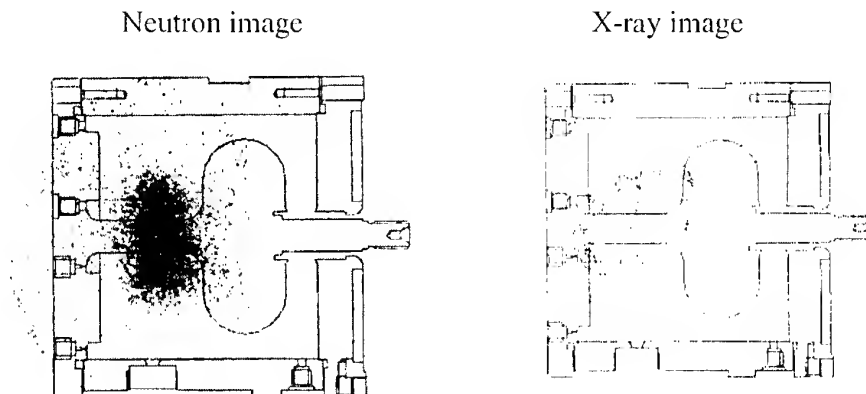
Fig. 2

However, the same calculations show that only a small portion of plasma (< 5% of a mass) is heated up to high temperatures and the lifetime of such a hot plasma is 1-1,5 μs. These data haue also been confirmed by the experiment. The main plasma mass has a temperature of 0,2-0,5 keV and a long lifetime. Such a temperature level of the main mass of magnetized plasma let us hope to get the thermonuclear reaction iguition at a relatively low degree of this plasma compression. The study of such a «warm» plasma have been carried out by the x-ray Si-diodes and pinhole cameras. Plasma temperatures of 0,15-0,35 keV have been registered in the experiments and this level of temperatures can be kept for more thah μs. When the radius of the MHD-nozzle chamber is ~5 cm (the majority of the experiments have been performed with the chambers of this caliber), for additional plasma compression the velocity of the compressing liner should be ~ 10 km/s. This can be achieved taking into account modern level of the quipment, what has already been experimentally shown [5].

Thus, at present the MHD-nozzle device is a leading candidate for a thermonuclear target in the MAGO/MTF (compression of magnetized heated plasma) approach to CTF (controlled thermonuclear fusion).

Reference

1. I. Lindemuth, V. Chernyshev, A. Demin et al, «MAGO/MTF: controlled termonuclear fusion with existing pulsed power systems???» Proc. 11th IEEE Int. Pulsed Power Conf., Baltimore, MD, USA, 1997.
2. I. Lindemuth, V. Chernyshev, A. Demin et al. Target plasma formation for magnetic compression/ magnetized target fusion (MAGO/MTF) Phys.Rrev.Lett.V75,No.10,p.1953,1995.
3. V. Chernyshev, V. Korchagin, V. Mokhov et al. Investigation of a possibility to form thermonuclear megnetized plasma in a magnetic compression system MAGO. Zababakhin' Scientific Readings, Kushtym, Russia, 1992.
4. I.Morozov, V.Korchagin, A.Demin et al. Study of plasma in MAGO chamber by own neutron radiation. Proc.11th Conf.High Power Particle Beams, Prague, 1996.
5. V. Chernyshev, I. Lindemuth, V.Mokhov et al. HEL-I: a DEMG based demonstration of solid liner implosions at 100 MA. Proc. 11th Int. Pulsed Power Conf. Baltimore, USA, 1997.

DISK EXPLOSIVE MAGNETIC GENERATOR WITH LOW RISETIME IN THE LOAD

V.A.Demidov, A.N.Demin, S.A.Kazakov, Yu.V.Vlasov, V.A.Yanenko

VNIIEF, Sarov, 607190, Russia

At present the multi-element disk explosive magnetic generators (EMG) are the most powerful sources of electromagnetic energy. They allow to obtain currents of hundreds megaamperes and current of hundreds megajoules at the times of dozens microseconds. They find application when performing pioneer experiments in the field of high energy densities, in the field of controlled thermonuclear fusion researches; they can also be used for radiation generation, etc. [1,2].

Nowadays, the use of the disk EMGs for the acceleration of the solid-state liners is one of the most promising applications [3]. But in this case the EMG current flows through the liner load during the whole time of the device work, i.e. 20-50 μs. This can lead to a liner deformation in the initial stage of EMG work, when the currents are not so high and the deformations may serve as the initial perturbations for a development of instabilities in the process of liner acceleration under the high currents.

Disk EMG with a diameter of 400 mm and with an explosive opening switch built-in to the EMG transmission line has been proposed and successfully tested in VNIIEF. This EMG is capable of providing currents of 50-100 MA with the risetime of ~5 μs instead of usual 20-50 μs; it is also capable of releasing the energy of dozens megajoules in the load, i.e. at approximately the same level as in the usual disk EMGs. It can be achieved because the additional compression of the disk generator volume and the effective cumulation of energy continue after the opening switch has actuated and the EMG has been connected to the load, and because the inductance of the opening switch is small.

The obtained value of the opening switch inductance turned out to be small because the initiation of the HE charge of the switch, used for destruction of the current-carrying foil, is carried out by the way of the disk EMG main charges detonation transmission (Fig.1) without the usage of any special initiation systems (unlike the usual way to do that).

Besides, it is possible to change the current risetime from 3 μs to 10 μs by changing the distance between some elements of the disk generator; and this may be helpful in some cases.

The serviceability of the disk EMG with the opening switch built-in to the transmission line has been successfully tested in the experiment. Two-element disk EMG was used in this experiment. Copper foil with a thickness of 0.2 mm and a layer of plastic explosives with a thickness of 3 mm have been used in the opening switch. The disk EMG was initially powered by a helical preamplifier, which provided the current of 3.8 MA for initial powering. Current of the disk EMG, to the moment the fast opening switch started working, was 21 MA; the maximum current derivative by that moment reached the value of 4.9 TA/s; current increase characteristic time was 6.7 μs.

The disk EMG current derivative, obtained in the experiment, is presented in Fig.2.

The current pulse presented in Fig.3 has been formed in the load at the actuation of the explosive opening switch. The same Fig.3 shows dependence of the current derivative in the load on time.
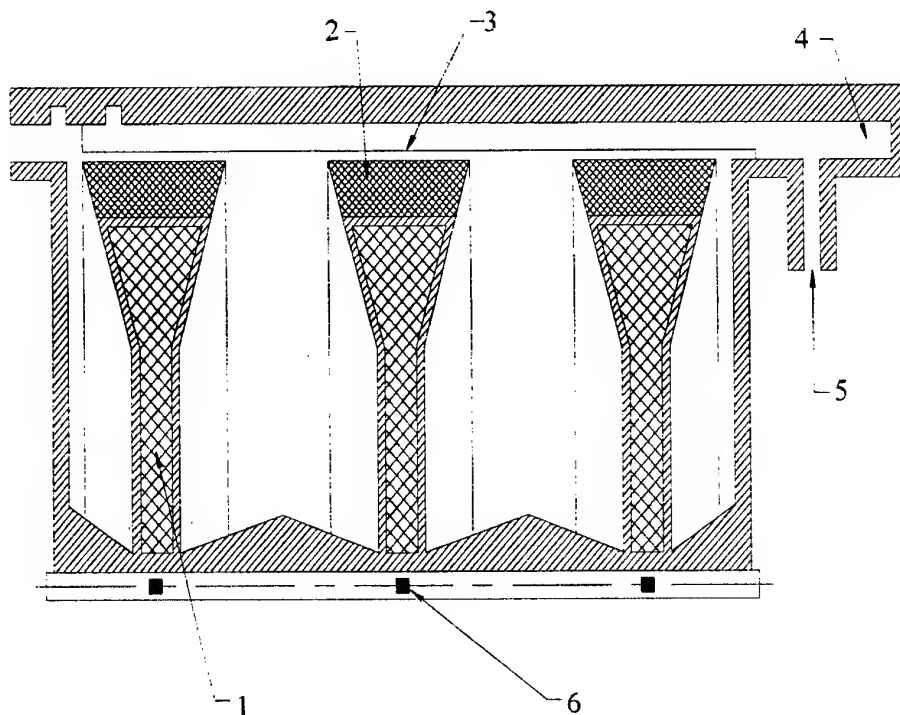
Fig.1. Disk EMG sketch.
1 - HE charge of the disk EMG, 2 - HE charge of the opening switch,
3 - foil of the opening switch, 4 - the load, 5 - the load switch, 6 - the detonator

The total duration of the load current pulse leading edge is 5 μs. The current reaches the maximum in two stage: at first, due to a throw-over of a magnetic flux from a ruptured contour, the current increases quickly (in ~1 μs) up to ~ 20 MA; further on it increases slowly up to ~ 50 MA due to a magnetic flux additional compression within the disk EMG volume. The characteristic time of the pulse's "fast" part growth is 0.55 μs. Energy of 2 MJ was obtained in the load with the inductance of 1.6 nH.
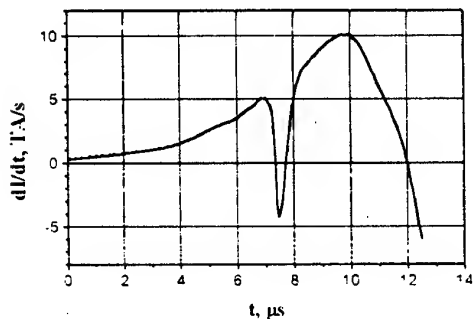
Fig. 2. Disk EMG current derivative
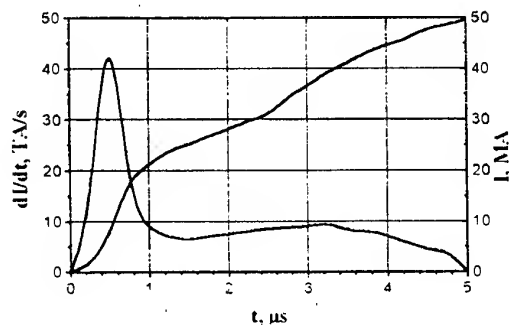
Fig.3. Current derivative and current in the load

A small value of the characteristic time of the pulse "fast" part current increases testify to a possibility to apply the above-described source of energy not only for liner acceleration, but for some other purposes as well. It is quite possible that for the majority of applications the energy level obtained in the experiment will be insufficient. But it can be increased up to the required values by increasing the number of generator disk elements. And owing to the increase of the ruptured conductor length, and consequently of the opening switch resistance, it is possible to connect up the loads with bigger inductance. Thus, if we increase the load inductance up to 10 nH, the number of disk elements in the generator up to 12 (under the same conditions of its initial powering), the load current pulse will be same as that obtained in the experiment.

REFERENCES

1. The questions of modern experimental and theoretical physics // Edited by A.P. Aleksandrov. L.: Nauka. 1984.
2. High density energy accumulation and commutation. // Edited by U. Bostik. Moscow.: Mir. 1979.
3. V. Chernyshev, I. Lindemuth, V. Mokhov et al. HEL-1: a DEMG based demonstration of solid liner implosions at 100 MA. Proc. 11th Int. Pulsed Power Conf. Baltimore, USA. 1997.

MICROSECOND PLASMA OPENING SWITCH AS A BREMSSTRAHLUNG GENERATOR

N. U. Barinov, G. I. Dolgachev, D.D. Maslennikov, M. S. Nitishinsky,
A. G. Ushakov, L. P. Zakatov,

*Applied Physics Dept., Russian Research Center Kurchatov Institute,
Moscow, 123182, Russia,*

Abstract

Experiments on efficiency increase of X-ray sterilizer RS-20 are reported. Increase in x-ray output for a given wall plug power may be obtained due to growth of both electron energy and electron diode current. In first experiment to increase electron beam energy (up to 3 MeV) a coaxial POS in applied external magnetic field was utilized. An electron diode with anode-converter was parallel to POS. 25% of total current was transmitted to the diode. A dose per pulse was 0.024 Gy at 1 m from the converter. The second experiment used POS with planar anode in open circuit regime so the anode was utilized for electron beam conversion into Bremsstrahlung. Electron beam energy was 1.7-2.0 MeV all 100% of generator current reached the POS anode-converter with the dose 0.022 Gy. An inverted pinch scheme of POS was proposed to combine advantages of those above in one unit: external magnetic field for obtaining high voltages and 100% of generator current utilization.

RS-20 SET-UP

X-ray sterilizer RS-20 was built in 1991 [1] with the parameters as follows: 0.8 MV - Marx working voltage, 0.6 μs - current quarter-period, 10 Ohm - wave resistance of the main circuit, and 1-2 p.p.s. repetition rate. The machine usually workes at positive polarity of the central electrode that makes maximum electric strength of the insulator.

The machine was used for sterilization experiments and , as well, for repetitive POS scheme testing and elements life-time increase. Different versions of repetitive plasma injectors have been designed with a life-time of 1-10 million shots together with x-ray radiator working at 10 million shots as well - both at power load 50-70 W/cm² [1-2]. Depending specific POS design, the voltage obtained lays between 1.5 to 3 MV and is limited with electron leakage in power supply circuits. Having that voltage x-ray irradiation is directed mainly along the direction of initial electron beam propagation. The use of coaxial POS design results in necessity to make a diode with planar anode-converter - to extract maximum irradiation to the sample. POS performance could be characterized by a voltage multiplication coefficient: ratio of POS/Marx voltages $k=U_{POS}/U_0$ and η - wall plug to e-beam efficiency. Two schemes may be outlined: POS in external magnetic field allowing maximum voltage [2] and POS with planar anode which allows to combine anode and converter in one unit and to avoid parallel diode circuit. In that case all generator current is utilized for Bremsstrahlung generation.

POS IN EXTERNAL APPLIED MAGNETIC FIELD

Under relatively low currents and, correspondingly, magnetic fields, additional measures should be used to provide a magnetic insulation of POS. [2]. The most simple one is a use of applied external magnetic field [3]. POS (Fig. 1-a) contains coaxial cathode with a water cooled solenoid providing 5-10 kGs at the center of the coil and graphite radiation-cooled anode. Cathode-anode gap is 3 cm. POS geometry was chosen so, that magnetic field lines, coming from anode, do not cross the cathode (vacuum chamber) in order to prevent electron explosive emission. To protect plasma guns dielectric surface, a capillary type guns were used - with a thin hole in the graphite disk placed outside the dielectric surface. Diode having anode-converter was switched parallel to POS. Maximum voltage was obtained without the load. The current in the POS (I_{POS}) is switched faster, than that in the circuit (I_G) (Fig. 1-b). The difference between them is determined by electron leakage (to 15 kA) and limits the voltage at 3 MV. In x-ray generation mode the diode takes ~20 kA resulting in some voltage drop. Maximum voltage multiplication $k=3.3$, and $\eta=20\%$. The absorbed dose in water 1 m distance from the anode is 2.4 rad/pulse.
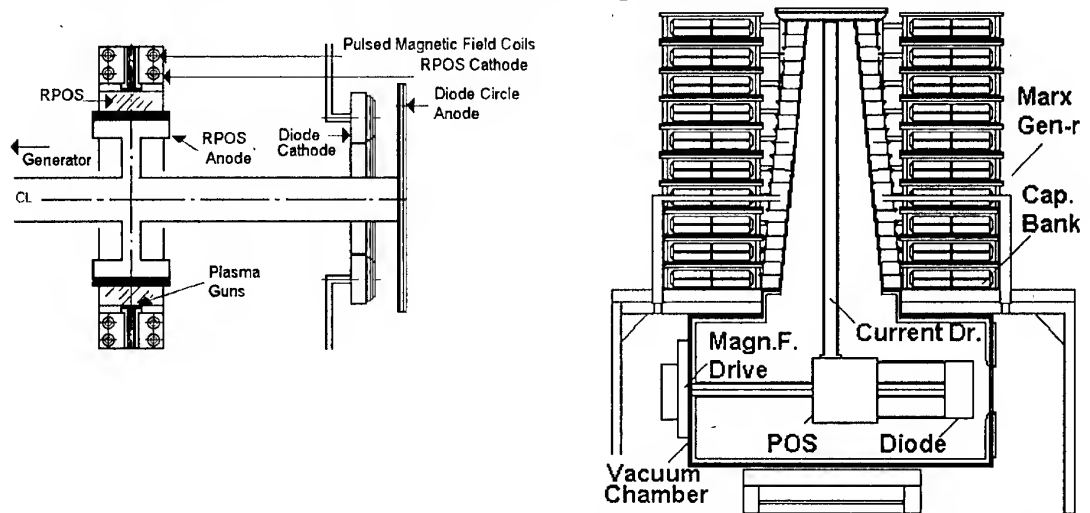
Fig.1-a. POS in external applied magnetic filed. RS-20 generator view (right).
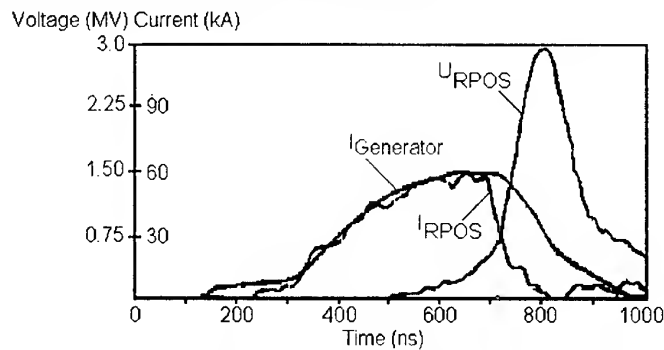
Fig.1-b. Typical waveforms of electrical signals in a short circuit regime.

PLANE POS

Plane POS allows to use all electron current of the generator to generate x-rays. The scheme, aswell, becomes lesser complicated and easy to operate. Despite sufficiently low POS voltage ~1.7-2.4 MV (Fig. 2), a dose 1 m from anode is almost the same as that in the previous case (2.2 rad/pulse at 1 m dist. from the cathode). ($k=2$, $\eta=\sim70\%$). But the planar anode allows to compensate the voltage loss due to current increase and to obtain same dose as POS in applied external magnetic filed does.
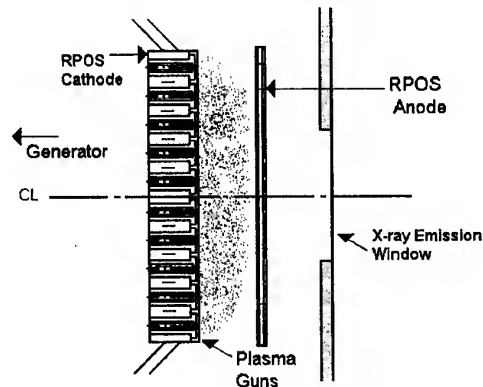
Fig. 2-a. POS with planar anode.
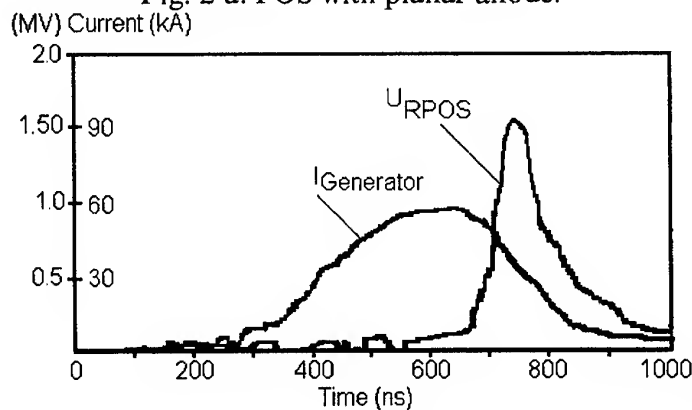
Fig. 2-b. Typical waveforms of main signals for the POS system with planar anode.

INVERTED PINCH POS CONFIGURATION

To improve the efficiency of x-ray output a POS with a disk anode-converter and external applied radial magnetic field is proposed [4] (Fig. 3). This system may allow to obtain high voltage using magnetic insulation and increase the current on the x-ray converter. This scheme is planned to be used at RS-200 [5] with the parameters being proposed: 5 MeV, 100 kA, 200 kW - in electron beam with $k=2.5$ and $\eta=\sim70\%$.
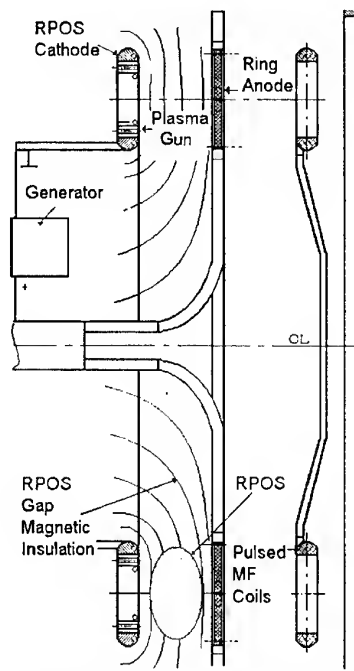
Fig. 3. A scheme of POS with radial magnetic field and disk x-ray converting anode.

CONCLUSION

Thus, POS efficiency in electron beam, in case when POS anode is used for e-beam/x-ray production, may be increased up to 70%. This corresponds to the expected efficiency of the most electron accelerator concepts recently developed (if one compares their efficiency in e-beam). Additional magnetic insulation for repetitive POS systems may sufficiently increase POS voltage and be effective enough: magnetic field system takes 5-10% of power consumption and increases POS voltage 50% as high in MV range. A new inverted pinch POS geometry which utilizes both approaches was proposed for 5-6 MV production in 200 kW generator concept.

REFERENCES

[1]. V.M.Babykin, R.V.Chikin, G.I.Dolgachev et. al.: Proc. of the 9th International Conference on High-Power Particle Beams, Washington DC, 1992, v.1, p.517.

[2]. N.U.Barinov, G.S.Belenki, G.I.Dolgachev, et al.: "Plasma-Opening-Switch-Based Repetitive Generator" // IEEE Trans. on Plasma Science, 1995, v. 23, N.6, p. 945.

[3]. G.I.Dolgachev, L.P.Zakatov, V.A.Skoriupin, Sov. Journ. Plasma Phys. "Fizika plasmy", vol. 13, pp. 760-763, 1987.

[4]. G.I.Dolgachev M.S. Nitishinsky Pat. of the Russian Federation #96119429 27.09.1996.

[5]. Dolgachev G. I., Zakatov L.P., Ushakov A.G. 11th IEEE International Pulsed Power Conference June 29- July 2, 1997, Proceedings, P2-65, v.2, pp. /In the Book of Abst.p.355

Ion Beam Measurements in a Small Plasma Focus Operating in Hydrogen/Gas Mixtures

P. Silva, M. Favre, P. Choi*, C. Dumitrescu-Zoita*, H. Chuaqui, and E. Wyndham

Facultad de Física, Pontificia Universidad Católica de Chile
Casilla 306, Santiago 22, Chile
*LPMI, Ecole Polytechnique, Palaiseau 91128, France

INTRODUCTION

Dense transient plasmas of high energy density, can be easily produced in a Plasma Focus device, on a cost effective basis. High energy ion beam emission is one, among several others, of the very interesting transient plasma phenomena observed in plasma focus discharges[1]. Although some of the properties of these ion beams have been investigated in the past, the physical mechanisms involved in their generation are still not clear, and further investigations are required on order to establish the exact correlations of the ion beam emission with other plasma focus phenomena[2]. We present a preliminary series of measurements on ion beams in a plasma focus operating with Hydrogen/Gas mixtures, using an XRD probe array, which allows the characteristic ion energy to be determined from the time of flight across the probe array, and the time of the ion beam emission to be correlated with plasma emission events associated with the soft X-ray pulses detected by the probes.

EXPERIMENTAL APPARATUS

The experiments have been performed in a small 3.8 kJ Plasma Focus, PFP-I, operating up to 30 kV, 140 kA peak current. The discharge is formed between a hollowed anode, 1.2 cm radius and 14 cm length, and six cathode rods, symmetrically arranged in a 3.2 cm radius circle. The general diagnostics includes voltage and current measurements, multi pinhole and slit-wire X-ray photography, filtered PIN diode array, and beam target electron beam detector. Further details on the device and the associated X-ray diagnostics have been published else where[3]. A novel hybrid XRD-Faraday cup detector array is used to measure the ion beams. The probes are made of standard 50 Ω solid coaxial cable, in which a portion of the central conductor is arranged as a 1 cm diameter circle, perpendicular to the plasma focus axis. The central conductor is negatively polarized at 120 V. In this way, the probes behave as XRD detectors, given a positive polarity
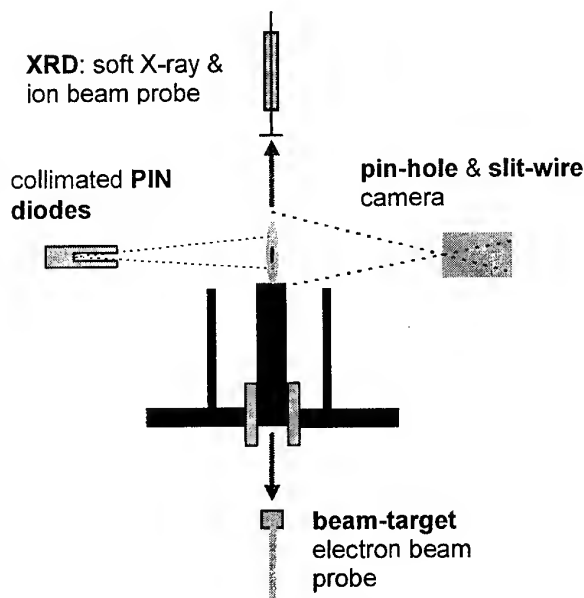
Figure 1: schematics of plasma focus device and associated diagnostics

signal under pulsed XUV illumination, and as a 50 Ω Faraday cup, giving also a positive polarity signal when reached by a pulsed ion beam. This arrangements allows the ion beams to be accurately timed with respect to the pinch phase of the focus discharge. Information on the ion energy distribution is obtained from time of flight measurements. Two XRD probes separated axially by 10 cm and coaxial with the focus gun are used in this investigation, with the lower one located at 21 cm from the anode rim. The electron beam probe consists of a 40 μm Copper target with a block of NE102 scintillator located behind the target. A 17 μm Aluminium filter is located between the target and the scintillator, to reduce signal due to target fluorescence. Light from the scintillator is fed into a fast 2.5 ns rise time photomultiplier. The simultaneous recording of ion and electron beams, together with the X-ray emission, provides a comprehensive set of single shot data which is used to correlate the ion emission with other plasma phenomena. A schematic of the different diagnostics as relative to the position of the plasma focus gun is shown in figure 1. The experiments have been performed in Hydrogen/gas mixtures, including Argon, Neon and Nitrogen as the additional gas, at different mixing ratios. For each mixture, the pressures is adjusted to keep a constant mass load, such as to achieve radial collapse at around peak current.

EXPERIMENTAL RESULTS

Figure 2 shows a slit-wire image corresponding to a shot with 100%, at 1.3 Torr pressure. A 100 μm width slit, filtered with 12 μm Beryllium was used to produce the image. A one dimensional image of a single hot-spot can be observed in the upper part of the image. Emission from the anode is seen in the lower part. Six different wires, 250 μm Silver, 160 μm Tin-Copper alloy, 80 μm Tungsten, 50 μm Tin-Copper alloy, 25 μm Tungsten, and 100 μm Copper were used and there shadows across the hot-spot image are identified by the arrows from right to left respectively. The Figure 3 shows the associated electric signals, around focus time, for the same shot than in Fig. 2. Voltage, electron beam, and side-on PIN diode, with 15 μm aluminium filtering, are shown in the upper graph. The signals from the axial XRD probes are shown in the lower graph. Two strong voltage spikes are observed, with associated electron beam pulses. The first electron beam pulse coincides with a simultaneous excursion in the XRD probes and PIN diode. These signals can be associated with beam target emission by electron beam collision with the anode electrode. Characteristic peaks in the XRD probes signals which do not coincide in time can be attributed to ion beam impact. This is the situation for peaks labeled "1" and "2" in both signals. If each pair is attributed to a single ion beam, the characteristic energy for the beams can be inferred from the time of flight between probes. In this case, the characteristic energies are found to be 30 and 19 keV for peaks labeled "1"
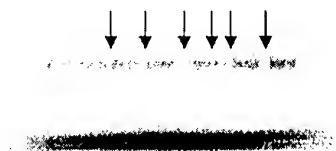
Figure 2: slit-wire image of a single hot-spot in pure hydrogen

time (100 ns/div)
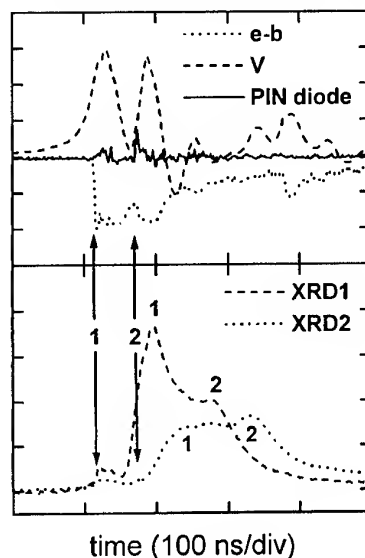
Figure 3: characteristic signals associated with slit-wire image shown in Fig. 2

and "2" respectively. If the ion beams are emitted from a region next to the anode edge, the time of the emission can be associated with the onset of the electron beams, as indicated by the arrows superimposed in the XRD traces. The onset of the second beam event coincides also with a soft X ray pulse detected by the PIN diode. The hot spot seen in Fig. 1 is probably associated with the emission of the soft X-ray pulse. A characteristic hot-spot size of 300 μm is inferred from the shade of the wires.

A similar behavior in terms of time correlations of the ion beam emission with electron beams and soft X-ray pulses is observed when the plasma focus is operated with a hydrogen/gas mixture. Figures 4 and 5 show slit-wire and associated signals corresponding to a shot with 30% neon, at 0.35 Torr pressure. The same wire array than in Fig. 2 has been used in this case. The pinch structure is found to be much more complex than in the pure hydrogen. A plasma column with embedded elongated hot-spots is observed. Hot-spot structures are observed next to and 8 mm above the anode. Characteristic diameter of the hot-spots inferred from the wire shadow is around 300 μm. A first radiation pulse coincident with the onset of an electron beam is also observed in this case. An ion beam can be associated with the time delayed pulses observed at later time in the XRD probes. If the ion species are assumed to be hydrogen a characteristic energy of 30 keV is obtained from the time of flight measurement. A neon ion beam is unlikely, as the energy required for the measured time of flight is of the order of 600 keV. If the emission time for the ion beam is traced back, it is again found to correlate with the onset of the initial electron beam. A ~10 ns soft X-ray radiation pulse is emitted in association with onset of a second electron beam. As the PIN diode is collimated to exclude direct anode emission, this radiation pulse can be attributed to plasma emission from the hot-spots. A possible ion beam associated with the second electron beam pulse can not be discriminated from the long decay tail of the first beam.

Figure 4: slit-wire image of a single hot-spot with 30% Neon

time (100 ns/div)
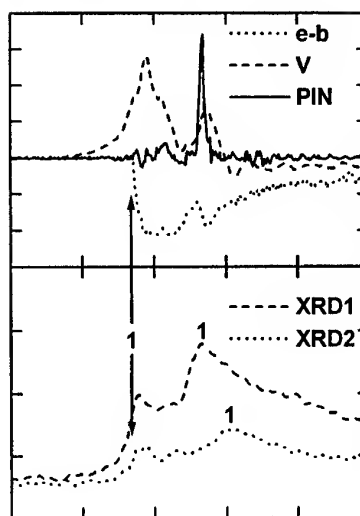
Figure 5: characteristic signals associated with slit-wire image shown in Fig. 4

This is also the case for the detection of Neon ion beams of the same characteristic energy.

Similar results are observed over the range of conditions investigated, including Argon, Neon and Nitrogen as the additional gas. The observations are consistent with the emission of Hydrogen ion beams of characteristic energy in the 10's of keV always associated with the onset of electron beams. In general, if a second hydrogen ion beam is observed, this tends to be of lower characteristic energy and is produced immediately after the emission of a short soft X-ray pulse, which is probably associated with hot-spot formed in the plasma column.

DISCUSSION

Most of the measurements of the ion spectra in Plasma Focus discharges rely on Thomson analyzers, which due to geometrical constraints and lateral spreading of the ion beams, have a characteristic energy threshold at around 100 keV in most of the reported

observations. As an example, magnetic spectrometer and time of flight measurements of fast deuterons produced in a small 1 kJ Plasma Focus indicate that the energy spectrum above 70 keV extends up to more than 400 keV[4]. If the exponential low obtained in ion spectra measurements[5] is extrapolated to lower energies, it can be inferred that in small Plasma Focus devices a significant fraction of the ions has a characteristic energy in the 10's of keV range, as it has been measured in our experiments. The data presented here can be further analyzed. From the time interval between the onset of the ion beam induced signals in the ion beam probes shown in Fig. 1, a high energy threshold of ~80 keV can be estimated for pure Hydrogen operation. These measurements do not contradict previous observations, due to the fact that our preliminary analysis does not take into account radial scattering of the beams and higher energy ions of lower characteristic flow can not be discriminated at present from the available data.

Our data provides good enough characterization of the beam energy to time correlate with the emission of electron beams and soft X-ray pulses. At least two ion beams pulses can be identified in most of the cases investigated. The first one is associated with the radial collapse of the current sheath and coincides with the emission of a high energy electron beam. At this time no significant soft X-ray emission from the compressed plasma is observed. The second pulse coincides with the emission of a second electron beam. At this time a soft X-ray emitting plasma column with embedded hot-spots of characteristic temperature ~400 eV[3] has been formed and a ~10 ns FWHM radiation pulse is emitted, as it is seen in Figs. 3 and 5. The emission of the soft X-ray pulse marks the onset of the charged particle beam emission. This time correlation of events appears to support hot-spot formation models based in the post evolution of $m = 0$ instabilities, in which radiation cooling and magnetic compression accounts for the local increase in plasma density, and fast local inductance increase across the instability neck provides the acceleration mechanism[6].

COLCLUSIONS

Preliminary observations on the time correlation between the emission of ion beams and other dense transient plasma phenomena have been performed in a small plasma focus operating with Hydrogen/Gas mixtures. Further experiments are been conducted in order to include time and spaced resolved measurements of the soft X-ray emission, which combined with an improved analysis of the ion beam measurements will provide a suitable data set to assess the validity of theoretical models of high energy plasma phenomena in Plasma Focus.

REFERENCES
[1] N.V. Filipov and T.I. Filipova, *Sov. JEPT Lett.* **29**, 689 (1979)
[2] M. Zadowski et al., *Phys. Lett.* **83A**, 435 (1981)
[3] M. Favre et al., *IEEE Trans. Plasma Sci.*, in press (1998)
[4] H. Kropholz and L. Michel, *Appl. Phys.* **13**, 29 (1977)
[5] H. Kelly, A. Lepone, and A. Márquez, *IEEE Trans. Plasma Sci.* **25**, 455 (1997)
[6] K.N. Koshelev et al, *J. Phys. D: Appl. Phys.* **21**, 1827 (1988).

PECULIARITIES OF WIRE RESISTANCE BEHAVIOR
ON INITIAL STAGE OF EXPLOSION.

A.V.Branitskii, E.V.Grabovskii, I.N.Frolov, G.M.Oleinik, A.A.Samokhin,
P.V.Sasorov*, V.P.Smirnov, G.S.Volkov, M.V.Zurin,
R.B.Spielman**

*Troitsk Institute for Innovation and Thermonuclear Investigation,
Troitsk, Moscow reg. Russia*
* - Institute for Theoretical and Experimental Physics, Moscow, Russia
** - Sandia National Laboratories, USA

During last time the large achievements in soft X-ray production were obtained by Sandia with multywire array implosion. The efficiency of the generator energy conversion to radiation strongly depends upon the quality of plasma shell. Thus the investigation of initial stage of wire explosion and the way of plasma shell creation are very important. To study the different process of plasma creation at initial stage of wire explosion the precision voltage on wire array axis and current measurements have been carried out.

THE ARRANGEMENT OF THE EXPERIMENT.

The experiments were done for different wire arrays from 8 up to 16 wires for W and Mo. Wire array diameter varied from 8 mm up to 20 mm, wire diameter: $4\mu m$, $6\mu m$, $10\mu m$, $20\mu m$ and $30\mu m$; the anode-cathode gap of 1cm.

To provide a good contact of wires with the electrodes and a homogeneous current distribution through wires the special design of electrical feeders has been used (see fig.1).
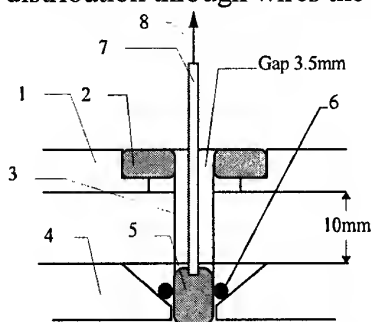
Fig.1. The layout of 8 - mm diameter wire array and voltage probe connection. 1-anode electrode of Angara-5-1 output, 2- anode electrode of array, 3- the wires, 4-cathode electrode of Angara-5-1 output, 5- cathode electrode of array, 6- metal balls for uniform electric contact, 7 - metal cylinder for connection of the voltage probe with the cathode, 8 - to voltage probe.

Single Angara-5-1 module was used in this experiment. The microsecond prepulse suppression was done by the using of prepulse switch. This switch provides the voltage level on wires during prepulse smaller then 10V. The heating of $4\mu m$ W wire during prepulse was less then 10°C.

The voltage on wire array axis was measured by the voltage probe (see fig.1). Temporal resolution of voltage probe is about 3 ns. Current through the wire array was recorded by means of coaxial resistive shunt probe with time resolution of 5 ns inserted in cathode electrode.

EXPERIMENTAL RESULTS. WIRE ARRAY RESISTANCE EVALUATION.

The values of voltage amplitude for different arrays were about 5-15kV with pulse duration of 10ns. Both the voltage amplitudes and voltage profile widths were significantly smaller than those in the case of the array absence. Small voltage can mean small wire resistance value. The voltage and current measurements allow to evaluate both the wire resistance and the wire temperature.

There are two different ways to get the wire resistance value:

1) by application of measured voltage U(t) and current J(t) profiles - as ratio U(t)/J(t);

2) by only U(t) profile - taking into account the wire heating and dependence of resistance on temperature.

Both ways of resistance evaluations were performed.

The difference between the voltage on array axis and the voltage on the wire surface is equal to d(L*J)/dt. This term was taken into account, but the input of such term is relatively small.

The results of mentioned above evaluation are presented on fig.2 for typical shot with tungsten wire array.

At the top part of fig.2 the voltage U(t) on the axis and the current J(t) per one wire measured by shunt at initial stage of the discharge are presented.
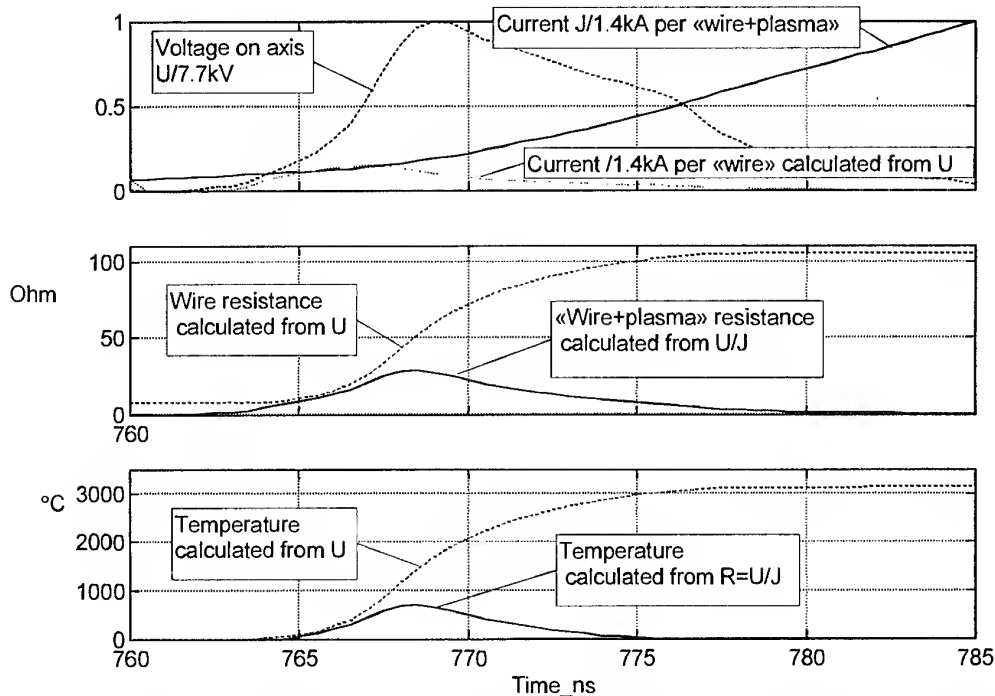
Fig.2. The typical voltage and current profiles and results of resistance and temperature evaluations. The wire array composed of 8 W- wires. Wire array diameter - 8 mm, wire diameter - 10μm.

In the middle part of fig.2 the temporal dependencies of wire resistance evaluated are presented. The lower curve is the resistance value calculated from the voltage/current ratio. The upper curve is the resistance value calculated from voltage taking into account the wire heating with dependence of resistance on temperature. Using the latter curve and voltage

measured it is possible to calculate the current in the wire. The result of such calculation is shown on the top part of fig.2.

At the bottom of fig.2 the calculated temporal dependencies of wire temperature are presented. Both these curves correspond to two calculated resistance dependencies presented in the middle part of fig.2. The lower curve is the temperature profile calculated on the base of voltage and current temporal profiles. The upper curve is the temperature profile calculated on the base of single voltage signal.

For the time moment t > 768 ns both the resistance calculated from U/J and the temperature calculated from U/J are decreased. The diminishing of the wire resistance for the time moment t > 768 ns is not possible for metal wire. Thus, it can be assumed that the wire resistance diminishing after the time moment t = 768 ns is due to the plasma on wire surface production under action of current pulse.

The existence of the plasma on the wire surface drastically reduces the resistance of the "wire + plasma" composition. The amplitudes of two currents presented on the top part of fig.2 are equal to each other for time moments which are preceded the 768-th ns. Measured «wire+plasma» current increases after 768-th ns but the calculated current on metal wire (lower curve on the fig.2 upper part) decreases. The wire temperature calculated from wire resistance at this moment is less than 2000°C.

At this moment for different shots and for W and Mo maximum current density in wire reached 3-6 A/μm^2 and maximum wire temperature was less than 2500°C - less than melting one for both used materials. The energy deposition transferred in wire by Ohms heating to this moment is not sufficient for complete melting of wire substance. The plasma production on wire surface takes place before melting of tungsten or molybdenum.

SIMULATION OF WIRE RESISTANCE BEHAVIOR.

For better understanding of results of the experiments we performed some simulations of tungsten wire electric explosion. Equation of state in wide range of density and temperature takes into account phase transition from metal to gas (and then plasma).

We compared simulations of naked tungsten wire explosion with explosion of tungsten wire dressed with thin envelope formed by light substance (that is impurity) covering of tungsten wire surface before current pulse. We simulate the wire dynamics under the action of given electric current with amplitude of 5kA/wire and the duration from the beginning to maximum -70ns, tungsten wire diameter of 6μm.

Fig.3 shows electric field at the wire axis and electric current for naked wire. Electric field achieves about 120 kV/cm that is much higher than measured voltage on the array.

We conclude that the wire doesn't explode as naked one. The most probable reason of strong decreasing of the voltage amplitude and of the delivered energy, is that the wire is covered before the current pulse with very thin impurity layer. It is evaporated in course of discharge quite before the moment of tungsten evaporation. A few of preliminary shootings shown that evaporation of impurities at about 200-300°C is quite enough for explanation of experimental data. To demonstrate this we stop the simulation of naked wire at t=6.75ns and then the simulation was continued with introducing a thin layer of carbon gas with thickness of 0.3 μm (1.8$\times$10^{-10} g/cm.). It corresponds to a few atomic layers of carbon. Fig.4 shows the results of such simulation - the voltage pulse on the wire. Its form and amplitude have much more satisfactory fitting to the experimental results. The temperature of tungsten wire surface

reaches of 0.05 eV at the moment of transition from the first simulation to the second one. The breakdown is possible only with some delay (~2.5 ns) after strong expansion of the carbon layer. After breakdown of the corona the current leaves the wire so its heating is stopped after this moment. The typical temperature of tungsten after the breakdown is of order of 0.23 eV. It corresponds to evaluated temperature of tungsten using measured values of voltage and current. The simulation shows that about 4 mJ/cm of energy is delivered to tungsten wire before the breakdown. After the plasma corona breakdown, the wire heats mainly due to heat flux from the corona to the wire surface.
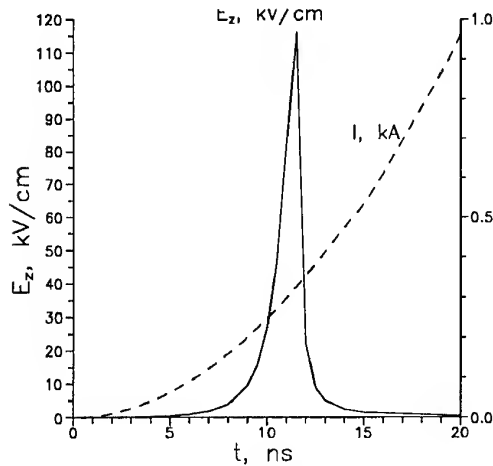
Fig.3. Electric field at the wire axis (solid line) and electric current per one wire (dashed line) versus time for electric explosion of naked wire.
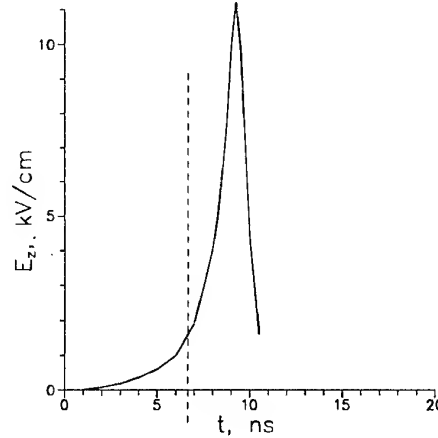
Fig.4. Electric field at the axis versus time for simulation of explosion of "dressed" tungsten wire. The vertical dashed line indicates the moment of evaporation of impurity layer.

Simulations presented can give only the rough estimations of the process of tungsten wire explosion. Nevertheless we may conclude that assumptions of early impurity evaporation and further evaporation of tungsten do not contradict experimental data, at least.

CONCLUSION

Main result obtained for molybdenum and tungsten wires is that the voltage on axis drops during first 10 ns. The voltage value measured on axis at the current beginning is too small for metal wire array resistance increasing upon temperature. The plasma appearance on the wire surface during first 10 ns could explain the measured voltage dropping. Thus, the wire array resistance is resistance of plasma produced on the wire surfaces.

The energy deposition in wire up to moment of plasma production is too small for complete wire substance melting by Ohms heating of metal wires. So, the wire at initial stage of current action can be presented as solid or liquid wire with plasma on the wire surface.

The reason of plasma appearing at wire surface could be a thin layer of light impurities at the wire surface. After voltage applying the wire temperature will increase; the temperature increasing would produce the vaporization of light impurities from the wire surface and the appearance of a gas (and then a plasma corona) near the wire. In the region of nearest vicinity of wires the plasma productive layer is originated due to Joule current heating of plasma corona and thermal flux transfer to wire surface.

ON AZIMUTHAL MAGNETIC FLUX PENETRATION DURING DOUBLE LINER IMPLOSION

A.V.Branitskii, E.V.Grabovskii, I.N.Frolov, A.Yu.Krukovskii*,
G.M.Oleinik, V.P.Smirnov, S.V.Zakharov, M.V.Zurin

*Troitsk Institute for Innovation and Thermonuclear Investigation,
Troitsk, Moscow reg., Russia
* Institute for Mathematical Modeling, Moscow, Russia*

Experiments performed at the beginning of 90-h year on the installation «Angara-5-1» with superfast double liner (the DL) implosion [1,2] demonstrate principle possibility of soft X-ray radiation pulse shortening up to 3-5ns. The DL configuration is a promising way in Z-pinches to diminish Rayleigh-Taylor instability, sharp soft X-ray burst and create the dynamic hohlraum for the ICF. The DL consists of the external and coaxial internal shells. A current through the external shell ionizes it and causes its implosion. The strike of shells produces high power soft X-ray radiation. The following compression brings to a formation of enhanced quality z-pinch and the second peak of soft X-ray radiation is produced (fig.1,2).
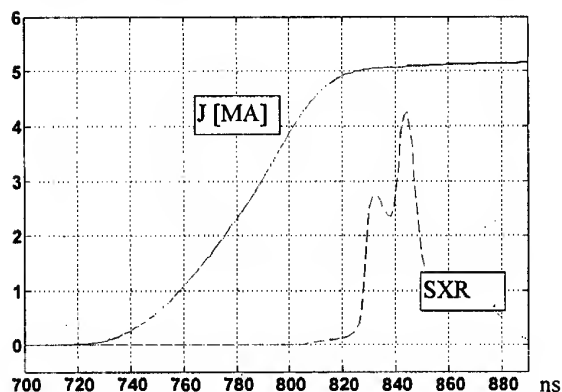
Fig.1. Current (J) and soft X-ray radiation (SXR) in DL experiment on Angara-5-1.

SIN period 10ns
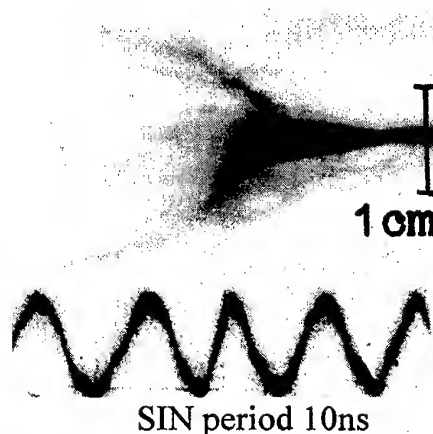
Fig.2. Optical streak picture of DL implosion. Slit perpendicular to DL axis.

According to the DL scheme concept [3] during the strike the external liner herewith plays a role of screen which reduces a radiation flux to outer space. Thus, it is possible to create conditions to irradiate a thermonuclear target placed into the cavity of the internal liner. The compression of a target takes place together with an implosion of the internal liner. Therefore this scheme is named by dynamic hohlraum.

There is an important question about an azimuthal magnetic flux penetration through the external liner during the DL implosion. Anomalous resistance of external liner plasma and MHD instabilities like Rayleigh-Taylor or Hall effect could be reasons of this process. Phenomena of the azimuthal magnetic flux penetration through the low density external liner is considered in [4], formation of the plasma precursor - in [5]. This flux can change the dynamic of the strike. The strike will be more elastic and the radiation power will be reduced.

In this paper investigations of a magnetic flux penetration through the outer shell in experiments on the installation Angara-5-1 are presented.

STATEMENT OF EXPERIMENT

The experiments were conducted on the installation Angara-5-1. The anode-cathode gap was of 1cm. The external liner was produced by hollow xenon jet with high Mach number (~6) and diameter of 32 mm, generated by pulse annular nozzle. The specific mass of the external shell was 200μg/cm. To prevent of a gas accumulation between the cathode and the anode, last was made as a grid (see fig.3).

Fig.3. The scheme of plasma shell implosion to shunt.
1 - cathode, 2 - anode, 3 - outer shell, 4 - anode grid, 5 - shunt, 6 - metal cone for protection from plasma and radiation action on divider, 7,8 - resistances of divider.
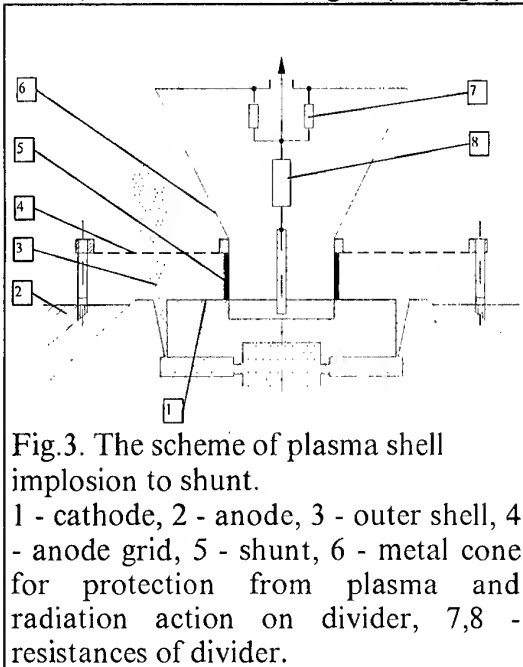
Penetration of magnetic flux should excite the current through the internal liner. In these experiments cylindrical shunt was established on the axis of the charging gap instead of the internal liner to measure this current. The shunt diameter was the same as inner liner one - 4-5mm. A shunt length was of 1cm. This shunt allows to check the penetration of the magnetic flux to the axis as the appearance of the current at the shunt. Shunt time resolution was of 5ns.

Current of some megaamper level will course high voltage appearance on the shunt and shunt heating. To diminish a measured voltage the resistive divider was installed in the vicinity of the shunt. The shunt resistance increasing was take into account for current calculation from shunt signal.

The total load current was measured with the help of eight B-dot probes, located on radius of 55mm on direction of each module. Current was calculated as integral and mean values of 8 signals.

The experiments were made at current level 4-5MA with front rise time about 80ns.

RESULTS OF EXPERIMENT

Check of a technique (without gas). There is a natural question about an accuracy of conducted measurements and a correctness of the shunt heating inclusion. On fig.4 the results of calibration shot for measurements accuracy checking are presented. The relative difference of currents on radius 55mm and through a shunt on radius 16.5 mm (after correction on heating) was not more than 15 % in a maximum of a current. The correction on heating for a current of 3.5MA was a fraction of 40%. From here it follows, that the correction on heating is quit necessary, and the heating inclusion permits to receive reasonably authentic results.

Magnetic flux penetration. Typical signals for large specific mass xenon outer shell implosion on the shunt are presented on the fig.5. It is seen a normal picture of implosion. Soft X-ray and visible radiation arise at strike. Minimum on a total load current derivative corresponds to a moment of strike. After the collision of a external liner with a internal one the current is redistributed and the part of a current of a external liner begins to flow through the shunt. The current in a shunt is away before strike and appears only after strike of the external shell with the shunt - approximately after 5ns from a maximum of soft X-ray radiation. A time of increasing of a current in a shunt is about 10ns.

The current amplitude in the shunt is sufficiently small: from 4.2MA on radius 55mm, through a shunt on radius 2.5mm flows only 0.8MA. The rest of current flows through a plasma around the shunt.

DISCUSSION

Outer shell shadowgraphy and soft X-ray frames show the existence of Rayleigh-Taylor instability with wave length about 3mm up to 30ns before strike. Nevertheless the current through the shunt from the beginning up to the strike is absent with the accuracy of 1% of the main load current amplitude. The current absence through the shunt before strike with the existence of the instability in this time is the evidence that magnetic flux does not penetrate through inner surface of the outer shell. It could mean that instabilities take place mainly on the outer surface of the outer shell and anomalous magnetic flux diffusion through the inner surface of the outer shell is absent.

It should be noted that a replacement of the internal liner by a dense metal shunt changes conditions of experiment. Nevertheless valuations show that a resistance of the shunt and plasma of the internal liner are comparable. An absence of a current on the shunt before strike means as appear the absence of a current through the inner liner before strike.

The current amplitude through the shunt after strike reaches not so large values - 0.3-0.8MA.
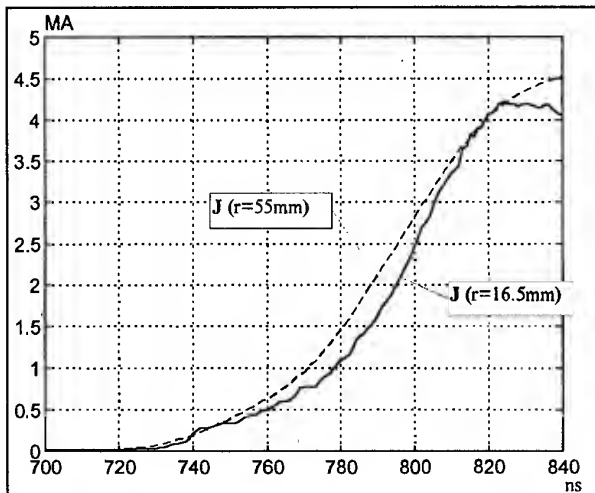
Fig.4. Results on calibration shot (without gas) for measurement accuracy checking.
Currents on radius 55mm and through the shunt on radius 16.5mm (with inclusion of shunt heating).

The increasing of a current growth rate through the shunt in comparison with a current growth rate of a generator in two times was observed. So phenomenologically the external liner can be considered as plasma MHD switch which ensure a current growth rate of $1.2*10^{14}$A/s.

It should be noted that one could explain the results obtained as the absence of magnetic flux penetration through outer shell before the moment of soft X-ray appearance and magnetic flux penetration in the moment of soft X-ray appearance. Anomalous resistance of external liner plasma in this moment could be the reason of both the soft X-ray production and the current switching to central region. This point of view on behavior of low density external liner is described in [4]. However the whole complex of experimental data which were obtained in previous DL investigations is the evidence of normal high density outer shell acceleration up to strike (see fig.1 and 2).

2-D simulations of the Xenon annular gas puff implosion and collision with the tungsten foil cylinder similar to the experimental set up at the Angara-5-1 facility were performed by means of the complete radiative magnetohydrodynamic code ZETA [6] with taking into

account kinetics of ionization, equations of state, radiation transport, spectral characteristics of non-equilibrium plasma, ion acoustic and LHD anomalous resistivity and the Hall effect.
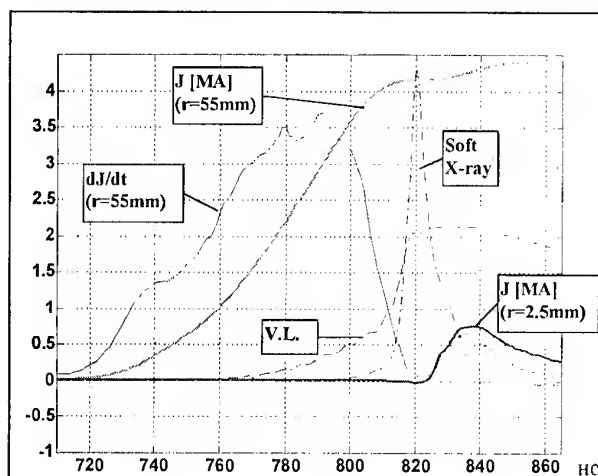
Fig.5. Results of experiment of outer shell implosion on the shunt.
J[MA] - Currents on radius 55mm and on radius 2.5mm (with inclusion of shunt heating).
Soft X-ray- Relative intensity of soft X-ray radiation.
V.L. - Relative intensity of optical radiation.

The plasma implosion is accompanied by development of short and long wave instabilities of different types. The initial gas puff distribution was inhomogenious macroscopically in an axial direction. At the beginning of the current pulse thermal and radiative instabilities produce short (about skin depth) wavelength perturbations. Then MHD Rayleigh-Taylor and non-isothermal (the last one in low density plasma) modes amplify them but mainly on the outer surface of the liner up to the moment of strike with the foil. According to simulations the inner part of outer shell together with a magnetic field front is almost straight. A diffusion of the magnetic field is close to classical, influenses of an anomalous resistivity or the Hall effect are negligible. The current through the foil begins at the moment of strike about 120ns from the voltage pulse start, though an explosion of the foil outer surface begins earlier by radiation and first shock wave outstripping the shell since about 95ns.

CONCLUSIONS

The main result is the absence of a current in the shunt before strike. It is possible to assert that an anomalous resistance of plasma of the external liner is absent up to the strike moment with the internal one. A penetration of a magnetic flux with cross plasma jets or due to sliding of a liner on electrodes is absent too.

The experimental confirmation of the theoretical predictions on the DL scheme is obtained: up to the moment of strike the current does not penetrate into the internal area and flows just through the outer plasma shell.

[1] A.V.Branitsky, V.D.Vikharev, E.V.Grabovsky, et all. Proc of the 8-th Int. Conf.on high-power particle beams (Beams'90). Novosibirsk, 1990, v.1, p.437.
[2] A.V.Branitsky, V.D.Vikharev, S.V.Zakharov et all. Sov. J. of Plasma Physics. v.17, N.5, p.531, 1991.
[3] Zakharov S.V., Smirnov V.P. et all. Collision of Current Driven Cylindrical Liners. Kurchatov Institute of Atomic Energy. Moscow. Preprint 4587/6, 1988.
[4] A.V.Branitsky, S.A.Dan'ko, A.V.Gerusov et all. Plasma Physics Rep. v.22, N4, p. 307, 1996.
[5] I.K.Aivazov, V.D.Vikharev, L.B.Nikandrov et all. Letters in JETPh, 1987, v.45, N.1, p.23.
[6] S.V. Zakharov, A.G. Lisitsyn, A.A. Otochin et all. 4 Int. Conf. On Dense Z-Pinches. Vancouver, Canada.1997, B1p11.

FOAM LINER PREIONISATION BY EXTERNAL CURRENT SHELL ON "PF-1000" AND "ANGARA-5-1"

L.Karpinski, M.Scholtz, W.Stepnewski, (*Institute of Plasma Physics and Laser Microfusion, IPPLM, Warsaw, Hery,23, Poland,.*

A.Szydlowski,(*Soltan Institute for Nuclear Studies,Swerk, n. Warsaw,Poland),*

A.V.Branitski, M.V.Fedulov, I.N.Frolov, E.V.Grabovskii, S.F.Medovschikov, S.L.Nedoseev, G.M.Oleynik, G.V.Rjabtsev, V.P.Smirnov, M.V. Zurin (*Troitsk Institute for Innovation and Fusion Research, TRINITI, 142092, Troitsk, Moscow reg., Russia.).*

ABSTRACT

Results of first experiments on powerful plasma focus PF-1000 (IFPiLM) [1], loaded by low mass foam liners, produced for „Angara" (TRINITI) liner implosion program [2], are presented in this report. An interaction of PF current plasma shell and the liner was the problem of main interest in our joint experiment. The main goal is to elaborate new method of plasma liner production for its compact implosion using multiterawatt pulsed power driver.

INTRODUCTION

As the matter of fact, all multiterawatt drivers for liners and Z-pinch implosion use "cold start" of the process. It means that plasma generation and posterior plasma liner implosion are realized by the same current generator. The initial current through cold liner substance is filamented in high extent due-to ionization instabilities. This current contraction is provided by plasma electric conductivity and effects of magnetic pressure are small initially. But these magnetic forces become significant with the current rise. So, the initial current filament could evolve under effect of two alternative factors: expansion due-to Joule current heating and compression due-to the current magnetic pressure. It is possible to propose that the current rise rate, specific for the powerful drivers , is too high to allow the filaments to expand, to flow together and produce azimuthally homogeneous liner plasma; magnetic field around the separate current filament could confine it. Being responsible for liner azimuthal inhomogeneities, the filaments could enhance axial inhomogeneities of initial liner plasma, which are especially dangerous as R-T and MHD- instabilities basis. Moreover, it is shown in experiments on "Angara-5-1" that cold start effects can destroy liner earlier liner implosion beginning [2].

Consequently, an effective preionization of liner substance is the necessary condition for the compact liner implosion. We treat the PF current shell as the one of possible preionizers for multiterawatt driver. The high current plasma shell, being accelerated during some microseconds in PF accelerator, could deliver its kinetic, thermal and magnetic energy in rather short period, ~ 100 ns, to liner, positioned in the shell focus region, providing appropriate initial conditions for fast implosion. It is necessary to mention here that PF current shell fall onto bubble or gas liners was investigated elsewhere [4-6]. We used the microgeterogeneous solid foam as the plasma producing substance, because our foam liner technology allowed to produce liners with different sizes, shaping and radiative dopants. Homogeneity of plasma liner produced was the main problem of interest.

EXPERIMENTAL SCHEME AND DIAGNOSTICS

The experimental scheme is shown on Fig.1. PF current shell imploded onto agar foam liner, positioned on the top of inner electrode of PF-1000 coaxial accelerator. Foam liners were produced by vacuum drying of thin wall cylinders made from frozen agar gel (1.5 - 3 mg agar in 1 g of water). Liners had diameter 20 mm, 15 mm length, 200 microgram/cm or diameter 5.4 mm, 15-20 mm length, 250-280 mg/cm. An axial insulating rod of 5 mm diameter was used to support in horizontal position the ϕ20 mm foam liner with top electrode. The 5.4 mm foam liner had no axial support and no top electrode. The metallic foil current shunt - ϕ 20 mm liner imitator was installed in some shots.
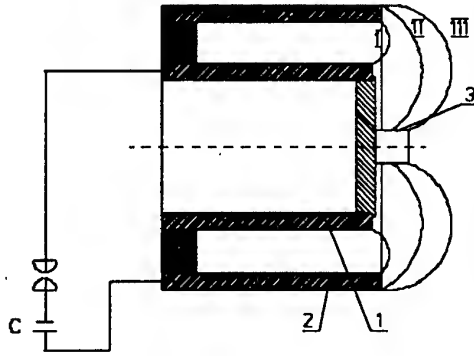
Fig.1. Experimental scheme.

1. - PF inner electrode, anode; 2-PF external electrode, cathode; 3-foam liner; I, II, III- different positions of the PF current shell.

Operating parameters of PF-1000 were: C~ 0.001 F, Vmax=25 kV, hydrogen pressure ~5 Torr, current Imax~1MA, current rise time 4-5 microsecond.

Measurements of dI/dt and V(t) were done to evaluate the total active power in discharge circuit Wact = VI - LI(dI/dt), L=L(t)-total inductivity of the circuit with moving current shell. Visible light streak camera with radial slit at the liner middle and optic frame camera (10 frames, 1.6 ns interval between frames) were used for current shell and liner dynamics investigation. Time integrated soft X-ray pinhole camera, filtered by 10-25 microns Be, allowed to analyze soft X-ray radiation during shell - liner contact and the composition implosion. Time resolved VUV and soft X-ray radiation were measured by a set of filtered vacuum photodiodes (XRDs). The VUV and soft X-ray radiation power was computed by linear combinations method, described in [6]. Signals were registered by Tektronix 2430A and THS-700 oscilloscopes and synchronized with of dI/dt and V(t) traces.

EXPERIMENTAL RESULTS

Typical signals of **dI/dt** (Idot, MA/(mks.div), voltage **V** (10 kV/div), current **I** (MA/div), active power W_{act} (10 GW/div)are shown on Fig.2.

Measured maximum of W_{act} during shell acceleration (~4 ms) was ~20 GW, it achieved 20-30 GW in period of the shell - liner collision and implosion, its duration being 150-300 ns. After hydrogen current shell coming to the ϕ20 mm liner the external margin of foam plasma becomes to expand during ~100 ns till ϕ22 mm, after that it implodes to axial rod with specific velocity ~2 cm/ms.

The liner plasma reflects from the rod with almost the same velocity after implosion (see Fig.3a).The visible external margin of 5.4 mm liner had no significant compression or expansion during ~0.6 ms after the shell - liner contact
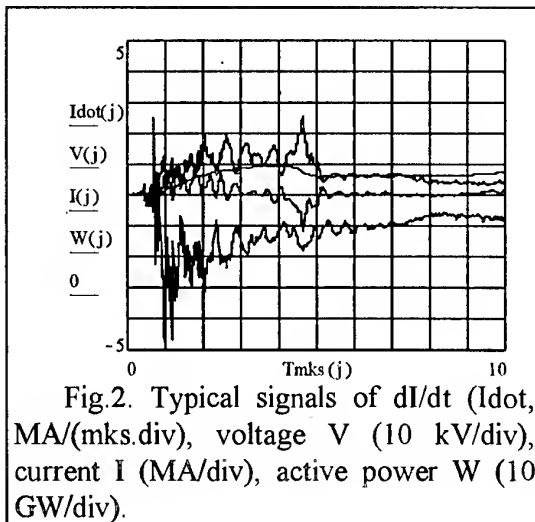
Fig.2. Typical signals of dI/dt (Idot, MA/(mks.div), voltage V (10 kV/div), current I (MA/div), active power W (10 GW/div).

(see Fig.3b). Nevertheless, the pretty shaped plasma column of ~2 mm diameter and ~10 mm length with the core of ~1 mm diameter was registered by pinhole camera in quanta energy >600 eV(see Fig4a). No „hot spots" present on this picture.

X-ray measurements.

VUV and soft X-ray radiation arises during 300-500 ns to 10-30% of maximum value. Then intensive narrow (~100-200 ns) peak of emission occurs with front rise time ~50 ns. This is close to frequency band of oscilloscope used. The peak appears in the moment of pinch
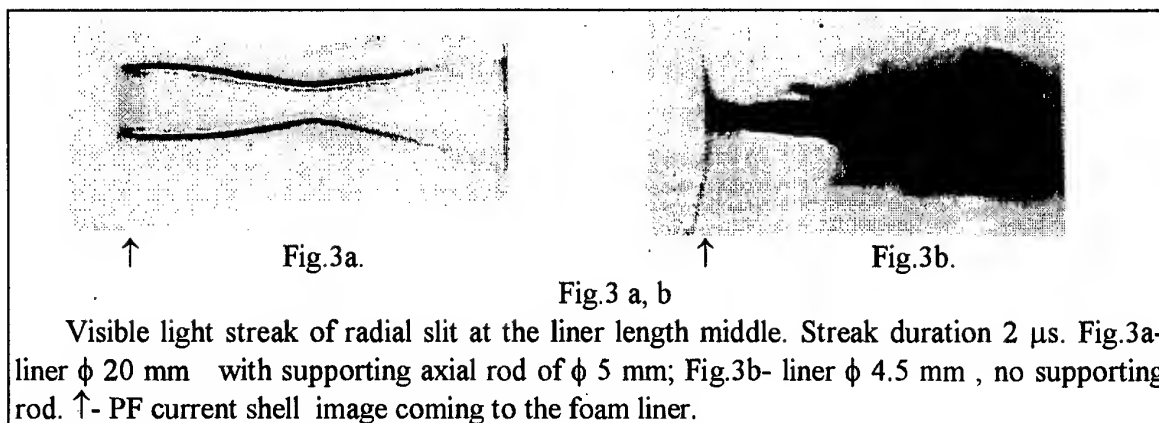
Fig.3 a, b

Visible light streak of radial slit at the liner length middle. Streak duration 2 μs. Fig.3a-liner φ 20 mm with supporting axial rod of φ 5 mm; Fig.3b- liner φ 4.5 mm , no supporting rod. ↑- PF current shell image coming to the foam liner.

collapse and corresponds to maximum W_{act}. After the peak emission the radiation intensity continues about 1mks at the level of ~0.3-0.5 of maximal value. This time is some more than the period of „stable" pinch on axis, viewed by optic streak. Then VUV drops during some microseconds.
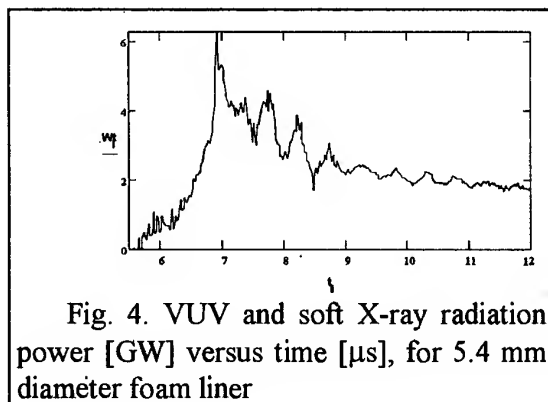
Fig. 4. VUV and soft X-ray radiation power [GW] versus time [μs], for 5.4 mm diameter foam liner

Maximal measured power of VUV and soft X-ray radiation for 5.4 mm diameter foam liner achieved ~2 GW, about 1 GW being measured in 10-120 eV band and almost the same power in 0.12-1 keV region. Taking into account absorption by hydrogen leads to higher power at 10-120eV band. Total power should be estimated as 3.5-8 GW with ~1 GW part harder than 120 eV. Emission in 0.1-1 keV region should be bound probably with more heated internal region of plasma column. (hv>0.6keV) This picture shows the pinch of φ 4.5 mm foam liner. The hot core was about 1mm diameter and of almost all initial foam liner length. Plasma corona diameter was about 3-5 mm as measured by optic streak camera. The intensity of hydrogen PF shell radiation, collapsed behind the foam liner of 15 mm length, was relatively small.

Preliminary analysis of the radiation spectra gives the plasma temperature evaluation as T=30-50 eV. This value is close to temperature evaluation by Bennett equation at the current of ~ 1MA. Radiation is significantly softer before the maximum peak during the phase of implosion.

DISCUSSION OF EXPERIMENTAL RESULTS

We consider results of this first experiment as optimistic.

1. The low mass PF current shell interaction with higher mass foam liner has produced rather homogeneous foam plasma liner. We couldn't see filaments in liner plasma. Foam liner didn't expand during the process dramatically.

2. The foam plasma produced has temperature $T \geq \sim 20$ eV and , consequently, liner electric conductivity is sufficient for effective implosion beginning by 3-5 MA current with $dI/dt \geq 5.1013 A/s$

PF junction with multiterawatt driver and their synchronized operation are possible in principle. We can't couple PF-1000 and "Angara-5-1 " to test preionization effects of ≥ 1 MA current, available on PF-1000. We believe this current level will be good for the drivers, being more powerful than "Angara-5-1". Consequently, testing of this preionization method at ~ 100 kA current level is planned on "Angara-5-1".
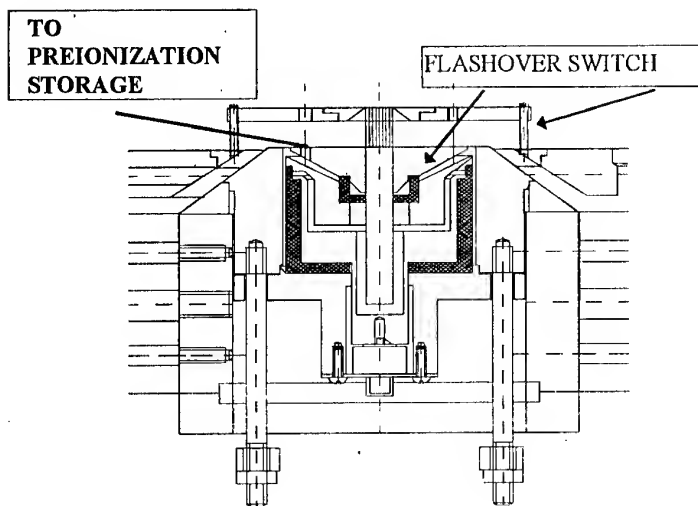
PLASMA FOCUS CURRENT SHELL PREIONIZATION ON ANGARA-5-1.

For Anagara-5-1 conditions the plasma shell microsecond current is produced by capacity storage with parametes: $C = 12\mu F$, $U = 25 kV$, $T1/2 = 14\mu s$, $Imax = 90$ kA.

The electrical testing and sinchronization of preionization current pulse with Angara-5-1 main pulse is performed using multywires liner, as presented on Fig. 6. Insulator inserted into cathode is flashover switch. This switch has'nt breakdown up to the moment of main Angara-5-1 pulse. In case of a gas shell using the columns 2 will work as a flasover switches.

REFERENCES

1. M.Scholz, M.Borowiecki, L.Karpinski, R.Miklaszewski, M.Paduch, W.Stepniewski, K.Tomaszewski, M.Sadowski, A.Szydlowski, V.Gribkov, S.Dubrowski, I.Volobuev. "Investigation of the PF-1000 facility". 2nd National Symposium PLASMA'95,Research and applications of plasmas,Warsaw, Poland, June 26-28, 1995, vol.2, p.15-21.

2 Branitski A.V., Grabovski E.V. et.al. "Angara-5-1" Program Development on Superfast Liner Implosion for ICF Physics Study and Basic Research". Proceedings of 11 Intern. Conf. "BEAMS'96", Prague, Czech Rep., June 10-14, 1996, vol.1, p.140-145.

3. R.Appartaim, A.Dangor, H.Kilic, J.G.Linhart, H.Schmidt. "Z-pinch driven foil implosions using liquid film bubbles". Proc. of workshop on Physics of Alternative Magnetic Confinement Schemes, Villa Monastero - Varenna, Italy, October 15-24, 1990. p.985-992.

4. A.Bortolotti, J.G.Linhart, J.Kravarik, P.Kubes. "Plasma driven implosions of a bubble liner". AIP Conference Proceedings 299, Dense Z-pinches, 3rd Intern. Conf., London, UK, 1993, p.372-380.

NUMERICAL AND EXPERIMENTAL STUDY OF BEHAVIOR OF GAS-PUFF Z-PINCH PLASMA PRODUCED BY INDUCTIVE PULSED POWER GENERATOR

K. Imasaka, Y. Kawauchi, K. Kawazoe, J. Suehiro and M. Hara

Department of Electrical and Electronic Systems Engineering, Kyushu University,
6-10-1 Hakozaki, Higashi-ku, Fukuoka, 812-8581 JAPAN

ABSTRACT

Magnetohydrodynamic(MHD) instabilities, such as kink and sausage instabilities, appeared on the gas-puff z-pinch plasma during the pinching process prevent spatial stability of hot spots, which are high energy density plasma regions produced by those instabilities on the z-pinch plasma column locally. Spatial stabilization of hot spots in the axial direction is very important to have practical applications.

In this study, radius and velocity of the inwardly tilted gas-puff z-pinch plasma during the compression and efficiency of energy conversion were analyzed theoretically by solving one dimensional snowplow model(1D-SPM) and circuit equations which considered inductive pulsed power generator. Those results were compared with experimental results measured with framing photograph of the pinching plasma. Efficiency of energy conversion of an input energy supplied from the inductive pulsed power generator into kinetic energy of the z-pinch plasma and final pinching velocity of the plasma exceeded that in comparison with fast bank method. These results received benefit from the fast and large pinching current transferred from the inductive pulsed power generator.

1. INTRODUCTION

In gas-puff z-pinch, hollow-shaped neutral gas injected between electrodes causes breakdown and the hollow plasma is produced. The plasma is compressed by Lorentz force inwardly and intensive soft x-ray is emitted. Since the gas-puff z-pinch device has a compact configuration and high density and temperature plasmas are easily produced, it received much attention as soft x-ray sources [1, 2].

If a conventional fast bank method which only utilizes discharge from a capacitor is used as a pulsed power source, the spatial stabilization of local hot spot as a soft x-ray emitter is difficult. Inductive pulsed power generator can drive fast rising current to the z-pinch plasma much faster than the fast bank and is expected to improve the plasma stabilization. So far, we observed pinching process of the z-pinch plasma column produced by fast bank method and inductive pulsed power generator with image-converter camera and recognized that instability mode differed with each other in both methods [3].

In this study, we measured the radius and radial velocity of the z-pinch plasma by using framing photograph. Moreover, we carried out numerical calculation according to one dimensional snowplow model based on momentum conservation and obtained satisfactory agreement between calculated and experimental values about the radius and radial velocity. Kinetic energy and conversion efficiency in the pinching process were also discussed.

2. EXPERIMENTAL SETUP AND EQUIVALENT CIRCUIT

Schematic diagram of the experimental setup with inductive pulsed power generator is shown in Ref.[3]. The inductive pulsed power system has 19.8kJ of primary energy and fine copper fuses as an opening switch. By removing fuses from the system, it is also worked as a

fast bank system. Operational gas, Argon, is puffed into through an introverted hollow shaped anode with an internal diameter of 4mm and an external diameter of 8mm. A conical cathode with 4mm in tip diameter is used. Gap space is 10mm. The charging voltages of the capacitor for fast bank and inductive pulsed power methods are controlled to 25kV and 28kV respectively so as to make equal the peak plasma current in both methods. Pinching plasma is observed with image-converter camera(ICC). Equivalent circuit of the inductive pulsed power system is shown in **Fig. 1(a)**, where $I_g(t)$, $I_L(t)$, R_s, L_1, and L_2 are generator current, load current, equivalent resistance, equivalent inductance of the circuit through the fuses and inductance of the load, respectively. $R_F(t)$ and L_F denote the resistance and inductance of fuses. Plasma inductance, $L_p(t)$, is obtained from an equation of inductance for a cylindrical inductor and plasma resistance, R_p, is calculated from Spitzer's equation. Efficiency, η, which is a ratio of plasma kinetic energy, $E_{kinetic}$, to electrical energy supplied to the plasma, E_{in}, is defined with load voltage, $V_{load}(t)$. η and $V_{load}(t)$ are given by

$$\eta = \frac{E_{kinetic}}{E_{in}} = \frac{\frac{1}{2} m(t) v(t)^2}{\int_0^t \left\{ V_{load}(t) I_L(t) \right\} dt} \tag{1}$$

$$V_{load}(t) = \frac{d}{dt} \left\{ L_p(t) I_L(t) \right\} + R_p I_L(t) \tag{2}$$

where $m(t)$ is plasma mass and $v(t)$ is radial velocity. Parameters in the present numerical calculation were taken as $R_s = 0.1\Omega$, $R_F(0) = 50m\Omega$, $L_F = 50nH$, $r_0 = 4mm$ and $r_i = 2mm$.

3. GAS-PUFF Z-PINCH PLASMA MODEL

We calculated the plasma radius and velocity by combing one dimensional snowplow model with the circuit equations. The model is based on momentum conservation and extremely accurate in spite of raking little trouble of calculation [4]. In order to carry out numerical calculation, initial pressure in the puffed gas should be given. The followings are assumed for simplicity.

(a) All load current flows through the outer shell of the cylindrical plasma which is symmetrical with respect to the z-axis and thin infinitely. Behavior of the pinching plasma is only dominated by difference between the pressures working in the current layer. At this time, the diffusion of gases is ignored.

(b) The plasma compressed under fixed volume is adiabatically imploded and the pressure by expanding gases is considered after internal radius of the plasma reaches the z-axis.

(c) The plasma is an ideal gas and a fully ionized plasma.

The initial pressure was determined by comparing experimental value with calculation. The model of cylindrical pinching plasma is illustrated as shown in **Fig. 1(b)**, where r_i, r_o and $r(t)$ is the initial inner radius, initial outer radius and plasma radius respectively. $P_{out}(t)$ shows the outer pressure which is produced by Lorentz force and $P_{in}(t)$ is the pressure by expanding gases. The equation for the motion of the plasma per unit length is written as follows:

(1) In case of $r(t) > r_a$

$$\rho \pi \frac{d}{dt} \left[\left\{ r_0^2 - r(t)^2 \right\} \frac{dr(t)}{dt} \right] = -2 \pi r(t) \frac{\mu_0 I_L(t)^2}{8 \pi^2 r(t)^2} \tag{3}$$

(2) In case of $r_i < r(t) < r_a$

$$\rho \pi \frac{d}{dt} \left[\left\{ r_0^2 - r(t)^2 \right\} \frac{dr(t)}{dt} \right] = -2 \pi r(t) \left\{ \frac{\mu_0 I_L(t)^2}{8 \pi^2 r(t)^2} - P_0 \left(\frac{r_a}{r(t)} \right)^{\frac{10}{3}} \right\} \tag{4}$$

(3) In case of $r(t) < r_i$

$$\rho \, \pi \left(r_0^2 - r_i^2 \right) \frac{d}{dt} \left\{ \frac{dr(t)}{dt} \right\} = -2 \, \pi \, r(t) \left\{ \frac{\mu_0 \, I_L(t)^2}{8 \, \pi^2 \, r(t)^2} - P_0 \left(\frac{r_a}{r(t)} \right)^{\frac{10}{3}} \right\} \qquad (5)$$

where ρ is the gas density and μ_0 is permeability of vacuum, respectively. r_a is the radius when inner radius of the plasma reaches the z-axis.

4. RESULTS and DISCUSSIONS

Framing photograph taken by ICC is shown in **Fig. 2**. The exposure time of each frame is 10ns and the time interval between adjacent two frames is 20ns. The times labeled in **Fig. 2** show the time after the z-pinch current begins to flow. It is recognized that there are few constrictions on the axis at $1.03\mu s$. These contractions are due to sausage instability and this region is considered hot spot as the soft x-ray source. Plasma radius and velocity at final stage of implosion measured from **Fig. 2** at the position of 7.2mm away from the anode were 0.2mm and 9.8km/s, respectively.

Plasma radius and imploding velocity by numerical calculation are shown in **Fig. 3** and **4**, respectively. Experimental values of the radius and velocity obtained from **Fig. 2** are also plotted in both figures. Effective initial pressure at calculation, P_0, is chosen so as to fit with experimental results. P_0 is turn out to be 90 Torr. Calculated results of generator current, I_g, and load current, I_L, are also shown in these figures. Calculation results of plasma radius and imploding velocity also agree well with experimental results. As a results, the present snowplow model with cylindrical pinching plasma near the maximum compression describes very well the experiments even if electrodes used actually is introverted shape.

Fig. 5 shows the Calculation results of η, $E_{kinetic}$ and E_{in} with inductive pulsed power generator. Time=$0\mu s$ in this figure corresponds to the time when I_L begins to flow, that is $2.44\mu s$ in **Fig. 3** and **4**. It is found from this figure that $E_{kinetic}$ in the plasma and E_{in} supplied to the plasma have maximum as well as η when the z-pinch plasma extremely imploded. The maximum efficiency for the studied system is about 30%. Under same condition, calculated results of the efficiency and energies with fast bank method are shown in **Fig. 6** for comparison. It is argued that E_{in} is more efficiently supplied to the pinching plasma in the case of inductive pulsed power method as compared with fast bank method.

5. CONCLUSIONS

In this work, 1D snowplow model confined with the circuit equations for the inductive pulsed power generator is calculated and compared with experimental results. The results may be summarized as follows.

(1) Plasma radius and implosion velocity calculated with 1D snowplow model agree well with experimental results.

(2) Efficiency estimated by numerical calculation reaches to about 30%.

(3) The input energy can be more efficiently supplied to the pinched plasma produced by inductive pulsed power generator as compared with fast bank method.

REFERENCES

[1] J. Bailey, et al., "Evaluation of the gas-puff z-pinch as an x-ray lithography and microscopy source", Appl. Phys. Lett., 40(1), pp.33-35, 1982

[2] S. Maxon, et al., "A gas puff soft x-ray laser target design", J. Appl. Phys., 57((3), pp.971-972, 1985

[3] K. Imasaka, et al., "Gas-puff z-pinch plasma produced by inductive pulsed power generator", Proc. of 11th IEEE Int. Pulsed Power Conf., 1997

[4] K. T. Lee, et al., "Numerical study on the dynamics of Z-pinch carbon plasma", Phys. Plasmas, 3(4), pp.1340-1347, 1996
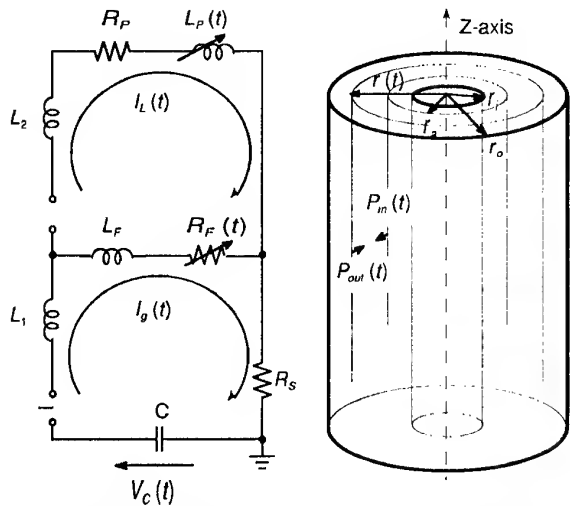
(a) Equivalent circuit of inductive pulsed power system.

(b) Gas-puff z-pinch plasma model.

Fig.1 Calculation model
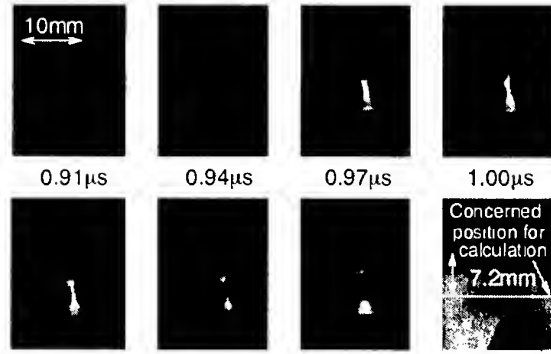
Fig.2 Framing photograph of the pinching plasma driven by inductive pulsed power generator.
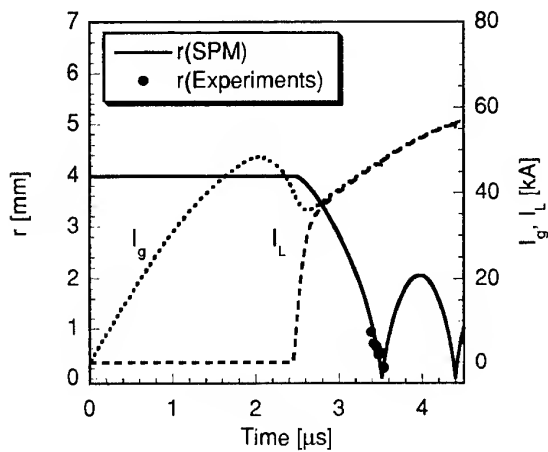
Fig.3 Plasma radius in case of inductive pulsed power system.
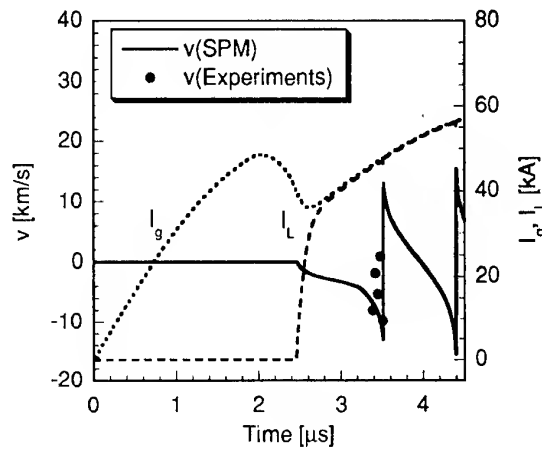
Fig.4 Imploding velocity in case of inductive pulsed power system.
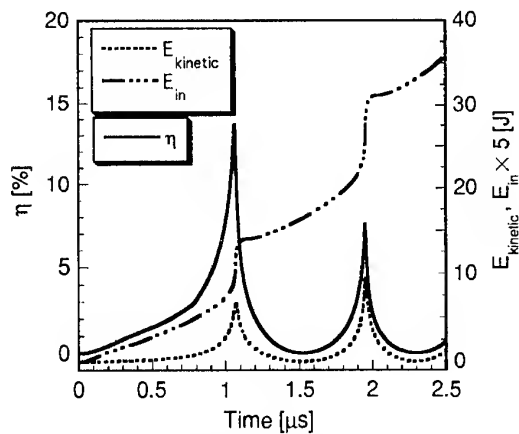
Fig.5 Calculated results of efficiency and energy with inductive pulsed power generator.
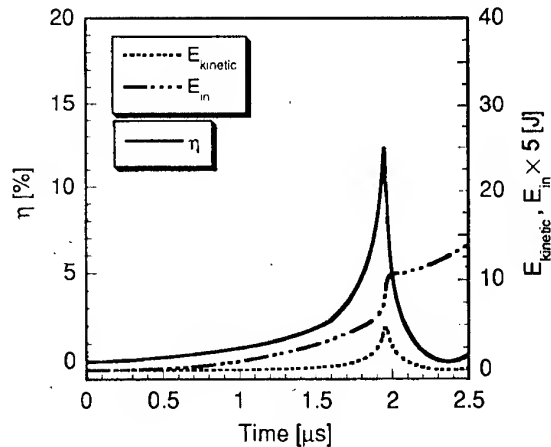
Fig.6 Calculated results of efficiency and energy with fast bank method.

ELECTRON BEAMS AND X-RAY POLARIZATION EFFECTS IN PLASMA-FOCUS DISCHARGES

L. Jakubowski*, M. Sadowski*, E.O.Baronova**, and V.V. Vikhrev**

* The Andrzej Soltan Institute for Nuclear Studies, 05-400 Swierk, Poland
** Nuclear Fusion Institute, RRC Kurhatov Institute, 123182 Moscow, Russia

Abstract: The generation of intense electron beams during the formation of „hot-spots" within a dense magnetized plasma of PF-type discharges has been confirmed by reproducible experiments [1]. Recently discovered phenomenon of the polarization of X-rays emitted from the hot-spots [2] seems to be strongly coupled with the emission of the intense electron beams. This paper presents results of recent experimental studies of the phenomenon in question and some mutual relations.

1. INTRODUCTION

Pinch columns, as produced within Plasma-Focus (PF) facilities (i.e., in devices equipped with two coaxial electrodes separated by a tubular insulator at one end), are sources of intense corpuscular and X-ray emission. In PF-type discharges performed with a gas mixture of deuterium and argon (or xenon) one can easily observe the formation of distinct miniature regions of an increased X-ray emission (so-called „hot-spots"), which are characterized by higher electron concentrations and higher electron temperatures.

In order to determine these basic plasma parameters by means of spectroscopic methods, we used two X-ray spectrometers with dispersion planes oriented in mutually perpendicular directions . The two Johanson-type spectrometers were equipped with concave quartz crystals with an interlayer distance equal to $2d = 8.5Å$ and $6.67Å$, respectively. The both X-ray spectrometers were placed side-on at 80 degrees to the z-axis , and the spectral measurements covered the wavelength range from $3.5Å$ to $5.0Å$. The dispersion plane of the first spectrometer was parallel to the discharge axis, while that of the second one was perpendicular to this axis. Typical X-ray spectra obtained from PF discharges have been presented in Fig.1.

A characteristic feature of the spectra appears to be a distinct difference in relative intensities of the resonance and intercombination lines (ArXVII-^{1}P, ArXVII-^{3}P) registered with the two spectrometers simultaneously. This effect can be explained by a different polarization of the considered spectral lines (taking into consideration that they should be polarized in the direction
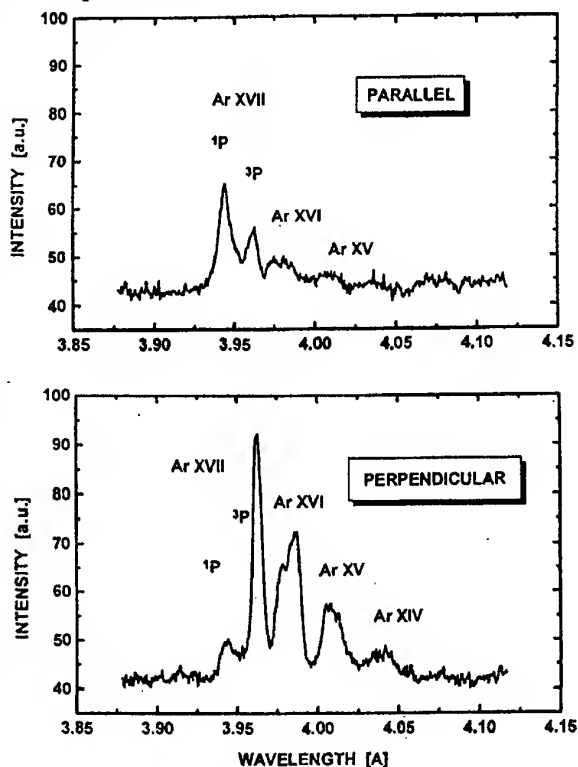
Fig.1. X-ray spectra demonstrating argon-ion lines as registered for a single PF shot by means of two crystal spectrometers with the dispersion planes oriented in mutually perpendicular directions.

perpendicular to the discharge axis). Since the plasma parameter (temperature and concentration values) are determined on the basis of relative intensities of selected spectral lines, an appropriate interpretation of the polarization effect in required.

A theory of the polarization for the X-ray wavelength region offers two possible explanations of this effect: appearance of strong local electric fields, in which the plasma emits the spectral lines under consideration, or anisotropy of the electron velocity distribution function .The polarization of the X-ray emission gives an evidence that highly-charged ions interact with free electrons of kinetic energy equal to about 3 keV (since there are excited the spectral lines corresponding to about 4Å wavelength). Some theoretical studies of electron beams within z-pinches [3] suggest that such 3 keV electrons appear always when there are formed "hot-spots" emitting e-beams of higher energy (> 100 keV). It has been suspected that such e-beams are generated within strong electric fields appearing at the z-axis due to the run away effect and they propagate along the pinch axis.

The main aim of this work was to find some experimental evidence of the appearance of the electron beams which might induce the polarization of X-rays emitted from a PF pinch column.

2. EXPERIMENTAL SET-UP AND DIAGNOSTIC METHODS

The experiments were carried out at the MAJA PF facility [1] which was equipped with two coaxial electrodes of 7.2 cm and 12.4 cm in dia., respectively. The system was powered from a condenser bank of a nominal energy equal to 45 kJ, at the initial charging voltage of 35 kV. The power supply system made possible to achieve the maximum discharge current equal to about 500 kA. Before PF shots the main experimental chamber was pumped out and filled up with a deuterium or deuterium and argon mixture (up to 20%) under an initial pressure of 1-3 Torr.

Time-integrated X-ray pictures of the PF discharges were taken with a pinhole camera equipped with a 100-μm-dia diaphragm and a 10-μm-thick Be-foil filter. Time resolved measurements of fast electrons were performed by means of Cerenkov-type detectors placed at different angles (45^0, 90^0, and 180^0) to the z-axis. Those detectors were equipped with special radiators (made of rutil crystals) which enabled the registration of electrons of energy above 50 keV to be performed [4].

Electron energy spectra were registered with a miniature magnetic analyzer equipped with two permanent magnets which deflected analyzed electrons by 180 degrees. This device made possible the registration of electrons within energy range from 5 keV to 1 MeV. In order to perform time-resolved measurements of electron beams of different energy there were used miniature scintillation detectors coupled through separate optical cables with a multichannel digital analyzer of the HP-16500 type. Other channels were used to register soft- and hard-X-rays, neutron pulses, VR emission from a pinch column and electrical discharge waveforms (voltage and current traces) .

3. STUDIES OF ELECTRON BEAMS

In our previous studies [1-2] there were observed correlations between the appearance, number and duration of "hot-spots", and fast electron beams registered with the Cerenkov-type detectors, placed behind the main collector plate (i.e.,at 180^0). Such correlations suggest that the fast e-beams are evidently involved , and their interaction with high-ionized species (within a hot plasma) can result in the polarization of emitted X-rays..

3.1 Electron energy spectra
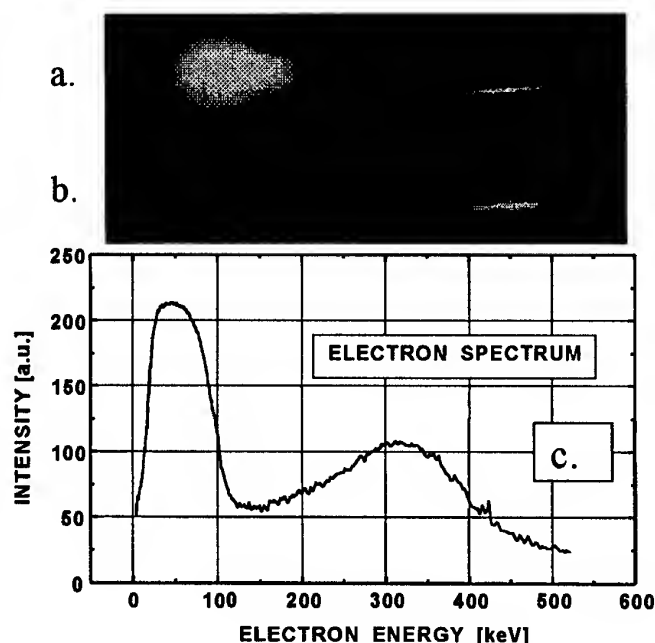
Fig.2. Electron energy spectrum obtained from a single PF discharge by means of the magnetic spectrometer: a – with the registration directly upon the X-ray film; b – with the registration behind a filter which constituted the base layer of the film; c – a diagram showing a dependence of intensity versus electron energy

Energy spectra of e-beams emitted along the z-axis (through the hollow inner electrode) were measured with the miniature magnetic analyzer placed at a distance of about 50 cm from the pinch column center. That spectrometer was equipped with a 100-µm-dia. entrance aperture, and a Kodak X-ray film. An example of the registered spectrum has been shown in Fig.2. An analysis of numerous electron images showed that the e-beams emitted from the pinch region (in the upstream direction) contain electrons of energy ranging from several keV to about 600 keV. The registered electron images are not uniform and one can discern regions of high intensity upon a weaker background or even behind it (see Fig.2a&b). It means that there are emitted e-beams within a relatively narrow energy band. Such electron beams can originate from different local sources, which might be identified with "hot-spots" (or their close surroundings). A spatial spread of the electron images in the direction perpendicular to the symmetry axis of the picture on the X-ray film can be explained by an effect of the electrical charges repulsion as well as by elastic and non-elastic scattering of electrons by working gas atoms.

According to the previous observation [5] the "hot-spots" are formed successively, starting from the front plane of the inner electrode and propagating with the current sheath colliding upon the z-axis. If different e-beams, corresponding various parts of the electron energy spectrum, are generated within (or nearby) different "hot-spots", time-resolved electron signals should appear at different instants.

3.2. Time resolved studies of e-beams

Time-resolved electron signals, corresponding to selected regions of the electron energy spectrum, were registered by means of the miniature scintillators placed inside the magnetic analyzer. Some examples of such signals, as obtained from fast photomultipliers coupled with the HP digital oscilloscope, have been presented in Fig. 3. Each oscilloscope channel shows electron-induced pulses belonging to a narrow energy band, which can be estimated as a determined average value ±10%, because of given dimensions of the miniature scintillation detectors.

On the basis of a comparative analysis of different electron signals from various energy bands, one can formulate the following conclusions:

– Individual peaks may correspond to different "hot-spots". It can be substantiated if one takes into consideration a shape , an appearance time, and a duration time of the pulses in
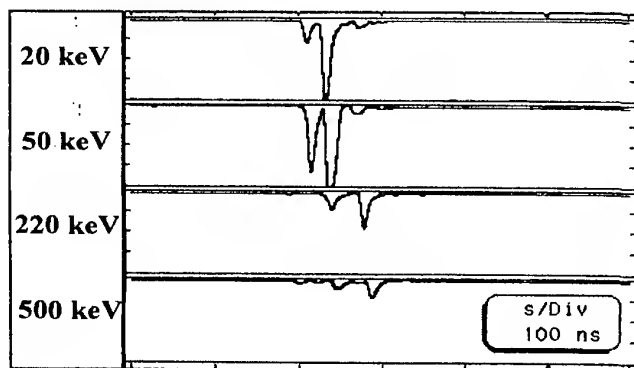
Fig..3. Time resolved signal from electrons registered within a chosen energy bands.

question. It can also be proved by a comparison of those signals with time-integrated X-ray pinhole pictures, taking into account that such pictures are in fact the flash photos.

-- During a single PF shot (discharge) the "hot-spots" can emit e-beams within narrow energy bands, which are different for various "hot-spots".

– Intensity of the electron beams reaches the maximum at about 50 keV.

It should be noted that the Cerenkov-type detectors, placed a 45^0 and 90^0 in relation to the z-axis, have also registered some weak signals induced by fast (>50 keV) electrons. Along the z-axis there were also measured ion (deuteron) beams reaching the detector plane with a time delay of about 100 ns. An estimated energy value of those deuterons amounted 300-500 keV. Results of the ion measurements will be presented in a separate paper.

4. SUMMARY AND CONCLUSION

The most important results of our recent studies of e-beams, generated by the MAJA-PF facility, can be summarized as follows:

1. The pulsed e-beams, emitted mostly along the z-axis in the upstream direction, contain the low-energy (about several keV) electrons as well as high energy (above 500 keV) electron bunches.

2. Individual „hot-spots" can be identified as local sources producing different e-beams of energy within relatively narrow bands.

3. During a single PF discharge the „hot-spots", formed successively along the x-axis, can emit e-beams of an average energy value different for each "hot-spot".

4. The experimental results suggest that the low energy electron beams can be responsible also for anisotropy of the velocity distribution function. It means that they can induce the polarization of some X-ray spectral lines.

5. Numerous high-energy e-beams (of energy ranging several hundred keV) give evidence that inside a pinch column there are formed strong local electric fields, inducing also the emission of some spectral lines. It means that the both mechanisms can cause the polarization of the X-ray emission from pinch columns produced by PF-type discharges.

References:

[1] L.Jakubowski, M.Sadowski, E.O.Baronova; Proc. 1996 Int.Conf. on Plasma Phys. (Nagoya 1996), Pt 2, p.1326.

[2] L.Jakubowski, M.Sadowski, E.O.Baronova, V.V.Vikhrcv; Proc. 4th Int. Conf. on Dense Z-Pinch (Vancouver 1997), p. 443.

[3] V.V.Vikhrev, E.O.Baronova; Proc. ICPP'96 (Nagoya 1996), p. 438.

[4] L.Jakubowski, M.Sadowski, J.Zebrowski; Journal of Technical Physics 38, 1, 141-150 (1997).

[5] L.Jakubowski, M.Sadowski; Proc. 22nd EPS Conf. CF&PP (Bournemouth 1995), Pt.2, p.181.

COMPARISON OF COMPUTED AND MEASURED PARAMETERS OF A DRIVER FOR FAST CAPILLARY DISCHARGE

K. Koláček, V. Boháček, J. Schmidt, P. Šunka, J. Ullschmied, M. Řípa

*Institute of Plasma Physics, Academy of Sciences of the Czech Republic,
Za Slovankou 3, P. O. Box 17, 182 00 Prague 8, Czech Republic*

1. INTRODUCTION

The capillary discharges (or sliding spark devices - as they were sometimes called) have been studied since the year 1965 [1] primarily as high-intensity pulsed light sources. Only about ten years ago they were recognised as potential soft X-ray lasers [2-8]. Most of these pioneering papers describe amplified emission of the Balmer alpha (H_α) line {3p-3s transition, $\lambda = 18.22$ nm} of hydrogen-like carbon (C VI), which occurs due to inversion population of the appropriate atomic energy levels. The active element - carbon - is ablated to the discharge from capillary walls usually made of polyethylene or polyacetal. The population inversion is reached according to the recombination pumping scheme - due to rapid conductive cooling of a hot plasma by capillary walls. The capillary diameter does not much exceed 1 mm and capillary length is up to 50 mm. Anyhow, the amplification has been achieved only during the first few shots (therefore, the capillaries had to be replaced frequently) and the gain of these lasers was relatively small (up to 2.8 cm^{-1} [8]). Also at gain scaling with length the values close to the saturation ones have not been reached.

One of the first papers proposing the amplification in a gas filled capillary (at that time called the ultrafast small diameter Z-pinch discharge) appeared in 1991 [7]. The authors were focused on 4f-3d and 4d-3p transitions {$\lambda = 51.97$ and 49.85 nm respectively} of lithium-like oxygen (O VI). Also in this case the recombination pumping scheme played decisive role, but the capillary diameter was as large as 14 mm and the capillary length was prolonged up to 90 mm. This experiment might be characterised by enhanced reproducibility, increased repetition rate and lifetime, but much smaller gain (0.28 cm^{-1} and 0.24 cm^{-1} for the first and the second transition, respectively [8, 9]).

In 1992 two independent groups [10, 11] came nearly simultaneously with an idea to build up the population inversion in gas filled capillaries with the help of collisional - excitation pumping scheme. In next few years the Rocca's group reported [12-14] strong amplification of neon-like argon (Ar IX) line {3p-3s transition, $\lambda = 46.88$ nm}, demonstration of lasing and finally achievement of saturation limit. The key point of this approach is the fast current rise-time (~ 1-4.10^{12} A/s) in a pre-ionised gas, which ensures a rapid detachment from the capillary walls (by Z-pinch effect) to limit the amount of material ablated from the walls and in this way to control the number of particles to be heated. These results triggered a burst of interest and a number of papers appear and specialised sections in conferences are organised.

Even we were attracted by numerous applications of coherent soft X-rays and decided to build a fast capillary discharge, despite it is generally understood as a relatively sophisticated apparatus. Since the beginning we paid grate attention to its design: we performed a lot of modelling and optimisation [15,16]. The present paper aims at comparison the designed (computed) parameters with the measured values.

2. APPARATUS

The designed apparatus (see Fig. 1) consists of a Marx generator, a coupling section (spacer), a fast capacitor (pulse forming line) with a closely coupled main spark gap and a capillary. Attached is gas filling and pumping assembly.
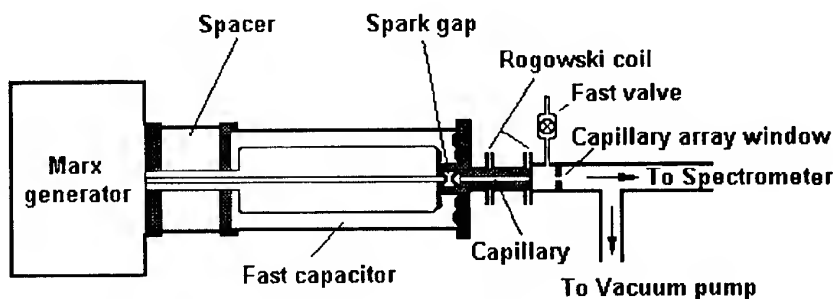
Fig. 1 Schematic drawing of the apparatus.

Contrary to the situation described in our previous papers [15,16], we use now a newly adopted fully screened oil insulated Marx generator (originally used at REBEX machine) as a power supply. After reconstruction it has 8 stages, each of them containing two couples (positively and negatively charged) of two 400 nF/100 kV condensers in series. The whole generator (erected capacity 12.5 nF) was successfully tested up to the charging voltage of 25 kV (erected voltage 400 kV). Its short-circuit inductance is 14.2 μH and serial resistance 5.7 Ω.

The coupling section (spacer) is a short SF_6 gas filled coaxial cylindrical line of the dimensions $\varnothing 426 \times \varnothing 88 \times 287$ mm ($L_{spacer} = 95$ nH, $C_{spacer} = 10$ pF, $Z_{spacer} = 95$ Ω), which functions as an interface between the oil insulated Marx generator and the water filled pulse forming line.

As a fast capacitor we used a coaxial cylindrical line of the dimensions $\varnothing 262 \times \varnothing 158 \times 675$ mm with de-ionised water as a dielectric. It has capacitance $C_{line} = 6.01$ nF, inductance $L_{line} = 68.28$ nH and characteristic impedance $Z_{line} = (L_{line}/C_{line})^{1/2} = 3.37$ Ω. At the end of the line the main spark gap is placed, to which a capillary assembly is attached. The inner part of the spark gap is filled (through the Marx generator, the coupling section and the fast capacitor) by SF_6 gas for reducing its longitudinal dimensions, while the outer part of the electrode gap is filled by water. In this way the spark gap capacity is significantly enlarged, which is one of the factors determining the pre-breakdown current. This current pre-ionises the gas in the capillary and ensures thus the sufficiently fast main-current rise-time mentioned in the Introduction. Thus the plasma in the capillary is very rapidly de-coupled from the capillary walls (by Z-pinch effect) and the number of particles ablated from the wall remains limited.

The 20 cm long capillary is directly attached to the main spark gap (having one common electrode). It is placed in a shielding and circuit closing metallic cylinder of the diameter of 60 mm. The working gas is injected as well as the generated radiation is monitored through orifices in the outer electrode.

Such a design is very critical: on one hand the fast current rise-time requires to diminish both the capacitance of the fast capacitor and the inductance of the circuit (and, therefore, the circuit dimensions) as much as possible, on the other hand it is necessary to have a sufficient amount of energy for ionisation of the gas atoms up to their K-shell. It means to elevate the voltage up to the upper limit of the power supply and the condenser bank, and to scale up the insulators accordingly.

In order to test the design, the Laplace-Poisson equation in the most exposed regions was solved (see in more detail [15,16]). This helped us to determine not only the minimum save dimensions of insulators and the optimum roundness of the conductor edges but also the mutual capacitance of individual components.

3. MODELLING AND COMPARISON WITH THE EXPERIMENT

For model calculations an equivalent circuit (see Fig. 2) was constructed, in which both the measured and the calculated values were substituted. The Marx generator is represented by a serial connection of capacitance C_m, inductance L_m and resistance R_m, while the spacer is a simple coaxial line. The fast capacitor is modelled as a line with distributed parameters having k = 10 identical elements (consisting of capacitance C_i and inductance L_i). The parts of the circuit that correspond to the spark gap and to the capillary differ prior to and after the spark gap breakdown: while prior to the breakdown the spark gap can be represented by its pure capacitance C_s (~ 300 pF), after breakdown it changes into a parallel combination of capacitance C_s and a serial connection of the inductance L_s (~ 60 nH) and the resistance R_s (in the first approximation we take it constant). Finally the capillary is represented by a serial combination of the inductance L_c (~100 nH), and the
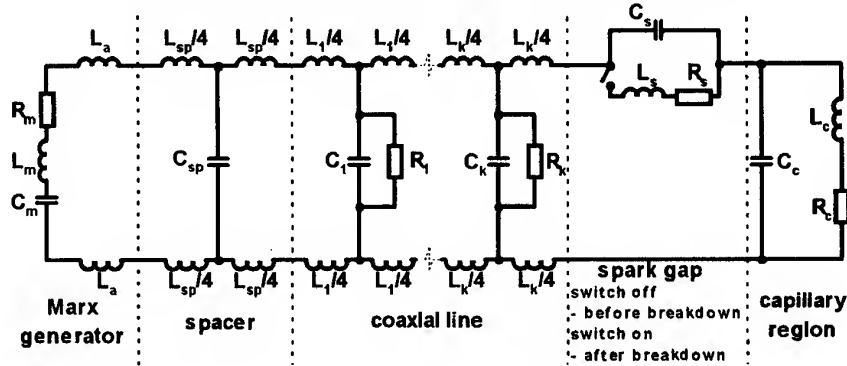
Fig. 2 Equivalent circuit of the soft X-ray driver

resistance R_c (also the later is taken to be constant in our approximation {900 Ω prior to and 0.01 Ω after the breakdown}) to which both the capillary capacity C_c^* (~ 15 pF) and the parasitic capacity C_p (~ 35 pF) of the second electrode of the spark gap to the casing (together C_c ~ 50 pF) are connected in parallel. The transient characteristic of this circuit is solved first, till the voltage on the spark gap reaches its breakdown value (see Fig. 3). Then the solution continues with the changed circuit (see Fig. 5, 6). The erected voltage of the Marx generator was U_0 = 160 kV in all cases. It turned out that charging of the fast capacitor takes ~800 ns (Fig. 3) and during this time the line voltage (measured by combined capacitance -resistance divider) rises up to ~ 130 kV. Fig. 4 shows the capillary current (having the amplitude ~ 100 A) as measured by a Rogowski coil as long as the pressure-distance product is higher than its breakdown value in the main spark-gap. In the moment of the main spark gap breakdown (t = 0) the capillary voltage rises steeply and then oscillates with a reasonable damping (see Fig. 5). The current-rise is as fast as 1.3×10^{12} A/s and the current amplitude reaches ~20 kA (Fig. 6).
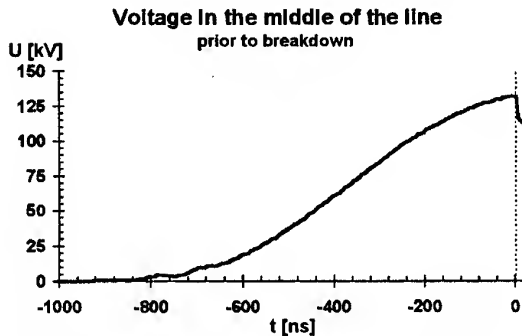
Fig. 3 Measured voltage in the middle of the line prior to breakdown
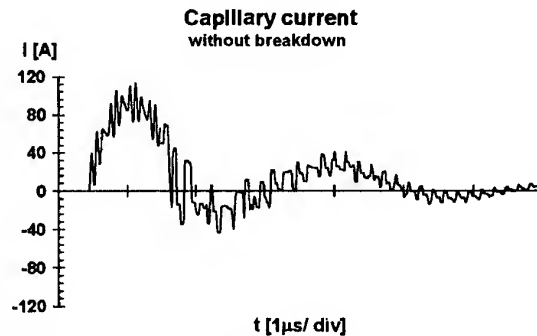
Fig. 4 Measured capillary pre-breakdown current

Voltage at the middle of the line
after breakdown

Capillary current
after breakdown
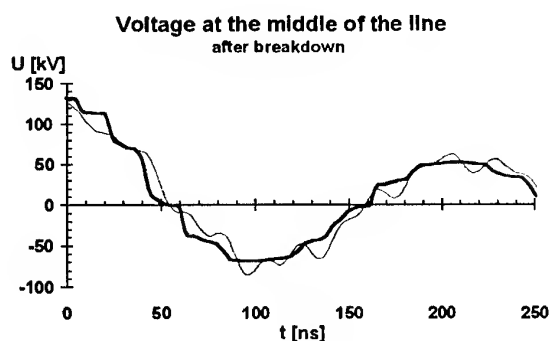
Fig. 5 Voltage in the middle of the line after
breakdown
bold line - measured curve
thin line - result of simulation
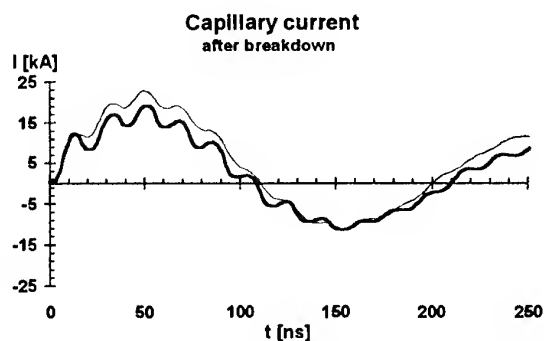
Fig. 6 Capillary current after breakdown
bold line - measured curve
thin line - result of simulation

4. CONCLUSION

First, it was shown that results of combination of a simple electrostatic field mapping (which on one hand warns against local voltage overloading, on the other hand it enables to calculate mutual capacities of individual components) and a classical equivalent circuit analysis gives an excellent agreement with measured curves and, therefore, its use at the design of future devices is strongly recommended.

Second, our test shots with the half charging voltage (160 kV) demonstrated that our driver for a fast capillary discharge has very similar parameters as the apparatus at the Colorado State University, where saturated stimulated emission in soft X-ray region (in Ne-like Ar line $\{\lambda = 46.9 \text{ nm}\}$) has been demonstrated [14].

References
[1] P. Bogen, H. Conrads, and D. Rusbüldt, Z.Phys. **186**(1965), 240
[2] J. J. Rocca, D. C. Beethe, and M. C. Marconi, Opt. Lett. **13** (1988), 565
[3] C. Steden and H.-J. Kunze, Phys. Lett. **A 151** (1990), 1534
[4] C. A. Morgan et al., Bull. Am. Phys. Soc. **37** (1992), 1459
[5] F. G. Tomasel et al., Bull. Am. Phys. Soc. **37** (1992), 1501
[6] H. Shin, D. Kim, and T. N. Lee, Bull. Am. Phys. Soc. **37** (1992), 1502
[7] W. Hartmann et al., Appl. Phys. Lett. **73** (1991), 2619
[8] T. Wagner et al., Phys. Rev.. Lett. **76** (1996), 3124
[9] E. Eberl et al., Laser and Particle Beams **15** (1997), 589
[10] J. J. Rocca et al., in Proc. 3rd Intenat. Colloquium on X-Ray Lasers, Schliersee, Germany, 1992 (Inst. of Phys., Bristol, UK, 1992), p. 427
[11] E. P. Ivanova et al., in Proc. Int. Conf. on Lasers '92, Huston, TX, 1992 (STS Press, McLean, VA, 1993)
[12] J. J. Rocca et al., Phys. Rev. E **47** (1993), 1299
[13] J. J. Rocca et al., Phys. Rev.. Lett. **73** (1994), 2192
[14] J. J. Rocca et al., Phys. Rev.. Lett. **77** (1996), 1476
[15] K. Koláček et al., Proc. Plasma '97, June 10-12, 1997, Jarnoltówck, Poland, Vol. 1, p. 69
[16] K. Koláček et al., Proc. 18th Symp. on Plasma Phys. and Techn., June 17-20, 1997, Prague, Czech Rep., p. 86

DENSE Z-PINCH NECK DEVELOPMENT DYNAMICS INVESTIGATION ON S-300 GENERATOR.

Bakshaev Yu.L., Blinov P.I., Chernenko A.S., Dan'ko S.A., Gordeev E.M., Korolev V.D.
Medovschikov S.F.*, Mizhiritskii V.I., Nedoseev S.L.*, Smirnova E.A., Tumanov V.I.

Russian Research Center "Kurchatov Institute" 123182, Moscow, Russia.
*Troitsk Institute Innovative and Fusion Research 142092, Troitsk, Russia.

INTRODUCTION

The experimental investigations of neck development dynamics in the Z-pinch with 0.1 g/cm^3 density were carried out on an 8-module pulsed power generator, the S-300 (4 MA, 100 ns) [1]. The objective of these experiments was a study for the possibility of obtaining plasmas with extra-high parameters in the Z-pinch neck region, corresponding to the fusion ignition conditions.

In the articles [2,3] it was suggested to initiate a wave of thermonuclear fusion in the Z-pinch neck region propagating to the main bulk of plasma column. In this case one can expect the theoretically predicted ignition of D-T mixture compressed from the initial cylinder of 1 cm diameter to the micron cross-size neck by passing through dense hot plasma in these experiments it a 10 MA current. In the first experiments which pursued this project's objective carried out on the Module A5-01 generator (1.5 MA, 100 ns) was demonstrated the possibility of a hot plasma formation (Te = 0.8-1 keV, Ne = 10^{22} cm^{-3}, r = 100 microns) as a result of profilled hydrocarbon fibres of 0.01 g/cm^3 density and 1 mm diameter compession [4]. In the given work are presented the experimental results obtained in the S-300 generator on the compression dynamics investigation of carbon Z-pinch with initial density of 0.1 g/cm^3 and preliminary formed neck.

EXPERIMENTS

The experimental investigations of plasma compression in the Z-pinch neck region were carried out at currents up to 3 MA with a rise time of 100 ns. The initial plasma was produced by an electrical breakdown of profiled carbon filled agar-agar fibres with density of 0.05-1 g/cm^3. The best matching with the load at the level of incident energy wave of 70 kJ transmitted to the vacuum concentrator unit occurs for the fibres diameter of 3-5 mm and length of 8-10 mm. The neck mass per unit length being chosen between 0.1-5 mg/cm.

Various X-ray diagnostics were used for plasma parameters measurements: X-ray framing cameras with 5 ns exposure time, X-ray pinhole cameras, quick response detectors with filters, crystal Roentgen spectrographs. Besides, optical streak and framing cameras were used.

It was established that plasma formation essentially depends on the initial density and radius of the neck. At the initial fibre density lower than 0.05 g/cm^3 the plasma corona was

formed with the diameter exceeding that of the neck [5]. Chaotically arising bright spots were observed in the space occupied by the rare plasma (the corona). At increasing the initial fibre density up to 0.1 g/cm^3 the time integrated pinhole camera and X-ray frame camera pictures show the plasma formation in preliminary made neck. The mean compression velocity as determined from X-ray frame camera pictures proved to be 5·10^6 cm/s (Fig.1,a). The highest compression for the initial neck diameter of 1 mm corresponded to the moment of current maximum. From time-integrated pinhole camera pictures follows that as a result of compression the plasma formation occurs with the least diameter dimension of 40-70 microns as observed behind 10 thick mylar filter (Fig.1,b). Approximately the same dimension values of the hot plasma were obtained in X-ray spectroscopic measurements of the penumbra width from the edge of the horisontal slit.

The compression was accompanied by the soft X-ray radiation pulses (Fig.2). The moment of the hot plasma appearance determined by soft X-ray radiation burst behind the 10 microns thick mylar filter corresponds to the current's maximum. It should be noted that the VUV-diode with 10 microns mylar filter is most sensitive to 2 keV X-ray radiation. The hot plasma life-time measured by the half intensity of soft X-ray decay is less than 5 ns, while the radiation power for 2 keV quanta exceeds 5·10^9 W and the total irradiated energy is to be 20-50 J.

In some experiments in which a diagnostic admixture of KCl was used, the luminous region length of helium-like chlorine radiation measured by a spectrograph proved to be 100-150 microns with its diameter of 200 microns. At the same time measured diameter for helium-like potassium is in one and a half times smaller. The electron density and temperature, calculated from the spectral lines intensity ratio of hydrogen-like and helium-like ions, proved to be: $N_e = (0.3-1.0) \cdot 10^{22}$ cm^{-3} , $T_e = (0.8-1.5)$ keV. The Fig.3 shows a typical spectrum of potassium admixture ions [6]. The line broadening measurement analysis shows that there maybe exists significant difference between the ion and electron temperatures.

The plasma parameters at the initial density of 0.1 g/cm^3 were essentially depended on the neck profile. The highest parameters were obtained when the load neck was like two truncated cones with their tops directed opposite to each other and the cone angle not exceeded 90°. By increasing the initial load density up to 1 g/cm^3 the plasma parameters decreased and became lower than for the density of 0.1 g/cm^3.

CONCLUSION

The experiments carried out on the S-300 generator show that at Z-pinch current increase from 1 to 3 MA the effect of deep neck development is remained. The hot dense plasma with typical cross-size dimension in 40 - 70 microns was formed in the region of a preliminary made neck as a result of electrical breakdown of carbon filled agar-agar fibres.

The highest plasma parameters $N_e = 10$ cm^{22} , $T_e = 1-1.5$ keV, were obtained by using fibres of 0.1 g/cm^3 density. The hot plasma life-time proved to be smaller than 5 ns. The power and full energy of soft X-ray radiation in the range of quanta energy h = 2 keV proved to be 5·10^9 W and 20-50 J, correspondingly. If we take for granted that almost all the

Z-pinch current flows through the neck region, then it comes out that for the smallest measured neck diameter values of 40-70 microns which at the same time correspond to the space resolution of used used diagnostics, the magnetic pressure $H^2/8\pi$ around the neck would be much higher than the kinetic pressure $(nT_e + nT_i)$. Therefore it may be thought that the plasma compression might still be going on to the smaller values of neck diameters.

ACKNOWLEDGEMENTS

REFERENCES

[1]. Chernenko A.S.et al, Proc.of Beams 96, Prague,1996, Vol.1, p.154.

[2]. Yan'kov V.V. Phys. Plasmy (Sov), 1991, 17, 521.

[3]. Vikharev V.V., Ivanov V.V. Sov.Phys. Dokl. 30 (6), June 1985 (492-493).

[4]. Gordeev E. M.et al, Proc.of Beams, San Diego,1994,Vol.1,p.167.

[5]. Bakshaev Yu.L., et al. Proc. of 18th Symposium on Plasma Physics and Technology, Prague, June 17-20, 1997, p.50.

[6]. Dan'ko S.A., "X-ray spectroscopy at S-300 facility" - these proceedings paper No.0045.

FIGURES
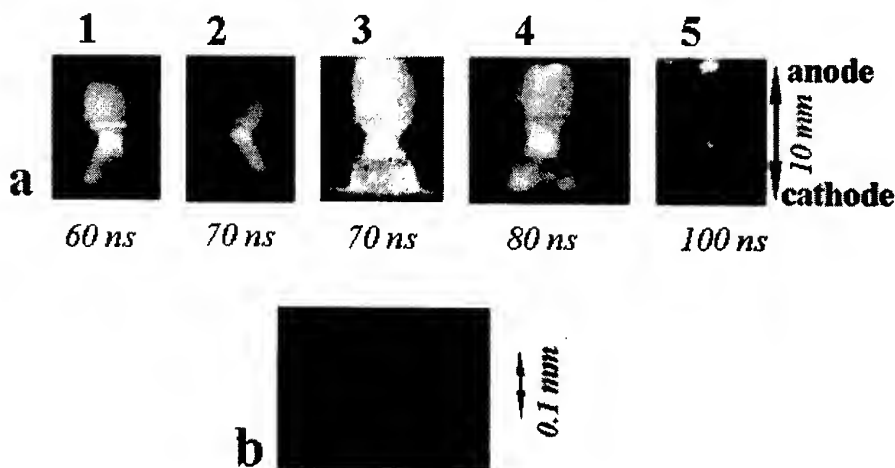
Fig 1. *a*.Optical (1, 2) and soft X-ray (3, 4, 5) frames for carbom filled agar-agar fibres of 0.1 g/cm^3 density with a neck region of less than 1 mm diameter. Numbers beneath – moment of frame. *b*. Pinhole-camera picture of carbon filled agar-agar fiber of 0.1 g/cm^3 density and with the initial neck diameter less than 1mm.
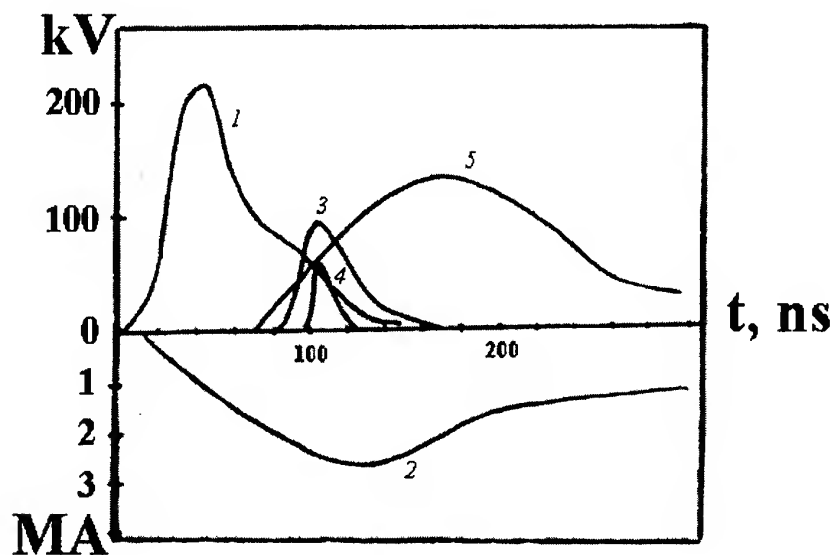
Fig 2. Voltage (1), current (2) oscillographic traces and soft X-ray radiation signals obtained with 5 microns mylar filter (3), 10 microns mylar filter (4) and no filter at all (5). (The Z-pinch load - a carbon filled agar-agar fibrs of 0.1 g/cm³ density and with neck diameter < 1 mm).
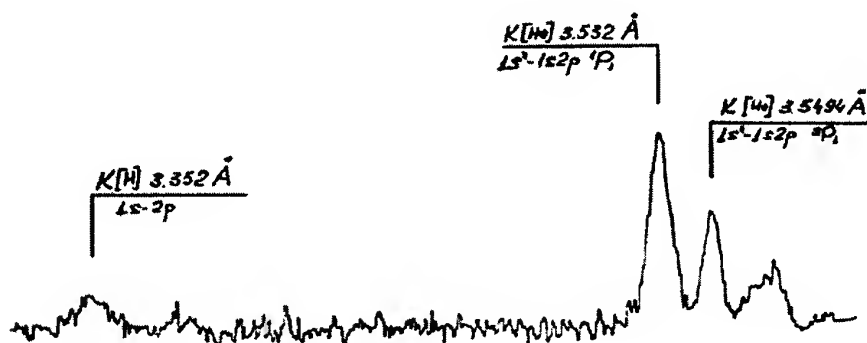
Fig 3. Typical spectrum of potassium admixture ions.

MONOCHROMATIC VUV-RADIATION OF Z-PINCH CARBON ROD

[1]P. Kubeš, J. [1]Kravárik, L. [2]Karpinski, [3]L. Aschke, [4]Ž.Andreić, ^{3}H-J. Kunze

[1]*FEE Czech Technical University, Technická 2, 16627 Prague 6, Czech Republic*
[2]*Institute of Plasma Physics and Laser Microfusion, P.O.Box 49 00-908 Warszaw, Poland*
[3]*Institut für Experimentalphysik V, Ruhr-Universität, 44780 Bochum, Germany*
[4]*Ruder Bosković Institute, Bijenička 54,10 000 Zagreb, Croatia*

A spectral VUV and visible and a laser schlieren diagnostics were used for the discharge load from graphite for pencil of 1 cm length and 2 mm of diameter between two cooper conical electrodes. The electric discharge was initiated by a small capacitor bank of 20 kV voltage and a 1 μF capacitos. The current reached its maximum at 40 kA during 360 ns after the increase of the current. The authors reported diagnostic results and the correlation of VUV emission with the explosion of the plasma corona.

For the detection of radiation, PIN diodes, sensitive to XUV-ray wavelength with 1 ns temporal resolution, were used in the axial direction along the length of the rod and in the radial direction perpendicular toward the axis of the rod. The detection of an axial radiation was enabled due to a 5 mm diameter hole in the center of the electrode near the detector. The PIN diode was also used in conjunction with a grazing incidence Si mirror, which essentially acts as a filter with selectable wavelength range by adjusting the angle at which the PIN diode observes the reflected XUV radiation. For the visual schlieren and the differential interferometer diagnostics two 3-ns beams, optically separated from one laser pulse, were used with a time delay of 12 and 55 ns or for perpendicular image in two radial directions. The plasma corona was observed side-on with a VUV flat–field spectrograph [1,2] based on a Hitachi flat-field grating. The line of sight was parallel to the rod axis. The spectral region observed was 10-25 nm and a spectral resolution of about 0.02 nm was achieved. The spectrum was converted into visible light with the help of a gated micro-channel plate (MCP) whose output surface was re-imaged onto a CCD camera chip [3]. The recorded spectrum was transferred into a computer for storage and further processing. With this arrangement it was possible to take time resolved spectra with a temporal resolution of 50 ns as given by the gate time of the MCP. The detection area was about 2 mm wide and 10 mm high, thus the spectra were integrated over the whole length of the rod. The spectra were observed sideways to the rod, at a distance of about 1 mm from the rod surface. The visible spectral region of 400 – 600 nm was observed by a ISP-51 spectrograph .

The emission and explosion of the corona of the carbon fiber of 20 μm diameter with the inner layer in solid phase, were reported from a previous device with a non-regular, random and weak radiation intensity [4]. The shorter increase of the current from 1 to 0.36 μs and the greater diameter of the rod caused the ten-times energy enhancement of XUV radiation to 0.1 J (power 500 kW), the increase of the probability of this emission from random to stable regime (from 30% to 100%) of the discharges, and it enabled the usage of the VUV spectrograph.

The emission started 55 – 80 ns after the increase of the current, reached its maximum at 380 ns (at current maximum) and finished at 600 – 1000 ns with FWHM of 90 – 450 ns and with mean value of 230 ns. The radial radiation had similar behavior as in the axial direction. When an oscilloscope signal had its local maximum, then its position in radial and axial direction was the same, but the ratio of their intensities could not be the same. The emission had good radial symmetry. The intensity of the visible wavelength was lower than 10% of the total intensity. The 0.8 μm thick Al foil applied in front of the PIN reduced the

emission intensity to 10 – 20 %. The 1.5 μm mylar foil reduces radiation maximaly to 2 %. The dependence of the intensity of the reflected emission on the angle of incidence at a silicon plate is illustrated in Fig.1.
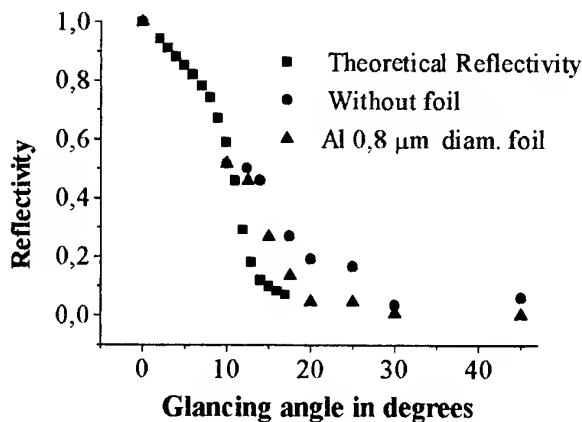
Fig.1. The dependence of the intensity of the reflected emission on the angle of incidence

The diagnostics by VUV spectrograph proved the line character of the dominate emission in the region 15-20 nm. The intensities of these lines were dependent on the discharge current but the line ratios were temporally independent during a few hundreds ns emission.

The plasma corona and its temporal evolution generated around the solid graphite rod showed some interesting features. The width of the corona evaluated from the visual diagnostics were dependent on the sensitivity of the schlieren method. For a deflection angle $\alpha > 3$ mrad, the corona width of 200 μm was regularly spread around the rod with electron densities higher than 2×10^{25} m^{-3}. For a deflection angle $\alpha > 1.5$ mrad $^{-3}$ (with electron densities higher than 10^{25} m^{-3}) the width increased to 500 μm and in the schlieren pictures the radial explosions from the corona were observable to 1 mm distance from the rod. For a lower deflection angle $\alpha > 0.75$ mrad $^{-3}$ (with electron densities higher than 5×10^{24} m^{-3}) the local explosions extended to 2-3 mm distance from the rod. It implied the local explosion of the plasma from the corona. The velocities of the radial plasma explosions, higher than 10^5 m/s, were evaluated .

At visualization of the corona, by Wollaston interferometry, a helical form of these plasma explosions was observed. Along the length of the rod the 3-6 winds are imagined with an axial width of ~ 0.5 - 1 mm and a pitch of ~ 1 - 2 mm (Fig.2). The axial velocity of the variation of positions of the winds was evaluated till $2-4 \times 10^4$ m/s. In some pictures the connection of neighbor winds and the formation of a toroidal ring around the rod can be seen. The velocity of connection was evaluated as ~ 10^5 m/s . Time of connection correlates with local maximum of VUV emission. The orientation of helical form is random, sometimes right and sometimes left. This conclusion was induced by the comparison of two pictures of diagnostic beams from two perpendicular radial directions. The dependence of the electron density on the radius of the exploded plasma is depicted in Fig. 3. During the discharge the main part of the rod remained in solid phase. The number of evaporated particles (3×10^{18}) was evaluated by measuring the volume of the graphite rod after discharge. For one evacuation of the chamber it is possible to realize a few hundred of discharges with one rod

and at this form of the load enables high frequency of experiments. The number of particles present in plasma corona reached value of ~10^{17}. The number of photons with an energy value of 50 – 100 eV (2 – 4×10^{15}) was evaluated from the absolute measurement of the intensity of the emitted radiation.
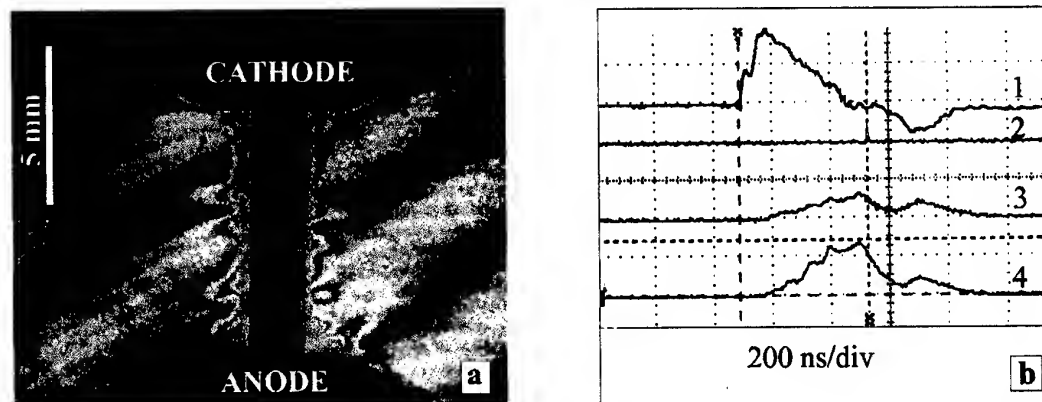
Fig.2: Shot No.206: a) Helical form and b) oscillogram. Trace 1:derivative of current. Trace 2: position of fig. Trace 3: axial PIN signal. Trace 4: radial PIN signal
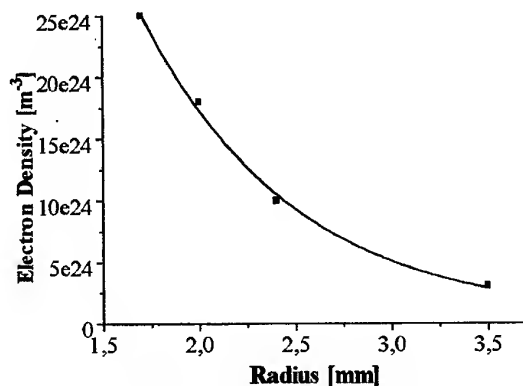
Fig.3: Dependence of the deflected angle and the electron density on the radius of the explosion.

From these experimental results it is possible to induce some considerations and conclusions.

The interval of emitted wavelength was determined from the combination of results of the Al and mylar filters and from the measured dependence of the intensity of the reflected emission on the angle of incidence. The Al foil absorbed less than 90% of the 0 – 2.7 nm and 17 – 60 nm wavelength, whereas the mylard foil did the same for the 0 – 2.4 nm and 5 – 11 nm wavelength. For the   observed absorption it is possible to suppose that the dominant emission in Al L window is between 17 – 60 nm. From the results of the incidence reflection spectroscope it is possible to exclude the wavelengths above 30 nm [6]. The emitted lines

belong to OV and OVI ions. The lines of CV and CVI ions were not confirmed. The visual lines are produced by CII and OII ions.

The typical helical form is imagined in Fig. 2. The helical form demonstrates an example of self-organization in magnetized plasma with the high energy density. Its nature and character can be deduced from the measured parameters of the plasma. It is possible to calculate the kinetic plasma pressure from the velocity of transition (2-4x10^4 m/s) and from the carbon ion density (5x10^{24} m^{-3}):

$$\frac{1}{2}\rho v^2 = \frac{1}{2}mnv^2 = 10^8 - 10^9 \; Pa.$$

This pressure must be directed by a magnetic confinement pressure generated by a current of 20 – 40 kA. The relations for the magnetic pressure and the magnetic field

$$\frac{B^2}{2\mu}, \quad B = \frac{\mu I}{2\pi r}$$

enable estimation of the necessary magnetic field of 20 – 40 T produced by a current channel with a radius r ~ 0.2 – 0.3 mm. This radius is less than 1 mm of the radius of the rod. A current conduction through a helical tube is then more probable than a conduction along the cylindrical channel around the rod. The dense part of the helical form can be a helical current tube wound on the rod. The kinetic pressure of the plasma explosions has the same value as the kinetic pressure of the transmission of a helical form, 10^8 – 10^9 Pa. The idea of magnetic confinement of plasma is supported by the stability of the corona. A dynamic of the connection of neighbor winds may be in conformity with the interaction and extinction of the opposite magnetic fluxes around the helical tube. The accelerated dynamics of the extended opposite magnetic fluxes may be probably the reason for the formation imagined as a small ring near the corona in Fig.2. This formation is located around the azimuthal periphery, winding around the rod circumference   0.5 – 1.5 times. It causes a pinch of the plasma corona, and an intensive plasma explosion in the area located in the opposite diameter of the rod.

A very important parameter for corona plasma   is its temperature. The temperature related to the velocity is higher than 2-5x10^4 m/s, and for a plasma pressure higher than10^8 – 10^9 Pa could be higher than 30   eV . This value, unrealistically higher than the emitted intensity evaluated for recombination processes [7], would be higher than the measured value 10^6 W. A real corona temperature of 2 - 3 eV was calculated from observed CII and OII lines. For an electron density of 10^{25} m^{-3} and for a temperature of 3 eV, from the Saha equation, the CII and OII ions can dominate. The dynamics of the corona plasma and the emitted radiation are governed by a strong non-thermal behavior.

When the line emission is induced by electron beams, accelerated during the transformation of the helical configurations, the energy of the electron beams is sufficient for OV and OVI generation but it is insufficient for CV and CVI ions.

References:[1] T.Kita, T.Harada, N.Nakano, H.Kuroda, Appl. Opt. 22, (1983), 512.[2] W.Schwanda, K.Eidmann, M.C.Richardson, J. of X-Ray Sci.Tech. 48 (1993),

[3] Ž.Andreić, L.Aschke, H-J.Kunze, J.Phys. D, Appl.Phys., to be published.

[4] P.Kubeš, J.Kravárik, Proc. Int. Conf. 4th Dense Z-pinches, Vancouver 1997, 449.

[5] R.L.Kelly, J.Phys.Chem. Ref. Data, 16, Suppl.1, 1987..

[6] L.Pína, private comunication.

[7] L.A.Arcimovitch, R.Z.Sagdeev, Fizika plazmy dlja fizikov, Moskow, Atomizdat 1979, 47.

OPERATIONAL MODE OF «COLD CATHODE» FLASH X-RAY TUBES WHICH PROVIDES SUBMILLIMETER FOCAL SPOT SIZE AND ELECTRON BEAM ENERGY ADJUSTING.

A. Dunaevsky*, K. Golubinsky, A. Lomako, O. Morgun

LRMT Ltd., P.O.B. 3025, Kharkov 310145, Ukraine
*Department of Physics, Technion, Haifa 32000, Israel

INTRODUCTION

From early times of compact pulse x-ray generators (PXG) with «cold cathode» flash x-ray tubes (CCXT) applications were made a lot of efforts to build a suitable equipment for needs of medical x-ray visualization. Moreover, in 1976 L.S. Birks [1] found that powerful pulse x-ray illumination of phosphor screens produce much more intense light yield and increase the quantum efficiency of the conversion of x-ray radiation to visible light. This phenomenon implemented in medical x-ray imaging could drastically reduce the patient dose loading, because only screen-film combinations are used for imaging in medicine at present.

Up to now, we find no reports of flash equipment systematic utilization in medical x-ray imaging and no descriptions of commercially available x-ray flash equipment for medical imaging. We suppose that is due to some major problems of PXG, which are unsolved at present to adapt it for medical needs. At first it is large focal spot size of existing CCXT, and at second it is the problem of x-ray energy control. PXG with less than 1 mm focal spot size during more than 500 000 shots and controlled x-ray energy could satisfy to medical imaging requirements.

In this paper we shall describe the operational mode of CCXT, which agrees with determined requirements of the medical imaging.

EXPERIMENTAL RESULTS

It is known that CCXT application requires a number of complicated technical problems to be solved mostly related with specific conditions of CCXT ignition. As a rule, it is necessary to apply a very sharp voltage pulse to form a plasma emitter due to quick electrode surface overheating from intense field emission. Anode-Cathode geometry of CCXT with small focal spot usually shows a kind of axial symmetry so the plasma emitter region and, correspondingly, the focal spot region is approximately circularly shaped.

Further, fast voltage raisetime is usually provided by a spark gap with fixed value of breakdown voltage. This voltage and its instability determine the dose of x-ray radiation and maximum of x-ray energy.

Below we shall describe an operational mode with different approach to CCXT ignition and emitting behaviors.

1. Voltage raisetime

In [2] we described a pulse voltage generator, which produces high voltage pulse with raise- and fall-time about of 50 ns and amplitude about of 200 kV on open circuit. During

investigations of 100 kV CCXT IMA6D produced by Svetlana-Rentgen, Russia, we found that the voltage raise-time accompanied with special generator loading characteristics provides no circular, but «point» focal spot in the place of smallest electrodes distance. We carry out a set of experiments, where CCXT x-ray emission was registered by a set of collimated p-i-n detectors SPPD3 (7 ns time resolution at 600 V bias voltage). Each collimator cuts an angle from CCXT emission area without overlapping and totally they cover the whole emission area. We clearly notice a «walking» of focal spot point around the focal spot size determined by the producer (about of ⌀2 mm). Moreover, we registered no occasions of two- or more point emissions. With the help of special CCD-based x-ray area sensor we estimate the upper limit of point-like focal spot size while obtaining digital pictures of spatial resolution grid. The upper limit of registered focal spot size is about of 200 μm.

However, this micro-focus operational mode requires very careful selection of CCXT current limiting technique. When a long voltage pulse is applied to CCXT there is a possibility of AC gap shortening by electrode plasma and thus a vacuum arc forming. If this occurs sequentially, intense erosion of tube electrodes will raise the tube ignition voltage and even totally destroy the tube. In Fig. 1a you can see IMA6D current in case of vacuum arc. To provide a safe tube operation we insert a time-limiting capacitor serially with the tube from the ground side. The IMA6D electron current with time-limiting capacitor is shown in Fig. 1b.
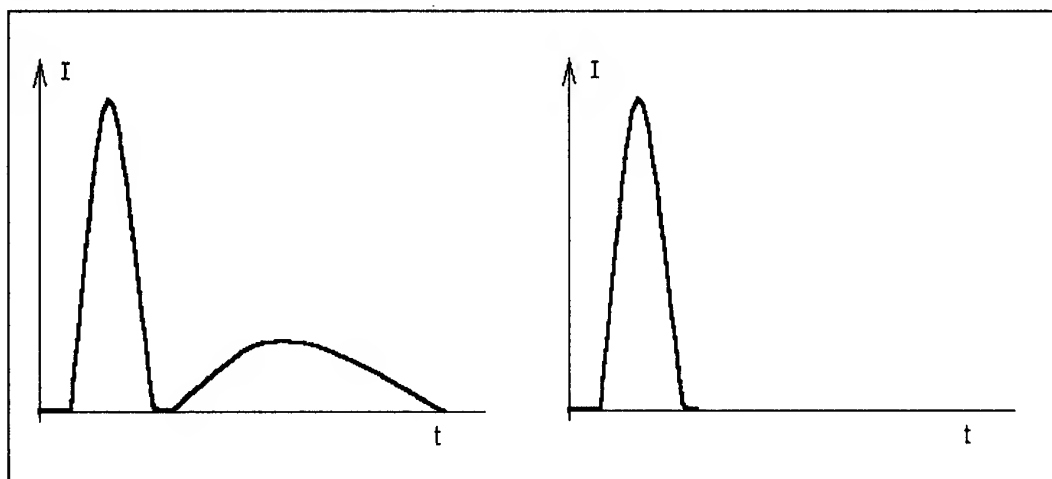
Figure 1a.   Figure 1b.

2. *X-ray energy*

CCXT micro-focus operational mode provides one more useful feature - x-ray energy could be controlled by means of easy changeable parameters.

Voltage pulse generator that was mentioned in Chapter 1 is an inductive storage device with solid-state opening switch. Initially the generator is loaded only on the tube capacitance. In such case it produces a voltage pulse with magnitude, which could be calculated by simply equation from primary capacitor voltage:

$$U_{OUT} = U_{PRIM} * K$$

where K = 6.

This means, that with 25-30 kV voltage at generator primary storage could produce voltage pulse which will be capable to «turn on» 100 kV IMA6D tube. Further, tube impedance is determined only by the behavior of explosive plasma in the anode-cathode gap

[3]. This means that after tube ignition the generator output voltage will fall down to the value that is determined by output load characteristic of the generator. Thus, adjusting solid-state switch pumping current by means of changing primary voltage we could adjust maximum x-ray quantum energy.

To prove the possibility of x-ray energy adjusting we successfully carried out a set of experiments, where CCXT emission was registered by a set of p-i-n detectors with filters of various thickness. X-ray energy was estimated using precalculated values of detector responses for various electron energies. After that we optimize generator parameters to provide 55-75 keV electron beam maximum energy adjusting with IMA6D CCXT to work in Digital Dental Diagnostic System DIRA.

X-ray yield measurements were carried out by three different diagnostics: TLD detectors, ionization chamber and soft energy p-i-n detectors SPPD3. The results shown excellent performance of the design: x-ray yield at 6 cm from the tube was found of 10 mR per single shot with instability less than 10 % under high voltage amplitude of 65 kV.

Conclusions

The micro-focus operational mode of «cold cathode» flash x-ray tubes is realized in order to provide some new advantages of CCXT utilization. They are - focal spot size reduction down to hundreds of micrometers and x-ray energy control by simple means. Compact pulse x-ray generators with micro-focus operational mode of CCXT completely satisfy to up-to-date digital visualization system, providing required resolution with lower yield of x-rays due to source-sample distance decreasing, high x-ray yield stability and x-ray energy controlling. This new properties and traditional benefits of flash generators such as small size and weight, high reliability and operational period, make this-mode-based flash x-ray generators very attractive for medical imaging applications.

References

1. L.S. Birks, J. W. Sandelin, C. M. Dozier. Calibration of Rare-Earth X-Ray Intensifying Screens in the 15-70 keV Energy Range For Use on Pulsed X-ray Sources, *Rev. Sci. Instrum.* 1976, V. 47, 12, pp.1475-1478.
2. A.Dunaevsky, K. Golubinsky, A. Lomako, O. Morgun, Compact pulse «cold cathode» flash x-ray tube power supply unit with solid-state opening switch, *Beams'98 proceedings*
3. R.B. Miller, *Intense Charged Particle Beams*, Plenum Press, New York, 1982

THE EXPERIMENTAL STUDY OF PLASMA PARAMETERS IN MAGO CHAMBER

V.K. Chernyshev, A.N. Demin, Yu.N. Dolin, V.I. Dudin, V.P. Korchagin, I.V. Morozov,
A.N. Subbotin, G.I. Volkov, P.L.Usenko

*Russian Federal Nuclear Centre,All-Russia Scientific Research Institute of Experimental
Physics,607190, Sarov, Russia.*

INTRODUCTION

The design and the working principles of the MAGO chamber (acronym for words "MAGnitnoe Obzhatie" in Russian, the same as "magnetic compression" in English) were firstly published in 1992 [1]. The chamber is a plasma gas-discharge device generating the thermonuclear neutrons.

The chamber is considered as a prospective object for the CTF concept realization: compression of a preliminary heated magnetized plasma (MAGO/MTF) [2]. MAGO/MTF is based on two main tenets. The first one is the use of a preliminary heating (up to the temperature of hundreds electron-volts) of DT-gas (plasma), the ensuring of a required heat insulation of the fuel and the confinement of the nuclear reactions charged products within the chamber volume. The second one is the use of a subsequent compression by a moving wall of a volume with a preliminary heated gas. Namely this preliminary heating allows to simplify the demands for the gas volume compression degree. In comparison with the inertial fusion the demands are 100 times lower. In the experiments the MAGO chamber was used, for the present, only as a device intended for plasma preliminary heating. The explosive magnetic generators with a stored energy of 1-10 MJ are used in the experiments as the sources of electromagnetic energy. The explosive magnetic generators (EMG) are the superpower sources of electric energy. The use of the explosives' energy allows to realize the parameters typical of the large expensive stationary capacitor facilities in the energy-production facilities having a relatively small size.

At present the explosive magnetic generators give a chance to carry out the research with the energy up to several hundred megajoules in the load.

OBJECT OF THE RESEARCH
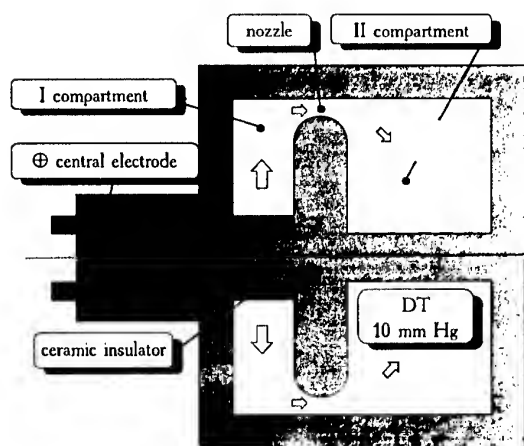
Fig. 1. Scheme of plasma chamber MAGO.

The scheme of the chamber is presented in Fig.1:

it is a hollow copper thick-wall cylinder 200 mm in inner diameter and 165 mm in length with a central electrode 60 mm in thickness separating the internal chamber space into two compartments (25 and 80 mm in height) connecting to each other with a narrow annular nozzle whose minimum width was 12 mm.

The vessel of the chamber with the central electrode constitutes a coaxial, short-circuited turn. The internal space of the chamber is filled with DT or DD-gas. At the

separated from the vessel with ceramic insulator 20 mm in outer radius. Initial gas pressure in the chamber is 10-20 mm Hg. In the chamber initial magnetic field was preliminary created through gradual increase of electric current in the short-circuited turn up to 1.5-2.2 million amperes. Then the current abruptly, during 1-3 microseconds, increased up to 10 MA.

During the abrupt current growth, according to the theoretic model, in the first chamber compartment, where the insulator is located, volume gas discharge occurs. Under the action of ponderomotive forces gas begins to flow out of the first chamber compartment to the second through the narrow nozzle. At the nozzle outlet the gas flow becomes supersonic. Plasma deceleration and heating occur in the second compartment of the chamber. In the hot plasma the thermonuclear reactions take place and stop in some time in consequence of hot plasma mixing with cold plasma.

In the first experiment, carried out in 1982, $2*10^7$ DD neutrons were obtained.
The following parameters were varied in the process of the research:
- dimensions of the first and the second chamber compartments;
- nozzle width; preliminary current magnitude;
- gas density;
- material of the chamber walls;
- current polarity.
The process resulted in the obtaining of $5*10^{13}$ neutrons on DT in a pulse of 2 μs duration and with a 200 mm diameter chamber, and $2*10^{11}$ neutrons with a 120 mm diameter chamber.
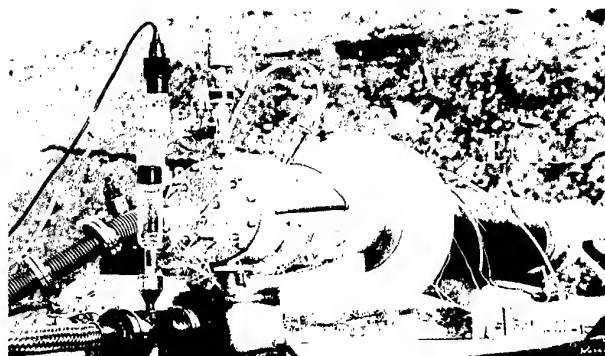
Fig2. 1 MJ facility.

Basic sources of information about the process parameters:
- Current probes;
- Voltage probe;
- Neutron measurements;
- Light probes;
- X-rays diodes with filters.

Due to collaboration with Los Alamos National Laboratory (LANL, USA) we got the information about the X radiation spectrum with time scanning taken from crystal spectrometer and the data about the electron density evolution of plasma.

Fig.2 and 3 give a general view of the experiment with EMG and MAGO chamber.

Chamber +EMG   Neutron imaging box

Neutron collimation wall
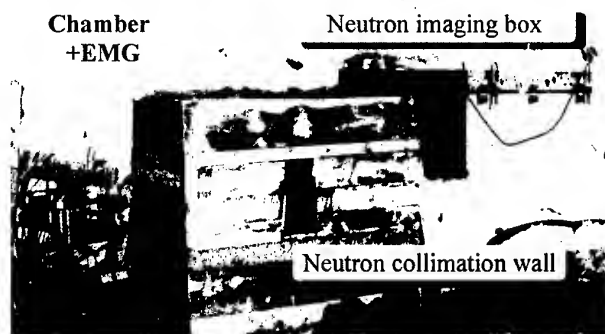
Fig. 3. Fire point equipment.

In more detail:
The current probes are located in the corners inside the chamber in special annular grooves. The location of the probes and the installation method are not casual: the probes introduction into plasma in these very points does not lead to worsening of plasma parameters. All the attempts to install the probes in plasma thickness lead to a sharp decrease of neutron yield in the chamber. The total number of oscillograms of current derivatives from the probes is up to 20 in one experiment.

The voltage measurements are made by a capacitive sensor only at the chamber inlet.

Neutron measurements are presented by an activation technique of the neutron yield and the average neutron energy measurements using a couple of indicators Cu/Mo and by a time of flight technique. An important results of neutron measurements is an establishment of the fact of a real isotropy of the energy of neutrons emitted in various directions. Average energy of neutrons emitted in various directions is practically constant and close to 14.1 MeV. The time integral image of the neutron source in neutrons was obtained by using pin-hole camera and bubble chamber. The photo of the source with the image of the chamber superimposed on the photo are shown in Fig.4.
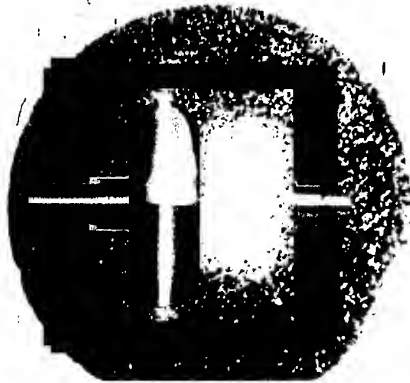
Fig.4 Neutron image.

The source of neutron is composed of two parts: 10% - a nozzle area, 90% - a central volume of the chamber's second compartment.

Light sensors are mainly used to estimate the symmetry of the discharge initiation inside the chamber.

The data about the X-radiation spectra were obtained mainly due to x-ray diodes with thin-film filters. This technique was used to estimate the lifetime and the electron temperature of the main plasma mass. In a hard part of the spectrum >0.5 keV the radiation is of pulse character, that strongly correlates with neutron radiation. In a soft part ~100 eV the radiation duration exceeds tens of microseconds.

Owing to collaboration with LANL (USA) the measurements of the x-ray spectra with high energy and time resolution were carried out. The measurements were performed by using crystal spectrometer with the registration done by the image converter. The principal objective of the experiment was to establish the presence or absence of considerable amount of admixtures in the plasma. The results of measurements showed a inessential radiation in the lines. Besides, owing to participation of the American specialists the data on plasma electron density were obtained (by using the lazer interferometry).

At present, the experimental data testify to the absence of obvious obstacles on the way of realization of a subsequent additional compression of plasma in the chamber of such a design.

SPECIFIC CHARACTER AND PROBLEMS OF DIAGNOSTICS.

1. The main distinctive feature of the experiments is the explosion character of the electromagnetic energy source operation. This not only gives the advantages but determines the main limit which is the use of only distance-type methods. The existing protection means allow to save the devices at the distance of 1 m from the chamber. Nevertheless, we should not neglect the risk to lose the expensive equipment. The advantage of EMG is in the absence of energy limitation and in the exceptional "purity" of the current signals form. It helps to easily and exactly interpret any peculiarities in the current sensors oscillograms (unlike the records of oscillating processes in the capacitor banks with transmission lines).

2. Hot plasma occupies almost the total volume of the second compartment that causes the difficulties in observation of the process in the chamber upon the whole. The diagnostic holes give a possibility to observe only small volumes of the chamber. The situations reminds a well-known parable which tells about the attempts to describe the elephant using the descriptions of its separate parts: the legs, the trunk, the tail, etc...

3. Probes introduction inside the plasma volume destroys the plasma. All the attempts to introduce the current sensors inside plasma led to a sharp decrease of neutron yield.

THE MAGO PLASMA DIAGNOSTICS DEVELOPMENT PLANS.

A series of experiments aimed at verification of scenario MAGO process in the chamber is expected to be carried out. Today a notion about the starting conditions and about the introduction of new processes is of hypothetical character. The measurements are planned to be conducted with a great number of current sensors located on the chamber surface.

The second trend is the introduction of the technique of the sequence (frame by frame) recording of plasma image in the X-rays. We suppose to have several frames of hot plasma image in several parts of the spectrum, i.e. an attempt will be made to record the whole process but not its fragments.

Of course, any other ideas concerning the diagnostics that may advance us in understanding of the processes going on in MAGO chamber will be welcome.

REFERENCES

1. Buyko A.M., Chernyshev V.K., Demidov V.A., Dolin Yu.N., Garanin S.F., Ivanov V.A., Korchagin V.P., Lartsev M.V., Mamyshev V.I., Mokhov V.N., Mochalov A.P., Morozov I.V., Moskvichev N.N., Pavlovskii E.S., Pak S.V., Trusillo S.V., Volkov G.I., Yakubov V.B., Zmushko V.V., «Studying of a feasibility to form thermonuclear magnetized plasma in the magnetic compression system MAGO», 3-d Zababakhin Scientific Readings, Kyshtym, Russia, January 1992.
Digest of Technical Papers: Proc. IX IEEE International Pulsed Power Conf., edited by K. Prestwich and W. Baker, Institute of Electrical and Electronics Engineers, New York, V. I, pp. 156-162, 1993. ДАН, т. 344, №3, с. 323-327, 1995.

2. Lindemuth I.R., Reinovsky R.E., Chrien R.E., Christian J.M., Ekdahl C.A., Goforth J.N., Haight R.C., Idzorek G., King N.S., Kirkpatrick R.C., Larson R.E, Morgan G.L., Olinger B.W., Oona H., Sheehey P.T., Shlachter J.S., Smith R.C., Veeser L.R., Warthen B.J. Younger S.M., Chernyshev V.K., Mokhov V.N., Demin A.N., Dolin Y.N., Garanin S.F., Ivanov V.A., Pak S.V., Morozov I.V., Korchagin V.P., Pavlovskii E.S., Seleznev N.Y., Skobelev A.N., Volkov G.I., Yakubov V.B., «Target plasma formation for Magnetic Compression/Magnetized Target Fusion (MAGO/MTF)», Phys. Rev. Lett. V. 75, No. 10, p. 1953, 1995.

Neutral Atoms Influence on the dynamics of Z-Pinch Capillary Discharge X-ray laser

R. Nemirovsky, A.Ben-Kish, M. Shuker, A. Ron

Technion - Israel Institute of Technology, Technion City, Haifa, 32000, Israel

Abstract. We investigate the dynamics of Z-pinch Ar plasma using a one-dimensional magneto-hydrodynamics (MHD) code, in a regime for which a large soft-x-ray amplification has been observed and reported [1]. While some of the model's numerical results are in good agreement with the experimental data, other features are not. Achieving better agreement with the experimental data requires some major adjustments in the plasma parameters relative to their classical values (as has been reported in previous works).
We attribute some of the discrepancies to the high percentage of neutral atoms in the plasma. Therefore we suggest to extend the standard MHD model, by introducing a neutral-species fluid, in addition to the charged-species fluid (ions and electrons).

INTRODUCTION

In a recent work by Rocca et. al. [1,2] large amplification of XUV light was demonstrated in Ne-like Ar and S plasma, created by a fast (~ 40 ns) capillary discharge Z-pinch. This Z-pinch, with length to diameter L/D≈ 50-500, was shown to have a remarkable stability. Therefore, modeling this type of experiment is usually performed using 1-D MHD codes, combined with atomic physics models, in order to calculate ionization abundance and electron population [3-5]. These codes are highly complicated, and usually contain a large number of physical effects, some of them of second order. Despite this, agreement with the experimentally measured data is still achieved in a phenomenological way, by some major adjustments in plasma transport parameters (up to 40 times their classical values) [3].

In this work we present MHD numerical calculations for a Z-pinch capillary discharge with parameters as in [1-3]. Our study points out that, in this regime, the standard MHD model might be inadequate, since it neglects the special effect of neutral atoms. This may suggest an explanation for the discrepancies found between theory and experiments.

PHYSICAL AND NUMERICAL MODEL

We start with a standard one-fluid two-temperature 1-D MHD model, similar to that used in previous numerical calculations [3-5]. It considers hydrodynamic flow including shock waves, heat conduction, heat exchange (between ions and electrons), magnetic field dynamics, magnetic forces, ohmic heating, radiative cooling and ionization. The MHD model assumes local charge neutrality (the ions and electrons flow together), and neglects the displacement currents as well as the neutral atoms in the plasma [6]. For the regime discussed here these assumptions are reasonable, except for the one neglecting the neutral component, as will be shown later on. Under these assumptions, the equations of motion of the system (see [3-6]) are solved implicitly in a lagrangean mesh. We use a simple ionization model and assume a quasi steady state, taking into account collisional ionization, and 2-Body and 3-Body recombination. Ionization and excitation by radiation is neglected, since we assume an optically thin plasma. The latter assumption should hold at least to the end of the collapse.

NUMERICAL RESULTS

The model described above was used to calculate Ar Z-pinch inside a plastic capillary. The initial and boundary conditions (after an ionizing pre-pulse) were [3]:

1. Electric current: $I(t) = I_0 \cdot sin(2\pi t/\tau_0)$, $I_0 = 39kA$, $\tau_0 = 64$ ns
2. Argon: $\rho_0 = 1.7 \cdot 10^{-6}$ gram/cm^3, $n_0 \approx 2.5 \cdot 10^{16}$ 1/cm^3, $T_0 \approx 0.5$ eV, $Z_0 = 0.1$.
3. Plastic wall: $\rho_0 \approx 1$ gram/cm^3, A = 14 (Mean atomic mass), $T_0 < 0.1$ eV, $Z_0 = 10^{-2}$.

Figure 1 (a): Electron Density – $log_{10}(n_e)$

Figure 1 (b): Electron Temp. (T$_e$) [eV]

Figure 1 (c): Mean ionization (Z$_{mean}$)

Figure 1 (d): Current Density (J$_z$) [MA/cm^2]
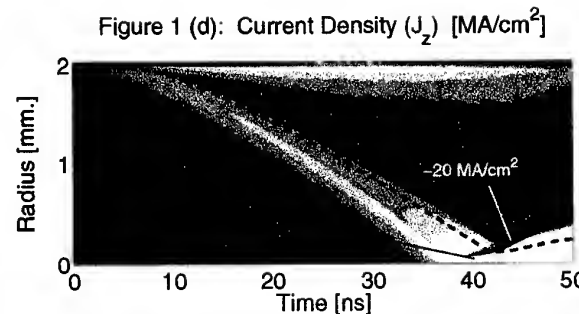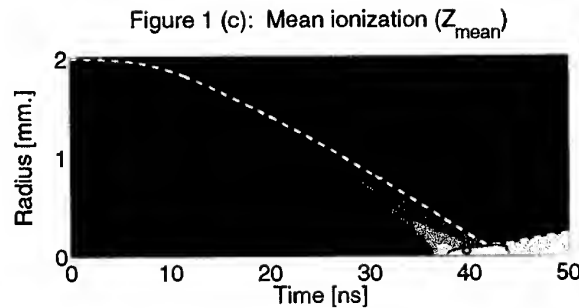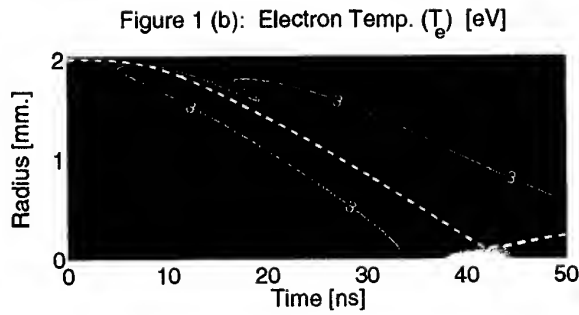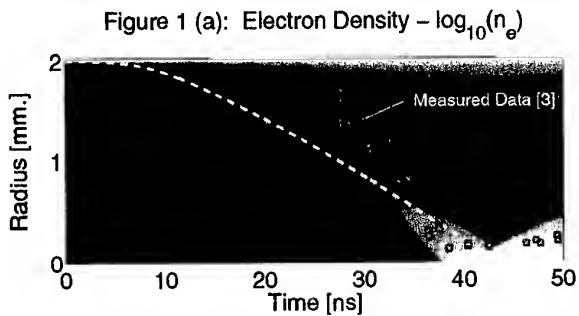
Results of these calculations are depicted in figures 1 (a)-(d). The figures display electron density, electron temperature, mean ionization and current density, respectively. During the pinch, the plastic capillary wall heats up, ablates and gets ionized. The boundary between the Argon and the ablated plastic is shown as a thick dotted line in the figures. Figure 1 (a) also presents experimentally measured data, obtained by Rocca et al. [3], of the radius of emitting plasma (below 300Å) as a function of time. The agreement between the measured and calculated pinch times was obtained by multiplying the classical electrical conductivity [7] by a factor of 15 (calculations made without this factor, resulted in a faster pinch, with its peak about 5 ns earlier). The state of the Argon plasma at the peak of the collapse is in good agreement with measured data: electron density of $5 \cdot 10^{19}$cm^{-3}, electron temperature of 65 eV, and mean ionization of about 8 (Ne-like Ar). However, some other features of the calculated results do not agree with the measured data. From figure 1 (a) it is clear that in practice the plasma collapse starts later and goes faster, compared to the calculation. Experimental compression velocity ~3 times higher implies that the kinetic energy is ~10 times greater, and as a consequence ion temperature at stagnation should be higher as well. According to [3], getting full agreement between the calculations and the experiments requires more artificial adjustments in the plasma transport parameters, up to 20-40 times their classical values.

Figure 1 (d) presents the calculated current density in the plasma during the pinch (the grayscales range was chosen to show maximum details, so it does not cover the whole range

of values achieved - ±20MA/cm² at the center of the pinch). According to figure 1 (d) the current flows mainly in the outer shells of the ablated wall plasma, and as a current sheath along the shock wave in the Ar plasma. It seems that the main effect of the wall is to keep most of the current out of the Ar plasma, and therefore to delay the pinch time. Figure 1 (d) also shows that after the collapse of the shock wave on the capillary axis, there is a narrow region where the current density changes sign (however with the same total current supplied by the power source). This effect is a result of a compression of the magnetic field in that region, and serves as one of the mechanisms (in addition to adiabatic and shock compression) for transforming the kinetic energy of the collapsing plasma to thermal energy at stagnation.

THE NEED FOR NEUTRAL FLUID

We suggest that the discrepancies between theory and practice, mentioned above, may be attributed to one of the model's assumptions - neglecting the neutral species in the plasma. Figures 2 (a) and (b) present the percentage of neutral atoms as a function of electron temperature, based on our ionization model, in Ar and C plasma, respectively (Carbon represents the plastic capillary wall). According to these figures, plasma of electron temperature lower than ~3 eV contains an appreciable amount of neutrals. From the solid white line in figure 1 (b) we also note that the Ar plasma starts to heat up above 3 eV only ~5 ns after the beginning of the pinch, and its central part stays below this temperature for the next 25 ns. Major portion of the plastic wall plasma remain below 3 eV even after the pinch collapse at the axis. Hence, the plasma is mostly neutral at the first stages of the collapse. The ablated wall material remains mostly neutral even longer, to the last stages of the collapse.

Figure 2 (a): % Neutrals in Ar plasma

Figure 2 (b): % Neutrals in C plasma
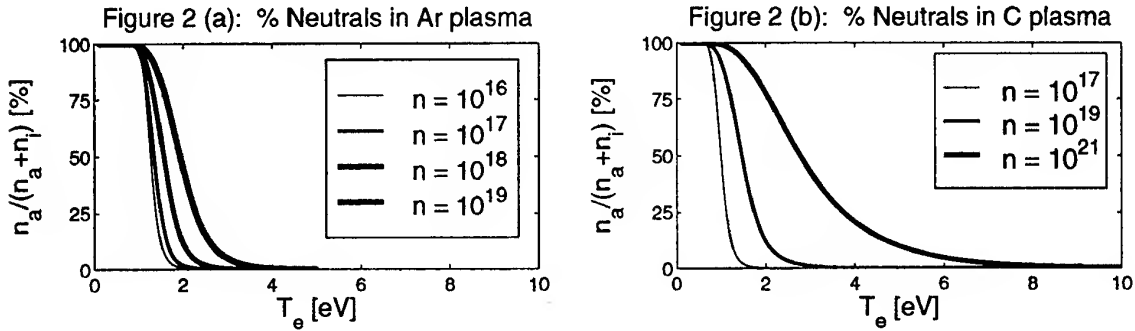
Since neutral atoms are not affected by magnetic forces, but only by the much weaker mechanical forces, they are expected to flow differently. To account for this effect we suggest to introduce a neutral-species fluid, in addition to the standard charged-species fluid (ions and electrons). The momentum equations for the two fluids are [6]:

(1)
$$\rho_i \frac{d}{dt} u_i = -\nabla(P_e + P_i) + \frac{\vec{j} \times \vec{B}}{c} - Coupling\ Term$$

(2)
$$\rho_a \frac{d}{dt} u_a = -\nabla(P_a) + Coupling\ Term$$

Where ρ stands for density, u for particle velocity, P for pressure, j for current density and B for the magnetic field. The indices e, i, a refer to electron, ions and atoms respectively.

Figures 3 (a) and (b) present an estimate for the forces that are expected to act on the charged and neutral fluids during the pinch, respectively. The grayscales are again limited

Figure 3 (a): JxB/c – grad(P_e + P_i) [dyn/cm^3]

Figure 3 (b): – grad(P_a) [dyn/cm^3]
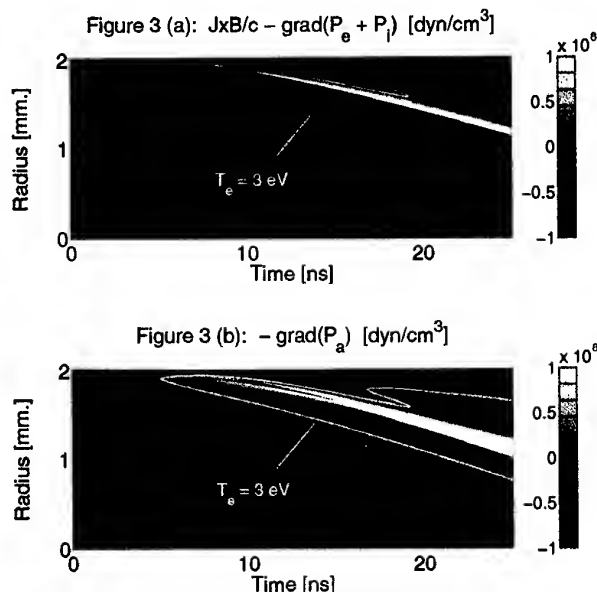
only to a small part of the total range, in order to clarify the details. It is clear that there are significant differences between the forces on the two fluids, particularly in regions where the plasma is colder than 3 eV (the solid white line), i.e. where the plasma may contain a significant amount of neutral atoms. The maximal difference between the forces on the two fluids in regions of cold plasma, obtained in this calculation, exceeds 10^9 dyn/cm^3 (not seen in figures 3 because of the limited scales).

The coupling term in equations (1) and (2) describes the momentum exchange due to collisions between the atoms and ions fluids, and due to exchange of particles between the two fluids (by ionization and recombination). Neglecting the latter effect (since we are dealing with a very cold plasma), we can estimate the collisional momentum transfer, by assuming hard spheres approximation. In that case, the collision frequency per unit volume equals $\alpha \cdot r_a^2 \cdot n_a \cdot n_i \cdot |u_a - u_i|$, and the momentum transfer rate per unit volume is thus $\alpha \cdot r_a^2 \cdot m_a \cdot n_a \cdot n_i \cdot (u_a - u_i)^2$, where α is coefficient of about 8. Here r_a is the atom radius, m_a it's mass, n_a, n_i are the number densities of atoms and ions respectively, and u_a, u_i their flow velocities. Assuming $n_a \approx 10^{16}$, $n_i \approx 10^{15}$ (10% ionization), and $|u_a - u_i| \approx 10^6$ cm/s we get for Ar plasma a coupling term of the order of 10^6 dyn/cm^3, i.e. very weak coupling, 2-3 orders of magnitude less than the difference between the forces.

CONCLUSIONS

Our numerical results agree with the MHD calculations, e.g. [3,4]. In particular, we agree with the conclusion that in the framework of the standard MHD model, good agreement with the experimentally measured data can be achieved only by some artificial adjustments in plasma transport parameters [3]. However, our work points out that neglecting the neutral component in the plasma may be unjustified for the regime discussed in [1-4]. Large portions of the plasma contain a significant amount of neutral atoms, which are expected to have different flow velocities, than the charged-species fluid. Introducing a neutral-species fluid to the model seems to be important, and may bring to better agreement with the experiments.

REFERENCES

[1] J. J. Rocca, V. N. Shlyaptsev, F. G. Tomasel, O. D. Cortazar, D. Hartshorn, J. L.A. Chilla, *Phys. Rev. Lett.* **73**, pp. 2192 (1994).

[2] F. G. Tomasel, J. J. Rocca, V. N. Shlyaptsev, C. D. Macchietto, *Phys. Rev. A.*, **55** (2), pp. 1437-1440 (1997).

[3] V.N. Shlyaptsev, J. J. Rocca, A. L. Osterheld, SPIE J., **2520**, pp. 365-372 (1995).

[4] N. A. Bobrova, S. V. Bulanov, T. L. Razinkova, P. V. Sasorov, *Plasma Phys. Rep.*, **22**, pp. 349-362 (1996).

[5] K. T. Lee, S. H. Kim, D. Kim, T. N. Lee, *Physics of Plasmas*, **3** (4), pp. 1340-1347 (1996).

[6] N. A. Krall, A. W. Trivelpiece "Principles of Plasma Physics", McGRAW-Hill, Inc. (1973).

[7] S. I. Braginskii, in *Review of Plasma Physics*, edited by M. A. Leontovich, **1**, pp. 216 (1965).

PULSED HIGH-VOLTAGE SOURCE BASED ON HELICAL MCG FOR POWER SUPPLY OF HIGH-CURRENT REB ACCELERATORS

E.V.Chernikh, V.E.Fortov, K.V.Gorbachev, E.V.Nesterov,
S.A.Roschupkin, V.A.Stroganov, I.O.Zolotikh

*High Energy Density Research Centre, Russian Academy of Sciences,
IVTAN, Izhorskaja St. 13/19, Moscow, 127412, Russia*

INTRODUCTION

At present, the creation of compact sources for power supply of high-current accelerators is connected with MCG usage. In spite of considerable progress in creation of capacitors with high specific characteristics, the capacitive storages are not competitive with MCG when energies of generated pulse are higher than several kJ.

On the basis of the experience collected in HEDRC for a long time of design and experimental investigations of high-current REB accelerators supplied by MCG and literature analysis as well, the design of self-contained high voltage source (SCHVS) have been accomplished with following characteristics:

Resistance of the load	2 Ohm
Inductance of the load	100 nHn
Voltage height U_m	450 kV
Pulse length at 0.8 U_m	200 ns
Voltage rise-time 0.1–0.9 U_m	$\leq$ 540 ns
Maximum power	80 GW
Pulse energy	$\sim$ 20 kJ.

PRELIMINARY CHOICE OF CHARACTERISTICS OF SELF-CONTAINED PULSED HIGH-VOLTAGE SOURCE BASED ON MCG

First of all, it is worth mention, that the usage of intermediate inductive storage of energy (IS) for generation of high voltage pulse has no alternative for compact SCHVS based on MCG, as well as a choice of electrically exploded wires as an opening switch (EEOS) is beyond any doubt. This is why, for preliminary choice of SCHVS characteristics the simplest electrical circuit with inductive storage was used (fig.1).
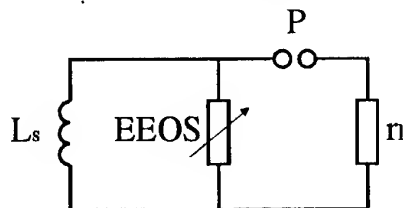
Fig.1. Circuit diagram for calculation of pulse characteristics generated with help of inductive storage and EEOS.

For EEOS description, the simulation model with exponential growth of interrupter resistance was used:

$$R(t) = R_0 \exp (\beta t), \tag{1}$$

where b – resistance growth increment, R_0 – EEOS resistance at the moment of heating stage termination, when the current action integral is equal to $Y = \int_0^t j^2 dt = Y_c$, where $j = I/S$ and

$$S = \frac{n\pi d^2}{4}, n - \text{number of fuses}, d - \text{their diameter. For copper } Y_c = 2*10^{17} \text{ A}^2\text{s/m}^4.$$

The ideal discharger P is switched on at the moment $t = 0$ when the current I_m in IS is a maximum. It is easy to derive $U=U(t)$ when $dR/dt = \beta R$ is valid at current breaking. Maximum voltage

$$U_m = L_s I_m \beta \left(\frac{\alpha}{\alpha+1}\right)^{\alpha+1}\left(1+\frac{R_0}{r_l}\right)^\alpha ; \tag{2}$$

is reached at the moment $t_{\max} = \frac{1}{\beta}\ln\frac{L\beta}{R_0}$, where $\alpha = \frac{\eta}{\beta L_s}$. $\tag{3}$

EEOS model was complemented with condition for electrical strength of explosion products $U_m < E_m * l$: the peak voltage across EEOS must be less than breakdown voltage of explosion products. We used the semiempirical model [1], where both breakdown voltage and resistance increment β are the functions of parameter called by authors as "reduced heating rate" $j^2 d$. At the explosion stage the increment of EEOS resistance growth is:

$$\beta = \frac{v_0}{d}\exp\left(-\frac{B_1}{j_R^2 d}\right) \tag{4}$$

where j_R – current density at the instance of start of explosion. The maximum electric strength of EEW is:

$$E_m = \frac{A}{\sqrt{d}}\exp\left(-\frac{B_2}{j_R^2 d}\right) \tag{5}$$

Here v_0, B_2, B_1, A – constants determined by the experiment. Representing j^2 as

$$j^2 = Y_c / k_f t_b, \text{ where } k_f = \frac{\int_0^{t_b} I^2 dt}{I^2 t_b} - \text{form-factor of current pulse, } t_{ef} = k_f * t_b - \text{effective time}$$

of wire heating, one can obtain

$$d_{opt}^\beta = \frac{B_1 k_f t_b}{Y} \text{ and } \beta_{opt} = \frac{v_0 Y}{k B_1 e t_b}. \tag{6}, (7)$$

From the energy balance equation written for the circuit in fig.1: $W_m + W_s = W_0 \, k_e k_t$, where W_0– the energy spent for generation of initial magnetic flux in MCG, k_e – MCG energy gain, k_t– energy transfer to IS ratio, $W_m = I_m^2 L_s / 2$ – magnetic field energy stored in IS up to the instance of load connection, W_s – losses in interrupter, one can derive the optimum L_s value:

$$L_s = 0.093 \, r_l \, t_{ef} \text{ [mH]}, \tag{9}$$

corresponding to the minimum in energy

$$(W_m + W_s) = 0.275 \, Ð \, t_{ef} \text{ [J]}. \tag{10}$$

For given L_s values the direct power supply of IS with MCG current is absolutely impossible. For MCG matching to high-inductive storage it is necessary to use pulse

transformer (PT) (Fig.2). It is easy to show that the losses of energy will be minimised when the transformer integrates the services of both matching unit and inductive storage – so-called transformer inductive storage of energy (TIS). This is followed by $L_s = L_2 (1 - k_c^2)$, where L_2 – inductance of secondary winding of transformer, k_c – coupling coefficient of PT windings. To eliminate the losses during energy transfer from MCG to PT connected with stray inductance of coupling line L_p, PT and MCG both are integrated into one unit (transformer MCG).
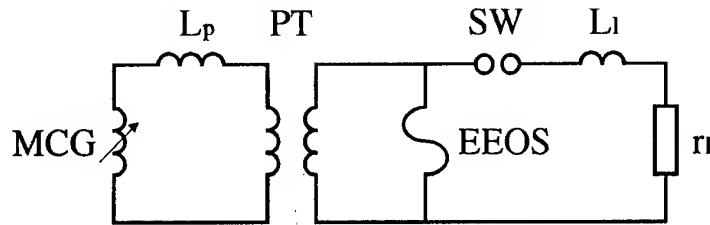
Fig.2. Schematic of SCHVS with transformer inductive storage.

For reduction of t_{ef} it is possible to connect the power peaker between PT and MCG, for example, an explosive breaker (EB), that is, to implement the two-stages way of power peaking. Apparently, this is the most effective conversion circuit design. Indeed, EB allows to achieve $t_{ef} \cong 1$ ms for IS, moreover, the most important fact is that $k_t = k_c^2$ – is much higher than without EB. The matter is that interruption of current flowing through the primary winding prevent from reversal energy transfer into primary winding circuit at EEOS operation.
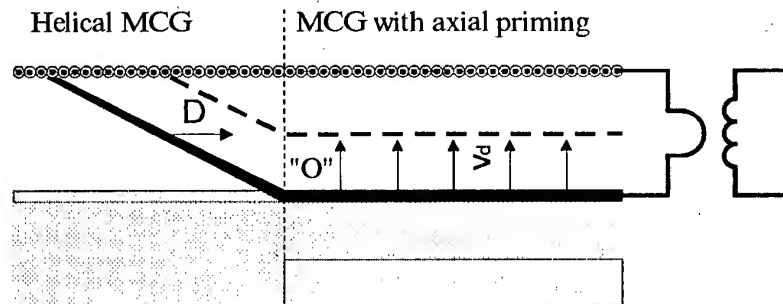
Fig.3. Schematic of MCG with axial priming in the last stage.

Alternative way of t_{ef} reduction – the use of axial priming of HE in the last section of MCG (Fig.3). The first stages of such MCG operate as in usual MCG with face priming. When detonation wave close in on the point "O" corresponding to the boundary of the last section, the simultaneous priming of HE along the axis takes place to shape the detonation wave to be smooth cylindrical when reaching the armature surface. Such procedure allows to reduce sharply the operation time of the last stage as well as effective operation time of MCG itself.

RESULTS OF CALCULATIONS

By use of the above method of optimisation we have made multi-tradeoff calculations of proposed circuit. The calculation technique for the first four sections of attached MCG design is drawn upon [3]. The calculations of the fast-run last stage of MCG were made with usage of data abstracted from [4]. The exponential decay of voltage was used for discharger simulations. Calculations have shown the necessity of employment of two spiral MCG with an axial priming in the last stages. The most characteristic initial and output properties of the system are given in the table:

Peak MCG current	2.6 MA
Duration of MCG work before EEOS operation	66 ms
Initial inductance of MCG pair	40 mH
Inductance of primary PT winding	0.14 mH
Inductance of secondary PT winding	5 mH
Diameter of EEOS wires	0.15 mm
Length of EEOS wires	600 mm
Number of EEOS wires	60
Effective time of MCG operation	3.8 ms
Peak current through EEOS	0.297 MA
Peak voltage across the load	436 kV
Maximum current through the load	0.209 MA
Peak power delivered to the load	88.1 GW
Length of voltage pulse at 0.8 U_m height ($t^{0.8}$)	215 ns
The rate of voltage growth from 0.1 U_m to 0.9 U_m	50 ns

SCHVS DESIGN

The following main units are included as compounds of a source: IS with explosive commutator for generation of initial magnetic field for MCG excitation; axial priming system for the final MCG stage; two spiral MCGs with windings connected in series, supplied with systems for axial priming of HE charges in the last stage of the helices; the system for generation of high-voltage pulse; pulsed transformer storage.

Helical MCG consists of multi-turn helix and an armature tube filled with HE charge. The helix has four sections, the first of which is winded with two insulated wires 2.5 mm in diameter (has two starts). The next two sections double the number of wires (the number of starts of the winding), and the last section triple the number of starts. The armature is made of copper tube with outer diameter 40 mm and the wall width 2 mm.

The pulse transformer is a coil-type one. The primary winding of transformer is a copper ring. Inside the ring the secondary winding is placed winded with a thin foil having the same width as a primary winding. Inter-turn insulation consists of a few layers of lavsan film and capacitor paper impregnated with a liquid dielectric.

The high voltage generation unit is made in kind of hermetically sealed stainless steel container filled with transformer oil where EEOS case and sharpening discharger are situated.

REFERENCES

[1]. Azarkevich E.I., Kotov Yu.A. Raschet electrovzryvnogo kaskada dvyxkaskadnogo preryvatelya toka. ("Design of explosive stage of two-stages current interrupter") // in: *Abst. of reports of cooperative shop of sections of science soviets of AS SU*, Tomsk,1986, p.111 (in Russian).

[2]. Boryskin A.S., Brodsky A.Ya. Eksperimentalnie issledovania po generatsii electronnogo pouchka na vzryvnom electrofizicheskom stende ("Experimental study of electron beam generation at explosive electrophysical installation"). // *Book of Abstracts MG-VII*, p. 132.

[3]. Pavlovsky A.I., Luidaev R.Z. et al. Mnogosectsionnyi generator MK–2. ("Multistage generator MK–2") //In: *Sverkhsilnie magnitnie polya. Fizika. Tekhnika. Primenenie.*, Nauka, 1984, p. 312 (in Russian).

[4]. Zharinov E.I., Demidov V.A., Chernyshov V.K. Predelnie vozmozhnosti koaksialnix VMG s osevim initsiirovaniem zaryada. ("Extreme capabilities of coaxial MCG with axial priming of HE") // *See [3]*, p. 298 (in Russian).

THE STUDY OF VARIABLE MASS LINER ACCELERATION IN ORDER TO CREATE THE SOURCE OF SOFT X-RAYS.

A.M. Bujko, V.K. Chernyshev, S.F. Garanin, Y.N. Gorbachev, V.A. Demidov,
G.G. Ivanova, V.N. Kostyukov, S.D. Kuznetsov, A.I. Kuzyaev, A.B. Mezhevov,
V.N. Mokhov, A.A. Petrukhin, V.N. Sofronov, A.I. Startsev, V.B. Yakubov

*All-Russia Scientific Institute of Experimental Physics,
607200, Sarov (Arzamas-16), N.Novgorod region, Russia*

B.G. Anderson, C.A. Ekdahl, J.L. Kammerdiener, I.R. Lindemuth,
R.E. Reinovsky, P.J. Rodriguez, L.R. Veeser, S.M. Younger,
W.D. Zerwekh, D.A. Poling, R.C. Kirkpatrick

Los-Alamos National Laboratory, New Mexico, USA

T.J. Englert, G.F. Kiuttu

Phillips Laboratory, Albuquerque, New Mexico, USA

INTRODUCTION

High power pulsed energy sources are required to produce large amount of X-rays. The leading role in creation of ultra-high power stationary machines belongs to the USA National laboratories.

VNIIEF has made much progress in creation of ultra-high power explosive magnetic generators (EMG) of a single action, which allow experiments up to 200 MJ of the stored energy and up to 10^{13} W of the power in the load [1].

Estimations show, that the shot cost on the stationary machine with the stored energy of ~100 MJ is higher than the experiment with EMG.

Relatively soft X-ray (quantum energy is about 0.3 keV) may be produced by acceleration and the following deceleration of the liner or plasma cluster up to a velocity of v ~300 km/s. That means that if the plasma cluster acceleration way is several cm, the time of plasma motion must be about 0.1 of a microsecond. This results in a difficulty, associated with the problem of plasma stability and the liner having low thickness and very small initial thickness and density tolerance. Besides, quick energy input into the load requires complicated fast opening switches, which need to be experimentally tested [2].

In experiments with EMG it is reasonable to have more simple systems to reach mass velocities about 300 km/s. The paper [3] theoretically considers one of these systems, where a liner mass during its magnetic acceleration significantly decreases and the velocity increases, i.e., a variable mass liner (VML). The same paper suggests two experimental designs to test a new concept: full-scale experiment, including X-rays generation and a model experiment, including testing of the initial stage of VML formation (v<100 km/s).

The current paper describes the first model experiment design and results (joint experiment "X-Ray-1" between Russia and the USA, 1995, VNIIEF).

1. EXPERIMENTAL LOAD OPERATION STAGES

A 5-module DEMG having a diameter of 40 cm and powered by a helical EMG was used to power a ponderomotive unit (PU) in the model experiment «X-ray-1».

Fig.1 schematically shows the load operation stages. At the first stage of operation during tens of microseconds up to the moment, when DEMG reaches the current maximum, the liner-switch serves as a load. Liner was fabricated of aluminum (alloy AMg6, σ_f =15 kg/mm^2, ρ=2,64g/cm^3, σ_0 =1,4×10^5 (Ohm×cm)$^{-1}$). The initial parameters were: thickness d=0.5 mm, radius r_0 =196.6 mm (m=16.7 g/cm) and length l_0 =50 mm. This experiment did not applied methods to deliver current to the liner in a highly symmetrical way, initial electrical contact between the liner and the wall was provided very simply: the liner was seated conically on the electrodes (the angle ~12° relatively to the liner axis).

Figure 1. Generation of a Plasma Bubble
The figure shows one half of a cross section through a cylindrically symmetric chamber. a) Current begins to run through the thick aluminum liner. The current generates a magnetic field and the magnetic pressure accelerates the liner inward toward the clipper. b) At peak current, the liner moves past the clipper. The break in electrical continuity causes a "spark," or an arc of plasma, to form between the liner and the wall. c) The magnetic pressure expands the plasma arc into a "bubble." Due to its low mass, the bubble rapidly accelerates towards the implosion axis (the axis of symmetry). d) The remainder of the slow-moving heavy liner stays behind while the bubble races inward. Upon reaching the implosion axis, the plasma collides with plasma coming from other sides of the chamber, stagnates, and emits x rays as it cools.

At the second stage of facility operation the liner breaks loose with the current conductive wall. The high-current arc discharge appears in the gap between the liner edge and the wall. The arc of plasma, effected by the magnetic pressure goes through the gap under the liner. This process reminds blowing up the "bubble" of a toroidal shape, in which the real surface will be only its portion in space under the condensed liner. Mass per square unity in the "bubble" will decrease in the process of its blowing up. Both speed and acceleration increase. Initial mass of the plasma arc is significantly less than that of the condensed liner. In the experiment, which studied the liner opening switch [4], the aluminium liner ~0.7 mm thick was accelerated up to a velocity of ~10 km/s, the maximum current was ~70 MA, arc mass was from 2 to 5g.

To decrease wall effects, associated with the properties of strength and elasticity of liner and wall materials, the liner (in a liquid state) was cut by a "clipper" as a result of that the current arc was formed at a liner portion with less perturbation. The minimum "clipper" radius R_{ext}=171 mm was chosen based on the consideration that the liner sliding of the

"clipper" was in a condensed state, not reaching the boiling point (q<2 kJ/g), not to increase the mass of the plasma arc. The height of the clipper was 1 cm. Thick "clipper" provided attenuation of a shock wave caused by the liner impact, and consequently the higher speed **u** of the increase of the gap between the clipper and the condensed liner after the arc of plasma was formed. To provide additional attenuation of shock waves the impact area between the "clipper" and the liner was covered by a layer of foam having a density of ~0,5 g/cm^3. That gave us hope that unloading and spall effects at the inner surface of the clipper would be less dangerous in terms of increase of plasma arc mass.

"X-Ray-1" experiment was designed in such a way that the slow balk liner (~ 6 km/s, M_l~100 g) could operate as a fast opening switch, the "bubble", which was formed had significantly less mass (M_b<10 g). The experiment planned to study only the initial stage of plasma shell formation and flight. Consequently the accelerated chamber had low vacuum (P_0~0,02 mm Hg), a central measuring unit (CMU) was located at the R_f=100 mm. CMU surface shape was made close to the calculated shape of the "bubble".

Current derivatives in the EMG units (VNIIEF measurements), voltage (VNIIEF) and voltage derivative (PL) in the transmission line from DEMG to the load, voltage at the CMU (PL) were registered in the experiment. VNIIEF probes were located at the walls of the accelerated chamber in the load: at the left side wall in three uniformly distributed azimuthal sectors the open light probes (LW#1-6) were located at the radii R=156 mm and R=107,5 mm and directed along the chamber axis; while at the right wall there were located the inductive B-dot probes IL at the radius R=165 mm, IBW at the radii R=160 mm and R=122 mm, and the light probes LW #13-24 at R=160 mm (directed along the chamber axis) and R=122 mm (directed perpendicular to the wall). Three groups of LANL inductive probes were installed above the CMU surface at R=105 mm and in 120° along the azimuth: A_1-A_5, B_1-B_5, C_1-C_5. A big variety of VNIIEF probes was located in the CMU: open light collimated probes Lk #1, 2 facing the clipper, non-collimated probes LMU #1-12, manganine probes, etc., and besides that LANL light probes.

2. BASIC EXPERIMENTAL RESULTS

DEMG was powered by the current 7.7 MA (t=105 μs after HEMG started its operation) with the maximum current derivative 0.21 MA/μs. DEMG produced in the load the current pulse with the amplitude 64,4 MA (t=27,9 μs) with the maximum current derivative of about 0,98x10^{13} A/s (t=25,65 μs). Fig.2 presents experimental values of the current derivative and current in the load as a function of time. Time is counted, when the electrical pulse comes from a detonating unit to DEMG detonators.

X-RAY-1   DMG   Probe ITL

Fig.2 Current derivative and current in the load as function time

The analysis of experimental data showed a deviation in the phenomena expected in the load.

First of all inductive probes measured that the magnetic field penetrated under the liner very early. The beginning of the field penetration was observed at the 24.6-24.9 μs (IL_1-IL_2 probes) and at the 24.6-28.4 μs (A_1-C_5 probes).

Second, VNIIEF light probes LMU, located in the CMU, measured light appearance at the joint area between the liner and the walls even at the stage of HEMG operation. The earliest increasing signals were measured by LMU_{10} probes ($\varphi=75°$) at the 2.4 μs. The latest time for the light measured by other probes of this group LMU corresponds to the 19 μs (LMU_8, $\varphi=315°$). LANL light probes also measured early light (~23 μs). Besides, LANL light probes at ~23.4 μs registered impact apparently with plasmoids (light intensity decreased sharply, presumably as a result of plasma sticking on the light-guide surface). According to the calculations the liner breaks loose with the clipper at t=28.4 μs (see the next section).

Based on the measurement of collimated light probes Lk the following picture of the initial "bubble" motion was obtained. The beginning of its formation, which manifested itself by the light flash, was recorded at the time t^{exp}_{ob}=29.3 μs (probe Lk_2, $\varphi=30°$). The second probe (Lk_1, $\varphi=210°$) recorded the glow Δt^{exp}_{ob}=0.3 μs later.

The light collimated probes at the left wall parallel to the load axis recorded the glow at the radius R=156 mm in the range from 22.8 μs (LW_1-$\varphi=90°$, LW_5-$\varphi=330°$) to 25.4 μs (LW_3-$\varphi=210°$). During ~3 μs the glow intensity had been increasing, and within the time range between 31.1 μs (LW_3-$\varphi=210°$) and 32.7 μs (LW_5-$\varphi=330°$) each of the probes measured sharp increase of the light signal, which could be associated with the "bubble" arriving at the radius of the probe location. Thus, angular difference in time of the "bubble" at the radius 15.6 cm was already 1.6 μs.

The "bubble" had the fastest speed at the radius R=156 mm in the angular section $\varphi\leq210°$ - 1,5 μs (the most intensive glow according to the probe LW_3 was observed at the time 32.7 μs), the "bubble" had the slowest speed in the angular sector $\varphi\geq330°$ - no less than 3,5 μs (the most intensive glow according to probe LW_5 was observed at t=32,7 μs). Thus, the average velocity of the plasma shell radial motion differed about a factor of two by the angle.

Experimental data on the following "bubble" expansion obtained from readings of non-collimated light probes (from R=107.5 mm on the left wall and from R=160 and 122 mm on the right wall) does not contradict to this angular picture of the "bubble" motion and testify to further growth of its asymmetry.

We measured the voltage in a transmission line from DEMG to the load and the voltage in the CMU. The analysis of those important measurements is given in paragraph 4.

3. ABOUT THE TECHNIQUE OF CALCULATIONS

The main results of 1D MHD calculations for a ponderomotive unit (PU) with a cylindrical liner-switch (and a transmission line (TL) to it) and for a variable mass liner (VML, "bubble") formed after the clipper "cuts off" a part of cylindrical liner-switch are given below.

The calculations have been made with help of a code designed to solve for calculating one-dimensional elastic-plastic and magnetic-hydrodynamic problems developed on the UP program basis [5].

The equation of state and the Al-liner conductivity were described by the formulas from [6]. The MHD calculations for the VML accounted for the radiant heat conduction.

According to this calculation the liner-switch collision with the clipper started with the velocity of 3.8 *km/s* at t = 26.8 μs (R_{int}=17.8 *cm*) and was over with the velocity of 6.0 *km/s* at t = 28.4 μs (R_{ext}=17.1 *cm*); the liner-switch collision with the CMU would have begun at t = 35.5 μs with the velocity of ~12 km/s if the liner had been accelerated by the current $I_{exp}(t)$.

The "bubble" shape prior to the collision with the PU walls (see Fig.1) was supposed to be a toroidal, with a toroid small radius

$$r = R_n - R, \qquad R_n \cong 17.5 \; cm, \qquad R < cm \qquad (1)$$

here $R = R_{int}$ is the minimal distance from the toroid inside surface from the rotation axis, R_n is the toroid large radius which is close the clipper minimal radius. Only a small "bubble" fragment of fixed mass $M_O = M_b/7.5\pi$ located in the vicinity of R radius (1) was computed; here M_b is the "bubble" total initial mass. This fragment was supposed to be a cylindrical and moved along the radial channel bounded by hard walls and having the width of

$$\Delta Z = \begin{cases} 0.05 cm, & R \geq 17 \; cm \\ \\ 1.75 - 0.1R, & R < 17 \; cm \end{cases} \qquad (2)$$

The 1D MHD-equations in the "channel" approximation are presented, for example, in [7]. The calculations were made from the moment $t_{ob} \cong 28.4$ μs which was assumed to be the start of the "bubble" formation; the initial "bubble" state in these calculations $\rho_{ob} = 2.4 \; g/cm^3$, $\varepsilon_{ob} = 2 \; кДж/г$, $v_{ob} = 0$.
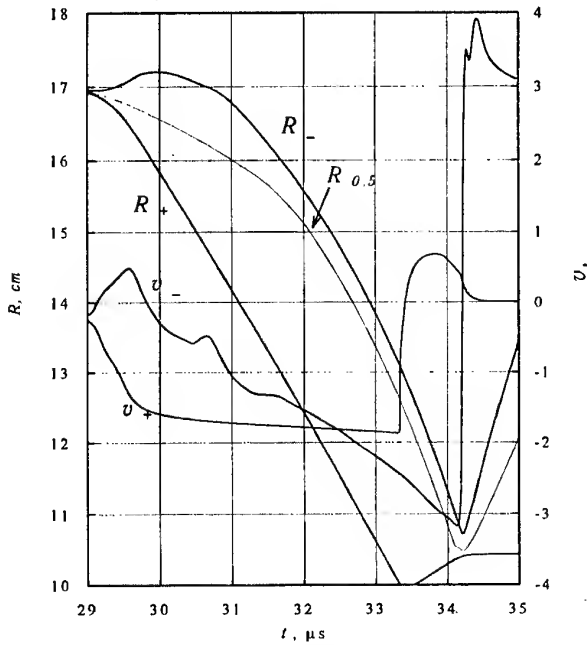
Fig. 3 The (R-t) and (v-t) diagrams of movement of the "bubble" surfaces from computation with $M_b = 7g$

Fig.3 represents the calculation results with $M_b = 7g$.

For a more detailed "bubble" angular asymmetry imitation that took place in the experiment this asymmetry might be associated with some angular distribution of the "bubble" mass $M_b(\varphi)$ supposing that the "bubble" movement in each angular sector $\Delta\varphi$ is close to the "bubble" 1D MHD-calculation with some M_b mass. Such model does not contradict to the experimental picture of the "bubble" formation and movement according to which the time difference of at "bubble" formation start Δt_{cf} was considerably small (~ 0.3 μs), at passing the first 15 mm was no less than 1.5 μs and increased as the "bubble" continued to move. One method of imitation of the supposed angular distribution $M_b(\varphi)$ (version M_{5b}) is given below: $M_{5b} = (6-7.5-8.5-10.5-11.5)g$, $\Delta\varphi/2\pi = (0.1-0.18-0.21-0.29-0.22)$ respectively.

The "bubble" parameter estimation results which are compared to the experimental data in the next part of the paper have been obtained by the "bubble" MHD-calculations described above for the $M_b = 7g$ ($\Delta t_{cf} = \pm 1.5$ μs) and for the M_{5b} version.

4. THE EXPERIMENTAL AND CALCULATION DATA DISCUSSION.

Comparison of the characteristic parameters of current pulse and current derivative experimental values with the analogous parameters taken from computations of DEMG+PU system, made before the experiment without regard for "bubble" formation, showed a satisfactory consistency.

The tendency $dI_{exp}/dt < dI_c/dt$ in value relation is evident, beginning before the moment of obtaining the $(dI/dt)_{max}$ value. This can be accounted for by the additional losses of the magnetic flux in the DEMG+PU current circuit, which were observed in the experiment. Besides, in the experiment a deeper minimum of current derivative $(dI/dt)_{min}=-9.4$ MA/μs was obtained compared to the calculations in calculations: $(dI/dt)_{min}=(-6)-(-7,4)$ MA/μs which testifies to the "bubble" formation in the experiment.

To estimate the "bubble" experimental characteristics the analysis of the voltage measurement results was performed. There were as well compared the experimental and the computational voltages in the DEMG' transmission line, the voltages and the magnetic fluxes between the clipper and the liner-switch, the inductance values of the "bubble" when taking different "bubble" mass values M_b in the MHD-calculations. Fig.4 presents comparison of experimental and computational voltages in the DEMG' transmission line at $M_b=7$ g, while Fig.5 presents comparison of experimental voltage $U_0*(t)$ with calculated voltage on the "bubble" outer surface $U_{b+}(t)$ for the M_{5b} version. In general, quite a satisfactory agreement can be observed.
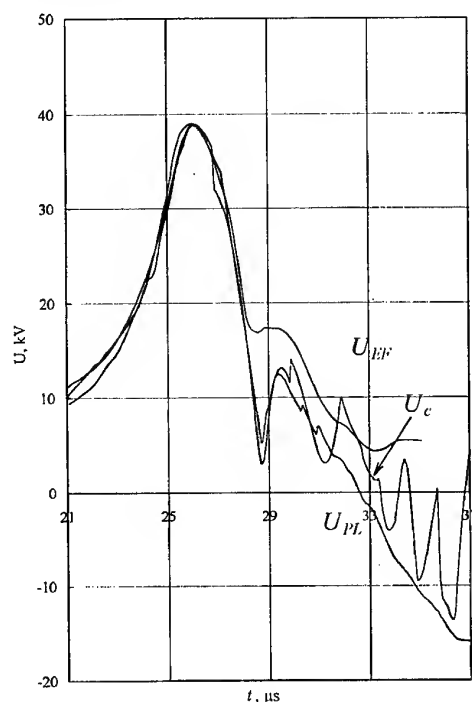
Fig. 4 Experimental U_{PL}, U_{EF} and
computational U_c voltages in the DEMG TL
(from computation with $M_b=7$g)
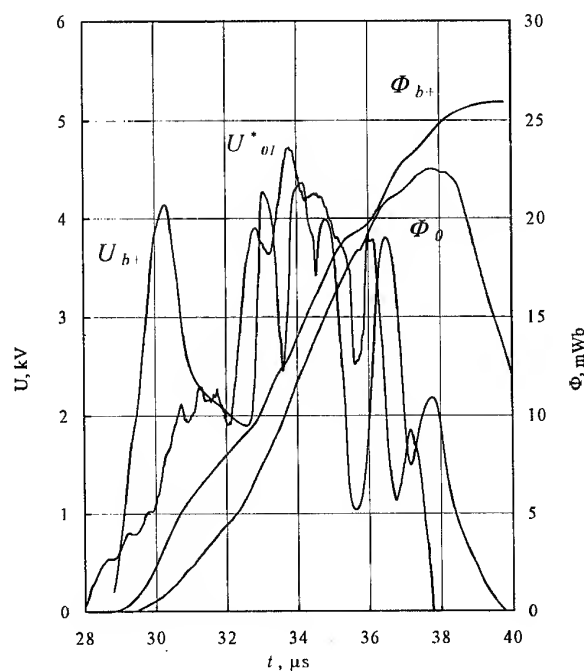
Fig. 5 Comparison of experimental voltage U_{0l}
with voltage on the external "bubble" surface U_{+}
for $M_{5b}(\varphi)$ case and comparison of the
corresponding magnetic fluxes

Let us note that a fine structure of the experimental curve $U^*_0(t = 32 \div 38 \ \mu s)$ main peak is qualitatively and in some parameters quantitatively depicted better in the M_{5b} version than in the case with $M_b=7$ g calculation. In particular, two late peaks at t = 36÷38 μs are reproduced by the contribution of $M_b=10.5$ g and 11.5 g values and the calculated $\Phi_{b+}(t)$ and experimental $\Phi_0(t)$ magnetic fluxes agree better.

The observed picture of the "bubble" movement (see paragraph 2) might be explained in the following way in the frames of the "bubble" $M_b(\varphi)$ model.

The fastest "bubble" movement taking place in the angular sector $\varphi \approx 210°$, corresponds to the "bubble" smallest sector mass $M_b^{(min)} \approx 5.5$ g, here the "bubble"

maximum velocity ~50 km/s was obtained. The value of this sector is ~10%. The "bubble" collision with the CMU in this angular sector has defined the first peak ($t \approx 33$ μs) in the fine structure of the experimental voltage $U*_0(t)$ recorded at CMU. The calculated time of the "bubble" hot part approach to the 15.6 cm radius corresponds approximately to the experimental start of maximum glow recorded by the photo collimated probe LW_3 (≈ 31.2 μs).

The slowest "bubble" movement which had place in the angular sector $\varphi \approx 330°$ corresponds to the $M_b^{(max)} \approx 11$ g maximum sector mass. Here the "bubble" maximum velocity is ~20 km/s, the sector dimension is 15–20%. This "bubble" mass collision with the CMU has defined the latest in time peak $(t \approx 37$ $\mu s)$ in a fine structure of $U*_0(t)$ voltage experimental curve. The calculated moment of the "bubble" hot part approach in this angular sector to the LW_5 photo collimated probe placed on the 15.6 cm radius corresponds approximately to the experimental $(\approx 32.7$ $\mu s)$.

In the intermediate angular sectors whose total sum is 70–75 % the "bubble" was characterized by the "leading" sector masses M_b close to 10 g, 9 g, 8 g and 7 g. The latter of these sector masses has defined the central peak $(t \leq 34$ $\mu s)$ in a thin structure of the $U^*_0(t)$ experimental curve main peak. The calculated moment when the "bubble" reaches LW_1 photo collimated probe placed in the angular sector $\varphi \approx 90°$ on the 15.6 cm radius in this sector corresponds approximately to the experimental moment ≈ 31.7 μs when the "bubble" hot part appeared here. The velocity of the "bubble" impact on the CMU in this sector is more than 30 km/s.

The picture of the "bubble" possible angular asymmetry built by these three angular sectors ($\varphi=90°$, $210°$, $330°$) is presented in Fig.6; here the maximal angular asymmetry of the "bubble" before its impact on the CMU reaches $(\varnothing_b-\varnothing_{CMU})/\varnothing_{CMU} \cong 0.17$.

The above-presented results of comparison of the experimental and calculated "bubble " characteristics estimations should be considered as satisfactory ones, taking into account their significant errors.
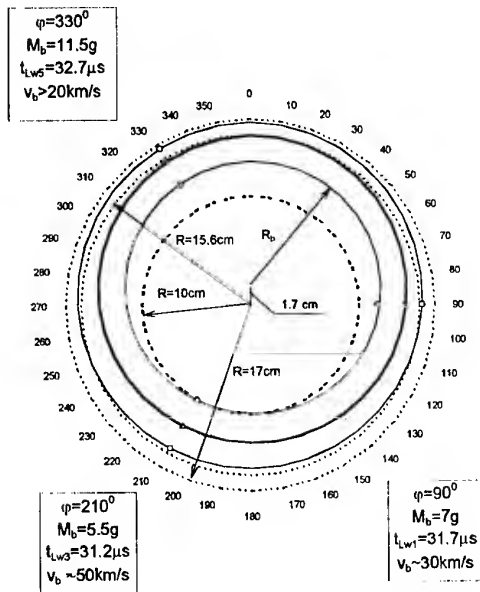
Fig. 6 Possible angular asymmetry of the "buble" prior impact on the CMU (t<32.4μs)

CONCLUSION

Valuable information on the liner PU operation including the process of the plasma "bubble" formation has been obtained. The results of theoretical and computational analysis of the experimental data available definitely indicates to the fact of the plasma "bubble" formation, a main new phenomenon expected in the experiment. The "bubble" basic experimental parameters have been estimated: a total mass ~5-10 g, maximum velocity at the collision with the CMU~50 km/s, angular asymmetry, etc. Besides this, the experiment has shown the presence of considerable discrepancies in the experimental picture of phenomena in

the liner PU unit from the expected one. These discrepancies, first of all, comprise an unexpectedly large angular asymmetry in the processes accompanying the plasma "bubble" formation, a very early appearance of the visible currents and, possibly, plasma in the central area under the liner and a large "bubble" mass as well. A possible reason of deviation from the expected phenomenon scenario and of the differences mentioned might be an insufficiently reliable contact of aluminum liner with copper conical current-feeders. We suppose that the area of the insufficiently good contact caused by its overheating with joule heat might be the cause of unexpected copper-aluminum plasma and magnetic field penetration under the liner and might cause a large asymmetry and, probably, higher "bubble" masses. We hope to change the liner unit design so that to provide a reliable liner contact with the walls and a symmetrical supply of current to the liner, to avoid the side effects described above and to diminish the initial mass of the plasma "bubble".

REFERENCES

1. V.K. Chernyshev, M.S. Protasov, V.A. Shevtsov, A.A. Petrukhin, V.B. Yakubov, et al., "Explosive magnetic generators of "Potok" family", Eighth IEEE Intern. Pulsed Power Conference, San-Diego, 1991.

2. P.J. Turchi, J.F. Davis, M.L. Alme, G. Berd, C.N. Boyer, S.K. Coffey, D. Conte, S.W. Seiler, W.L. Baker, J.H. Degnan, D.J. Hall, J.L. Holmes, W.F. McCullough, D.W. Price, M.H. Frese, R.E. Peterkin, N.F. Roderick, J.D. Graham and E.A. Lopez, "Generation of High-Energy x-Radiation Using a Plasma Flow Switch. J. Appl.

3. A.M. Buyko, O.M. Burenkov, V.K. Chernyshev, S.F. Garanin, S.D. Kuznetsov, A.I. Kuzayev, V.N. Mokhov, I.V. Morozov, E.S. Pavlovsky, A.A. Petrukhin, A.I. Startsev, V.B. Yakubov, B.G. Anderson, C.A. Ekdahl, J. Kammerdiener, I.R. Lindemuth, R.E. Reinovsky, P. Rodriguez, P.J. Sheehey, L. R. Veeser, S.M.Younger, and W. Zerwekh "Changing mass liner system for generation of soft X rays", J. Laser and Particle Beams (1997), vol. 15, no. 1, pp.133-138.

4. A.A. Petrukhin, N.P. Bidylo, S.F. Garanin, V.M. Danov, V.V. Zmushko, A.I. Kuzyaev, V.N. Mokhov, E.S. Pavlovsky, V.A. Prokopov, M.S. Protasov, V.K. Chernyshev, V.A. Shevtsov, V.B. Yakubov. «Current pulse generation using an opening switch actuated by magnetic field.» /Ultrahigh magnetic fields. Physics. Technology. Application. /Ed. by V.M. Titov, G.A. Shevtsov. Moscow, Nauka Publishers, 1984. p. 406.

5. V.A. Batalov, V.A. Svidinsky, V.I. Selin, V.N. Sofronov «UP code for solution of one dimensional gasdynamic and plastic–elastic problems of continuous media mechanics», VANT Methods and programs of numerical solution of mathematical physics problem, 1978, 1(1), p.21

6. A.M. Buyko, S.V. Garanin, V.A. Demidov et al. «Investigation of the dynamics of a cylindrical exploding liner accelerated by a magnetic field in the megagauss range». Megagauss fields and pulsed power systems (MG-V). 1989,p.743.

7. A.M. Buyko, V.M. Danov, V.I. Mamyshev, V.B. Yakubov. A technique for numerical simulation of disk exploded magnetic generator with electro – exploded current opening switch and liner load (VANT, Mathematical modeling of physic processes, 1995,4,p.12) .

SIMULATION OF MULTI-WIRE LINER DYNAMICS DURING Z-PINCH IMPLOSION

S.Semushin, B.Etlicher

Laboratoire de Physique des Milieux Ionisés, Laboratoire CNRS, Ecole Polytechnique
91128 Palaiseau, France
e-mail: sem@lpmi.polytechnique.fr

The physics of multi-wire liner compression is analysed by two dimensional simulations in r-z plane and in r-φ plane.

Sandia experiments with multi-wire liners provide encouraging experimental results. But a threshold effects of the number of wires has not been entirely explained. This complex three-dimensional problem nevertheless can be investigated by means the two dimensional simulations in two orthogonal planes. The simulations were done with original adaptive mesh refinement algorithm [1, 2], using a two temperature plasma model with and without radiation effects. Different models were used for equations of state and transport coefficients.

Three dimensional simulations are expensive, and they can't be realised with rather full physical model. So, firstly, the stability of tungsten double liner was analysed in assumption of cylindrical symmetry. Than some features of multi-wire dynamics are analysed from simulations in Z-pinch cross section.

Parameters of multi-wire liners

For two-dimensional simulations in r-φ plane the cold start becomes very complicated, because of almost point singularity of initial density distribution. For small number of wires it is possible to start computations in one dimensional approximation, assuming the independent explosion of each wire. Let's analyse the topology of magnetic field around such multi-wire liner. In plane case the magneto-static field around infinite array of wire is well known (Fig.1). In this case we have multiple zero point of magnetic field between each pair of wires. Such zero points have rather complicated physics, related with interconnection of magnetic lines. But the situation is drastically changed for the cylindrical geometry (Fig.2). The cylinder composed of multiple wires produces magnetic field with the only one zero point, namely at the axis. This is the principal difference between the plane and cylindrical cases.

Outside the wire cylinder the magnetic field very quickly approaches to limit of the homogenous current in cylinder. But near the wires magnetic field variations are significant.
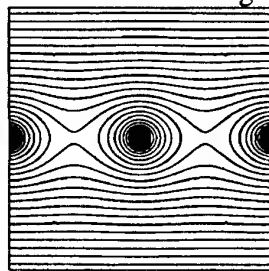
Fig.1 Magnetic field topology in plane geometry.
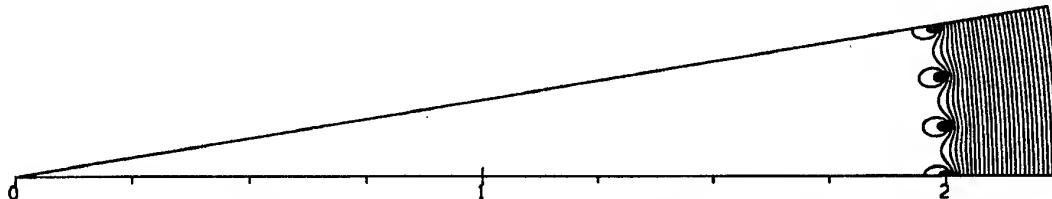
Fig.2 Magnetic field topology in cylindrical geometry.

For the large number of wires the variation of magnetic field on the wire surface is proportional to the square root of wire number (for fixed mass load). Analyse shows, that for the last targets of Sandia laboratories[3], composed of 300 wires, the variation of magnetic filed on the wire surface is more than 15 percents. This means, that the variation of magnetic pressure and Joule heating is two time more. Thus, the explosion of each wire is essentially two dimensional from the beginning, and it is necessary to make fully two dimensional simulations. Some estimations for others multi-wire arrays are given in the table along with wire and cylinder diameters:

N	d	D	?B/B
300	12.15 μm	2 cm	0.18
240	7.5 μm	4 cm	0.05
180	10. μm	3 cm	0.06
120	18. μm	4 cm	0.05

Simulations in r-z plane

If we suppose that the wires are already exploded and homogenised in in angular direction, it is possible to make simulations in r-z plane. Such simulations provide wery useful physical information about development of instabilities. The instability here was induced by random perturbations of the initial density distribution.

The computations were done by ASTRE code [2], with uses original adaptive mesh refinement algorithm. Equations of state and transport coefficients for tungsten were used in analytical form. Radiation was taken in account as radiation losses, such model is valid for initial stage of implosion.

Mass load was 2.5 μg/cm, an internal shell has diameter 1 cm and mass load 1 μg/cm, external - 3 cm and 1.5 μg/cm. The density in external liner was randomly perturbed. Current parameters are 20 MA with 120 ns rise time, what corresponds to PBFA-2Z.

The figures 1-4 present the evolution of the lines. The isolines of density along with the radial cross section are given.

Despite the external liner perturbation, initial compression is almost homogeneous. The impact of shells, which begins near 80 ns, induces the instabilities, which continue to increase. The instabilities are evident as at the internal side of the liner, as at the external. The velocity of liner before interaction is 30 cm/μs, and after the merging the velocity of the heavy resulting liner is 25 cm/μs.
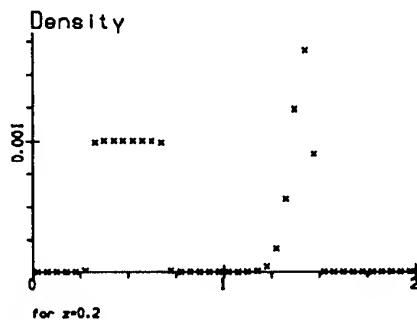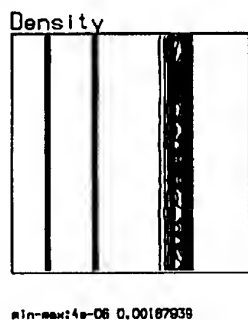
Fig.1 Density, t=50 ns
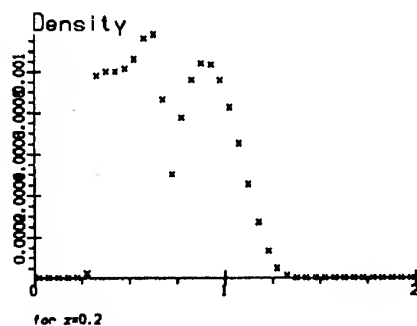
Fig.2 Density, t=80 ns
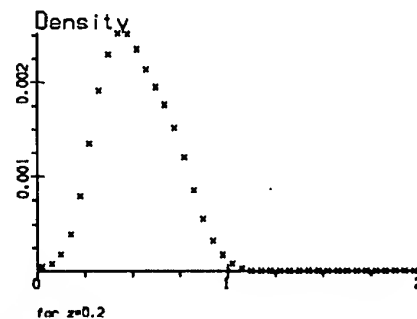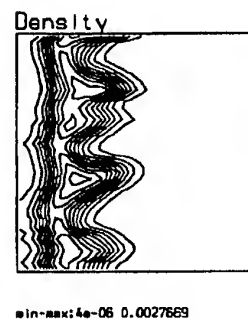
Fig.3 Density, t=90 ns
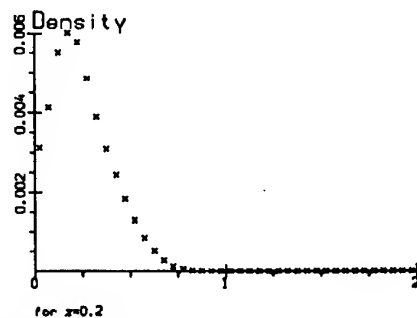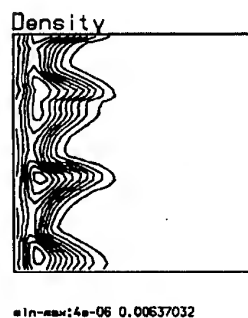
Fig.4 Density, t=100 ns

Simulation in r-φ plane.

These simulations were done by ASTRE code version, which works in polar coordinates. The physical model was the same, as in the previous item.

The symmetry of multi-wire liner allows to realise the computations in the sector of angle $0.5\dfrac{2\pi}{N}$, where N – is the number of wires. In the presented computation the target was composed of 30 tungsten wires, which were distributed over the cylinder with 3 cm diameter. Boundary conditions on the lateral sides correspond to symmetry. Because of analytical equation of state, the computations start from already distributed liner (Fig.5). Current corresponds to PBFA-2Z values and is 20 MA during 120 ns. The initial implosion is not homogeneous, and it is possible to see that variations of magnetic field on the wire surface are essential. The form of plasma is not symmetric, and we have intensive interaction between the wires. The penetration of magnetic field is negligible for such choice of parameters

Density

min-max:4e-05 0.000937821

Fig.5 Initial conditions, t = 0.

Density

min-max:4e-05 0.000597499

Magn.field
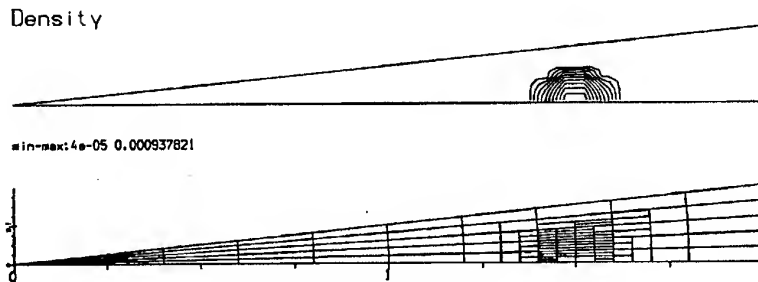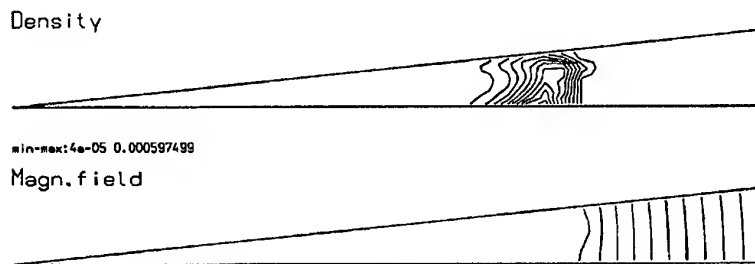
Fig.6 Multi wire Z-pinch simulation, t = 50. ns

The first simulations, presented here, provide a physical understanding of the process. The simulations with more sophisticated physical model will give more accurate analysis of the multi-wire target.

References.

[1]   S.Semushin, Adaptive Mesh Refinement approach for simulation of gas dynamics and magneto hydrodynamics problems. *Proceedings of 15th IMACS Word Congress. vol.3,* Wissenschaft & Technik Verlag, 1997, 109-114.

[2]   S.Semushin, B.Etlicher Tools for MHD simulation of hot dense plasma. *These Proceedings.*

[3]   http://zpinch.sandia.gov/

DEVELOPMENT OF ACCELERATOR FOR HIGH-POWER MICROWAVE APPLICATIONS BASED ON THE FORMING LINE SUPPLIED WITH CURRENT

V.E. Fortov, V.A. Kamensky, V.M. Mihailov, E.V. Nesterov,
V.Y. Petrov, S.D. Plaksina, S.A. Roschupkin, V.P. Shumilin, V.A. Stroganov

*High Energy Density Research Centre, Russian Academy of Sciences,
IVTAN, Izhorskaja St. 13/19, Moscow, 127412, Russia*

At present, explosive magnetic generators (EMG) are the most energy containing sources for pulsed power applications. The use of MCG for power supply of microwave generators significantly reduce the weight and sizes of installation as a whole. Modern fast-run MCGs are capable to transmit into load dozens or even hundreds of KJ during only few microseconds. For matching with relatively high-resistance load, which is the most of microwave generators, it is very useful to take the advantage of intermediate inductive store with electroexplosive opening switch (EEOS).

In papers [1,2] it was suggested to use the cut of a long wire current supplied instead of inductive coil. The high-voltage source based on the line has an active output resistance over a wide frequency range and allows to generate a square pulse with a high efficiency of energy conversion. Unlike DFL, the high voltage impacts the line insulation for a short time only, which doesn't exceed the generated pulse duration. This allows the use of polymer films as a main insulation under extremely high electric field intensities. So, the total volume of forming line is comparable with that of inductive store for the same energy stored.

Following the above concept we have built the installation and carried out experiments, in that number with use of MCG, which proved the idea. This helped us to design a new accelerator having the ability to utilize the dozens of kilojoules of energy.

DESIGN

The circuit diagram of installation (Fig.1) is absolutely the same as that of the previous design. The design arrangements are alike when the accelerator is composed of two main parts (Fig.2):
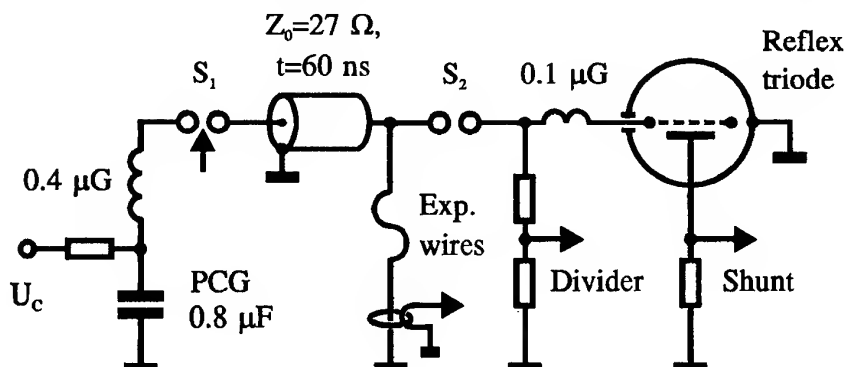
Fig. 1. The equivalent circuit for the experimental installation.

vacuum chamber and oil volume, separated from each other by bushing section insulator. The case with EEOS and sharpening gas discharger are placed inside the oil volume. In addition, the oil volume has four cable leads-in, gas entrance for pressure control inside the sharpening discharger, voltage divider as well as oil pumping out, filling in and draining units, pressure gauges and compensator of temperature expansion of the oil. With help of the cables being the intermediate stores of energy, the installation is connected to either MCG or capacitive stores. The installation allows to adjust the output parameters within the wide range of values by variation of cables length or their number (from 2 to 4) or capacity of stores as well (from 2×0.8 μF to 4×1.6 μF, 100 kV).
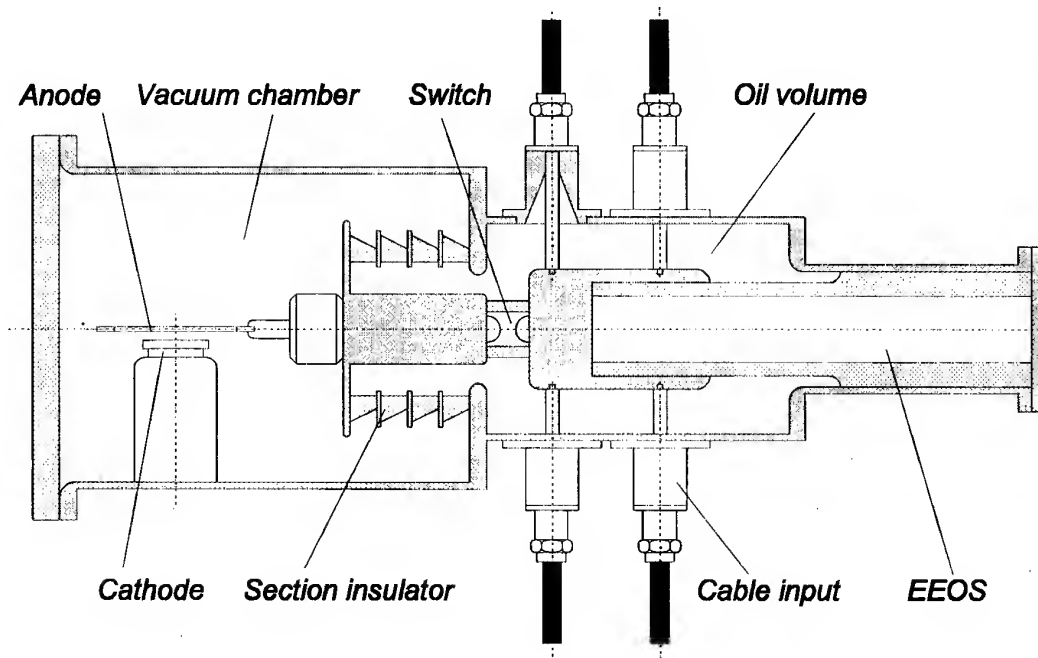
Fig.2. Scheme of acelerator.

The both codes AXIAL and ATLAS as well as own laboratory-made codes have been widely used. The main attention was paid to minimize the spurious circuit elements at a considerably higher energy and power of the beam. As a result, we were succeed to provide the 1.5–2 folds safety factor and decrease the installation in sizes in comparison with the prototype.

RESULTS OF CALCULATION

Mathematical simulation have been made with help of ATLAS code including the subprograms for EEOS, reflex triode and sharpening discharger calculations. The mathematical model used for EEOS calculation is given in [3]. The reflex triode was simulated by "3/2" law under relativistic conditions with account of transparency of the grid and cathode plasma movement. The discharger was accounted for by exponentially decreased resistance mainly, since the further refinement of the model had no influence on the results of calculations practically.
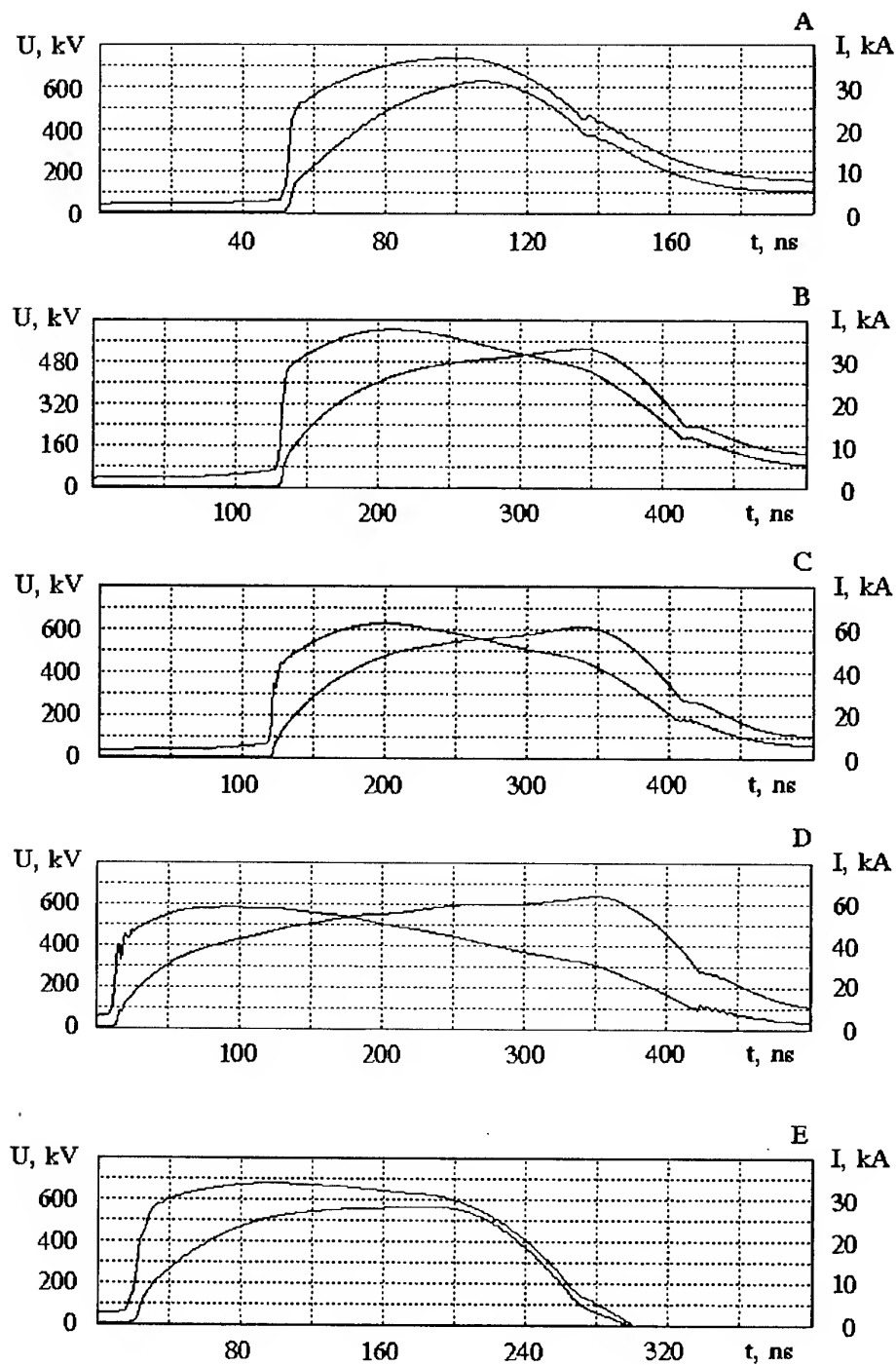
Fig.3. Mathematical simulation with help of ATLAS code.

Initially, the accelerator was assumed to operate under three main conditions:

A. U = 800 kV, τ = 80 ns, Z_{FL} = 25 Ω, Z_L ~ 25 Ω.

B. U = 600 kV, τ = 240 ns, Z_{FL} = 25 Ω, Z_L ~ 25 Ω.

C. U = 600 kV, τ = 240 ns, Z_{FL} = 12,5 Ω, Z_L ~ 13 Ω.

Calculations reveal two more interesting conditions to be realized:

    D. $U = 600$ kV, $\tau = 400$ ns, $Z_{FL} = 12,5\ \Omega$, $Z_L \sim 13\ \Omega$.

    E. $U = 600$ kV, $\tau = 200$ ns, $Z_{FL} = 12,5\ \Omega$, $Z_L \sim 25\ \Omega$.

Initial data as well as results of calculations are given in Table 1 and Fig.3.

Table 1

Variant	A	B	C	D	E
Storage capacity, μF	3.2	3.2	6.4	6.4	3.2
Voltage, kV	100	100	100	100	50
Wires diameter, μm	50	100	100	100	50
Wires number	80	21	40	38	90
Wires length, mm	700	700	700	650	600
Peak power, GW	22.6	16.9	31.0	28.4	18.2
Energy in load, kJ	1.46	3.74	6.89	8.61	1.69
Efficiency, %	9.1	23.0	21.5	26.9	10.6

One can notice, that under condition D the peak power of the beam is 28 GW and pulse duration at the level of 20 GW is more than 300 ns while the resistance of the load changes by almost 3.5 times. Experimental data as well as numerical simulation results gives us the reasons to believe in obtaining microwaves with power higher than 1 GW and energy of the pulse ~100 J. We plan to use this new installation with microwave generators of other types.

REFERENCES

[1]. Chernych E.V., Fortov V.E., Gorbachcv K.V., Nesterov E.V., Stroganov V.A., Shumilin V.P. "Accelerator for High Power Microwave Gcneration", Proceedings of thc 11th International Conference on High Powcr Particle Beams, Beams'96, June 10-14 1996, Prague, Czech Republic, V.1, P.457-460.

[2]. Bezrukov M.Y., Gorbachev K.V., Chernykh E.V., Zolotykh I.O., Lisichkin A.L., Nesterov E.V., Plaksina S.D., Roschupkin S.A., Stroganov V.A., Fortov V.E., Shumilin V.P., Yakovlev D.G. Petrov V.Y. "High Powcr Microwave Generation by Current Supplied Accclerator with Low Energy Capacitive Storagc or MCG", Seventh International Conference on Megegauss Magnetic Field Generation and Relatcd Topics, Sarov (Arzamas-16), August 5-10, 1996, Book of Abstracts, P.130. (in Russian).

[3]. Azarkevich E.I., Kabluchko A.V., Luchinskiy A.V., Lisetchkaya T.A. //Tezisy dokladov sovmestnogo zasedaniya sektchiy nauchnyh sovetov AN SSSR. Tomsk, 1986, P.12-20 (in Russian).

Two mechanisms of high energy ions generation
in the Z-pinch

V.V.Vikhrev and E.O.Baronova

Nuclear Fusion Institute, RRC Kurchatov Institute, Moscow 123182

Abstract. An analysis of high energy ion generation mechanisms in the Z-pinches is given in the paper. A particular attention is paid to a mechanism of ion generation in the process of high temperature plasma expansion and to a mechanism of ion acceleration up to the Alfven velocity in a zone surrounding the pinch plasma column.

Introduction

The presence of high energy of about few MeV region is well known fact for Z-pinch discharges. The origin of the such ions in the MeV energy range can not be explained by a simple acceleration between the discharge electrodes, since the energy of such ions is many times greater than the voltage, applied to the electrodes. It is also known that the spectra of high energy ions outgoing from discharges has the power dependence on the energy ($\sim 1/E^k$) with the power index in the range from 2 to 3 [1]. One should note that the same spectrum of protons is observed in the space plasma. As known ions can be accelerated in the electric fields or obtain the energy from other particles possessing of a higher energy. Let us consider the energy production under acceleration in the electric plasma fields.

A few mechanisms are proposed for explaining the high energy ion generation. Some of them turned out to be wrong. For example, the high electric field, caused by pinch border motion with the velocity $\mathbf{v}$, is sometimes involved for explaining the ion acceleration, when the field, $E=[\mathbf{v}\times\mathbf{B}]/c$, emerges in the laboratory set of co-ordinates. However, this field is absent in the set of co-ordinates, related with the plasma. Thus it cannot be responsible for acceleration of particles.

The Ohmic electric field ($E=j/\sigma$) is related with the friction between electrons and ions, when the current passes through the plasma. In such a field the electron acceleration is possible due to the mechanism of electron runaway effect in the plasma. Thus mechanism is related with that the frequency of collisions between electrons and ions is reduced with a rise in the electron energy. Therefore a part of electrons, having a rather high velocity can practically interrupt their interaction with the plasma ions and acquire the energy equal to a potential difference in the Ohmic field. However the similar run away mechanism for ions is absent. It is related with that the frequency of electron-ion collisions depends on a relative velocities of electrons and ions, i.e. on the electron velocity. In this case, the ions with different energies are accelerated in the similar way under collisions with electrons, and among them there are no ions which could dominantly acquire the energy in comparison with other ions.

The third electric field which exists in the plasma is the Hall one: $E=[\mathbf{j}*\mathbf{B}]/nec$. Due to a presence of a such the field a ponderomotive force, $F=[\mathbf{j}*\mathbf{B}]/c$ affecting electrons, is transferred to ions. This field in a stationary Z-pinch produces the potential difference, in a radial direction, equal to the ion temperature. Therefore in the stationary z-pinch this field retains the ions in the radial direction from the expansion. However it can not accelerate ions up to energies greater than their temperature. In non-stationary z-pinch ions can be accelerated in the Hall field up to very high energies.

Two mechanisms of generating high energy ions in such a field have been found: one of them is related to the generation in dense plasma column of the pinch: Another, to regions surrounding the pinch column.

High energy ion production in the z-pinches due to a high temperature plasma expansion

The first mechanism to be considered and related to the main part of fast ions, is related to a high temperature plasma, expanding from a dense z-pinch region, when both ion and electron thermal energies are converted into the kinetic energy of fast ions. A dense-high temperature plasma is produced in the z-pinches due to the plasma column compression by the magnetic field of the pinch.
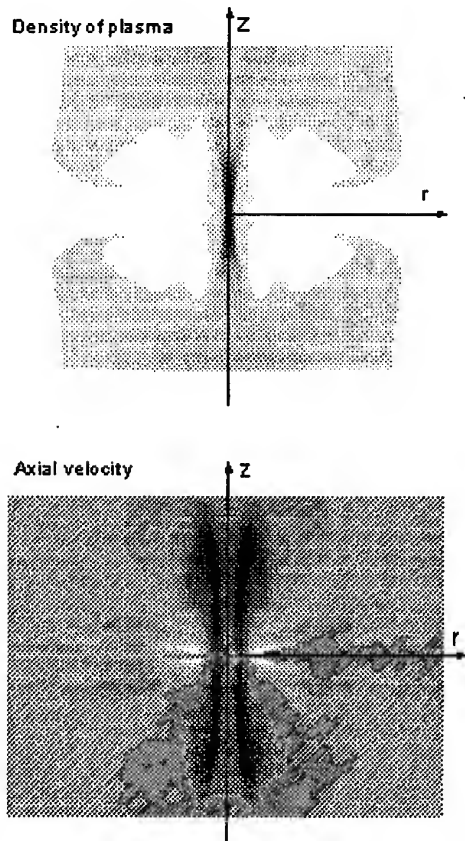
Figure 1. **The results of 2D MHD modeling of Z-pinch neck development for the moment of presence of strong z-axis stream of plasma.**

The particle expansion from the neck in axial direction results in a reduction in the number of particles in the N-cross-section and an average energy of the left particles (i.e. temperature, T) is increases due to satisfaction of the Bennet condition ($NT=I^2/4c^2$). The plasma dynamics in the z-pinch necks is such that the plasma temperature there is continuously rising, and the number of particles in the cross-section is reduced.

If one assumes that ions, expanding from the neck, have the Maxwellian spectrum and the plasma temperature attains high values, the total energy distribution of expanding ions will be determined by the expression [2]:

$$dn/dE=3\ h/8cE^2.$$

This expression determines the energy spectrum of particles, when there is no limit to the temperature rise in the pinch. If such a limit exists, the ion energy distribution power index k, $dn/dE\sim1/E^k$, will be in the range from 2 to 3 [1], that corresponds to the spectra, observed in the pinch discharges.

As a result, the emergence of the main part of high energy ions, their amount and the spectrum can be explained as a result of the high temperature plasma emergence in the compressed z-pinch regions. At present, such an approach to the high energy ion flux determination from z-pinches has been developed in the papers by Trubnikov, Zhdanov and Vlasov [3,4].

Ion generation in a plasma surrounding the pinch

Another mechanism of ion generation has been found in the analysis of plasma flows in a region, surrounding the plasma column of a pinch.

Density of plasma

Radial velocity
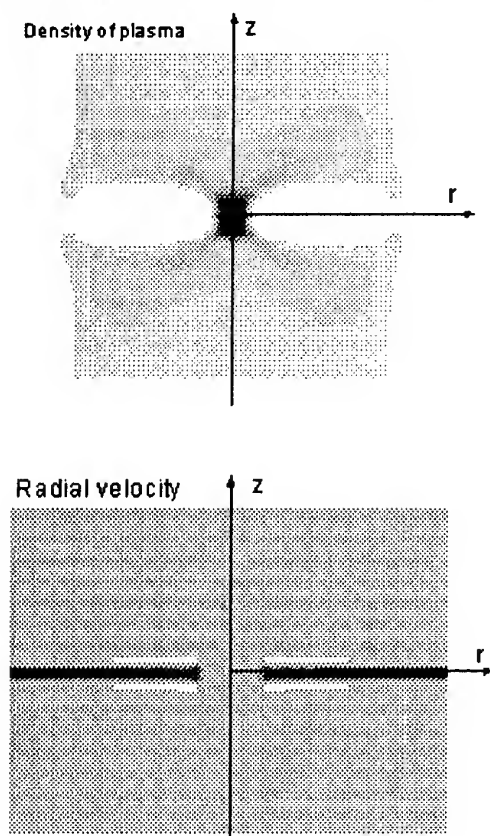
Figure 2 The results of 2D MHD modeling of Z-pinch neck development for the moment of presence of strong radial ion stream.

So, simulating the short wave perturbation development in the pinch plasma column a fast expanding cavity is produced. This cavity is filled with a rarefied plasma with the magnetic field "frozen" into it. Frequently a situation emerges, when the magnetic field can enter the expanding cavity through a narrow slit only (Fig.2) In that case, to be able to fill the cavity, the magnetic field flow rate becomes very high, being limited by the velocity of light only in the absence of plasma. since the plasma acceleration inside the cavity is prevented by the inertia of the plasma, "frozen" into this magnetic field, a given velocity cannot exceed the Alfven one. As a result, the plasma flows at rates, corresponding to the Alfven velocity are produced in the region surrounding the pinch plasma column. A given situation is similar to that as if the rarefied plasma with the magnetic field "frozen" into it, started to expand rapidly into vacio. In that case, the magnetic field under expansion accelerates the plasma , and, in fact, the whole magnetic field energy of the plasma particles locates in that field. The similar high energy ion generation mechanism could take place in the stratosphere of stars, when the energy of an emerging magnetic fields could be converted into high energy particle fluxes.

Discussion about the models

One should note that the high energy particles in the mentioned mechanisms are driven symmetrically with respect to the pinch current direction, meanwhile there is an explicit asymmetry in the expansion from the pinch in the experiments.

Such an asymmetry is related with that their subsequent motion in the magnetic field of a pinch results in an advantageous motion towards the cathode. In [5] the high energy ion trajectories in the magnetic field of a pinch are considered.

An analysis of that particle trajectories has shown that the majority of high energy ions in the pinch plasma even under isotropic generation of high energy ions expands towards the cathode due to their drift in the magnetic field of a pinch.

The first mechanism, providing for our opinion, the main part of fast ions, is connected with high temperature plasma outflowing from dense z-pinch region, when both ion and electron thermal energy is converted into the fast ion kinetic energy.

Theoretical analysis shows the power dependence for high energy ion number on their energy with index of a power from -2 to -3.

The one more reason for high energy ions generation is plasma motion in the surrounding pinch regions. Plasma velocity in such the regions is appeared to be enough high, limited by alfven's one. Since Alfven's velocity might be great (about 10^9 sm/c) there, that due to low plasma density and high magnetic field, the fast ion energy is evaluated to be in MeV region. Both the mechanisms are examined in this paper, including the MHD approximation and the simple analysis of ion motion in electromagnetic fields.

Acknowledgments

Referenses

1. Vikhrev V.V., Ananin, C.A. Fiz. plazmy v.7, 494, (1981).
2. Ananin S.V., Vikhrev V.V. Preprint KIAE-3299/6, Moscow, (1980).
3. Trubnikov B.A., Zhdanov S.K. Vlasov V.P. IEEE Transactions on Plasma Science, 1992, v. 20, No. 6, p. 905.
4. Trubnikov B.A., Zhdanov S.K. Vlasov V.P 23 EPS Conference on Controlled Fusion and Plasma Physics, Kiev, 1995, p.431.
5. Vikhrev V.V., Ivanov V.V. and Rozanova G.A., *Nuclear Fusion*, **33**, 311 (1993).

Electron beam generation in the strong local electric fields of Z-pinch discharges

V.V.Vikhrev and E.O.Baronova

Nuclear Fusion Institute, RRC Kurchatov Institute,
Moscow 123182, Russia

Abstract. An analysis of a numerical simulation of the electron beam drive in Z-pinch discharges are represented in the paper. The results of the plasma inhomogeneity effect along the Z-axis on the plasma column resistance are given. The electron beam is generated as a result of the electron run-away mechanism at the places of the strongly-compressed plasma production in the vicinity to the pinch axis. The main electron beam fraction is generated at the stage of plasma column expansion.

Introduction

As known, the electron fluxes - the energy of which is equal to a few hundreds eV at the current of order of 1 MA - are generated in the Z-pinch discharges. The simplest estimates show what the electron generation occurs as a result of the electron run-away mechanism [1]. High energies of beam electrons - of the order of a few hundreds eV - are a serious difficulty in the explanation of electron beam parameters in the Z-pinches.

In order to produce the electron acceleration up to such an energy one should assume a rather high plasma column resistance essentially greater than the Colombian one or an anomalous resistance emerging as a result of driving the kinetic instability. Therefore in [1,2] a geometrical factor of the current passage through the pinch plasma column has been introduced for matching with the experiment, i.e. it has been a priori assumed that the plasma column resistance is 10÷20 times increase because of zigzag current passage through the pinch plasma column. Such an increase in the pinch resistance emerges only when there is the electron density inhomogeneitly along the pinch and the plasma magnetization parameter, $\omega\tau$, is essentially higher than unity.

An increase in the plasma column resistance because of a zigzag current passage through it

In [3] a problem of current distribution in the plasma column, in the presence of density inhomogeneities along the column, has been formulated for estimating an increase in the plasma column resistance, as a result of the zigzag current passage.

For finding the stationary current distribution an equation of a magnetic field change in space, taking account of the magnetic field diffusion in plasma and the Hall electric field, has been numerically solved. For simplicity, it has been assumed that the electric density is sinusoidally changed along the pinch axis

$$n = n_0 + n_1 \cos(2\pi z/\lambda), \tag{1}$$

where n_1 is the density perturbation along the plasma column, λ is the density perturbation wavelength. The equation for the φ-magnetic field component within, the framework of an electron hydrodynamics has the form:

$$\frac{\partial H}{\partial t} = \frac{\partial}{\partial z}\left(D\frac{\partial H}{\partial z}\right) + \frac{\partial}{\partial r}\left(\frac{D}{r}\frac{\partial rH}{\partial r}\right) + \frac{cH}{4\pi e r}\frac{\partial rH}{\partial r}\frac{\partial}{\partial z}\left(\frac{1}{n}\right) - \frac{cH}{4\pi e}\frac{\partial H}{\partial z}r^2\frac{\partial}{\partial r}\left(\frac{1}{nr^2}\right), \quad (2)$$

where $D_\sigma = \dfrac{c^2}{4\pi\sigma}$ is the magnetic field diffusion coefficient.

Previously, in [3], the stationary solution to Eq. (2) has been found for the case of long wavelength perturbations (i.e. $\partial H/\partial z \ll \partial H/\partial r$). Here, we give the results of the complete solution to Eq. (2), when $\partial H/\partial t = 0$. The solution has been done by the technique «of setting», when a change in the magnetic field is simulated, according to Eq.(2), and the solution to which the magnetic field distribution tends for a rather long time interval is found. Under such an approach the initial magnetic field distribution is of no importance. For certainly, the initial magnetic distribution has been taken as $H(r,z)\sim 1/r$, that is corresponds to the stationary current distribution in the absence of the electron density perturbation along the pinch. If one knowns the magnetic field distribution at a finite instant of time, one will be able to calculate the resistance R. This resistance may be presented as:

$$R = gR_0 = R_0 + (g-1)R_0, \quad (3)$$

where R_0 is resistance of the stationary homogeneous plasma column, g is geometrical factor. The result of numerical simulation of Eq.(2) are given in Fig. 1-3.
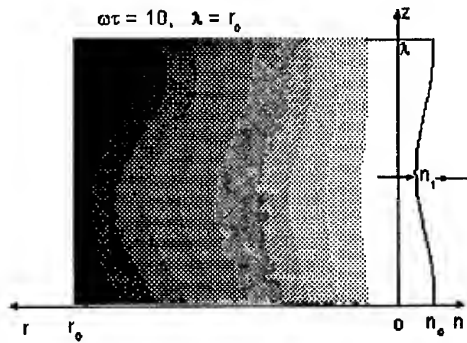
Figure 1 Stationary distribution of magnetic field under $\lambda = r_0$, $n_1/n_0 = 0.1$. and $\omega\tau = 10$
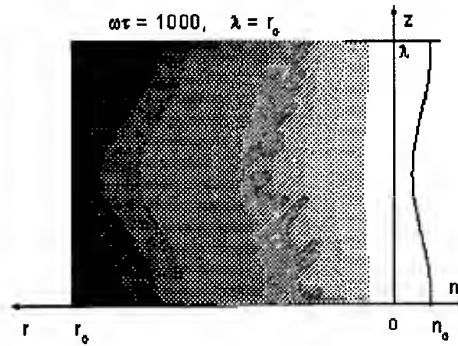
Figure 2 Stationary distribution of magnetic field under $\lambda = r_0$, $n_1/n_0 = 0.1$. and $\omega\tau = 1000$
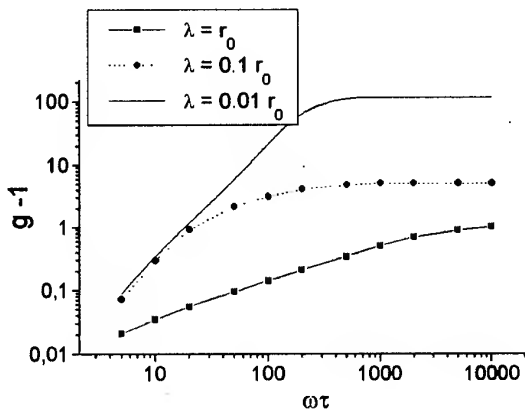
Figure 3. Dependence of geometrical factor (g-1) from λ and $\omega\tau$ under $n_1/n_0 = 0.1$

An increase in the plasma column resistance, is given, being dependent on the magnetization parameter, $\omega\tau$, and on the perturbation wavelength, λ, at the relatively pertubation amplitude, $n_1/n_0 = 0.1$. In Figure 3 one can see that, at $\omega\tau < 20$, the resistance coefficient, g, is increased with the parameter $\omega\tau$. At great values of $\omega\tau$ the attainment of a plateau (Fig.3) is observed, and, when the perturbation wavelength is in range $0.01r_0 < \lambda < 0.1r_0$ (where r_0 is the plasma column radius), an increase in g - because of a zigzag current motion - is in the range from 2 to 100.

One should note that in more early - done papers [4,5] dealing with Hall effect on the plasma resistance rise, an unlimited pinch plasma column resistance rise has been produced with a rise in the parameter $\omega\tau$. The effect of plasma column resistance rise saturation - found here and dependence on the parameter $\omega\tau$ - is related with the fact we - first - have found a stationary solution for the magnetic field distributions in a plasma column, taking account of the Hall effect and all the terms in Eq.(2). In the given solution the magnetic field diffusion in axial direction has turned out to be essential. The due regard for this diffusion results in the disappearance of the pinch plasma column resistance dependence on the magnetic field magnitude of high magnetization parameters $\omega\tau$.

As a result, the introducing of the geometrical parameter, $g=10\div20$, into the pinch plasma column resistance rise is justified in [1,2] and, probably, the due regard for this factor is also necessary in all the papers which deal with the Z-pinch discharge dynamics. Here we briefly represent - once more - the results of simulating the electron beam generation, taking account of this factor.

The electron beam genertion

That the concentration of the current in the vicinity of z-axis leads to the essential rise in the strength of the local electric field and electron beam might be generated in such the region.

Taking this factor into account electric field along the Z-pinch is:

$$E = g(I - I_{beam})/\sigma S, \tag{4}$$

where I is total pinch current, I_{beam} is electron beam current, $\sigma = ne^2/m_e(\nu_{ei} + \nu_{eff})$, $S = \pi r^2$, r - plasma column radius in the neck.

We used simple model of final stage of the Z-pinch for description of plasma dynamics in the neck of the Z-pinch [5]. According to this model the plasma temperature T is defined from radial equilibrium:

$$T = I^2/4c^2 N, \tag{5}$$

where N is number of ions per unit height of neck.

The loss of plasma from the neck can be described by the equation

$$dN/dt = -N/\tau, \tag{6}$$

where t is the characteristic time for escape of plasma out the neck, $\tau = h/2v_s$, h is length of neck, $h \approx 20r$ [5], v_s is the sound velocity. The energy balance in the neck is written as

$$3d(NT)/dt = -5NT/\tau - r B^2/4 \, dr/dt + Q_J, \tag{7}$$

where $B = 2I/cr$, Q_J is Joule heat release, $Q_J = (I - I_{beam})E$.

The equation, describing the generation of electron beam is as follows [1]:

$$dI_{beam}/dt = (G N e h - I_{beam}/h) v_b, \tag{8}$$

where e is electron charge, v_b is the electron beam velocity ($m v_b^2/2 = E h e$).

The results of numerical simulation of Z-pinch discharge at the current 1 MA and deuterium gas pressure 1 Torr, $g=20$ are given on Fig.4. Maximum of density is arise 10^{20} cm^{-3}, minimum radius of plasma column - 0.5 mm, maximum of accelerated voltage is 380 kV and maximum beam current - 10 kA.

Summary

Our theoretical investigation of electron beam generation and comparison with experimental data leads to following conclusions:
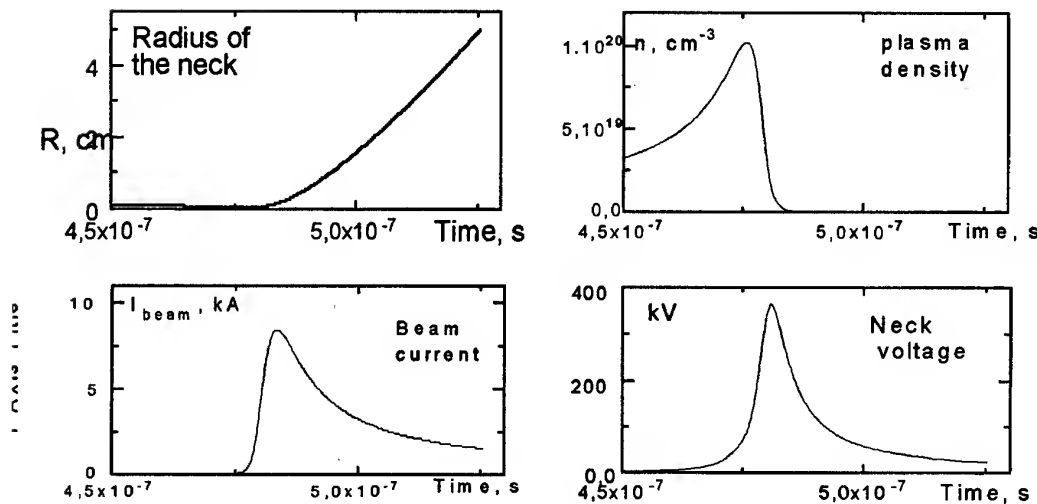
Fig.4. Radius of plasma column r, plasma density n, beam current I_{beam} and voltage on the neck U vs the time at the current 1 MA

1. Zigzag-like current motion is stated for the case of stationary plasma column with density inhomogeneity along z-direction. Such indirect current motion leads to increase of resistance of plasma column.

2. The dependence is obtained for resistance vs $\omega\tau$. If $\omega\tau<100$ then increase of $\omega\tau$ leads to continuous increase of resistance, with regard to resistance under homogeneous current motion; if $\omega\tau>100$, then increase of resistance becomes constant with regard to the value of homogeneous current motion resistance. Theory gives the reasonable value of geometrical factor $g=10\div20$.

3. Modeling of electron beam parameters, using $g=10\div20$ shows good agreement with experimental data (electron beam current 10 kA, voltage $200\div300$ kV, duration $20\div40$ nsec).

Acknowledgments

References

1. Vikhrev V., Baronova E. In:Proc. 996 Int. Conf. On Plasma Physics, Nagoya, 1996, v.1, p.322.
2. Vikhrev V., Baronova E. In: AIP, Conference Proceedings, #409, Dense Z-pinches 4th Int. Conf., Vancouver, Canada, May 1997, AIP Press, New York (1997), p.611,
3. Vikhrev V.V. In: AIP, Conference Proceedings, #409, Dense Z-pinches 4th Int. Conf., Vancouver, Canada, May 1997, AIP Press, New York (1997), p.615,
4. Kingsep A.S., Rudakov L.I. Plasma Physics Reports, v.21, No.7, p.576 (11995).
5. Grechikha A.V., Kingsep A.S., Sevast'yanov A.A, Plasma Physics Reports, v.21, No.7, p.305 (1995).
6. Vikhrev V.V, Sov. J. Plasma Phys., 3, 539 (1977).

MHD INSTABILITIES OF IMPLODED LINERS

S.V. Zakharov
LPMI, Ecole Polytechnique, 91128 Palaiseau, France
TRINITI, 142092 Troitsk, Russia
V.S. Zakharov
Moscow State University, Russia

Dense multicharged ion plasmas ($Z>>1$) of imploded liners [1] and z-pinches [2] are high effective powerful sources of thermal X radiation.

The magnetohydrodynamics of dense heavy ion plasma has qualitatively new physical properties. Due to the high radiation cooling the balance between radiation and plasma heating by shock waves or joule effect takes place at a relatively low plasma temperature, so that a thermal plasma pressure becomes much less the magnetic one: $\beta = 8\pi p/B^2 <<1$ (or Alfven velocity is much more than the sound one $c_A>>c_s$) and the plasma conductivity is not so high unlike low radiation plasmas. It means that the magnetic field pressure cannot be balanced by the thermal one *. The magnetic field pressure is balanced by inertia forces of accelerated plasma, the magnetic field and plasma density are distributed self-consistently in accordance with magnetic field diffusion due to the finite electrical conductivity of plasma [3]. In [3] the nonlinear equation for intense radiating plasma shells (liners) accelerated by magnetic field was derived. The initial problem in 1D was solved and shown that the singular asymptotic solution is realized for a wide class of initial and boundary conditions.

Different types of instabilities influence on plasma implosion and finally define the z-pinch radiation power. Thermal, radiative and non-isothermal instabilities of liners in azimuthal direction were investigated at [4-6] and others. The thermal instabilities [7] and MHD Rayleigh-Taylor in axial direction [7,8,9] for radiating plasma were studied numerically. The main influence on plasma implosion quality exerts the MHD Rayleigh-Taylor axial mode, thermal instabilities produce perturbations for it.

In this paper we develop the approach [3] to the MHD of intense radiating plasma implosion, consider the structure of the magnetic field - outer surface plasma border and its stability with respect to thermal and Rayleigh-Taylor axial modes and its modification by the electromagnetic field diffusion and radiation cooling. The interior part of imploded plasma shell is examined on stability and conditions for MHD Rayleigh-Taylor instability are obtained which are realized as a rule under significant compression degree near final stage of implosion just before pinching. Theoretical results and numerical complete simulations by means 2D ZETA code are compared.

ASYMPTOTIC SOLUTION FOR INTENSE RADIATING LINER

As shown earlier by one of the authors [3] the dynamics of magnetically accelerated dense radiating plasma liner in the planar geometry approximation may be overwritten by nonlinear wave equation. An arbitrary initial distribution evolves to the asymptotic solution in which the liner density and the magnetic field B have exponential distributions with characteristic scale - skin depth (the magnetic field twice wider):

$$B = B_0 e^{-\frac{x}{\Delta}}; \qquad \rho = \frac{B_0^2}{4\pi a \Delta} e^{-2\frac{x}{\Delta}}; \qquad v = x \frac{\dot{\Delta}}{\Delta} \qquad for \quad x \geq 0 \tag{1}$$

---

* Except the case of very low density high Z plasmas which are heated by intensive shock wave. In this case ions are heated mainly, radiation cooling is limited by ion - electron energy exchange rate and thermal pressure may be sufficiently high. Considering of such low density effects is out of a subject of this paper (see [5,6]).

here x is a coordinate in the frame of reference of moving liner in a direction of liner

acceleration a under action of applied magnetic field $B_0(t)$, $\Delta = \sqrt{\dfrac{\int \dfrac{c^2 a}{\sigma} dt}{2\pi a}}$ - liner skin-depth.

This solution was derived under condition that the plasma thermal pressure is negligible with respect to magnetic one. In order to obtain a plasma density distribution on the border magnetic field - plasma i.e. for $x<0$ it is necessary to take into account the plasma thermal pressure and some kind of anomalous resistivity at low density plasma. Due to $\beta<<1$ a

thickness of the transition layer δ is much less the skin-depth $\delta = \dfrac{c_s^2}{a} <<\Delta$ and therefore the

electric field is constant inside this layer and B changes there just in the next order by δ/Δ parameter. Then developing the procedure [3] for this region it is light to get the plasma density distribution inside the transition layer which has the next expression simplified with the accuracy of the main order by δ/Δ :

$$\rho(x,t) = \begin{cases} \rho_0 e^{2\frac{x}{\delta_a}}, & \delta_a = \dfrac{\delta\sigma\rho_a}{\sigma_a\rho_0 - \sigma\rho_a} \quad for \quad x \le -\lambda\delta \\ \rho_0(1 - e^{-\lambda-\frac{x}{\delta}}) + \rho_a e^{-\lambda-\frac{x}{\delta}}, & for \quad -\lambda\delta \le x < 0 \end{cases} \tag{2}$$

$\lambda = 0.5\dfrac{\delta_a}{\delta}\ln\dfrac{\rho_0}{\rho_a}$ is a parameter reflecting the concrete point of the conductivity transition from

anomalous σ_a at ρ_a to classical σ. The solutions (1) and (2) are sewed together at the point $x=0$,

$\rho_0 = \dfrac{B_0^2}{4\pi a\Delta}$ with the accuracy of the main order by $\rho_a/\rho_0 <<1$.

The solution (2) for the external surface of the liner is formal because of instabilities destroying it. Unlike of it the solution (1) for the liner interior structure has much more deep sense. As complete 2D radiation MHD simulations and theory below show the inner liner part is more stable during almost all implosion and distribution (1) realizes locally in spite of instabilities.

The external liner surface is unstable due to thermal and Rayleigh-Taylor instabilities.

AXIAL THERMAL INSTABILITY

The thermal instability of the liner external surface is a result of increase of the plasma conductivity versus temperature. Actually as mentioned above the electric field is almost constant in external plasma layers as they are thinner the skin - depth and joule heating rises with the temperature growth. As far as the layer is heated it intercept more the current from more deep layers. An electron thermal conduction cannot suppress the instability process as it is magnetized by transversal magnetic field as well as radiation transfer cannot do it also as external plasma is transparent. Detailed instability examination of the nonhomogeneous nonstationary distribution in the frames of MHD with ohmic heating shows that in a competition of the joule heating and electromagnetic field diffusion the instability on the external liner

surface takes place if $\dfrac{\partial\ln(\sigma)}{\partial\ln(T)} > 1 + \dfrac{\partial\ln(\sigma\varepsilon\rho)}{\partial\ln(T)}$, here ε is the plasma specific internal energy. The

minimum $min(\dfrac{\partial\ln(\sigma\varepsilon\rho)}{\partial\ln(T)}) \approx 0.5$ for heavy ion plasmas realizes for short wavelegth modes when

plasma has time to leave the hot points i.e. $c_s\tau > 2\pi/k$. (k - a wave number). The characteristic time of instability growth is typical for thermal instabilities i.e. the plasma heating time

$\tau = \dfrac{2\sigma\varepsilon\rho T}{j^2}$. The thermal instability develops as ring strata stretched in z direction on the external liner surface with a scale much less the skin-depth. Numerically this instability was observed in complete radiation MHD simulations of the argon shell implosion [7].

The nonisothermal instability of multicharged ion plasma due to shock wave heating of ions from one side and radiation cooling of electrons from another takes place also in low density plasma especially if the shock wave propagates through regions of falling down density where the shock wave accelerates, for example like for gas puff annular plasma [7].

Thermal instabilities develop on the stage before the main acceleration and produce short wave perturbations for the Rayleigh-Taylor instability.

RAYLEIGH-TAYLOR INSTABILITY OF LINER EXTERNAL SURFACE

The external surface of accelerated plasma shell is unstable due to MHD Rayleigh-Taylor instability classically as gradients of the magnetic field pressure and plasma density are in opposite directions. However the MHD Rayleigh-Taylor instability of multicharged ion plasmas has special features. In a long wavelength limit it is restricted by the finite magnetic sound speed and in the short wavelength limit it is suppressed by the magnetic field diffusion.

The stability examination of the solution (2) for exterior plasma border under simplifying condition $\dfrac{B\tilde{E}_z}{E_z\tilde{B}} \approx \dfrac{\Delta}{\delta} >> 1$ (where perturbations are with a symbol ~ and background values - without it) by linearisation procedure of MHD equations leads to the next linear equation for the relative perturbation $\zeta = \dfrac{\tilde{\rho}}{\rho}$:

$$\frac{\partial^2}{\partial t^2}(\Box_M - a\frac{\partial}{\partial x} + c_A^2 \frac{\partial \ln \rho}{\partial x}\frac{\partial}{\partial x})\varsigma = (D\frac{\partial}{\partial t}\Delta(\Box_S - a\frac{\partial}{\partial x}) - c_A^2 a k_z^2 \frac{\partial \ln \rho}{\partial x})\varsigma \qquad (3)$$

where k_z is a wave vector axial component; Δ is the Laplace operator; $\Box_M$, $\Box_S$ - operators of magnetic sound and ion sound respectively; $D = \dfrac{c^2}{4\pi\sigma}$ is the magnetic field diffusion coefficient. For the short wavelength limit where there is the increment maximum analysis of this equation is relatively simple and shows that the maximum corresponds to $k_z \approx \dfrac{c_A}{c_S}\Delta^{-1} > \Delta^{-1}$, the main effect restricting the increment in this limit is the magnetic field diffusion. Estimations for the typical liner implosion conditions $\beta \approx 0.1$, $\Delta \approx 1mm$ the most unstable harmonic has a wavelength $\lambda = 2\pi/k_z \approx 2 \div 3mm$ which corresponds to presented below 2D tungsten plasma liner simulations.

The liner external surface is unstable all time during implosion. This Rayleigh-Taylor instability leads to a redistribution of masses in external plasma layers, formation of bubbles and spikes and increase of the effective liner thickness.

MHD RAYLEIGH-TAYLOR INSTABILITY OF LINER INTERIOR

The inner part of the unperturbed liner is described asymptotically by distributions (1), gradients of magnetic field pressure and plasma density are in the same direction and it seems to be stable with respect to the Rayleigh-Taylor modes, gravitation waves only may be exited in it. Liner implosion simulations closely follow these notions up to some compression degree of the liner, but after it becomes unstable and the liner interior is destroyed quickly (see also, [7,9]). It cannot be explained by nonlinear development of bubbles from external surface as they have not penetrated yet so deep.

The stability analysis of the space and time dependent solutions (1) in the frames of MHD equations under conditions of $\beta<<1$ and $a >> c_S^2/\Delta$ leads to the next linear equation for the relative magnetic field perturbation function $\varsigma = \dfrac{\tilde{B}}{B}e^{0.5(\ln B_0 - k_z^2 \int Ddt)} \propto e^{ik_z z}$:

$$\ddot{\varsigma} + \varsigma\left[k_z^2(c_A^2 + c_S^2) - \tfrac{1}{4}(Dk_z^2 - \ln \dot{B}_0)^2 - \tfrac{1}{2}\ln \ddot{B}_0\right] = 0 \tag{4}$$

where logariphmic derivative is signed by $\dfrac{\partial}{\partial t}\ln B_0 = \ln \dot{B}_0$, with two points is the second order derivative respectively.

An instability takes place if the value in figured brackets let us sign it by letter A satisfies to two conditions $A<0$ and $/A/> \tfrac{1}{4}(Dk_z^2 - \ln \dot{B}_0)^2$ that occurs if second logarithmic derivative of B_0 by time is positive and sufficiently high). The liner inner part is unstable if the applied magnetic field changes quickly for example at the final stage of the implosion before pinching (the current is almost constant but radius diminishes and $B_0 = \dfrac{2I}{cr}$).

2-D RADIATION MHD SIMULATION RESULTS

The radiation MHD code ZETA [7,9] was used for the complete simulation of 2-D tungsten plasma liner implosion. The ZETA includes the quasi neutral plasma magnetohydrodynamics with self-consistent electromagnetic field, energy exchange between plasma electrons and ions, finite conductivity, heat conduction, radiation transport and tables for EOS, atomic constants, spectral opacities, emissivities and kinetic plasma coefficients. The radiation transport is calculated in a multigroup semianalytical self-consistent model both in LTE and in non-LTE regimes.

A coupling of the z-pinch with the pulsed power generator was modeled by an electrical circuit equivalent to the Z generator output parameters. During the liner implosion the total current reached *18-19 MA* depending on the load.

Single shell and double shell liners were simulated. The density of the liners were randomly disturbed with different levels (*5%, 10%*) or undisturbed. Results on the double liner implosion are discussed in the other report [9].

The initial dimensions of the single liner are: *2cm* radius, *2cm* height , shell thickness 1mm with different masses *m=4÷6mg*.

Initial liner mass perturbations causes instability at first on the external surface of the liner, after inside. Linear mass of the liner (the mass per length unit) redistributes, bubbles and spikes occur. The characteristic liner thickness (thickness averaged by the liner height) increases due to regular increase in time of the skin-depth and due to instability growth. On the figure 1 the linear liner mass in percents to the middle one versus liner length for different time moments is represented. Initial random mass perturbations was *10%* maximum for the total liner mass *m=4mg*. The time is shown from the beginning of the main voltage pulse at *0.1μs.*. Mass perturbations start to growth significantly since 163*ns* up to *+60% -80%* at *229ns* . It is possible to evaluate the characteristic wavelength of the most unstable mode $\lambda \approx 2.5mm$.

On the figure 2 the dynamics of the characteristic liner thickness $<dr>= \sqrt{\dfrac{\int r^2 \rho d\vec{r}}{m}} - <r>^2$ (where $<r>$ is the middle liner radius) versus time is shown for the same initial mass. The thickness without initial mass perturbations during implosion before pinching follows the skin-depth. But with *10%* mass perturbations it follows the skin-depth until *160ns*, after it increase due to instability at first linearly until approximately *200ns*, then nonlinearly and finally near *220ns* pinching on the axis begins.

This is shown on figure 3 where are represented the spatial distributions of mass density at different time moments. The external surface of the liner is unstable, its internal surface is closely stable up to compression degree about of 3. After that closer to the axis the perturbations of the inner surface as of the outer one increase and unhomogeneous z-pinch with the wide corona forms. The unhomogeneous z-pinch radiates at maximum 238TW which is more than twice lower homogeneous pinch.
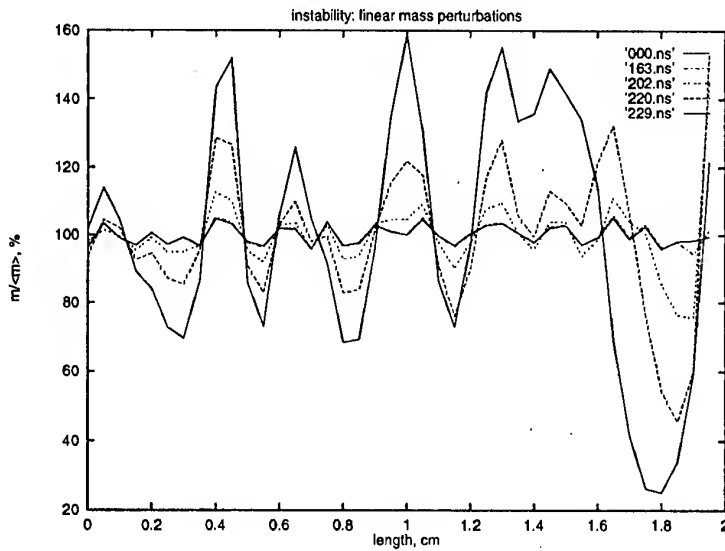
Figure 1. The relative linear mass distribution along the liner length for different time moments for *10%* initial mass perturbations.
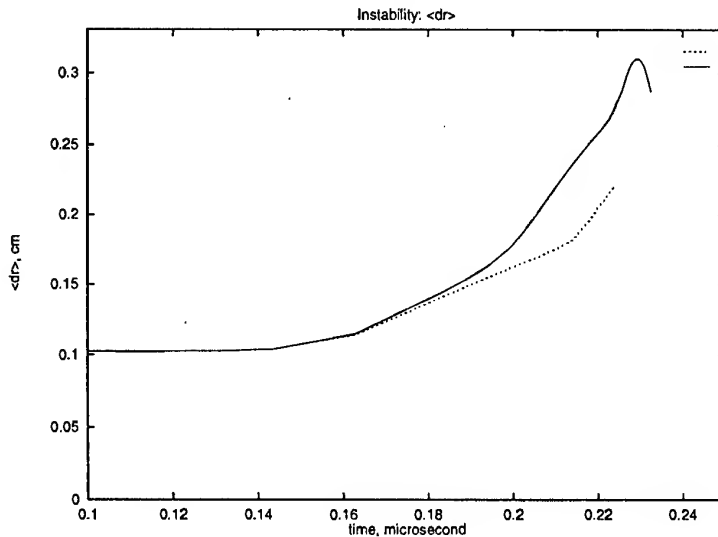
Figure 2. Characteristic liner thickness for 10% liner mass initial perturbations - solid line and 0% - dashed line vs liner implosion time.

a

b

c

d
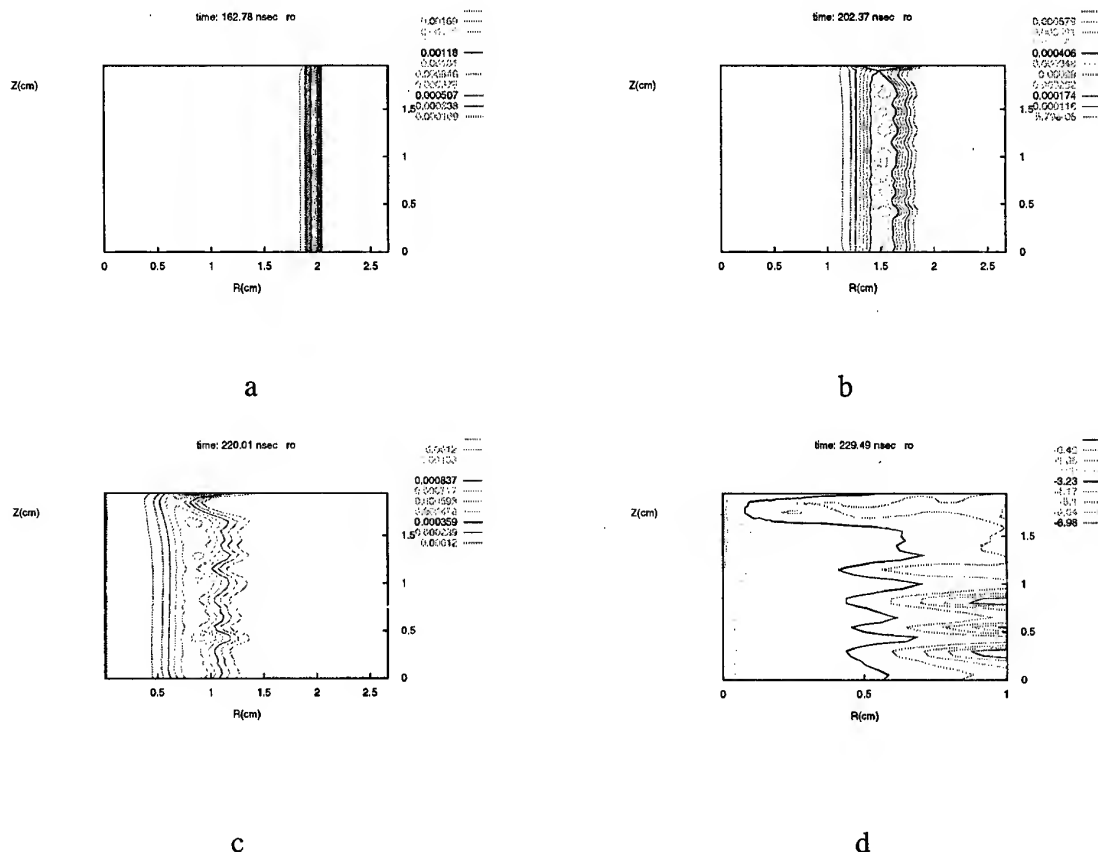
Figure 3. The history of implosion for the single liner simulation with *10%* initial mass perturbations as density isocontours at different time moments: a - instability start *162.78ns*, b - linear growth *202.37ns* , c - nonlinear growth and interior instability *220.01ns*, d - z-pinch *229.49ns*. The box for a, b, c has *2.67 cm* , for d - *1cm* along *R* axis and *2 cm* along Z axis. For d - logarithmic scale for density isocontours is applied. The initial positions of the liner at *R=2cm*.

ACKNOWLEDGMENTS

[1] Zakharov S.V., Smirnov V.P., Grabovskii E.V. et al. Proc. of the I.A.E.A Technical Commitee Meeting on Drivers for Inertial Confinement Fusion. Paris, France Nov. 14-18,1994. 395 (1995).

[2] Spielman R.B., Deeney C., Chandler G.A. et al. Phys. Plasmas, 5, 2105 (1998).

[3] Grigoriev S.F., Zakharov S.V. Sov. JTP Letters. 13, 254 (1987)

[4] Vikharev V.D., Zakharov S.V., Smirnov V.P. et al. Fizika plazmy. 16, 671 (1990) (in Russian).

[5] Branitskii A.V., Zakharov S.V., Smirnov V.P. et al. Fizika plazmy. 17, 531 (1990) (in Russian).

[6] Gasilov V.A., Zakharov S.V., Panin V.M. Influence of Azimuthal Instabilities on the Acceleration Dynamics of Radiating Liners. Preprint IAE 5464/6, 1992.

[7] Benattar R., Ney P., Nikitin A., Zakharov S.V., Starostin A.N., Stepanov A.E., Rerich V.K., Nikiforov A.F., Novikov V.G., Solomyannaya A.D., Gasilov V.A., Krukovskii A.Yu., 4th International Conference on Dense Z-Pinches Vancouver Canada 1997, AIP Conference Proceedings 409, 211.

[8] Peterson D.L., Bowers R.L., Brownell J.H. et al. Phys. Plasmas, 3, 368 (1996).

[9] R. Benattar, S.V. Zakharov, A.F. Nikiforov, V.G. Novikov, V.A. Gasilov, A. Yu. Krukovski. 12th Int. Conf. on High-Power Particle Beams: BEAMS'98. P2h, 0094.

STUDIES OF MULTIWIRE ARRAY PLASMA FORMATION USING X-RAY BACKLIGHTING

T.A. Shelkovenko[*], S.A. Pikuz[*], A.R. Mingaleev[*], D.A. Hammer and B.R. Kusse

Laboratory of Plasma Studies, Cornell University, Ithaca, NY 14853

ABSTRACT

Issues regarding the generation of cylindrically symmetric dense z-pinch implosions initiated from multiwire arrays in recent experiments on the Z accelerator at Sandia National Laboratories, Albuquerque, are investigated using the 420-kA, 100-ns XP pulser. Experiments to study merging plasmas from adjacent wires utilize 2 or more Al, Ti, Fe, Cu, Ni, Mo, Pd, Ag, W, Pt or Au wires (13-50 microns in diameter) separated by 0.1-1-mm with up to 125-kA per wire. The explosion phase of the wires is studied with wires carrying at most a few kA each for 30-70-ns. The influence of adsorbates on the wire-generated plasma is being tested by comparing results from initially hot and room temperature W wires. The wire plasmas are imaged using 13-25 micron Mo wire, and 20 micron Pd wire, 150-200-kA x-pinch x-ray backlighters which are < 5 microns in size and about 1-ns in duration. Two images with separations ranging from 5 to 20-ns are obtained with 2-4 keV x-rays. Experiments on plasma merging with 2-4 wires in a linear array show that the coronal plasmas which form around each wire coalesce within 50-ns into a dense plasma between the wires when the interwire spacing is less 0.2-mm. This plasma is significantly more uniform in the case of heated wires. For larger interwire spacings, a plasma which appears unstable forms close to the center of the interwire gap. We have also found that the physical properties of the wire material appear to influence the rate of expansion of the residual wire cores after initial plasma formation. For higher resistivity materials (Ti, Fe, Ni, Pd, W), the wire cores have expanded to 3-5 times the initial wire diameter by 40-50-ns after the start of the current pulse. By contrast, the expansion factor is 5-10 times for lower resistivity materials (Al, Cu, Ag, Au).

Recent experiments on the Saturn [1] and Z [2] pulsed power accelerators have shown that x-ray peak powers and total yields can be increased enormously from wire-array-initiated z-pinches when large numbers of wires in a cylindrical array are used. Qualitatively, these results can be understood as being a consequence of the improved cylindrical symmetry of the implosion when the number of wires increases, together with a reduction in the growth of instabilities due to the reduced current per wire which will improve both azimuthal symmetry and axial uniformity of individual wire plasmas, although other explanations are also possible. In this paper we report results of experiments which suggest two ways to improve the azimuthal symmetry and axial uniformity of wire-array-initiated z-pinches: 1.) Heating the wires to eliminate surface contaminants (adsorbed gases, grease, etc.) and 2.) using high conductivity metals for the wires, both of which we find experimentally to improve the apparent uniformity of plasma formation in wire-initiated z-pinches.

The principal means by which we monitored wire initiated z-pinch plasmas was x-ray backlighting, both direct [3] and monochromatic [4], using one or two X-pinch plasmas [5] as the backlighter x-ray source. The experiments were carried out using the 400 kA, 100 ns (fwhm) XP pulsed power generator at Cornell University, which is described elsewhere [6]. Mo and Pd X-pinches were used as backlighter x-ray sources using a combination of Be and Ti filters to restrict the energy range of the x-rays used to image the z-pinch plasmas to 3-5 keV. In this energy range, these X-pinches are observed to produce micron-scale x-ray source

[*]Permanent address: P.N. Lebedev Physical Institute, Moscow, Russia

points, with only a single such point obtained most of the time if a two-parallel wire array load mode of operation (to be described shortly) is used [7].

Other diagnostics used in these experiments included photoconducting diodes (PCDs) with subnanosecond time resolution used to monitor the moment of the x-ray burst from the X-pinch backlighter, Rogowski coils to monitor the current through different portions of the pulsed power generator load circuit, and x-ray pinhole cameras to obtain the time integrated images of the X-pinch(es) and z-pinch(es) in each pulse. Figure 1a shows a sample total current trace together with a typical PCD pulse from an X-pinch backlighter which illustrates the timing of the backlighter pulse relative to the start of the current trace; it also shows that there is only a single x-ray peak that has a ~ 1 ns width. Figure 1b illustrates the spatial resolution of the direct backlighter method under good conditions.
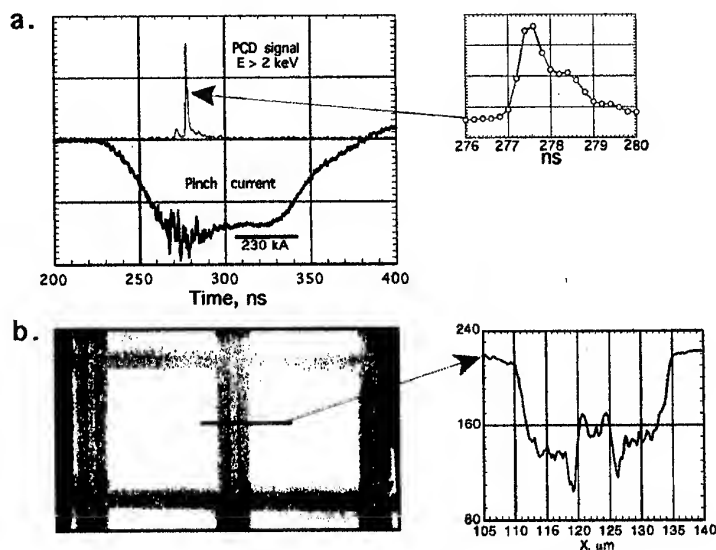
Fig.1 Examples Of data which demonstrate the spatial and temporal resolution of the direct backlighting method using a Mo X-pinch as the backlighter: a - typical total current and PCD traces showing the relative timing of the backlighting pulse relative to the start of the current trace; b. - an x-ray shadow image and densitometer tracing of a Ni mesh with wire substructure
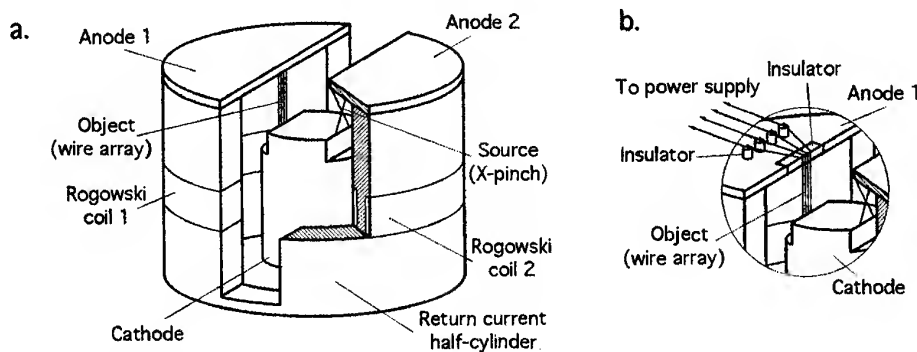
Fig.2 X-ray backlighting experimental setup with two loads in the diode in parallel, a - without heating and b - with heating.

Figure 2 illustrates the mode of operation of the x-ray backlighter and wire array z-pinch experiment when tungsten wire-initiated plasmas were imaged with and without heating them to a red-hot state for 5-30 minutes right up to the moment the high current pulse was applied. In this experimental arrangement, the wire array load and the X-pinch were parallel loads for the

pulser, and their separate currents were measured using Rogowski coils around the separate return current paths of the two loads. Figure 3 compares the results obtained using pairs of wires with and without pre-heating. These images were obtained at the time indicated in the current trace. For these pulses, there was about 40-60 kA per wire in the z-pinch. Notice that in both experiments, the W wires have expanded to about 4 times their original size. However, the dense core plasmas and the plasma between the wires appear to be more uniform for the preheated wires than for the wires which were initially room temperature. The axial nonuniformities apparently triggered by the adsorbates and/or grease on the wire surface evidently lead to a non-uniform blowoff of plasma from the surface. This plasma between the wires, is absorbing some tens of percent of the 3-5 keV backlighter x-rays and therefore cannot be composed of carbon or other low Z material but is most likely made up of tungsten from the wire itself.
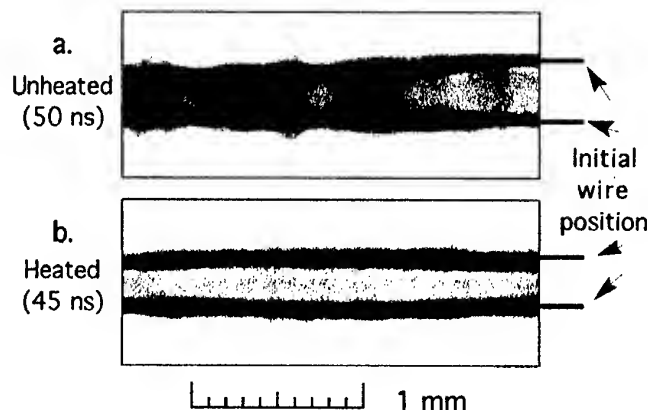
Fig.3 X-ray shadow image of two 20 μm W wires, a - unheated and b - heated.

Figure 4 shows the experimental geometry used to compare high conductivity wires (Al, Cu, Ag and Au) with comparable Z, lower conductivity wires (Ti, Ni, Pd, Pt, W, etc.). In these tests two X-pinches were in parallel as the inner load, and the z-pinch-generating wires were in the separately monitored return current channels.
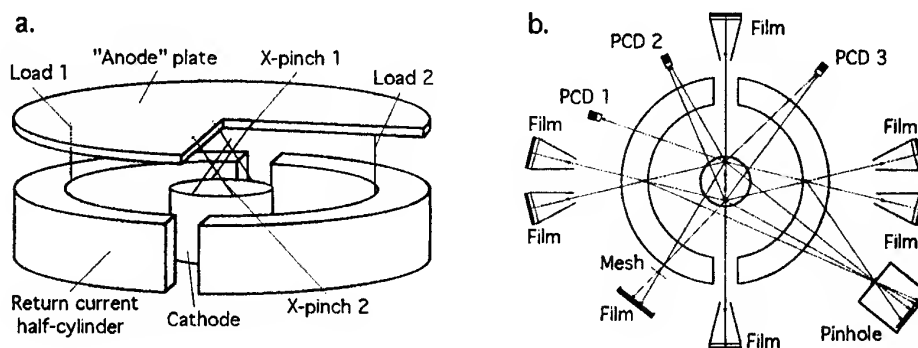
Fig.4 X-ray backlighting arrangement with two loads in the return current half cylinder circuits.

By using different X-pinch wire materials (25 μm Mo and Pd) or X-pinches from different size wires of the same material (17.5 μm and 25 μm Mo), images of the z-pinches were obtained at two times separated by 10-20 ns. As an example of images of two loads taken at the same instant by a single x-pinch is shown in Figure 5, which compares the dense core development

of Cu and Au wires relative to Ni and W wires. It is clear that not only do the Cu and Au wires expand more rapidly at the same current per wire, but also the plasma appears to be more axially uniform with the two higher conductivity wires. Images of loads at two times in a single pulse show that long scale length nonuniformities grow more slowly with the higher conductivity wires. These results suggest that the generation of azimuthally symmetric, axially uniform cylindrical plasmas from wire arrays will be more easily achieved with wires made from one of the four highest electrical conductivity metals, Al, Cu, Ag and Au, than with any other. We note that these results may have more to do with the way these metals draw into fine wires than with their conductivities, as suggested by Rick Spielman [8], but absent the ability to test a lower conductivity wire material that draws like Cu, Au, etc., we have not been able check out this hypothesis.
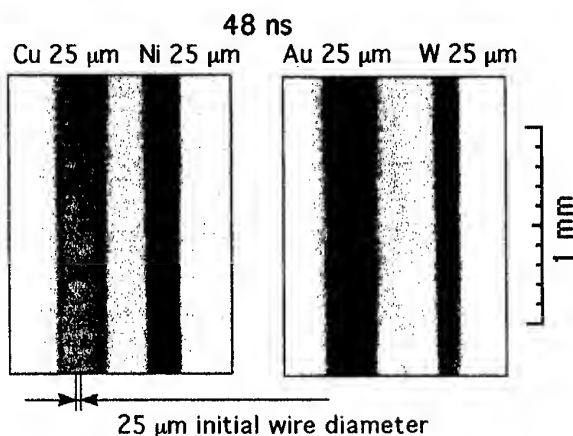
Fig.5 Dense core expansion comparison between Cu and Au (1.68 and 2.2. $\mu\Omega$-cm initial electrical resistivity) wires relative to Ni and W wires (6.84 and 5.5 $\mu\Omega$-cm).

[1] M.K. Matzen, Phys. Plasmas 4, 1519 (1997).
[2] R.B. Spielman, et al., Phys. Plasmas 5, 2105 (1998).
[3] D.H. Kalantar and D.A. Hammer, Phys. Rev. Lett. 71, 34806 (1993).
[4] S.A. Pikuz, T.A. Shelkovenko, V.M. Romanova, et al., Rev. Sci. Instrum. 68, 740 (1997).
[5] A.Ya. Faenov, S.A. Pikuz, T.A. Pikuz, V.M. Romanova, T.A. Shelkovenko, X-ray Sci. Technol. 5, 323 (1995).
[6] D.H. Kalantar and D.A. Hammer, Rev. Sci. Instrum. 66, 779 (1995).
[7] T.A. Shelkovenko, S.A. Pikuz, A.R. Mingaleev, D.A. Hammer, Bull. Am. Phys. Soc. 42 (1997).
[8] Rick Spielman, Sandia National Laboratories, Albuquerque, private communication.

BEAMS'98

12th INTERNATIONAL CONFERENCE
ON HIGH-POWER PARTICLE BEAMS
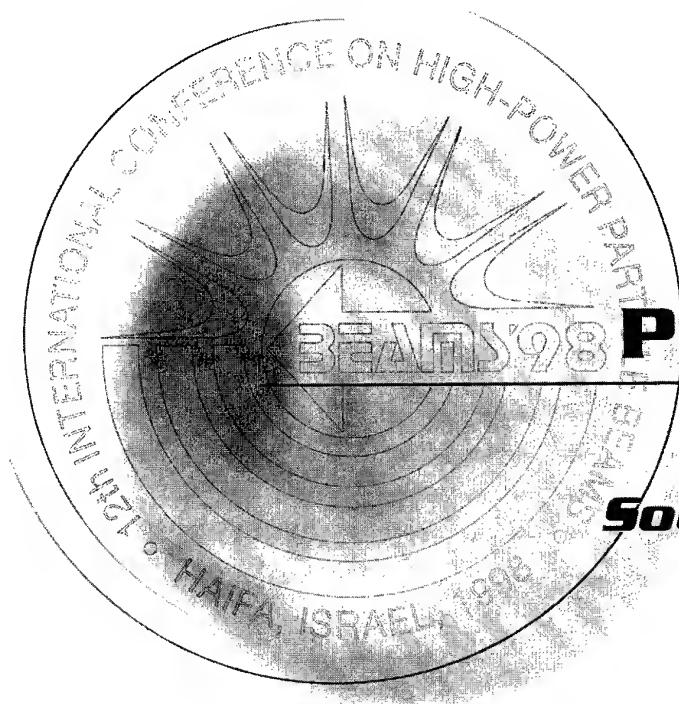
POSTERS

Radiation Sources, HPM

Vol. II

DESIGN OF A 7 MW, 95 GHz, THREE-CAVITY GYROKLYSTRON

M. R. Arjona and W. Lawson

*Electrical Engineering Department and Institute for Plasma Research,
University of Maryland, College Park, MD 20742 USA*

ABSTRACT

In this paper we present a three cavity design of a gyroklystron at 95 GHz. We present the design of the magnetron injection gun (MIG), the magnetic field coils, and the three-cavity microwave circuit. The MIG produces a 500 kV, 30-70 A small-orbit annular beam with an average perpendicular-to-parallel velocity ratio of 1.5 and a parallel velocity spread below 5%. The MIG requires a control anode with a voltage of about 65 kV, a magnetic compression of about 30, and a cathode loading near 10 A/cm^2. The circuit magnetic field is about 28.7 kG. The microwave circuit has a first-harmonic TE_{011} input cavity which is driven at 47.5 GHz, and second-harmonic TE_{021} buncher and output cavities which are resonant at 95 GHz. A peak power of 7.56 MW is obtained with 51.6 dB gain and 33.6% efficiency. A complete description of the system is presented along with a systematic study of the sensitivity of the device to parametric variations.

INTRODUCTION

The range in frequencies near 95 GHz is currently of great interest for radar applications due to the low atmospheric absorption. Because of the dependence of breakdown on frequency, there is interest to develop an amplifier for high energy RF acceleration of electrons in W-Band. The power tubes that are commercially available at these frequencies have maximum output powers of about 5 kW. At the University of Maryland, we have a program to develop high power gyrotron amplifiers for electron-positron collider applications. We have designed, constructed, and tested a variety of gyroklystron tubes, including a second-harmonic, two-cavity tube which produced peak powers above 30 MW at 19.7 GHz [1]. In this paper we scale the 19.7 GHz tube to 95 GHz. The 7.5 MW output power that simulations predict for our 95 GHz amplifier is three orders of magnitude above the current state-of-the-art. There are two main parts to the system: the MIG design is presented in the next section, followed by the design of the microwave circuit.

MAGNETRON INJECTION GUN

The magnetron injection gun which generates our injected beam is shown in Fig. 1. The gun design is based on the 19.7 GHz gun. A scaling code was used to obtain the starting dimensions. After scaled, the design was adjusted by changing the boundaries in both anodes and cathode until the required parameters were obtained with the minimum velocity spread. The square mesh code *Egun* is used to simulate the performance of the electron gun.

Two codes are used to generate input data for *Egun*. *Mesh_plt* takes data about the gun's boundaries which is specified by a set of line segments and arcs and generates the gun's actual boundary as a function of the meshes (grid) in the radial and axial dimensions as required by *Egun*. *Coil* takes the current and position of the coils (8 in our case) and generates the magnetic field on the z-axis mesh points. In order to run *Egun*, we put together all the previously obtained information from the magnetic field (*Coil* output), boundaries (*Mesh_plt* output) and some other input parameters such as the control anode voltage and number of rays to be simulated. *Egun*'s output details the characteristics of the produced beam which we can see in Fig.1. We also obtain several statistical beam parameters, for example the velocity spread in the z direction (Δv_z), maximum and average beam radius, and average velocity ratio (α).

To verify the accuracy of our results, a numerical check in the code calculations was done by varying the number of rays and number of particles until convergence was found. Accurate results were obtained when we used a mesh size of 0.05 cm (20 mesh/cm) and when we modeled the beam with 17 rays. All simulation results presented here were obtained with those values.

Our optimal gun was designed for the best results at an input current of 45 A. The parameters of the gun and the results of the simulation are summarized in Table I. The control voltage required to produce the proper velocity ratio was 65.1kV. The cathode loading is a little high, but well within the state-of-the-art and the peak electric fields are relatively low.

Fig. 2 shows how the axial velocity spread varies with beam current. As expected, the lowest velocity spread is at 45 A. This plot also shows how the control anode voltage needs to be varied to keep α at 1.5. The required change in the voltage is within a range of ± 3.5kV. It's important to notice that the Δv_z remains below 10% for all currents from 30 A to 65 A.

For the gun output beam we are mainly concerned with the velocity spread because of the strong dependence of efficiency on this value. The axial velocity spread can be lowered by decreasing the control voltage and then the velocity ratio

Fig.1 The 500 kV, 45 A Electron Gun Simulation
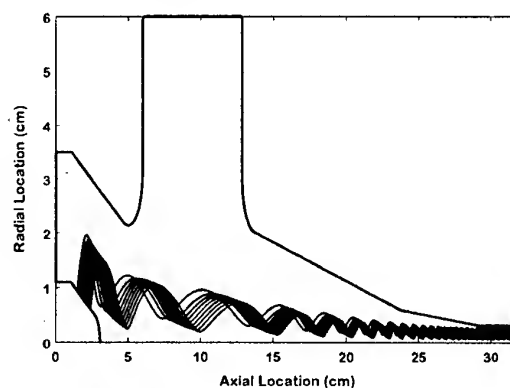
Table I: Electron gun specifications and simulated performance.

Emitter radius (cm)	0.78
Emitter width (cm)	0.958
Emitter angle (deg)	20
Cathode loading (A/cm²)	9.58
Cathode magnetic field (G)	900
Cathode-anode gap (cm)	2.262
Average velocity ratio	1.5
Axial velocity spread (%)	4.69
Average beam radius (cm)	0.163
Peak anode field (kV/cm)	81
Peak cathode field (kV/cm)	94
Space-charge current (A)	98

Fig. 2 Dependence of Velocity Spread on Current

-684-
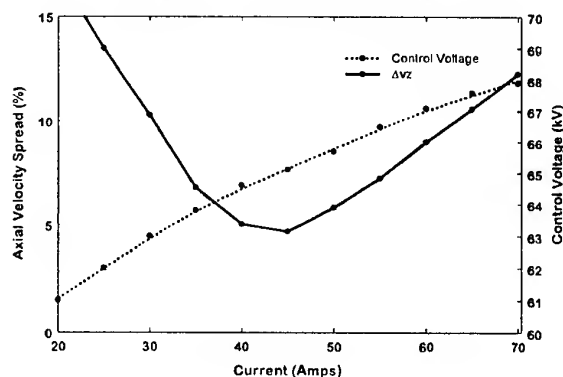
would be lowered as well. Lowering the velocity ratio makes the tube more stable but decreases the efficiency. Changing the control voltage from 58-69 kV varies α from 1 to 2. In our gun design, these values are optimized so that efficiency is maximum and spread is minimum.

MICROWAVE CIRCUIT

Our amplifier circuit is made of input, buncher, and output cavities that are connected by drift regions. The input cavity interacts at the first harmonic in the TE_{011} mode. Simulations showed that a buncher cavity was necessary in order to increase the power that can be extracted from the output cavity at the second harmonic (TE_{021}). A picture of the circuit design is shown in Fig. 3. The starting parameters for the circuit came from scaling the input and output cavities from the 19.7 GHz design and adding the buncher cavity. The buncher and output cavities have dolph-chebychev radial transitions. This proved in simulations to minimize the mode conversion from the TE_{02} to the TE_{01}. The initial dimensions were adjusted to get the desired first (47.5 GHz) and second harmonic (95 GHz) frequencies. This is done using a simulation code called *Coax*. This code takes for input the cavity's dimensions and starting points for the frequency and Q search. It then iterates the frequency and Q until it finds a solution. The azimuthal mode is an input to the code, but a field plotting routine is required to verify that the mode found by *Coax* has the correct radial and axial mode numbers.

After the dimensions were modified to the correct values, other codes were run to get the system efficiency for each cavity individually. These codes are *Hpm_gen* and *Gycoax*. They both simulate the beam's trajectory in the three cavities and the two drift regions. *Hpm_gen* takes *Coax* output and it also takes the output beam simulation parameters from *Egun*. This code takes for input all the dimensions from the circuit along with the coil locations and sizes. It then iterates changing the electric field phase and amplitude to obtain the highest efficiency. It outputs the maximum efficiency and the required Q for each cavity. The second code (*Gycoax*) takes a different approach to solve this same problem. *Gycoax*'s input includes the same information that *Hpm_gen* uses. The difference in this code is that it iterates to find optimal currents for a given electric field to get the highest efficiency. It outputs these currents, the efficiency and the required Q. Rather than use the actual ray data from *Egun*, the statistical results (e.g. velocity ratio, axial velocity spread) are used as inputs. The efficiency codes are iterated many times, changing the magnetic fields, the lengths of the drift regions, and the lengths, shapes, and quality factors of the cavities until the optimal values are achieved. *Egun* and *Coax* are rerun as necessary so that the simulations are self-consistent. The dimensions of the microwave circuit and the simulated results from *Hpm_gen* are given in Table II. Note that the quality factors are at least an order of magnitude below the resistive Q of a copper cavity. That means that over 90% of the output power can

Fig. 3 The 95 GHz Circuit Design
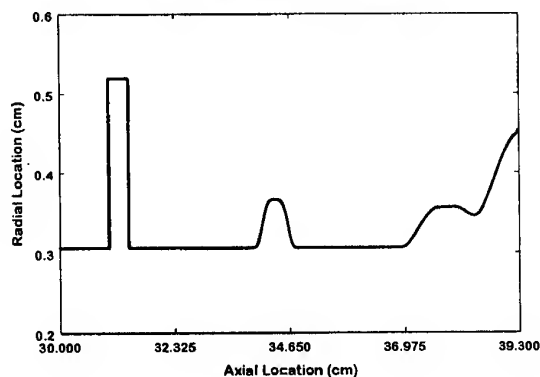
be extracted from the system and that the buncher Q must be realized with additional loss (e.g. lossy ceramics [1]).

To assure stability another code was used: *Qpb*. This code gives the Q (for each cavity) below which the device will be stable. This result and the simulated Q for each cavity (given by *Hpm_gen* and *Coax*) are shown in Fig. 4. The simulated Qs are positioned at the average magnetic field in each cavity. The system is clearly seen to be stable.

Another important parametric study is to see the relation between efficiency and velocity spread. Our MIG is predicted to produce a beam with 4.7%. We can see in Fig. 5 that the efficiency for an ideal beam is over 36%. Note that this our design's efficiency is less than 3% lower than that of the ideal beam and that the efficiency remains above 30% up to velocity spreads of about 6.5%

SUMMARY

The three cavity gyroklystron presented in this paper is the first amplifier which is predicted to produce more than 7 MW (7.56 MW) at 95 GHz. This high power is obtained from the interaction with a 45A, 500kV beam. We also designed a MIG that was proven by simulations to produce a high quality beam with the necessary characteristics. Using second harmonic allows a higher peak power since the beam's size is increased in proportion to the dimensions of the input cavity, which interacts with the beam at the 1st harmonic. This results in a very high gain of 51.6 dB and efficiency of 33.6%. In the future we hope to build and test this microwave system.

Table II: Microwave circuit parameters and simulated results.

Input Cavity	
Drive frequency (GHz)	47.5
Operating mode	TE_{011}
Resistive quality factor (Q)	600
Radius (mm)	5.19
Length (mm)	4.00
Input drive power (W)	52

Buncher Cavity	
Maximum radius (mm)	3.663
Length (mm)	20.20
Required Q	1075

Output Cavity	
Main section radius (mm)	3.457
Overall length (mm)	23.70
Required Q	1345
Power (MW)	7.56
Efficiency (%)	33.6
Gain (dB)	51.6

Fig. 4 The Start Oscillation Threshold
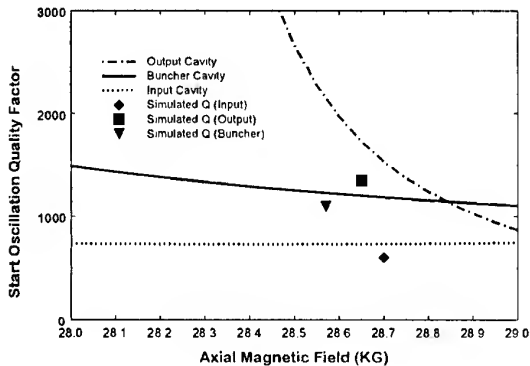
Fig. 5 Dependence of Efficiency on Velocity Spread
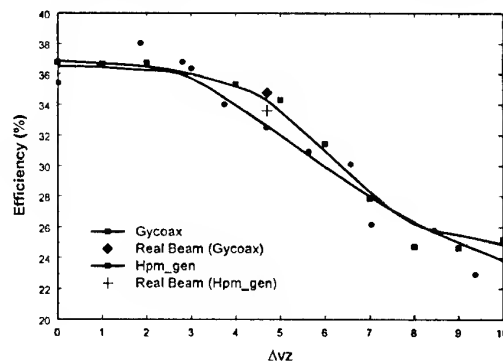
REFERENCES

[1] V. L. Granatstein and W. Lawson, "Gyro-Amplifiers as Candidate RF Drivers for TeV Linear Colliders" IEEE Trans. on Plasma Science, vol. 24, pp. 648-665 (1996).

PROGRESS IN INVESTIGATIONS ON MICROWAVE FEL DRIVEN BY MICROSECOND SHEET BEAM

N.V. Agarin, A.V. Arzhannikov, V.B. Bobylev, V.G. Ivanenko, S.A. Kuznetsov,
V.S. Nikolaev, M.A. Shcheglov, S.L. Sinitsky and V.D. Stepanov
N.S. Ginzburg[*] and N.Yu. Peskov[*]

Budker Institute of Nuclear Physics, Novosibirsk, 630090, Russia
*Institute of Applied Physics, N-Novgorod, 603600, Russia

INTRODUCTION

For production of mm-radiation with 10 GW power one needs a few tens of kAs current of 1MeV electrons passing through a generator. Ribbon or sheet E-beams allow one to reach this value of the current [1]. In the result of our investigations at U-2 accelerator in 1994 this type of the beams with 30 kA current at 10 μs duration was generated and transported through the slit vacuum channel [2]. In 1996 at this accelerator in modelling experiments with the beam current 3-5 kA in a passive magnetic undulator of 4 cm period we also obtained 200J energy of 4mm radiation in a few μs pulse [3].

The next step of investigations was aimed to reach the maximal efficiency of the microwave generation at a single mode operation of the generator. On this goal in 1997-98 we made reconstruction of the experimental setup intended to investigate FEM-oscillator. In order to increase productivity of the investigations this setup was replaced from the U-2 accelerator to the U-3 one that was specially reconstructed for generation of sheet beams.

EXPERIMENTAL SETUP

Schematic of the modified experiment that has been called "ELMI" is shown in Fig.1. In differ from the experiments at the U-2 device we have put between a ribbon diode and a slit vacuum channel with an undulator a special former to increase quality of the sheet beam. In this former with the length of 0.5m the electron beam is passing in a slit channel which gap between graphite walls smoothly decreases down to 4mm and then increases up to the value 10mm that is equal to a gap between walls in a Bragg resonator. The Bragg resonator is placed in an active undulator situated in a vacuum channel with the inner cross section of 4x25cm and the length of 1m. Transverse component of the undulating magnetic field can be varied from zero up to 2 kG by increasing the current in the coils of the undulator up to 1.6kA. Longitudinal component can be varied independently from transverse one by changing the current in coils wound on the vacuum channel. The maximal value of the longitudinal field is 13 kG.

THEORETICAL AND EXPERIMENTAL RESULTS

Regime of the microwave generation essentially depends on the value of these components of the magnetic field and on a smoothness of an increase in the amplitude of the

transverse one at the entrance of the undulator. Results of the computer simulations of the beam electron motion for the undulator used in experiments, are presented in Fig. 2. The ratio of an amplitude of the cyclotron parasitic harmonic in the transverse motion of the electron to an amplitude of the undulating harmonic is shown there for two cases. The first one shows this ratio as a function of the longitudinal magnetic field at zero angular spread of
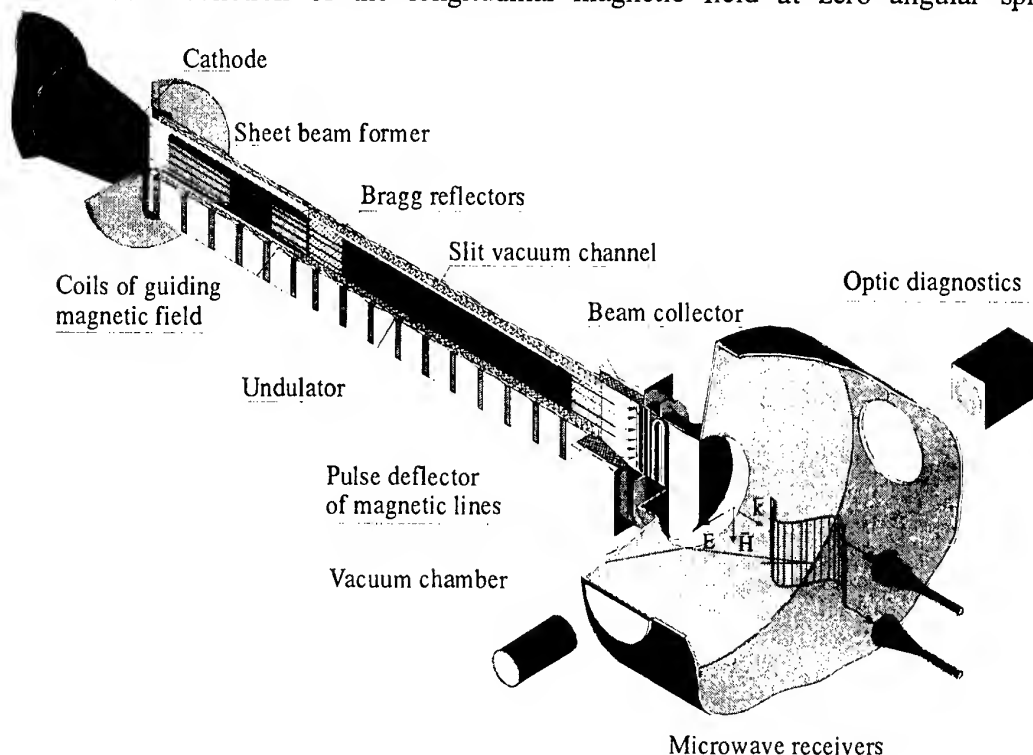
Fig.1. Schematic of the ELMI experiment at the U-3 accelerator.

the beam electrons. The second one demonstrates the influence of the initial angular spread of the electrons on this ratio at a certain values of the magnetic fields. Two curves in the both figures refer to various values of the smoothness of the undulator field increasing. (The smoothness is changed by varying the current in the entrance coils of the undulator at the fixed current in its homogenous part. The coefficient K is the ratio of these currents.) One can see that to depress the cyclotron harmonic in the electron motion we have to inject into the undulator the beam with the electron angular spread smaller than 2 degrees and the
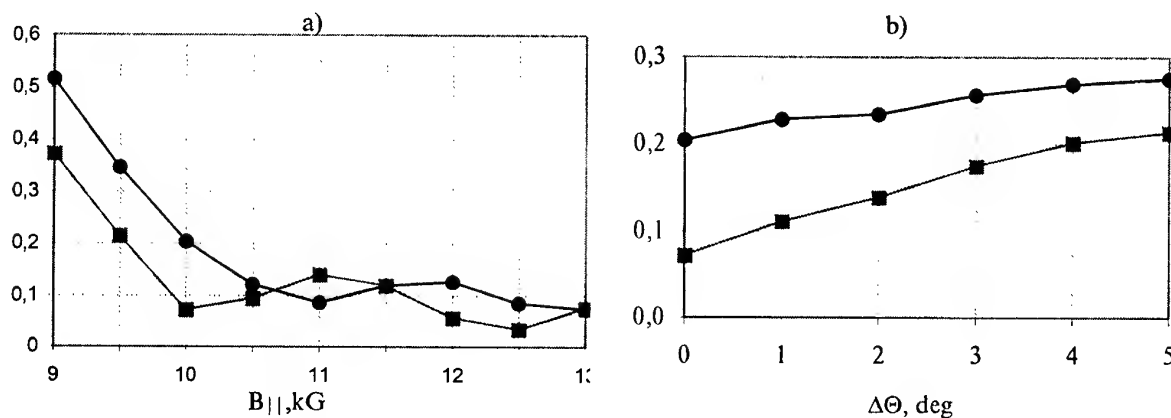
Fig.2. Ratio of the amplitudes of the cyclotron and undulating harmonics as a function of the longitudinal magnetic field(a) and initial angular spread of the beam electrons at $B_{||}$ =10kG and $B_\perp$=1kG (b). K=1 -circles, K=0.7 -squares.

smoothness in the increase of the undulating field has great importance at these conditions of the experiments.

A planar 1-D Bragg resonator is formed from the regular waveguide section of length $l_0=64$cm and two Bragg reflectors of lengths $l_1=18$cm and $l_2=10$cm. In case when the gap between the plates is equal to 10 mm, a corrugation period of the Bragg gratings is 2mm and a corrugation depth is 0.2 mm. These Bragg reflectors provide at a certain frequency the reflection coefficients $R_1=0.95$ and $R_2=0.75$ correspondingly. The Q-factor of eigen modes of such resonator is 3400 (See [3]). 2-D Bragg resonator is constructed by replacing 1-D Bragg gratings by two-dimensional ones. A corrugation period of the 2-D Bragg gratings is 3mm and a corrugation depth is 0.3 mm. These 2-D gratings provide mutual scattering of four partial waves: $\mathcal{A}_\pm$ propagating along the axis of the slit channel in $\pm z$ directions and having s field variations over transverse y-coordinate (the gap between the walls) and $\mathcal{B}_\pm$ propagating in $\pm x$ directions and having p field variations over y (See Fig.1). A stationary theory shows that the TM and TEM waves for which $\bar{E} \parallel \bar{y}$ can be used in such FEL versions as ubitron with guiding magnetic field and cyclotron autoresonance maser (CARM). The Q-factor is maximal for the lowest modes of these waves. Position of the modes of the "cold" resonator for the cases of using 1-D gratings and 2-D ones is shown in Fig. 3. It is seen that to reach a single mode operation is more easy in the case of the 2-D resonator.

Fig.3. Spectra of eigen modes for «cold» resonators.

Dynamics of FEL operation with a two-mirror Bragg resonator was studied by use of a time domain analysis taking into consideration the dispersion properties of the Bragg reflectors (See [4,5]). It is established that there is a significant difference in a process of growth oscillations in FELs with 1-D and 2-D distributed feedback. In FEL with 1-D distributed feedback a single-mode oscillation regime is established at nonlinear stage of evolution due to mode competition mechanism and caused by electronic mode selection. In contrast, in FEL with 2-D feedback the most high-Q mode is established from $t=0$ and accumulation e.m. energy in this mode takes place after that. Thus, an electrodynamics mode selection is realised in this FEL scheme.

The output for e.m. energy fluxes from a 2-D Bragg resonator is provided along four directions: longitudinal and transverse as well. This leads to practical difficulties in construction of the FEL. However, the single-directed output of radiation (both longitudinal and transverse one) may be provided using additional Bragg structures.

The active undulator with the plane resonator was tested with an operated current in the coils at the U-2 device. For example, one of the shorts for these testing experiments is presented in Fig.4. These experiments demonstrated good stable operation of the active undulator in the band of the required field.

CONCLUSION

New installation ELMI intended to investigate the FEM-oscillator with a sheet beam has been created on the base of the reconstructed U-3 accelerator. For this installation an active plane undulator with the longitudinal field up to 13kG and the periodical transverse one up to 2kG was manufactured and tested. Two-dimensional Bragg resonator to select a single mode of the radiation was also made. A vacuum chamber added to the exit of the slit channel to prevent influence of the microwave pulse shortening on measurements of the radiation parameters.
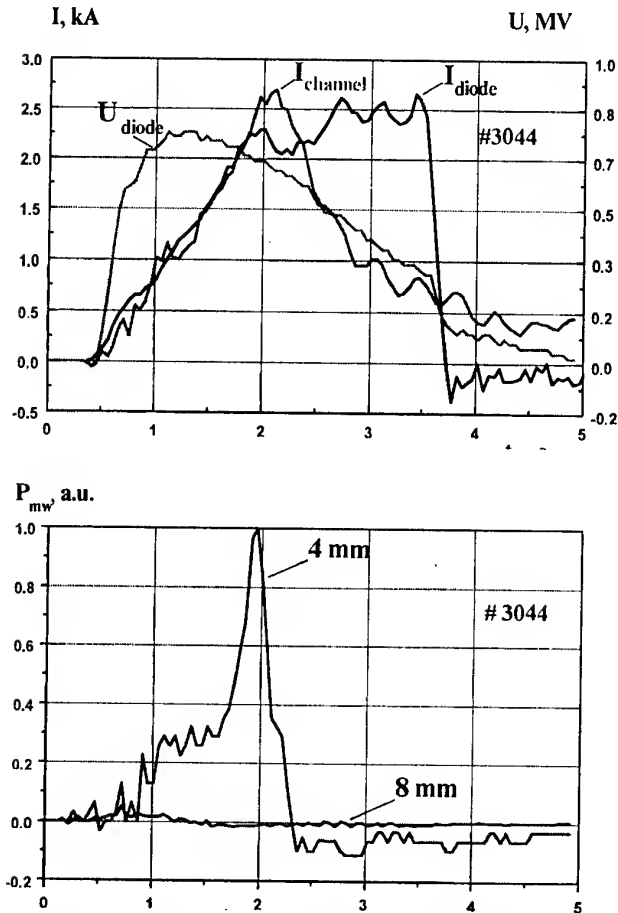
Fig4. Signals characterising generation of the mm-wave radiation at the active undulator

REFERENCES

1. A.V.Arzhannikov et al. Proc. of 9-th Int. Conf. on High-Power Particle Beams, Novosibirsk, Russia, 1990, vol.1,p 256-263.
2. A.V.Arzhannikov et al. Proc. of 10-th Int. Conf. On High-Power Particle Beams, San Diego, USA, 1994, p. 136-139.
3. M.A.Agafonov et al. J. Digest of technical papers of Int. Workshop on High-Power Microwave Generation and Pulse shortening, Edinburgh,UK,1997, p.185-190.
4. N.S.Ginzburg et al. II-Asian symposium on Free Electron Lasers, Novosibirsk, Russia, 1996, p.150-157.
5. A.V.Arzhannikov et al. Nucl. Inst. and Meth. in Phys. Research, 1994, vol. A358, p. 189-192.

GENERAL SCALING OF PULSE SHORTENING IN EXPLOSIVE-EMISSION-DRIVEN MICROWAVE SOURCES

James Benford*
Microwave Sciences
1041 Los Arabis Lane, Lafayette, CA 94549
and
David Price
Maxwell Physics International
2700 Merced Street, San Leandro, CA 94577

Microwave generation in devices that depend on synchronization between an electron beam and a resonant cavity or slow wave structure can be disrupted by changes in either. Explosive-emission-driven microwave sources use plasma as the electron source in the diode. This plasma is conductive enough to act as the boundary for both the applied diode voltage and the microwave electric field. The motion of this plasma can effectively change the dimensions of either the electron beam diode or the cavity and will thereby cause resonance destruction. This shortens the microwave pulse length τ_μ. Using simple models of cathode plasma motion and plasma speed dependence on diode current, we derive a scaling relation between microwave power and microwave pulse length. This general model of the process predicts that, for a Child-Langmuir diode, microwave power falls as $P \propto \tau_\mu^{-5/3}$ and that pulse energy falls as $E \propto \tau_\mu^{-2/3}$. Therefore, energy efficiency declines as the pulse length is extended. We compare with data from magnetrons, MILOs and BWOs, with good agreement. Explosive-emission-driven microwave sources are fundamentally limited by the speed of the diode plasma and can be improved by finding cathode materials that generate slower plasmas.

One principal cause of microwave pulse shortening at high power is the presence of plasmas in the diode or interaction regions[1]. Diode plasma is the root cause of many shortening mechanisms, such as electron beam expansion, detuning of the resonances upon which the source operation depends, gap closure in diodes and beam interception along its path. Other related mechanisms are high microwave field breakdown, multipactor, and beam-plasma instability. Here we address only pulse shortening caused by plasma expansion in the accelerating gap. It is widely observed that microwave power falls as pulse duration increases, and it falls at a rate such that energy in the pulse falls as well.

We advance a general proposition that all explosive emission devices will eventually be driven out of resonance (detuned) by plasma motion which produces either a sufficiently large change in the dimensions of the diode or a change in the dimensions of the slow wave structure or microwave cavity. Using simple models of cathode plasma motion and plasma speed dependence on diode current, we derive a scaling relation between microwave power and microwave pulse length. Both the scalings predicted here and those observed in experiments run counter to attempts to produce high energy microwave pulses by lengthening the pulse: higher energy will be obtained in shorter pulses, not longer pulses. Gains can be made by making the plasma heavier, thereby slowing down the perturbing plasma effects.

GENERAL SCALING

The simplest expression for output power, P, from any microwave source is:

$$P = \eta VI = \eta VjA \qquad (1)$$

with V and I the diode voltage and current, j, the cathode current density, A, the cathode surface area, and η the electronic conversion efficiency at resonance. We assume that the

emission characteristics are represented by a general scaling similar to the Child-Langmuir relationship:

$$j \propto \frac{V^n}{d^l},$$ (2)

with d the AK gap spacing and n and l diode physics dependent exponents. For Child-Langmuir scaling, appropriate for parallel-field linear beam sources, n = 1.5, l = 2. For parapotential diodes, such as for most vircators and magnetically insulated line oscillators (MILOs), n ~ 1, l = 1. (Here we have approximated the voltage dependence of parapotential flow as linear, a good fit for the domain of HPM experiments, where the diode voltage is typically between 300 kV and 1 MeV.)

Next we make the key assumption that the microwave pulse length τ_μ is limited by plasma expansion across the accelerating gap. In Figure 1 this gap is in the radial direction in the magnetron and MILO, but it can be both radial and axial in the linear beam sources. In fact the radial gap in linear beam geometry is usually smaller than the axial gap, so it is crucial to the pulse shortening phenomenon. When the plasma expands across some fraction of the gap, resonance is destroyed and microwaves cease. Therefore, the microwave pulse length scales like the cathode plasma transit time across the gap:

$$\tau_\mu \propto \frac{d}{v_p} \propto d \sqrt{\frac{m_p}{T_p}}.$$ (3)

T_p is the temperature of the cathode plasma and m_p is the mass of the (hottest and lightest) ion species which governs the location of the conducting surface.

Finally, following Mesyats and Proskurovsky[4], we assume that the cathode plasma temperature is derived from the joule heating due to the diode current:

$$T_p = \int_0^t \rho j^2(t')dt' \propto \rho j^2,$$ (4)

with ρ the cathode plasma resistivity. Equation 4 should be considered more a construct than a detailed theoretical model of the cathode plasma. Here we simply imagine that a number of different dissipative mechanisms (plasma expansion, radiation, electron thermal conduction) balance the joule heat flux input and rapidly establish an equilibrium temperature at a given current density level.

Combining Equations 1 and 2 and using Equation 4,

$$P \propto \eta j^{\frac{n+1}{n}} \propto T^{\frac{n+1}{2n}} \propto \frac{m_p^{\frac{n+1}{2n}}}{\tau^{\frac{n+1}{n}}}.$$ (5)

Using Equation 3, the pulse-shortening relation becomes:

$$P \propto \tau^{-(\frac{n+1}{n})}.$$ (6)

There are two consequences of this model. The first is that the fundamental pulse length dependence on the square root of the plasma ion mass means pulse lengths can be extended at a given power by increasing the plasma ion mass number. The second consequence is that the microwave pulse energy E, the product of power and pulse length, will scale as:

$$E \propto \tau^{-\frac{l}{n}}.$$ (7)

In this model, the energy in a pulse does not rise linearly with the pulse duration. For example, with Child-Langmuir scaling, $P \propto \tau^{-5/3}$, and $E \propto \tau^{-2/3}$. To double the pulse duration requires power be reduced by a factor of 0.32, and as a result energy efficiency decreases by a factor of 0.64. Clearly, if more energy per pulse is the goal, it doesn't pay to extend the pulse duration. Pulse shortening due to plasma in the diode drives seekers of higher energy efficiencies to shorter pulses.

COMPARISON WITH EXPERIMENTS

We have compared the above relations with data by using measured exponents in (2) for each source where available and inserting in (7). A complete discussion is in press (IEEE Trans. Plas. Sci., Special Issue on High Power Microwaves, Vol. 26, June 1998). The table shows that the power relation with pulse length is remarkably good for magnetrons (Figure 1) and BWOs, mixed for MILO. We know of no data for vircators, but for the variety of vircator with pinched flow, i.e., parapotential flow, the prediction is a scaling of 2.

<u>Scaling relations for exponent of power with pulse length</u>

Source Type	Predicted scaling	Experimental scaling
Magnetron	1.63	1.68± 0.23
MILO	1.6	1.24± 0.18
BWO	1.67	1.63
Vircator	2.0	?

The magnetron data gives essentially Child-Langmuir scaling, indicating the cross-field flow is limited only by space-charge. This may be due the flow interacting only weakly with the microwave fields and agrees with the observation that experimental values of microwave production efficiency are typically half that of theory and $\ll 1$ in all cases[2]. Perhaps microwaves are sufficient to allow flow across the gap but not strong enough to determine the flow.
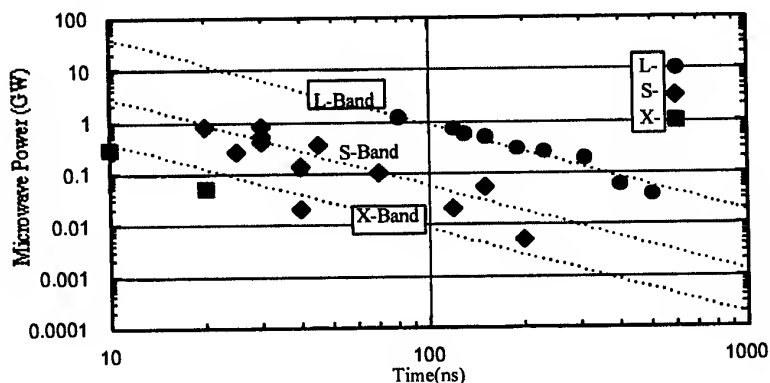
Figure 1. The maximum attainable microwave pulse length from relativistic magnetrons with explosive emission cathodes decreases as the peak output power increases. The data shown are collected from magnetron experiments conducted over the past two decades at Maxwell Physics International, MIT, NCSU, IAP, NRL, Stanford Univ., Rafael, Varian and T-CSF. In these various magnetron experiments the microwave power, P, scales with the frequency f, and the pulse length τ, like $P \sim f^2$ and $P \sim \tau^{5/3}$, respectively[2]. (Curves normalized to the L-band, 80 ns, 1.2 GW point.)

The increased scatter in the MILO data may indicate that several different pulse shortening mechanisms are competing. Alternately, choosing only the <u>maximum</u> power at each pulse length produces an observed scaling much closer to the expectation $P \propto \tau^{-1.6}$.

The Backward Wave Oscillator (BWO) consists of a foilless diode that injects a thin annular beam into a slow wave structure (SWS). The beam couples to the microwave fields in the SWS most efficiently if it skims the wall closely. Cathode plasma expands axially (along magnetic field lines) at fairly high speed and radially (across field lines) at lower speed. The radial plasma motion can expand the beam's annular width, changing the BWO coupling efficiency and therefore changing the microwave power.

As voltage and current are raised to produce higher power, the higher currents in the diode cause faster radial plasma expansion and shorter pulses. Equations 1, 2 and 3 should still apply, with the gap in Equation 3 the BWO diode's radial gap. The foilless diode operates with a Child-Langmuir characteristic, so the model predicts $P \propto \tau^{-5/3}$, $E \propto \tau^{-2/3}$.

Applying this to data from a 3 GW BWO at the Institute for High Current Electronics at Tomsk[3], up to about 2 GW the scaling is: $P \propto \tau^{-1.63}$, corresponding to n = 1.59, which fits the Child-Langmuir expectation (n = 1.5) well. Above 2 GW, the scaling is: $P \propto \tau^{-0.50}$. Clearly, another mechanism (with a different characteristic scaling) operates at higher powers and depresses the power relative to the plasma motion model prediction. RF breakdown is the likely culprit. The exponent, -0.50, is close to the range -1/2 to -1/3 that is normally[4] observed when RF breakdown at the output gap limits the microwave pulse of high power klystrons. The data suggest that the power saturates in the experiment of Gunin $et.$ $al.$ above 2 GW when RF breakdown takes over.

Gunin, $et.$ $al.$ assume that the pulse shortening mechanism in their experiment is microwave induced explosive emission in the SWS. At 3 GW, the very high microwave fields in the SWS (~1500 kV/cm) make the mechanism plausible. The scaling for this mechanism, from Mesyats and Proskurovsky[5], is $P \propto \tau^{-2/3}$. The data do not fit such a scaling. More observations on BWO's will be required to sort out the mechanism that causes the pulse shortening at lower powers. Currently, some manifestation of RF breakdown appears to limit the BWO pulse length at its highest achievable output power levels.

The agreement between this analytical model and the measurements on a large variety of magnetrons and a BWO experiment supports the hypothesis that cathode plasma motion is a culprit causing pulse shortening observed in many types of high power microwave sources. An implication of the model (Equation 6) is that the mass of the material causing diode gap closure is a key determinant of pulse duration. Three clear ways to extend the microwave pulse duration are: 1.) to reduce the plasma temperature by decreasing the current density, 2.) to eliminate the plasma, or 3.) to increase the plasma ion mass. The first tack leads to either large devices with large cathodes at moderate impedances or higher impedance designs that require high voltage (> 1 MV) in order to obtain high power. The second tack requires the development of high current density cathodes that do not rely on explosive emission. As for the third tack, most HPM source experiments have not had wall cleanliness sufficient to prevent the plasma formed by explosive emission from being determined by contaminants. The usual surface layer of water and hydrocarbons is quickly disassociated into hydrogen and other light elements. The lightest, fastest atoms determine the plasma speed. Therefore, improved surface conditioning is essential to lengthening pulses. From Equation 6, using heavier cathode materials will increase pulse energy. Some success with this approach has been reported with carbon fiber doped with Cesium Iodide[6].

The model of pulse shortening scaling proposed here agrees remarkably well with a variety of HPM devices. We urge other workers to compare their data with this model and to produce models of the other pulse shortening mechanisms.

ACKNOWLEDGMENTS

[1.] J. Benford and G. Benford, "Survey of Pulse Shortening in High-Power Microwave Sources," $IEEE$ $Trans.$ $Plasma$ $Sci.,$ Vol. 25, pg. 311-317, 1997.

[2.] J. Benford and J. Swegle, $High$ $Power$ $Microwaves$, Boston, Artech House, Chap. 5, pg. 172, 1992.

[3.] A. V. Gunin, A. I. Klimov, S. D. Korovin, I. V. Pegel, S. D. Polevin, A. M. Roitman, V. V. Rostov, A. S. Stepchenko, "Relativistic X-Band BWO with 3 GW Pulse Power," $Proc.$ $Int'l$ $Workshop$ on HPM $Generation$ and $Pulse$ $Shortening$, Edinburgh, U.K., pg. 173, 1997.

[4.] Private communication, Glen Westenskow, LLNL J. Wang and G. A. Loew, SLAC-PUB-4866, 1989.

[5.] G. A. Mesyats and D. I. Proskurovsky, $Pulsed$ $Electrical$ $Discharge$ in $Vacuum,$ Springer-Verlag, Berlin, pg. 87, 1989.

[6.] E. Garate, "Novel Cathode for Field-Emission Application," $Rev.$ $Sci.$ $Instru.,$ Vol. 66, pg. 2528, 1995. "Lowered Plasma Velocity with Cesium Iodide/Carbon Fiber Cathodes at High Electric Fields," J. Benford, D. Price and W. DeHope, Proc. Beams '98.

LOWERED PLASMA VELOCITY WITH CESIUM IODIDE/CARBON FIBER CATHODES AT HIGH ELECTRIC FIELDS*

James Benford
Microwave Sciences Inc.,
1041 Los Arabis Lane, Lafayette, CA 94549

and
David Price and William DeHope
Maxwell Physics International,
2700 Merced St., San Leandro, CA 94547

We have demonstrated reduced CsI plasma speed for macroscopic electric fields of up to 285 kV/cm with cesium iodide-coated (CsI) carbon fiber cathodes, sufficient for the diodes of GW microwave sources. Plasma speeds is 0.6×10^6 cm/sec, 3.5 times less than the bare carbon fiber. The apparatus had oil-free high vacuum conditions (metal seals and glass insulator) and the cathode was baked both before assembly at atmospheric pressure and in vacuum after assembly, to temperatures of >600 °C. A residual gas analyzer showed burnout of the water; base pressure was $\sim 10^{-6}$ Torr. An unexpected benefit of the CsI coating is that diode current and voltage traces are substantially more reproducible than with bare carbon fiber. With reduced plasma velocity, CsI cathodes should produce an extension of the HPM pulse length and an increase in pulse energy by a substantial factor in sources now limited by low-Z contaminant cathode plasma motion.

When explosive emission cathodes are used in higher power (>100 MW) devices, microwave pulse shortening can occur because of motion of the cathode plasma at speeds 1 to 5×10^6 cm/sec, which can limit present-day high power microwave (HPM) sources to a few hundred joules. In previous work[1-5] introduction of cathodes made from cesium iodide-coated (CsI) carbon fiber has shown plasma speeds reduced by factors of a few from uncoated carbon fiber, but previous work was at low diode fields of a few 10's of kV/cm. We have extended the CsI cathode to much higher fields, such as occur in HPM sources of the GW class.

We used a 450 kV, 500 ns, 50 Ω modulator. The cathode base is of POCO graphite, 8.0 cm diameter, 0.635 cm thick with full radius. To avoid contamination, no cutting fluid was used during the machining. The cathode tip assembly is made entirely of components compatible with high-vacuum operation--metals, no plastics. The region around the cathode consists of the anode and the downstream region beyond it. The anode is a mesh of copper 50-mil (0.127 cm) wire, 80% transmissive. Immediately behind it is an anode from an inactive L-band relativistic magnetron, made of ~300 pounds of stainless steel. A halogen lamp is inserted toward the anode along the axis from the downstream end.

The cathode was baked both before assembly at atmospheric pressure and in vacuum after assembly, to temperatures of >600 °C. During shooting, which followed immediately, the block cooled slowly, due to the large thermal inertia of the 300 pound block, so the diode region stayed heated. The residual gas analizer registered a large amount of water when heating began and a steady decline in water as the bakeout procceded. No water re-condensation could occur on the cathode surface between shots or bursts.

We first conducted a study of the bare carbon fiber cathode, then coated the cathode and repeated. Diode current and voltage traces for the CsI-coated cathode are substantially more reproducible than those for the bare carbon fiber cathode. The CsI diode is clearly more repeatable, with less "hash"—short-time fluctuations, compared to bare fiber. With bare fiber, the coupling between the 50 Ω driver and the ~125 Ω diode load varies as the diode impedance fluctuates. This matters because microwave generation depends sensitively on the electron beam. Higher levels of noise in the flow gives fluctuating microwave power levels. This beneficial effect may be because CsI emits copious UV, lighting up the surface much more uniformly, eliminating jets or flares of emission.

In Figure 1 the current begins at ~25 ns, when the voltage reaches ~290 kV across the 1.4 cm gap. The voltage drops momentarily, loaded by the beginning of emission, then resumes its rise. For bare carbon fiber the average value of this turn-on field is 67 kV/cm. For CsI-doped carbon fiber it is 124 kV/cm. Previous workers quote ~50 kV/cm for CsI-doped carbon fiber[1-5]. Previous work on carbon fiber may well have been essentially dominated by water and other volatiles so the lower turn-on field was characteristic of the volatiles, not the fiber.
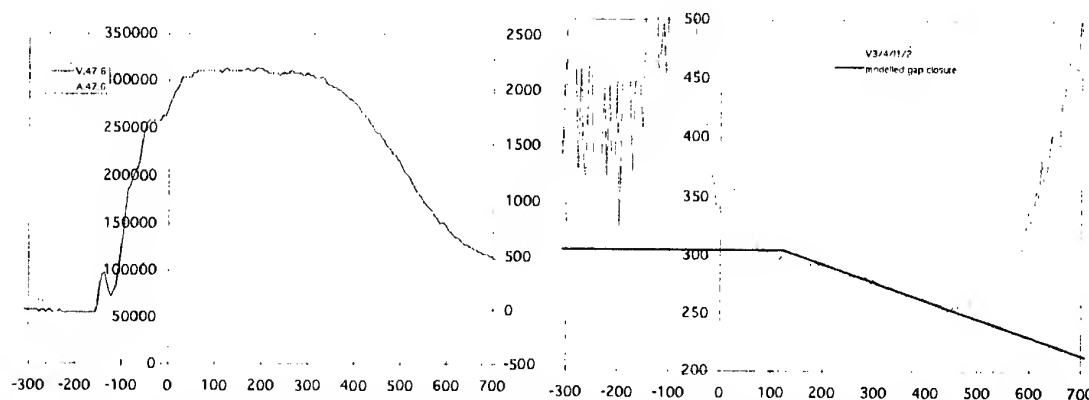
Figure 1. V(t) and I(t) for a CsI shot (tenth in a burst of 20 at 3 Hz) on the left. On the right are the inverse square root of perveance and the modeled gap vs. time, using the data on the left.

Figure 2 shows that for macroscopic electric fields of up to 285 kV/cm, sufficient for the diodes of GW microwave sources, closure speed for CsI on carbon fiber is 0.59±0.16 cm/µs. With the bare carbon fiber the magnitude and the shot-to-shot variation is much larger For bare fiber, closure speed is 2.08±0.71 cm/µs. Note that the ratio of speeds is 3.5, and the 1σ data spread varies by a factor of 4.4.

The ratio of closure speeds with and without CsI is 3.5. Therefore, we expect a factor of 3.5 extension of the pulse duration and the pulse energy at high power with properly cleaned cesium iodide-coated cathodes.

When plasma motion is the mechanism causing closure (and, in microwave sources, shortening the microwave pulse duration):

$$\tau_\mu \propto v_p^{-1} \propto \sqrt{m_p} \quad .$$ (6)

Therefore

$$\frac{m_{CsI}}{m_f} = 3.5^2 = 12.25$$ (7)

Closure Velocity vs. Electric Field
With and Without CsI Coating
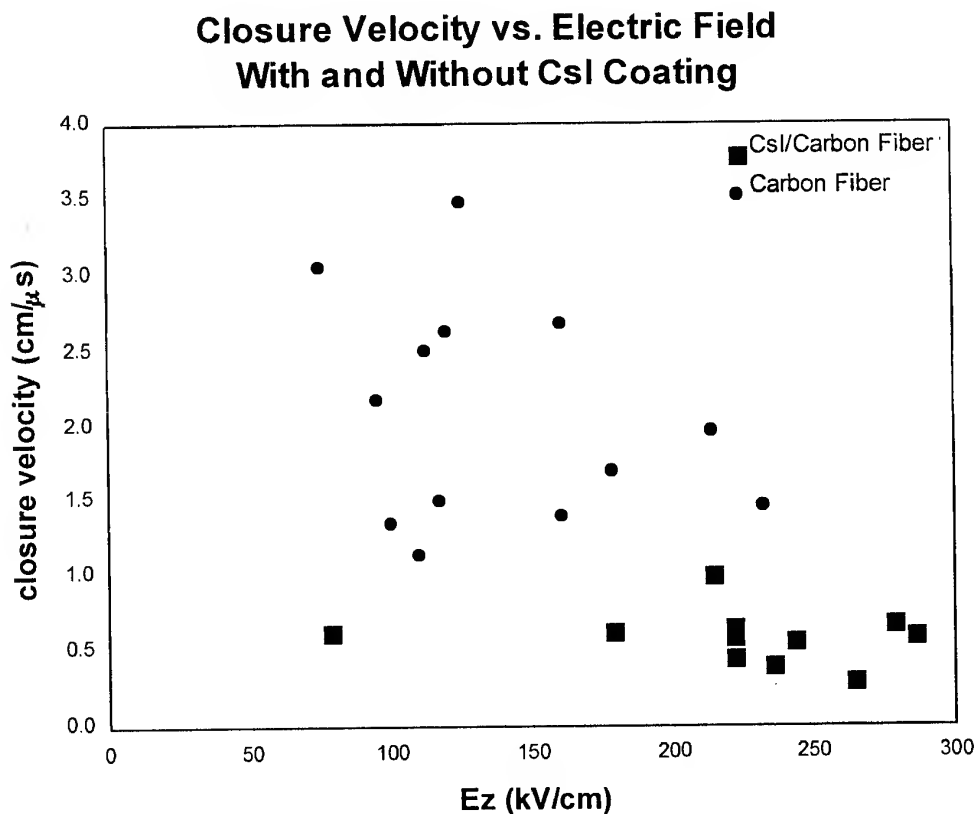
Figure 2. Closure rate with bare carbon fiber and CsI-coated fiber.

where m_f is the mass of whatever ion determines the closure speed with bare carbon fiber. The simplest interpretation is that heated bare fiber still contains hydrogen, so $m_f = 1$.

Therefore, $m_{CsI} = 12$, and expansion is evidently governed by the next lightest, available, ion: the carbon from the fibers or the substrate.

Our interpretation of the physics of bare carbon fiber is that the lightest, fastest ion, which determines the closure speed, is residual hydrogen from the fiber, probably from chemisorbed sources, not from water, most of which we boiled off under vacuum. As a check, recall that the plasma thermal velocity is:

$$v(cm/\mu s) = \sqrt{T(eV)/m} \tag{8}$$

where m is the mass relative to the proton. Then for hydrogen from the bare carbon fiber, T= 4 eV gives a speed of 2 cm/μs, as we observe. This fits, because we expect such collision-dominated cathode plasmas to have temperatures of a few eV[6].

Note we found that baking under vacuum removed copious amounts of water from the CsI cathode, which had already been baked at atmosphere. Previous workers either did no baking or baked at atmosphere only. Therefore, we can explain most of the work preceding ours as basically water-dominated.

For CsI-covered carbon fiber, the hydrogen from the fiber or the water is captured by the process of covering it with CsI. Perhaps the hydrogen is bound up into hydrogen iodide, HI. (Note from Figure 5 the RGA detects a molecule with this mass). This leaves carbon as the lightest, fastest ion. To get the closure speed of CsI, assume the temperature remains about the same 4 eV, insert in Eq. 8 the carbon mass, 12, giving 0.6 cm/μs, fitting the observed 0.59 cm/μs. (Here we assume the density is high enough to give rough equivalence of electron and ion temperatures, which seems likely from comparison with the literature on cathode densities.)

1. R. Prohaska and A. Fisher, "Field Emission Cathodes using Commercial Carbon Fibers", Rev. Sci. Instrum. 53, pg. 1092, 1982.

2. R. J. Adler, G. Kiuttu, B. Simpkins, D. Sullivan and D. Voss, "Improved electron emission by use of a cloth fiber cathode", Rev. Sci. Instru., 56, pg. 766, 1985.

3. E. Garate, R. MacWilliams, D. Voss, A. Lovesse, K. Hendricks, T. Spencer. M. C. Clark and A. Fisher, "Novel Cathode for Field-emission Applications", Rev. Sci. Instru., 66, pg. 2528, 1995.

4. K. Hendricks et. al., "Recent Results on Pulse Shortening of GW Class HPM Sources", APS Plasma Physics Mtg., Denver, CO, 1996.

5. R. B. Miller, "Repetitive pulse operation of reltron tubes", SPIE 3158, pg. 2, 1997.

6. D. D. Hinshelwood, "Cathode Plasma Formation in Pulsed High Current Vacuum Diodes", IEEE Trans. Plasma. Sci., PS-11, pg. 188, 1983.

EFFECT OF PLASMA NONLINEARITY ON RADIATION SPECTRUM IN PLASMA-FILLED TRAVELING-WAVE TUBES

Yu.P.Bliokh, Ya.B.Fainberg, M.G.Lyubarsky, V.O.Podobinsky,
*Institute of Plasma Electronics & Advanced Acceleration Methods, National Science Center
``KhPhTI'', 1 Akademicheskaya Str., Kharkov 310108, Ukraine;*
G.S.Nusinovich, Y.Carmel, V.L.Granatstein, S.Kobayashi,
*Institute for Plasma Research, University of Maryland, College Park, Maryland 20742-3511,
USA.*

INTRODUCTION

It is typical for many microwave sources that as the beam current increases the device exhibit successive transitions, first from self-excitation of constant amplitude oscillations to automodulation, and then to chaotic oscillations. Such transition were found in devises based on the absolute instability of electron beams (backward-wave oscillators (BWO) [1,2,3], gyrotrons [4]). They were also studied in devices based on the convective instability (traveling wave amplifiers) in which an additional feedback providing a self-excitation can be caused either by reflection of a certain amount of radiated power from the exit (internal feedback) or by the external feedback loop (see, e.g. [5]). In all these studies the sources of microwave radiation from electron beams propagating in vacuum were analyzed. The aim of this report is investigation of plasma influence on transit to the chaotic oscillations and spectral characteristics of such oscillations in the microwave sources filled with plasma.

The fact that the filling of interaction region of slow wave structures (SWS) with plasma can significantly enhance efficiency, power and bandwidth was predicted theoretically and observed experimentally in many papers. However, the plasma as a medium with a large number of degrees of freedom can also complicate the radiation processes in these tubes and promotes to development of stochastic processes [6,7]. Our study described below is devoted only to the effect of the magnetosonic waves, excited in the plasma due to the pondermotive force, on the dynamics of plasma-filled traveling-wave tubes.

GENERAL FORMALIZM

The initial equations of the problem under consideration are, first, equations of for excitation of the SWS eigen wave by an electron beam and, second, equations which connect perturbations in the plasma density with the excited wave amplitude.

The effect of the electromagnetic waves on plasma can be described by the pondermotive force $\vec{F}_p = -\nabla \psi$, potential ψ in external magnetic field can be determined [8] as

$$\psi = \frac{e^2}{4m\omega^2}\left(|E_z|^2 + \frac{\omega^2}{\omega^2 - \Omega^2}|E_\perp|^2\right)$$ Here ω is the frequency of TM_{0n} wave with axial E_z and

transverse $E_\perp$ components of electric field; Ω is the electron cyclotron frequency. Since the $E_\perp$ near the axis is much less than E_z, the second addend in ψ may be neglected.

Below, we will assume minority of the plasma column radius in comparison with the reverse plasma-beam spatial instability increment. In this case transverse perturbations in

plasma due to the effect of $F_{p,\perp}$ can be described by linearized one-fluid magneto-hydrodynamic equations [9], which for axially symmetric system can be rewritten as:

$$\frac{\partial^2(\delta n)}{\partial t^2} - \left(C_A^2 + C_S^2\right)\frac{1}{r}\frac{\partial}{\partial r}\left(r\frac{\partial(\delta n)}{\partial r}\right) = \frac{e^2 n_0}{4mM\omega^2}\frac{1}{r}\frac{\partial}{\partial r}\left(r\frac{\partial|E_z|^2}{\partial r}\right) \tag{1}$$

Here, δn – is a plasma density disturbance around the average value n_0; $C_A = H_0/\sqrt{4\pi n_0 M}$ and $C_S = \sqrt{T_e/M}$ are, respectively, the Alfven and ion acoustic wave velocities; T_e is the plasma electrons temperature; M is the ion mass.

For long systems with plasma column of a small radius we may neglect time derivatives in Eq. (1). Then, the reduced equation can easily be integrated, which yields:

$$\frac{\langle \delta n\rangle_p}{n_0} = -\frac{e^2\langle|E_z|^2\rangle_p}{2Mm\omega^2(C_A^2 + C_S^2)S_p}, \tag{2}$$

where $\langle...\rangle_p$ means averaging over the plasma cross section S_p.

Equations and boundary conditions that describe the plasma-beam TWT-oscillator operation with the delayed feedback may be obtained assuming the results of [10] and , for example [11, 12]. The first one investigates a beam interaction with non-homogeneous plasma, and in the second and third are shown the equations that describe a beam oscillator with the delayed feedback operation in vacuum or homogeneous plasma conditions. In the case of a non-homogeneity that comes from Eq. (2), the following equations and boundary conditions take place:

$$\frac{\partial a}{\partial \tau} + \frac{\partial a}{\partial \xi} - i\gamma|a|^2 a = -\frac{1}{2\pi}\int_0^{2\pi} e^{i\varphi}d\varphi_0, \qquad \frac{\partial^2\varphi}{\partial \xi^2} = -\mathrm{Re}\left(ae^{-i\varphi}\right), \tag{3}$$

$$\varphi(0) = \varphi_0 \in [0, 2\pi], \quad \left(\partial\varphi/\partial\xi\right)\big|_0 = 0, \quad a(0,\tau) = qa\left(\xi_{out}, \tau - \Theta\right).$$

Here τ and ξ are the normalized time and longitude coordinate, a is the normalized complex amplitude of the high-frequency wave, γ is a coefficient, that determines the degree of the high-frequency fields influence on plasma non-homogeneity. Θ is the normalized delay time, q is a reflection coefficient and ξ_{out} is the normalized length of the interaction region.

Equations (3) present the simplest mathematical model of the TWT oscillator with plasma-filled SWS, which takes into account a non-linear effect of plasma density variation under excited waves action. Description of this effect by introduction of only one additional term and one new parameter γ is possible due to selection of the most sensitive element of a beam-wave interaction - the resonance condition. The local connection between plasma density variation and wave amplitude is possible only under excitation of the given non-propagated magnetosonic waves.

RESULTS

In the absence of the pondermotive force ($\gamma = 0$), Eqs. (3) with corresponding boundary conditions describe the vacuum TWT studied in [11,12]. The behavior of such systems with feedback is similar to that of vacuum BWO,s studied in [1,2,3] and of the hyrotron studied in [4], namely, when the wave is amplified after one pass around the loop the system starts to oscillate. As q or ξ_{out} grow and reach a certain limit, the constant amplitude oscillations are

replaced by automodulation. Then, at even larger q and ξ_{out}, stochastic oscillations appear. This general description is illustrated by Fig. 1 in which the region of constant amplitude, automodulation and stochastic oscillations are shown in plane ``reflection coefficient q vs. normalized length ξ_{out}''. This plot corresponds to the solution of Eqs. (3) for $\gamma = 0$. Note that stochastic oscillations appear only in the regime of deep saturation in the process of beam electrons debunching, i.e. at rather large distances $\xi_{out} \geq 5 \div 6$. Therefore the plot shown in Fig. 1 was started from $\xi_{out} = 8$ where stochasticity appears at reasonably small q's.
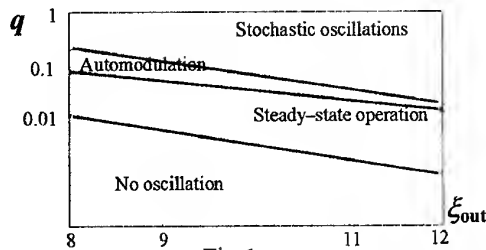
Fig 1.
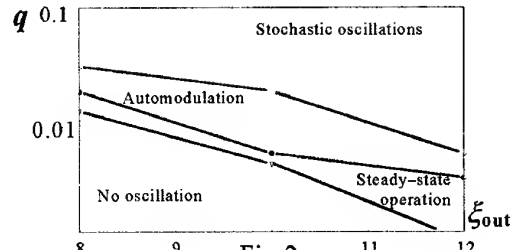
Fig 2.

Similar regions for the system with $\gamma \approx 0.1$ are shown in Fig. 2. As one can see, the threshold for oscillations (lowest curve) in both systems is the same; however, the region of constant amplitude oscillations is much more narrow than for $\gamma = 0$. Because normalized length ξ_{out} depends on a beam current ($\xi_{out} \approx I_b^{1/3}$), decreasing of a threshold value of ξ_{out} when automodulation rise means decreasing of corresponding threshold current value. This illustrated the effect of a new nonlinearity caused by magnetosonic oscillations in plasma and can be explain in the following way.

In the TWT–amplifier the term $\sim \gamma$ in Eq. (3) influences sufficiently on beam-wave interaction dynamics if $\gamma \geq 1$ and may be neglected if $\gamma << 1$. In the TWT oscillator considered in this paper the role of this term is noticeable under much smaller values of γ. It can be explained in the following way. The mechanism of regular or stochastic automodulation appearance in the TWT oscillators is connected with dependence of phase of amplified wave on wave's amplitude – non-linear phase shift $\Delta\phi(|a|^2)$. The third term in the first Eq. (3) under $\gamma << 1$ changes namely this dependence $\Delta\phi(|a|^2)$. Really, instability increment $\mathrm{Im}\,\delta k$ depends on phase velocity shift quadratically, therefore dependencies $|a(\xi)|$ for various $\gamma << 1$ differ little (in all considered below range of γ variations these differences do not exceed some percents).

Additional phase shift $\Delta\phi$ caused by beam-wave interaction is determined by $\mathrm{Re}\,\delta k$: $\Delta\phi \sim \int_0^{\xi_{out}} \mathrm{Re}\,\delta k\,d\zeta$. In opposite to $\mathrm{Im}\,\delta k$, $\mathrm{Re}\,\delta k$ is a linear function of the phase velocity shift, and the additional phase shift caused by the third term in Eqs. (3) $\Delta\phi \sim \gamma \int_0^{\xi_{out}} |a(\zeta)|^2 d\xi$ can be about unit even for $\gamma << 1$.

Nonlinear phase shift caused by nonlinearity of beam particles motion under beam–wave interaction development is the main reason of a signal stochastization in the vacuum TWT oscillator [11]. Therefore additional phase shift $\Delta\phi$ influences namely on stochastization mechanism and can change the value of threshold current and radiation spectrum.

Now let us discuss the radiation spectra in the presence and absence of magnetosonic oscillations. In Fig. 3 the spectrum of stochastic oscillations is shown for $\gamma = 0$, $\xi_{out} = 10$,

$\Theta = 10$ and $q = 0.08$. This spectrum consists of many isolated spikes. In the case of non-zero γ's the spectrum becomes much more continuous and wider. This is illustrated by Fig. 4 where, for the same q, ξ_{out} and Θ as before, the spectrum is shown for $\gamma = 0.1$.
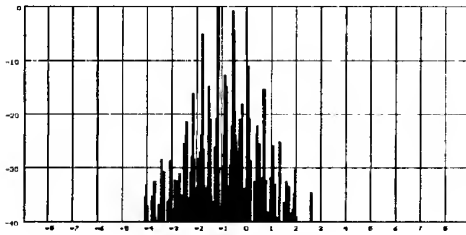
Fig.3
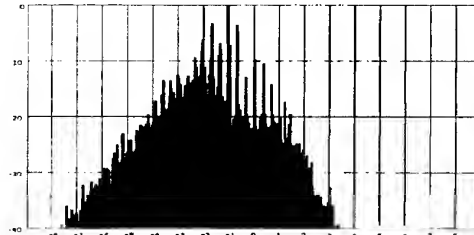
Fig.4

CONCLUSION

We have shown that in plasma-filled microwave sources of coherent Cherenkov radiation the radial non-homogeneity of the axial field of the EM wave may cause magnetosonic oscillations in plasma. These oscillations can be described by an additional reactive nonlinearity in the wave envelope equation, and thus lead to some changes in the phase of the amplified wave. In traveling-wave tubes with end reflections or with an external feedback loop where the signal passes many times through the interaction region, this nonlinear effect leads, first, to a complication in the transition processes in nonstationary regimes which are ended by constant amplitude oscillations. Second, this effects shrinks significantly the regions of constant amplitude oscillations and automodulation processes. Third, stochastic oscillations appear at much smaller values of the feedback coefficient and their spectrum is almost continuous while in the absence of this effect the spectrum contains a large number of quite isolated frequency components.

REFERENCES

1. N.S. Ginsburg, S.P. Kuznetsov and T.N.Fedoseeva, Izv. VUZov. Radiofiz. 21, 1037 (1978); [Radiophys. and Quantum Electron. 21, 728 (1978)]
2. B.P. Bezruchko, S.P. Kuznetsov, and D.I. Trubetskov, Pis'ma ZhETF 29, 180 (1979) [JETP Lett. 29, 162 (1979)]
3. B. Levush, T.M. Antonsen, Jr. A. Bromborsky et al, IEEE Trans. Plasma Sci. 20, 263 (1992)
4. N.S. Ginzburg, G.S Nusinovich and N.A. Zavolsky, Int. J. Electron. 61, 881 (1986)
5. V.Ya. Kislov, N.N. Zalogin and E.A. Myasin, Radiotekhnika i elektronika 24, 1118 (1979) [Radioeng. Electron. Phys. 24, No. 6, 92 (1979)]
6. Berezin A.K., Bolotin L.I., Fainberg Ya.B. et al., Plasma Phys. and Contr. Nuc. Fusion Res., 1, 515 (1966)
7. Fainberg Ya.B., A Surrey of Phenom. In Ionized Gases, Inv. Pap., Vienna, p.149 (1968)
8. A.V.Gaponov, M.A.Miller, JETP, 34, 515 (1958)
9. L.D.Landau, E.M.Lifshitz, L.P.Pitaevskii, Electrodynamics of Continuous Media (Pergamon Press, 1984).
10. Yu.P.Bliokh, Ya.B.Fainberg, M.G.Lyubarskiy et al., SPIE. Proc.V3158. Intense Microwave Pulses V. p. 182-193 (1997)
11. Yu.P.Bliokh, Ya.B.Fainberg, M.G.Lyubarskiy et al., Plasma Phys. Rep., 20, 675 (1994)
12. N.S.Ginzburg, Sergeev, Sov. Phys. Tech. Phys., 36, 665 (1991)

INSTATIONARITY OF E-BEAM PUMP PROCESSES IN SHOT-PULSE-DURATION GAS LASERS OF VUV-RANGE

V.A. Burtsev

*Efremov Scientific Research Institute of Electrophysical Apparatus,
St.-Petersburg, 189631, Russia*

Abstract

The results of analytical and numerical research of questions connected with instationarity of E-beam pump processes of active media in short-pulse-duration lasers of VUV-range on excimers of inert gases are reported. The determining influence on parameters of active medium regard a competition of processes of gas ionization by fast electrons and recombination of ions and secondary electrons is shown. The instationary processes of accumulation of an electrical charge owing to thermalization of beam electrons and it pour down by means of opposite currents should be taken into account in subnanosecond range of pulse pump duration.

Introduction

At numerical research and optimization of electron beam pumping in gas lasers with life time of upper laser levels in tens and more nanoseconds (for example, excimer lasers on halides of inert gases) the method of Monte-Carlo in stationary approach [1] is usually applied. Incidentally one consider, that stationary values of plasma electron density, intensity of an internal electrical field and opposite electrical current density are established practically instantly, tracing changes of electron beam parameters. Such approach was used at complex numerical modeling of large aperture excimer amplifiers for ICF [2].

At pulse duration, essentially exceeding the flight time of beam electrons through an active zone, this approach allows in quasi-stationary approach to determine spatial - temporary distributions of specific pump power corresponding to running values of initial energy of injected electrons and beam current density on an entrance in a zone of interaction with gas [3]. Such by a rather simply way one can take into account real temporary dependencies of initial energy of beam electrons and its current.

In the given report the questions connected with finiteness of time of development of relaxation collision processes in laser active media at pumping its by an short-pulse electron beam (all accounts were curried out with reference to argon). The interest to these questions is caused by attention, which recently has become again to be given to creation of VUV-gas lasers based on the use excimers of inert gases as active media (Xe$_2$ - λ = 172 nm, Kr$_2$ - 146 nm, Ar$_2$ - 126 nm) [4]. Despite of the extremely high requirements to specific pump power and pulse pump duration, beam current density (hundreds MW/см^3, units ns, units кA/cm^2 correspondingly), the successes of modern physics of excimer lasers [4] and high current electronics [5], allow to hope for the successful decision of this problem.

Interaction of electron beams with dense gas

It is possible to write down the system of the equations describing 3-component medium ($n_e + n_i + n_0$ = const), arising at interaction of an electron beam with gas, as

$$\frac{\partial n_e}{\partial t} = -div \vec{j}_e - \beta n_i n_e + q + \psi,\tag{1}$$

$$\frac{\partial n_i}{\partial t} = -div \vec{j}_i - \beta n_i n_e + q,\tag{2}$$

$$div \vec{E} = \frac{e}{\varepsilon_0}(n_i - n_e),\tag{3}$$

$$\vec{j}_e = -e n_e \mu_e \vec{E},\tag{4}$$

where $q = \upsilon(W_e)Pj_b / e$ - specific speed of formation electron-ion pairs in gas at pressure P by beam electrons with energy W_e at density of a current j_b,

$\upsilon(W_e) = \varepsilon^{-1} dW_e / dz$ - number of pairs formed by fast electron on unit length of penetration in medium at P = 1,

ε - average energy, spent by beam electron on formation one electron-ion pair with account of atom excitation,

$\psi = e^{-1} \mathrm{div} \vec{j_b}$ - specific velocity of beam electron thermalization.

The typical distributions of velocities of formation of electron-ion pairs and fast electron thermalization on the depth of penetration of a homogeneous beam in gas are given on fig.1 at presence of a strong longitudinal magnetic field (stationary approach, one-dimensional geometry). As it is possible to see, the locations of q/P and ψ/P maxima are dispersed on depth of penetration; the maximal velocity of thermalization lies in area where the velocity of electron-ion pair formation is sufficiently less its maximal value.

The location of maximum q/P is enough well predicted by the estimated formula for the maximal depth of penetration of beam electron in gas [6]

$$z_{max} \approx 0{,}19(\gamma^2 - 1)^2 / P\gamma^2, \tag{6}$$

where γ- relativistic factor of a beam. Moreover, the location of ψ/P maximum practically coincides with $z^*_{max} \approx 2z_{max}$. It has enabled to propose non-stationary 0-dimentional model for analytical research of interaction of an electron beam with gas.

In the proposed model the distribution $q/P = f_1(Pz)$ of a kind submitted on fig.1, is replaced on homogeneous distribution with depth $z = z^*_{max}$ and magnitude of specific energy losses of fast electrons corresponding to set condition on W_e^0. As to function $\psi/P = f_2/P$, in the model it is accepted that all beam electron are thermalized on the depth z_{max}^* creating a plane layer of a negative charge with density σ, which partially pours down by means of opposite plasma currents j_e. In this case for definition of an electrical field instead of the Puasson equation (3) it is possible to make use the expression for field of the plane condenser with thickness z^*_{max} and dielectric constant ε_0 of kind $dE/dt = (j_b - j_e) / \varepsilon_0$. In result we have

$$\frac{dE(t)}{dt} + \frac{e\mu_e}{\varepsilon_0} n_e(t)E(t) - \frac{1}{\varepsilon_0} j_b(t) = 0 \tag{7}$$

The equation of balance of plasma electrons (1) in the proposed model has a following kind

$$\frac{dn_e(t)}{dt} + \beta n_e^2 = q \tag{8}$$

The velocity of electron-ion pairs birth can be defined as $q = W_e^0 j_b / \varepsilon e z^*_{max}$.

The system of the equations (7) and (8) is sufficient to estimate the times of an establishment of a stationary regime at interaction of high current electron beam with dense gas.

Definition of times of stationary regime establishment

Solving the system of equations (8,9), we receive

$$n_e^*(\tau) = \frac{n_e(\tau)}{n_{e\infty}} = \mathrm{th}\tau, \tag{9}$$

$$E^*(\tau,\delta) = \frac{E(\tau,\delta)}{E\infty} = \delta(\mathrm{ch}\tau)^{-\delta} \int_0^\tau (\mathrm{ch}\xi)^\delta d\xi, \tag{10}$$

$$j_e^*(\tau,\delta) = \frac{j_e(\tau,\delta)}{j_{e\infty}} = \delta(\mathrm{th}\tau)(\mathrm{ch}\tau)^{-\delta} \int_0^\tau (\mathrm{ch}\xi)^\delta d\xi, \tag{11}$$

Here, $\delta = a/\beta$, $a = e\mu_e/\varepsilon_0$, $\tau = \sqrt{q\beta} t$ - dimentionless time,

$n_{e\infty} = \sqrt{q/\beta}, E_\infty = \dfrac{j_b}{\varepsilon_0 \sqrt{q\beta a/\beta}}, j_{e\infty} = j_b$ - established values of sought parameters.

On fig.2 the dependencies (9-11) are given at various values of parameter δ.

The analysis of these expressions and its plots shows, that after stepped switching the constant homogeneous plane beam and reaching by its front limited depth of penetration z^*_{max} the stationary values of plasma electron density are established with characteristic time $t_{n,\,est} \approx (q\beta)^{-0,5}$. So, in argon at P = 10 atm the electron density reaches stationary value for ~ 0,5 ns at $j_b = 1$ kA/cm^2; at increasing of current density this time decreases as $(j_b)^{-0,5}$, pressure - as $(P)^{-1}$. As known this fact is explained by competition of processes of gas ionization by fast electrons and recombination of ions and secondary electrons.

The establishment of stationary values of electrical field intensity and opposite electrical currents occurs in more complex way. At $\delta \leq 1$ (the small values of parameter δ correspond high gas pressure P as $\delta \propto P^{-2}$) the establishment of stationary values of E and j_e occurs on the whole with the same time: $t_{E,\,est} \approx t_{j,\,est} \approx t_{n,\,est}$. However, at increasing of parameter δ (reducing of P) temporal dependencies $E^*(\tau,\delta)$ and $j_e^*(\tau,\delta)$ acquire maximum, the location of which is displaced to short times with increasing of δ. This fact can be explained by competition of processes, determined by electron mobility and charge recombination ($\delta \propto \mu_e/\beta$).

The time at which the electric field intensity reaches of maximum value is determined by expression $t_{e,\,max} = (q\beta)^{-0,5}.\mathrm{arcth}(1/\delta)$, at indicated above conditions this time is less $t_{e,\,est}$ by factor of 200. The temporary delay of a beginning of the opposite current determined on a flex point of the plot $n_e^*(\tau,\delta)$ is given by expression $t_{j,f} = (2q\,a)^{-0,5}$. At the same conditions it come to 0,02 ns. It is interest to note that as unlike dependence $E^*(\tau,\delta)$ the maximal values of opposite electrical current maximum poorly depends on parameter δ. This produces an impression about more fast establishment of stationary values of opposite current j_e in comparison with $t_{j,\,est}$.

Conclusion

The carried out researches have shown, that at account e-beam pumped active medium on excimers of inert gases the use of the stationary approach is in common illegitimate . The further researches together with consideration of kinetic processes are necessary for study of influence of the considered non-stationary processes on efficiency of short-pulse pumping .

1. M.I Avramenko, V.A. Burtsev, P.A. Ivanov, N.I. Kazachenko, V.S. Kuznezov. Numerical investigations of electron beam deposition into gas medium of an excimer laser. Fusion Technology, v.19, May 1991, p440-8.
2. V.A. Burtsev, A.G. Grad, V.S. Kuznezov, R.P. Fidelskaya. Ecimer laser for inertial confinement fusion. Plasma Devices and Operations, v.1, 1991, p. 213-226.
3. M.1. Avramenko, V.A.Burtsev, P.A. Ivanov, N.I. Kazachenko, V.S. Kuznezov. Pumping of excimer lasers by high current electron beams. Preprint K-0819.- M.: ZNIIatominform, 1989 (in Russian).
4. V.F. Tarasenko, S.I. Yakovlenko. Rare-gas dimer and halide lasers. Quantum electronics, т. 24, № 12, 1997, p. 1145-1153 (in Russian).
5. G.A. Mesyats, V.G.Shak, M.I. Yalandin, S.A. Shunailov. RADAN-EXPERT portable high-current accelerator .In Proc. Of 10th IEEE Intern. Pulsed Power Conf. (Albuquerque, NM, USA, 1995), Vol.1, P.539-543.
6. M.I. Avramenko, V.A. Burtsev, N.I. Kazachenko, N.V. Kalinin, V.S. Kuznezov, P.V.Mikhailov, R.P. Fidelskaya. Distribution of energetic loses of high current electron beam in gas medium. Preprint P-K-0702.- M.: ZNIIatomizdat, 1985 (in Russian).
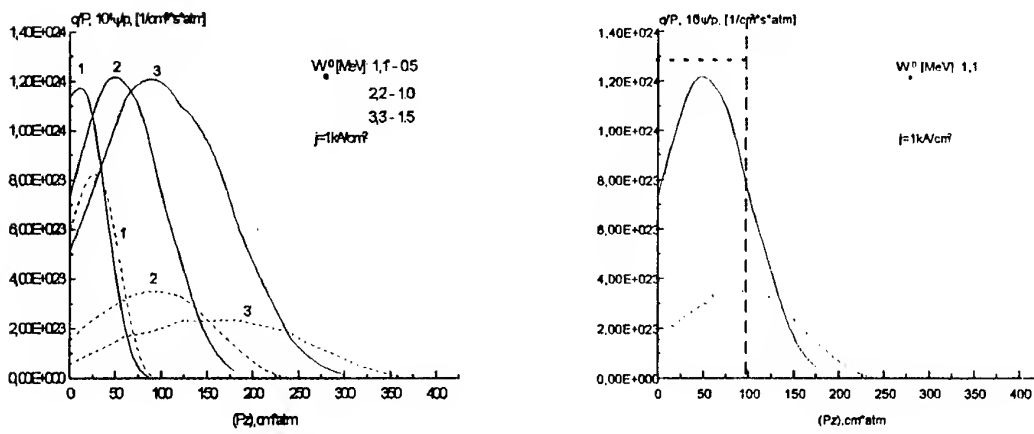
Fig.1. Dependencies of specific velocities of e-i pair formation q and e-thermalization ψ
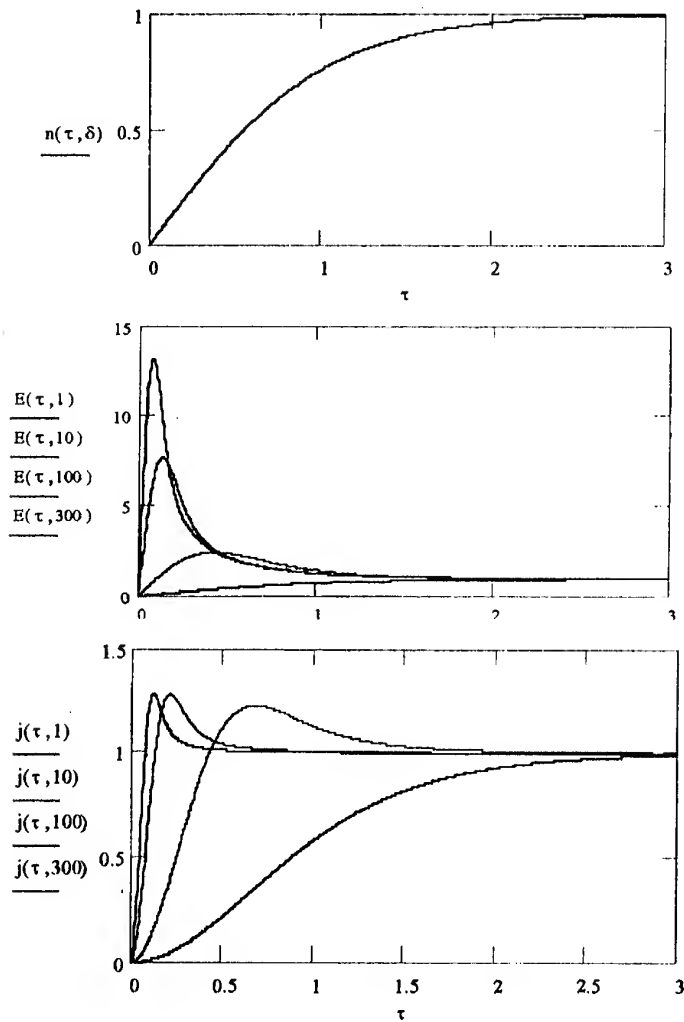
Рис.2. Dependencies of the dimentionless parameters of active medium on τ and parameter δ

INFLUENCE OF AN OVERMODED SLOW-WAVE STRUCTURE MATCHING ON A CERENKOV GENERATOR EXCITATION

I.A.Chernyavsky, M.P.Deichuly, V.I.Koshelev

High Current Electronics Institute RAS,
4 Akademichesky Ave., Tomsk, 634055 Russia

ABSTRACT

Possibility to match overmoded periodic slow-wave structures and to regulate a resonance factor contribution into the process of microwave generators self-excitation is shown by means of a linear stationary theory methods. It has been obtained experimentally that matched structures use resulted in a sharp (by two-three orders of magnitude) drop of generation power level.

INTRODUCTION

Experimental and theoretical investigations [1,2] have shown that in the absence of matching in the frequency region near the π-type of TM_{01}-mode, periodic slow-wave structures (SWS) of a finite length have the properties of distributed resonators inside which the circuits of internal back coupling can form effectively that promotes the self-excitation of microwave devices based on such structures. Recent detailed experimental and theoretical investigations [3-7] of interaction process of electron beam and fields of overmoded one- and two-section SWS at the frequencies near the π-type of TM_{01}-mode has confirmed once more the importance of a resonance factor at self-excitation of microwave generators on the basis of mismatched SWS.

In the given paper, the results of numerical and experimental investigations of possibility to decrease essentially a resonance factor part by introducing matching at the SWS ends are presented. Instead of a widely used introduction of additional periodical nonuniformities with decaying heigh it is suggested to select the gap value $d \neq d_0$ between the nonuniformities on the SWS ends (Fig.1). The effect obtained is analogous to the optics elucidation well-known in physics and can find an application in the microwave region. More detailed information can be found in [8].
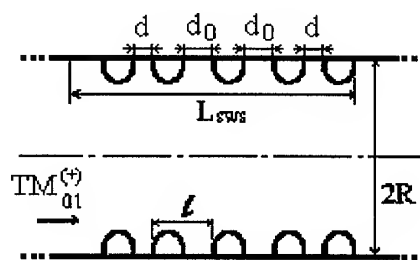
Fig.1. A model of an overmoded periodical slow-wave structure of the radius R, period l and length L_{sws}; d_0 and d are values of gap inside SWS and on its ends, respectively.

RESULTS OF NUMERICAL INVESTIGATIONS

Numerical investigations were carried out by means of methods of a linear stationary theory [9], in which only axial-symmetrical structures and TM-type fields are considered. In

the absence of matching, overmoded one-section periodical SWS in the frequency region near the π-type of TM_{01}-mode have strongly pronounced resonance properties [3-5], which are convenient to be studied by means of transmission coefficient $T(\lambda)$ dependencies (here λ is the radiation wavelength in free space). Fig.2 presents the calculation results of such depen-

dence for the case of setting the initial power flow of TM_{01}-mode of a smooth waveguide at the input of an overmoded SWS ($2R/\lambda \approx 4$) containing 17 nonuniformities. In case of a uniform SWS (when $d=d_0$ and $L_{sws}=17l$) a number of maxima of transmission coefficient related to the excitation of longitudinal resonances of $TM_{01,n}$-type along the length of the mismatched SWS is seen on the dependence $T(\lambda)$ (curve 1 on Fig.2).

As it follows from calculations, change of the value of the end gaps d ($\neq d_0$) results in a strong transformation of resonance properties of the SWS under consideration and, particular, in the possibility of their effective matching with the input and output waveguide

Fig.2. Dependencies of a transmission coefficient T on the radiation wavelength λ near the π-type of TM_{01}-mode for uniform (curve 1) and nonuniform (2-4) slow-wave structures.

parts. Decrease of the value d ($< d_0$) results in gradual smoothing of the dependence $T(\lambda)$ (curve 2) which acquires the most smoothed view at a certain optimal value of the gap $d=d'$ ($\approx d_0/2$, curve 3). It can be supposed that in this case end nonuniformities have the part of matching quarter-wave transformers [10] for a surface field part transfered by TM_{01}-wave of a SWS. Further decrease of the value d ($< d'$) again increases the SWS mismatch (curve 4).

When a hollow relativistic electron beam propagates near the surface of SWS under consideration, a possibility of their self-excitation appears. Calculations in the approximation of an infinite magnetic field have shown that at the diode voltage $U_d =1,0$ MV and electron beam current $I_b=10$ kA, self-excitation of a uniform SWS ($d=d_0$) becomes possible only at the lengths $L_{sws} \geq 15l$ and similar to [4,5] is realized at the frequency of the first from π-type

"hot" longitudinal resonance. With the increase of number of periods of a uniform SWS ($> 15l$) wavelength of its self-excitation changes weakly, but starting current decreases quickly and at the length $L_{sws}=17l$ achieves the value $\approx I_b/2$.

Further, for SWS with fixed number of nonuniformities, influence of the gap value d of the wavelength and generation starting current of the given device has been studied. The results of such study for the SWS containing 17 nonuniformities are presented on Fig.3. One can see that

Fig.3. Wavelength λ and starting current I_{st} of the device generation versus value d of the end gaps; I_b is the value of the electron beam operating current.

the most essential changes take place at the decrease of the gap value d ($< d_0$) when the starting current sharply increases from its initial (at $d=d_0$) value I_{st}^0 achieving maximum value $\geq 2I_b$ at a certain $d=d''$ ($\approx d_0/3$). Further decrease of the gap d ($< d''$) results in decay of the starting current value to the ones $\leq I_b$. Such behaviour of the starting current allows to mark out an interval Δ of the gaps d values at which starting current exceeds its operating value I_b and, hence, self-excitation of the given SWS is impossible. Thereby, possibility to regulate resonance mechanism contribution into the self-excitation process of the studied microwave device appears.

When matching the SWS under consideration, an essential electromagnetic field redistribution in the whole generator volume takes place. In particular, it is seen from consideration of the transverse structure of the longitudinal field normalized amplitude in the internal SWS cross-section (Fig.4), that at transition from the case $d=d_0$ (curve 1) to the case $d=d''$ (curve 2), a sharp amplitude decrease of the surface field part occurs. At the same time the content of the highest modes ($TM_{02}\div TM_{04}$) in the output radiation of the device being increased from 30 to 50 %.
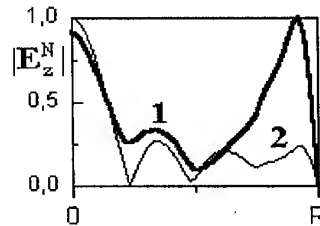
Fig.4. Transverse structures of a normalized amplitude of a longitudinal electrical field inside the devices based on the mismatched (1) and matched (2) slow-wave structures.

RESULTS OF EXPERIMENTAL INVESTIGATIONS

The experiments were carried out at the SINUS-7M accelerator. A hollow relativistic electron beam was formed in a coaxial diode with magnetic insulation and transported in a guiding magnetic field with induction value $B\approx 10$ kG. Voltage pulse with the amplitude of $\approx 1,0$ MV and duration of ≈ 40 ns was applied to the diode. Electron beam current was $I_b\approx 10$ kA. Radiation power was determined by the pattern measured in the atmosphere.

Searches of the starting length in case of a uniform slow-wave structure ($d=d_0$) have shown that generation with the wavelength $\lambda\approx 3,3$ cm is observed only at the SWS length $L_{sws} \geq 15l$ that is in good agreement with the linear theory calculations. Black circles in Fig.5a indicate the result of the pattern measurements typical of the case of generation of the devices on the SWS
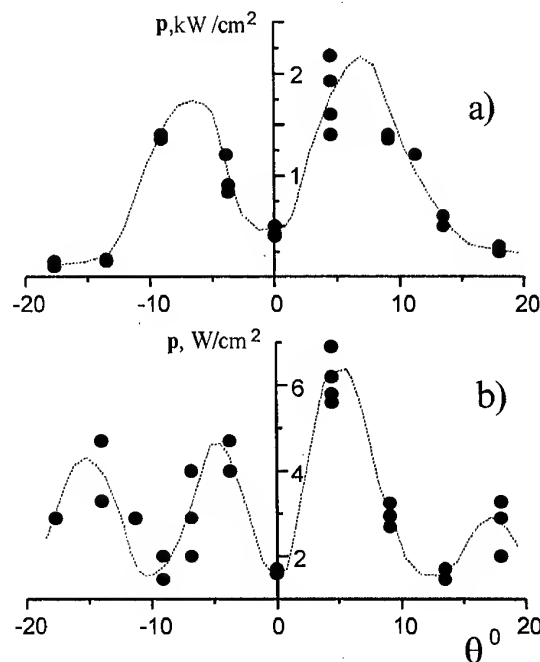
Fig.5. Measured radiation patterns of microwave generators with mismatched (a) and matched (b) slow-wave structures.

basis with the length equal to $15l$ $(16l)$ and characteristic of radiation on the TM_{01}–mode; the power obtained was equal to ≈ 20 MW (80 MW) at the efficiency $\approx 0{,}2$ % (0,8 %).

Later on, experiments with a device based on the SWS containing 17 nonuniformities and with a suggested optimal matching at the ends (d=d″) were carried out. In spite of the theory results in this case very weak generation by power ≈ 90 kW (at the efficiency $\approx 0{,}001$%) was still observed at the same wavelength. The pattern (Fig.5b) was characterized by the appearance of a power sidelobe that correlates good with predictions of the theory about increase of the content of the highest modes in the matched generator output radiation. The analogous results have been also obtained for SWS with 18 nonuniformities though the power level observed was already more essential ($\approx 1{,}3$ MW), that can be explained by using of nonoptimal in this case the same value of end gaps d=d″ [8].

CONCLUSION

As a result of numerical investigations it has been shown that by means of selection of the gap values at both ends of overmoded periodical structure one succeeded in obtaining its effective matching with the input and output waveguide parts in the wavelength region near the π-type. As the result essential increase of generation starting condition and field redistribution by the microwave device cross-section accompanied by the decrease of its surface component and increase of the highest mode contents are occur. It has been shown experimentally that the use of the suggested slow-wave structure matching results in sharp decrease of generation power level of the studied microwave device (by two-three orders of magnitude) and appearance of additional sidelobe in the output radiation pattern. The results of the investigations that have been carried out allowed to draw a conclusion that at SWS lengths higher than/or the order that the starting one, resonance mechanism made the main contribution into the Cerenkov microwave device self-excitation and operation in the frequency region near the π-type.

REFERENCES

[1]. A.F.Alexandrov, S.Yu.Galuzo, V.I.Kanavetz, V.I.Pletyushkin, A.I.Slepkov. Zhurn. Tech. Fiz. 1980. V.50. N 11. P.2381-2389.

[2]. A.P.Kuznetsov, A.G.Roznev. Electronnaya technika, Seriya Electronika SVCh. 1985. N 9(381). P.3-6.

[3]. I.A.Chernyavsky, V.M.Pikunov. SPIE Proc. 1994. V. 2154. P.396-407.

[4]. I.A.Chernyavsky, V.M.Pikunov. SPIE Proc. 1995. V. 2557. P.480-491.

[5]. M.P.Deichuly, V.I.Koshelev, V.M.Pikunov, I.A.Chernyavsky. Radiotechnika i electronika. 1995. V.40. N 9. P.1440-1449.

[6]. M.P.Deichuly, V.I.Koshelev, V.M.Pikunov, I.A.Chernyavsky. Radiotechnika i electronika. 1996. V.41. N 2. P.228-235.

[7]. V.I.Koshelev, M.P.Deichuly, I.A.Chernyavsky, A.A.Petkun. SPIE Proc. 1997. V.3158. P.298-307.

[8]. M.P.Deichuly, V.I.Koshelev, I.A.Chernyavsky. Radiotechnika i electronika. (to be published).

[9]. V.M.Pikunov, I.A.Chernyavsky. SPIE Proc. 1993. V. 1872. P.358-367.

[10]. I.V.Lebedev. Technika i pribori sverhvisokich chastot. V.1. M.: Gosenergoizdat. 1961.

ON THE LIMITING ADMISSIBLE POWER LEVEL OF PULSED MICROWAVE GENERATORS BASED ON HIGH-CURRENT ELECTRON ACCELERATORS

A.N.Didenko

Russian Academy of Sciences, 32a Leninsky prosp., Moscow, 117334, Russia

At present, various powerful microwave devices capable of generating microwave pulses of nanosecond duration and with a power of several gigawatts are constructed on the basis of high-current electron accelerators with energy on the order of several megaelectronvolts [1]. These generators are on major interest for high-resolution radio detecting and ranging [2], designing charged-particle accelerators of super-high energies [3], and for solving a number of problems of pulsed microwave power engineering [4, 5]. For all these regions of application of the microwave technique, one of the important problems is increasing the pulsed power. A goal of the present study is to determine the maximum microwave power that can be generated in a certain relativistic microwave generator and to clarify the dependence of the power on both parameters of high-current electron accelerators used and the type of a microwave generator.

Thus, let the high-current electron beam with a kinetic energy $\mathcal{E}_k = mc^2(\gamma-1)$ enter a certain resonance cavity. As a result of high-frequency instabilities, an initially unmodulated electron beam is split into separate clusters, which is a direct reason for the appearance coherent microwave oscillations. Provided that the amplitude of the generated microwave oscillations is sufficiently high, this microwave field decelerating the electron beam can substantially affect the motion of electrons, resulting ultimately in stopping the electron beam. Such a situation, apparently, defines the maximum power that can he generated in a given microwave device. Here, we can consider this situation in more detail. We can write out the expression for the change in the energy of the electron beam with allowance for the effect of the generated microwave power in the following form:

$$\frac{d\mathcal{E}_k}{dt} = e\mathbf{v}(\mathbf{E}_{ex} - \mathbf{E}_{ind}) \tag{1}$$

or

$$d\mathcal{E}_k = -e\, d(\varphi_{ex} - \varphi_{ind}), \tag{2}$$

where φ_{ex} and φ_{ind} are the external-field and induced potentials that are defined by the electron-beam energy and by the level of generated power, respectively; $\mathbf{E}_{ex} = -\nabla\varphi_{ex}$, $\mathbf{E}_{ind} = -\nabla\varphi_{ind}$, and $\mathbf{v}$ is the velocity of electrons. It is shown in [6] that the particle motion in alternating fields (which vary with the frequency ω) can be described in terms of the potential $\varphi_{hf} = \dfrac{eE_0^2}{4m\omega^2}$, where E_0 is the amplitude of the induced electric field. Taking into account that $\varphi_{ind} = \varphi_{hf}$ and $\varphi_{ind} = \dfrac{mc^2(\gamma-1)}{e}$, where $\gamma = \dfrac{\mathcal{E}}{mc^2}$, we are able to show that the maximum

generated power can be determined from the expression $\mathcal{E}_k = e\,(\varphi_{ex} - \varphi_{ind}) = 0$, or

$$mc^2\,(\gamma - 1) = \frac{(eE_0)^2}{4m\omega^2}. \tag{3}$$

The latter expression can be transformed in the following manner. As is well known, generated microwave power can be expressed through the Poynting's vector

$$W_{rad} = \frac{c}{8\pi} \int_S [\mathbf{EH}^*]\,dS', \tag{4}$$

where it is necessary to perform the integration over the area of the radiating hole. Therefore, expression (3) can be written in the form

$$mc^2\,(\gamma - 1) = \left(\frac{2\pi\,e^2}{mc\omega^2}\right)\frac{W_{rad}}{\alpha\,S} \tag{5}$$

or

$$W_{rad} = \frac{1}{2\pi}\,\frac{m^2 c^5}{e^2}\,\alpha\,(\gamma - 1)k^2 S. \tag{6}$$

Here

$$\alpha = \frac{\int_S [\mathbf{EH}^*]\,dS'}{E_0^2\,S}$$

is a certain dimensionless coefficient depending on the type of the microwave generator used, on the types of oscillations being excited in it, and also on the shape and the position of the hole for extracting the energy, while $k = \omega/c$ is the wave number. The quantity $m^2 c^5/e^2$ has the dimensional representation of power and is equal to 8.5 GW. Therefore, introducing the notation $W_A = m^2 c^5/e^2$ it is possible to rewrite formula (6) in the following form:

$$W_{rad} = \alpha\,(\gamma - 1)\frac{k^2 S W_A}{2\pi} = 2\pi\alpha\,(\gamma - 1)\frac{S}{\lambda^2}W_A, \tag{7}$$

where λ is the wavelength of the oscillations generated. For example, if a cylindrical cavity, in which a E_{011} wave is excited, is chosen as a generating object, and the energy is extracted in the axial direction, then

$$\alpha = \frac{kk_z J_1^2(2.405)}{k^2 - k_z^2} = \frac{0.27 kk_z}{k^2 - k_z^2},$$

where $k_z = \pi/L$ is the zth wave-vector component, L is the cavity height, and $J_1(x)$ is the Bessel function of the first order. For the most acceptable parameters, $\alpha \approx 0.2 - 03$, and therefore $W_{rad} \sim (\gamma - 1)SW_A/\lambda^2$. This implies that, in the case of exciting the basic form of oscillations, $S \sim \lambda^2$ and

$$W_{rad} \approx (\gamma - 1)W_A = \frac{\beta^2\gamma^2}{\gamma + 1}W_A. \tag{8}$$

It follows from this formula that, similar to the fact that the Alfven current $I_A = mc^3/e = 17$ kA defines the value of the limiting current, the quantity $W_A = m^2 c^5/e^2 = 8.5$ GW defines the limiting power generated in powerful microwave facilities. In the first case, I_A defines the value of the current for which its own axial magnetic field essentially influences the motion of

particles causing the curving of their initial trajectories. Similarly, in the second case, W_A defines the generated microwave power for which the induced voltage is comparable to that of high-voltage generators used for acceleration of charged particles.

Thus, the limiting power that can be generated in powerful microwave-generator facilities based on high-current electron accelerators is comparable to W_A = 8.5 GW and depends insignifcantly on the type of microwave generator. This fact explains the unsuccessful attempts to surpass this level in modern powerful microwave generators.

As follows from formula (7), a substantial increase of generated microwave power can be attained by either increasing the energy of the particles used or exciting in the system oscillations of the highest types, as in many-wave Cherenkov generators, or vircators, in which realization of the inequality $S >> \lambda^2$ is possible. Experimental results on the generation of super-power microwave oscillations obtained at the most powerful Aurora accelerator (γ = 17, W = 40 GW) and in many-vave Cherenkov generators (W = 10 GW) confirm this conclusion.

REFERENCES

[1] *High-Power Microwave Sources,* Granatstair V. and Alexeff I., Eds., Massachusetts: Artech House, 1987.
[2] Bunkin B.V., Gaponov-Grekhov A.V., Elchaninov A.S., et al., *Abstr. IX Int. Conf. High-Power Particle Beams,* p.269, Washington, 1992.
[3] Galanin V.E. and Skrinskii A.N., *Trudy XIII Mezhdunarodnoi Konferentsii po Uskoritelyam Vysokikh Energii,* Novosibirsk: Nauka, 1987.
[4] Didenko A.N., *Dokl. Akad. Nauk,* 1993, vol. 331, no. 5, pp. 571 – 572 [*Phys.– Dokl.* (Engl. transl.), vol. 38, no. 8, pp. 344 – 354].
[5] Didenko A.N. and Zverev B.V., S*VCh-energetika* (Microwave Power Engineering), St. Petersburg: Nauka, 1995.
[6] Gaponov A.V. and Miller M.A., *Zh. Eksp. Teor. Fiz.,* 1958, vol. 34, no. 1, pp. 242-243.

AN AXIALLY TWICE ACCELERATION LOW IMPEDANCE HPM SOURCE

Wu   Ding

Institute of Applied Physics and Computational Mathematics
(P.O.Box 8009,Beijing 100088,China)

1.INTRODUCTION

M.J.Arman presented a new low impedance HPM source –Radial Acceletron[1],it has the following new characteristics:(1) There are very high harmonic currents in the device because it combines the oscillator and the diode into one;(2)The impedance of the diode is very low due to being coaxial,thus allowing larger input and output powers. We try to make two improvements for the device:(1) Add a accelerating section after the diode/ oscillator,make the bunched beam to be accelerated again,then extract the radiation emitted by the bunched and postaccelerated beam in the extraction cavity.Therefore one can not ony raise the power and conversion effiency of the beam,but also select output frequency of the waves.While in the Radial Acceletron, the conversion efficiency is not high enough,and the output frequency can not be tuned;(2) Change the radial acceleration to axial acceleration.In the configuration of radial outward twice acceleration,radius of the cavity should be very large ,and the field and beam in it are divergence;In the configuration of radial inward accelaration,the power capacity is very small; While the new configuration of axially twice acceleration does not have these problems.The Coaxial axially twice acceletron needs no maganetic guide field like the Super-Reltron.But its modulation cavity is TTO rather than SCO, and compared to SCO, it is not easy to be breakdown due to its larger power capacity and the bunching of the beam is much better because of the combining of the oscillator with the diode.

2.BEAM BUNCHING IN THE DIODE/OSCILLATOR

The conceptual diagram of the Coaxial axially twice acceletron is shown in Fig.1.
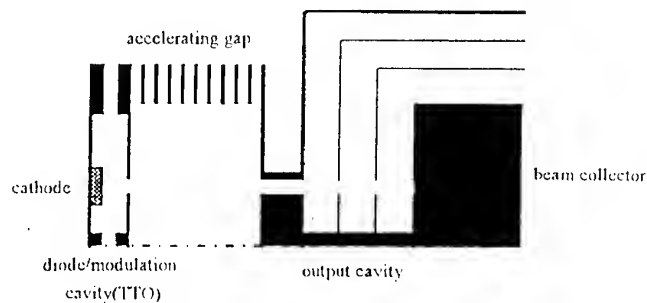
Fig 1. Coaxial axially twice acceletron

Its microwave generation is based on the principle of the transit time oscillator(TTO): when the transit time of the electron in the oscillator exceeds the oscillating period of the wave,it will emit radiation. We will study the bunching and radiation of the beam in the diode/oscillator at first.

2.1.FORM OF THE FIELD INTERACTING WITH THE BEAM

In the coaxial diode/oscillator with standing RF waves,the beam interacts with the waves to generate radiation and bunching .Asssume only one mode resonate with the beam,the form of its electromaganetic field then can be written as[2]

$$E_z^{rf} = [E_{pz}(r,z)\epsilon(z,t) + E_{scz}(r,z,t)]e^{-i\omega t} + c.c \tag{1}$$

where $E_{pz}(r,z) = f_{al^*}(r)cos(\gamma_{al^*}z)$ is the z direction component of the eigenmode of the diode/oscillator;f_{al^*} is a linear combination of Bessel functions determined by the radial boundary conditions, $\gamma_{al^*}$is determined by the axial boundary conditions, $\gamma_{al^*} = \frac{l^*\pi}{d}$,$l^*$is the definite axial wave number;$\epsilon(z,t)$ is the slow varying complex amplitude of the field; $E_{scz}(r,z,t)$ is the z direction component of the space charge wave field on the electron beam,it can be expressed as [2]

$$E_{scz}(r,z,t) = \frac{\frac{\omega_b^2}{\gamma^3(\gamma_{al^*}\nu_z - \omega)^2} + \frac{\omega_b^2}{\gamma^3(\gamma_{al^*}\nu_z + \omega)^2}}{1 - \frac{\omega_b^2}{\gamma^3(\gamma_{al^*}\nu_z - \omega)^2} - \frac{\omega_b^2}{\gamma^3(\gamma_{al^*}\nu_z + \omega)^2}} E_{pz}(r,z)\epsilon(z,t) \tag{2}$$

Where $\omega_b^2 = \frac{4\pi e^2 n_0}{m}$ is the plasma frequency of the beam, ν_z and γ are,respectively,the axial velocity and the relativistic factor of the electron,ω is the frequency of the wave.The components E_{pr} and $B_{p\theta}$ of the field can be found from the source free Maxwell's equations.

Substituting (2) into(1),we obtain

$$E_z^{rf} = \beta E_{pz}(r,z)\epsilon(z,t)e^{-i\omega t} + c.c \tag{3}$$

$$\beta = \frac{1}{1 - \frac{\omega_b^2}{\gamma^3(\gamma_{al^*}\nu_z - \omega)^2} - \frac{\omega_b^2}{\gamma^3(\gamma_{al^*}\nu_z + \omega)^2}} \tag{4}$$

Equation (3) is the form of the wave field interacting with the beam.

2.2.BEAM BUNCHING CAUSED BY THE EXPONENTIAL GROWING FIELD

Assume the voltage of the diode is relatively low,one can make nonrelativistic approximation on the motion of the electrons,and assume $E_r^{rf} \ll E_z^{rf}$ in the mode resonating with the electrons,that is ,only the axial motion of the electrons will be considered.Before the radiation reaches saturation,$E_z^{se} \gg E_z^{rf}$,so the velocity and time of the electrons travaling from cathode to anode is determined mainly by the static electric field E_z^{se}.Their expressions can be written as

$$\nu_z^{se} = \sqrt{\frac{2|e|V}{md}}z \tag{5}$$

$$t = \sqrt{\frac{2md}{|e|V}}z \qquad \tau = \sqrt{\frac{2m}{|e|V}}d \tag{6}$$

where V is the voltage on the anode of the diode,d is the distance between the cathode and the anode(or the length of the resonator) and τ is the total time of the electrons

traveling from the cathode to anode.

Beam bunching is that the velocity changes of the electrons caussed by the RF field lead to the phase modulation of the electrons.In the exponetial growth regime,when the beam travels from the cathode to the anode,the amplitude of the phase modulation of the electrons can be calculated from the following equations

$$\omega t = \omega t_0 + \omega \int_0^z \frac{dz}{\nu_z} \approx \omega t_0 + \omega \int_0^z \frac{dz}{\nu_z^{se}} - \omega \int_0^z dz \frac{\nu_z^{rf}}{(\nu_z^{se})^2} \tag{7}$$

$$\nu_z^{rf} = -\frac{|e|\beta}{m} \int_0^z dz_1 \frac{f_{al\cdot}(r)cos(\gamma_{al\cdot}z)\epsilon(z,t)}{\nu_z^{se}} e^{-i\omega \int_0^{z_1} \frac{dz_2}{\nu_z^{se}} - i\omega t_0} + c.c \tag{8}$$

Where t_0 is the Lagrangian time coordinate of the electrons.The third term on the right side of Equation (7) is the modulated phase of the electron at the coordinate z,It is marked as

$$\Delta\theta = \omega \int_0^z dz \frac{\nu_z^{rf}}{(\nu_z^{se})^2} \tag{9}$$

Assume that the beam is a thin ring and its pulse length is much longer, and the RF field is in the exponential growth ragime of the steady state,i.e.

$$\epsilon(z,t) = \epsilon(z) = |\epsilon_0|e^{\Gamma z + i\phi_1 z} \tag{10}$$

where Γ and ϕ_1 are the growth rate of the amplitude and the phase of the electromagnetic field respectively.

Substituting (5),(8) and (10) into (9),we obtain the amplitude of the modulation phase $\Delta\theta$ of the electrons when they travel from the cathode to the anode.

$$\Delta\theta = -[F_1 cos\omega t_0 + F_2 sin\omega t_0] \tag{11}$$

$$
\begin{aligned}
F_1 &= A\int_0^d \frac{dz}{z} \int_0^z dz_1 \frac{e^{\Gamma z_1}}{\sqrt{z_1}} \{cos[(\phi_1 + \gamma_{al\cdot})z_1 - \frac{\omega z_1^{\frac{1}{2}}}{\sqrt{\frac{|e|V}{2md}}}] \\
&+ cos[(\phi_1 - \gamma_{al\cdot})z_1 - \frac{\omega z_1^{\frac{1}{2}}}{\sqrt{\frac{|e|V}{2md}}}]\}
\end{aligned}
\tag{12}
$$

$$
\begin{aligned}
F_2 &= A\int_0^d \frac{dz}{z} \int_0^z dz_1 \frac{e^{\Gamma z_1}}{\sqrt{z_1}} \{sin[(\phi_1 + \gamma_{al\cdot})z_1 - \frac{\omega z_1^{\frac{1}{2}}}{\sqrt{\frac{|e|V}{2md}}}] \\
&+ sin[(\phi_1 - \gamma_{al\cdot})z_1 - \frac{\omega z_1^{\frac{1}{2}}}{\sqrt{\frac{|e|V}{2md}}}]\}
\end{aligned}
\tag{13}
$$

$$A = \frac{\omega\beta|\epsilon_0|f_{al\cdot}(r_b)}{2\sqrt{\frac{|e|}{m}}(\frac{2V}{d})^{\frac{3}{2}}} \tag{14}$$

Equations (11)–(14) show that the amplitude of the modulation phase of the electrons increases rapidly as the distance d between the anode and cathode is enlarged($\Delta\theta \sim d^2 e^{\Gamma d}$),but decreases as the voltage V of the diode is rised ($\Delta\theta \sim V^{-\frac{3}{2}}$).

The harmonic component of the modulation current of the electron beam can be derived from its modulation phase[2]:

$$
\begin{aligned}
I_{zn} &= \int 2\pi r dr \frac{1}{2\pi/\omega} \int_{-\frac{\pi}{\omega}}^{\frac{\pi}{\omega}} j_z(r,z,t) e^{in\omega t} dt + c.c \\
&= -|e|n_0\nu_z(d)s_b \sum_l i^l J_l(F_1)(-1)^{l+n} J_{l+n}(F_2) + c.c
\end{aligned}
\tag{15}
$$

The fundamental mode of the radiation is generated by the first harmonic current, which can be obtained from the Equation (15) above

$$
\frac{I_{z1}}{I_{z0}} = 2J_0(F_1)J_1(F_2) + 2J_2(F_1)[J_1(F_2) - J_3(F_2)]
\tag{16}
$$

where $I_{z0} = |e|n_0\nu_z(d)s_b$ is the direct current of the beam reaching the anode; J_n is the first kind of Bessel function with order n.

2.3.BEAM BUNCHING CAUSED BY THE SATURATION FIELD

Every time each electron group transits the diode/resonator, the wave will be amplified once. The transit time τ of the electron group from the cathode to the anode, for the parameters given in the reference[1], equals 0.24ns. If the work time t_c of the diode/resonator equals 200ns, then the wave amplification times N will be $N = \frac{t_c}{\tau} = 833$. The quality factor Q of the diode/resonator is relatively small(the impedance is lower due to the coaxial structure), but it allows higher injection current, therefore the radiation can still start up and reach saturation.

When the radiation field in the diode/resonator reaches saturation, the emition and bunching of the electron group will show new phenomena. the saturation condition is

$$
|E_z^{rf}| \geq E_z^{se}
\tag{17}
$$

The relation between the current and voltage of the diode, according the reference[3], is

$$
I_0^l = \begin{cases} aV^{\frac{3}{2}} & \text{nonrelativistic} \\ bV & \text{ultrarelativistic} \end{cases}
\tag{18}
$$

where I_0^l is the current emitted by the cathode far from saturation. If we make the system operate at $|E_z^{rf}| = E_z^{se}$, then the current emitted at saturation I_0^s can be written as

$$
I_0^s = \begin{cases} 0 & E_z^{rf} \text{ in the opposite direction with} E_z^{se} \\ 2.8I_0^l & E_z^{rf} \text{ in the same direction with} E_z^{se}, \text{nonrelativistic} \\ 2I_0^l & E_z^{rf} \text{ in the same direction with } E_z^{se}, \text{unltrarelativistic} \end{cases}
\tag{19}
$$

At saturation electron emitting on the cathode is completely controlled by rf field with the period T, therefore the cathode emits electron bunches one by one with period T. The emitted current can be written as

$$
I(t) = I_0^s T \sum_{n=0}^{\infty} \delta(t \pm nT)
\tag{20}
$$

Here $T = \frac{2\pi}{\omega}$.Making Fourier expansion on $I(t)$,we obtain

$$I(t) = I_0^s + 2I_0^s \cos\omega t_0 + 2I_0^s \cos 2\omega t_0 + \cdots \tag{21}$$

It is obvious from Equation (21) that under the action of the saturation field ,the beam emitted by the cathode reaches ideal bunching and the peak current of each harmonic is twice the direct one at saturation,that is,5.6 times and 4.0 times the direct one far from saturation in the nonrelativistic condition and in the ultrarelativstic condition respectively (In the reference [1],it is found by numerical simulation that the rf peak current is approximately 4 times the direct current far from saturation at the voltage of 250KV).Therefore by the design of the extracting cavity,one can acquire not only high power but also hign frequency microwave pulses.

3. EVOLUTION OF THE ELECTROMAGNETIC FIELD

Using the same method as in reference [4],we can derive the evolution equation of the electromagnetic field of the nth harmonic in the extraction cavity

$$\frac{\partial \epsilon_n}{\partial t} + \nu_{gn} \frac{\partial \epsilon_n}{\partial z} = -\frac{1}{U_n} \int_{z-\frac{\lambda_{zn}}{2}}^{z+\frac{\lambda_{zn}}{2}} dz \int d^2 \vec{x}_\perp \vec{j}_n \cdot \vec{E}_q^{(n)*} e^{-ik_{zn}z+in\omega t}$$

$$= -\frac{1}{U_n} \int_{z-\frac{\lambda_{zn}}{2}}^{z+\frac{\lambda_{zn}}{2}} dz \int d^2 \vec{x}_\perp j_{nz} E_{qz}^{(n)*} e^{-ik_{zn}z+in\omega t} \tag{22}$$

$$\nu_{gn} = \frac{c}{4\pi} \int_{z-\frac{\lambda_{zn}}{2}}^{z+\frac{\lambda_{zn}}{2}} dz \int d^2 \vec{x}_\perp \frac{\hat{e}_z \cdot (\vec{E}_q^{(n)*} \times \vec{B}_q^{(n)} + \vec{E}_q^{(n)} \times \vec{B}_q^{(n)*})}{U_n} \tag{23}$$

$$U_n = \int_{z-\frac{\lambda_{zn}}{2}}^{z+\frac{\lambda_{zn}}{2}} dz \int d^2 \vec{x}_\perp \frac{[|\vec{E}_q^{(n)}|^2 + |\vec{B}_q^{(n)}|^2]}{4\pi} \tag{24}$$

where $\vec{E}_q^{(n)}$ and $\vec{B}_q^{(n)}$ are the eigenmodes of the extraction cavity,which are determined by the source free Maxwell's equations and the boundary conditions; $\epsilon_n, \lambda_{zn}, k_{zn}, \nu_{gn}$ and U_n are,respectively,the slow varying complex amplitude,axial wavelength,wavenumber, group velocity and energy per $|\epsilon_n|^2$ contained in the nth harmonic axial wavelength $\lambda_{zn} = \frac{2\pi}{k_{zn}}$.

The ideal bunched beam is accelerated again after it passes through the slot on the anode of the diode/oscillator,in this process its energy is raised while its bunching remains unchanged.Then the prebunched and post-accelerated beam will radiate in the extraction cavity.Its prebunched current is

$$j_{nz} = \int \nu_z^{(0)} dt_0 \int 2\pi r_0 dr_0 2j_0^s \cos(n\omega t_0)\delta(z - z_e(t,t_0,r_0)) \times \frac{\delta(r - r_e(t,t_0,r_0))}{2\pi r} \tag{25}$$

where $\nu_z^{(0)}$ is the electron velocity after post-acceleration;j_0^s is the current density emitted by the cathode at saturation.

Substituting (25) into (22),we obtain the scaling law of the radiation power of the nth harmonic

$$P_n \sim |\epsilon_n|^2 \sim (I_0^s)^2 \tag{26}$$

where I_0^s is the current emitted by the cathode at saturation.From Equation (26),the radiation emitted by the beam in the extraction cavity is superradiation.

REFERENCE

[1] M.Joseph Arman "Radial Acceletron,A new Low-Impedance HPM Source" IEEE Trans.Plasma Sci.,24(3) (1996),964-969.

[2] Wu Ding "Mechanism of microwave generation in Super-Reltron",Intense Microwave pulse V,ed. H.E.Brandt,SPIE Vol.3158(1997) 104-112.

[3] Ronald C.Davidson "An Introduction to the Physics of Nonneutral Plasmas" Addison- Weslay Publishing Company(1990).

[4] Baruch Levush,Thomas M.Antonsen,Jr.,Alan Bromborsky,Wei-Ran Lou,Yuval Carmel, "Theory of Relativistic Backward-Wave Oscillators with End Reflections" IEEE Trans.Plasma Sci.,20(3) (1992),263-280.

MICROWAVE GENERATOR WITH VIRTUAL CATHODE, WORKING IN STOCHASTIC RESONANCE REGIME (STOCHASTRON)

A.Dubinov, K.Mikheyev, V.Selemir, A.Sudovtsov

*Russian Federal Nuclear Centre - VNIIEF,
Mira 37,Sarov, 607190, Russia*

Such phenomena as parametric resonance, three wave resonance and similar are well known in the theory of dynamic systems, but in 1981 [1] a new dynamic phenomenon, named stochastic resonance, was discovered.

This phenomenon develops itself in the following way: if a bistable system is a subject of a simultaneous influence of harmonic noise signals, then under some circumstances, the amplitude of harmonic signal and signal to noise ratio can be increased. On the contrary to ordinary resonance, where the increasing of signal's amplitude takes place during the matching of the system's eigenfrequencies with the frequency of the external signal, stochastic resonance appears when the frequency of the external signal matches with the average frequency of the system's jumps from one stable state to another under the influence of noise. That means that during the stochastic resonance, the noise energy partly transfers into the energy of regular oscillations.

The theory of stochastic resonance for bistable potential systems is described in [2,3]. It is rather interesting to apply the theory of stochastic resonance to constructing of high-power microwave oscillators.

The most promising impulse high-power microwave oscillators are oscillators based on virtual cathode (so-called vircators) [4-6]. In such oscillators, stochastic resonance can be realized very simply. In this paper, theoretical model of vircator, working in stochastic resonance regime, is investigated. We called such vircator – stochastron.

The phenomenon of stochastic resonance can appear under the influence of the following factors:

1. the existence of bistable potential between real and virtual cathodes, which in our case can be provided by inserting of the additional anode grid. The space between grids is chosen for promoting of the electron beam transferring without creation of the virtual cathode between grids, and the potential barrier between grids forms because of space charge of the beam. The similar double-grid reflection systems that are used for collective acceleration of the positively charged ions [7,8] and for microwave generation [9] are well known. In the last case the additional grid is necessary for smoothing of the potential profile at the bottom of the potential well.

2. the existence of the energy noise which provides irregular excitation of the electrons-oscillators. Such noise in vircators appears as a result of irregular oscillations of the virtual cathode which, in its turn, causes the appearance of the noise component of longitudinal electric field near virtual cathode:

$$\langle E(t)\rangle = 0; \quad \langle E(t)E(t+\tau)\rangle = \frac{E_n}{\tau^d} \tag{1}$$

here E_n – noise amplitude d – correlation index, it was calculated for different microwave devises in [10]. In the same paper was found that in the major cases $d>10$ that is why we can write:

$$\langle E(t)E(t+\tau)\rangle = E_n\delta(\tau) \tag{2}$$

fig.4a, the spectrum of double grid vircator working in stochastic resonance regime (stochastron) is shown at fig.4b (the locations of the grids at both figures are the same). The difference between those two spectrums is very noticeable. The main pick at fig.4b is at the frequency Ω_0 = 2,3 GHz, harmonics with frequencies $2\Omega_0$ and $3\Omega_0$ are also noticeable. Spectrum of the longitudinal component of the electric field E_z also has maximum at the frequency close to Ω_0.

The facts presented above demonstrate that stocastron generates electromagnetic radiation in narrower spectral band then the ordinary vircator.

Fig.3. Transitional current diagram.

a)

b)

Fig.4. Frequency characteristics of the transitional current:
a) ordinary vircator;
b) stochastron.

Indeed, thus in a presence of a high power magnetic field in the area of beam spreading, stochastron and comparable with it vircator generate the electromagnetic wave of TM-type. That means that in stochastron, the magnetic component of the wave - H_φ is proportional to the transitional current and so, the Poynting vector also has maximum at the frequency Ω_0, which has been proved.

As a rule, the increasing of the signal to noise ratio during the increasing of the noise amplitude is considered to be the proof of the existence of the stochastic resonance regime. That lead to the appearance of maximum in the dependence of signal to noise ratio from noise magnitude at some noise value. However, in our case, there is no external regular signal, that is why such criteria of the existence of stochastic resonance regime can't be used. We consider, that in this case the most provable confirmation of the existence of stochastic resonance regime is the existence of pick in the transitional current spectrum which can't be explained by another reason in resonator with low quality factor such as the emitting microwave oscillator.

Thus, the possibility of stochastic resonance regime realization in microwave devices with virtual cathode

Also, the regenerative coupling provided by the charge density waves, raised by electrons reflected from the virtual cathode, will lead to the oscillation of the height of the potential barrier between grids.

3. the existence of a harmonic signal of the appropriate frequency. Actually, this signal can appear because of the existence of spectral component with appropriate frequency in noise. But, moreover in microwave oscillator, harmonic signal can be risen with one of the eigenfrequencies of the electrodynamic system.

For numerical simulation of stochastron authors used computer code "KARAT" [11], which used PIC-method. The geometry of the model is demonstrated at fig.1. A homogeneous magnetic field equal to 50 kGs was applied to the whole area of simulation.

Diode in the model provides an electric current with magnitude about 65 kA at potential difference – 300 kV. The instant phase portraits of the system are
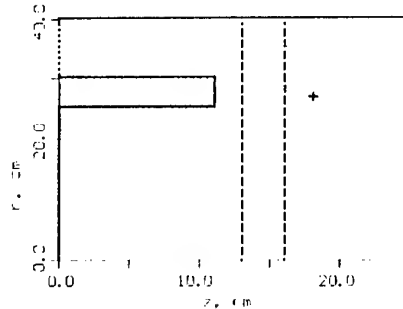
Fig.1. Model (all sizes in cm., cross identifythe sensor location.

a)

b)
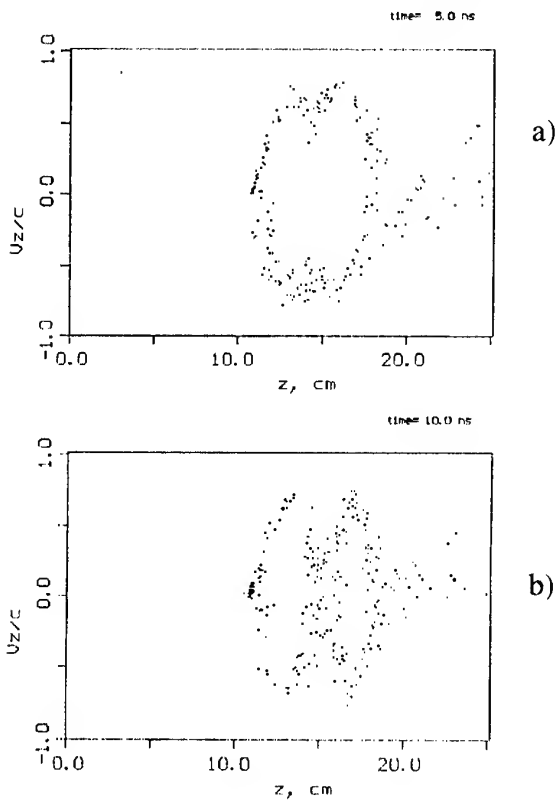
Fig.2. The instant phase portraits of the electrons beam (points - electrons):
a) t = 5 ns; 6) t = 10 ns.

demonstrated at fig.2a,b. It is easy to see at those figures that firstly all electrons pass the potential barrier between grids, but then system transfer to regime with some locked electrons around each grid. The existence of the diffuse electron's layer nearby separatrix confirms the possibility of existence of stochastic resonance regime in this model.

During choosing of the geometry of the anode system, the space between grids was varied, but the diode region, zone of virtual cathode forming and the location of the main point – "sensor" (cross at fig.1) relatively to the second grid, was kept invariant. In a result of variation it was found that the stochastic resonance regime most brightly develops itself in a model with the size of the gap between grids - 3 cm.

For additional confirmation of the existence of stochastic resonance regime in stochastron, the spectral characteristics of microwave oscillator were analyzed. For that purpose the spectrums of the transitional current were investigated at the profile of the system where sensor was located. The typical picture of the transitional current temporal evolution is demonstrated at fig.3.

In comparison to the spectrum of the ordinary - single grid vircator, demonstrated at

was demonstrated. The existence of stochastic resonance regime in microwave oscillators allows generating of some sort of monochromatic radiation. The way of energy transformation in degrees of freedom is shown at fig.5

There are no other methods of generation of highly monochrome radiation with appropriate power in microwave oscillators with virtual cathode. It seems that it is possible to increase the quality factor of resonator and in such way to increase the level of monochromatism of the radiation, but this will lead to diminishing of the emitting aperture. In [12] vircator with closed cylindrical drift area without any emitting window was investigated, the generated radiation was highly monochromatic, but of cause the emitted radiation in such case is close to zero. That is why microwave oscillators working in the stochastic resonance regime could be a good solution for emitting of highly monochromatic radiation in comparison to the increasing of the quality factor of the electrodynamical system.

Fig.5. The energy transformation in degrees of freedom

In conclusion notice, that if in some reason one can't achieve ordinary resonance in the oscillating system (in our case such reason is turbulence of the electrons flow with virtual cathode), it could be useful to achieve in stochastic resonance.

Authors would like to thanks V.P.Tarakanov for the giving an opportunity of usage of the computer cod "KARAT" developed by him.
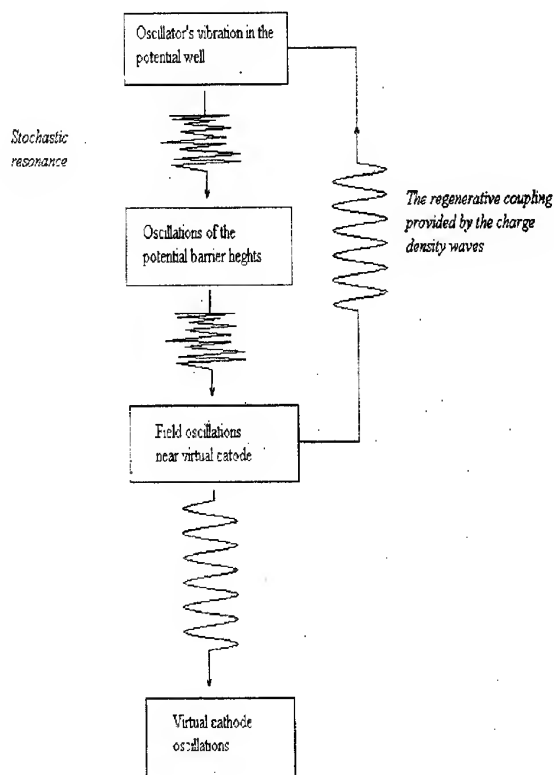
1. Benzi R., Sutera A., Vulpiani A. // J. Phys. A, 1981, v. 14, p. L453.
2. McNamara B., Wiesenfeld K. // Phys. Rev. A, 1989, v. 39, N 9, p. 4854.
3. Anishenko V.S., Postnov D.E., Hovanov I.A., Shul'gin B.V. // Radiotehnika i electronika, 1994, v. 39, N 12, p. 2004 (in Russian).
4. Rukhadze A.A., Stolbetsov S.D., Tarakanov V.P. // Radiotehnika i electronika, 1992, v. 37, N 5, p. 385 (in Russian).
5. Alyokhin B.V., Dubinov A.E., Selemir V.D. et al. // IEEE Trans. Plasma Sc., 1994, v.22, N 5, p. 945.
6. Dubinov A.E., Selemir V.D. // Zarubejhnaya radioelektronika, 1995, N 4, p. 54 (in Russian).
7. Pasour J.A., Mahaffey R.A., Golden J., Kapetanakos C.A. // Phys. Rev. Lett., 1978, v. 40, N 7, p. 448.
8. Arbuzov A.I., Bystritski V.M. // ZhETF, 1981, v. 51, N 11, p. 2383 (in Russian).
9. Miner L.M., Voss D.E., Koslover R.A. et al. // IEEE Trans. Elect romagnetic Compatibility, 1992, v. 34, N 3, p. 229.
10. Vatrunin V.E., Dubinov A.E., Selemir V.D., Stepanov N.V. // In book: Fractals in the applied physics, edited by Dubinov A.E., Arzamas-16, 1995, p. 47 (in Russian).
11. Tarakanov V.P. User's manual for code Karat, Berkley Research As sociate, Inc., Springfield, VA, 1992.
12. Fazio M.V., Freeman B.L., Hoeberling R.F. et al. //IEEE Trans. Plasma Sc., 1992, v. 20, N 3, p. 305.

HIGH-FREQUENCY ELECTRON BEAM MODULATION IN A DIODE WITH AN ACTIVE PLASMA CATHODE

Ya. E. Krasik, A. Dunaevsky, and J. Felsteiner
Department of Physics, Technion, 32000 Haifa, Israel

We have carried out experiments with an active plasma cathode showing the possibility to generate a modulated electron beam with a repetition rate of 2Hz without the use of a high-frequency power supply. The modulation of the beam current amplitude reaches values ≥30%. This modulation is found to have a frequency of 325±5 MHz for a discharge capacitor of 1nF and a duration ≥1μs. In addition, the modulated electron beam is accompanied by electromagnetic radiation with the same frequency. We suggest that this high-frequency modulation is caused by electron oscillations within the potential well which is created inside the cathode structure by the positive potential of the plasma.

In the present experiment, an electron beam is produced by the use of a plasma source (see Fig. 1).
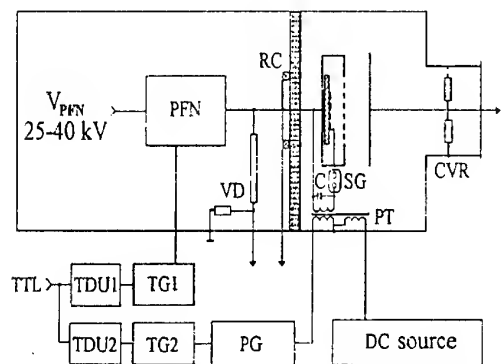
Fig. 1. Experimental setup. TDU – time delay unit; TG – trigger generator, PG – pulse generator; VD – voltage divider; RC – Rogovskii coil; CVR – current view resistor; PT – pulse transformer; SG – spark gap; C – capacitor.

To produce a plasma inside the cathode we have used a TiBa sample (∅44 mm, 3.5mm thickness). The front surface of the sample is covered by by strips (distance between strips of 1.5mm, strip width of 1.5mm). The diameters of the front electrode and the rear disk electrode are 20mm each. The TiBa

sample is placed inside an aluminum box. The box window is covered with a stainless steel grid placed at a distance of 10mm from the sample. The plasma is created by applying a positive voltage pulse (6-10kV), produced by a pulse generator (PG), to the front electrode of the sample. The sharp rise time ($\tau_r \leq 10$ns) of the pulse is provided by a capacitor (C) and a spark gap (SG). Due to the "triple point" effect,[2] a surface discharge is initiated which leads to surface plasma formation. The anode, made of a brass disk or a stainless steel grid, was placed at different distances (5 – 40 mm) from the cathode. A negative voltage was applied to the cathode by a PFN generator ($\varphi_{ch} \leq 40$kV, $\rho_{PFN} = 10\Omega$, $f \leq 5$Hz) with a variable time delay with respect to the PG firing. A pulsed transformer (PT) was used for decoupling PG from the PFN generator.

The plasma parameters were measured by a biased collimated Faraday cup (CFC) and by floating probes. The voltage and the diode current were measured by an active

voltage divider (VD) and a current view resistor (CVR). The electron beam current density was measured by the CFC. HF electromagnetic radiation was detected by B-dot loops placed inside and outside the vacuum chamber. The plasma density, plasma electron temperature and the plasma expansion velocity were found to be 2×10^{12} cm^{-3} at 1 μs, T_e =5±2eV and v_{pl} =1.2±0.2×10^6 cm/s, respectively. Thus, the saturation current density of the plasma can be estimated as $j_{ep} \cong 0.4\, n_e e v_{T_e} \geq 30$A/cm^2.

To achieve emission of electrons from the stationary plasma boundary the condition $j_{ep}=j_{sc}$ must be satisfied. Here j_{sc} is the space charge limited current density.[3] Otherwise, when $j_{ep}>j_{sc}$ or $j_{ep}<j_{sc}$ plasma expansion or erosion will take place, respectively. The condition $j_{ep} \approx j_{sc}$ was achieved by an adjustment of the time delay between the PG and the PFN. In this case, the electron beam generation ($I_e \leq 100$A, $E_e \leq 40$keV) was continuously pulsed at a repetition rate of 2Hz. A comparison of the electron current density with that predicted using the space charge law[3] shows satisfactory agreement during the first 200ns. Later on, the amplitude of the electron current density becomes less than the j_{sc}. These data were observed for the capacitance $C \leq 0.5$nF. When the value of the capacitor C was increased to >0.7nF, we observed large HF oscillations of the CVR signal, as shown in Fig. 2. These oscillations appear after ~2.5μs with respect to the beginning of the plasma formation. It was found that the HF oscillations could not be associated with electromagnetic noise. In addition, the appearance of the HF oscillations did not depend on the time delay of the PFN generator firing. The duration of these

HF oscillations was ≥1 μs, and in some shots, the duration was as long as 10μs.

Time (1000 ns/div)
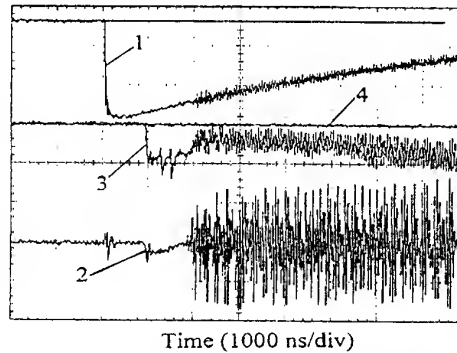
Fig. 2. Typical waveforms received by the CFC placed at 2 cm from the anode grid: (1) diode voltage (16 kV/div), (2) anode current (11 A/div) and the signals received (3) by the opened CFC2 (5 A/cm^2/div) and (4) by the closed CFC1 (3 A/cm^2/div). CFC1 is closed by a polyethylene foil with 180 μm thickness. V_{PFN} = 40 kV. Anode-cathode distance of 1.5 cm.

It was found that the appearance of the HF oscillations depended on the amplitude of the voltage pulse and on the value of the capacitor C. In addition, the appearance of the HF modulation depended on the diameter of the cathode output window and on the transparency of the cathode grid. Changing of other parameters (anode-cathode gap, diameter of the vacuum chamber, etc.) had no effect on the appearance of the HF oscillations.

The CFCs were used to study the modulation of the extracted electron beam. Two CFCs were placed at a distance of 20mm from the anode grid. One of them was covered by a polyethylene layer with a thickness of 180 μm. The data show that the non-covered CFC1 detects the electron beam with a HF modulated current amplitude, while the covered CFC2 shows zero signals (see Fig. 2). The amplitude modulation (I_e~20 A) reaches ≈30-60%, but modulation with 100% depth was also some times observed. By using the

windowed regime of the TDS640A digitizer, it was found that the amplitude modulation had a frequency of 325±5MHz (see Fig. 3).
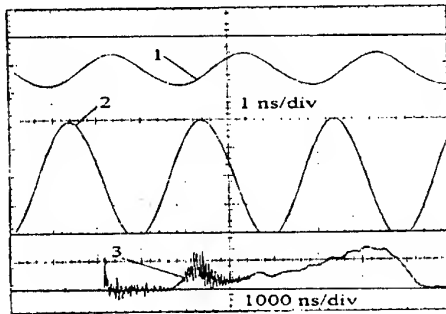
Fig. 3. Waveforms of the signals from (1) the CFC ($1A/cm^2$/div) and (2) the B-dot loop (10 V/div) in the windowed regime of the TDS 640A digitizer, and (3) the envelope of the attenuated B-dot loop signal (50mV/div). V_{PFN}=40kV. Anode-cathode distance of 2 cm.

It was found that the HF modulated electron beam was accompanied by electromagnetic radiatio. The frequency of the radiation was found to be the same as the frequency of the electron beam modulation, 325±5MHz, at $C = 1nF$. For a capacitance C =0.7nF the frequency of the radiation as well as the frequency of the electron beam modulation decreased to 290±5MHz. The frequency was not changed when varying the amplitude of the applied voltage and the anode and cathode radii. In addition, the change of the distance between the ceramic surface and the cathode grid and of the anode-cathode distance did not change the observed frequency.

The observed dependence of the amplitude of the HF signal on the applied high voltage showed that HF radiation disappears when the PFN voltage amplitude is < 30 kV, and increases by a factor 2 for each 5kV. A microwave detector (bandwidth of 0.01-12 GHz) was used to obtain an envelope of the attenuated B-dot loop signal (see Fig. 3). Regarding the value of the capacitance C, we have found that the HF modulation becomes unstable in the case of C<500 pF. In addition, it has been found that the decrease in the grid transparency as well as the decrease in the diameter of the output grid lead to the disappearance of the HF oscillations.

It should be noted that the electron beam modulation and the HF radiation occur only in the case when certain values of plasma parameters are achieved. For instance, for plasma density up to 10^{12} cm^{-3}, HF oscillations have not been observed. In addition, HF oscillations have disappeared when $n_e \le$ 10^{11}cm^{-3}. Therefore, the HF oscillation effect occurs for a comparatively narrow range of plasma density: 10^{11}cm$^{-3} \le n_e \le$ 10^{12}cm^{-3}.

The power of the radiation was estimated from the data obtained by a B-dot loop (S=3cm^2) at a distance of z=25cm from the diode. Taking into account that the measured induced voltage was $\varphi \approx$5V, and assuming the frequency of the radiation as $f \approx$325MHz, we estimate the power of the radiation as $P = 4\pi (z/\mu_0 S)^2 (\mu_0/\varepsilon_0)^{1/2} (\varphi/f)^2 \le 30$ kW.

Let us analyze the process which may occur during the plasma cathode operation. The positive voltage pulse is applied to the front electrode of the ceramic sample after the SG breakdown. Prior to the application of the PG voltage pulse the capacitance of the ceramic sample is about 240pF, and we have observed a short duration (~30 ns) high current (~250A) charging pulse through it. Then plasma begins to form on the ceramic surface due to electron avalanching.[2] The conductivity of the plasma allows it to serve as a dynamic electrode to provide an additional

charging current with amplitude of 50-70A during ~300ns. Simultaneously, the plasma extends in the space between the ceramic surface and the output grid with a velocity of 1.0-1.5cm/µs. After 0.7–1.0µs the plasma reaches the cathode grid and short-circuits both the secondary winding of the decoupling transformer and the capacitor C. The capacitor ($C = 1$ nF) begins to discharge through the plasma with a current density of $j_{pl} \approx 35$A/cm^2. This discharge current is carried by electrons and ions, and can be expressed as: $j_{pl} \approx j_i[1+(M_i/m_e)^{1/2}]$. To maintain the plasma quasineutrality, the ion current density should be $j_i \geq 0.7$A/cm^2. If the required ion current density $j_i \geq j_{is} \approx 0.4 Zen_i v_{pl}$, a cathode sheath can be formed at the vicinity of the sample surface.[4] Under our experimental conditions the ion plasma density is $n_i \leq 3 \times 10^{11}$cm^{-3} at a time of 2.5µs after the beginning of the plasma formation and corresponds to $j_{is} \leq 0.4$ A/cm^2. Therefore, the sheath formation can take place.

When a high voltage pulse of the PFN generator is applied between the anode and the cathode, the electrons accelerate from the boundary of the plasma which has already reached the cathode grid. The observed electron current density at that time was $j_{sc} \approx 6.5 \pm 1$ A/cm^2 which satisfactorily agrees with the expected j_{sc}. Further, the amplitude of the electron beam current decreases to 2.5 ± 0.5A/cm^2 which corresponds to the erosion of the plasma boundary and its movement beyond the cathode grid. This process may lead to a sheath formation between the plasma and the cathode grid. Thus, the plasma will have a positive potential with respect to the sample surface and the cathode grid. In this case, electrons will oscillate inside the potential well between the surface of the ceramic sample and the cathode grid, as in the reflex triode or vircator systems.[1,5] To estimate the frequency of the electron oscillations one has to know the floating potential of the plasma and this was not measured in the present experiment. However, according to the linear theory[1] for a non-relativistic electron beam, the frequency of electron oscillations

$$\omega_{osc} = (5/2)\omega_p = (5/2)(4\pi n_b e^2/m_e)^{1/2}$$

We assume that the density of the oscillating electrons is approximately the same as the electron density of the extracted modulated electron beam. In this case, the electron density can be estimated taking into account the observed current density $j_e \approx 1$A/cm^2 (see Fig. 3) as $n_b = j_e(2e^2 V_{PFN}/m_e)^{-1/2} \approx 5 \cdot 10^8$cm^{-3}. Thus, the frequency of electron oscillations is estimated as $f_{osc} = (5/2)\omega_p/2\pi \approx 500$MHz, which is in rough agreement with the observed frequency.

1. V. L. Granatstein and I. Alexeff, *High-power Microwave Sources* (Artech House, Boston, 1995).
2. G. A. Mesyats, Tech. Phys. Lett. **20**, 8 (1994), and references therein.
3. R. B. Miller, *An introduction to the Physics of Intense Charged Particle Beams* (Plenum, New York, 1982).
4. P. F. Ottinger, S. A. Goldstein, and R. A. Meger J. Appl. Phys. **56**, 774 (1984).
5. S. H. Gold and G. S. Nusinovich, Rev. Sci. Instr. **68**, 3495 (1997), and references therein.

VERSATILE e - BEAM PREBUNCHER FOR FEMs AND OTHER HIGH POWER BEAM DEVICES

A. L. Eichenbaum, H. Kleinman, M. Arbel, A. Gover

Faculty of Engineering, Dept. of Electrical Engineering-Physical Electronics,

Tel-Aviv University, Ramat - Aviv, ISRAEL

e-mail: eichenbm@eng.tau.ac.il

Abstract

Beam bunching is employed in microwave tubes, FEMs and in other devices. We shall characterize and point out the advantages of using a traveling wave type prebuncher in a table- top compact FEM, which operates successfully at Tel-Aviv University in C-band and for FEMs operating anywhere in the microwave or mm wave range.

Our prebuncher utilizes the e-gun and the first 2 "amplifier" sections of a 3-section Traveling Wave Tube (TWT). The 3rd "output" section was severed; an adopting flange was added to permit mounting and alignment of the prebuncher with the FEM resonator.

We shall characterize the density modulation of the e-beam exiting from the prebuncher as a function of the r.f. power input to the prebuncher and as a function of operating frequency. This characterization is made possible by scaling from data of small signal gain, saturation gain, power output vs. power input which was measured on the 3 section TWT for a large frequency range. From this measured data, from the knowledge of the prebuncher operating parameters and from existing information regarding the behavior of TWT bunched beams in the saturation region a good estimate of density modulation vs. input power and frequency is obtained for our prebuncher.

Among the features of our prebuncher are: great instantaneous bandwidth (in our case anywhere in the 3 GHz to 12 GHz band) obtained by varying the prebuncher input frequency, and the ability to vary the current density modulation level from 0 to near 100% (by varying the r.f. input power to the prebuncher from 0 to about 3 Watt).

This prebuncher allows selection and operation of our FEM at only one desired frequency for which net gain exists (this allows operation in the mode of highest efficiency). The r.f. power buildup time in the FEM oscillator is shortened by prebunching, and we can operate at different frequencies on a pulse-to-pulse basis by shifting the premodulation frequency in synchronism with the beam pulser. These unique capabilities to operate our FEM in a stable and narrow spectrum, at high efficiency and at any eigenfrequency are all made possible by use of our prebuncher.

1. Introduction

We proposed [1] and employ successfully, a short, efficient wide-band Traveling-Wave-type (TW) prebuncher in a table-top FEM (Fig. 1) operating at Tel-Aviv University [2] since 1994.

TW prebuncher-amplifiers can operate over more than octave bandwidths in the frequency range of 2 GHz to 120 GHz and can provide e-beam current modulation index of the fundamental and of the r.f. current harmonics from zero up to near unity (frequency and modulation level depend on the r.f. input to the prebuncher). Since the TW prebuncher is basically an amplifier prebuncher input levels of 0.1mW were sufficient to assure single mode selection in a FEM oscillator having an output power of 4kW. Maximal current modulation was obtained with a prebuncher r.f. input power level of about 1Watt.

The wide-band prebuncher, uses the e-gun and the first two helix sections of a TWT, (Fig. 1). It enables setting and adjustment of the prebunching frequency, level of r.f. current modulation, e-beam d.c. current and e-beam pulse width.

The fundamental prebunching frequency, determined by the r.f. input frequency to the prebuncher, can be chosen to be anywhere within the prebuncher bandwidth or in the FEM interaction bandwidth. The r.f. current modulation level can be set and adjusted by choice of the prebuncher input power level. The e-beam current level and the the pulse width are determined by the modulation voltage applied to a grid near to the cathode.

Use of this prebuncher in our FEM enabled single mode selection and stable operation of the FEM oscillator at any one desired eigenfrequency throughout the r.f. pulse and the suppression of other eigenfrequencies [2], reduction of required r.f. buidup time to reach FEM saturation [3], and efficiency enhancement in FEM operation [4]. Possibilities of operating the FEM as a frequency-agile high power source (on a pulse to pulse basis) by employing frequency hopping in the prebuncher were described [5]; recently oscillations and high amplification of the FEM in the spectral range near cutoff [6] were also observed. Pure prebunching radiation experiments using this prebuncher are being carried out at present.

2. Current density modulation level as a function of r.f. input power to the prebuncher

The premodulator operation in an FEM is characterized by I_{rf}/I (i.e. the fundamental frequency r.f. current density modulation index) at all frequencies of interest. We need to know it as a function of the r.f. input power to the prebuncher.

This I_{rf}/I_0 modulation behaviour has been investigated extensively for TWTs in an experimental study by C.C. Cutler [7] up to, and beyond saturation.

Prior to removing the third TWT section and collector from an operative TWT (to prepare the 2-section prebuncher for our FEM) we measured the gain and power vs. frequency, up to saturation of the complete TWT. The first 2 sections of our TWT have a length which is 0.6N of the complete TWT. Based on the TWT gain equation, we can scale and evaluate the s.s. gain G_{ss} of the prebuncher first 2 section vs. frequency. The large signal gain at saturation of the prebuncher (first 2 section) is similarly evaluated.

Based on the large signal gain we find the required r.f. input power which saturates the prebuncher, for various current levels and frequencies.

For a complete TWT Cutler [7] found that the ratio of the fundamental r.f. component of current I_{rf} to the d.c. beam current I_{dc}, $I_{rf}/I_0 \approx 1$ for saturation conditions.

As one reduces the input r.f. power to the prebuncher by several db from an input power P_{insat}, leading to prebuncher saturation, this current modulation ratio, I_{rf}/I_0 first goes

above 1; it is still near to unity for P_{insat}-10db (i.e. for an input level 10db below that which causes saturation). For r.f. input power levels below P_{insat}-10db, Cutler showed that the ratio $(I_{rf}/I_o)^2$ is nearly proportional to the input r.f. power.

On this basis we obtained the graphs of Fig. 2 for a frequency of 5GHz. Similar graphs were obtained for each frequency of interest which relate the current modulation level to the r.f. input level to the prebuncher. For simplicity $(I_{rf}/I_o)^2$ =1 in Fig. 2 (for P_{insat}-10db $\leq P_{in} \leq P_{insat}$).

ACKNOWLEDGEMENT

References

[1] A.L. Eichenbaum, "Proposed use of TWT prebuncher in mini FEM", Tel-Aviv University Res. Proposal (March1990).
A.L. Eichenbaum, H. Kleinman, M. Cohen, "Mini FEM for the study of microwave radiation from r.f. prebunched e-beams", Mini symposium on FEL, FOM Institute, The Netherlands, pp.20-24 (1991).

[2] M. Cohen, A. Eichenbaum, M. Arbel, D. Ben-Haim, H. Kleinman, M. Draznin, A. Kugel, I. M. Yakover, and A. Gover, "Masing and Single Mode-Locking in a Free Electron Maser Employing Prebunched Electron Beam", Phys. Rev. Lett., 74, 3812-3815 (1995).

[3] A.L. Eichenbaum, A. Abramovich, M. Arbel, M. Cohen, L. Gilutin, A. Gover, H. Kleinman, Y. Pinhasi, S. Volkovich, I.M. Yakover, "Performance Improvement of FEMs by Prebunching of the Electron Beam", Nucl. Inst. & Meth. in Phys. Res. A 393, pp.361-365, (1997).

[4] A. Abramovich, Y. Pinhasi, V. Sterngratz, L. Gilutin, H. Kleinman, A.L. Eichenbaum, I.M. Yakover, M. Cohen, A. Gover, B. Levush, T.M. Antonsen, V.L. Granatstein, "Measurements and simulation of the radiation build-up process in a prebunched free-electron maser oscillator", Nuclear Inst. and Methods in Phys. Res. A375, 164-168, (1996).

[5] A.L. Eichenbaum, M. Cohen, H. Kleinman, D. Ben-Haim, A. Kugel, D. Chairman, I. Ronin, M. Arbel, M. Draznin, I.M. Yakover, and A. Gover, "A Novel Free-Electron Maser as a High Power Microwave Source of Sophisticated Signals", Proc. 18th IEEE Convention, Israel, 95TH8044, (1995).

[6] L. Gilutin, A. Abramovich, M. Arbel, A.L. Eichenbaum, A. Gover, H. Kleinman, Y. Pinhasi, Y.M. Yakover, "Free Electron Maser Oscillations Near Waveguide Cutoff", Nucl. Inst. and Meth Phys. Res A, (1998).

[7] C.C. Cutler, "The nature of power saturation in Traveling Wave Tubes", Bell Sys. Tech. Jour. Vol. 35, #4, (1956).
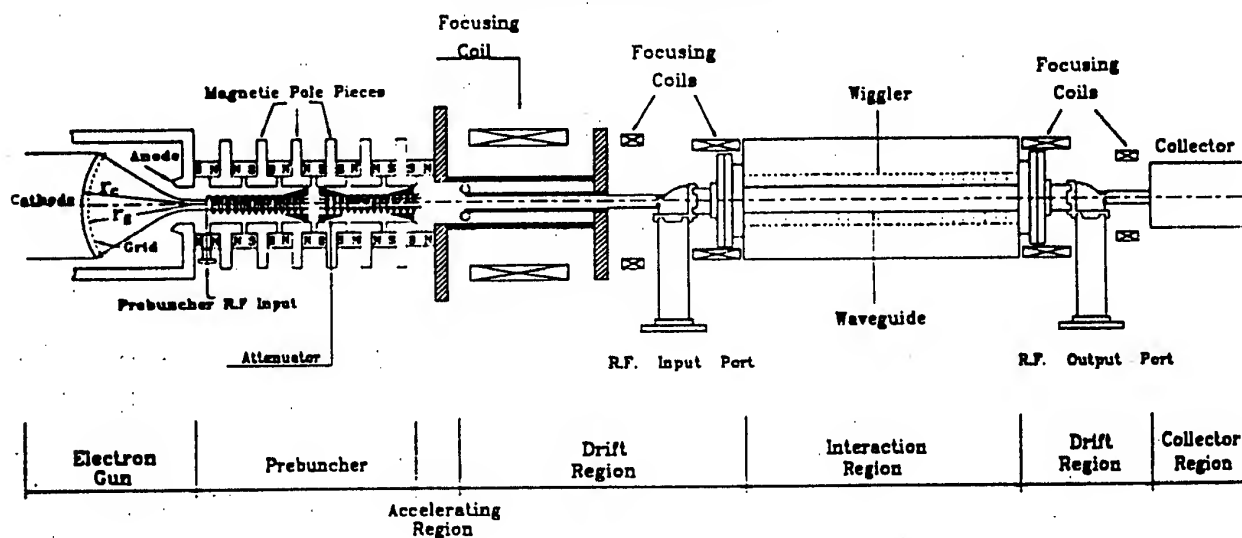
Fig. 1   Schematic Diagram of Prebunched FEM
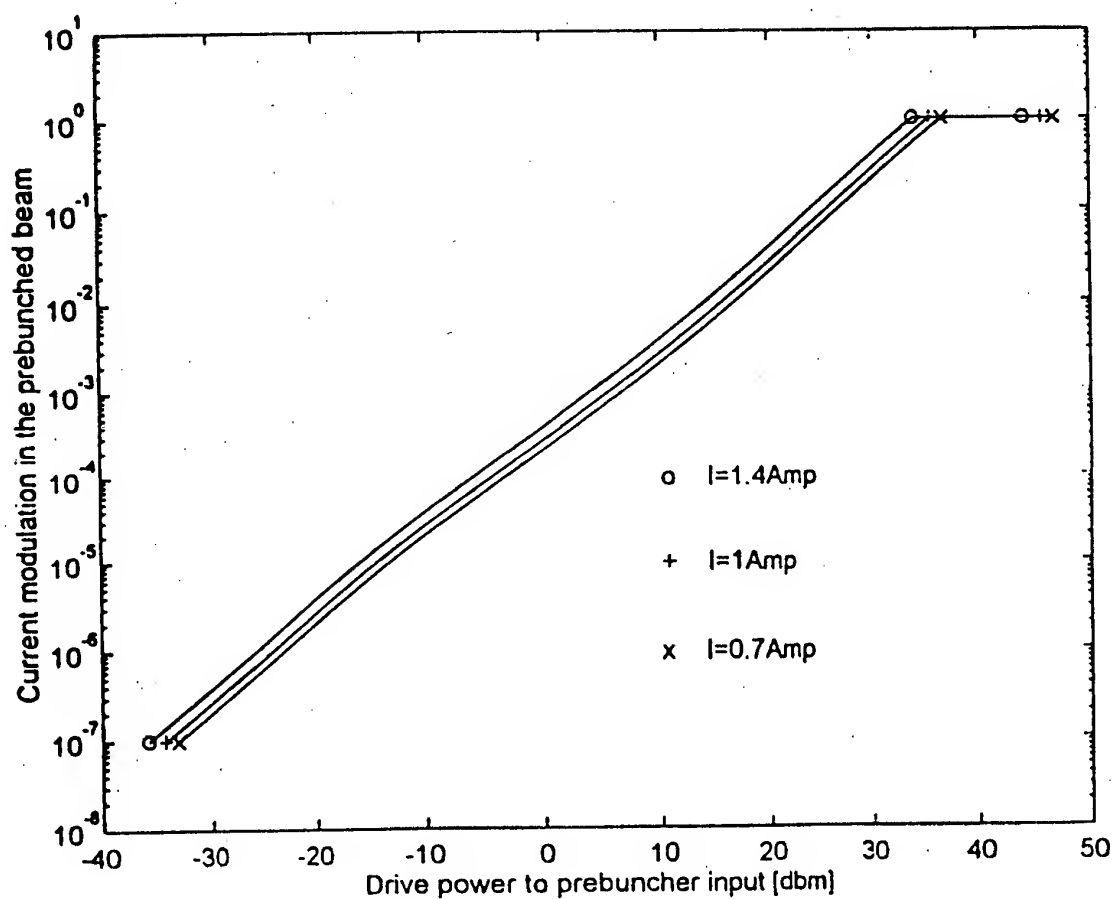
Fig. 2   Current modulation vs. prebuncher input power (for f=5GHz)

A HIGH-POWER RELATIVISTIC MAGNETRON OF NEW CONCEPTION: SIMULATION AND EXPERIMENT*

V. A. Bogachenkov, V. A. Papadichev,
P. N. Lebedev Physical Institute of RAS,
Leninsky Prosp. 53, Moscow 117924, Russia,

V. M. Fedorov, <u>V. P. Tarakanov</u>,
High Energy Density Researh Center of RAS,
IVTAN, Izhorskaya 13/19, Moscow, 127412, Russia,

V. A. Silin
General Physics Institute of RAS,
Vavilova, 38, Moscow, 117942, Russia

ABSTRACT

Investigations on increasing the power and efficiency of a relativistic magnetron microwave generator with "large anode" are presented. General parameters of the installation are: wavelength $\lambda = 10\,cm$ (S-band), anode-cathode gap is 1 cm, high voltage pulse of $150\,ns$ duration $V_0 = 500\,kV$ and axial pulsed magnetic field $B_0 = 0.5\,T$. Microwave power of $P_\sim \sim 1\,GW$ is emitted through a cylindrical waveguide with TM_{01} mode and a horn with a 28-cm output diameter. The first magnetron version VF-1 was limited to a microwave power level of $0.3\,GW$. It was determined primarily by RF-breakdown inside the cavities and the output space mode RF-converter (resonator structure – coaxial emitter). The new magnetron contains 12 resonators of the open saw-shape type. To eliminate the storage of electrons inside resonator cavities, we use additional permanent magnets in all vanes of the resonators. Finally, we changed the classical Boot-Pickering spatial RF-converter. The new semi-transparent RF-converter transforms both symmetrical and non-symmetrical magnetron modes to travelling waves of the output waveguide.

INTRODUCTION

High power microwave relativistic magnetrons (RM) of gigawatt power levels [1-4] operate with lower efficiencies ($\eta_\sim \sim 20\%$) and shorter pulse duration ($t_\sim \sim 100\,ns$) compared to classical magnetrons with efficiency $\eta_\sim \geq 50\%$ and $t_\sim \sim 1\,\mu s$ at $P_\sim = 1 - 50\,MW$ [5-7]. A cause of pulse shortening in RM due to expanding cathode-anode plasma was eliminated for $t_\sim < 100\,ns$ by using A–K gap of $d_0 \simeq 1\,cm$ [3,4,8]. It is suitable for high power magnetron (HPM) devices with $\lambda \geq 10\,cm$. For the sake of compactness, many researchers (like [2,3,8] and the present ones) choose S-band wavelength. The well known HPM relativistic oscillators of BWO type [9] use smaller A-K gap about 0.1 cm as well as shorter $\lambda \simeq 3\,cm$ and $t_\sim < 10\,ns$ for $P_\sim \simeq 1\,GW$. Typical parameters of S-band RM are $P_\sim \sim 1\,GW$, $\eta_\sim \simeq 0.2$, $V_0 \simeq 0.5\,MV$ and $I_0 \simeq 10\,kA$. Dimensions of a $10\,kA$ cathode are defined primarily by a space charge limit of current density in a gap d_0 with crossed $E \times B$ -fields, namely, $J_{EB} = 0.1 \times J_{CL} = 0.2 \times V_0^{1.5}d_0^{-2}\ kA/cm^2$ [10]. It predicts $J_0 \leq J_{EB} = 0.07\ kA/cm^2$ for $V_0 = 0.5\,MV$ and $d_0 = 1\,cm$. Finally, one obtains $2r_0 = (r_A + r_K) \geq I_0/(\pi l_K J_0) = 5\,cm$ with $l_0 = l_K = l_A \simeq \lambda = 10\,cm$, $d_A = 6\,cm$ and $d_K = 4\,cm$ for anode and cathode diameters respectively. Such parameters correspond to "large anode" magnetron ($l_A/\lambda \simeq 1$, $d_A/\lambda = 0.6$). The "large anode" means that the last values are greater than 0.5. Both π-mode instability and low efficiency were observed for classical magnetrons in this case [5,6]. Problems of large anode relativistic magnetrons

---

are analysed in this paper. Experimental results for the VF-1 version of RM are presented below.

EXPERIMENTAL ARRANGEMENT
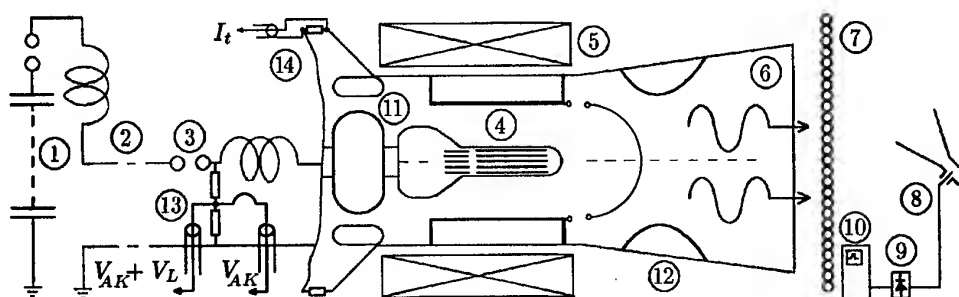
Fig 1. Schematic diagram of pulsed voltage generator and high-power S-band magnetron. 1 – Marx generator (700 kV, 40 Ohm); 2 – Single pulse forming line (0.5 MV, 12 Ohm, 250 ns); 3 – Main switch and transport vacuum line (2.3 m long, 1.1 μH inductance) followed by a parallel matching coaxial diode to improve voltage waveform; 4 – Magnetron (S-band, submicrosecond, gigawatt level); 5 – Solenoid (5 kG, T/4 = 3 ms); 6 – RF-radiation output horn (73 cm long, 28 cm output i.d.); 7 – Array of fluorescent lamps for mode identification (1 × 1 m^2 at 1.1 m from horn output of 28 cm i.d.); 8 – Receiver horn (at 3.2 m from the emitting horn) and signal transporting cable (l_{cab} = 20 m, 20 dB); 9 – Diode detector; 10 – Oscilloscope to record RF-envelope; 11 – Matching coaxial diode; 12 – Diaphragm for microwave reflection; 13 – Megavolt voltage divider with compensating loop; 14 – Resistor shunt of total current.

Table I

Main parameters of the VF-1 magnetron	
Operating voltage, V_0	$\approx 450\,kV$
Voltage pulse duration, t_0	$\approx 150\,ns$
Number of resonators, N	16
Outer radius of resonators, r_R	$6\,cm$
Inner anode radius, r_A	$4\,cm$
Cathode radius, r_K	$3\,cm$
Length of the anode, l_A	$20\,cm$
Resonator gap (at $r = 4.2\,cm$)	$0.7\,cm$
Magnetic field, B_{0z}	$4.5\,kGs$

Table II

Experimental results for the VF-1	
Frequency, f	$\approx 3.1\,GHz$
Maximum output RF power, $P_{\sim}$	$\geq 200\,MW$
Pulse duration of RF, $t_{\sim}$	$\leq 20\,ns$
Efficiency, η	$\geq 5\%$
Internal pressure	$2 \times 10^{-5}\,Torr$
The reason of power limitation	Micowave breakdown

Fig 2. Typical oscillograms: 1 – RF-power envelope (measured by a vacuum valve diode of 6D3D type); 2 – Total (magnetron and matching diode) current; 3 – Magnetron voltage.

Upgraded pulsed accelerator ERG [1] was used in the experiments. Typical acceleration voltage applied to the cathode equals $V_{AK} = -0.45\,MV$ with pulse duration

$t_0 = 150\,ns$ at the level of $0.9V_{max}$. Experimental set-up is drawn in Fig. 1. An additional element was used in the pulsed power circuit: the matching coaxial diode (see Fig. 1, position 11) with a cold emission velvet cathode and without applied magnetic field B_{0z}. It damped also voltage spikes which could occur during microwave breakdown in magnetron. On our opinion, the matching/damping diode could reduce electrical breakdown probability inside accelerating gap in the magnetrons.

Parameters of the VF-1 magnetron version are shown in Table I and Table II. The VF-1 is a large anode magnetron with $l_A/\lambda = 2$ and $d_A/\lambda = 0.8$ and with axial microwave power extractor of coaxial Boot-Pickering type [6].

The total extracted RF-power $P_\sim$ was estimated approximately by multiplication of the power measured at input of the receiver horn ($S_{RH} = 10^2$ cm^2, $P_{\sim RH} = 0.1 - 1\,MW$) to the ratio of $S_{0r}/S_{RH} \simeq 5 \times 10^2$, where S_{0r} is the averaged area of radiation pattern at the receiver horn distance. The S_{0r} was calculated using data of the light pattern size from fluorescent lamps (see Fig. 1). This estimation gives $P_\sim = 0.2 - 0.4\,GW$ with pulse duration of $t_\sim \leq 20\,ns$. The light lamp pattern indicates the multi-mode regime of the magnetron oscillator. Probably, pure magnetron π-mode was unstable in our magnetron generator.

On our opinion, the limitations of RF-power and pulse duration were occured previously due to microwave breakdown inside the cavities and the output microwave convertor (resonant structure — coaxial extractor). The cavity microwave breakdown can be triggered by a storage of large number of electrons inside the cavities (see Fig. 3) and increased electric field at the vane surfaces.

LARGE ANODE RELATIVISTIC MAGNETRONS

Computer simulations of the VF-1 and the VF-2 (see Fig. 3) were made by code KARAT [11, 12]. Cold RF-measurenemts of the magnetron resonance frequency have
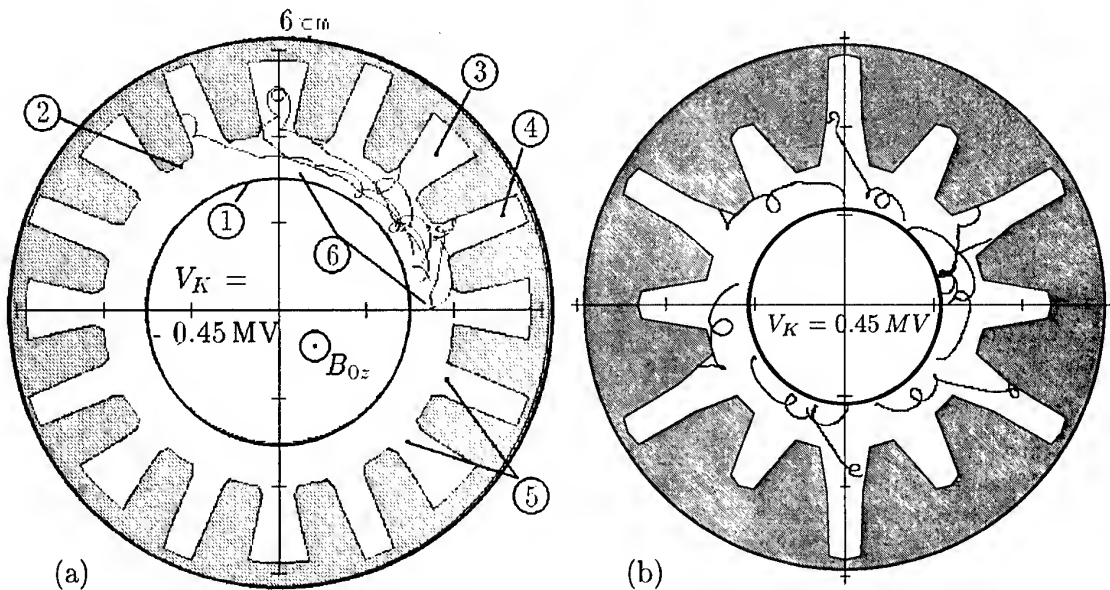
Fig 3a,b. Cross-section of the magnetrons (a: VF-1, b: VF-2). It shows trajectories of test electrons calculated by KARAT ($V_\sim \simeq V_0 \simeq 0.5\,MV$, $B_0 = 5\,kG$). 1 – Cathode electrode; 2 – Anode vanes; 3,4 – Cavities; 5 – Resonator gaps of $\simeq 0.7\,cm$ width; 6 – Trajectories of test electrons.

shown good agreement with simulation results. The VF-1 magnetron had a long anode

$(l_A/\lambda = 2)$, and classical type of the resonator cavities (Fig.3a). RF measurements show many resonance frequencies for VF-1 magnetron. As a rule, non-symmetrical resonant modes have been excited. There are some reasons for unstable π-mode of the VF-1 magnetron. First, weak coupling of cavities is due to lowering of azimuthal cross-currents caused by a larger cavity perimeter. This coupling operated quite good in classical rising-sun magnetrons of the AXD type [5] with lower azimuthal velocity of the synchronous wave ($v_{ph} < 0.1c$). This type of magnetron with high phase velocity ($v_{ph}/c = 0.22$ as in [3]) operated as good amplifier with a master magnetron and showed poor performance in generator regime. The RM were constructed with higher velocity of the $v_{ph}/c \geq 0.3$, for example, $v_{ph} = 0.33c$ for the VF-1, $v_{ph} = 0.45c$ in [3], and $v_{ph} = 0.54c$ in [1]. The second reason of the VF-1 low efficiency is poor extraction of microwave power from all cavities. Good solution for this problem would be to use the diffractional radiation extractor as in [1]. But it would be large and complicated device to use it in S-band magnetron.

Finally, we formulate some principal problems which are still to be solved for "good" relativistic magnetron. They are: 1) stabilizing magnetron π-mode in the case of $v_{ph} \geq 0.3c$; 2) eliminating storage of electrons inside magnetron cavities; 3) ensuring high current from cold cathode by secondary electron emission; 4) efficient extraction of microwave power from all magnetron cavities to output waveguide.

Cross-section of new magnetron of the VF-2 version is shown in Fig.3b. It has 12 resonators of the open saw-shape type. In addition we will use permanent magnets in all vanes of VF-2 and new semi-transparent RF-converter to couple the resonant cavities with output waveguide.

CONCLUSION

Relativistic magnetron of gigawatt power level can work without a breakdown of the accelerating A-K-gap $d_0 \simeq 1\,cm$ caused by plasma streams. The main problems are to construct large anode resonator structure which could stably operate on π-mode, eliminate the storage of electrons inside cavities, and use RF-mode converter which couples all cavities with output waveguide. Next VF-2 magnetron version is in progress.

REFERENCES

[1] Kovalev N.F., Krastelev E.G, Papadichev V.A., Fuks M.I. et al. Pis'ma v JTP, 1980, v.6, 459-462.

[2] Didenko A.N., Fomenko G.P. Gleiser I.Z. Krasik Ya.E. et al. 3rd Intern. Conf. on High Power Electron and Ion Beams, Novosibirsk, 1979, 683-691.

[3] Sze H., Smith R.R, Benford J.N., Harteneck A. IEEE Trans. on EM Comp., 1992, v. 34, 235-241.

[4] Benford J, Price D, G. Benford G. Proc. 11th Intern. Conf. on High-Power Particle Beams. Prague, Czech Republic, 1996, 217–220.

[5] Collins G. (ed.). Microvawe magnetrons. N.Y., 1948.

[6] Okress E. (ed.). Crossed-Field Microwave Devices. Academic Press. N.Y., 1961.

[7] Treado T.A., Bolton R.A, Hansen T.A., Brown P.D., Barry J.D. IEEE Trans. on PS, 1992, v.20, no.3, 351-359.

[8] Agafonov A.V, Bogachenkov V.A., Papadichev V.A., Fedorov V.M., Tarakanov V.P. Proc. of the 11th IEEE Intern. Pulsed Power Conf., USA, 1997. Preprint FIAN, no.46, 1997.

[9] Moreland L.D., Shamiloglu E., Lemke R.W., Korovin S.D., Rostov V.V., Roitman A.M., Hendriks K.J. and Spencer T.A. IEEE Trans. on PS, 1994, v.22, no.5, 554-565.

[10] Fedorov V.M. Theory Progress of Back-Bombardment Instability of Electron Emission Across Magnetic Field. 16th Symp. on Discharges and Electrical Insulation in Vacuum. Moscow, 1994 (unpublished).

[11] Tarakanov V.P. User's Manual of Code KARAT. Berkeley Research Ass., Inc., VA, USA, 1992.

[12] Agafonov A.V., Fedorov V.M., Tarakanov V.P. Proc of 1997 Particle Accelerator Conf. (PAC'97). Vancouver, Canada, 1997. Preprint FIAN, no.37, 1997.

EXPERIMENTAL INVESTIGATION OF ELECTRON ENERGY SPECTRUM IN GYROTRONS

M.Yu.Glyavin, A.L.Goldenberg, A.N.Kuftin,
A.S.Postnikova, N.P.Venediktov, V.E.Zapevalov

*Institute of Applied Physics Russian Academy of Sciences.
46 Ulyanov Street, 603600 Nizhny Novgorod, Russia*

INTRODUCTION

Powerful sources of coherent electromagnetic radiation operating in the millimeter wavelength range (gyrotrons) are used in such applications as electron-cyclotron heating of fusion plasma and high-temperature processing of some materials. Typical values of output efficiency of modern gyrotrons are 30–40%. A sufficiently easy and efficient way to further increase efficiency is recuperation: the process, during which electrons leave the interaction space and after that are decelerated by the electric field near the collector, the potential of which is lower than the initial beam potential. These electrons give up a part of their kinetic energy, which was not spared for interaction with the RF field, to the power supplies. Efficiency of energy regeneration is significantly depending on the energy spread of electrons after interaction with the RF field. As was shown by calculations, this spectrum depends, to a great extent, on the conditions of this interaction, especially in the region of transition from the cavity to the output waveguide. Although energy spectra have been studied theoretically in sufficient detail, direct measurement of the energy distribution function for used electrons is of special interest for interpretation of peculiarities in operation of various gyrotrons in the regime of single-stage regeneration and for development of the gyrotron with two- (multi-) stage regeneration. Multi-stage schemes of regeneration can be developed and realized basing on reliable data about the energy spectra of used electrons and confidence in accuracy of the existing methods for calculation of energy spectra.

On the other hand, a well-known feature of the gyrotron is its low criticality in terms of the spread of translational velocities of particles. This feature is caused by the quasi-transverse character of propagation of the operating mode, which provides smallness of the Doppler widening of the cyclotron resonance line. At the same time it is evident that due to relativistic dependence of the rotation frequency of electrons, on their complete energy, E, a weakly relativistic gyrotron must be sensitive to the spread of initial energy of particles. There are quite a few possibilities for appearance of noticeable energy spread of particles before they enter the operating space of the gyrotron; they may be connected, e.g. with excitation of spurious oscillations or development of inherent instabilities in dense beams in the forming space. These reasons may be responsible for somewhat lower efficiency of powerful gyrotrons as compared to the calculated values.

This paper describes experimental determination of the energy spectrum of the electron beam after interaction with the RF field in a short-pulse gyrotron operating at the frequency of 83 GHz with output power up to 1 MW [1]. Another subject matter of the paper is measurement of the energy spread in the gyrotron electron beam before interaction with the RF field. The authors also make an effort to explain appearance of this spread. As the most possible reason, development of inherent instability of the negative-mass-instability (NMI) type [2] is discussed; this instability is universal for gyrotrons. In principle, it can provide convective amplification of perturbations and appearance of energy spread in the electron

beam during its formation and propagation from the cathode towards the operating resonator cavity of the gyrotron.

MEASUREMENT METHOD AND EXPERIMENTAL SETUP

In order to determine the energy spectrum of electrons experimentally, one can use the method of the decelerating field. Usually such measurements can be performed only in modeling regimes, i.e. at lower values of magnetic field B, voltage U and beam current I. These values are chosen basing on similitude relationships that provide invariability of non-perturbed (with no account for NMI) electron trajectories. Unlike this, the analyzer proposed in and used in our experiments allows measurements not only in the modeling regimes, but also at nominal beam voltages (of the order of several tens of kilovolts) and measures also the spread of total electron velocity.

The analyzer is set in a tube connected to the collector of the gyrotron at the angle coinciding with the inclination angle of the force line of the magnetic field. Electrons enter this tube through a narrow longitudinal slot in the collector. Then they move towards the target set perpendicularly to the force line of the magnetic field, which in this region is much weaker than at the collector and, all the more so, than at the resonator. Along this way the electrons are decelerated by the electric field, and it is possible to determine their velocity by the dependence of the current to the target on the decelerating voltage.

In the region of the decelerating field of the analyzer rotational velocities of electrons are approximately 20 times lower than their translational velocities along the magnetic field. Thus, the method of the decelerating field in this system makes it possible to determine the total velocity (energy) of electrons, at which they enter the collector region. The electron energy distribution function is determined as a derivative of the collector current with respect to the voltage of the decelerating grid, and the velocity of the energy spread will be determined as $\delta\varepsilon = (U_{0.1} - U_{0.9})/U_0$ where $U_{0.9}$ and $U_{0.1}$ are voltages of the grid, at which the target current equals, respectively, to 0.9 and 0.1 of its maximum, and U_0 is total voltage of the beam that determines maximum energy of electrons. The signals proportional to the target current and decelerating voltage were transmitted to an automatic system for data acquisition and processing. Automation of data acquisition and processing made it possible to obtain a great number of points at the cut-off curve and a high rate of measurements, thus reducing errors caused by instability of power supplies. The large size of the data files obtained improves reliability of the measurement results.

ENERGY SPECTRUM OF ELECTRONS WITHOUT INTERACTION WITH RF-FIELD OF THE GYROTRON

Though the analyzer was designed for voltage up to 70 kV, a part of measurements of energy spectrum was made in the modeling regime. That made it possible to avoid distortions of the energy spectrum of the particles that appear, when powerful RF oscillations are excited in the operating space. Main characteristics of the experimental gyrotron are given in Table.

Mode	TE$_{11.3}$
Operating frequency, GHz	83
Output power, MW	1
Pulse duration, ms	100
Accelerating voltage, kV	70
Maximum beam current, A	40
Pitch factor	1.3–1.5
Magnetic field, T	3

The plots for dependence of the energy spread on the beam current at two values of the magnetic field, B_0 and 0.9 B_0, are shown in Fig. 1. For the nominal magnetic field, B_0, when the current changes from 5 A to 40 A (the latter corresponds to the generated output power over 1 MW at efficiency over 40%), the energy spread grows together with the beam current. Thus, the method proposed makes it possible to measure energy spectra of electrons in a wide range of parameters. The obtained results prove that when the beam is formed by a standard electron gun of a gyrotron and there is no interaction of particles with the RF field, in the modeling regime the spread of electron energy grows together with the spatial charge (beam current). At the operating values of the current at the system output it is several per cent. When the magnetic field becomes lower, widening of the spectrum occurs. At a relatively small decrease of the magnetic field this effect can be explained by NMI intensification. As the magnetic field decreases further and the number of particles reflected from the magnetic trap grows, the spectrum widens further. This is caused by the growth of the fields of the spatial charge due to a greater number of reflected electrons, and, probably, due to arising instabilities in the drift space between the cathode and the magnetic trap.

A possible reason that leads to a spread of particle energies in the region of electron beam formation and beam drift towards the resonator is negative-mass instability. Probably, it has the most general character, since it develops independently of the type of the electron-optical system and the presence of reflected electrons. This instability is caused, on the one hand, by non-isochronism of cyclotron rotation of electrons in the magnetostatic field, and, on the other hand, by Coulomb repulsion of electrons. Really, a fluctuation of electron density repels "neighboring" particles and makes their oscillatory velocity higher or lower depending on their position relative to the fluctuation. For example, linear velocity of the particles moving behind the fluctuation becomes lower. By that, their angular velocity grows, since, the frequency of cyclotron rotation is inversely proportional to the relativistic energy of the electron. At the same time the angular velocity of the particles moving in front of the fluctuations becomes lower. Thus, Coulomb repulsion of the particles oscillating in the magnetostatic field leads to their efficient rotation phase attraction.

In terms of the affect of the spread on efficiency of interaction of electrons with the RF field in the gyrotron resonator, the most interesting characteristic is the value of the spread not near the collector, but at the input to the resonator (near the maximum of the magnetic field). In the gyrotron under consideration, at the input to the resonator the spreads in the operating and modeling regimes actually coincide and prove to be less than 2%. Such a spread has almost no reducing effect on gyrotron efficiency. However, in the case of a smoother profile of the magnetic field and, correspondingly, longer drift space, in which the electron beam

Fig. 1. Dependencies of the energy spread from beam current for two different regimes.

travels from the cathode to the resonator, the spread at the input to the cavity can brow up to the value corresponding to the stage of NMI saturation, $\delta\varepsilon = 7\text{–}8\%$.

ENERGY SPECTRUM OF ELECTRONS AFTER INTERCONNECTION WIHT RF-FIELD

Varying experimental parameters were accelerating voltage, magnetic field and beam current. We will limit our consideration here to description of main regularities obtained by analyzing the data of measuring energy spectra of electrons.
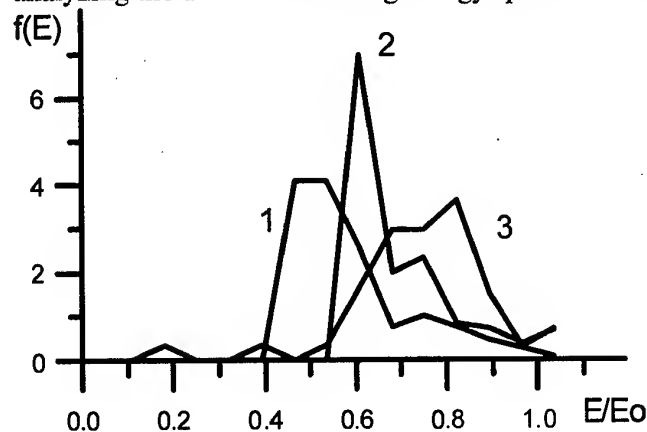
Fig. 2. Energy distribution function for different regimes Curve "1" - $B = B_{opt}$, $\eta \approx 40\%$, curve "2" $B \cong 1.015B_{opt}$, $\eta \approx 20\%$, curve "3" - $B \cong 1.02B_{opt}$, $\eta \approx 10\%$.

Figure 2 presents functions of electron energy distribution after electron interaction with the RF field at different values of the magnetic field within the generation band at nominal values of the current and voltage ($U_0 = 70\text{kV}$, $I = 30\text{A}$). For the distribution corresponding to the regime of generation with maximum efficiency the major part of electrons have the energy about twice as low as the initial energy of electrons, E_0, i.e. the energy before their interaction with the RF field determined by the complete accelerating voltage, U_0. To the left of the maximum (at lower energies) the number of electrons is insignificant, at to the right the slope of the distribution function is soft, and there are even electrons with energies exceeding the initial value.

CONCLUSION

The proposed method for measuring the energy spread in the electron beam of a gyrotron made it possible to obtain experimentally characteristic energy spectra for different regimes. Qualitative coincidence of the dependencies of electron energy spread on the current and value of the guiding magnetic field, which were found experimentally and calculated basing on the NMI theory, gives grounds to suppose that the role of other possible instabilities of the electron beam is not great.

One can state that the character of the spectrum of "spent" electrons depends significantly on generation conditions. In the regimes with maximum efficiency the spectrum begins at energies of the order of 30–40% of the initial beam energy. Comparison of the measurement results and calculations showed that efficiency values coincide with sufficient accuracy, but there are differences in details of energy distribution of "spent" electrons, which require further refinement of the calculation model.

REFERENCES

[1] A.N.Kuftin, N.P.Venediktov, V.E.Zapevalov // Gyrotrons, Gorky, 1989, p.21
[2] V.L.Bratman et all. // Digest of 22nd Int. Conf. On IR and MM Waves, 1997, p. 186

A REVIEW OF RECENT PROGRESS IN RELTRON TUBE DESIGN

R. B. Miller and Kerry W. Habiger
Titan Advanced Innovative Technologies
Albuquerque, NM 97119-9254

Titan's high-peak-power Reltron microwave tubes have proven to be useful for testing the vulnerability of electrical systems to high power microwave pulses. A description of this tube has been given previously.[1] The nominal frequency range of operation of the tubes is 0.5-6 GHz. Typical operating parameters for a high-peak-power L-band tube are summarized in Table 1. Over the past year we have continued to make progress on the following topics: **1.** A new modulating cavity design permits a useful tuning range of approximately +/- 15% about the nominal center frequency. **2.** An investigation of velvet cathodes has shed additional light on the behavior of dielectric cathode materials, permitting higher repetition rates with significant pulse durations. **3.** An analysis of pulse shortening mechanisms has identified the dominant mechanisms in Reltron tubes, resulting in significant improvements in the energy per pulse.

Table 1. Characteristic Parameters of L-Band Reltron Tubes

Parameter	Typical Value
peak power (MW)	500
efficiency (%)	40
instantaneous bandwidth (%)	0.1
tuning range (+/- %)	10
pulse width (μs)	0.5
energy per pulse (J)	>200
repetition rate (pps)	<10
MTBM[1] (# of shots)	5×10^4

[1]*Mean Time Between Maintenance*

ENHANCED TUNING RANGE

The beam bunching mechanism in a Reltron tube is essentially that of a two cavity klystron oscillator, the operating frequency of which is determined by the resonant frequency of the $\pi/2$ mode of the modulating cavity, down-shifted by beam loading effects. The modulating cavity itself consists of a three-cavity section of side-coupled, standing-wave rf linac. Tuning is achieved by moving plungers in the two "pillbox" cavities through which the beam passes, and by using a tuning screw in the offset, idler cavity. When all three cavities are tuned to approximately the same frequency, there are three lowest frequency TM_{01} modes of the modulating cavity structure, with the frequency separation between modes depending on the amount of magnetic coupling (the area of the coupling aperture) between cavities.

In the past we have used a "single-sided" tuning plunger, as shown in Figure 1(a). With the tuning plunger fully inserted, the resonant frequency of a "pillbox cavity" is essentially that of a right circular cylinder. As the plunger is withdrawn, the cavity becomes more rectangular, and the resonant frequency decreases approximately as

$$f/f_o = 2^{-1/2} [1 + (a/b)^2]^{1/2} \qquad (1)$$

with the minimum value of b being approximately equal to the pillbox radius a. Eq. (1) indicates that the maximum decrease in resonant frequency afforded by this one-sided plunger mechanism is approximately 29%. This tuning range cannot be realized, however, because the position of the peak axial electric field shifts away from the beam axis as the plunger is withdrawn, significantly decreasing the beam-cavity interaction strength, and decreasing the beam modulation over the lowest frequencies in the range.

To overcome this limitation we developed the two-sided plunger mechanism, as shown in Figure 1(b). With this arrangement, the peak electric field of the modulating cavity remains nearly centered on the beam axis over the entire tuning range. Also with this arrangement, the tuning range can be further increased because the area of the coupling aperture can be decreased somewhat as the plungers are inserted into the cavities. For the first modulating cavity constructed using this approach, the resulting frequency variation of the π/2 mode was 625-865 MHz, or +/-16%. Although beam loading effects decrease the tuning range somewhat, the hot test tuning range can still exceed 30%. This amount of tuning is comparable to the recommended frequency range of standard waveguide.

(a) asymmetric tuning plunger

(b) symmetric tuning plungers
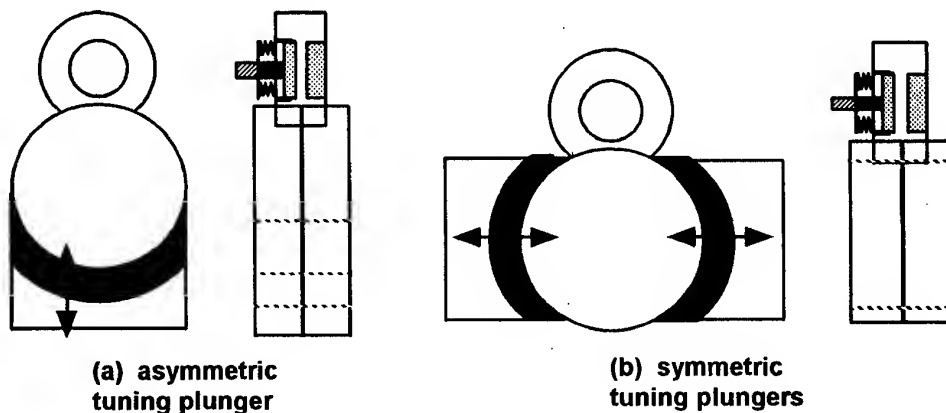
Figure 1. (a) Old-style asymmetric, single-sided tuning plunger configuration. (b) The newer symmetric, two-sided tuning plunger configuration.

CATHODE STUDIES

At the present time velvet cathodes are used in our high-peak-power Reltron tubes. In comparison with other explosive emission materials, velvet has some quite beneficial properties (low electric field threshold, high current density, low plasma closure velocity, inexpensive). Unfortunately, velvet discharges a significant amount of matter during a pulse. In fact, for standard velvets with a linear tuft density of typically 12 tufts/cm, the amount of material discharged into the vacuum system is of the order of $3x10^{15}$ molecules/cm^2 per pulse. The corresponding erosion rate limits the lifetime of a velvet cathode to about 10^5 pulses. Moreover, if a velvet cathode is operated repetitively, the increase in the background pressure resulting from this material release will limit the achievable PRF, depending on the vacuum system specifications and the desired pulse duration. This limiting behavior is believed to be

the result of avalanche breakdown in the anode-cathode gap. A useful equation which relates the allowable pulse duration to the pulse repetition frequency (PRF) is[2]

$$\tau \text{ (ns)} < (3300 \text{ S} / A_c \text{ PRF}) (d^*/0.07)^2 \qquad (2)$$

in which S is the effective pumping speed in liters/s, A_c is the cathode area in cm^2, and d^* is the separation between velvet tufts measured in cm.

As a result of these limitations, we have undertaken an investigation of the mechanisms involved in the explosive emission process for velvet cathodes, and we have examined several alternate cathode materials. Guided by our experimental data and the results of previous workers,[3] we hypothesize that the main features of the explosive emission process for velvet cathodes include the five steps illustrated in Figure 2:[4]
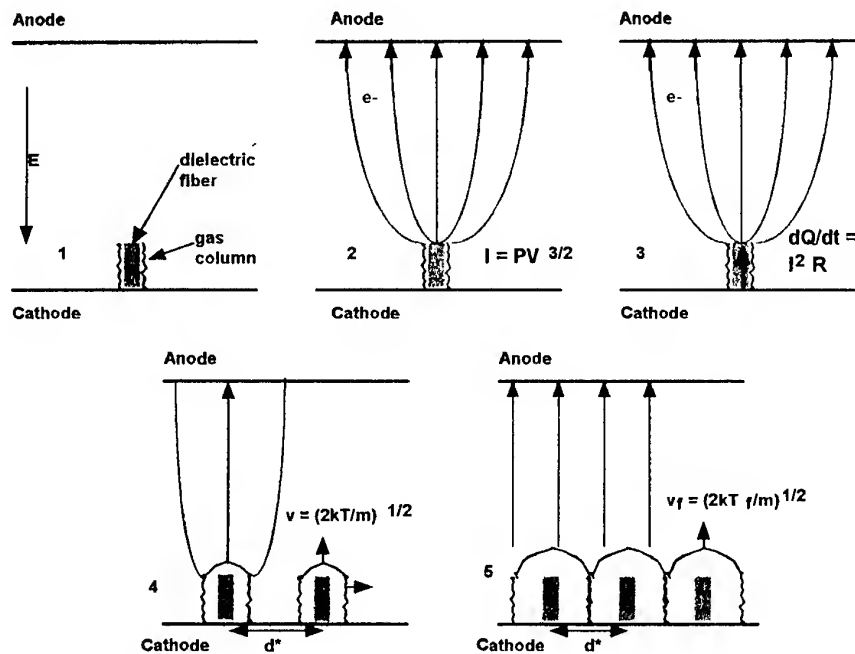
Figure 2. (1) Surface flashover generates a cold, dense plasma/gas column. (2) The electric field extracts a space-charge-limited current. (3) The current resistively heats the gas. (4) The gas columns expand at a rate determined by the gas temperature. (5) The gas continues to expand into the anode-cathode gap.

A scaling relationship deduced from a detailed modeling of these processes, which appears to give a good estimate of the plasma closure velocity, is given by

$$v_f \text{ (m/s)} = 100 \, (d^*/d)^{2/3} \, V^{1/2} \qquad (3)$$

with the diode voltage in volts. d^* is the separation between velvet tufts and d is the anode-cathode gap separation. Assuming that the useful pulse duration is limited by an increase in the diode perveance of 20%, then Eq. (3) leads to a limitation of the diode voltage pulse duration that can be approximately expressed as

$$\tau \text{ (s)} < 0.001 \, d^{5/3} \, (d^*)^{-2/3} V^{-1/2} \qquad (4)$$

with physical dimensions in meters and V in volts. Increasing the tuft spacing reduces the amount of material vaporized in a pulse resulting in a longer useful pulse duration for a given vacuum system and PRF. However, the increased tuft spacing can also limit the useful pulse duration by increasing the plasma closure velocity.

To investigate the validity of these scaling relationships we manufactured a cathode having a tuft density of 14 tufts/inch using rayon thread. With $S = 150$ liters/s, PRF = 25 Hz, and $A_c = 28$ cm^2, Eq. (2) predicts a limiting pulse duration of 4.4 μs, while with $V = 150$ kV and $d = 4.4$ cm, Eq. (4) predicts a limiting pulse duration of only 0.9 μs. Data obtained using this rayon thread cathode indicated that the useful pulse duration was limited to approximately 0.75 microseconds by diode closure effects, and not by the pulser repetition frequency.

PULSE SHORTENING

Pulse shortening previously observed in Reltron tubes is believed to be the result of processes observed in "dirty electrode" breakdown experiments,[5] which are summarized as follows: **1.** Local electric field enhancement at dust particles or microscopic protrusions causes electron field emission. **2.** These electrons are accelerated in the applied field and impact other surfaces, heating these surfaces and generating secondary electrons and photons. **3.** These processes result in gas desorption, via electronic excitations. **4.** The desorbed gas is collisionally ionized. **5.** The free electrons and ions are accelerated, absorbing more energy, heating the plasma, causing more gas desorption, more plasma, etc., leading to breakdown.

Detailed examinations of our experimental data suggest that if the peak field stress can be kept below about 150 kV/cm, then we should be able to generate rf pulses of nominally one microsecond in duration. To test this hypothesis we replaced the stainless mesh grids in the output cavities of an L-band tube with plates having small "nosecone" apertures (4.45 cm dia). **There was no apparent pulse shortening with these apertures**. Using apertures in a second extraction section as well, we were able to obtain a maximum energy per pulse of about 300 joules with a peak output power of about 400 MW at a charge voltage of 45 kV.[6] Experiments are now underway to further increase the energy per pulse using a lower frequency tube.

REFERENCES

[1] R. B. Miller, W. F. McCullough, K. T. Lancaster, and C. A. Muehlenweg, IEEE Trans. Plasma Sci. **20**, 332 (1992).
[2] R. B. Miller, Proc. of SPIE <u>3158</u>, 2 (1997).
[3] G. A. Mesyats and D. I. Proskurovsky, <u>Pulsed Electrical Discharge in Vacuum</u>, Springer-Verlag, Berlin (1989).
[4] R. B. Miller, submitted to Journal of Applied Physics, (April, 1998).
[5] J. Halbritter, IEEE Trans. Elect. Sci. <u>EI-20</u>, 671-681 (1985).
[6] R. B. Miller, to be published in IEEE Trans. Plasma Science (1998).

ELECTRON BEAM FORMATION FOR RELATIVISTIC CRMs

V.L. Bratman, Yu.D. Grom, Yu.K. Kalynov, V.N. Manuilov,
M.M. Ofitserov, and S.V. Samsonov

*Institute of Applied Physics, Russian Academy of Science
46 Ulyanov St., Nizhny Novgorod, 603600, Russia*

ABSTRACT

An electron-optical system with a thermionic cathode allowing production of a 0.6 mm diameter thin rectilinear electron beam with an energy of 250 keV, current of 15 A and pulse duration of 10 μs in an axial magnetic field of 16 kG is designed and constructed. A pumping system transforms the straight beam into a beam of electrons gyrating around the axis with a velocity ratio of 1.5 and sufficiently small velocity spread. Results of numerical simulations and experiments are presented. The obtained beam will be used for Cyclotron Resonance Maser experiments.

INTRODUCTION

Relativistic Cyclotron Resonance Masers (CRMs) are promising sources of coherent powerful radiation in the millimeter/submillimeter wavelength range [1-4]. In order to enhance mode selectivity a thin beam of electrons gyrating around the axis of an axi-symmetric microwave system is often used in a number of varieties of relativistic CRMs (Cyclotron Autoresonance Masers, High-Harmonic Large Orbit Gyrotrons, gyro-TWTs etc.). Such a beam can excite only co-rotating modes whose azimuthal indices are equal to the number of the resonant cyclotron harmonic.

The simulations and first experimental results on electron-optical system producing an electron beam with unique parameters are presented. The obtained electron beam will be used for a millimeter-wave Large Orbit Gyrotron (LOG) at the 5th cyclotron harmonic as well as a basis for further development to drive submillimeter CRMs.

PECULIARITIES OF ELECTRON-OPTICAL SYSTEM

As the 1st step to powerful submillimeter-wave CRMs, a high-harmonic LOG will be experimentally studied. The LOG is designed to operate at the 5th cyclotron harmonic, at 2 mm wavelength. For effective operation it should be driven by sufficiently relativistic and high-current electron beam. Based upon parameters of an existing high-voltage source [5] and preliminary calculations, the following requirements for the electron beam were determined: energy of 250 keV, current of 10-15 A, beam diameter of 0.6 mm, electrons should gyrate around the axis with minimum displacement of guiding centers and velocity ratio $v_\perp/v_\parallel \geq 1.5$ in a magnetic field of 16 kG. Efficient harmonic operation requires also enhanced quality of the beam compared to the fundamental gyrotron.

In order to produce such a beam, a two-stage electron-optical system was designed. First, a thin rectilinear beam is formed, and then the electrons acquire the necessary transverse

velocity passing through a short non-adiabatic pumping system, kicker [4]. The main cause of the particle velocity spread after passing a kicker is initial electron cyclotron oscillations which have different cyclotron phases even for a laminar axisymmetric beam and, therefore, are added or subtracted to operating value of the transverse velocity driven by a kicker. Thus, the system before the kicker should provide a rectilinear beam with minimum oscillations. Assuming a conventional current density for thermionic cathodes, 5 A/cm^2, one obtains the required area of emitting cathode surface of about 3 cm^2, and, correspondingly, a very strong compression, over 1000, for the beam cross-section. To achieve such a beam compression without excitation of parasitic cyclotron oscillations a system providing particle trajectories parallel to the guiding magnetic field lines has been designed and constructed.

FORMATION OF THE RECTILINEAR BEAM

Following the chosen concept of forming the required rectilinear beam we find that the axial magnetic field at the cathode should have a very low magnitude of 0.015 kG, which corresponds to about 8 m Larmor period. Certainly adiabatic magnetic compression, when the spatial scale of the magnetic field tapering is much smaller than the Larmor period, is very inefficient. Therefore, the particle motion in the near-cathode region is mainly determined by fields of the gun and the space charge, while a system of coils provides the matching of axial magnetic field profile to the particle trajectories. After achieving a sufficiently strong magnetic field a conventional adiabatic compression can be used for decreasing beam diameter to required level.

The emitting surface of the cathode operates in the space-charge-limited regime. The code EPOSR [6] was used for numerical simulations of the system. The current distribution was calculated directly from the condition $E_n=0$ on the emitter surface. In the cathode-anode gap, a quasi-Pierce configuration of the gun provides an electrical compression of the beam of about 20 times, while gun coils form the corresponding rapid magnetic field tapering (Fig.1).
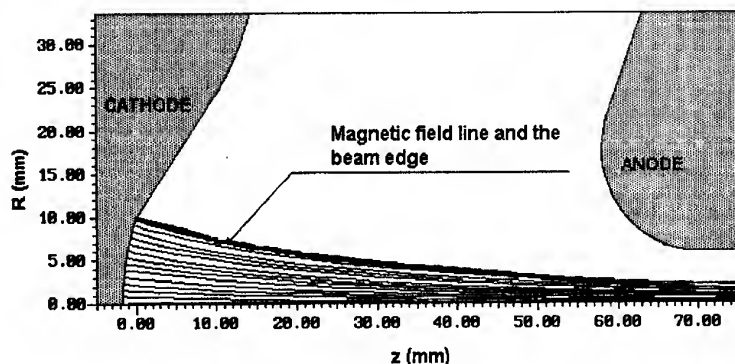
Fig.1. Configuration of the gun and electron trajectories.

After that the electron Larmor period is still quite large (about 300 mm), therefore an additional smooth magnetic field tapering should be used for about 10 times compression of the beam before a natural increase of the main coil field (Fig.2). For the optimized system the simulations predict a magnitude of the electron parasitic transverse velocity less than $0.05c$ in the rectilinear beam of 0.6 mm in diameter, which is sufficient for the formation of a helical beam with acceptable velocity spread.

The diameter of the straight beam for a few points along the system was measured experimentally in a modeling regime with a low voltage and current (22 kV/0.3 A/10 µs). Spots produced by the beam in a perpendicular scintillator plate were observed. Results of the measurements are in a good agreement with the results of corresponding simulations.
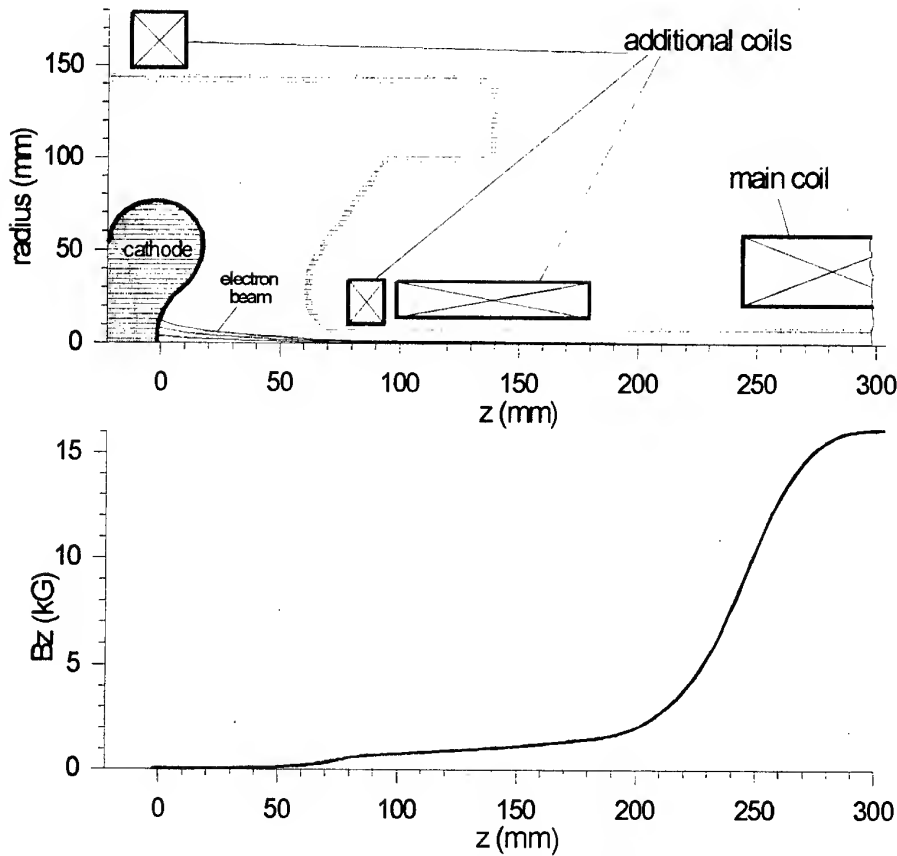
Fig.2. Schematic of the electron-optical system for the rectilinear electron beam formation and spatial profile of the axial guiding magnetic field.

FORMATION OF THE HELICAL BEAM

The pumping of the rectilinear beam up to required transverse velocity is based upon a known technique of the resonant excitation of the electron cyclotron oscillations in a wiggler producing a spatio-periodical magnetic field with a period close to the electron Larmor step. Obviously, reduction of the period numbers broadens operation of a pumping system over a magnitude of the guiding axial field. We use a single-period wiggler, so-called, kicker, which is formed by four rectangular current frames generating a perpendicular component of magnetic field (Fig.3). In order to simplify the pumping, the kicker is located in a region of relatively weak guiding field (of about 5 kG). After the kicker, the electron transverse velocity is further adiabatically increased in the tapered guiding field (Fig.3). The kicker was optimized to pump the beam up to necessary level of velocity ratio with minimum displacement of electron guiding centers from the axis and minimum sensitivity to electron position spread. For the operating parameters simulations predict a transverse velocity spread, $(\delta v_\perp/v_\perp)_{rms} \approx 7\%$, which is sufficiently small for an effective operation of the 5th harmonic LOG. The kicker can effectively pump the beam within a very wide range, about 50%, of the axial field.

The operation of the pumping system was checked experimentally. At the operating voltage of 250 kV and a very low beam current (low temperature of the emitter surface) marks made by the beam on a perpendicular scintillator target were observed in the region of operating magnetic field. The measured mean diameter of more than 2 mm and the thickness of 0.5-0.8 mm of the observed axially centered Larmor rings proved the correspondence of the obtained beam parameters to the designed ones.
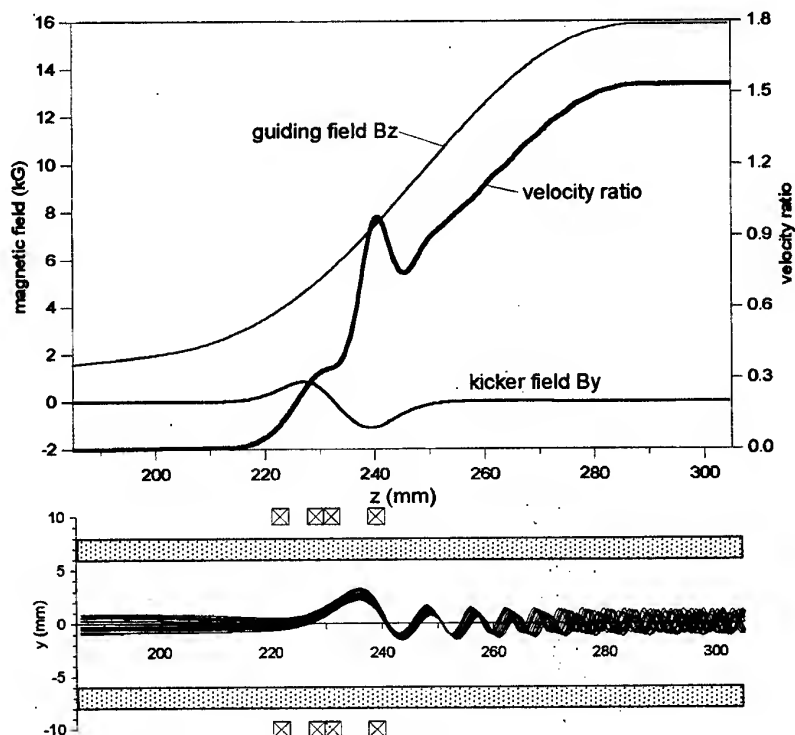
Fig.3. Magnetic fields, velocity ratio for the near-axis electrons, schematic of the kicker and particle trajectories in the helical beam formation region.

SUMMARY

An electron-optical system producing a 250 kV/15 A/ 10 μs high-quality electron beam gyrating around the axis in a magnetic field of 16 kG with a velocity ratio 1.5 is designed, constructed and checked experimentally. The formation of a very dense (about 5 kA/cm^2) rectilinear beam is based upon a combination of non-adiabatic electrical and adiabatic magnetic compression with a beam cross-section ratio exceeding 1000. The required particle transverse velocity is pumped by means of a short kicker having a very wide band over the magnitude of guiding magnetic field. The obtained electron beam will be used for the realization of a Large Orbit Gyrotron with a designed output power of 50-100 kW at the 5th cyclotron harmonic (the TE$_{5,1}$ operating mode at the wavelength of 2 mm).

The developed concept allows elaboration of relatively compact electron-optical systems for high-power millimeter/submillimeter sources.

[1] M.I. Petelin, Radiophys. Quantum Electron., 1974, 17, 686.

[2] D.B. McDermott, N.C. Luhmann, A. Kupiszewski, H.R. Jory, Phys.Fluids, 1983, 26, 1936.

[3] V.L. Bratman, Yu.K. Kalynov, V.N. Manuilov et al. Proc. of 11th Int. Conf. on High Power Particle Beams, Prague, Czech. Republic, 1996, 401.

[4] V.L. Bratman, G.G. Denisov, M.M. Ofitserov, M.I. Petelin, S.V. Samsonov, Nucl. Instr. Meth. Phys. Res. A, 1995, A385, 135.

[5] V.K. Lygin, V.N. Manuilov, Sh.E. Tsimring. Effective code for numerical simulation of the helical relativistic electron beam. Ibid, 385.

[6] V.L. Bratman, I.E. Botvinnik, Yu.D. Grom, Yu.K. Kalynov, M.M. Ofitserov, Proc. SPIE XVI Int. Symp. on Discharges and Electr. Insulation in Vacuum, Russia, 1994, 538.

OBTAINMENT OF ELECTROMAGNETIC RADIATION AT INTER-ACTION OF ELECTRON BEAM WITH RING PLASMA WAVEGUIDE

V.A.Balakirev, V.I.Karas', E.A.Kornilov, Ya.B. Fainberg, O.N.Shulika,
I.N.Onishchenko, V.O.Podobinsky

*National Scientific Center «Kharkov Institute of Physics & Technology»,
Academicheskaya St., 1 , Kharkov, 310108, Ukraine*

1. One of the principle purposes is the research of the most effective method of extraction of energy of the oscillations excited by an electron beam from plasma into the outer space or high frequency (HF) tracks. The most attractive solution of this problem is presented with hybrid plasma waveguides that combine advantages of the both plasma waveguides and the standard slow wave structures. In these systems a hybrid wave is generated [1, 2]. The wave electric field longitudinal component is maximum in the plasma volume and the super high frequency (SHF) power propagates in the vacuum structure. From the point of view of powerful microwave radiation generation the following structures are of a special interest: the plasma waveguide enclosed with a periodic system of rings with ideal conductivity and the plasma waveguide filled with plasma partially.

The Rieman-Gilbert method [3] is applied to solve the problem of microwave radiation excitation by an electron beam in the ring periodic structure filled with plasma. The radiation excitation nonlinear dynamics is investigated by numerical methods.

2. The slow wave hybrid system examined consists of a periodic chain of identical metallic rings with radius a. The ring avails are infinitely thin and ideally conductive. The structure period is l and the width of the gap between the rings is d. The ring waveguide is completely filled with homogeneous plasma. An external magnetic field is absent. The structure advantages are the compactness and the small weight. Along the system axis an annular nonrelativistic electron beam is propagating in plasma, it's modulated and its average radius is r_b. Here one neglects the beam thickness, presenting, the beam with its surface current.

The solution method is the following. Firstly, solving the Maxwell equations, one finds the HF field excited by the beam in the entire space. Then the EMF inverse influence on the beam particle motion is taken into account. As a result one obtains the self-consistent nonlinear system of the equations that describe the process of EMF excitation in the ring hybrid structure.

In general case the Flocke amplitude expressions are bulky. But for nonrelativistic beams and examining the boundary case of the narrow slots $d/l \ll 1$, one can simplify these expressions.

The electric field acting on the beam particles may be described with the expression:

$$E_z = \frac{2I_\omega}{i\omega a^2}\left(\frac{I_0(pr_b)}{I_0(pa)G} + \frac{p^2a^2}{\varepsilon}F_0\right)\frac{I_0(pr_b)}{I_0(pa)}, \tag{1}$$

where $p^2 = k_b^2(1-\beta_0^2\varepsilon)$, $F_0 = I_0(pa)K_0(pr_b) - K_0(pa)I_0(pr_b)$, $I_0(x)$, $K_0(x)$ are the cylindrical functions of an imaginary argument, $k_b = \omega/V_0$ is the longitudinal wave number of the beam modulation, ω is the modulation frequency, V_0 is the beam initial velocity.

The EMR energy flow per unit of the ring structure length may be described with the formula

$$S_\perp = \frac{c}{8\pi} H_\varphi^* E_z = \frac{2}{\pi} \frac{I_\omega^2}{\omega^2} \frac{I_0(pr_b)}{I_0(pa)} \frac{1}{|G|^2} \times \frac{1}{w_{-1}^2 a^2 \left[J_0^2(w_{-1}a) + N_0^2(w_{-1}a) \right]}, \tag{2}$$

where $w_n = \sqrt{k_0^2 - h_n^2}$, $h_n = k_b + 2\pi n/l$, $k_0 = \omega/c$.

The beam current Fourier amplitude may be presented as

$$I_\omega = I_b \rho, \qquad \rho = \int_0^1 \exp(2\pi i \tau)(1 + h_b \cos 2\pi \tau_0) d\tau_0. \tag{3}$$

Here $\tau = (t_L - z/V_0)/T$, $t_L(t_0, z)$ is time during which the beam particle reaches the z-coordinate if the particle enters the system at the moment t_0, I_b is the total beam current, $T = 2\pi/\omega$ is the s SHF oscillation period, h_b is the initial relative depth of the beam current modulation. In the (3) the integral is taken over the moments of the particle inlets into the system.

The expression (1) and the equation of the beam electron motion in the Lagrangian variables in the dimensionless form:

$$(1 - v\theta)\frac{dv}{d\xi} = \operatorname{Re} C \exp(-2\pi i \tau), \frac{d\tau}{d\xi} = \frac{1}{2\pi}\frac{v}{1 - v\theta}, C = i\rho \exp(-i\alpha), v = \frac{V_0 - V_L}{V_0 \theta}, \xi = \frac{\omega}{V_0}\theta z, \tag{4}$$

where $\theta^2 = \frac{2 I_B e}{m V_0 \omega^2 a^2} \frac{I_0(pr_b)}{I_0(pa)}|Q|, \exp(-i\alpha) = -\frac{|Q|}{Q}, Q = \frac{p^2 a^2}{\varepsilon} F_0 + \frac{I_0(pr_b)}{I_0(pa)}\frac{1}{G}$, V_L is the beam particle velocity.

As it's known, the Q-function has an imaginary part if the radiation condition is true for the Flocke harmonic with the number $n = -1$.
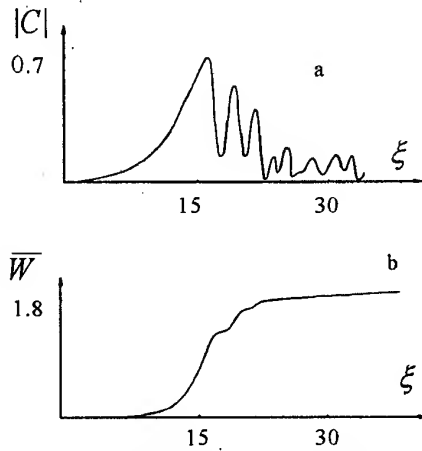
Fig. 1. Spatial dependencies of the wave amplitude $|C|$ (a) and dimensionless variation of beam particle energy flow $\overline{W}$ (b).
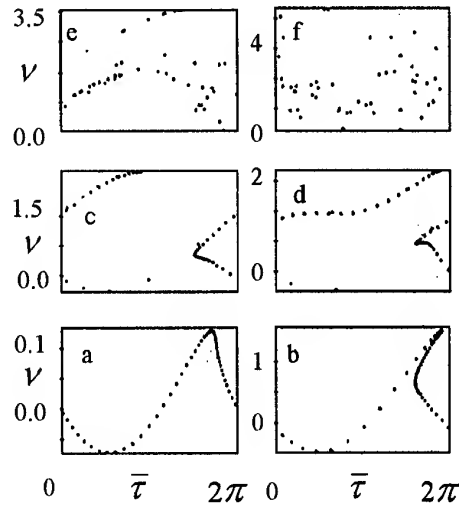
Fig. 2. The beam particle picture $v(\tau)$ at different points ξ: (a) - 13.8, (b) - 15.9, (c) - 17.8, (d) - 19.2, (e) - 23.1, (f) - 38.2.

The system of the equations (4) yields the integral [4]

$$\overline{W} - \sin\alpha \int_0^\xi |\rho|^2 d\xi = Const, \qquad \overline{W} = \int_0^1 v(1 + h_b \cos 2\pi \tau_0) d\tau_0 \tag{6}$$

that depicts the law of conservation of energy in the considered system. In the (6) the first addendum describes the dimensionless variation of the beam particle energy flow. The second

term represents the EMW total energy flow in the transversal direction.

3. The system (4) as been solved by the numerical methods for various values of the α ($\pi > \alpha > 0$) and for $h_b = 0.05$. The range $\pi/2 > \alpha > 0$ corresponds to the "vacuum" mode where the dielectric constant is positive ($\varepsilon > 0$).

The results of the numerical simulations are given at the Fig.1, 2 when $\alpha = \pi/4$. As one can see at the Fig.1a, at the nonlinear stage the wave amplitude reaches its maximum and then it extinguishes, performing oscillations. Correspondingly, (see the Fig.1b), at the beginning the $\overline{W}$ is increasing. Then, reaching the area of the field absence, it becomes constant. At the Fig.2 the beam phase picture is presented at different points (v, $\overline{\tau} = 2\pi\tau + \varphi$, φ is the field phase). The Fig.2 demonstrates that the beam particle bunching occurs at the linear stage. At the non-linear stage the bunches perform phase oscillations in the wave field. During this process the bunches are losing the particles and become deformed. Finally almost complete mixing of the particles takes place on the phase plane, i.e. the beam becomes demodulated, being spread in velocities. The wave is emitted only from the limited structure section where the beam modulation is still preserved.

The instability increment also grows with increase of the α-parameter. The distance to the first maximum of the beam field amplitude is diminishing. As a matter of fact, practically the amplitude value is not changed at the first maximum. Behind the first maximum and farther to complete extinction of the amplitude its oscillation number also increases.

4. In the plasma mode $\pi > \alpha > \pi/2$ and the plasma dielectric constant is negative $\varepsilon < 0$. In this case the excitation process essentially differs from the one observed in the vacuum
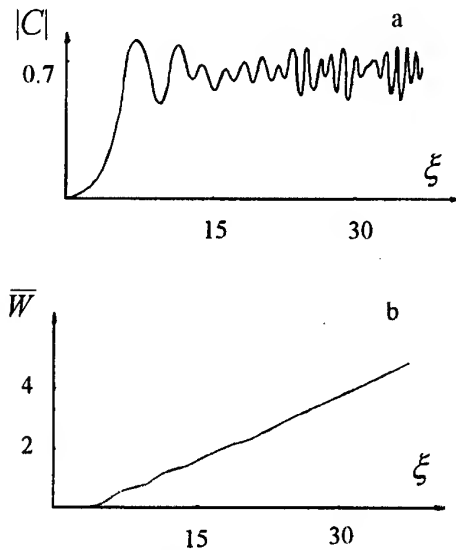
Fig. 3. a) Spatial dependence of the wave amplitude $|C|$, b) dimensionless energy flow losses of the beam particles $\overline{W}$.
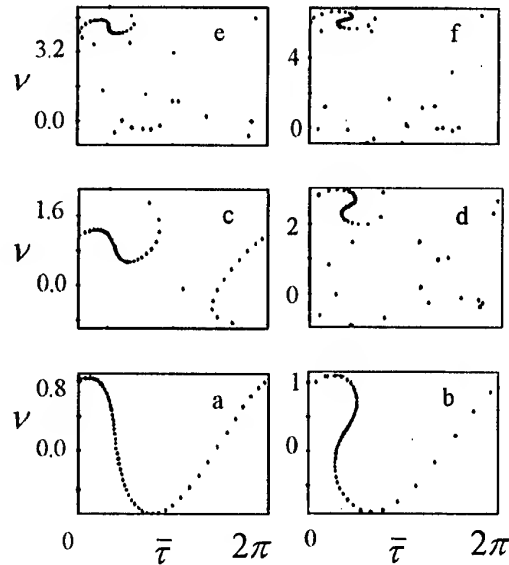
Fig. 4. The beam phase picture $v(\overline{\tau})$ at different points ξ: (a) - 5.5, (b) - 6.7, (c) - 9.3, (d) - 19.2, (e) - 26.2, (f) - 36.0.

mode. The fields induced in plasma modulate the beam. While the bunches formed this way are propagating along the diffraction grating built of the ring system, they excite radiation.

Let's examine the radiation influence on the instability nonlinear dynamics. The results of the numerical simulation are obtained for $\alpha = 7\pi/8$ and they are depicted at the Fig.3,4. Judging by these plots, one can be convinced of the fact that at the nonlinear stage the wave amplitude

also oscillates. The oscillation period decreases. The average amplitude is approximately equal to the one excited in absence of radiation. The energy flow losses $\overline{W}$ are increasing continuously. This fact testifies to the resulting deceleration of the beam. The wave phase velocity decreases. At the Fig.4 the beam particle dynamics is depicted on the phase plane. As it's evident, at the nonlinear stage two bunches are formed. Their phase oscillations are opposite in direction. Put the bunches oscillate with respect to the synchronous phase value corresponding to the beam deceleration by the field (in absence of radiation they would oscillate with respect to the potential pit bottom). Thus, the beam bunches are being decelerated continuously. Since the wave phase velocity is determined by the bunch motion velocity, the wave is being persistently decelerated in synchronous phase with the beam as well. This autoresonance effect results in the phase squeezing of the bunches, which can be clearly observed at the phase picture. One should notice that when the radiation conditions are broken because of the beam velocity decrease, the beam deceleration stops immediately. Notwithstanding the fact that at the first maximum the field value practically remains the same, the average field decreases behind the first maximum, if the value of the α is decreasing. The wave amplitude phase oscillation period diminishes too.

5. In this work for the first time we have elaborated the linear and nonlinear theories of the monoenergetic electron beam instability in the hybrid ring structure. Both the vacuum and plasma modes are possible. The type of the realized mode depends on the beam parameters, the ring waveguide geometry and plasma density. In the vacuum mode the instability is dissipative by nature, which is connected with existence of SCW energy losses by excitation of the fast SCW ($V_{ph} > c$) emitted into the outer space.

In the plasma mode ($\varepsilon < 0$) the beam instability (automodulation) is stimulated by the fields induced in plasma. When the bunches formed this way are propagating along the diffraction grating that consists of the system of periodic metallic rings, the bunches are emitting EMW. Numerical analysis demonstrates that in plasma mode of the radiation excitation the emission is accompanied by the bunch deceleration. If the EMW radiative condition becomes broken, the excitation process comes to an end. The transformation efficiency heightens when the relativistic beams are used.

Thus, in the hybrid ring system it's possible to realize conditions on which plasma provides for the beam effective instability (the beam modulation) and the ring system permits to transform the slow waves excited in plasma into EMR. One should notice that in the ring waveguide intensive disturbance of microwave fields takes place even in the case of the narrow slots. If the slot width is being narrowed $d \to 0$, the radiative field decreases as $1/\ln(l/d)$. In the ring waveguide its period may be rather short (about several mm in order of magnitude), which makes the difference between this and other types of the hybrid structures (such as a chain of coupled cavities, disk-loaded waveguides, etc.). Therefore usage of the ring structures is especially effective in the SHF band (in particular, for mm wavelengths).

[1] Ya.B.Fainberg. "Problems of Plasma Electronics". Plasma .Phys., Vol. 11, No 11, 1985, p. 1398-1406.
[2] Ya.B.Fainberg. Yu.P.Bliokh, E.A.Kornilov et. al. "Electrodynamics of Hybrid Plasrma-Waveguide Structures". Dokl. Ak. Nauk SSSR, se. Fiz.-Mat. i Tech. Nauk, vol. 11, 1990, p. 55.
[3] V.P.Shestopalov. "Method of Rieman-Gilbert Problem in Diffraction Theory and Electromagnetic Wave Propagation". Kharkov: Kh.G.U., 1971.
[4] V.A.Balakirev, G.V.Sotnikov, I.N.Onishchenko. "Nonlinear Autosynchronism in Beam-Plasma Interaction". Proc. of the X Intern. Conf. on High-Power Particle Beams. June 20-24, 1994, San-Diego. C.A. Vol. 2, p. 687-689.

TRANSFORMATION OF EXCITED BY ELECTRON BEAM PLASMA WAVES INTO ELECTROMAGNETIC RADIATION (EMR) OWING TO PARAMETRIC PROCESSES ON LAYER PLASMA WAVEGUIDE

V.A.Balakirev, V.I.Karas', E.A.Kornilov, Ya.B.Fainberg

National Scientific Center «Kharkov Institute of Physics & Technology», Academicheskaya St. 1, Kharkov, 310108, Ukraine

1. Let's investigate the transformation of the plasma oscillations excited by an electron beam into EMR during the nonlinear interaction of HF plasma with LF ion-sound waves in the magnetized plasma waveguide. While exciting a regular ion-sound wave in the nonisothermal plasma ($T_e \gg T_i$, $T_{e,i}$ are the electron- and ion temperatures), one creates the plasma density periodic inhomogeneity (the diffraction grating) with the depth of modulation $\delta n_s/n_0 = e\varphi_s/T_e$ (δn_s is the plasma density distortion amplitude, n_0 is the plasma equilibrium density, φ_s is the electric potential amplitude of the ion-sound wave). Plasma density periodic modulation provides for parametric coupling between the plasma- and electromagnetic (EM) waves. In the plasma waveguide the necessary condition of the process realization is coexistence of both the EMW and plasma wave at the same frequencies. In the waveguide filled with plasma partially this condition is realizable [1, 2]. In this waveguide the EMW can propagate at the frequencies $\omega \leq \omega_p$ between the plasma- and the outer conductive jacket boundary.

The parametric process in question is realizable if the conditions of time-spatial synchronism are fulfilled for the longitudinal wave numbers and for the frequencies of the interacting waves:

$$\omega_l = \omega_t + \omega_s, \qquad k_l = k_t + k_s. \tag{1}$$

Here ω_s, k_s are the frequency and the longitudinal wave number of the ion-sound wave and $\omega_{l,t}$, $k_{l,t}$ are the frequencies and the longitudinal wavenumbers of the plasma wave and EMW, correspondingly.

Acting on plasma, the HF feedback caused by the HF pressure amplifies the ion-sound wave (the plasma density modulation depth).

Let's consider a homogeneous plasma cylinder with the radius a. Plasma is placed into the co-axial jacket with ideal conductivity and the radius $d > a$. The system is situated in the intensive magnetic field directed along the waveguide axis z. Along this axis a monoenergetic electron beam is propagating (its radius b ($b \ll a$)). There are three waves excited in the waveguide: the plasma wave amplified by the electron beam, the ion-sound wave, and the EMW propagating in the vacuum gap between plasma and the jacket conducting ideally. All these waves move in the same direction (along the z axis). Below we limit ourselves with examination of the stationary processes of the wave interaction.

As it's already mentioned, the HF field feedback action on plasma amplifies the plasma density modulation depth. The following equation describes the process:

$$\frac{\partial^2 \delta n}{\partial t^2} - C_s \Delta \delta n = \frac{1}{16\pi} \frac{\omega_{pe}^2}{\omega^2 m} \Delta |E_z|^2, \tag{2}$$

E_z is the HF field longitudinal component. The Eq.(2) yields the reduced equation of the ion-sound wave amplitude. The amplitudes of the interacting waves are described with the system of the reduced equations in the dimensionless variables:

$$\frac{dC_l}{d\xi} = iWC_tC_s \exp(-i\Delta_v\xi) + \rho + i\Delta_b C_l, \quad \frac{dC_t}{d\xi} = iWC_lC_s^* \exp(i\Delta_v\xi), \quad \frac{dC_s}{d\xi} = iWC_lC_t^* \exp(i\Delta_v\xi). \quad (3)$$

Here one designates: $C_{l,t} = a_{l,t}/A_{l,t}$ are the dimensionless amplitudes of the HF plasma- and EM waves, $C_s = a_s/A_s$ is the dimensionless amplitude of the LF ion-sound wave, $A_t = A_l\sqrt{R_l/R_t}$, $A_s = A_l\sqrt{\omega_s R_l/\omega R_s}$, $A_l = m\omega V_0\theta^2/e\gamma_0$, $\theta = \gamma_0\left(I_b c^3/4I_A\omega^2 R_l\right)^{1/3}$,

$$I_A = mc^3/e \approx 17 \text{ kA}, \quad R_{l,t} = \frac{\omega}{8}\frac{k_{l,t}a^2}{\left(K_{l,t}\right)^2} J_0^2(\lambda_{l,t}) \times \left[\frac{\omega_p^2}{\omega^2} + \frac{4}{\pi^2 K_{l,t}^2 a^2 \Delta_0^2\left(K_{l,t}, K_{l,t}\eta\right)}\right], \quad \lambda_{l,t}/a$$

are the transversal wave numbers of the plasma- and EM waves in plasma, $K_{l,t} = \lambda_{l,t}/\sqrt{-\varepsilon}$, $\eta = d/a$, $\Delta_v = \left(k_l - k_b - k_s\right)L$ is the difference between the 'wave numbers of the interacting waves, $\Delta_b = \left(k_l - k_b\right)L$ is the initial difference between the beam velocity and the wave phase velocity,

$$W = \frac{1}{8}\sqrt{\frac{\omega_s\omega}{R_s R_t}}\frac{\omega_p^2}{\omega^2}Qa^2\frac{mV_0^2}{2T_e}\theta, \quad Q = \int_0^1 J_0(\lambda_l x) J_0(\lambda_t x)x\,dx, \quad R_s = \frac{1}{8}\frac{\omega_{pi}^2}{c_s}, \quad (4)$$

ω_{pi} is the ion plasma frequency and c_s is the sound velocity.

In the presented expressions it's supposed that $\omega_t = \omega_l = \omega$ and the difference between the frequencies of the HF EMW and plasma wave is not taken into account. Physical sense of the coefficients R_α ($\alpha = t,l,s$) is clear. They represent the ratio of the energy flow of the corresponding wave S_α to the amplitude squared:

$$S_\alpha = R_\alpha |a_\alpha|^2. \quad (5)$$

In the right-hand side of this expression of the plasma wave amplitude the second term describes the plasma wave amplification by the beam.

2. To start with, let's consider a simpler physical case in which the plasma density modulation depth is given $C_s = C_{s0}$. In particular, the plasma layering may be produced by modulation of the external magnetic field [3]. In this situation the system of two coupled equations of the plasma- and EM waves amplitudes describes the process of radiation excitation. In this system, as in the equations of the beam particle motion, the integral describing the law of conservation of the system energy is included:

$$S_t + S_l + P_b = Const,$$

The $S_{t,l}$ is the total energy flow of the plasma- and EM waves, P_b is the beam power.

Numerical simulation of the nonlinear equation system in order to investigate the nonlinear stage of excitation of the coupled plasma- and EM waves for different values of the wave coupling parameter $\Lambda = WC_{s0}$ when the difference $\Delta_b = 0$, $\Delta_v = 0$.

The coupling parameter Λ is varying within the limits $0\ldots1.05$. If $\Lambda_{cr} = 1.05$, the instability derangement takes place. At the Fig.1 the dependencies of the plasma- and EM wave dimensionless amplitudes on the longitudinal coordinate are plotted for $\Lambda = 0.15$ (the Fig.1a) and $\Lambda = 1$ (the Fig.1b). When $\Lambda = 0.15$ and the energy pumpover length essentially exceeds the amplification length, after exponential increase the amplitudes of the both waves amplitudes reach their maximums and then they start to oscillate. An oscillation of the plasma- and

EM wave amplitudes are stipulated by the phase oscillations of the beam bunches trapped by this wave. The plasma- and the EM wave oscillations are opposite in phase. That's, the plasma wave amplitude maximum corresponds to the EMW amplitude minimum and v.v. comparing the dimensionless amplitudes, one can see that the plasma wave amplitude is approximately in 3 times higher than that of the EMW. The EMW amplitude reaches its maximum at longer
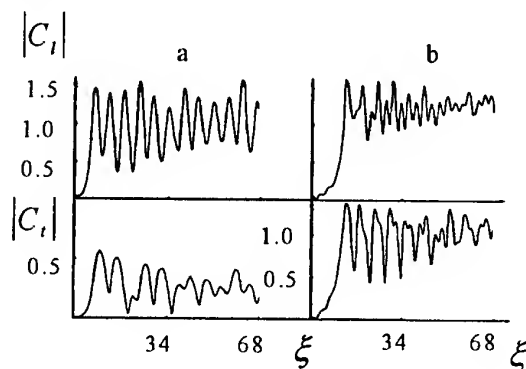
Fig. 1. Spatial amplitude dependencies of the plasma $|C_l|$ and electromagnetic $|C_t|$ waves for different values of the Λ -parameter.
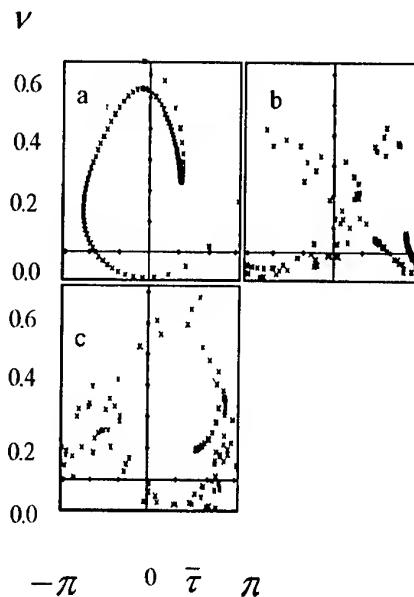
Fig. 2. The beam phase picture at the different points ξ: (a) - 120, (b) - 200, (c) - 280.

distances than the plasma wave. If $\Lambda = 1$, the energy pumpover period is equal to the inverse increment. In this case the picture of the coupled wave excitation is different in its essence. At the initial stage the plasma- and EM waves amplitudes are increasing nonmonotonically. Then they get into their maximums located approximately at the same point. At the initial stage the amplitude oscillations are stimulated by energy pumpover from the plasma wave to the EMW and v.v. One should take into account that, in contrast to the wave amplitude, the electronic efficiency is increasing monotonely during this stage. The fact testifies to existence of the wave energy pumpover effect. At the first maximum the dimensionless wave amplitude values are same approximately. Behind the maximums the amplitudes oscillate irregularly. At the Fig.2 the beam phase pictures are plotted for $\Lambda = 1$. Here it's depicted that at large distances the bunch is being destroyed and the particles become greatly mixed on the phase plane. As a result, the amplitude oscillations are diminishing.

The dependencies of the electronic efficiency and beam power relative losses by fast EMW excitation on the Λ parameter for $\theta = 0.2$ show evident, while the coupling parameter is increasing up to its critical value Λ_{cr}, the maximum electronic efficiency is also increasing continuously. At the mentioned critical point the instability decayes. In particular, when $\Lambda = 1$, the efficiency is approximately equal to 32%. This is in 1.8 times higher than in absence of the wave coupling. A part of the beam power expended on EMR excitation increases with increase of the Λ. When $\Lambda = 1$, approximately the half of the total beam plasma losses is spent on radiation excitation and the plasma wave is excited by the other half of this power.

3. Let's examine the system of the equations that take into account the influence of the HF plasma- and EM waves feedback on the LF ion-sound wave. In absence of the electron beam the system (2) describes the decay instability of the plasma wave that produces the EM- and the ion-sound waves. This instability causes exponential increase both of the EM- and ion-

sound waves. The corresponding dimensionless spatial increment is $\Gamma_d = W|C_{I0}|$.

The decay instability increment is $\Gamma_d \approx W$ for the amplitude value $|C_{I0}| \approx 1$ determined by the beam particle trapping by the synchronous plasma wave field. If $W \geq 1$, the decay instability essentially influences the beam-plasma instability. Thus, the analysis demonstrates that HF plasma- and EM waves stimulate the ion-sound wave increase, i.e. they amplify the plasma density modulation depth.

The results of the numerical solutions of the systems (2) are presented in the [4], in which the plasma decay process is investigated. While the electron beam is being continuously injected into infinite homogeneous plasma, the decay of the plasma wave produces the plasma- and ion-sound waves. Numerical analysis demonstrates that the plasma wave transformation into EMW essentially influences the plasma-beam instability dynamics when $W^2 > 0.1$.

Energy interchange between the plasma- and EM waves modulates the wave amplitudes with the spatial period ξ_{mod} ($\xi_{mod} \sim W^{-2}$). The decay process stimulates the efficiency of the power pumpover from the beam. If $0.1 < W^2 < 2$, the beam power losses keep on increasing. At the maximum they are in 2 times higher than in the case of $W = 0$, in which the HF plasma wave is not transformed into EMR. When $W^2 > 2$, periodic modulation of the HF plasma wave parameters causes development of the stochastic instability [5]. This instability originates in phase mixing of resonance particles. The length of the effective energy interchange of the HF plasma wave with EMW decreases with growth of the wave nonlinear interaction parameter W. For example, if $W = 1$, the EMW amplitude reaches its maximum when $\xi = 15$.

4. In this work the process of EMR excitation by an electron beam is also investigated in the case of the plasma waveguides where the plasma density varies along the system according to the periodic (harmonic) law. In the examined system the plasma wave is synchronous with the beam. The plasma wave is parametrically coupled with the fast EMW propagating in the vacuum gap between the plasma boundary and the conductive jacket. The coupling is stimulated by the plasma density periodic inhomogeneity.

It's demonstrated that in this system the process of the plasma wave parametric transformation into EMR stimulates increase of efficiency of the power pumpover from the electron beam.

Plasma density periodic inhomogeneity may realized by excitation of the short ion-sound wave in plasma. In this case the ponderomotive force of HF pressure creates the feedback of the plasma- and EM waves, which causes increase of the ion-sound wave (the plasma density modulation depth amplification) and, correspondingly, diminution of the length of the plasma wave energy transformation into radiation.

[1] A.K.Berezin et. al. "Numerical Analysis of Dispersive Properties of Plasma Cylindrical Waveguides Placed into Magnetic Field". Preprint KhPhTI 86-25, Moscow: CNI Atominform, 1986.

[2] M.B.Kiselev et. al. "Spectra of Proper Oscillations of Co-Axial Plasma Waveguide in Finite Magnetic Field". Preprint 23. Moscow: IOFAN, 1991.

[3] P.I.Markov, I.N.Onishchenko et. al. "Electrodynamics of Corrugated Plasma Waveguide". Plasma Phys., Vol. 19, No 1, 1993, p. 14-19.

[4] N.G.Matsiborko, I.N.Onishchenko et. al. "Decay Instability of Plasma and Ion-Sound Oscillations during Stationary Injection of electron Beam into Plasma". Plasma Phys., Vol. 1, No 5, 1975, p. 765-771.

[5] G.M.Zaslavsky. "Stochasticity of Dynamic Systems". Moscow: Nauka, 1984.

DIELECTRIC WAKE-FIELD GENERATOR

V.Kiselev, A.Linnik, V.Mirny, N.Zemliansky,
R.Kochergov, I.Onishchenko, G.Sotnikov, Ya.Fainberg

*NSC Kharkov Institute of Physics & Technology,
Academic 1, Kharkov 310108, Ukraine*

Abstract

Wake-fields excited in a dielectric media can be applied both for particles acceleration and for HF-power generation. In the present work theoretical and experimental investigations are represented on the generation of the electromagnetic wake-fields in the dielectric tube by a sequence of the relativistic electron bunches. The obtaining of the peaked high power due to the coherent superposition of the wake-fields of the regular sequence of bunches and multi-mode operation has been investigated. The measurements of wake-fields output power and the beam electron energy losses and were performed.

1. INTRODUCTION

Using of the wake-fields exited in dielectric by a sequence of electron bunches for high-gradient particle acceleration is proposed and investigated in [1-3]. Recently [4] wake-fields are considered as an effective means for HF-generation in plasma-filled klystron. In the present work the theoretical treatment, simulation, and experimental investigations of the wake-fields excitation in dielectric-lined waveguide for the generation of peaked high power emission. As it was revealed in [2,3] two essential virtues are being exploited. First of them is the excitation by many bunches regular sequence that allows to superpose coherently the wake-fields excited by each bunch. The second one [3] concludes to multi-mode operation that leads to peaking of the excited HF-power. So obtained HF-field represents a sequence of soliton-like spikes of alternative signs with correspondingly higher amplitude comparatively to one principle mode excitation.

In Sec.2 of the paper the theory of wake-field excitation by a single electron bunch in the dielectric-lined circular waveguide is developed in contrast to plane geometry considered in [3]. The simulation of the wake-fields excitation for parameters of the experimental investigations are represented in Sec.3. Sec.4 deals with the description of the experimental set-up. The results of performed experiments on beam energy losses and HF-power measurements are reviewed in Sec.5. Conclusions are made in the last section.

2. THEORY

Let slow wave structure represents a dielectric pipe enclosed by a metal shell of the radius b and having the vacuum channel of the radius a located along pipe axiz. Along the channel bunch of the radius r_0 and length Δz moves with a velocity v_0. At first we find the fields of an infinitely thin tubular bunch, the charge density is given by $\rho = -(eN_0/2\pi r_0)\delta(r - r_0)\delta(z - v_0 t)$, where e is electron charge , N_0 is number of electrons in the bunch. To receive the equations for all components of an electromagnetic field of TE wave we use the follow Maxwell equations:

$$\nabla_\perp^2 \tilde{E}_z + \kappa_\perp^2 \tilde{E}_z = -(4\pi i/\omega)\kappa_\perp^2 \tilde{j}_z ; \tilde{E}_r = (i\kappa_z/(\omega^2\varepsilon/c^2 - \kappa_z^2))\partial\tilde{E}_z/\partial r ; \tilde{H}_\varphi = \omega\varepsilon/c\kappa_z \tilde{E}_r \quad (1)$$

where for all field components magnitude $\widetilde{F} = \int\limits_{-\infty}^{\infty} F\, e^{-ik_z z + i\omega t}\, dz\, dt$, the z-component of the current density $j_z(r, z, t) = v_0 \rho$, value of a dielectric permeability ε in vacuum is equal to 1, and in the dielectric medium it is ε_d, the transversel wave number $\kappa_\perp^2$ is equal to $\kappa_v^2 = -\omega^2/v_0^2\gamma_0^2$ for vacuum and $\kappa_d^2 = \omega^2(\beta_0^2\varepsilon_d - 1)/v_0^2$ for the dielectric, ω-frequency of ocsillations, c - light velocity, $\kappa_z = \omega/v_0$ - longitudinal wave number, γ_0 is relativistic factor of the beam electrons.

To solve the equation (2), we shall divide the whole area inside a waveguide on three parts: I - $r < r_0$, II - $r_0 < r < a$, III - $a < r < b$. The solutions in these areas look like: $\widetilde{E}_z^I = C_1 I_0(\kappa_v r)$, $\widetilde{E}_z^{II} = C_2 I_0(\kappa_v r) + C_3 K_0(\kappa_v r)$, $\widetilde{E}_z^{III} = C_4 J_0(\kappa_d r) + C_5 Y_0(\kappa_d r)$. Here J_i, Y_i, I_i, K_i are Bessel functions of i-th order. C_i should be found from boundary conditions.

To find wake field for relativistic bunch as a disc of a finite length, it is necessary in the expressions for infinitely thin bunch make a replacement $t \to t - t_0$ (t_0- the entry time for an infinitely thin bunch) and, using expression $N_0 = 2\pi r_0\, j(r_0, t_0)/e\, dt_0 dr_0$, to integrate over entry time and entry radius r_0. Here $j(r_0, t_0)$ is the bunch current density at $r = r_0$, $z = 0$. If the charge density distribution of the bunch has an step view, the longitudinal component of the wake field behind the bunch is equal:

$$E_z = -\frac{4\pi r_b j}{a^2} \sum_s \frac{I_0(\kappa_{vs} r) I_1(\kappa_{vs} r_b)}{I_0^2(\kappa_{vs} a)} E_s^{-1} \Theta(t - \frac{z}{v_0}) \frac{\sin(\omega t_*/2)\cos(t - z/v_0 - t_*/2)}{\kappa_{vs}\omega_s/2} \qquad (2)$$

where t_*-duration of the bunch, r_b -beam radius, j-bunch current density, ω_s-eigen frequency:

$$D(\omega_s) = \varepsilon_d \kappa_{vs}\frac{B}{A} - \kappa_{ds}\frac{I_1(\kappa_{vs} a)}{I_0(\kappa_{vs} a)} = 0; E_s = \varepsilon_d - \frac{4\varepsilon_d}{\pi^2\kappa_d^2 a^2 A^2} + \frac{\varepsilon_d B^2}{A^2} - \left(1 - \frac{I_1^2(\kappa_{vs} a)}{I_0^2(\kappa_{vs} a)}\right)$$

$$B = J_1(\kappa_d a)Y_0(\kappa_d b) - J_0(\kappa_d a)Y_1(\kappa_d b), A = J_0(\kappa_d a)Y_0(\kappa_d b) - J_0(\kappa_d a)Y_0(\kappa_d b)$$

3. RESULTS OF SIMULATION

The further evaluations are produced with the help of numerical methods for the following sets of parameters, being used in experiments: $b = 3.5$ cm, $a = 1.1$ cm, $\gamma_0 = 5.0$, $r_b = 1.0$ cm, $r = 0.0$ cm, $\Delta z = 1.7$ cm. Two cases were considered: $\varepsilon_d = 10.0$ and, $\varepsilon_d = 2.6$, the number of included mudes in expression (2) is equal to 50. As well as in work [3], the multimode considerations for large values ε_d leads concentrating the electrical field in narrow, periodically spased peaks (fig. 1a). The E_z is normalized on value $4\pi r_b j/c$, ξ is equal to $(t - z/v_0)c/a$. For smaller ε_d ($\varepsilon_d = 2.6$), only a few first peaks can be determinated clearly, while there is nonregular oscillation of the electrical field on the remaining part of the wake field dependence on the length (fig. 1b). For $\varepsilon_d = 10.0$ the resulting electrical field exceed the first harmonic 10 times, while for smaller $\varepsilon_d = 2.6$ this ratio is only 3. The nonregularity caused by the violation of the equaly spacing of the eigen frequencies ($\omega_s = \omega_0(n + 1/2)$, n-integer) at small value of ε_d. Besides, increasing ε_d leads to magnifying amount of first modes having amplitudes of the same order, i.e. bringing noticeable contribution to the resulting field.
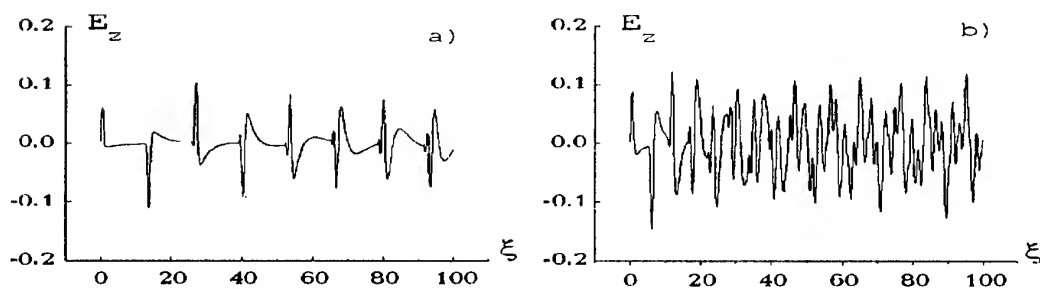
Fig.1.

It shows necessity to take into account a great number of eigen modes excited in the structure considered.

4. EXPERIMENTAL SET-UP

Experiments have been run to investigate wave excitation in the dielectric structure by a sequence of relativistic electrons bunches. The schema of the experimental installation is shown in Fig.2. The electron beam was produced by a linear accelerator and had the following parameters: energy 2 MeV, each bunch length 60 ps, number of bunches 300 to 6000, bunch diameter 1 cm, length 1.7cm, number of electrons per bunch $2 \cdot 10^9$, beam modulation frequency $f_0 = 2825\,MHz$. The energy spectrum of beam electrons was $\Delta W / W = 8\%$. Parameters of dielectric structures (DS) were: inner radius $R_1 = 1.1cm$, outer radius $R_2 = 3.5cm$, length $l = 70cm$, $\varepsilon = 2.6$. For comparison, experiments were carried out with both DS and thin glass tube, whose inner diameter coincides with that of the DS.
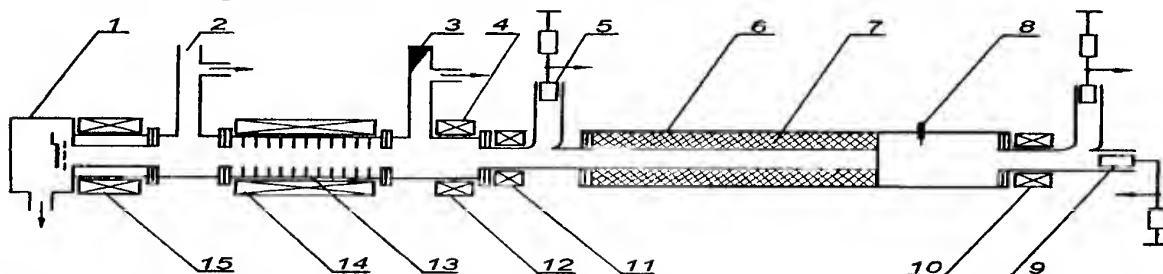
Fig. 2. The schema of the experimental installation: 1 - electron gun; 2 - waveguide; 3 - matching load; 4, 10, 11 - corrector coils; 5, 9 - Faraday cups of magnetic analysers; 6 - cuper tube; 7 - dielectric structure,8 - HF probe, 13 - disk loaded waveguide; 14, 15 - solenoids.

5. RESULTS OF EXPERIMENTAL INVESTIGATOINS

The probes arranged at the output of the structure have indicated the presence of intense microwave radiation at the wavelength λ=10cm with both E_z and E_r field components. The spectrum width of radiation ($\Delta f = 10 - 12\,MHz$) is of the spectrum width order of the accelerator driving generator ($\Delta f_0 = 8\,MHz$). The microwave radiation amplitude as a fraction of the number of bunches that have passed through the structure (beam current pulse length) has shown (see Fig.3) that the field grows by nearly a linear low up to 3000 bunches. Then the saturation sets. The same conclusion follows from the comparison between the oscillogram of the radiation signal and the beam pulse oscillogram.
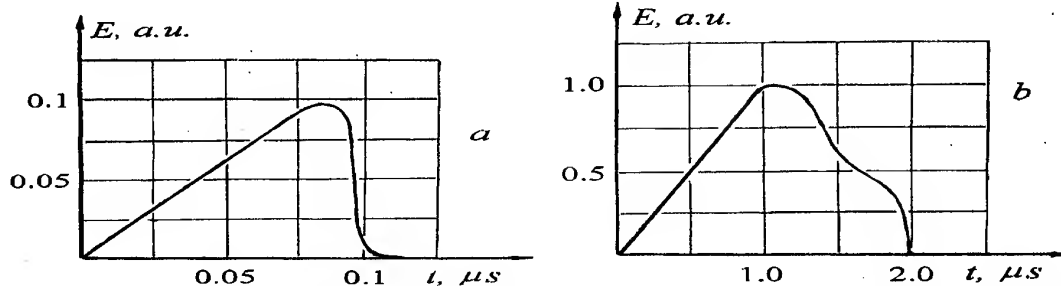
Fig. 3. Oscillograms of the HF radiation pulse ($\lambda = 10$ cm) for the number of bunches a - N = 300, b - N = 6000.

Energy spectrum measurements by a magnetic analyzer at the exit DS are represented in Fig.4. It is seen that the spectrum peak is shifted by 500 keV, i.e. 25% of the beam energy are lost. At the same time, there are some electrons (about 10%) which have energy higher than their initial one. for a small number of bunches (N=300) the shift of the spectral peak decreased down to 100-200 keV. The measurements of 'instantaneous' spectra have shown that the greatest energy losses were in the middle of the beam current pulse ($t=2\mu s$), while the losses were at the head of beam pulse.
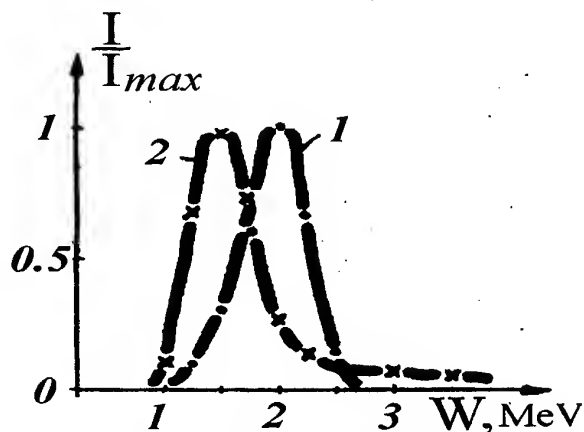
Fig. 4. Electron beam energy spectra. 1- initial spectrum, 2 - spectrum after interaction with dielectric structure.

6. CONCLUSIONS

Based on the results obtained we can draw the following conclusions:
1. The presence of probe-detected microwave radiation at the DS exit, as well as the dependence of microwave radiation amplitude on the number of bunches passed through structure, give the evidence for the summation of wake field of the first 3000 bunches. Power intensity enhancement due to power peaking in multi-mode operation is being investigated.
2. In the process of the bunches sequence interaction with a dielectric structure, the electron energy losses up to 25% of its initial value are experimentally observed.

ACKNOWLEGMENTS

REFERENCE
[1] W.Gai, P.Schoessow, B.Cole, R.Konecny, J.Norem, J.Rosenzweig, and J.Simpson, *Phys. Rev. Lett.* **61**, 2756 (1988).
[2] I.N.Onishchenko, V.A.Kiselev, A.K.Berezin, G.V.Sotnikov et al. Proc. 1995 Particle Accelerator Conf., PAC'95, pp. 782-3.
[3] T.B.Zhang, J.L.Hirshfield, T.C.Marshall, B.Hafizi, and A.K.Ganguly, Proc. 1997 Particle Accelerator Conf., PAC'97.
[4] J.A.Pasour et al, Rev. Sci. Instrum. **68**, 3229(1997).

Plasma Nonlinearity Influence on HF Oscillation Excitation by the Electron Beam in Hybrid Plasma Waveguides.

V.S. Antipov, A.N. Antonov, V.A. Balakirev, Yu. P. Bliokh, A.M. Egorov, Ya. B. Fainberg, V.I. Karas', O.F. Kovpik, E.A. Kornilov, M.G. Lubarsky, K.V. Matyash, V.O. Podobinsky, G.V. Sotnikov, V.G. Svichensky.

Institute of Plasma Electronics & New Acceleration Methods, National Science Center «KhPhTI», 1 Akademicheskaya Str., Kharkov 310108, Ukraine

1. The tasks of increase of the HF power under excitation and the microwave energy extraction into the outer space are the key-problems of microwave electronics. In order to solve them, it has been proposed the application of hybrid plasma waveguides [1]. The hybrid plasma waveguide is the slow-wave structure with its passage channel filled with plasma. (HPSWS). In such waveguide, the principal advantages of plasma electronics characteristics are realizable. Although there are many works dedicated to the oscillation excitation by the electron beam in plasma, practically, any analysis is not given to the problem of plasma nonlinearity influence on this process - in hybrid plasma waveguides at present.

In the given brief report, we have presented the first experimental investigations which demonstrate the dynamics of the microwave oscillation excitation in a plasma of HPSWS. On the ground of the examination performed, one can suppose that the limiting of the oscillation power level is conditioned by the plasma motion stimulated by ponderomotive microwave forces. We have also presented the theoretical model which describes the process observed; this model can make the basis of the self-consistent theory of the beam-plasma interaction in HPSWS. Besides the most prospective hybrid plasma waveguide for the microwave beam plasma devices has been shown.

2. The experimental investigations have been performed with the test bench installed according to the scheme of the beam-plasma generator. In this device, the hybrid plasma waveguide is formed due to the plasma generation by the electron beam in a chain of cavities coupled inductively (CCI) [2,3,4].

The characteristics of the electron gun of the test bench are the following: the cathode is the LaB_6 tablet; the accelerating voltage is 1-40 kV; the beam current is 0.5-10 A; the beam diameter is 10 mm; the operating regime the pulse and continuous. CCI are placed in the magnetic field up to 0,1 T. Some gas (argon, nitrogen) is inflated by the device CHA-1 (an automatic system of the gas inflation) through the pipe into the end of the slow-wave structure. The electron-gun cell is pumped out by the turbomolecular pump. Behind the slow-wave structure either the collector diagnostic unit or the current collector capable of scattering the beam power up to 200 kW may be placed, which depends on the experiment program.

The plasma nonlinearity manifestation must be accompanied with excitation of the proper low frequency (LF) ion oscillations. Therefore, the experimental determination of the frequency spectrum and wavelength of the ion oscillations makes one of the most important stages in creating the analytical model of description of the beam-plasma interaction in the hybrid plasma waveguide.

Low frequency ion oscillations must influence all the interaction parameters. In this connection, the spectra and amplitudes of LF oscillations (20 kHz - 200 MHz) are registered

through the collector current, plasma density and the envelope of HF oscillations. The mutual correlation of these measurements is carried out.

The dispersion characteristics of LF oscillations can be restored through the autocorrelation functions of the plasma density fluctuations registered with the help of suspended single and double Langmuir probes placed in the beam fringe on the both sides of the hybrid plasma waveguide section. A special method, based on the analytical analysis given to deformation of the video pulse propagating in the waveguide, has been supplementary elaborated for the same purposes [4].

3. The hybrid plasma waveguide is intended for excitation of the fundamental zeroth spatial harmonic by the electron beam with the energy 30-40 keV in the frequency band 2.4-4.4 GHz when the plasma density is 10^{11} $1/cm^3$. As it has been determined experimentally, such plasma density in the waveguide passage channel is obtainable under the gas pressure 10^{-4}-$5*10^{-5}$ mm Hg. If the beam velocities are synchronous, the beam efficiency related to the microwave oscillation excitation makes 40%, and the oscillation power reaches 40 kW in this case.

The plasma resonant density, which provides the maximum power of the oscillations excited, is obtainable under a certain correlation between the pressure and current of the beam when the energy of the latter is fixed. There is an optimal value of the pressure if the beam current is fixed and vice versa.

Instantaneous investigation of the amplitude of the microwave oscillations excited, which has been performed with the rapid-record oscillograph, indicates that they are purely sinusoidal if either the beam current is being increased (under the fixed pressure) or the pressure is being heightened (under the fixed current) and the power reaches 30-40% of the maximum value. A further increase of the power causes distortion of the signal. In the oscillation spectrum, the satellites of the resonant frequency arise, and the amplitude modulation takes place at the frequency of ion-acoustic oscillations and higher frequencies (20 kHz - 200 MHz). The amplitude splashes occur in the packets 5.0-300 μs. When the average value of the power is maximum, its magnitude in the pulse packet can be 2-4 times as much. Increase of either the current or pressure causes excitation of the oscillations which have the form of a sequence of short pulses recurring periodically. Before the oscillation derangement, the number of the pulses becomes smaller.

There are the oscillograms in Fig.1 which demonstrate the variations of the power of the microwave oscillations excited. The oscillogram of the plasma density variation and the envelope of the microwave oscillation power indicate that the temporal variation of the oscillation power correlates with the variation of the plasma density. (Fig.2).

The analytical calculations indicate that there are three brunches of ion oscillations in the hybrid plasma waveguide - the ion-acoustic, ion-plasma oscillations and those of the low hybrid resonance. The frequencies belonging to these oscillations are registered in the envelope of microwave oscillations. The frequencies of ion-acoustic oscillations have been determined through the plasma density fluctuations (the depth of modulation of the plasma density is more than 50%).

The emergence of LF oscillations in the plasma is accompanied by excitation of supplementary currents of particles along the beam axis.

As phase velocities of LF oscillations are essentially lower than the electron beam velocity, one can suppose that emergence of the LF oscillations is conditioned by the nonlinear mechanism for the oscillation excitation owing to the energy of HF oscillations.

4. We have studied the self-consistent stationary solutions to the equations describing the beam instability in the HPSWS filled with plasma, the density of which is disturbed by a ponderomotive force. It has been demonstrated that the instability saturation can be

conditioned by the plasma inhomogeneity (plasma nonlinearity) if the beam current is high enough. In other words, plasma nonlinearity can make a mechanism for the power limiting in hybrid structures.. The ponderomotive force must be taken into account in the experimental device if the microwave radiation power is higher than several kW's.
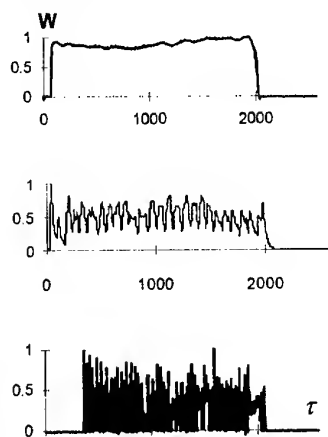
Fig.1
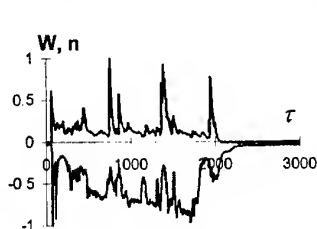
Fig. 2
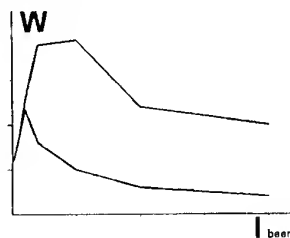
Fig. 3

Fig. 1 Dependence of HF power W (in relative units) on time τ (μs) under increasing pressure in waveguide. **Fig. 2** Dependence of HF power **W** and plasma density n (lower curve) (both in relative units) on time τ(μs). **Fig. 3** Dependence of the pulse power (upper curve) and the mean power (lower curve) on the beam current (numerical simulation).

Ponderomotive forces condition a transition from the oscillation persistent excitation by the electron beam to the pulsed excitation. The power of the microwave oscillations excited increases with the heightening of the beam current. As a consequence of this, the plasma density decreases further in the output area of HPSWS, and the wave phase velocity becomes decelerated within the plasma inhomogeneity. Nearing the waveguide output, the beam loses its energy as well, and its velocity decreases. At a certain moment, the autotuning of the beam velocity in to the wave phase velocity takes place in this area, which provides the increase of the effectiveness of the beam energy transfer to the oscillations. The HF wave energy increase is accompanied by some heightening of the HF pressure. The plasma inhomogeneity is being displaced by the pressure towards the waveguide input, which reduces the interaction effective length. In the long run, this causes derangement of the oscillations under excitation.

So, the theory elaborated predicts the following behavior of the microwave oscillator in the case of the beam current increase. At first, some regular excitation of the oscillations, the power of which increases simultaneously with the beam current growth, takes place. If the beam current reaches a certain threshold value, low-frequency self-modulation of the microwave signal envelope comes into existence. Under the consequent current increase, the self-modulation becomes deeper, and it takes the form of isolated short pulses. In the last stage, the radiation principal power decreases when the beam current increases.

The numerical simulations are in the qualitative agreement with the system behavior observed experimentally. In the self-modulation regime, demonstrated in Fig.1, the pulse power increases when the beam current grows - to the contrary to the average power. The corresponding dependencies of the pulse- and average powers on the beam current have been presented in Fig.3.

The theory also shows that the efficiency of the beam-wave interaction in the HPSWS depends on plasma density or gas pressure in the system and reaches its maximum under some density value. It can be explained in the following way. The part of plasma density inhomogeneity increases under the plasma density growth. If the density is small, the beam-wave instability saturation is conditioned by the beam particles motion nonlinearity; maximum value of the wave amplitude increases under plasma density growth do to the

increase of the beam-wave coupling coefficient. If the plasma density is large enough, the instability saturation is conditioned by plasma non-linearity as it was mentioned above and the maximal amplitude of the excited wave increase under the plasma density growth. This is conditioned by the fact that the dispersion characteristics of the SWS are determined by the plasma density, and the increase of the latter as well as the inhomogeneity causes more stronger alterations in the wave phase velocity.

The numerical simulations have shown that, for the given experimental device, the maximum efficiency (relation of the microwave radiation power to the beam power) reaches about 40% (radiation power about 30 - 35 kW). The power value calculated is very close to the one obtained experimentally.

5. The results obtained confirm that the plasma nonlinearity plays a large part in the mechanisms limiting the power of the oscillations excited by the beam in HPSWS. Naturally, the question about the concrete hybrid structures which would be preferable in designing powerful beam-plasma microwave devices may arise. The performed analysis [6,7] indicates that at least three types of waveguides can be chosen: the hybrid plasma waveguide, the boundary of which is formed with the slow-wave structures coupled inductively (a chain of the cavities coupled inductively or a structure of the meander-ring type), the hybrid plasma waveguide on the basis of comb-like coaxial slow-wave structures, the annular plasma waveguide. The last one is the most preferable in designing the beam-plasma microwave generators and amplifiers in the millimeter and submillimeter ranges of the wavelengths. For the beam-plasma generators, in which the waveguide of the given types is applied, the increase of the radiation power is performed without heightening the amplitudes of electric fields in the plasma.

6. The aim of our further investigations is to determine the part played by the HF wave decay processes, which take place simultaneously with the emergence of short-wave LF oscillations in HPSWS and which can stimulate acceleration of the plasma particles and heating of the plasma. The high temperature of electrons in plasma (~100 eV) and supplementary flows of charged particles, which are registered with the current collector, indicate that the existence of such processes is possible.

As a whole, all the investigations aim at finding the methods in controlling the process of the pulse generation of the oscillations and heightening the level of power of the microwave oscillations excited in hybrid plasma slow-wave structures.

References.

1. Ya.B. Fainberg, Yu.P. Bliokh, E.A. Kornilov et al. Electrodynamics of a hybrid plasma slow-wave structures. DAN, USSR, A. Phys.-mat. and technical sc. 1990.
2. Yu.P. Bliokh, E.A. Kornilov, L.A. Mitin, Ya.B. Fainberg. Experimental investigates of HF oscillation exitation by electron beam in the hybrid plasma slow-wave structure. Pl. Phys. V.20, №9, 767-776 (1994).
3. A.N. Antonov, Yu. P. Bliokh, Ya. B. Fainberg, O.F. Kovpik, E.A. Kornilov, L.A. Mitin et al. Plasma-beam generator with hybrid plasma waveguide. Pl. Phys., V20, №9, 777-781 (1994).
4. «Preparing the experimental testing grounds for investigating the stability of high amplitude waves in the hybrid plasma waveguides». //Technical report T6 on STCU 's Project #256, 1998.
5. Yu.P. Bliokh, Ya.B. Fainberg, M.B. Lubarsky, V.O. Podobinsky. Self-consistend plasma motion as a possible mechanisms of the power limiting and the pulse shortening in the plasma-filled TWT-devices. SPIE. Proc. V3158. Intense Microwave Pulses V Editor H. Brandt. p. 182-193 (1997).
6. P.I. Markov, E.A. Kornilov, G.V. Sotnikov. Excitation of broadband oscillations by electron beam in coaxial disk-loaded transmission line (in the proceedings).
7. V.A. Balakirev, V.I. Karas', E.A. Kornilov, Ya.B. Fainberg. Obtainment of electromagnetic radiation of electron beam with ring plasma waveguide (in the proceedings).

RELATIVISTIC MILLIMETER-WAVELENGTH RANGE CERENKOV GENERATORS

V.I.Koshelev, V.A.Popov

High Current Electronics Institute RAS,
4, Akademichesky Ave., Tomsk, 634055 Russia

ABSTRACT

Beam geometry influence on the selection of the lowest slow-wave modes of an overmoded periodic waveguide near the π-type oscillations in a 8-mm wavelength range has been investigated. Possibility of linearly polarized radiation generation has been shown. Radiation power up to 500 MW has been obtained.

INTRODUCTION

The aim of the investigations that are carried out is the development of gigawatt- power level generators in 8-mm wavelength range. To realize the task that has been set, multiwave Cerenkov generators (MWCG) are promising. In the previously made MWCG investigations [1], ~1-GW power 8-mm wavelength range radiation pulses have been obtained and injected into atmosphere. These experiments were carried out at the GAMMA accelerator with microsecond beam current pulse duration at a long leading edge and large beam thickness owing to cathode plasma expansion across magnetic field. The external beam diameter was limited by the diameter of a collimator installed in front of the slow-wave structure (SWS). Generation of radiation was realized at the beam currents close to the starting ones owing to a high duration of the voltage pulse leading edge. Radiation pulse length was much less than the beam current pulse duration that made difficult the separation of influence of nonlinear and plasma processes on the radiation pulse length limitation.

In the paper, the results of experimental investigations under conditions when radiation pulse length is close to the beam current pulse length and much longer than the voltage pulse leading edge length are presented. Two series of experiments were carried out. In the first part of the paper the main attention is given to the problem of electron selection near the π-type oscillations of the lowest axially symmetric TM_{01}-mode and nonsymmetric hybrid HE_{11}-mode in one-sectional overmoded SWS. The second part of the experiments is devoted to MWCG investigation.

EXPERIMENTAL SETUP AND MEASURING TECHNIQUE

The experiments were carried out at the SINUS-7M accelerator. Hollow electron beam with the mean diameter $D_b = 107 \div 111$ mm and a 2-mm thickness was formed in the diode with magnetic insulation at the voltage $U_d = 0.7 \div 1.1$ MV. Voltage pulse length $\tau_p = 40$ ns, leading edge pulse length was $5 \div 7$ ns. Magnetic field was changed in the limits of $6 \div 14$ kG. The main part of the experiments (if it is not mentioned specially) is carried out at $U_d \approx 1$ MV, beam current $I_b \approx 10$ kA, and magnetic field $B = 12$ kG.

In the experiments, SWS sections with the internal diameter D_w = 118 mm were used. Diaphragms were made as half-tores with a 1.1-mm radius, period ℓ = 3.8 mm. Section length could be regulated with a 2ℓ step. Slow-wave structures were made of a duralumin alloy.

Radiation power was determined by the patterns measured for (θ, φ) polarizations in the atmosphere. Radiation losses in the transmitting antenna were not taken into account. Pattern form was visualized by means of a gaseous lamp board. Radiation spectrum was measured by bandpass filters with band width of 0.5%.

GENERATORS WITH ONE-SECTIONAL SLOW-WAVE STRUCTURES

Hollow electron beam ellipsity influence on the selection of the lowest slow-wave modes of an overmoded periodic wavegude has been studied experimentally. Initially, the experiments were carried out with the beam large and small diameters of which differed in 3 mm, the mean one D_b = 110 mm. A linearly polarized radiation with maximum in the pattern center that corresponded to HE_{11}-mode excitation was registrated at the generator output. Cross-polarized radiation power didn't exceed 5% of the main radiation power. Wavelength λ = 8.8 mm in the limits of the experiment accuracy didn't depend on the diode voltage, structure length, magnetic field (9-14 kG). At B < 9 kG generation was unstable. Radiation spectrum width was 1%. Radiation pulse length at half-amplitude was 20 ns. Fig. 1 presents radiation power versus SWS length at U_d = 1 MV. Starting length L_{st} = 24ℓ. At SWS length increase up to L = 56ℓ radiation power decreased relative to maximum practically by a factor of two.
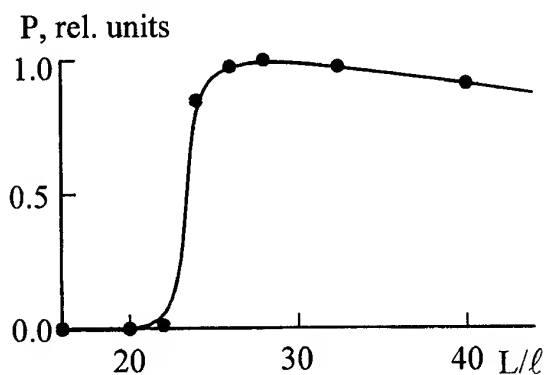
Fig. 1.
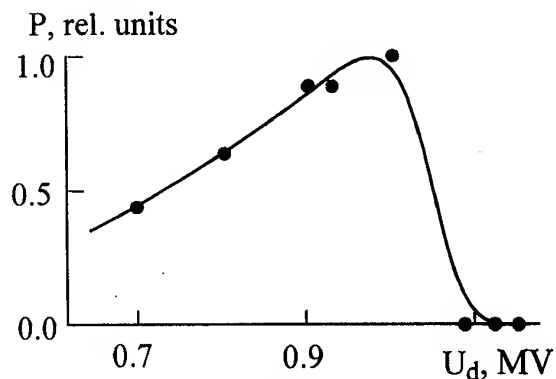
Fig. 2.

Radiation power versus diode voltage at L = 28ℓ is presented in Fig. 2. Power reached $100 \div 150$ MW in maximum. At U_d > 1 MV generation was absent. Radiation power sharply depended on the beam diameter. In particular, SWS heating in the pulsed magnetic field was found to result in the beam diameter decrease and generation disappearance. This circumstance was taken into account when carrying out experiments.

Beam ellipsity decrease (difference of the large and small diameters) to 1 mm allowed to realize generation regimes with preferential excitation of TM_{01}-mode. At the mean beam diameter D_b = 108.5 mm, SWS length L = 48ℓ radiation pulses with the power up to 150 MW at the wavelength λ = 8.6 mm and spectrum width 1% have been obtained. Cross-polarized

radiation power was ~10 MW. Diagram and polarization of the main radiation corresponded to TM_{01}-mode excitation. Beam diameter decrease by 1 mm resulted in the power decrease by an order of magnitude.

MULTIWAVE CERENKOV GENERATOR

A two-sectional SWS and a beam with small ellipsity and mean diameter $D_b = 108.5$ mm were used in the experiments that allowed, as it was shown above, to realize beam and field interaction near the π-type of TM_{01}-mode. The first section length $L_1 = 36\ell$ was less than the starting one. The length of the second section and drift tube L_{dr} varied in the experiments. Figs. 3 and 4 present the power versus L_{dr} at $L_2 = 32\ell$ and L_2 at $L_{dr} = 28\ell$, respectively.
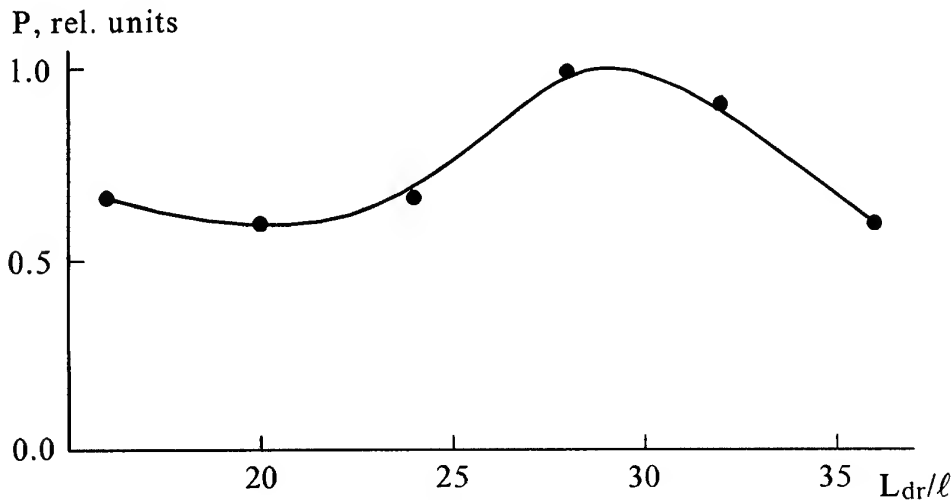
Fig. 3.
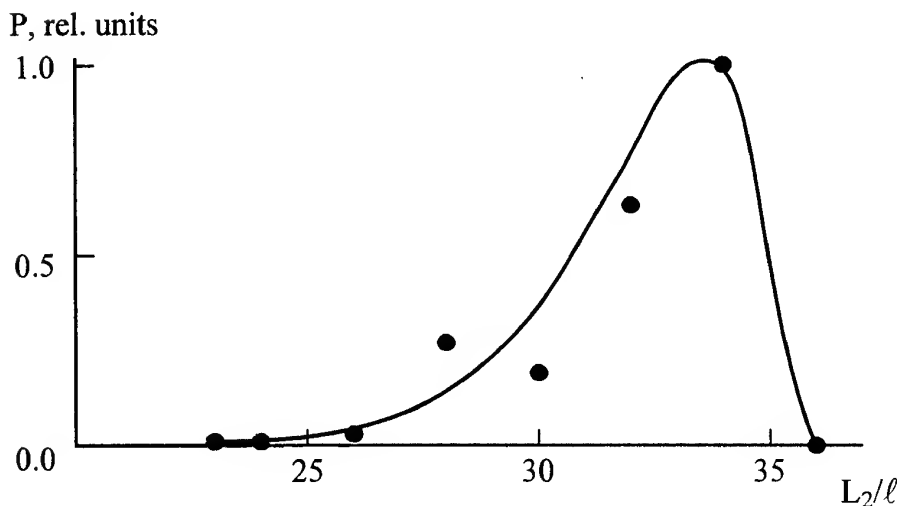
Fig. 4.

In the optimum regime (Fig. 4) radially polarized radiation power reached $P_\theta = 500$ MW that corresponded to a 5÷6 % efficiency. Cross-polarized radiation power didn't depend on P_θ and was ~ 10 MW as in a one-sectional generator. Fig. 5 presents typical patterns for two polarizations for regime with maximum power. Wavelength $\lambda = 8.8$ mm, spectrum width was

less than 1%. Radiation pulse length corresponded to the diode voltage pulse length. Fig. 6 presents typical oscillograms of U_d and radiation pulse with θ-polarization.

p, kW/cm^2
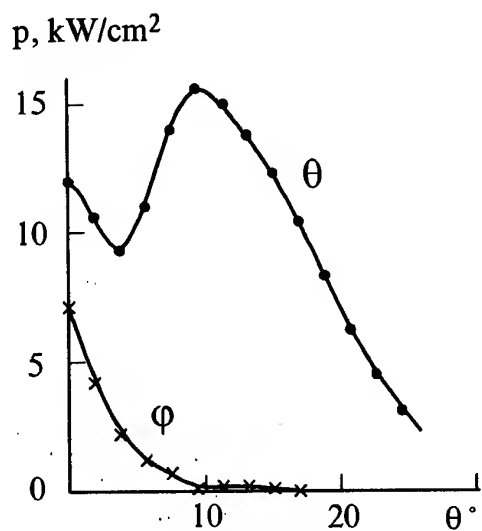
Fig. 5.
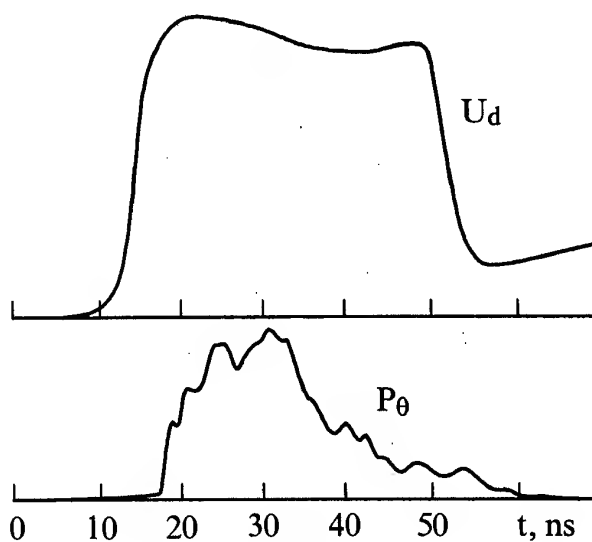
Fig. 6.

CONCLUSION

Beam geometry influence on the lowest mode selection of an overmoded periodic waveguide has been shown experimentally. Ellipsoidal electron beam use allows to obtain linearly polarized radiation without application of special converters. Improvement of electron beam characteristics in MWCG allowed to decrease the part of cross-polarized radiation by a factor of 5 as compared with [1].

REFERENCES

[1] S.P.Bugaev, V.I.Kanavets, V.I.Koshelev, V.A.Popov, A.I.Slepkov, A.F.Fedorov, V.A.Cherepenin. Proc. 7 Inter. Conf. on High Power Particle Beams. 1988. V. 1. P. 454-459.

MWCG WITH BIPERIODIC OUTPUT SECTION

M.P.Deichuly, V.I.Koshelev

High Current Electronics Institute, RAS,
4 Akademichesky Ave., Tomsk, 634055 Russia

ABSTRACT

Multiwave Cerenkov generators (MWCG) with overmoded two-sectional slow-wave structures (SWS) and different geometry of the output section have been investigated. MWCG with biperiodic output section has shown to have a remarkable property, and namely, microwave radiation power more weakly depends on the distance between electron beam and SWS surface than in MWCG with uniform section.

INTRODUCTION

Investigations of overmoded SWS carried out earlier [1, 2] have shown that essential part in the electron beam – electromagnetic field interaction near the π-type of TM_{01}-mode have longitudinal electron-electromagnetic resonances of SCSW – TM_{01}(SCSW is the space charge slow wave). Investigations [3, 4] of MWCG with uniform sections have revealed a determining influence of the drift tube length on the behaviour of electron-electromagnetic resonances and microwave radiation characteristics, and namely, efficiency, stability from pulse to pulse, wavelength, and pattern. The drift tube multifunctionality advantageously distinguishes MWCG from a one-sectional generator. However, simultaneous usage in full measure of all possibilities of the drift tube is a difficult and frequently contradictory task. As the experimental test and numerical simulation analysis have shown [4], application of properties of only one drift tube isn't enough to solve the problems of stable generation at generation efficiency higher than 15%. First of all, it is related to the interaction of longitudinal modes resulting in the phases and amplitudes beating. To solve this problem, it seems to be logical to pass to a generator with nonuniform SWS sections.

The aim of investigations is the search of SWS which should allow to obtain small deviations of microwave radiation parameters when changing electron beam parameters and magnetic field value and should serve as a basic constituent part of more complex microwave generator. Investigation results of three variants of MWCG with the same uniform input sections but different output ones are presented in the given paper. In the first and second variants the output sections are uniform and differ by the period and diaphragm geometry. In the third variant the output section is biperiodic.

RESULTS OF EXPERIMENTAL INVESTIGATIONS

Experimental investigations were carried out at the SINUS-7M accelerator with a voltage pulse length $\tau_p = 40$ ns. Hollow beam diameter $D_b = 2 r_b = 10$-11.8 cm, magnetic field in the SWS region B = 5-15 kG. Radiation power was determined by the pattern with θ-polarization measured in atmosphere. Radiation power losses in a transmitting antenna were not taken into

account. Radiation spectrum was measured by the bandpass filters with a band width of 0.5%.

Fig. 1 presents schematically three variants of two-sectional SWS. In the first sections period $\ell_1 = 1.45$ cm. In the variants with uniform output sections (Fig. 1a, $\ell'_2 = 1.45$ cm; Fig. 1b, $\ell''_2 = 1.4$ cm) diaphragm geometry was chosen so that the frequencies of the upper boundary of TM_{01}-mode passband should be close. In the third variant (Fig. 1c) the output section is formed from the diaphragms of the output sections of the first two SWS variants. The internal diameter of periodic waveguides and drift tube $D = 2R = 13$ cm, the length of the first and second sections are $L_1 = 13\ell_1$ and $L_2 = 10\ell_2$, respectively, the drift tube length $L_{dr} = 9.4$ cm .
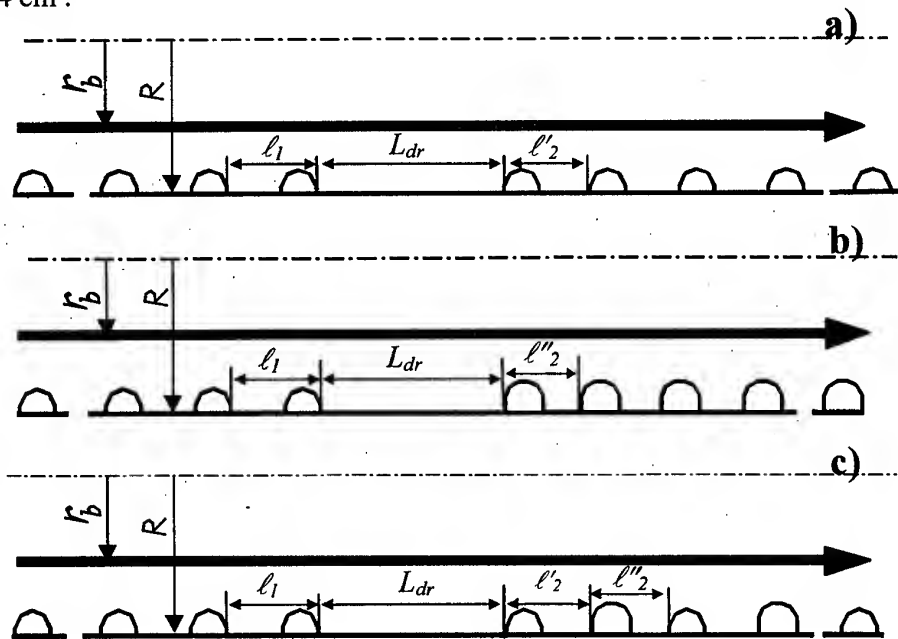
Fig. 1.

MWCG with uniform sections were investigated at two values of the diode voltage (U_d) – 800 kV and 1000 kV. Beam current (I_b) was, respectively, 6.6 kA and 10 kA. Figs. 2 and 3 present, respectively, the dependencies of microwave radiation power on the gap between the beam and SWS surface ($b = R - r_b$) and radiation spectra at $U_d = 800$ kV and $I_b = 6.6$ kA.
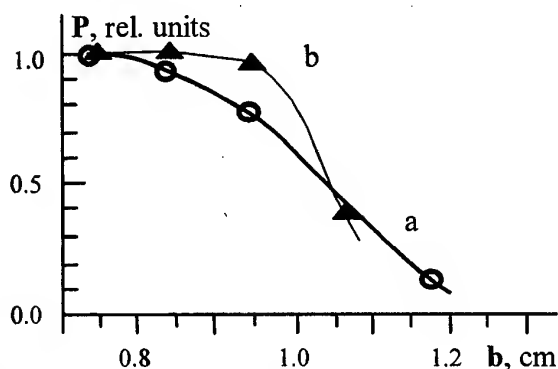
Fig. 2.
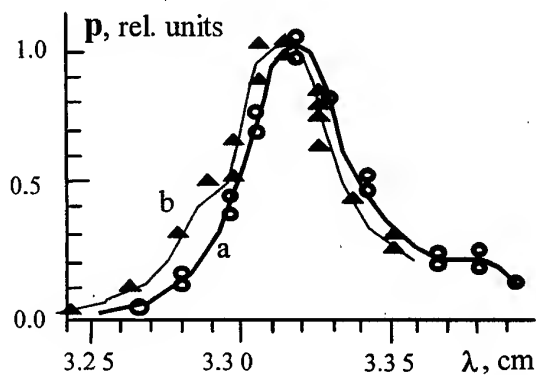
Fig. 3.

Here and below in Figures the curves are designated by the letters corresponding to SWS numbering in Fig. 1. The efficiency of radiation generation in both cases was 6÷8%.

At U_d = 1000 kV and given L_{dr}, the MWCG efficiency with SWS depicted in Fig. 1b decreased to 1÷3%. Strong generation instability from pulse to pulse made difficult measuring of microwave radiation parameters. Figs. 4 and 5 present, respectively, the dependencies of microwave radiation power on the gap between the beam and SWS surface and radiation spectra at U_d = 1000 kA for two other MWCG variants.
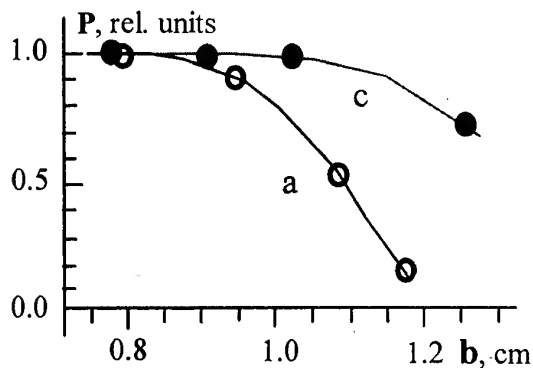
Fig. 4.
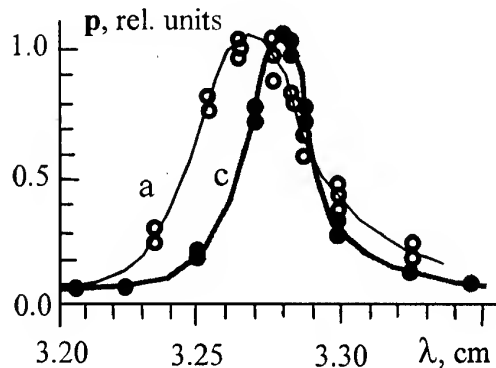
Fig. 5.

Maximum efficiency of MWCG with biperiodic and uniform sections was 7% and 10%, respectively. Microwave radiation pulse duration was limited by the beam current pulse duration.

Fig. 6 presents the MWCG pattern with a biperiodic section. The patterns in all cases had analogous form. Narrow spectrum of microwave radiation (spectrum width at half maximum practically equals to the filter band width) and relatively weak dependence of microwave radiation power on the gap between the beam and SWS surface for MWCG with a biperiodic section attracts attention.
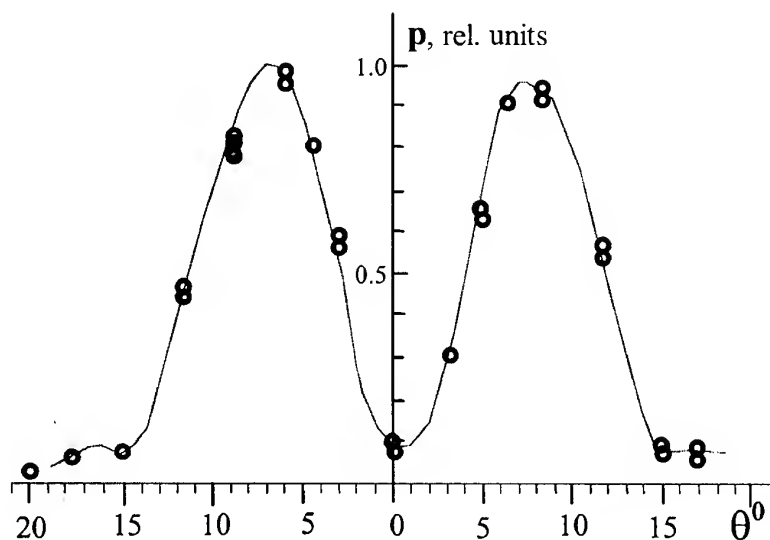
Fig. 6.

Comparison of stable generation regions at the plane (B, b) depicted in Fig. 7 seems to be interesting. Painted region of stable generation ($\Delta P/P < 20\%$) relates to MWCG with uniform sections (Fig. 1a). Shaded region ($\Delta P/P < 20\%$) relates to MWCG with a biperiodic section. In this case instability of microwave radiation power at optimum relation between the gap b and

magnetic field B (line in Fig. 7) was less than 10% at the beam power scattering $\Delta P_b/P_b <$ 20%.
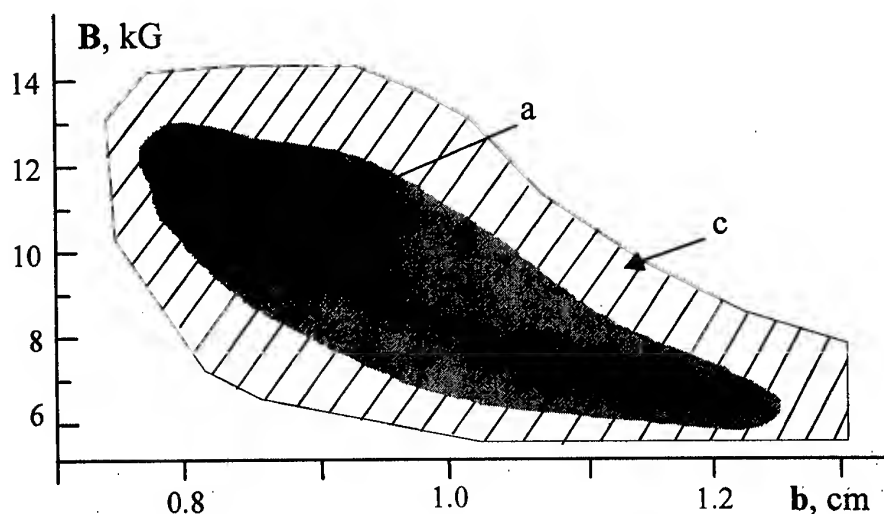
Fig. 7.

CONCLUSION

Application of MWCG with biperiodic output section of a slow-wave structure essentially extends the region of microwave radiation stable generation relative to the changes of electron beam and magnetic field characteristics that is especially important when using high-current electron beams formed in the diodes with explosive-emission cathodes to generate long pulses (> 100 ns) of microwave radiation.

REFERENCES

[1] M.P. Deichuly, V.I. Koshelev, V.I. Pikunov, I.A. Chernyavsky. Radiotekhnika i Elektronika. 1995. V. 40. N9. P. 1440-1449.
[2] M.P. Deichuly, V.I. Koshelev, V.I. Pikunov, I.A. Chernyavsky. Radiotekhnika i Elektronika. 1996. V. 41. N2. P. 228-235.
[3] M.P. Deichuly, V.I. Koshelev, A.A. Petkun. Proc. 11 Inter. Conf. on High Power Particle Beams. 1996. V. I. P .221-224.
[4] V.I. Koshelev, M.P. Deichuly, I.A. Chernyavsky, A.A. Petkun. SPIE Proc. 1997. V. 3158. P .298-307.

HIGH-POWER MICROWAVE GENERATION BY AN AXIAL TRANSIT-TIME OSCILLATOR

J. J. Barroso, K. G. Kostov*, R. A. Corrêa, and I. P. Spassovsky*

Associated Plasma Laboratory
National Institute for Space Research (INPE)
P.O. Box 515, 12201-970 São José dos Campos, SP, Brazil

*On leave from Dept. of General Physics
Sofia University, 5 J. Bourchier Blvd.
Sofia 1126, Bulgaria

Abstract

A description is given of a microwave tube based on the transit-time effect and conditions accounting for its feasibility as a high-power, pulsed microwave source are outlined. The device comprises a temperature-limited diode gun operating at 33-kV cathode voltage and 40-A beam current. As indicated by 2.5D particle-in-cell simulations, a 5.7-GHz single frequency radiation has been generated at the peak-power output level of 100kW.

Introduction

The mechanism by which a stream of electrons crossing a resonant structure transfers energy to cavity's characteristic modes is called a transit-time effect. Without requiring an external magnetic field, perhaps the simplest microwave tube is the transit-time oscillator [1, 2], which consists of a cylindrical cavity with the end plates forming a diode in which propagates a rectilinear electron beam. Early works on transit-time effect date back to the 1930's with a developmental 3-GHz device of 0.25% efficiency [3]. Nevertheless, the transit-time based oscillator can achieve a significant efficiency to be worth considered as an attractive microwave source by virtue of its simplicity, as diode and resonator are combined into a single unit that makes for a compact, lightweight device. Recent advancements in the pulse technology has revived the concept of Transit-Time Oscillator (TTO) as an attractive source of high-power microwaves.

This article deals with computer simulation of an axial transit-time oscillator, which operates without external guiding magnetic field. Fully electromagnetic 2.5D, particle-in-cell computer code KARAT [4] has been used to simulate TTO operation. The device is driven by a coaxial transmission line, whose high-voltage inner electrode serves as the gun cathode. The collector plate is provided by a similar coaxial line from which microwave energy is extracted. The diode runs in the temperature-limited regime and produces a 40-A beam current at 33 kV cathode voltage. The device is designed to operate at 5.74GHz in the lowest order TM_{010} cavity mode. The chosen mode and frequency are arbitrary and design at other modes and frequencies are likely achievable. Peak output power of 100 kW, which translates into a 7.5% beam to microwave power conversion efficiency, is obtained.

Numerical Simulation

Fig. 1 shows the elements of the oscillator, which, besides its mechanical simplicity, has circular symmetry for easy machining and assembly. From the cathode, the electrons are accelerated through the diode gap and then collected at the anode to the right.
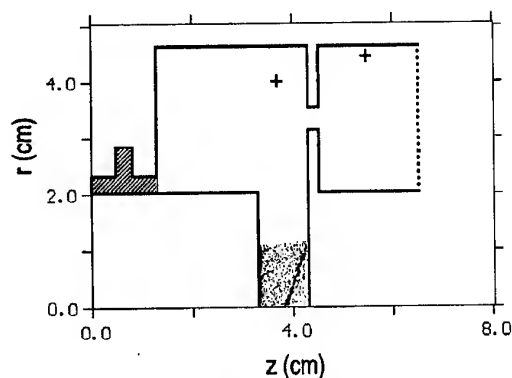
Fig. 1. Simulation setup.
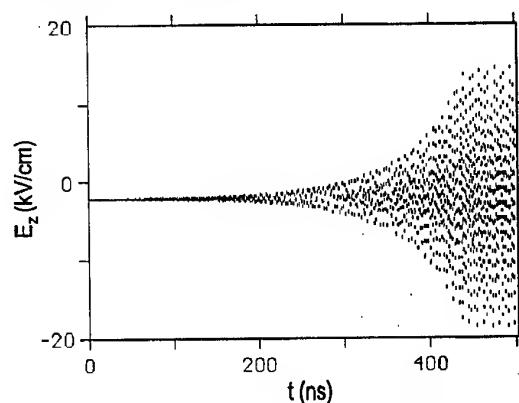
Fig. 2. Time history of the RF field

The annular aperture in Fig. 1 couples the intermediate cavity into the output coaxial line of characteristic impedance $Z_0 = 60 \ln R_w/R_c = 50\Omega$ that guides the radiation out of the oscillator.

For insulation purposes, at the left of Fig. 1 is a structure filled with dielectric material and composed of a radial line connected to a short-circuited coaxial line. The outer conductor of the coaxial line is interrupted by the radial line whose external radius is properly determined such as with the given cathode radius R_c=2.0cm and the operating wavelength, the radial line has zero input impedance seen from the coaxial line [5] . At the same time, the coaxial line is made a half-wavelength long (measured in the dielectric medium with relative permittivity $\varepsilon_r = 4$), and hence the input impedance seen looking toward the short-circuited termination at $z = 0$, is zero, so that the gap in the cavity end wall appears as a perfect conducting surface at the RF operating frequency, but is open circuit at DC.
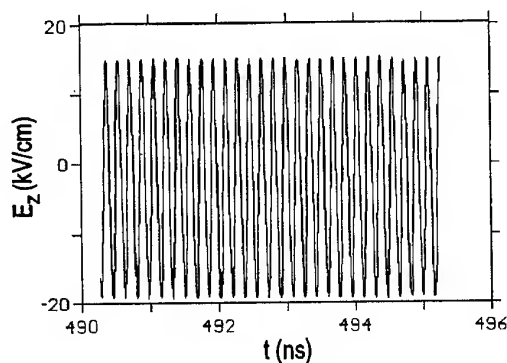
Fig. 3(a). Time variation of electric field
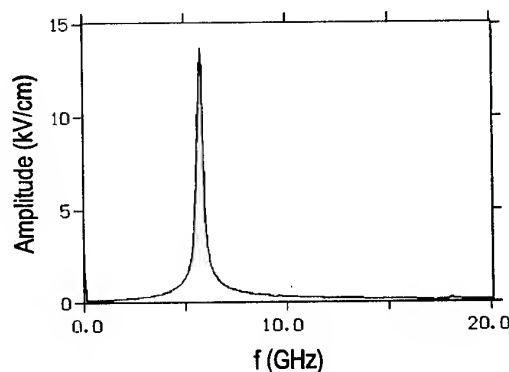
Fig. 3(b). Spectrum of the electric field

In the simulation of the transit-time oscillator operation, square cells of 1mm in size have been used with over one thousand particles representing the 40-A electron beam, whose configuration space is shown in Fig. 1. This plot is a snapshot at time t=470ns when the beam has become density-modulated so that RF currents are induced on the cavity walls to sustain the oscillations. The RF fields have started to grow after a time span of 200ns as indicated in Fig. 2, that displays the time history of the electric field at the observation point z=3.8cm, R=4.0cm

lying on the mid plane of the diode gap. We can see that, apart from a 2.0kV/cm shift from the origin due to the cathode voltage, the RF field has reached the steady-state regime at around t=450ns with a peak value of 14.0kV/cm. More detailed information about the axial electric field is provided by Fig. 3(a) which shows the field time variation over the interval 490-495ns; it is clearly seen that the signal oscillates with constant amplitude and at the frequency of 5.7GHz as evidenced by Fig. 3(b).
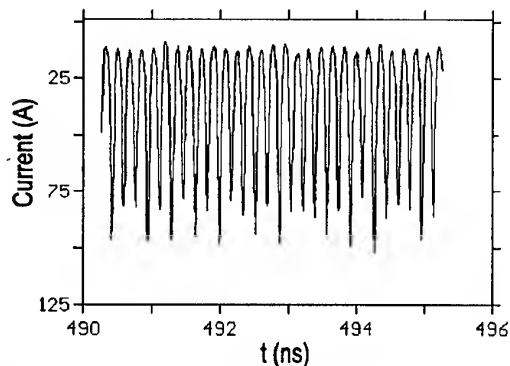
Fig.4(a). Time plot of total beam current
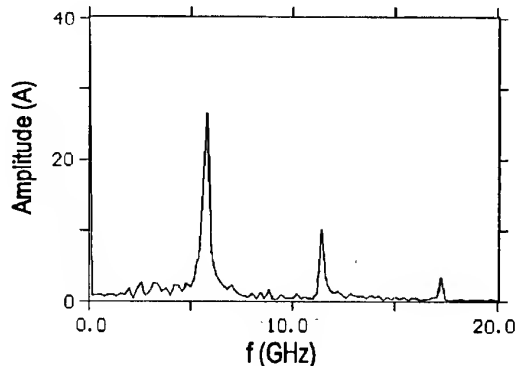
Fig.4(b). Fourier spectrum of the current

The time plot of the beam current crossing the section at z=3.8cm in the steady-state regime is given in Fig. 4(a), and when Fourier analyzed its spectrum shows up to three harmonics present (Fig. 4(b)), with the amplitude (27.0A) of the fundamental component being comparable to the 40-A DC beam current.
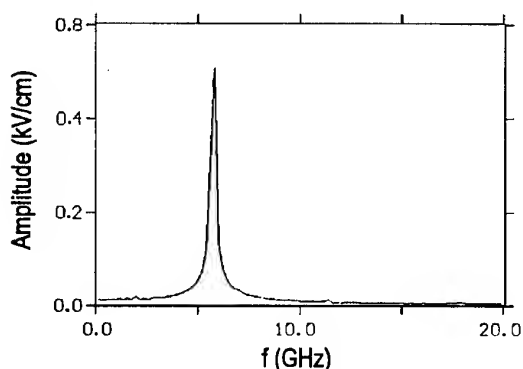
Fig.5 Frequency spectrum in TEM guide
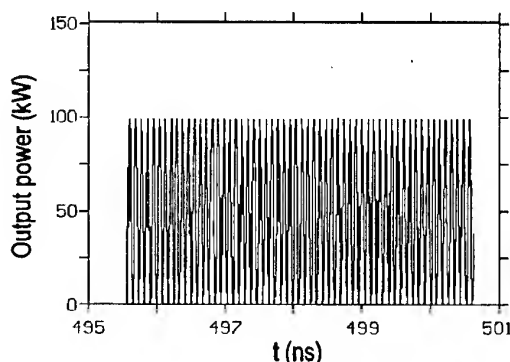
Fig.6. Time plot of the output RF power

As for the radiation that leaks into the output TEM guide through the annular aperture, is in Fig. 5 the spectrum of the radial electric field at the point z=6.0cm, r=4.5cm. The spectrum has a sharp peak of 0.7kV/cm in amplitude centered at 5.7GHz. The corresponding output power (Fig. 6) is obtained by integration of the Poynting flux across the section at z=6.0cm of the outlet. First we note in Fig. 6 that the pulsating power is always positive, implying that the output signal is a pure traveling wave that propagates to the right. We can see also that within a 1ns interval there exist twelve peaks, twice as much as in the time plots of the electric (Fig. 3(a)) fields. This corresponds to two pulses per period, as expected from the Poynting vector calculation involving the cross product $E \times B$.

Finally, we should mention that the 33.0kV accelerating voltage used has been indicated by a preliminary parameterization study, as long as at lower voltages the peak output power has been less than 100kW and at $V_0 \geq 34kV$ no emission has been observed after a sufficiently long

running time.

Conclusions

We have devised a single-frequency oscillator that comprises a temperature-limited diode gun operating at 33kV cathode voltage and 40A beam current. The diode gap acts as a mode resonator that excites an intermediate coaxial TM_{010} cavity, which in turn is coupled by an annular aperture to an output TEM coaxial guide having characteristic impedance of 50Ω.

On the basis of 2.5D particle-in-cell simulations, the device has produced an output peak power of 100kW which translates into a DC to RF power conversion efficiency of 7.5%. Oscillations reach the steady-state regime on a time scale of a few hundreds of microseconds after the beam has become density-modulated in high-voltage gap, where RF electric field intensities of 65kV/cm have been noticed. However, this is far below the Kilpatrick limit [6] for electrical vacuum breakdown at short wavelength which predicts according to $E_{br} = 2.5 \times 10^2 \sqrt{f(\text{GHz})}$ a maximum electric field of 6.0×10^2 kV/cm at 5.7GHz.

The device, rugged from both a mechanical and thermal standpoint, has a simple structure with cylindrical symmetry for easy machining and assembly. The peak power density of 420kW/cm^2 restrains the oscillator from operating in CW regime, since this value far exceeds the limit of 3kW/cm^2 for presently available cooling techniques. Nevertheless, for a pulse duration τ_p=10μs and repetition frequency of 250Hz the average ohmic heating density on the anode inner surface reaches the acceptable value of 1.0kW/cm^2. For OFHC copper, the corresponding temperature rise during the application of the pulse can be estimated by [7] $\Delta T(^{\circ}C) = 0.3P_s(\text{W/cm}^2)\sqrt{\tau_p(\text{s})}$, where P_s is the peak power density at surface, giving 400°C. As for the emission density, the cathode should operate at a current density of 13.0A/cm^2, for which an efficient pulsed thermionic emitter can fulfill this requirement.

Acknowledgment

References

[1] A. B. Brownwell and R. E. Beam, *Theory and Application of Microwaves*, New York: McGraw-Hill 1947, Sec. 4.03.

[2] C. H. Birdsall and W. B. Bridges, *Electron Dynamics of Diode Regions*, New York: Academic Press, 1966, Sec. 1.06.

[3] F. B. Llewellyn and A. E. Bowen, "The production of ultrahigh frequency oscillator by means of diodes", *Bell System Technical Journal*, vol. 18, pp. 280-284, 1939.

[4] V. P. Tarakanov, *"User's Manual for Code KARAT"* 1994, Berkeley Research Associates, Inc., Springfield, VA, USA.

[5] S. Ramo, J. R. Whinnery, and T. van Duzer, *Fileds and Waves in Communication Electronics*, New York: John Wiley & Sons, Inc., 1965, Sec. 8.12.

[6] G. S. Nusinovich, T. M. Antonsen Jr., V. L. Bratman, and N. S. Ginzburg, *"Applications of High-Power Microwaves"*, Ed. by A. V. Gaponov-Grekhov and V. L. Granatstein, Boston: Artech House, 1994, Chapter 2.

[7] G. B. Collins, *"Microwave Magnetrons"*, (M.I.T. Radiation Laboratory Series, vol. 6), New York: McGraw-Hill, 1948, Sec. 12.6.

NUMERICAL SIMULATION AND EXPERIMENTAL STUDY OF THE HELICAL ELECTRON BEAMS OF 170 GHZ/1MW GYROTRONS

A.N.Kuftin, V.K.Lygin, A.S.Postnikova, V.E.Zapevalov

*Institute of Applied Physics Russian Academy of Sciences,
46 Ulyanov Street, 603600 Nizhny Novgorod, Russia*

ABSTRACT

The report presents the results of the numerical simulation and experimental study of the helical electron beams (HEB) formed in magnetron-injection guns of 170 GHz/1MW gyrotrons. The dependence of HEB parameters on the beam current is analyzed. The evolution of the transverse velocity distribution functions is traced at the variation of the beam current.

INTRODUCTION

High quality helical electron beams with required parameters is one of the main problem for the creating of powerful high efficiency 170 GHz gyrotrons for ITER. For example achievement of 1MW output power of gyrotron with an operating voltage U =80 kV and the efficiency $\approx$ 35 % or more is required to a beam with a current I $\approx$40 A and a pitch-factor g $\approx$1.25 or higher (g = $v_\perp$ /v_z , $v_\perp$, v_z -oscillatory and longitudinal velocity in operating space). Thus a magnetron-injection gun (MIG) should provide formation of a such beam.

The specified restrictions were accepted in attention at account of particular guns for gyrotrons with different working mode. The results of four possible versions of guns with different radiuses of cathodes R_c are presented. The design parameters are summarized in Table 1.

Table 1: Main parameters of 170 GHz/1 MW/CW gyrotrons

Operating mode	$TE_{28.7}$	$TE_{31.8}$	$TE_{25.7}$	$TE_{25.10}$
Output power, MW	1.0	1.0	0.5-0.8	0.7-1.0
Accelerating voltage, kV	80	80	80	80
Maximum beam current, A	45	45	45	45
Voltage depression at resonator center (40A), kV	5.12	5.29	5.47	6.95
Resonator radius, mm	15.86	17.9	14.84	17.77
Mean beam radius in resonator, mm	8.26	9.13	7.4	7.4
Radius of the cathode R_c, mm	45.2, (47.5)	50, (51)	41.5	41.5
Electrical field on the cathode Ec, kV/mm	6.3, (5.6)	6.3, (5.8)	5.8	5.8
Pitch-factor	1.25	1.25	1.25	1.25

NUMERICAL SIMULATION

The results of a new numerical simulation procedure and experimental data for the basic types of beams are presented. For each beam type the dependencies $t_\perp$ and $\delta v_\perp$ on the beam current, including results, received in the model with finite initial velocities are received. It was found, that there are the small devergenses between the data obtained from numerical simulation at the total formation length and the ones find out from calculation in the cathode region only. The received distinctions are caused by different value of the beam potential, used at the finding $t_\perp$ and $\delta v_\perp$. According to results of the trajectory analysis, the value of the beam voltage depression is rather close to the theoretical estimations [1]. Evolution of $f(v_\perp)$ for each beam type along the formation region and when the current grows is traced.

The allowable value of radius of the cathode for a chosen operating mode is defined by the value of an acceptable electrical field on the cathode E_c, which, as a rule, is necessary not above than 6 kV/mm. Width of the emitter is selected with the account of extreme allowable density of an emission current (usually it is not recommended to exceed 3 A/cm^2). At selection of an optimum configuration of electrodes the value of velocity spread $\delta v_\perp$ was not allowed above than 30 %. The specified restrictions were taking into account of particular guns for gyrotrons with different operating modes. Then from numerical simulation dependencies $\delta v_\perp(I)$ and $t_\perp(I)$ for each gun were received. Calculations were performed as using model with zero initial velocities (EPOSR [2]) as taking into account initial velocities (EPOS-V [3]). Evolution of transverse velocity distribution function $f(v_\perp)$ is traced with a beam current growth. The sensitivity of the beam parameters to influence of thermal deformations of a gun and possible technological errors is investigated. The transformation of distribution function $f(v_\perp)$ can serve one of attributes of loss of beam stability [4]. In considered guns infringement unimodality of oscillatory velocity distribution function is not registered at currents of a beam, even exceeding design value of the current (I=40A). The specified circumstance allows to hope, that offered MIG will provide formation of a stable beam with acceptable parameters.

For the operating mode TE$_{31,8}$ in the frame of limitations on an electrical field E_c, optimum radius of the cathode R_c =51mm. Thus on the cathode $E_c \approx 5.8$ kV/mm. For gyrotron with an operating mode TE$_{28,7}$ two versions of guns with different radiuses of cathode were designed. In the first version a gun with R_c =45.2mm was used. The necessary g value need an increased electrical field on the cathode $E_c \approx 6.3$ kV/mm. In the second variant the reduction E_c to 5.5-5.7 kV/mm was reached by using of the cathode with increased average emitter radius (R_c =47.5mm). Finally for the operating mode TE$_{25,10}$ R_c =41.5 mm was chosen. For all gun variants dependencies $\delta v_\perp(I)$ and $t_\perp(I)$ and evolution $f(v_\perp)$ are investigated (Fig.1-Fig.4), and at presence of the disturbances factors.
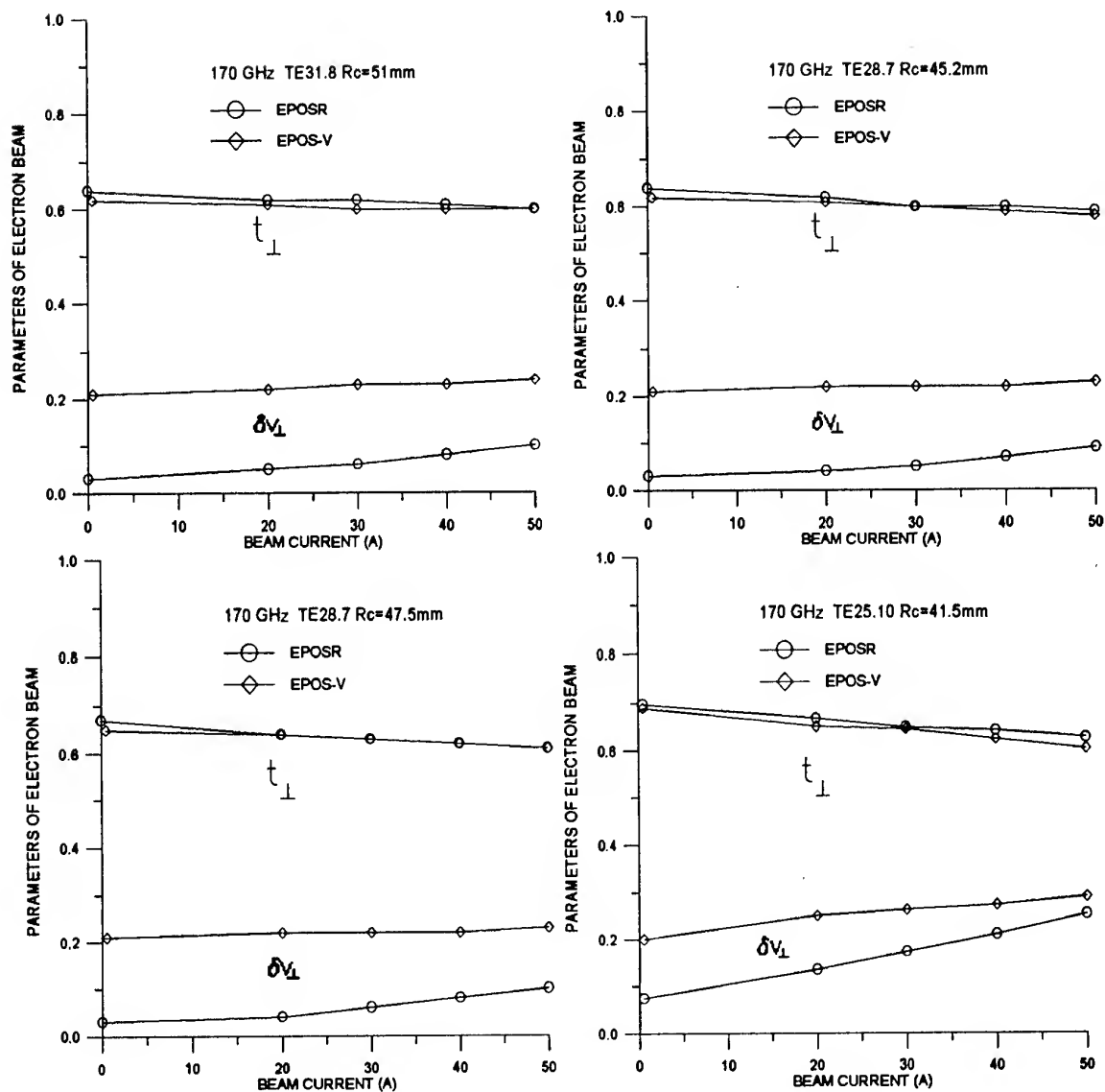
Fig.1-Fig.4. Velocity spread $\delta V_\perp$ and oscillatory energy of electrons $t_\perp$ as a function of beam current.

EXPERIMENTAL RESEACH

The measurements were carried out for guns with R_c =45.2mm and R_c=41.5mm by the modified method of the retarding field in the scale down regime [5] at the automated experimental set up [6]. Beams with caught electrons are compared with beams, in which these electrons are intercepted by a special additional diaphragm. HEB formed in such conditions we shall name "primary beam". Besides knowledge of the characteristics even for a primary beam allows to predict real beam stability and stability of gyrotron operation in oscillation regimes, when reflected electrons take places. A beam, which is measured without interception of reflected electrons, we shall name "resulting beam". Below we will mark for simplicity resulting beam measurements as 1D regime, and primary beam measurements as 2D regime.The velocity spread, average oscillatory energy and oscillatory velocity distribution function dependencies on the beam parameters were traced (Fig.5-Fig.8). The received dependencies $\delta v_\perp$ and $t_\perp$ are compared with results of numerical simulation and good correlation is observed.
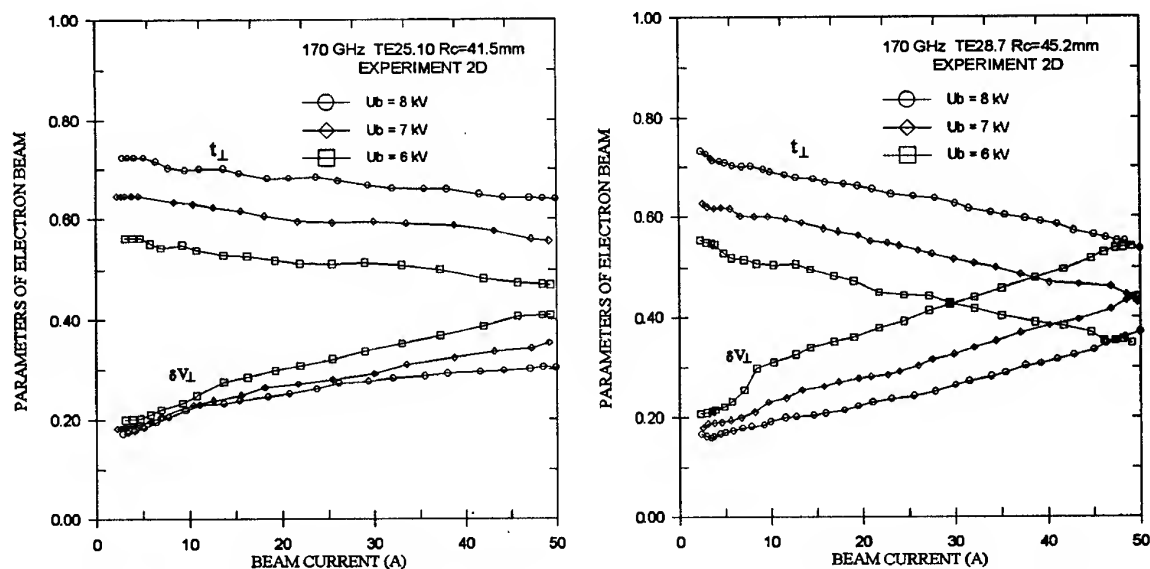
Fig.5-Fig.6. Velocity spread $\delta V_\perp$ and oscillatory energy of electrons $t_\perp$ as a function of beam current.
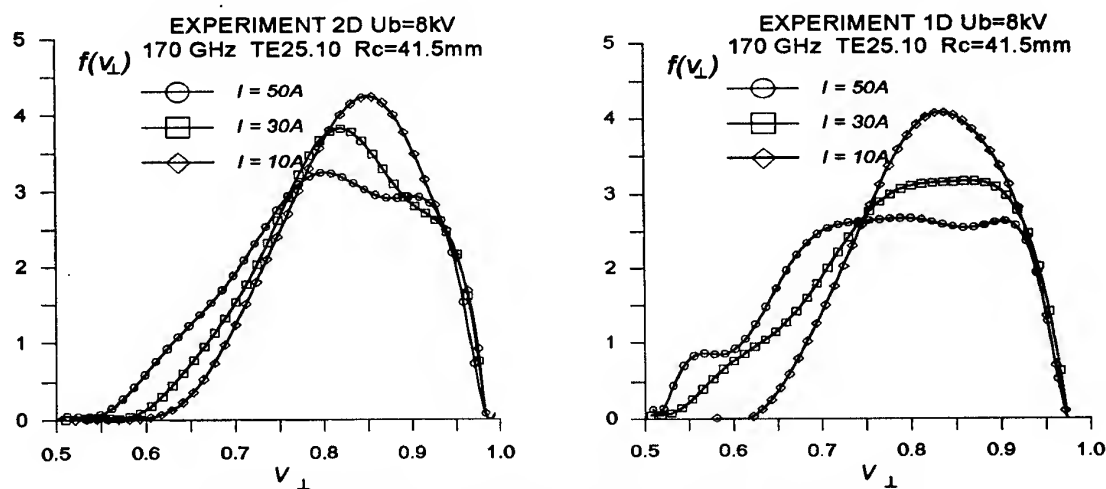
Fig.7-Fig.8. Oscillatory velocity distribution functions at various currents.

CONCLUSION

Methods of numerical simulation and experimental research of HEB were developed. HEBs properties including the electron distribution functions over transverse velocities were studied numerically and experimentally in various regimes. In result of numerical simulation and series of experiments an electron gun, ensuring formation of an electron beam with parameters, necessary for 170 GHz/1MW gyrotron, is created.

REFERENCES

[1] Tsimring Sh.E. . Int. J. of Infrared and MM waves, v.14, n.4, p.817, 1993.

[2] Lygin V.K., Manuilov V.N., Tsimring Sh.E. Elektron. tekhnika, ser.1,Electronika SVCH, n.7,p.38, 1987.

[3] Lygin V.K. Int. J. of Infrared and MM waves, v.16, n.2, p.363, 1995.

[4] Flyagin V.A., Goldenberg A.L., and Zapevalov V.E. Conference Digest, 18th Int. Conf. on Infrared and Millimeter Waves, University of Essex, Colchester, UK, v.2104 , p.581, 1993.

[5] A.L.Gol'denberg, E.G.Avdoshin. Izvestiya Vysshikh Uchebnykh Zavedenii, Radiofizika, 16(1973), p.1605.

[6] A.N.Kuftin, et al. Digest of 21nd Int. Conf. On IR and MM Waves, p.188,1997.

EXPERIMENTAL STUDY OF TRAPPED ELECTRONS INFLUENCE ON THE HELICAL ELECTRON BEAM PARAMETERS FOR MILLIMETER WAVE RANGE GYROTRONS

A.N.Kuftin, V.E.Zapevalov

*Institute of Applied Physics Russian Academy of Sciences,
46 Ulyanov Street, 603600 Nizhny Novgorod, Russia*

ABSTRACT

The basic properties (velocity spread, average oscillatory energy and oscillatory velocity distribution function) of helical electron beams (HEB) formed in the magnetron -injection gun (MIG) of powerful millimeter wave range gyrotrons are investigated experimentally at the presence of electrons, reflected by the magnetic mirror and locked in adiabatic trap. Guns for 83GHz, 110GHz, 140GHz and 170GHz, 1 MW power level gyrotrons, forming quasilaminar, regularly intersecting, mixed and boundary HEB (between quasilaminar and regularly inter-secting HEB) are considered. The results of the experiments show that the trapped electrons significantly affect the beam parameters.

INTRODUCTION

In the magnetron-injection gun (MIG) of the powerful gyrotrons, which form helical electron beams (HEB), a portion of electrons acquired in the gun the surplus oscillatory energy owing to the velocity spread, appears to be caught in the adiabatic trap. It was mentioned [1], that the trapped electrons are the main factor that lead to electron flow instability. The trapped electrons' effect on the helical beam parameters for the case of stable beams was considered theoretically [2] and studied experimentally in centimeter wave range gyrotrons HEBs [3]. In [3] it was noted that the transition to more short-wave gyrotrons having a relatively small Langmuir radius and the trajectory step in the near-cathode region, should, facilitate the improvement of the HEBs quality. In this case, one should expect attenuation of the trapped electrons' phasing and, consequently, their influence on the velocity spread $\delta v_\perp$ and relative oscillatory energy $t_\perp$.

Parameters of HEBs can be different when the operating frequency changes and other conditions stay the same, due to variation of mirror ratio- α ($\alpha = B_o / B_c$, where B_o and B_c- are magnetic fields in the operating space and at the cathode, respectively). According to the adiabatic theory this coefficient α will be growing and average velocity falling in higher-frequency ranges at the same other conditions [1,4]. Therefore, at the same $t_\perp$ one should expect growth of relative initial velocity spread and, respectively, a greater share of the trapped and reflected electrons in the beam.

Below, the basic properties of helical electron beams (HEB) of a millimeter wave range gyrotrons are investigated experimentally at the presence of electrons, reflected by the magnetic mirror and locked in adiabatic trap. Guns for, 83GHz, 110GHz, 140GHz and 170GHz, 1 MW power level gyrotrons, forming HEB with the different topology are considered. Some results of the experiments, aimed at ascertaining the character of the trapped particles effect on the parameters of the millimeter wave range gyrotrons are given.

MEASUREMENTS

The measurements were carried out by the modified method of the retarding field in the scale down regime [3] at the automated experimental set up [4]. Beams with trapped electrons - "resulting beam" (or 1D regime) are compared with beams, in which these electrons are intercepted by a special additional diaphragm - "primary beam" (or 2D regime). Experimental MIG emitters are manufactured on LaB6 and therefore are high-temperature ones.

Scaled regimes are used, during which the magnetic field, voltage and current decrease in comparison with the operating values, according to the scaling relations which guarantee the invariability of the forms of trajectories. The relative velocity spread $\delta v_{\perp}$, relative oscillatory energy $t_{\perp}$, function of distribution electron on oscillatory velocities $f(v_n)$ changing with the beam current grow are traced.

EXPERIMENTAL RESULTS

a) MIG for 83 GHz gyrotron, $\alpha = 19$

The measurements were carried out for 83 GHz gyrotron guns [4]. in a scale down regime on automated installation described above. According to [4] HEB parameters depend significantly on HEB topology. Guns forming mixed (irregularly intersecting), regularly intersecting, boundary (between quasilaminar and regularly crossed HEB) and quasilaminar HEB are considered.
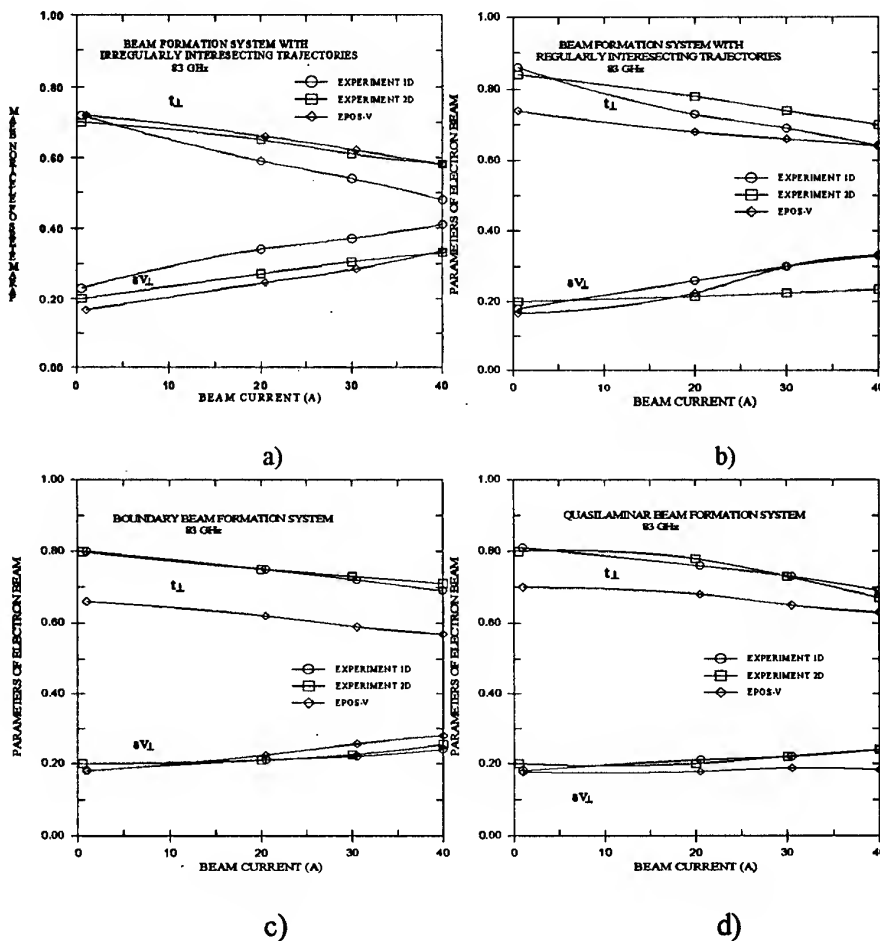
Figure 1. The relative oscillatory energy $t_{\perp}$ and the velocity spread $\delta v_{\perp}$ as the beam current functions.

In Fig. 1a-1d the 1D-marked lines show the average relative oscillatory energy $t_\perp$ and the oscillatory velocities spread $\delta v_\perp$ in MIGs with different beam topology [6], as functions of the beam current in the 1D case. The characteristics of the MIG substantially acquire another form in the 2D case - fig. 1a-1d. It is seen that the dependence become different but not in the great degree as [3], the velocity spread decreases and the oscillatory energy increases. Unlike the previous case, the changing of values $\delta v_\perp$ and $t_\perp$ satisfactorily agrees with the results of the trajectory analysis performed without taking into account reflected electrons (see [4,6]).

b) MIG for 110 GHz gyrotron, $\alpha = 25$

For 110 GHz gyrotron guns forming boundary and quasilaminar HEB[8]were also investigated in 1D and 2D regimes. The attributes of the MIG primary beam acquire another form in 1D-regime compare with 2D case. It is seen that the dependence become a little bit different, the velocity spread decreases and the oscillatory energy increases. The changing of values $\delta v_\perp$ and $t_\perp$ satisfactorily agrees with the results of the trajectory analysis.

c) MIG for 140 GHz gyrotron, $\alpha = 28$

For 140 GHz gyrotron guns forming boundary and quasilaminar HEB[8], were also investigated in 1D and 2D regimes and dependencies of the average relative oscillatory energy $t_\perp$ and the oscillatory velocities spread $\delta v_\perp$ as functions of the beam current were received. The velocity spread dependence $\delta v_\perp$ (I) of the MIG primary beam get another form for quasilaminar HEB, and practically the same for boundary one. It is seen that the oscillatory energy $t_\perp$ (I) dependence have no changes for both HEB topology. Like the previous case, the change of values $\delta v_\perp$ and $t_\perp$ satisfactorily agrees with the results of the trajectory analysis. More detail information on electron beam property are included at the electron distribution function in the oscillatory velocities $f(v_\perp)$ [6,9]. Evolution of the $f(v_\perp)$ as the beam current grows has been traced. For 140 GHz gyrotron gun with current 10, 30, and 50A. Fig.2.a,b presents such $f(v_\perp)$ functions for the primary boundary beam and resulting one respectively. The distribution functions even for the relatively small beam current 10A have the Gaussian like shape in the 2D case only. When the beam current grows the $f(v_\perp)$ shape becomes more wide, especially for resulting beams. Even at the 50 A beam current the distribution functions have no tendency to get additional maximum.
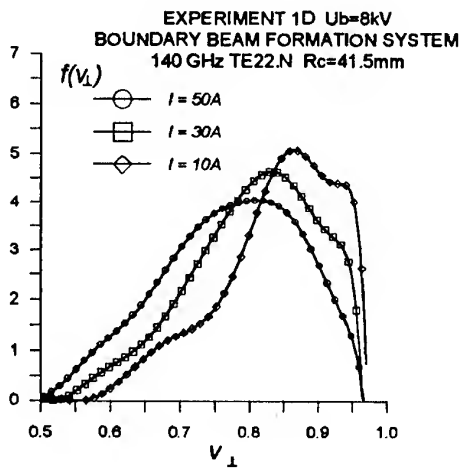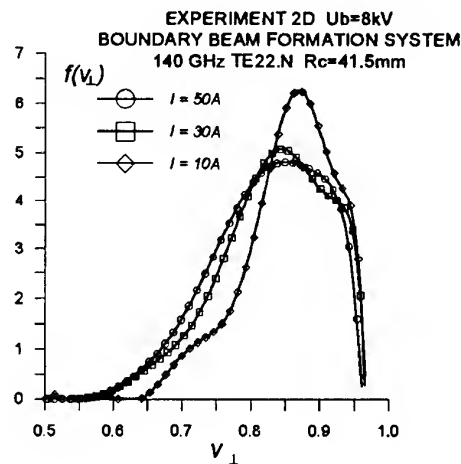
a)   b)

Figure 2. The electron distribution function upon the oscillatory velocities.

Two version of the 170 GHz gyrotron guns (for TE $_{25.10}$ and TE $_{28.7}$ operating modes [10]) forming boundary HEB also are considered:

d) MIG for 170 GHz gyrotron, $\alpha=31.5$

The average relative oscillatory energy $t_\perp$ and the oscillatory velocities spread $\delta v_\perp$ in MIGs with. Rc=41.5mm (for TE $_{25.10}$ operating mode), as functions of the beam current were investigated in 1D and 2D regimes. The characteristics of the MIG substantially acquire another form in the 1D regime compare with the case 2D regime. It is seen that the dependence become different, the velocity spread decreases and the $t_\perp$ increases in the 2D regime. $f(v_\perp)$ functions for the 170 GHz TE $_{25.10}$ gyrotron gun primary and resulting beams with currents 10, 30 and 50A were studied. The distribution functions for the beam current 10A have the Gaussian like shape in both the 1D and 2D cases. When the beam current grows the $f(v_\perp)$ shape becomes more wide and flat-headed, especially for resulting beams. Only at the 50 A beam current the distribution functions have a tendency to get additional maximum.

e) MIG for 170 GHz gyrotron, $\alpha=30$

MIG for 170 GHz gyrotron, with. Rc=45.2mm (for TE $_{28.7}$ operating mode)[10], demonstrates practically the same behavior as the previous one.

In all the investigated cases, the beam corresponds the operating current value does not lose its stability. We may state that, in spite of the considerable influence of the reflected electrons on the velocity distribution of helical beams, there is a mechanism of particle removal from the trap that does not disturb HEB stability.

CONCLUSIONS

The results of experiment in the wide mirror ratio interval show essential influence trapped electrons on parameters of a millimeter wave range gyrotrons HEB. The interception of the reflected electrons decreases the velocity spread. The beam parameters with the excluded trapped electrons satisfactory agree with the calculated ones obtained from the trajectory analysis. Attenuation of the trapped influence on the velocity spread and $t_\perp$ of millimeter wave range gyrotrons beam compare centimeter one are shown.

ACKNOWLEDGMENT

REFERENCES

[1] Sh.E.Tsimring, Lectures on Microwave Electronics at the Third Winter Workshop -Seminar for Engineers. Book 4, p.3, Saratov, Sar. State University, (1974).
[2] V.E.Zapevalov, V.N.Manuilov, Sh.E.Tsimring Izvestiya VUZov, Radiofizika, 33 (1990), p.1406.
[3] Sh.E.Tsimring, V.E.Zapevalov, Int. J. Electronics, 81, No2, (1996), p.199.
[4] A.N.Kuftin et al, Int. J. Electronics, 72, (1992), p.1145.
[5] Tsimring Sh.E. 1972, Izvestiya Vysshikh Uchebnykh Zavedenii, Radiofizika, 15(8), 1247-1259
[6] Lygin V.K. 1995, Int. J. Infrared and Millimeter Waves, 16, 363-376..
[7] Denisov G.G., Kuftin A.N., Maligin V.I. et al. 1992, Int. J. Electronics, 72(5-6), 1079.
[8] V.E. Mjasnikov et al.,. Conf. Proc. 21 Int. Conf. on IR & MM waves., Berlin, Germany, 1996, PP. ATH1
[9] Antakov I.I., Ginzburg V.A., Zasypkin E.V. and Sokolov E.V. 1975, Izvestiya Vysshikh Uchebnykh Zavedenii, Radiofizika, 18(8), 1196-1200
[10] V.E.Zapevalov et al.,. Conf. Proc. 22 Int. Conf. on IR & MM waves. Wintergreen, USA. pp. 108-109., (1997).

INVESTIGATION OF SMALL--DIMENSIONAL MAGNETRON SECONDARY EMISSION GUNS WITH EXTERNAL TRIGGERING[1]

M.I. Ayzatsky, A.N. Dovbnya, P.I. Gladkich, V.V. Zakutin, V.A. Kushnir,
V.V. Mitrochenko, V.F. Pokas, N.G. Reshetn'yak, V.P. Romas'ko, Yu.D. Tur

*National Science Center, Kharkov Institute of Physics & Technology,
1 Academicheskaya st., Kharkov, 310108, Ukraine*

ABSTRACT

The investigation of beam generation in magnetron guns with small anode-cathode gap has been carried out. The main attention was paid to study of an initial stage of space charge arising and providing steady-state regime of secondary emission multiplication.

INTRODUCTION

The problem of pulse and average capacity raise of UHF source, increase of their durability is closely connected to development of electron guns with unheating cathode [1-4]. As known, magnetron gun, cold secondary emissive metal cathode to be used in, is characterized by long lifetime [2] and high density [4-6] emission of electrons from the cathode, by relative simplicity of its design and can be used for decision of this problem. Besides that the magnetron gun with secondary emissive cathode take an interest for creation of the electron guns for accelerators [7] and high-speed high-voltage pulse engineering [8]. Despite of all these advantages there is insufficient quantity of both experimental and theoretical works to explain some effects connected with beam generation. Particularly, the question on conditions and time of spatial charge accumulation [9, 10] is one of the poorly investigated.

EXPERIMENTAL INSTALLATION

The present work is devoted to an experimental research of beams formation and their parameters measurement with nanosecond times of a starting pulse recession, numerical modeling of electrons trajectories in magnetron guns with secondary emissive process start by recession of voltage pulse from the external generator. Experiments were carried out at the installation which circuit is shown in fig. 1. The gun supplies from the modulator that forms a rectangular voltage pulse with amplitude of 4 -- 100 kV, pulse duration of 2 -- 10 μs, pulses frequency of 10 -- 50 Hz. The pulse of negative polarity gives to the cathode 3 of the gun. Anode 4 of the gun is grounded.

The external pulse generator 2 with voltage amplitude of 1.5 -- 15 kV and duration of recession from 1.5 up to 70 ns was used to start the secondary emissive process. It allowed to change a steepness of voltage recession from 50 up to 1500 kV/μs. The magnetic field was formed by the solenoid 4 with magnetic field intensity up to 3000 G and heterogeneity of ~±8% in the longitudinal direction. Fig. 2 shows the distribution of

---

magnetic field intensity along the solenoid axis, the arrangement of magnetron gun and Faraday cup. The measurement of beam current was made with the help of the Faraday cup 7 and resistor R4 and sizes of the beam - with the help of imprint on a x-ray film and on Mo foil.
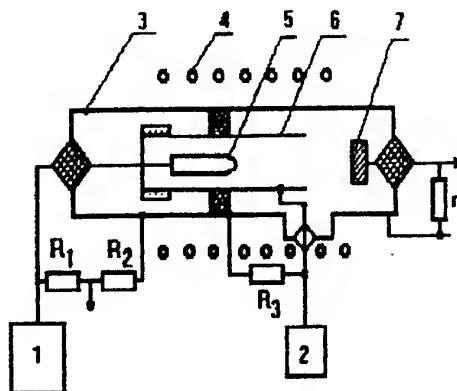
Fig. 1 - Experimental installation circuit.
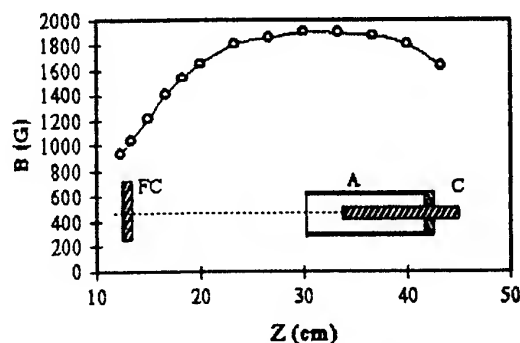
Fig. 2 - Distribution of magnetic field along the solenoid axis and gun arrangement (FC - Faraday cup, A - anode, C - cathode).

RESULTS AND THEIR DISCUSSION

The parameters dependence of electron beam from the geometrical sizes of the gun were investigated within the limits of change of the cathode and anode diameters 1 -- 3 mm and 5 -- 14 mm, respectively (gun length -- 100 mm). The researches have shown that the start of the gun occurs only at recession of starting pulse. The current could be generated in the various moments of time on the voltage pulse plateau by changing the beginning moment of secondary emission start. Fig. 3 shows typical oscillograms of voltage pulses on the cathode, pulse of secondary emission start and current of the beam from the Faraday cup. The measurement of beam's current dependence from the steepness of recession has shown that the dependence has threshold character. So, the start of the magnetron gun (cathode and anode diameters are 2 mm and 7 mm, respectively) with the cathode voltage ~ 7 kV occurred only with the steepness of recession more than 1000 kV/μs (voltage amplitude of starting pulse ~ 2.4 kV, duration of recession ~ 2 ns). The electron beam with the current of ~ 2 A was received with the minimal meaning of cathode voltage ~ 7 kV and magnetic field ~ 3000 G.

The generation of beam with the minimal voltage on the cathode of 5 kV occurs with the minimal steepness of recession of 300 kV/μs (voltage amplitude of starting pulse is 4 kV, duration of recession is 13 ns) at magnetron gun start with other geometry (cathode and anode diameters are 2 mm and 10 mm, respectively).

Thus, the current of the electron beam 0.7 -- 0.9 A was received with the magnetic field of about 1900 G.

The received experimental results show, that in the first case the electronic beam arises through ~ 1.5 -- 2 ns and in second one through ~ 10 ns after amplitude recession of start pulse. It was also observed on downloading of voltage pulse on the cathode (see fig. 3). Thus the temporary instability of the beam's current pulse beginning does not exceed the duration of start pulse and can reach the nanoseconds units. In these experiments the magnetic field changed according to change of electrical one and

optimized from the beam's generation point of view. Thus, the generation of electron beam occurred in narrow limits of magnetic field change ± 10%.

Changing cross sizes of beam, it was revealed that in both cases the beams in crossed section look like rings with uniform distribution of intensity on azimuth with internal diameter approximately equals to that of the cathode with thickness of the "wall" of ≈1 mm. The measurement of the beam's sizes was made on distance of 180 mm from the anode cut off. Thus, as follows from a curve (see fig. 2), the magnetic field near to x-ray film arrangement decreased approximately in 1.8 times in comparison with that the magnetron gun is situated in.

The given results show that electron beam is enough strongly magnetized because moving in falling down defocusing magnetic field its sizes practically do not change in comparison with that ones at 5 cm distance behind the anode cut off. It can be used with injection of electron beam from the magnetron gun into other systems.
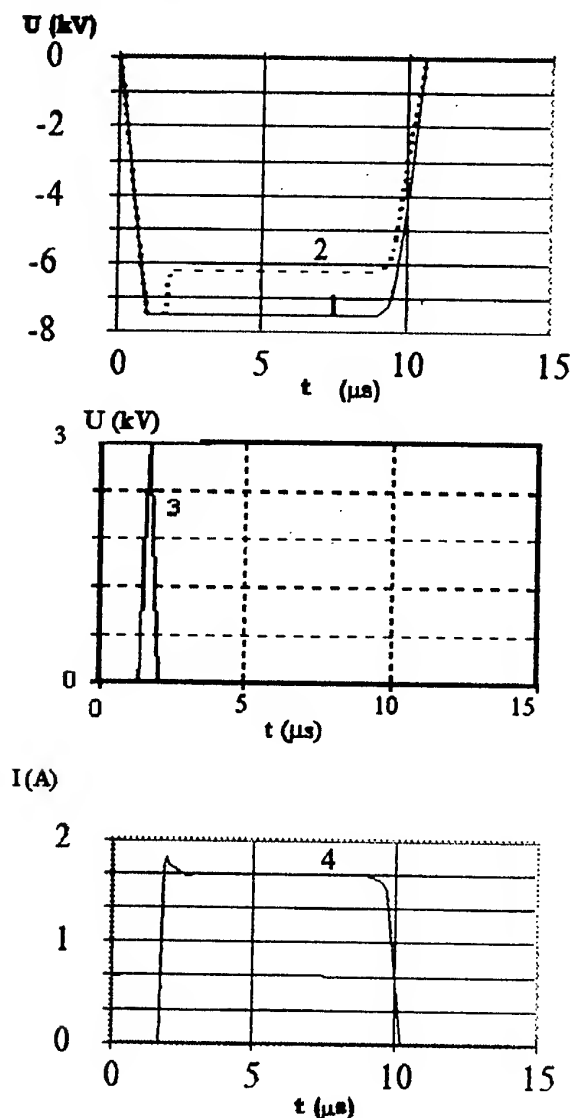
Fig. 3. Oscillograms of voltage pulses (1 - x.x. of modulator, 2 - with beam generation, 3 - primary pulse, 4 - current of the beam).

Calculations executed in one-partial approximation confirm the above given results. They show that electrons flowed from the cathode at recession of the start pulse voltage can collect the energy > 300 eV which is sufficient for secondary emissive duplication during 1 ns. It does not contradict to calculations executed in the work [9] for cylindrical magnetron diode with the secondary emissive cathode. In this case the quantity of primary electrons is insignificant but as the steepness of recession is great the process of secondary emissive duplication goes rather effectively.

It is necessary to notice that in experiments executed with magnetron guns within the limits of cathode diameter change from 5 mm up to 30 mm and anode one from 26 mm up to 140 mm in the mode of autostart [4] with the steepness of recession 20... 50 kV/μs, the start of the gun occurred through 100... 500 ns (depending on experiment conditions) from the recession beginning of the voltage pulse. In this case it is necessary to accumulate significant number of primary electrons for creation of the electron layer of spatial charge. Therefore, the process of accumulation is longer in time and also carries a statistical property with disorder of tens nanoseconds that defines the temporary instability of the current pulse beginning.

The results of researches of various magnetron gun types in the mode of secondary emission start from the external pulse generator are given in the table.

Catode diameter (mm)	Anode diameter (mm)	Cathode voltade (kV)	Gun current (A)	Magnetic field (T)	Trigger voltage (kV)	Trigger duration (ns)
2	7	7	1.9	0.3	2.4	2
2	10	5	0.8	0.19	4	13
2	10	7	1.6	0.21	3	11
3	14	8	2.3	0.14	3	14

CONCLUSIONS

The carried out researches have shown the possibility of spatial charge accumulation during 1.5 -- 2 ns and reception of electron beam with the cathode voltage of 5 -- 7 kV. The tubular electron beams with the current range of 1 -- 2 A are received and (voltage range of 5... 7 kV) with internal and outside diameters of 2 mm and 3.5 -- 4 mm, respectively, at the magnetic field of 1900... 3000 G.

REFERENCE

[1] Lomakin V.M., Panchenko L.V. "Elektronnaya technika "b ser. 1, "Electronika SVCh", 1970, vyp. 2, s. 33-42 (in russian).

[2] Skowron J.F. The Continuouce-Cathode (Emitting-Sole) Crossed-Field-Amplifier. Proc. of the IEE 1973, v. 61, #3, p. 69-101.

[3] Cherenshikov C.A. "Elektronnaya technika " ser. 1, "Electronika SVCh", 1973, vyp. 6, c. 20-28 (in russian).

[4] Dovbnya A.N., Zakutin V.V., Zhiglo V.F. et. al., Proc. of the Fifth EPAC 10-14 June 1996, vol. 2, p. 1508-1509.

[5] Dovbnya A.N., Mitrochenko V.V., Reshetnyak N.G. et. al., Abstract of PAC-97, Vancouver, 1997, v. 42, N 3, p. 1235.

[6] Dovbnya A.N., Gladkikh P.I., Zakutin V.V. et al., VANT, ser.: Yaderno-fizicheskie issledovaniya, vyp. 2,3 (29, 30), Tom 1, s. 204-206 (in russian).

[7] Ivanov G.M., Cherenshikov C.A., Tezisi dokladov 13go Kharkovskogo seminara po lineynim uskoritelyam zaryazhennih chastits, (Kharkov, 25-28 May 1993), Kharkov, 1993, s. 27 (in russian).

[8] Vishnevsky A.I., Soldatenko A.I., Shendakov A.I., Izvestia vuzov, ser. Radioelectronika, 1968, t. 11, #6, s. 555 - 564 (in russian).

[9] Agafonov A.V., Tarakanov V.P., Fedorov V.M., VANT, ser.: Yaderno-fizicheskie issledovaniya, vyp. 2,3 (29, 30), Tom 1, s. 134-140 (in russian).

[10] Churyumov G.I., Radioelectronika, 1997, #7, s. 77 - 80 (in russian).

OPERATING CHARACTERISTICS OF EFFICIENT, HIGH POWER COAXIAL GYROKLYSTRON AMPLIFIERS*

W. Lawson, M. Castle, J. Cheng, V. L. Granatstein, B. Hogan, M. Reiser, and X. Xu

*Electrical Engineering Department and Institute for Plasma Research,
University of Maryland, College Park, MD 20742 USA*

ABSTRACT

We are currently conducting a series of experiments on coaxial tubes which are designed to produce peak powers in excess of 100 MW in X- and Ku-Band. Preliminary results have indicated peak powers in excess of 75 MW at 8.57 GHz in a three-cavity first-harmonic tube with a gain near 30 dB and an efficiency near 32%. In this paper we detail the optimal results of this tube. We also discuss designs and preliminary cold test results of a three-cavity second-harmonic device, which is expected to give comparable results at 17.14 GHz.

INTRODUCTION

At the University of Maryland, we have been investigating the suitability of high power gyro-amplifiers as drivers for linear colliders for over a decade. [1] To this end, we have designed, constructed, and tested a variety of gyroklystron and gyrotwystron tubes operating from X-Band to Ka-Band. With a 440 kV, 160-260 A beam, we were able to produce about 30 MW of peak power in 1 μs pulses near 9.87 and 19.7 GHz with first- and second-harmonic gyroklystron tubes, respectively. The peak efficiencies were near 30% and the large-signal gains were 25-35 dB. Circular electric modes were used in all cavities and the average beam velocity ratio was always near one. Efficiency was limited by instabilities in the beam tunnel preceding the input cavity and beam power was limited by the electron gun.

The focus in the past few years has been to upgrade the system to achieve peak powers approaching 100 MW in X- and Ku-Band. The increase in power results from a larger beam current, which is achieved by maintaining the same current density, but enlarging the average beam radius. Subsequently, the tube cross-sectional dimensions are increased and an inner conductor is required to maintain cutoff to the operating mode in the drift regions. In this paper we first discuss the experimental test facility. Then we discuss the computer simulations before describing the experimental results from our X-Band tube. Finally, we mention our Ku-Band progress before closing with our near and long term goals.

EXPERIMENTAL TEST FACILITY

The voltage pulse is generated with a line-type modulator which is capable of producing 2 μs flat-top pulses at up to 2 Hz with voltages and currents up to 500 kV and 800 A, respectively. A capacitive voltage divider and a current transformer are used to measure the time evolution of the voltage and current. Our single-anode MIG is capable of producing a 500 kV, 720 A beam with an average orbital-to-axial velocity ratio of $\alpha = 1.5$ and an axial velocity

spread of $\Delta v_z/v_z < 10\%$. The beam parameters are given in Table I for the operating point where maximum amplification occurs. The voltage and current are measured quantities; all other values come from the EGUN simulations and are based on the MIG geometry and the magnetic field profile. The actual theoretical fields at the centers of the three cavities are given in Table I. The axial field is detuned by -3.5% in the input cavity, -8.8% in the buncher cavity and -15.4% in the output cavity.

Figure 1. The three-cavity microwave circuit.

The microwave circuit is shown in Fig. 1. The key dimensions are given in Table I. The inner conductor is supported by two 2 mm diameter tungsten pins which intercept approximately 3% of the beam. The primary function of the inner conductor is to force the drift tubes to be cutoff to the operating mode. The inner conductor only extends a few centimeters into the downtaper and is rapidly terminated after the output cavity. Lossy ceramics are placed in the drift regions to help suppress spurious modes. The rings on the inner conductor generally alternate between carbon-impregnated alumino-silicate (CIAS) and 80% BeO-20% SiC. Two layers of lossy ceramics are placed along the outer conductor in the drift regions. The outer layer is BeO-SiC and the inner layer is CIAS.

The input cavity is defined by a decrease in the inner conductor radius and has a length that matches the width of X-band waveguide. The cavity loss is roughly evenly divided between the diffractive loss of the coupling aperture and the ohmic loss of the cavity. The latter loss is provided by a CIAS ring on the inner conductor which is placed adjacent to the cavity and is separated by a thin copper section which is adjusted to produce the proper Q. The power to the input cavity is supplied by a 150 kW coaxial magnetron. The buncher cavity has identical dimensions for the metal components. However, the Q is determined entirely by the ohmic loss of the adjacent CIAS ceramics. The output cavity is defined by radial changes on both walls and the lip radii are equal to the drift tube radii. The quality factor is dominated by the diffractive Q which is adjusted by changing the length of the coupling lip.

THEORETICAL AND EXPERIMENTAL FIRST-HARMONIC RESULTS

A partially self-consistent large-signal code is used to design the circuit and magnetic field configuration and to estimate the performance of the tube at the actual operating point. A small-signal start-oscillation code is used to determine the stability properties of the cavities and set limits on the cavity quality factors. The solid line in Fig. 2 shows the expected performance of the tube as a function of velocity spread for $\alpha=1.5$. The simulation predicts a zero-spread efficiency of 43%, and an efficiency of 34% for 10% spread. For the 6% spread predicted for a 500 A beam, the simulated interaction efficiency is about 40%. All microwave
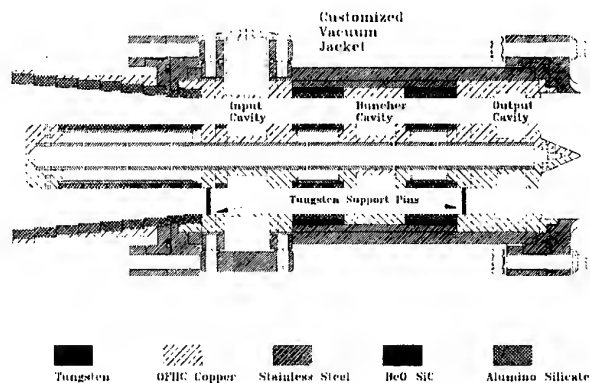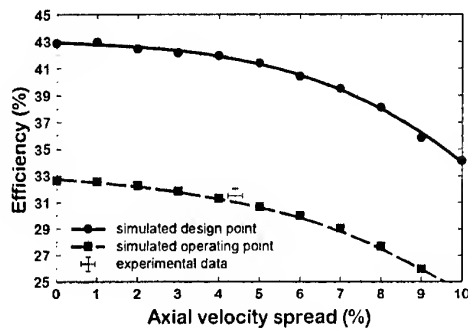
Figure 2. Efficiency versus velocity spread.

Table I. The system parameters.

Beam parameters	
Beam Voltage (kV)	470
Beam Current (A)	505
Average Velocity Ratio	1.05
Axial velocity spread (%)	4.4
Average beam radius (cm)	2.38
Magnetic field parameters	
Input cavity field (kG)	5.69
Buncher cavity field (kG)	5.38
Output cavity field (kG)	4.99
Input cavity parameters	
Inner radius (cm)	1.10
Outer radius (cm)	3.33
Length (cm)	2.29
Quality factor	65 ± 10
Buncher cavity parameters	
Inner radius (cm)	1.10
Outer radius (cm)	3.33
Length (cm)	2.29
Quality factor	75 ± 10
Output cavity parameters	
Inner radius (cm)	1.01
Outer radius (cm)	3.59
Length (cm)	1.70
Quality factor	135 ± 10
Drift tube parameters	
Inner radius (cm)	1.83
Outer radius (cm)	3.33
Length (between I-B) (cm)	5.18
Length (between B-O) (cm)	5.82
Amplifier Results	
Drive Frequency (GHz)	8.60
Output power (MW)	75
Pulse length (µs)	1.7
Gain (dB)	29.7
Efficiency (%)	31.5

cavities are expected to be stable at the design operating point for the quality factors indicated in Table I.

The optimal parameters and experimental results have been listed in Table I. The values are all taken from anechoic chamber measurements. The time dependence of the beam voltage, beam current, and the amplified signal are shown in Fig. 3. There is a slight droop on the flat top due to mismatches in the modulator. The peak values indicated in Table I represent the average value of the signal in the flat top region. The peak power is about 75 MW, which represents an efficiency of nearly 32%. The corresponding gain is almost 30 dB and the pulse width is 1.7 µs (FWHM). Attempts to increase the peak power further by raising the beam's velocity ratio result in a sharp cut in the output signal near the maximum value which is usually indicative of an instability (though none were detected by the microwave diagnostics).

An EGUN simulation using the parameters of the operating point indicate that the beam's velocity ratio at the entrance to the circuit is near one. There is a reasonably large uncertainty in this ratio due to the neglect of the self-axial magnetic field in EGUN and the uncertainty in the applied field at the cathode. In a previous experiment at the University of Maryland, for example, the measured average velocity ratio was consistently higher than the simulated ratio by about 15%. [2] Simulations of the amplifier performance at the operating point are given by the dashed line in Fig. 2. The simulated cathode magnetic field is adjusted slightly to produce the best match between the theoretical efficiency and the measured efficiency, which is indicated by the cross. The required field is about 20 G lower than the calculated ideal field and well within the uncertainties of the experimental data.

SECOND HARMONIC TUBE

The second harmonic tube is real-ized by keeping the first harmonic tube's input cavity but replacing the buncher and output cavities with ones that reso-nate at twice the drive frequency in the TE_{021} mode. Such cavities are normally difficult to realize, because the cavity's end walls generate other radial modes due to the beam tunnel opening. For cavity isolation, the fields must not leak substantially into the drift regions, yet the operating frequency is well above the cutoff of the TE_{01} mode. In circular waveguide systems, the usual way to avoid this problem is to introduce smoothly-varying wall radii, but the added length of these transi-tions is usually unacceptable. Fortunately, in coaxial tubes, making the radial wall transitions that define the TE_{021} cavity approximately equal on the inner and outer walls naturally leads to a mode with very little conver-sion to the TE_{01} modes and subsequent leakage fields. The principal design parameters for our three cavity 2nd harmonic tube are given in Table II along with the simulated performance estimates. At this point, the tube has been entirely constructed, the cavities have been adjusted to achieve the required frequencies and quality factors, And we are currently installing the tube in our test facility. Hot testing should commence soon.
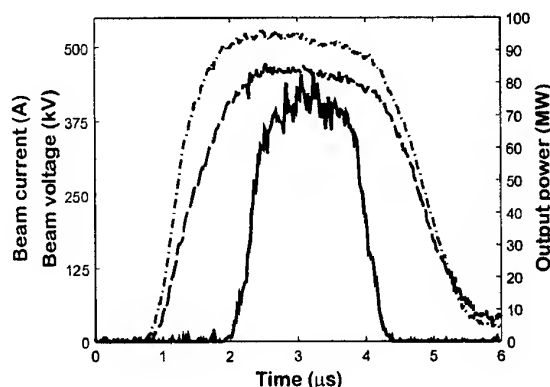
Figure 3. Time dependence of the output pulse.

Table II. The 2nd harmonic design.

Beam voltage (kV)	500
Beam current (A)	770
Velocity ratio	1.51
Input cavity Q	50
Buncher cavity Q	389
Output cavity Q	320
Gain (dB)	49
Efficiency (%)	41
Output power (MW)	158

SUMMARY

In summary, we have developed an X-band coaxial gyroklystron which has increased the state-of-the-art in peak power for gyroklystrons by nearly a factor of 3. In the near future we will test our 2nd harmonic tube, with the goal of obtaining about 100-150 MW of peak power at 17.136 GHz. We will investigate the limitations on velocity ratio in greater detail and at-tempt to increase the nominal velocity ratio to the original design value. In the long term we expect to build and power a 17.136 GHz accelerator structure with an accelerating gradient near 200 MV/m.

ACKNOWLEDGEMENTS

[1] V. L. Granatstein and W. Lawson, *IEEE Trans. on Plasma Science*, vol. 24, p. 648 (1996).
[2] J. P. Calame and W. Lawson, *IEEE Trans. Electron Devices*, vol. 38, p. 1538 (1991).

NUMERICAL SIMULATION STUDIES OF COAXIAL VIRCATORS

Hao Shao, Guozhi Liu, Zhimin Song, Yajun Fan, Xiaoxin Song

Northwest Institute of Nuclear Technology, P.O.BOX 69-13, 710024,Xi'an, P. R. China

Coaxial vircator is a novel high power microwave(HPM) generator, in which an annular virtual cathode is formed inside the anode screen due to the injection of electron beams along radial direction, and its temporal and spatial oscillation along with the reflected electron oscillating in the potential well give HPM output. Because of the preferable geometry for HPM generation, coaxial vircator can theoretically give higher efficiency and narrower output bandwidth than that of the planar vircators.

The main part of the coaxial vircator-coaxial diode is shown in Figure 1. Basically there are two type of coaxial diode, i.e. the inward emitting coaxial diode(IECD) and the outward emitting coaxial diode(OECD).
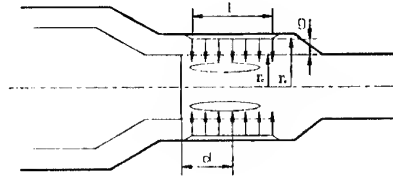
Figure 1 Schematic of inward emitting coaxial vircator

1. FREQUENCY STUDIES OF COAXIAL VIRCATOR

The simulation results shows that IECD takes great advantages over the planar diode in the generation of HPM. In the stable case, the inward emitting electron beam in IECD has an increasing density as the radius decreases because of the conservation of charge. Therefore within a IECD, electron beam of higher density is formed than a planar diode has the same cathode area. The dominant frequency of the coaxial vircator is directly proportional to the plasma frequency of the virtual cathode, $\omega_{out} \propto \omega_p$, where $\omega_p = \left(4\pi n e^2 / m\gamma\right)^{1/2}$ is the relativistic plasma frequency of the virtual cathode. The simulation geometries of a coaxial vircator and a planar vircator of the same cathode area are given in Figure 2and 3.
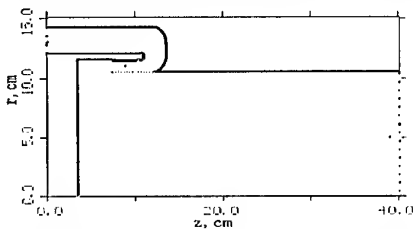
Fig 2 Simulation geometry scheme of coaxial vircator
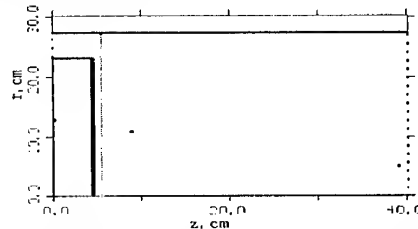
Fig 3 Simulation geometry scheme of planar vircator

From the FFT graphs for coaxial and planar vircator output shown in Figure 4 and 5

respectively, a peak frequency of 7.14GHz can be clearly identified for coaxial vircator much higher than 4.06GHz for the planar vircator. This result was obtained under 0.6MV peak input voltage, 144.4cm^2 cathode area and 1cm diode gap.
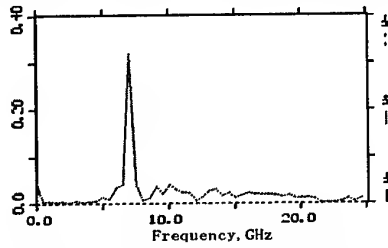
Fig 4 FFT for a coaxial vircator
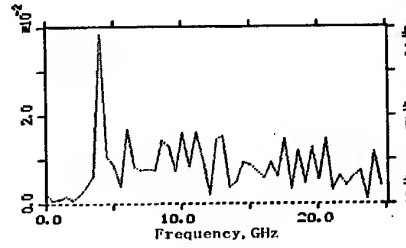
Fig 5 FFT for a planar vircator

Within the coaxial diode, a quasi-cavity is formed by the anode screen and anode base. When virtual cathode was formed in the cavity, oscillation of radically injecting electrons and virtual cathode strongly interacts with the cavity TM_{0n} modes, inducing the virtual cathode oscillation frequency to the characteristic frequency of the cavity mode. By diagnosing the electric field distribution at the waveguide output end, the output microwave mode was verified to be TM_{01}, the same as the lowest mode of the cavity.

Since the width of injection region generally shorter than the half of cutoff-wavelength of TM_{01}, it is reasonable to assume that the electron injection region locates at strongest position of TM_{01} mode electric field perpendicular to the waveguide wall. The axial wavelength λ of the induced output microwave has a direct relation with distance **d** from centerline of injection region to anode base. Consequently,

$$\left. \begin{array}{l} d = \dfrac{4i+1}{4}\lambda \\ or \\ d = \dfrac{4i+3}{4}\lambda \end{array} \right\} i = \quad 0,\ 1,\ 2,\ 3,\ \cdots \tag{1}$$

From Equation 1 we can expect a relatively stable **i** for different parameters of the simulation geometries. So a preferable **d** for certain geometry can be chosen out from simulation results and ultimately achieve the highest couple coefficient and energy efficiency.

The parameters of one simulation geometry are the width of emission region L=2cm, cathode radius r_c=11cm, anode radius r_a=10cm, diode gap g=1cm, length from centerline of emission region to anode base d=5cm. The simulation result is shown in Figure 4.

According to Equation 1, when $i = 0,1,2$, $\lambda = 4d, \dfrac{4}{5}d, \dfrac{4}{9}d$, under these wavelength, the frequency of TM_{01} is $f = \dfrac{c}{2\pi}\sqrt{\beta^2 + T^2_{TM_{01}}}$, where, $\beta = \dfrac{x_{01}}{r}$, x_{01} =2.405 is the 1st root of 0 step Bassel function, **r** is the radius of the cylindrical cavity, the transverse wave vector $T = 2\pi / \lambda$ Hence, for $i = 0,1,2$, we have

$$f(\lambda = 4d) = 1.6GHz \tag{2}$$
$$f\left(\lambda = \frac{4}{5}d\right) = 7.59GHz$$
$$f\left(\lambda = \frac{4}{9}d\right) = 13.55GHz$$

Comparing with the simulation results, we obtained that when **d** satisfies $d = 5\lambda / 4$, the characteristic frequency of TM_{01} is 7.59GHz approximately equals the dominant frequency of output microwave 7.14GHz.

During the numerical simulations, all the results suggest that oscillating frequency of virtual cathode keep relatively unchanged when vary the value of **d** only, but microwave conversion efficiency vary with **d**. This indicate coupling coefficient between virtual cathode and TM_{01} mode in the anode cavity change with **d**. Hence, we can change **d** to improve the

efficiency to the highest point.

In the simulation, we test this deduction by the geometry with previous refereed parameters. Varying **d** make the TM_{01} mode of anode cavity have a characteristic frequency at 7.14GHz, we have $d=5\lambda/4=4.26cm$, and it have attained a energy conversion efficiency more than 10%.

Fig 6 Schematic of efficiency of a coaxial vircator with optimal **d** value

2. ENERGY CONVERSION EFFICIENCY OF COAXIAL VIRCATOR

The coaxial vircator have an efficiency much higher than planar vircator according to the simulation results. Generally, an inward emitting diode is used in coaxial vircator for HPM generation. It can operate in positive pulse(see Figure 1) or negative pulse(see Figure 7). A variation simulation structures together with the peak output frequency are presented in Table 1 and Table 2,the applied voltage is a 40ns half-period sinusoidal pulse of positive and negative

Fig 7 Schematic of Negative pulsed coaxial vircator

Table 1 Efficiency of Positive pulsed coaxial vircator under different structure

Parameter NO.	r_a(cm)	r_c(cm)	L(cm)	Peak efficiency
1	10	11	2	4.8%
2	10	12	2	3.4%
3	10	11	3	3.6%
4	9	11	2	2.8%

Table 2 Efficiency of negative pulsed coaxial vircator under different structure

Parameter NO.	r_a(cm)	r_c(cm)	L(cm)	Peak efficiency
1	10	11	2	10.6%
2	10	12	2	8.2%
3	10	11	3	8.4%
4	9	11	2	7.2%

respectively.

We also find in the electron distribution graph and electron trace graph(see Figure 8), the reflected electrons always oscillate in potential well formed by the real cathode and virtual cathode for 2~3 periods then drift down to the waveguide region to be absorbed. By this way, the reflected electrons give part of them energy to the output microwave, the same time, the reflected electron modulates the injecting electron beam and avoid the low energy electron stay in the potential well for too long time. Hence, this nature mechanism eliminating reflected electron can be treated as the plate in Reditron. It provides a single modulation to the beam, and ultimately improve the energy conversion efficiency.

According to the simulation results, when the impedance of diode match the transmission line, the efficiency of high power microwave generation is maximum. One matching case in the simulation is shown in Fig 9. It was got under 10Ω transmission line and has the highest peak in efficiency curve before 30ns.

Figure 8 Electron trace graph of coaxial vircator

Fig 9 The impedance scheme in a matching condition

3. CONCLUSION

The characteristic frequency and energy conversion efficiency of the coaxial vircator are studied by numerical simulation method. Comparing with planar vircator, the coaxial vircator generates much narrow bandwidth and higher center frequency. The simulation results also evince that by adjusting **d** can tune the output microwave frequency in about two octave range under certain conditions. The negative pulsed coaxial vircator can significantly improved efficiency from about 4% of positive pulsed coaxial vircator to about 10%.

The experimental apparatus are setting up, the experimental results will be given in future.

REFERENCE:

[1] Liu, S. Qiu, et. al., NINT, "Coaxial diode and vircator", SPIE Proceeding of Intense Microwave Pulse, San Diego, 1997.
[2] Banford, Ja. Swegle, "High power microwave source", 1992.
[3] Irv. Langumuir, "Electrical discharge in gases", Review of modern Physics, Vol. 3, No. 2, 1931.
[4] Woolverton, M. Kristiansen, et. al., "Computer simulations of coaxial vircator", Proceeding of SPIE, Intense Microwave pulse V, San Diego, 1997.
[5] Woolverton, M. Kristiansen, et. al., "Coaxial vircator source development", IEEE International Conference on Plasma. Science, 1995.

NUMERICAL STUDY OF FOILLESS DIODE

Zhimin Sung   Guozhi Liu   yajun Fan   Hao Shao

Northwest Institute of Nuclear Technology,
P.O.BOX 69-13, 710024,Xi'an, P. R. China

I. INTRODUCTION

The foilless diodes have been studied extensively in theoretical analysis, numerical simulation and experimental testing[1-5], because of their potential application beam-wave interaction devices and microsecond pulse accelerator. Theoretical models of beam generation in foilless diodes have been of two types. The first one is the space charge limited model under infinite applied magnetic field [2-4], which assumes that the current depends on the conditions in the acceleration region. According to the OAL model, diode current and diode impedance for a thin ultra-relativistic beam are given approximately by[2]

$$I_{OAL} = 17\left(\gamma_0^{2/3} - 1\right)^{3/2} \frac{R_c}{\delta} \ln^{-1}\left(\frac{8\delta}{a}\right) \quad (kA) \tag{1}$$

$$z = 30 \frac{\delta}{R_c} \ln\left(\frac{8\delta}{a}\right) \quad (\Omega) \tag{2}$$

where $\gamma_0 = 1 + eU/mc^2$, Rc is the cathode outer radius, and a is the beam thickness, δ is the distance between the beam and anode wall. While for a thin non-relativistic beam, diode current is given approximately by[4]

$$I_b = 17\frac{(\gamma_0 - \gamma_b)\sqrt{\gamma_b^2 - 1}}{2\gamma_b} \ln^{-1}\left(\frac{R_a}{R_c}\right) \quad (kA) \tag{3}$$

where $\gamma_b = 1/\sqrt{1 - (v_b/c)^2}$, v_b is the velocity of the beam electron, Ra and Rc are the radii of the drift-tube and cathode respectively. The other model assumes that the diode current can be determined by the equilibrium that the beam reaches in the hollow anode-drift tube[5], and it gives diode current formula as

$$Iequ = 34\left\{\left[\gamma_0/\left(1 + 4\ln\left(R_a/R_c\right)\right)\right]^2 - 1\right\}^{1/2} \quad (kA) \tag{4}$$

Although these models could yield some scaling laws, they do not provide quantitative results for realistic conditions. Numerical simulations have proved to be an optimum method to study foilless diode[1,5], because the beam behavior can be examined under the influence of complex diode configuration, shank emission and finite magnetic field, etc. In this paper, a fully relativistic electromagnetic, 2.5-D PIC code(KARAT)[6] was used to model the generation of an annual relativistic electron beams by a magnetic field-immersed foilless

diode in consideration of shank emission. The effects of guiding magnetic field, applied voltage and diode geometrical construction on the diode behavior were considered mainly.

II. SIMULATION RESULTS AND ANALYSIS

The schematic diagram of the diode is shown in Figure 1. A TEM wave of 5-ns risetime is input from a 40Ω coaxial transmission line at the left side, and drives the cathode negativly. The high field causes a space-charge-limited emission on the cold cathode where the electric field is above the field threshold of 500kV/cm, and the electron beam transports into the drift tube under the action of the applied magnetic field which is provided by a solenoid coil. The self-consistent space-charge-limited emission is modeled in the code by correcting the emission current until the normal electric field at the emission region becomes zero for each time step. In the simulation, the beam current, diode impedance and beam quality were diagnosed with the variation of the geometry and electromagnetic parameters.
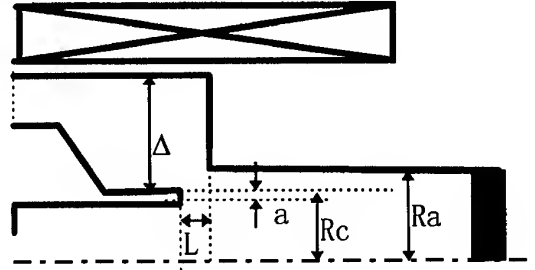
Fig. 1.Schematic diagram of the field-immersed foilless diode

1) The Effect of the Magnetic Field

In order to control the transportation and expansion of the electron beam in the absence of the anode foil, the applied magnetic field should be above a critical value Bcr, which is chosen based on the condition that the electron emitted from cathode could not go through the cathode-anode gap when a voltage applied on the diode. The critical magnetic field Bcr can be obtained considering the magnetic-flux conservation for relativistic beams as:

$$B_{cr} = \frac{0.17}{d}\sqrt{\gamma_0^2 - 1} \quad (Tesla) \tag{5}$$

where d refers to the minimum gap distance between cathode and anode (cm). When L≤0, d equals to Ra-Rc. When the amplitude of the inputting TEM wave is 800kV, and L=0cm,d=0.5cm, the diode voltage varies from 400kV to 980kV due to the mismatch of diode-transmission line impedance. The variation of diode current and impedance with the applied magnetic field are shown in Fig.2. According to the result of simulation, the Bcr is about 0.85 Tesla, which is in agreement with that calculated estimate given by Eq.(5). For an electron in an electromagnetic field, the Larmor orbit radius has the relation of $r_L \propto V/(B^2 d)$. In the case of B<Bcr, a large proportion of electrons reach the anode wall due to the r_L is larger than the diode gap. Hence, the diode current is relatively small. With the increasing of the magnetic field, more and more electrons could transport into the drift tube and the diode current also increases and reach to maximum till B=Bcr. When B>Bcr, the electrons emitted from the cathode shank return backward due to the decreasing of the Larmor
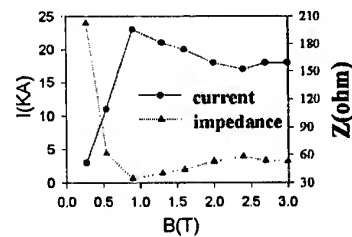
Fig.2 Diode current(solid line) and impedance(dot line) as a function of magnetic field

orbit radius. Meanwhile the current decreases. When the magnetic field is strong enough, the diode current is mainly provided by the electrons emitted from the cathode tip, while the contribution of those emitted from the shank can be neglected.

2) the Effect of the Diode Voltage

The diode gap voltage is changed by varying the amplitude of the input TEM wave. The current increases with the diode voltage while the impedance decreases (Fig.3). A comparison of the simulation with several theoretical models is also shown in Fig.3 . The simulation results indicated that the diode current agrees well with the non-relativistic space-charge-limited model (Equ.4) at low voltage. While in the relativistic case, the diode current can be described by the model of beam equilibrium in the drift tube at very high voltage. At relatively low voltage the OAL model gives suitable result.

3) the Effect of the Geometry Parameters

There are two important geometry parameters for foilless diodes, L and δ, which influence the diode current and impedance significantly. The simulation results appear to be coincident with the theoretical predictions of the diode current.

In Fig.4 the simulated diode current and impedance as a function of axial gap spacing L are presented when the amplitude of the inputting TEM wave is 600kV. For very small axial gap the diode current and impedance is governed by the beam thickness and δ. For large L they are determined by the beam thickness and the separation from the cathode shank to the anode wall Δ (see Fig.1). For intermediate L the current will decrease with increasing gap separation. The simulation results agree with the experimental results in Ref.1 and this can be explained as that the normal electric field decreases with increasing L.

We can change the δ by varying the radius of the cathode and that of the drift tube respectively, and the increasing of diode current and decreasing of the impedance with increasing δ is presented in Fig.5 and Fig.6, which are in good agreement with the description of OAL model.

In the simulation the effect of the cathode tip thickness is also examined. Keeping the other parameters constant, it can be found that the beam current changes slightly with the cathode tip thickness, and that the electrons are concentrated in the region whose radial thickness is about 1mm, indicating the electron beam is exactly hollow. In the simulations, cathode tip thickness varies from 2mm to 8mm, the diode current and impedance are 12kA
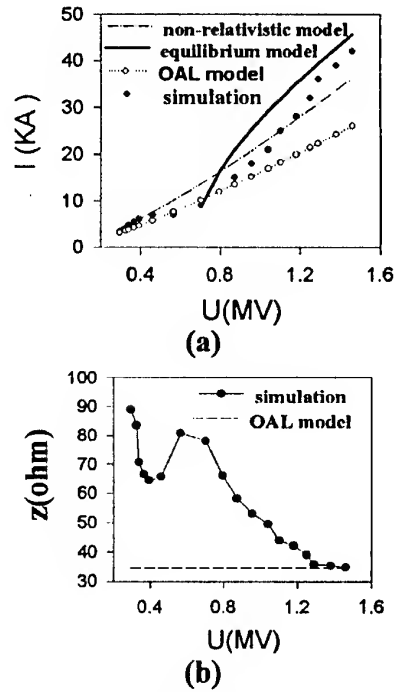
Fig.3 Diode current (a) and impedance (b) variation with the diode voltage
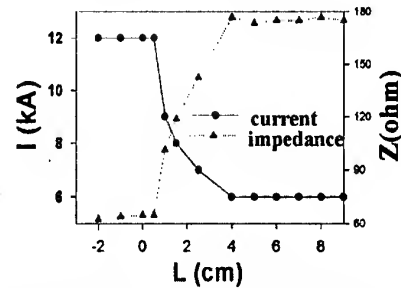
Fig.4 Diode current(solid line) and impedance (dot line) as a function of the axial gap spacing L (B=2T, Ra=1.8cm, Rb=1.3cm, a=0.2cm)
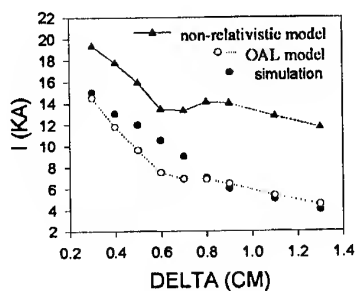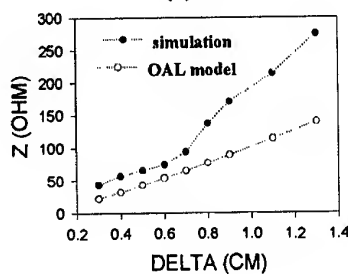
Fig.5 Diode current (a) and impedance (b)
variation with δ by changing the cathode
radius (L=0,B=2T,Ra=1.8cm)
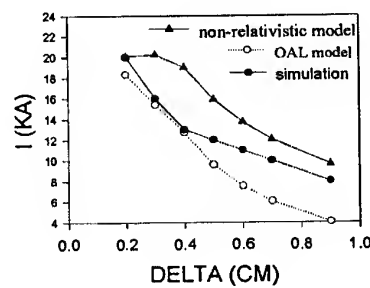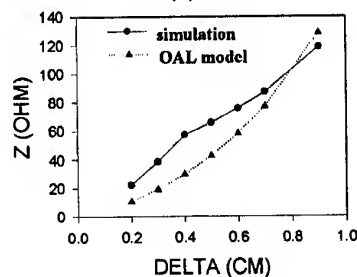
Fig.6 Diode current (a) and impedance (b)
variation with δ by changing the drift tube
radius (L=0,B=2T,Rb=1.3cm)

and 65ohm respectively.

III. SUMMARY

Based on the numerical simulation of the foilless diode presented above, the following conclusions can be summarized.

(1)At finite magnetic field, the effect of the shank emission on the electron beam could not be neglected. Although shank emission increase the beam current, it reduces the beam quality, which could be solved by increasing the applied magnetic field and decreasing the radial electric field at the cathode shank.

(2)For the diode current, the beam equilibrium model is valid in ultra-relativistic case, while the space-charge-limited model is suitable for relatively low voltage.

ACKNOWLEDGMENTS

The authors wish to thank zeng zhengzhong, chen changhua, song xiaoxin for their assistance and helpful suggestions.

REFERCE:

1.R. B. Miller, K. Prestwich etc, J. Appl. Phys. 51(7),3506(1980)

2.E. Ott , T. M. Antonsen and R. V. Lovelace , Phys. Fluids, 20(7), 1180(1977)

3.J. Chen and R. V. Lovelace , Phys. Fluids, 21(9), 1623(1978)

4.G.A.Mesyats ,High Power Microwave Generation and Applications(edited by E. Sindoni and C. Wharton), Bologna,1992,P.245

5.M. E. Jones and L. E. Thode, J. Appl. Phys. 51(10),5212(1980)

6.V. P. Tarakanov, Users' Manual for Code KARAT ver.7.06.02, 1998

EFFECT OF EMISSION INHOMOGENEITIES ON LOW-FREQUENCY OSCILLATIONS IN GYROTRON-TYPE ELECTRON BEAMS

V.N. Ilyin[*], O.I. Louksha, V.E. Mjasnikov[*], L.G. Popov[*], G.G. Sominski

Saint-Petersburg Technical University,
29, Polytechnicheskaya St., St.-Petersburg 195251, Russia
[*]GYCOM Ltd., 52, Obrucheva St., Moscow 117393, Russia

INTRODUCTION

Plasma heating in large tokamaks is one of the most attractive applications for millimeter-wave gyrotrons. Gyrotrons designed and created in Russia for this purpose have megawatt microwave power level in quasi-CW regime (in single pulses with duration t > 1 s) [1,2]. Their effective operation is impeded by low-frequency (~ 100 MHz) spurious oscillations of electron space charge accumulated in the trap between gun cathode and magnetic mirror [3,4]. These oscillations often develop after a long-term operation of a gyrotron. Modification of cathode emission characteristics can be one of the most probable causes of this phenomenon.

Our paper reports the results of the study of space charge oscillations in gyrotron trap and effect of emission inhomogeneities on their characteristics. Investigations were performed on a gyrotron model at the Physical Electronics Dept. of St.-Petersburg Technical University in cooperation with GYCOM Ltd. and Institute of Applied Physics RAS.

EXPERIMENTAL APPARATUS

The schematic drawing of experimental tube representing a gyrotron-type electron optical system without a special microwave cavity is shown in Fig. 1. Measurements were made for
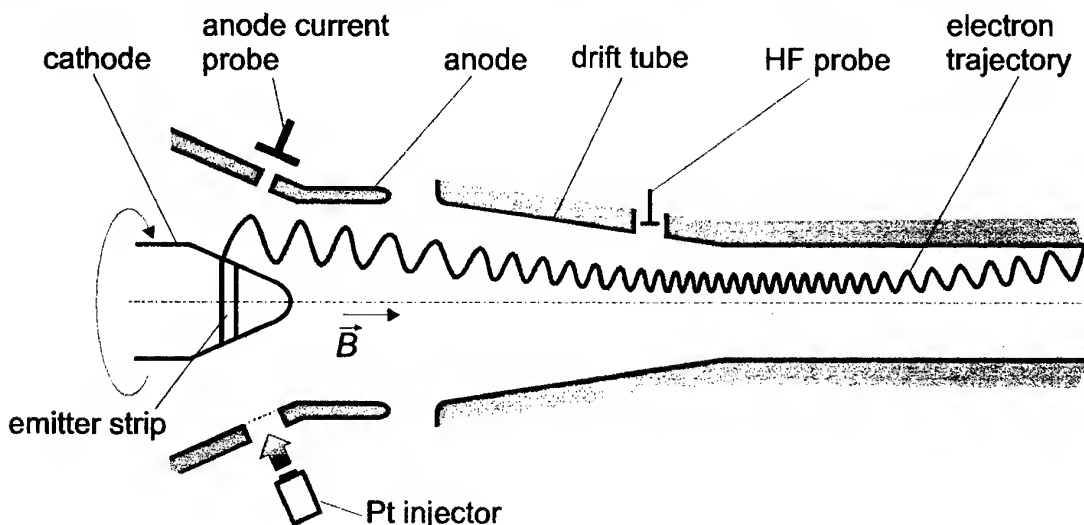
Fig.1. Experimental set-up

wide range of working parameters including scaling regimes of high-power gyrotrons. The basic parameters are given in Table 1.

Characteristics of space charge oscillations were measured with broadband probe registering the induced signals from helical electron beam (HEB) near-zone [2]. Probe was placed in the magnetic field compression region (Fig. 1). Information about oscillations characteristics was obtained as a result of computer analysis of probe signals oscillograms with duration from 10 ns to 100 μs.

Impregnated metallic-porous cathodes were used as an electron source. In temperature-limited regime (typical for gyrot-

Parameter	
Cathode diameter	83 mm
Distance cathode-anode	7 mm
Distance cathode-magnetic field plateau	22 cm
Drift tube diameter in plateau region	22 mm
Beam voltage	7-12 kV
Plateau magnetic field	2.0-3.0 T
Magnetic compression (ratio of plateau magnetic field to cathode magnetic field)	25
Beam current	0-10 A
Beam pulse duration	5-100 μs
Pitch-factor (ratio of transverse velocity to longitudinal velocity) in plateau region	0.7-2.0

Table 1. Main experimental parameters

rons) the work function inhomogeneities result in non-uniform distribution of current density in HEB. It was possible in our experiments to control of spatial distribution of work function by platinum deposition onto cathode surface. Platinum passed from injector through a gridded slot in anode and was deposited onto surface increasing the work function of this region (Fig. 1). The deposition region was selected by rotating of cathode.

Fig. 2. Azimuthal distributions of emission current density

Azimuthal distributions of emission current density $j_e(\theta)$ were obtained by measuring the current of electrons passing through a pin-hole in anode 0.5 mm in diameter (Fig. 1) vs cathode azimuthal position in the absence of applied magnetic field. Fig. 2 shows distributions $j_e(\theta)$ measured before (curve 1) and after (curve 2) platinum deposition. In this case deposition

resulted in smoothing of emission inhomogeneities. "Amplitude" of inhomogeneities could be described by parameter m defined as

$$m = \frac{\frac{1}{n}\sum_{1}^{n} j_{ci} - j_c}{j_c},$$

where $j_{ci} = j_c(\theta_i)$ $(\theta_i = \frac{360}{n}, \frac{2 \cdot 360}{n}, ..., 360)$, $j_c = \frac{1}{n}\sum_{1}^{n} j_{ci}$. For distributions presented in Fig.2: $m = 0.295$ (curve 1) and $m = 0.187$ (curve 2) for $n = 72$.

RESULTS AND DISCUSSION

Current of electrons reflected from magnetic mirror in gyrotron can be estimated for known HEB transverse velocity spread $\delta v_\perp$ and average pitch-factor g. For typical values $\delta v_\perp = 20\%$ and $g = 1.4$ coefficient of reflection has to be about 10^{-3}. Previous investigations [4] demonstrated that excitation of space charge oscillations in gyrotron trap occurs when value of beam current I exceeds the threshold one $I_{th} \sim 0.1$-0.5 A. Fig. 3 presents probe signals oscillograms for different HEB current values varied by cathode temperature adjustment. For current I not much above the I_{th} oscillations were observed only near the pulse front (Fig. 3a). Duration of the oscillations increased (Fig. 3b-d) and their spectra became more complicated with current growth. But when HEB current approached a maximum value I_{max}, , amplitude of oscillations rapidly fell to zero (Fig. 3e). Current I_{max} was found to be approximately equal to the boundary value I_{sc} of space-charge limiting current regime of the magnetron-injection gun. One of mechanisms of suppression of the oscillations could be connected with decrease of average HEB pitch-factor g due to effect of electron beam space charge on static electric field distribution in gun region. On the other hand, current growth results in reduction of non-uniformity of emission and space-charge fields, and so velocity spread caused by these fields can decrease also.

| a | b | c | d | e |
| (10 mV/cm) | (10 mV/cm) | (10 mV/cm) | (20 mV/cm) | (20 mV/cm) |
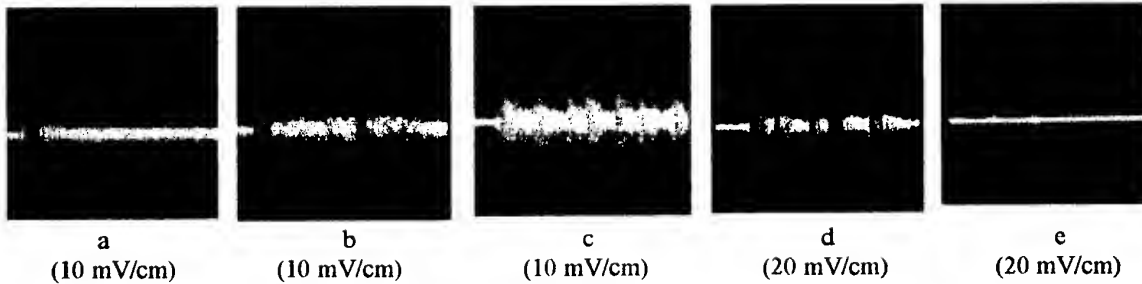
Fig. 3. Oscillograms of probe signals with duration of 15 μs.
Beam voltage $U_0 = 8$ kV, plateau magnetic field $B_0 = 1.89$ T. Beam current I (and ratio I/I_{sc}):
a - 0.29 A (0.04), b - 0.63 A (0.1), c - 4.1 A (0.06), d - 4.35 A (0.71), e - 6.34 A (1).

Our experiments demonstrated that varying of cathode emission inhomogeneities for a constant beam current results in alteration of oscillations intensity. Fig. 4 shows dependencies of oscillations energy W_{osc} (defined as their amplitude multiplied by duration of oscillatory process) vs HEB current I for different values of m. Current range $I_{th} < I < I_{max}$, where

oscillations were registered, narrowed with decrease of m. Maximum value of W_{osc} in this range decrease also.

With the results obtained in this work, we can predict considerable decrease of spurious low-frequency oscillations in gyrotrons with more homogeneous emission distribution over the cathode surface. Inhomogeneity of modern metallic-porous cathodes for gyrotrons can be made less then 10 % of average value of emission density ($m <$ 0.1) [2]. Though during gyrotron operation cathode emission non-uniformity may increase due to inhomogeneous disactivation of its surface. Cathode manufacturing technology imperfections, ion bombardment, micro-breakdowns are known to be the factors causing this disactivation. For gyrotrons cathode bombardment with electrons reflected from the magnetic mirror have to be taken into account as one of such factors.
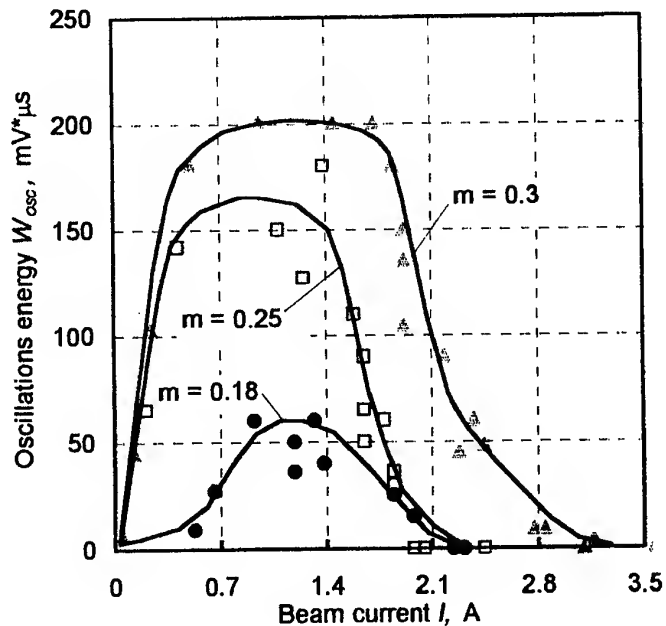
Fig. 4. Oscillations energy W_{osc} vs beam current I.
$U_0 = 8$ kV, $B_0 = 2.2$ T.

CONCLUSIONS

In this paper new techniques for control of emission distribution over the surface of metallic-porous gyrotron cathodes is presented. Influence of emission non-uniformity on spurious low-frequency oscillations' development had also been investigated. Following the emission homogeneity requirements established in this work, it would be possible to prevent excitation of intensive spurious oscillations.

[1] M.V. Agapova, et al., Digest of 20th Int. Conf. IR&MM Waves, Orlando, USA, (1995), 205.

[2] A.N. Andronov, et al., Proc. Int. Vacuum Electron Sources Conf., Eindhoven, The Netherlands, (1996), G13.

[3] Tsimring Sh.E.: in Lectures on Microwave Electronics and Radio Physics [in Russian], 3rd Winter School-Seminar, Saratov, (1974), 3-94.

[4] O.I. Louksha and G.G. Sominski, Proc. 11-th Int. Conf. On High Power Particle Beams, Prague, Czech Rep., (1996), 418-421.

NON-STATIONARY SIMULATION OF THE GYROTRON HELICAL ELECTRON BEAMS

A.N.Kuftin, V.K.Lygin, V.N.Manuilov

Institute of Applied Physics Russian Academy of Sciences,
46 Ulyanov St., Nizhny Novgorod, 603600, Russia

ABSTRACT

The results of non-stationary simulation of helical electron beams (HEBs) parameters based on the PIC method and quasi-stationary model of electric field are presented. The beam types with different topology (laminar, boundary , regular intersecting) are considered. The evolution of the oscillatory velocity distribution is investigated. The space charge value of locked into adiabatic trap electrons and their life-time are obtained. The bombardment of the cathode by reflected electrons is studied.

INTRODUCTION

During recent years in many countries the intense efforts to develop the high power CW and quasi-CW gyrotrons for nuclear fusion (ITER program) and technology applications have been undertaken. Formation of HEBs in gyrotrons is performed by magnetron-ingection guns (MIGs) - see Fig.1. The characteristic feature of MIGs is rather large oscillatory velocity spread $\delta v_\perp$ in the formed helical electron beam.
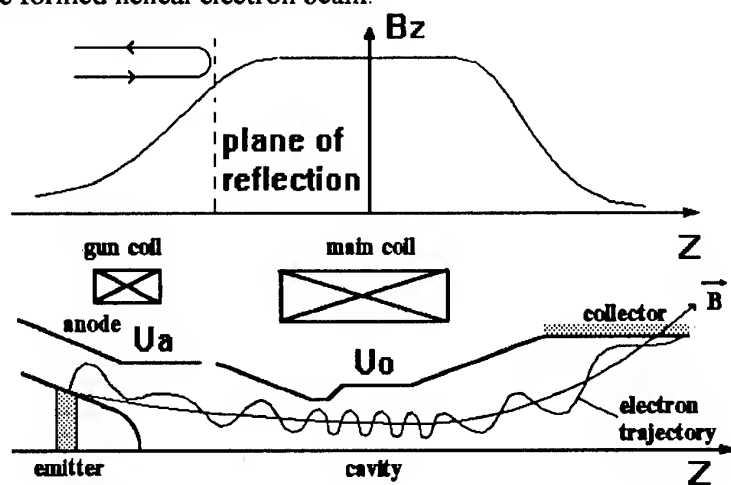
Fig.1. The scheme of the gyrotron electron-optic system and the axial magnetic field distribution.

The latter factor decreases the gyrotron efficiency and causes the reflection of a part of electrons with the maximum oscillatory velocity from the magnetic mirror between the cathode and the working space. Reflected electrons may initiate the beam instability in some regimes[1].

The static model of the HEBs and corresponding codes [2-4] allow to predict the variation of the $t_\perp$ value (the ratio of the beam oscillatory energy to the total one) as the beam current I grows with good enough accuracy . However the difference in calculated and measured values of $\delta v_\perp$ in spite of the identical methods of the $\delta v_\perp$ definition [4] remained still essential [5]. The main reason for this deviation is evidently the absence in the static numerical model of the electrons reflected from the magnetic mirror and then captured into the adiabatic trap between the cathode and the cavity. The correct including of the trapped electrons in the numerical model may be performed by transition from static codes to the ones based on the PIC method.

The first works dealing with the non-stationary processes in HEBs were [6,7]. Below some new results of the HEBs properties simulation based on the quasi-stationary model of electric field [8] are described.

THE RESULT OF NON-STATIONARY ANALYSIS

The calculations were performed for MIGs in the regime close to critical that is typical of the HEBs formation systems of the centimeter wave length range (Fig.2). The diode type guns with accelerating potential $U_o=60$ kV were considered. The emission current value I was chosen in such a manner as to provide the ratio $t_j=I/I_L\approx0.1$-0.2. Here I_L – Langmuir current of the gun. The variation of the pith-factor value g_0 (the ratio of the longitudinal drift velocity to the oscillatory one, $t_\perp=g_0^2/(1+g_0^2)$) in "cold" system from $g_0=1$ up to $g_0=2.0$ was provided by changing the amplitude B_0 of the magnetic field in the working region.

The calculations were performed for three values of $g_0=1$, 1.2 and 2.0 for each gun. The dispersion of initial velocity distribution was chosen using the static code so that $\delta v_\perp\approx20\%$ for $t_j=0$. When $g_0=1$ and 1.2 there are no reflected electrons and the beam parameters are close to the calculated ones using the static model. The most interesting are the versions with $g_0=2.0$. In this case for $t_j=0.1$ the character of the processes in the electron beam changes essentially. In time interval T_1 a little bit less than $T_\parallel$ ($T_\parallel$ is the time of the particle motion from the cathode to the interaction region) the part of particles from the "head" of the beam with maximum oscillatory velocities reflects in the plane $z\approx3.8$ R_k (here $B(z)/Bo\approx0.8$) from the magnetic mirror and then turns back to the cathode. Finally in time ~ 2.5 T_1 the reflected electrons reach the cathode. From this moment the cathode bombardment by reflected electrons having the energy $W > U_0$ at the moment of reflection begins (at this moment maximum electron energy W_{max} may exceed $1.25 Uo$ for $t_j=0.1$). On the average the zone of bombardment is to some extent shifted (~ 0.2-$0.3d$, d- the larmour diameter in the cathode region) to the left in comparison with emitter edges (see Fig.3). The averaged energy W_c of electrons bombarding the cathode may exceed some kilovolts. For laminar flow the values of W_c and W_{max} are to some extent greater than for the regular intersecting flow. It is interesting to note that even when the current time t exceeds 10 $T_\parallel$,W_{max} is still about 1.01-$1.02 Uo$. Trapped electrons form the halo of the initial beam (Fig.3). The space charge density ρ in the halo usually do not exceed 5% of maximum ρ in the cavity for the initial beam. However the full space charge Q_r of locked into the adiabatic trap electrons may reach $1.1 Q_o$ for laminar flow and $0.3 Q_o$ for regular intersecting one when the relaxation processes are finished. Here Qo - full charge of the initial beam.

According to the results of numerical simulation the time of the relaxation proses Tr in any case exceeds 10-15 $T_\parallel$. The value of Tr is greater for laminar flow. The middle life-time of the electrons in the adiabatic trap is about 3-5 $T_\parallel$.

When reflected electrons reach the cathode region they cause the additional cathode electric field depresion ΔE . However, it is not exceed 50% of ΔE caused by the initial beam.

The value of $t_\perp$ becomes lower and $\delta v_\perp$ - greater in comparison with the static model of the beam (Fig.4). It is seen that the maximum deviation in $\delta v_\perp$ is observed for the laminar flow and minimum - for boundary one.

When the current grows by two times (t_j=0.2), the qualitative picture of the relaxation processes in the considered beams remain the same.
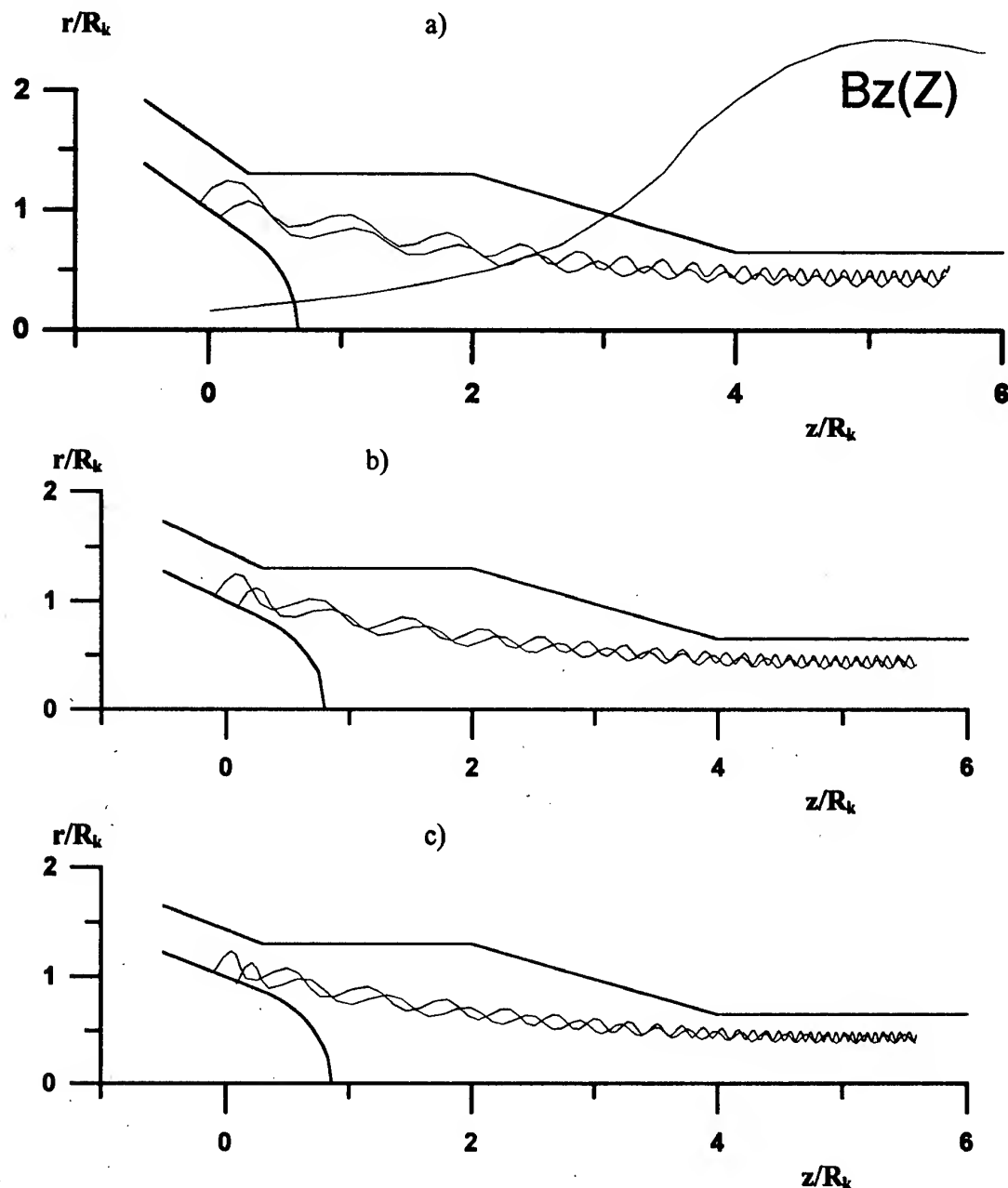
Fig.2. The guns forming electron beams with different topology: a) laminar flow, b) boundary flow, c) regular intersecting flow. All linear dimensions are normalized on cathode radius R_k.
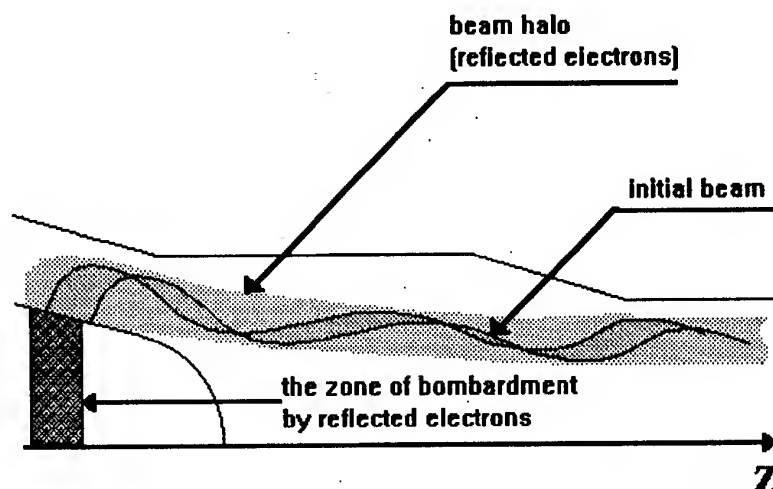
Fig.3. The qualitative picture of the space charge distribution formed by the initial beam and reflected electrons.

a)   b)   c)
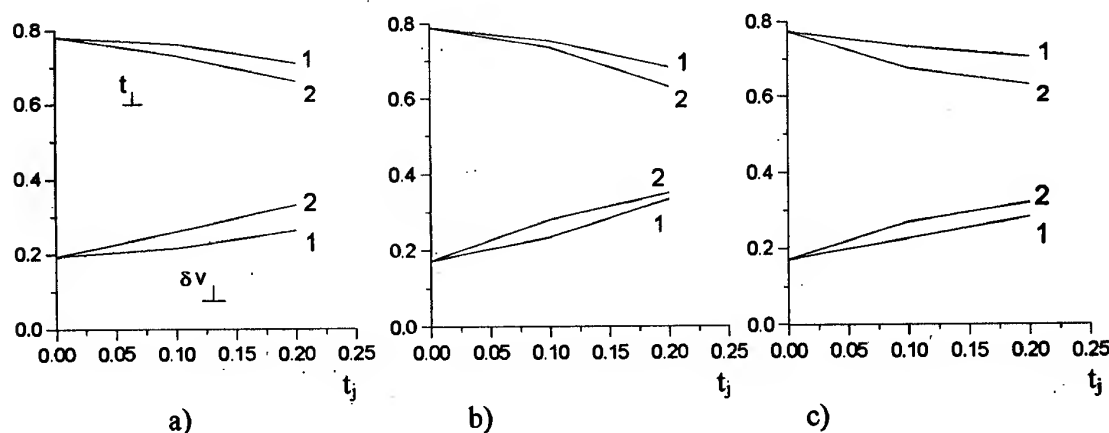
Fig.4. Calculated beam parameters : 1 static code, 2 - time dependent code (t > Tr) ;
a) - laminar flow, b) - boundary flow , c) - regular intersecting flow.

ACKNOLEDGMENT

REFERENCES

[1] Sh.E.Tsimring. Izvestiya Vysshikh Uchebnykh Zavedenii, Radiofizika, 15(1972) 1247.

[2] V.K.Lygin, V.N.Manuilov and Sh.E.Tsimring, Elektronnaya tekhnika, ser.1, Electronika SVCH, 7(1987).

[3] V.N.Manuilov and Sh.E.Tsimring, Izvestiya Vysshikh Uchebnykh Zavedenii, Radiofizika, 4(1981)491.

[4]. V.K.Lygin, Int. J. of IR and MM waves, 16(1995) 363.

[5] A.N.Kuftin, V.K.Lygin, Sh.E.Tsimring, V.E.Zapevalov, Int. J.Electronics, 72(1992) 1145.

[6] E.Borie, C.Cruber, T.Westermann. Int J. Electronics, 78(1995) 789.

[7] B.V.Raisky, Sh.E.Tsimring. IEEE Transactions on plasma science 24(1996) 992.

[8] V.K.Lygin, V.N.Manuilov and Sh.E.Tsimring. Proc. of the 5th Int.Conf. on Charged Particle Optics (1998).

CONTROL REGIMES POSSIBILITY IN SYSTEM WITH VIRTUAL CATHODE AND INTERNAL FIELD FEEDBACK

Yury P. Bliokh and Igor I. Magda

*Institute for Plasma Electronics and Advanced Acceleration Methods;
Akademicheskaya str. 1, Kharkov 310108, Ukraine;
phone: 38-057-240-4464, fax: 38-057-235-3564; e-mail: nsc@kipt.kharkov.ua*

ABSTRACT

The simulation results of a variety beam system with a supercritical current including electromagnetic feedback - VIRTODE [1] have been discussed. It has been shown, that beam dynamics and the output radiation parameters are the most sensitive to conditions of the cathode emission current modulation. These conditions may be produced by fields of a space-charge created in the acceleration area by reflected particles, and also by electromagnetic feedback fields, which are used for the radiation parameters control. The model results are in good qualitative correspondence with data obtained in experiments with real device.

INTRODUCTION

An interest to the structurally simple and effective HPM devices - vircators does not weaken in connection with necessities of their radiation parameters control. The present work proceeds a series of research in this field where the control factor is an external electromagnetic fields. The one-dimensional vircator mathematical model studies the system generation scheme including internal electromagnetic feedback (EMFB).

It is well known that vircator system generation is based on a strong feedback mechanism, stipulated by particle reflection from the virtual cathode (VC) area. As it had been shown [2], a space-charge fields formation in the acceleration area due to this beam feedback (BFB) produces emission current beam modulation in diode and forms preliminary conditions for vircator radiation parameters control. To maintain a vircator generation efficiency some special means should be performed. The radiation efficiency problem may be solved by removing particles that are randomly reflected from VC, returned in the acceleration area and disturbed the modulation process [3]. A virtode concept, produced by a series of our works, establishes that an arbitrary weak control signal injection into the acceleration area is efficient for both the power and the spectra control mechanisms. It is in connection with some obvious conditions:

• cathode emission current regime (the space-charge current limiting) due to strong nonlinearity of the volt-ampere diode performance is very sensitive to fields magnitude and configuration in the acceleration area;

• beam current preliminary modulation in the acceleration area improves a klystron bunching effect for particles that pass through anode and form a non-stationary VC [4];

• fields of a control signal in the drift area cannot compete to ones of a non-stationary VC.

Thus, the control vircator regime corresponds to some conditions of external fields formation and their interaction with beam particles in the acceleration area. Obviously, these conditions should promote the beam oscillation spectrum narrowing and the current preliminary modulation efficiency magnification in the range of specific frequencies.

PROPERTIES OF A MODEL

For the electron beam dynamics description in configuration close to real virtode scheme, it has been used a simple one-dimensional model, fig. 1, that includes two parts: the vircator traditional elements:

- cathode emission current is limited by the beam space-charge fields in diode;
- anode is half-transparent for particles moving in both directions, thus a BFB between the VC area *I* and the acceleration area *II* is created;
- electromagnetic fields, produced by a non-stationary VC, are completely radiating;

and some novel assumptions introducing electromagnetic feedback (EMFB) [1]:

- arbitrary small efficiency of a real vircator assumes a negligible backward effect of radiating fields on beam particle dynamics in area *II*;
- according to real system configuration the radiating fields are uniform over the VC area;
- internal EMFB is modeled by a waveguide of a variable length L_w that directs a portion of the output radiating power into area *II*;
- EMFB parameters take into account the feedback coefficient q_{FB} and the waveguide transparent function G_{FB}.

For simplicity a waveguide time delay is in proportion to L_w and its transparency is non-dispersive. Function G_{FB} assumes a low-frequency cutoff at $f_{cutoff} = 1/3 F_{max} \cong 1/3$ *a.u.* and a high-frequency exponential damping beginning at 6 F_{max}, where $F_{max} \cong 1$ *a.u* corresponds to the maximum in vircator generation spectrum without EMFB (autonomous generation regime).

The high-current relativistic beam experimental data show, that a beam particle passing through the half-transparent anode in arbitrary strong focusing magnetic field experiences minor energy losses. The losses are mainly caused by particle scattering in anode foil and on focusing magnetic field non-uniformity. Therefore it is assumed that electrons make no more than 2-5 half-oscillations around anode foil. Thus, in the present model the current and energy loss coefficients are $q_e = 0.9$, $q_E = 0.7$, correspondingly, and the minimum energy of oscillating particles is $E_{min} = 0.8$, that are typical values for such systems.

The set of equations describing a particle dynamics in an external accelerating and a self-consistent BFB fields, as well as in the EMFB circuit fields have been solved numerically using method of plane sheets [5]. As parameters of the model data that define the anode transparency, the EMFB signal delay and the feedback coefficient have been used.

SIMULATION RESULTS

The previous model study of the autonomous generation regime with the switched off BFB (simulation of the non-transparent anode) [2], had shown an intensive generation with no significant control effect of an external fields in the range of vircator frequency and its harmonics. As it has been shown, an efficient vircator radiation control assumes complex conditions for well formed BFB and an effective EMFB. This stipulates the main features of the examined model regimes - the half-transparent anode and the EMFB circuit, produced by matching the radiation and the acceleration areas.

In the noted conditions of a combined feedback a strong generation intensity dependence on the EMFB signal magnitude is observed. Indicated on fig. 2 data correspond to a field feedback coefficient $q_{FB} = 0.1 - 0.4$. As it is seen, an essential magnification of a control efficiency corresponds to the EMFB power coefficient of 0.1 - 0.15.

The EMFB influence also essentially modifies a character of vircator generation spectrum, that is obvious from comparison of function P_{output} (*f*), obtained for autonomous and controlled regimes, fig. 3, 4. Multifrequency and almost noisy a spectrum at the autonomous regime comes to more intense narrow-band spectrum with dominant lines when the

feedback coefficient increases up to $q_{FB} = 0.3 - 0.4$. The dominant frequencies are formed in the range of 1-2 F_{max}.

The EMFB effect on the radiation spectrum narrowing may be understood assuming that:

- BFB is principally broadband because of absence of severe constraints on the beam particle energy selection;

- EMFB operation essentially narrows the initial beam particle modulation spectrum in diode, and further grouping effect in traveling beam strengthens the process of narrow-band and high-power radiation formation.

Thus, the generation efficiency increase and spectrum narrowing are the result of a combined feedback (BFB + EMFB) effect. It is necessary to take into account, that each feedback has its own frequency spectrum and delay times. Therefore, when one of these feedbacks alternates its frequency spectrum (in the present model it may easier be done by EMFB), the system amplification as a whole may vary significantly.

This EMFB effect is well exhibited by the EMFB waveguide length L_w alternation. From the output power dependence P_{output} (L_w), fig. 3, 4 it may be seen, that this effect allows to vary the output radiation amplitude over a wide range. The radiation power in the EMFB regime for $q_{FB} = 0.3 - 0.4$ and for selected dominant frequency from 6 to 20 times exceeds the power maximum for autonomous generation.

The simulation results also show that the power dependence P_{output} (L_w) in a wide range of $L_w = 2$-20 $a.u.$ has a periodic character in correspondence to similar dependence for the real device [1]. Under variation of L_w as a parameter at $q_{FB} = 0.4$ the output radiation power ratio P_{max}/P_{min} achieves 6-6.5.

It is interesting to note that parameter L_w variation in rather broad limits is accompanied by the dominant frequency tuning up to 40% that also confirms the combined feedback effect.

One of the main problems of the present studies is place for the control EMFB signal injection. Similarly to the previous study [2], it is checked up by the emission current eliminations from a model of the EMFB regime. In fig. 5 there are plots of vircator generation dynamics, appropriate to conditions of the diode current modulation mechanism stipulated by the EMFB, and without modulation. As it may be seen, an amplitude increase and a more regular output signal formation for the first case testifies a high vircator sensitivity of the EMFB injected in the acceleration area. The presence of an analog to this mechanism among devices of a traditional vacuum electronics - a grid control of the anode current in triode configuration, confirms a principal importance of the selected mechanism for the radiation parameter control in vircators.

CONCLUSIONS

1. The acceleration area in vircator is a beam source with nonlinear property of electric field. The fields formed in this area, essentially influence to the VC dynamics and the device operation as a whole. Due to this a possibility appears for vircator system to be controlled by means of arbitrary weak signals injected into the particle acceleration area.

2. Vircator with the EMFB circuit changes essentially the output radiation parameters. The dominant radiation frequencies are formed that exceed 10 - 20 dB the spectral background repeating a monotonous configuration of spectrum for the autonomous regime. The output radiation power increases by the factor of 10-15 dB.

3. Variation of the EMFB coefficient module allows to alternate the output radiation power over a wide range.

4. The EMFB time delay factor determines characteristic dominant frequencies for the given regime within the limits of the basic generation spectral maximum.

REFERENCES

1. N.P. Gadetski, I.I. Magda, S.I. Naisteter, et al.,The virtode: a generator using supercritical REB current with controlled feedback. Plasma Phys. Rep., 1993, v. 19, No. 4, p. 273.

2. Yu.P. Bliokh and I.I. Magda, Controlled regimes possibility in system with virtual cathode by external electromagnetic signal. Proc. of the Int. Conf. on LASERS'97. New Orleans, USA, Dec. 1997.

3. H. Davis, R. Bartsch, T. Kwan, et al., Experimental configuration of Reditron concept, IEEE Trans. Plasma Sci., 1988, v. 16, p. 192.

4. D.J. Sullivan, J.E. Walsh and E.A. Coutsias, Virtual cathode oscillator (Vircator). Theory, in: *High-Power Microwave Sources*, V. Granatstein and I. Alexeff, ed., Artech House, Norwood, 1987, p. 441.

5. A.P. Prevezentsev, N.I. Sablin and G.P. Fomenko, Nonlinear dynamics of virtual cathode in high frequency field. Radiotechnica i Electronika, 1990, v. 35, No. 4, p. 832.
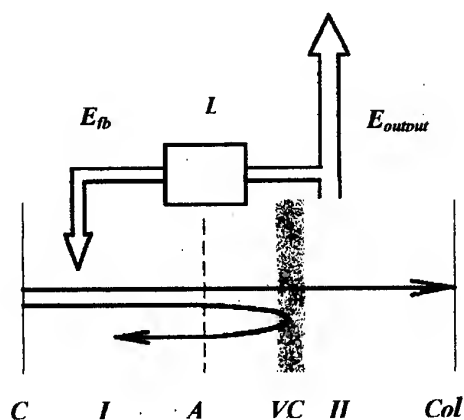
Fig. 1. Configuration of the studied 1D vircator model. C - cathode, A - half-transparent anode, VC - virtual cathode, I and II - acceleration and drift areas, correspondingly, L - pathlength of the EMFB waveguide.
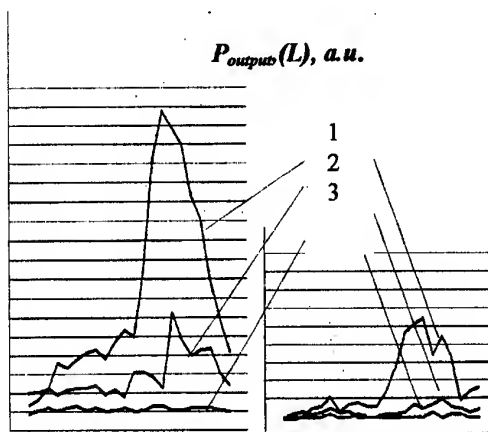
Fig. 2. The normalized output radiation power as a function of a waveguide length L_w in $a.u.$ for different emission current regimes: *left* - space-charge current limit, *right* - constant current. Curves 1, 2, and 3 correspond to a feedback coefficients q = 0.4, 0.3, and 0.1.
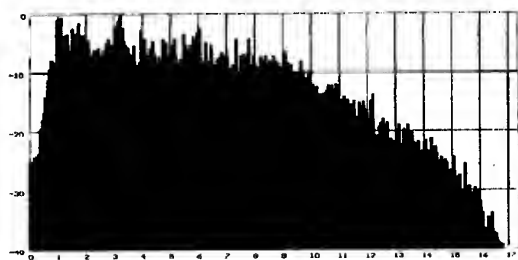
Fig. 3. The radiation power spectrum $P(f)$ in dB and f in $a.u$ for the autonomous regime.
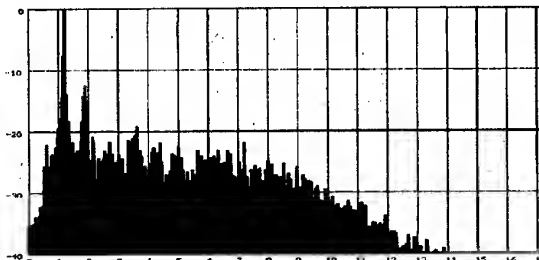
Fig. 4. The radiation power spectrum $P(f)$ in dB and f in $a.u.$ for the EMFB regime for a feedback coefficient $q = 0.4$ and a waveguide length $L = 8$ $a.u.$
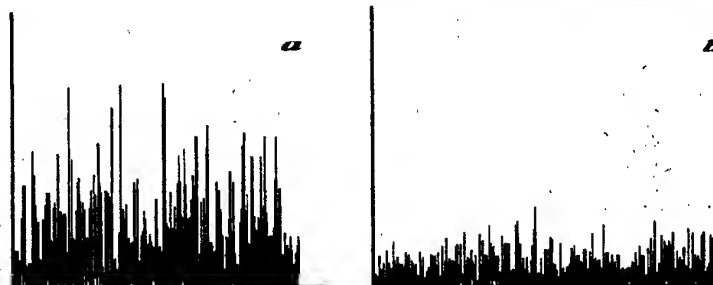
Fig. 5. Time evolution of the output radiation power. Plot *(a)* corresponds to the system with modulated emission current. Plot *(b)* corresponds to the system with fixed emission current.

GENERATION OF DENSITY MODULATED
ELECTRON BEAM IN AN OPEN RESONATOR[*]

B. Maly, J.A. Nation[*] and L. Schächter

*Department of Electrical Engineering, Technion – Israel Institute of Technology,
Haifa 32000, Israel*

The energy carried by density modulated electron beams with low spread in velocity can be converted into high power microwave radiation with high efficiency. The density modulated beam is generated by applying both rf and dc fields. This is possible in an __open cavity__ that consists of a Bragg reflector region. We examine the conditions for beam generation taking into account regular field emission (Fowler-Nordheim) and space-charge effects. The concept is demonstrated when a density modulated beam is injected in a tapered traveling wave structure; simulations indicate that the highest efficiency is achieved when in the first 15% of the interaction region the phase velocity of the wave is higher than the average velocity of the electrons.

In a klystron, the electromagnetic field stored in a closed cavity generates velocity modulation on an otherwise uniform beam; no dc field can be applied in the cavity region. The velocity modulation is utilized down stream to enhance the modulation and eventually to convert kinetic energy into electromagnetic power. On the other hand, the simplest configuration we can conceive for the generation of a uniform beam is an anode–cathode gap. Here we can apply a dc field but can not apply an rf field since this energy will leak out of the system. In order to combine the features of a diode on one hand and a cavity on the other hand we suggest an open cavity configuration as illustrated schematically in Fig. 1.
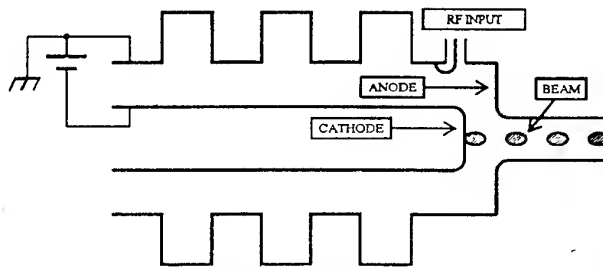
Fig. 1: Schematics of the open cavity which facilitates the generation of a density modulated beam.

The cavity consists of two metallic surfaces, which are electrically insulated facilitating application of a dc field that, in turn, enables to reach the threshold for significant field emission. The latter is exceeded by applying an rf field that is confined by a "Bragg reflector" [1]. Contrary to klystrons where the cavity gap is much smaller than the radiation wavelength, here we chose the geometry such that the transit time of the electrons is equal to the rf period. If we further assume that the electric field experienced by the electrons does not vary in space, then the electrons at the anode can be considered as *mono-energetic;* their energy is determined only by the dc field.

The Bragg reflector consists of several cells of a periodic coaxial structure; the inner cylinder is smooth (in order to avoid emission from the edges) and the outer cylinder is corrugated. Since our rf source operates at 9.25GHz, the geometrical dimensions of the periodic structure were adjusted such that the forbidden band (3GHz) will be centered at this frequency; see left frame of Figure 2. The propagation number in this frequency range has an imaginary part, therefore the field decays rapidly along the longitudinal direction. For this reason only a small number of cells is needed in order to achieve a high quality factor; the entire cavity including the output waveguide was simulated with Superfish - see right frame of Fig. 2. This design satisfies the condition mentioned above regarding the transit time of an electron over the gap comparing to the rf time period.

Fig. 2: Left frame. The dispersion relation of a periodic coaxial corrugated waveguide. The geometry was designed such that there is a wide cut-off band between the first two propagating modes, centered about 9.25 GHz. Right Frame. The first resonant mode in the open resonator at 9.25 GHz. The simulation was performed with "Superfish". All dimensions are in [mm].

The electron beam characteristic is considered assuming two quasi-static effects: space-charge effect and field emission. The current density assuming a planar diode with a voltage V_0 applied to the anode and an electric field at the cathode is E (Child-Langmuir limit is achieved when the latter is zero) is given by

$$J = \sqrt{\frac{2e}{m}}\frac{\varepsilon_0}{9g^2} \cdot \begin{cases} 2V_0^{\frac{3}{2}} + \sqrt{4V_0^3 - 27E^2g^2 \cdot (V_0 - E \cdot g)}, & E \le \frac{2}{3}\frac{V_0}{g} \\ 2V_0^{\frac{3}{2}} - \sqrt{4V_0^3 - 27E^2g^2 \cdot (V_0 - E \cdot g)}, & E > \frac{2}{3}\frac{V_0}{g} \end{cases} \qquad (1)$$

where m is the electron mass, e is the electron charge, J is the current density, ε_0 is the vacuum permitivity and g is the diode gap. The second effect considered is the field emission described by the Fowler-Nordheim formula:

$$J = 3.44 \times 10^{-7} \cdot (\beta E)^2 \cdot \exp\left(-\frac{6.54 \times 10^{10}}{\beta E}\right) \qquad \left[\frac{A}{m^2}\right] \qquad (2)$$

where E is expressed in [V/m] and β (=120) is the surface enhancement factor. The current density at a given voltage is determined by the intersection point of the (1) and (2) as illustrated in the left frame of Fig. 3. The resulting non-linear current-voltage characteristic is presented in the right frame of the same figure.
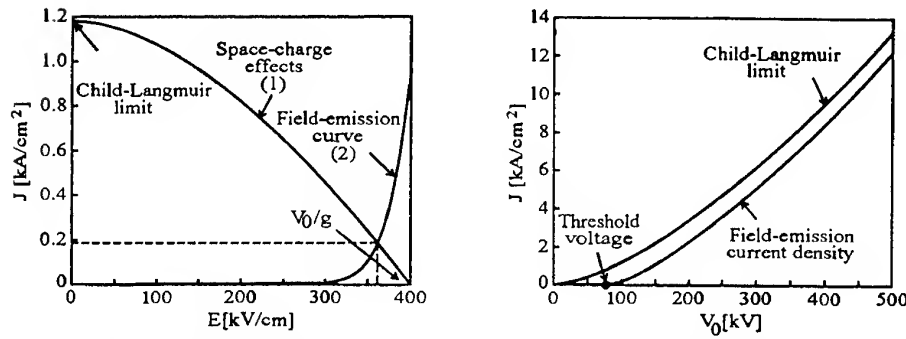
Fig. 3: The current density is determined by the intersection point of (1) and (2) accounting for space charge and field emission effects (left frame). The lower curve in the right frame describes the emission process as a non-linear impedance. There is a threshold voltage at which the cut-off region ends. The current density approaches the Child-Langmuir limit (upper curve) at high voltages.

With the characteristic of the beam established we may simulate the operation of this system and determine the system's dynamics. For this purpose the system is modeled by a lumped circuit illustrated in Fig. 4 (left frame). In this circuit R_0 represents wall loss, Z stands for the non-linear diode impedance, V_0 is the dc accelerating voltage and V_1 represents the rf input voltage. Simulation indicates that a peak current of 10 A can be achieved (right frame) during about 30% duty-cycle. The dc voltage applied in this simulation is 70kV and the input rf power is 48kW. The calculated output average power carried by this beam is 240 kW.
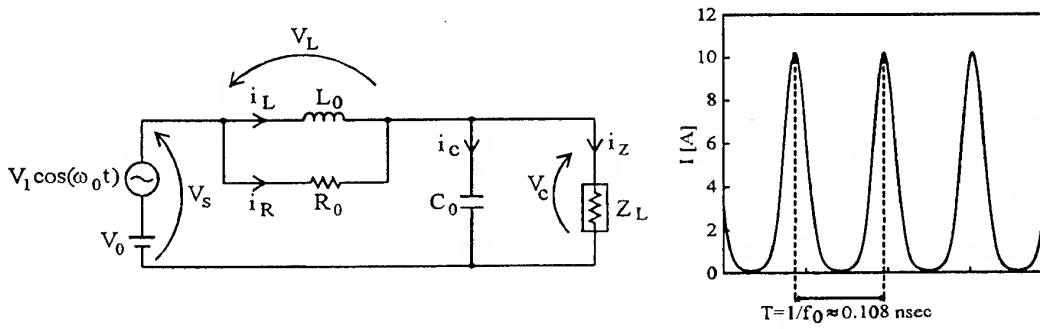
Fig. 4: Left frame. The lumped circuit model by which the dynamics of the system is determined. Right frame. The current that can be achieved at the output.

In order to show the potential of a density modulated beam we consider next the build-up of electromagnetic energy in a tapered traveling wave structure. For simplicity we assume that the interaction is with the TM_{01} mode in a dielectric filled waveguide [2] such that the relation between the coupling coefficient α and the normalized wavenumber K is given by

$$\alpha = \frac{1}{\pi} \cdot \frac{eI\eta_0}{mc^2} \cdot \frac{1}{p_1^2 J_1^2(p_1)} \cdot \frac{u^4}{u^2 + K^2} \cdot \frac{\Omega}{K} \tag{3}$$

where η_0 is the vacuum impedance, I is the average current, $u = p_1 d/R$, R is the radius of the waveguide, d is the interaction length, $\Omega = \omega d/c$; ω is the angular frequency, p_1 is the first zero of zero order Bessel function of the first kind and J_1 is the first order Bessel function of the first

kind. With this relation, the equations that control the dynamics of an ensemble of electrons in the presence of a normalized electric field $a = eEd/mc^2$ are given by

$$\frac{d}{d\zeta}\left(\frac{a}{\sqrt{\alpha}}\right) = \sqrt{\alpha} \cdot \left\langle e^{-j\chi_i}\right\rangle_i \;, \quad \frac{d}{d\zeta}\gamma_i = -\frac{1}{2}\left(a \cdot e^{j\chi_i} + c.c.\right) \;, \quad \frac{d}{d\zeta}\chi_i = \frac{\Omega}{\beta_i} - K \quad (4)$$

where χ_i is the relative phase of the i'th particle, β_i is the normalized velocity of the i'th particle, $K (= kd)$ is the normalized wavenumber, $\gamma_i = (1 - \beta_i^2)^{-1/2}$ and $\zeta = z/d$.

These equations were solved numerically. The initial value for the complex electric field is zero and the initial spread in kinetic energy is about 0.2% rms. The initial spread in phase of the macro particles is 40 degrees and the current is assumed to have a <u>square shape</u> in the initial phase-space. The calculated efficiency is about 90% (see left frame of Fig. 5). In order to reach this high efficiency the initial phase velocity of the wave has to be somewhat faster than the average velocity of the electrons. In this way the bunch is actually <u>compressed</u> before it is decelerated by the wave. The right frame of Fig. 5 illustrates the way that the (active) phase velocity of the wave should develop in space; with the exception of the first 15% of the interaction region the particles should be resonant with the wave. If the resonance condition is imposed from the input (upper curve of right frame), the conversion efficiency is substantially reduced as illustrated in the lower curve of the left frame;
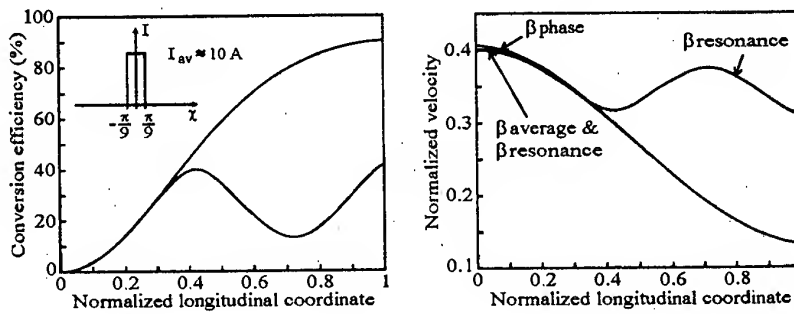
Fig. 5: The conversion efficiency in the interaction region may reach the level of 90% (left frame -upper curve) for an ideal density modulated mono energetic beam with a spread in phase of 40^0 and average current of 10 *A*. At the beginning of the interaction region the (active) phase velocity of the wave should exceed somewhat the average velocity of the particles (right frame -lower curves). However, if these velocities are equal then the efficiency decreases (left frame –lower curve and right frame -upper curve).

In conclusion, taking advantage of the non-linear effects associated with space-charge and field-emission, together with the ability to confine rf energy in an open resonator; it was shown that a density modulated electron beam with low energy spread is achievable. The potential of such a scheme was demonstrated theoretically when we calculated the interaction of an ideal density modulated beam with an electromagnetic wave in a tapered slow wave structure; simulation indicates that very high efficiency can be achieved provided that in the first 15% of the interaction region, the phase velocity is higher than the average velocity of the electrons.

REFERENCES

[1] T. Shintake: "The Choke Mode Cavity", *Jpn. J. Appl. Phys.*, Vol. 31 (1992), pp. L 1567-L 1570.
[2] L. Schächter:"Beam Wave Interaction in Periodic and Quasi Periodic Structure",Springer,1997,pp.157.

LINEAR ANALYSIS OF INSTABILITIES
IN A PLASMA-FILLED DIELECTRIC-LINED CIRCULAR
WAVEGUIDE IMMERSED IN A FINITE AXIAL MAGNETIC FIELD

Masaru Masuzaki, Hiroshi Tsukuda, Norio Toyosugi, Keiichi Kamada, Ritoku Ando,
Tsuguhiro Watanabe,* and Cha Yeol Lee**

Department of Physics, Faculty of Science, Kanazawa University, Kanazawa 920-1192, Japan
*National Institute for Fusion Science, Toki 509-5292, Japan
***Department of Physics, College of Natural Sciences, Pukyong National University, Pusan
608-737, Korea*

Abstract: A dispersion relation is derived for waves excited by an intense relativistic electron beam in an infinitely long plasma-filled dielectric-lined circular waveguide immersed in a finite axial magnetic field.

Recently much attention has been paid to plasma-filled high-power microwave devices such as backward-wave oscillators and dielectric Cherenkov masers (DCM). It is thought to be one advantage of such devices that the current of the driving electron beam can be raised due to charge neutralization and accordingly output power of radiation is enhanced. There are some theoretical treatments for DCM with an infinite axial magnetic field [1], and without axial magnetic field [2]. However, as far as the authors know, there is no full treatment for the case with a finite axial magnetic field.

In this work we derive a dispersion relation for waves excited by an intense monoenergetic linear relativistic electron beam (IREB) in a plasma-filled dielectric-lined cylindrical waveguide immersed in a finite axial magnetic field, B_0. Figure 1 shows the configuration of the system under the consideration. The waveguide is supposed to be infinitely long. Radii of the plasma and the IREB columns are assumed to be the same. Also it is assumed that there is a vacuum gap between the dielectric liner and the beam-plasma column. We take account of all field components and three dimensional perturbed velocities of beam and plasma electrons. Plasma ions are assumed to be stationary. We use cylindrical coordinates (r,θ,z) and consider only axially symmetric modes. All perturbed quantities are assumed to vary as

$$f = f(r)\exp i(kz - \omega t)$$

From equations of motion and continuity equations for beam electrons and plasma electrons, energy equation for beam electrons, and Maxwell's equations, all linearized, we obtain coupled differential equations for axial electric and magnetic fields, E_z and B_z, in the beam-plasma region. Bessel function of the first kind of zeroth order can be the solutions of these equations, and other components are derived from E_z and B_z. However, instead of solving these equations directly, we adopt following procedure. Assuming that each electric field components can be given as follows,
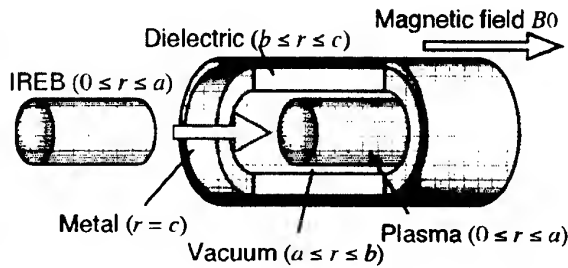
Figure 1. Dielectric lined waveguide filled with plasma and the beam immersed in a finite magnetic field.

$$E_{rb}(r) = \sum_p iA_pJ_1(pr), \quad E_{\theta b}(r) = \sum_p B_pJ_1(pr), \quad E_{zb}(r) = \sum_p C_pJ_0(pr),$$

the each magnetic field component is given as

$$B_{rb}(r) = -\frac{k}{\omega}\sum_p B_p J_1(pr), \quad B_{\theta b}(r) = i\sum_p \frac{kA_p - pC_p}{\omega} J_1(pr), \quad B_{zb}(r) = -i\sum_p \frac{pB_p}{\omega} J_0(pr).$$

Substituting these equations into equations of three dimensional perturbed velocity components and perturbed densities, which are derived from equations of motion and continuity equations for beam electrons and plasma electrons, and energy equation for beam electrons, we obtain three dimensional perturbed current density components expressed by field components. Substituting these into one of Maxwell's equations, rot $B = \mu_0 j + \frac{1}{c^2}\frac{\partial E}{\partial t}$, we obtain following simultaneous algebraic equations for A_p, B_p, and C_p.

$$d_{11p}A_p + d_{12p}B_p + d_{13p}C_p = 0, \quad d_{21p}A_p + d_{22p}B_p + d_{23p}C_p = 0, \quad d_{31p}A_p + d_{32p}B_p + d_{33p}C_p = 0,$$

where $d_{11p} = \omega^2 - c^2 k^2 - \gamma\omega_b^2\omega'^2/\omega''^2 - \omega_p^2\omega^2/(\omega^2 - \Omega^2)$, $\quad d_{22p} = d_{11p} - p^2 c^2$,

$$d_{12p} = \Omega\{\omega_b^2\omega'/\omega''^2 + \omega_p^2\omega/(\omega^2 - \Omega^2)\}, \quad d_{13p} = -p\left(\gamma\omega_b^2\omega'v_0/\omega''^2 - c^2 k\right),$$

$$d_{23p} = p\omega_b^2\Omega v_0/\omega''^2 \text{ and } d_{33p} = \omega^2 - \omega_p^2 - \omega_b^2\omega^2/\gamma^3\omega'^2 - p^2\left(c^2 + \gamma\omega_b^2 v_0^2/\omega''^2\right).$$

Here $\omega' = \omega - kv_0$, $\omega''^2 = \gamma^2\omega'^2 - \Omega^2$, $\Omega = eB_0/m$, $\omega_b^2 = n_{b0}e^2/m\varepsilon_0$, $\omega_p^2 = n_{p0}e^2/m\varepsilon_0$,

$\gamma = 1/\sqrt{1 - v_0^2/c^2}$, n_{b0} and n_{p0} are the beam and the plasma densities, and e, m and ε_0 have usual meanings.

By setting the determinant of this equation system to zero, a pair of radial wavenumbers p and p' is determined. And, for each p, B_p and C_p are expressed with A_p as

$$B_p = A_p\left(A_{2p}/A_{1p}\right) = A_p\left(d_{13p}d_{23p} - d_{12p}d_{33p}\right)/\left(d_{22p}d_{33p} - d_{23p}^2\right)$$

and

$$C_p = A_p\left(A_{3p}/A_{1p}\right) = A_p\left(d_{12p}d_{23p} - d_{13p}d_{22p}\right)/\left(d_{22p}d_{33p} - d_{23p}^2\right).$$

Carrying out usual procedure, E_z and B_z in the gap and the dielectric regions are given as follows. The subscripts "v" and "d" indicate gap and dielectric regions, respectively.

$$E_{zv}(r) = S J_0(qr) + T N_0(qr), \quad B_{zv}(r) = i\left(U J_0(qr) + V N_0(qr)\right),$$

$$E_{zd}(r) = S' J_0(q'r) + T' N_0(q'r), \quad B_{zd}(r) = i\left(U' J_0(q'r) + V' N_0(q'r)\right),$$

where $q^2 = \omega^2/c^2 - k^2$ and $q'^2 = \varepsilon_r\omega^2/c^2 - k^2$.

Boundary conditions at metal-dielectric and dielectric-vacuum interfaces are usual ones. At vacuum-plasma (beam) interface, considering the deformation of boundary shapes of beam and plasma regions due to the electrons' motion, surface charge and surface current are determined as $\sigma_s = -ie\left(n_{b0}v_{br}(a)/\omega' + n_{p0}v_{pr}(a)/\omega\right)$ and $j_s = -ien_{b0}v_0 v_{br}(a)/\omega'$.

The final dispersion equation is obtained by setting the determinant of the following system of simultaneous equations for ten unknowns, i.e., two A_p's, S, S', T, T', U, U', V, and V'.

$$\sum_p A_p\left(pA_{2p}J_0(pa)/\omega A_{1p}\right) = -\left(U J_0(qa) + V N_0(qa)\right),$$

$$\sum_p A_p\left(A_{2p}J_1(pa)/A_{1p}\right) = -\omega\left(U J_1(qa) + V N_1(qa)\right)/q,$$

$$\sum_p A_p\left(A_{3p}J_0(pa)/A_{1p}\right) = SJ_0(qa) + TN_0(qa),$$

$$\frac{\omega_b^2 v_0}{c^2\omega''^2}\sum_p A_p J_1(pa)\left(\gamma\omega' - \Omega\frac{A_{2p}}{A_{1p}} + \gamma p v_0\frac{A_{3p}}{A_{1p}}\right) = \frac{\omega^2}{qc^2}(SJ_1(qa) + TN_1(qa)) + \sum_p A_p J_1(pa)\left(k - p\frac{A_{3p}}{A_{1p}}\right),$$

$$(UJ_1(qb) + VN_1(qb))/q = (U'J_1(q'b) + V'N_1(q'b))/q',$$

$$SJ_0(qb) + TN_0(qb) = S'J_0(q'b) + T'N_0(q'b),$$

$$UJ_0(qb) + VN_0(qb) = U'J_0(q'b) + V'N_0(q'b),$$

$$(SJ_1(qb) + TN_1(qb))/q = \varepsilon_r(S'J_1(q'b) + T'N_1(q'b))/q',$$

$$S'J_0(q'c) + T'N_0(q'c) = 0,$$

and

$$U'J_1(q'c) + V'N_1(q'c) = 0.$$

The dispersion equation obtained is a complex transcendental equation. To solve it we must numerically calculate Bessel functions with complex arguments.

Figure 2 shows an example of the dispersion relation for the waveguide filled with

Figure 2. Dispersion relation for waveguide filled with plasma

Figure 3. Dispersion relation (a) and growth rates of instabilities (b) for waveguide filled with the beam.

plasma. Parameters are: radius of the plasma (beam) region $a = 8$ mm, inner radius of the dielectric liner $b = 9$ mm, inner radius of the metallic cylinder $c = 10$ mm, dielectric constant $\varepsilon_r = 2$, the plasma density $n_{p0} = 5 \times 10^{11}$ cm^{-3}, and the axial magnetic field $B_0 = 1.5$ T. In Fig. 2 we can see the waveguide modes and the Trivelpiece-Gould (T-G) modes. As expected there is no instability. Figure 3 shows an example of the dispersion relation for the waveguide filled with the beam which corresponds to the example in Fig. 2: Fig. 3(a) shows dispersion relation in real space and 3(b) shows growth rates of instabilities. The beam energy is 1.5 MeV and the beam current is 5 kA. In this Figure we can see Cherenkov instability (A) which is due to coupling of the slow space charge mode in the beam with the first waveguide mode (TM$_{01}$ mode), and cyclotron Cherenkov instability

(B) which is due to coupling of the slow cyclotron mode in the beam with the first waveguide mode. This is because the dielectric-lined waveguide is a slow wave structure. Appearance of the latter instability is due to the finite axial magnetic field. Figure 4 shows an example of the dispersion relation for the waveguide filled with the beam and plasma which corresponds to examples in Fig.'s 2 and 3: Fig. 4(a) shows dispersion relation in real space and 4(b) shows growth rates of instabilities. In addition to Cherenkov instability (A) and cyclotron Cherenkov instability (B) we can see instabilities due to coupling of slow cyclotron modes with lower branches of T-G modes (D), instabilities due to coupling of slow space charge modes with upper branches of the T-G modes (C) and instabilities due to coupling of slow cyclotron modes with upper branches of the T-G modes (E). We call instabilities (C), (D), and (E) as beam-plasma instabilities. Some detailed examinations indicate that the main coupling is between modes of the same order. Cherenkov instability is modified when plasma is present, and it connects to some mode in the beam-plasma modes (C).
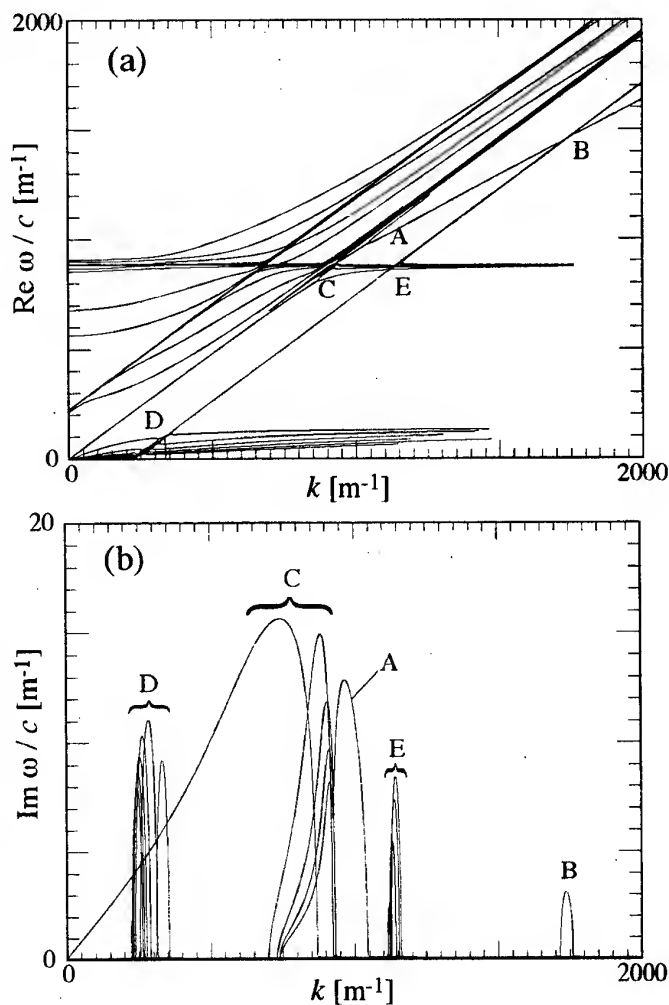
Figure 4. Dispersion relation (a) and growth rates of instabilities (b) for waveguide filled with the beam and plasma.

When B_0 is much less than 1.5 T its growth rate is the same as in Fig. 3. As B_0 is increased, resonance points of instabilities (C) approaches the resonance point of Cherenkov instability and its growth rate decreases. The order of beam-plasma mode (C) to which it connects changes. After the former pass the latter, Cherenkov instability is disconnected from the (C) mode and its growth rate returns to its former value. Other parametric researches are being carried out.

We are now applying similar procedures for annular beam case, no dielectric liner case, and coaxial waveguide case. Finally we note that the there is a possibility of nonlinear coupling of (C) modes with (E) modes by some means.

References

[1] Hiroyuki Kosai, Eusebio P. Garate, and Amnon Fishier, IEEE Trans. Plasma Science, **18**, 1002 (1990).

[2] Wu Jian-Qiang, Phys. Plasmas, **4**, 3064 (1997).

OBSERVATION OF SELF-MODULATION REGIMES OF GENERATION IN POWERFUL BWO

N.S. Ginzburg, N.I. Zaitsev, I.S. Kulagin, Yu.V. Novozhilova, M.I. Petelin, A.S. Sergeev,
A.K. Tkachenko
Institute of Applied Physics, Nizhny Novgorod, Russia

Self-modulating regimes of generation in powerful X-band BWO was studied experimentally. Periodic sinusoidal modulation of the output signal was observed, which became more complicated as the beam current grew, acquired the character of a series of spikes, and then lost its periodicity.

Complex dynamics in backward-wave generators was first studied theoretically in papers [1,2]. It was shown that as the current exceeds the start value, the regime of stationary single-frequency generation is replaced with the regime of periodic self-modulation, first sinusoidal and then acquiring the shape of a sequence of peaks. As the current grows further, the signal modulation becomes more complicated and loses its periodicity. For the large exceeding of current over threshold generation becomes stochastic. The such sequence of bifurcations was observed experimentally in the non-relativistic BWO with power levels of several milliwatt [3].

This report is devoted to the theoretical and experimental investigation of self-modulation regimes in BWO with power levels of tens to hundreds kW and configuration of the interaction space typical for relativistic BWO [4] (smoothly corrugated waveguide with cut-off narrowing at the cathode end and diffraction output of radiation from the collector end). It is evident that achievement of chaotic self-modulation in such generators opens prospects to create powerful noise sources operating in the X-band wavelength range.

As a source of electron pulses we used the "Saturn" accelerator based on a magnetron-injection gun with a thermal cathode that allowed formation of beams with duration up to 10 µs, energy of particles up to 300 keV, and current up to 300 A. This accelerator was used earlier in successful realization of the relativistic BWO with the power level 5 MW and pulse duration up to 10 µs [5].

The lowest mode, TE_{11} was chosen as the operating one to avoid the resonance interaction of the electron beam with other modes and the related problem of mode selection on the transverse index. The microwave system was made as a section of axially symmetric corrugated waveguide with mean radius 1.2 cm, period and amplitude of corrugations 1.7 cm and 0.25 cm, respectively. The waveguide had a cut-off narrowing at the cathode end and was smoothly matched to the output waveguide at the collector end. In order to reduce starting currents at fixed coupling impedance; the length of the interaction space was extended to 44 cm. The accelerating voltage was about 70 kV, the beam current changed in the range from 3 A to 35 A. At expected efficiency these parameters were chosen to avoid microwave breakdowns. The operating wavelength was 3.75 cm.

Preliminary simulation of multi-frequency processes in the BWO generator was performed basing on the self-consistent system of equations [1], which consisted of the equation describing evolution of the field amplitude

$$\frac{\partial A}{\partial \tau} - \frac{\partial A}{\partial \varsigma} = -\frac{J}{\pi} \int_0^{2\pi} \exp(-i\vartheta) d\vartheta_0 \qquad (1)$$

and relativistic equations for electron motion:

$$\frac{\partial \vartheta}{\partial \varsigma} = \frac{1}{\sqrt{1-\gamma^{-2}}} - \frac{1}{\sqrt{1-\gamma_0^{-2}}} \qquad (2)$$

$$\frac{\partial \gamma}{\partial \varsigma} = \text{Re}\left(A(\varsigma,\tau)\exp(i\vartheta)\right) \qquad (3)$$

Here $A = eE_z/(mc\omega)$ is dimensionless amplitude of the resonance (−1)st field harmonic, $\tau = \omega(t - z/v_0)/(1/\beta_0 + 1/\beta_{gr})$ and $\varsigma = \omega z/c$ are dimensionless time and longitudinal coordinate, respectively, $\vartheta = \omega t - hz$ is phase of electrons relative to the synchronous harmonic of the field, $J = eI|Z|/(2\beta_0^2 mc^2)$, Z is the impedance for this harmonic [6], I is beam current, γ is the relativistic mass-factor of electrons, ω is the frequency of precise synchronism, $\beta_0 = v_0/c$, $\beta_{gr} = v_{gr}/c$, where v_0 is initial velocity of electrons, v_{gr} is group velocity of the wave. The boundary and initial conditions for equation (1)–(3) have the following form:

$$A\big|_{\varsigma=l} = 0 \ , \ A\big|_{\tau=0} = A_0(\tau) \ , \quad \vartheta\big|_{\varsigma=0} = \vartheta_0 \in (0,2\pi) \ , \quad \gamma\big|_{\varsigma=0} = \gamma_0 \qquad (4)$$

where l is dimensionless length of the interaction space.

Coupling impedance and starting currents were calculated basing the results presented in [6]. The starting current of the BWO with the length of the decelerating system 44 cm was about 1 A. The relative excess of the current over the threshold, corresponding to the appearance of periodic self-modulation, is equal to 2.9. The stochastic regime is realized when this excess reaches 10–15. Fig. 1 shows the results of simulation of the output signal amplitude time dependence, as well as the spectrum of the signal at different values of current
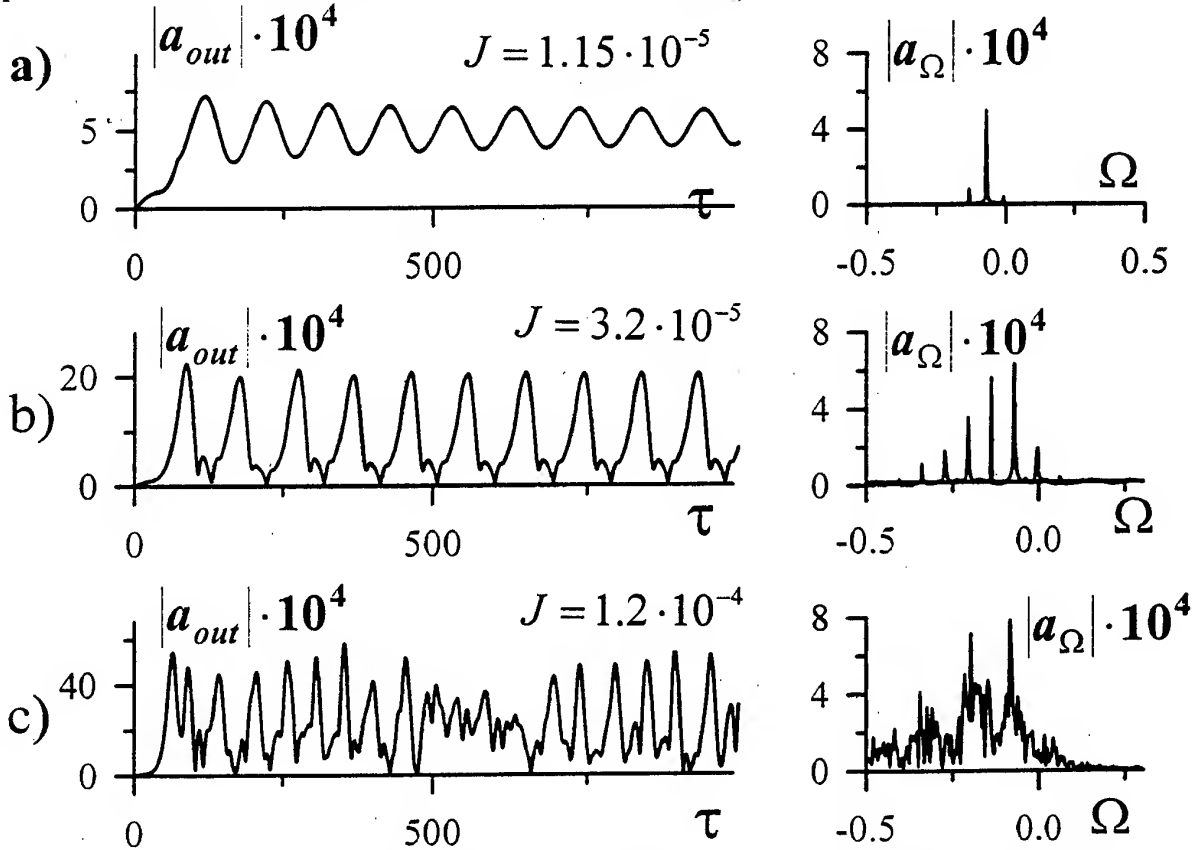
FIG.1. Evolution of wave amplitude and spectrum with increase of electron current (simulation)

and tube length 44 cm, which corresponds to $l = 70$. Figure 1a corresponds to sinusoidal self-modulation of the output signal, fig. 1b - to more complicated self-modulation in the form of a periodic sequence of spikes. In dimensionless variables the period of self-modulation is equal to $\sim 10^2$. The period of self-modulation in the operating point was about 12 ns in dimensional values. By that, in the case of the sinusoidal self-modulation the relative width of the radiation spectrum was 0.7%. Fig. 1c shows the variant of stochastic self-modulation corresponding to the spectrum width of 5%.

In the experiments the output signal was recorded with the digital Tektronix TDS-540A oscilloscope. It allowed storing in memory of all the envelope of the high-frequency pulse with total duration up to 10 µs for further analysis of its separate plots. The sections of oscillograms corresponding to equal accelerating voltages but different values of the operating current are shown in Fig. 2. Radiation was registrated on the collector end of the interaction space. As it is seen from Fig. 2, at current of 3 A the regime of sinusoidal self-modulation was observed, and as the current increased, the time dependence of the amplitude became more complicated. At the currents from 21 A to 28 A self-modulation had the complex periodical character, and at currents over 35 A it became stochastic. Note that in the above sequence of oscillograms there is no regime of stationary generation. It is explained by the fact that the decreasing of the current lower than 3 A was connected with great technical difficulties. At the same time, stationary regimes of generation in the current range from 3 A to 20 A were observed in a tube with the interaction space shortened to 29 cm.

In the experiment the regime of stochastic self-modulation was achieved when the current reached 35 A, which exceeded the bifurcation value, founded from numerical simulation. The period of sinusoidal self-modulation was actually higher than the estimate for the feedback time basing on the velocity of electrons and group velocity of the wave in the operating point. These deviations may be explained by the fact that theoretical model doesn't include a number of factors, among which one has to emphasize the possibility of synchronous interaction of the electron beam with the forward wave (the 'orotron' regime). This factor can have great effect on actual values of the starting current, group wave velocity and generation efficiency as compared to the expected values. One cannot exclude the effect of nonresonance components of the RF field, influence of the spatial charge, presence of spurious reflections at the collector end of the tube either. It seems that further research should take into account these factors consistently.

In the experiment carried out voltage and beam current were limited from consideration that output power did not exceed 100 kW. At higher voltages the duration of microwave pulses become limited due to RF breakdowns in the microwave system made of copper by the method of galvanic growing. It is shown by earlier experiment [5], there is the possibility to improve electric reliability by using thermal degassing of the electromagnetic system made of all-metal oxygen-free copper. At the next research stage it is planned to use a new tube assembled of separate sections made by this method. That will allow to increase the injecting current, thus to rise also the exceeding over threshold and the mean power of stochastic radiation.

[1]. Ginzburg N.S., Kuznetsov S.P., Fedoseeva T.N. Izv.vuzov. Radiofizika, 1978, 21, P.1037
[2]. Bezruchko B.P., Kuznetsov S.P., Trubetskov D.I. Nonlinear Waves. Turbulence and Stochastics. Gorky.IAP, 1980, P.29
[3]. Bezruchko B.P., Kuznetsov S.P., Trubetskov D.I. Pis'ma ZhETF, 1979, 29, P.180
[4]. Kovalyov N.F., Petelin M.I., Raizer M.D. Pis'ma ZhETF, 1973, 18, P.232
[5]. Ilyakov E.V., Zaitsev N.I. et.al. Intense Microwave Pulses III. Proc.SPIE,1995,2557,P.457
[6]. Kovalyov N.F. Elektronnaya tehnika. Seria 1. HF Electronics, 1978, N 3, P.102
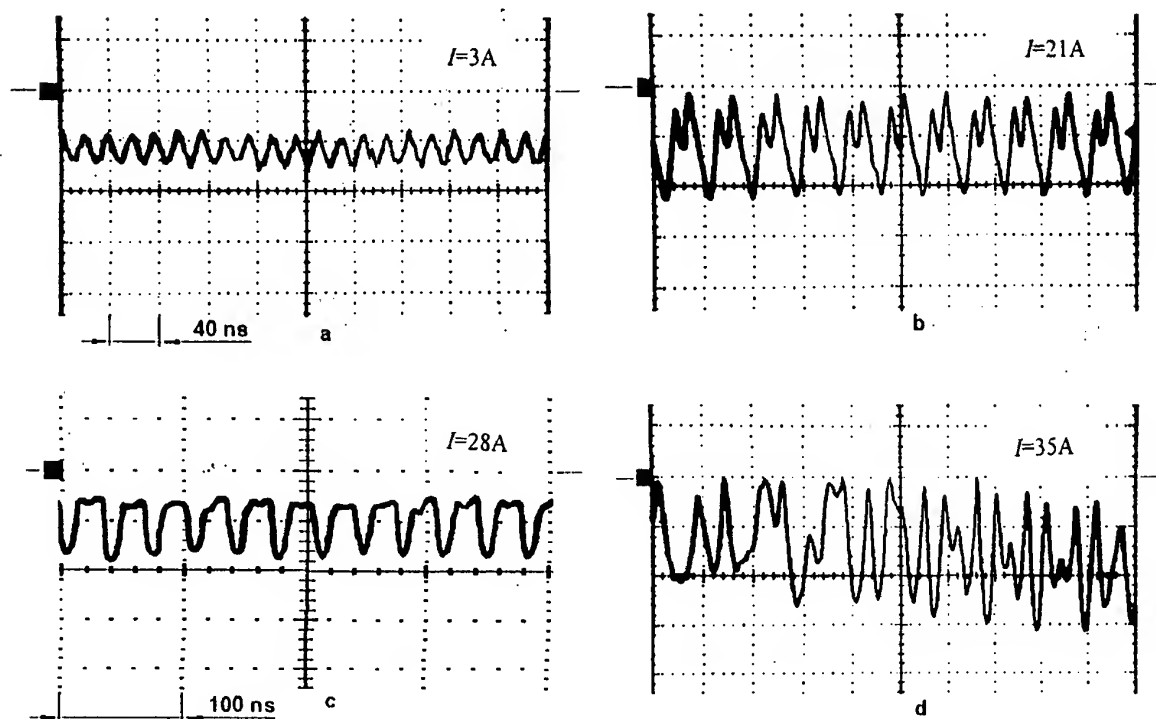
FIG.2. Experimental oscillograms of output signal amplitude under different electron currents.

INVESTIGATION OF PLASMA-BEAM AMPLIFIERS WITH REFERENCE TO THE USE IN COMMUNICATION SYSTEMS

V.Perevodchikov, Y.Kuznetzov, L.Mitin, , A.Shapiro, M.Zavjalov
All-Russian Electrotechnical Institute,
111250, Krasnokazarmennaya 12, Moscow, Russia

ABSTRACT

Quality characteristics of amplification of plasma travelling wave tube (TWT) are studied. It was shown linearity, phase stability, level of combined frequency signals and noises are close to such characteristics of vacuum TWT. Plasma TWT has higher power and wider range of operating frequency band. Plasma TWT-based power smallsize amplifier is worked out.

Earlier published works [1] discuss physically validated principles of construction of plasma traveling wave tube (TWT) based on hybrid decelerating structures i.e. a chain of coupled cavities, with a plasma-filled channel. Structure and technological developments conducted at VEI resulted in designing plasma TWT for S and C frequency range having parameters substantially higher those of similar vacuum devices. The presence of plasma in the channel of the decelerating structure load to markedly increase electronic efficiency up to 35%, to expand operating frequency band ($\Delta f/f=25\div30\%$) and to raise the power to 20 kW under continuous regime. This characteristics exceed noticeable parameters of developed vacuum TWT.

The role of plasma in operation of TWT is especially demonstrated by an amplitude-frequency characteristic taken for one and the same device working at vacuum and plasma regimes (Fig.1). It is clearly seen under plasma regime in out power efficiency of the device operation are increased, namely at a high frequency part of the specter.

Structure and technology of plasma TWT are designed so that plasma is produced by an electron beam, only at the cost of an increase of pressure in the devices with no additional means. Experiments showed the capability of devices to operate for continuous period (several hundred hours) at independent regime provided a required level of the pressure ($\sim10^{-3}$ Torr) is maintained. In this case cathode steadily emits electrons.

Thus, plasma TWT may be succesfully used in practice. The target of the present study is to examine the quality of plasma TWT amplified signals. We deem the use of an amplifier in communication systems requires especially high quality of the amplified signal. Our studies are carried out with the aim of defining the possibility of the use of plasma TWT for this purpose.

The amplification factors for three operating frequencies are shown in Fig.2. It is seen this characteristic is linear up to 25 dB with an output signal power at the level of $20\div25$ kW. Stability of the phase characteristic of the amplified signal is within $\pm$ 0.01 rad (Fig.3) that also proves a high quality of the amplified signal.

For the possibility of plasma TWT operation in multi-frequency communication systems with channel frequency multiplex to be estimated it is necessary to define the presence of signal intermodulation distortions tied with non-linear interactions of the waves having close frequency values. Evidently, plasma waveguides with a wide range of inherent fluctuations including low frequency waves (magnetosonic, ionosonic ones) may cause conditions for occurrence of combined fluctuations. Experiments showed when the plasma TWT input was supplied with a signal of monochromatic amplified with a vacuum TWT. The level of intermodulation frequencies of the input signal of plasma TWT was -30 dB. After amplification the level of intermodulation frequencies was raised to -20 dB (Fig.4a). When special measures are taken to suppress development of low-frequency components the level of combined components is decreased to -30 dB with the same input signal (Fig.4b). Thus, the characteristic of excitation of intermodulation fluctuations of plasma TWT is on a par with that of vacuum TWT.

Considering a wide spectre of native fluctuations of plasma waveguide characteristics noise of plasma TWT were studied in detail. Measurements of the spectral noise density within the operating frequency band were made by a gyromagnetic detectors. A value of the spectral density of the noise power was about 1 mW/MHz. The noises were distributed uniformly in the operating frequency band with a slight rise at the high adge. The main result was that for an operating frequency band $\Delta f/f = 25\%$, beam power ~60 kW without a signal at the input the noise level was ~ 500 MW that corresponds with a spectral density of power 1 mW/Mhz. Thus, with a signal amplification to 10 kW the noise level -47 dB.

Studies of noises by waveguide couplers showed at the second harmonic they were -35 to -45 dB versus the frequency of the amplified signal was near of the edge or in the middle of the operating frequency band. Noises at the third harmonic were between -50 to -55 dB. The noises were measured with an output power of the amplified signal of 10 kW.

The main conclusion from these studies is the following. The quality of plasma TWT signal amplification doesn't give way to that of vacuum TWT. At the same time power and width of the frequency band of plasma TWT considerably higher.

The use of vacuum TWT in preliminary amplification cascades by our experiments produced additional complexity to tune away from distortions generated by them. It is possible that actual distortions might be even lower with amplifications of signals by plasma TWT.

Relatively low levels of combined components and noises allow to use plasma TWT in communication lines with frequency-and-time-multiplex channel. In comparison to existing power vacuum TWT with $P_{min} = 3$ kW and $\Delta f/f = 10\%$ the plasma TWT under study having $P_{min} = 15$ kW, $\Delta f/f = 25\%$ make possible to increase a volume of information to be transformed per unit time by more than an order.

The opportunity to amplify and generate power microwave radiation of plasma TWT offers vast possibilities of their application. However, to convert to a level of voltages at a power 20 kW it is necessary to design a power supply source of $60 \div 100$ kW in power which should be technically adequate with a plasma TWT.

VEI has conducted developments of such power supply systems which were carried out in three trends:
- increase of the supply frequency to 5-8 kHz,
- creation of high voltage transformers with a solid insulation,
- utilization of specially designed switching electron tubes in high voltage circuits.

The block diagram of the developed amplifier is shown in Fig.5. It comprises a plasma TWT with a solenoid and power supply source. In creation of the invertor to convert a frequency there were used IGBT transistors. Besides the invertor, the power supply source includes a converter providing independence of the circuit load on the operation regime of a

plasma TWT. A high voltage transformer which steps up a circuit voltage to 25 kV has a core from amophous iron and monolit insulation. A special high voltage electron switching valve makes possible to carry out modulation of long pulses with a front 5÷10 mks duration, protection switchings and stabilization of plasma TWT currents.

The above-mentioned technical solutions allowed to design a power amplifier of minimum weight and sizes.

CONCLUSION

Studies were carried out to estimate the quality of plasma TWT signals amplification. It was found out linearity of the amplification factor, phase distortions of the signals of the combined frequencies and noises are close to similar characteristics of vacuum TWT. This permits to recommend to plasma TWT for utilization and communication systems. Considering the power and width of the operating frequency band of plasma TWT are substantially higher those of vacuum TWT it is possible to conclude the use of plasma TWT in communication systems will give the opportunity to increase a volume of information unit time. Plasma TWT was used as basis for development of a power wide-band amplifier having minimum weight and sizes.

The authors are very thankfull to all co-worker who were designed the amplifier and particulary, to S.Gusev, N.Matveyev, G.Mustapha, V.Shapenko.

REFERENCES

1. M.A. Zavjalov, L.A. Mitin, V.I. Perevodchikov, V.N. Tskhai, A.L. Shapiro et al. «Powerfull wideband amplifier based on hybrid plasma-cavity slow-wave structure', Plasma Science, vol. 22, N5, hh.-600-607, 1994.
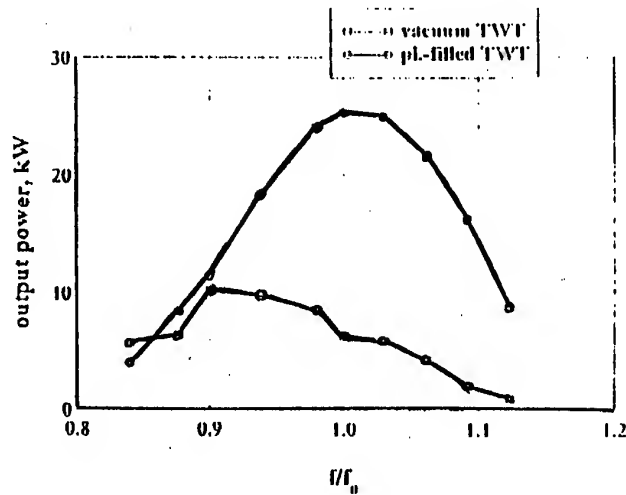
Fig.1 Amplitude-frequency characteristics of plasma TWT by vacuum and plasma operating
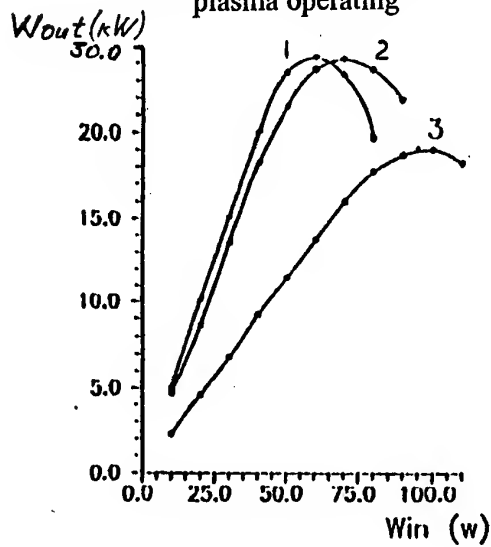
Fig.2 Amplification factor for three operating frequencies.
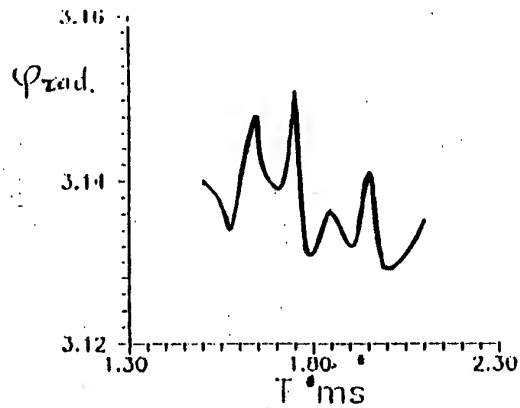
Fig.3 Stability of the phase characteristic.
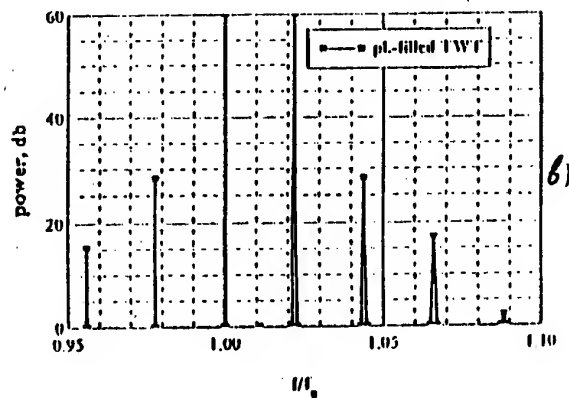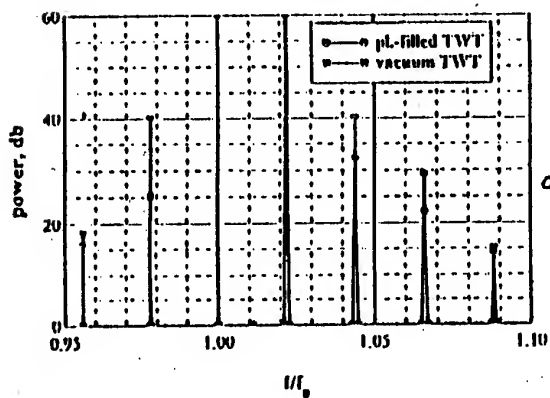
Fig.4 Level of two monochromatic signals and combined components after amplification by vacuum and plasma TWT (a) and by plasma TWT after correction (b).
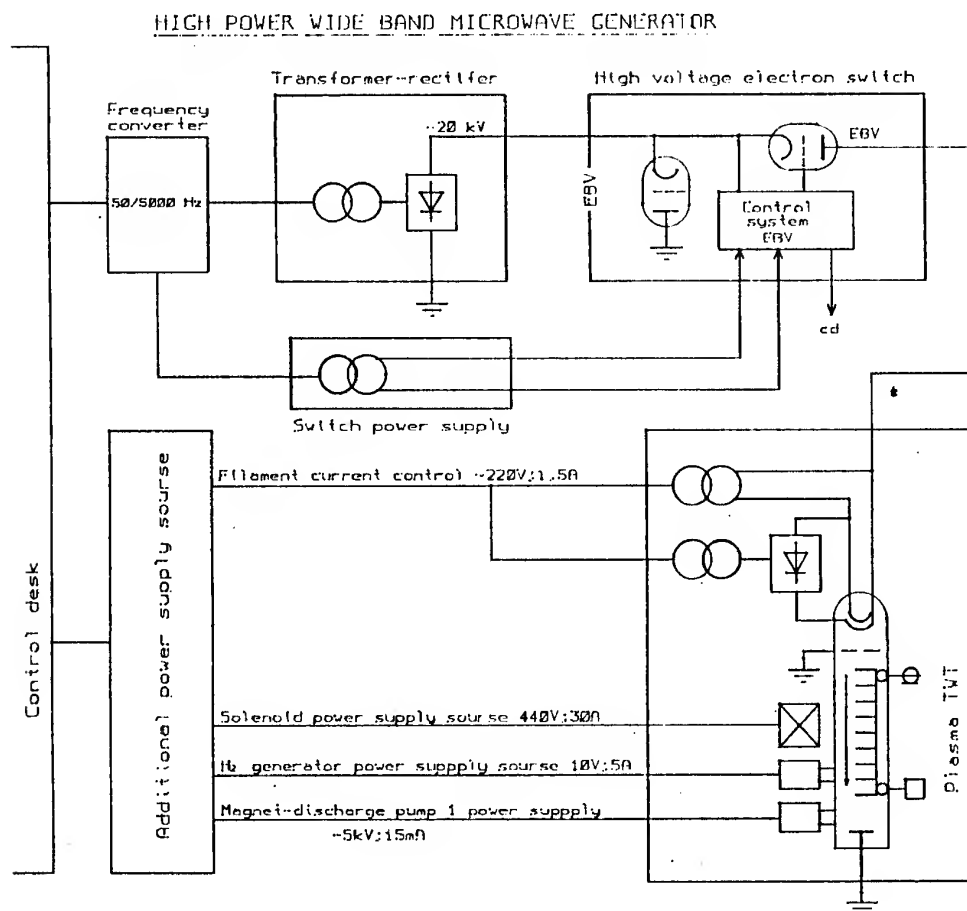
Fig.5 The block-scheme of the powerfull amplifier with plasma TWT.

EFFICIENT SCHEMES OF MILLIMETER WAVE FEM-OSCILLATOR AND AMPLIFIER

N.S. Ginzburg*, G.G. Denisov*, A.A. Kaminsky**, A.K. Kaminsky**,
N.Yu. Peskov*, S.N. Sedykh**, A.P. Sergeev**, A.S. Sergeev*

*Institute of Applied Physics RAS, 603600 Nizhny Novgorod, Russia
**Joint Institute for Nuclear Research, 141980 Dubna, Russia

The paper is devoted to a progress in experimental study of FEM with guide magnetic field based on a linear induction accelerator (1 MeV / 200 A / 200 ns). In Bragg FEM-oscillator a mode pattern in the resonators of different Q-factors was studied both theoretically and experimentally. In accordance with theoretical predictions single-frequency operation in a low Q-factor resonator and multifrequency operation in a high Q-factor resonator were observed. Under optimal resonator configuration at the frequency of 31 GHz single-mode generation with power of 37 MW and efficiency of 26% was obtained.

A new wideband scheme of RF-input based on the effect of microwave beams multiplication is studied in FEM-amplifier experiment. At the present stage at the frequency of 36.4 GHz amplification of 20 dB was obtained.

INTRODUCTION

Experimental study of FEM-oscillator with Bragg resonator is performed in cooperation of JINR (Dubna) and IAP RAS (N.Novgorod) during several years. At the previous stage of the experiments a record efficiency of 25% for millimeter wavelength FEM-oscillators with guide magnetic field have been obtained [1]. These experiments demonstrated an advantage of regimes with reversed guide magnetic field and capability to achieve the efficiency in FEM-oscillator comparable with efficiency realized before in FEM-amplifiers with reversed guide field [2, 3].

At the present stage we study dynamics of single-mode and multimode operating regimes in the oscillator. To record a mode pattern in different regimes, an oscilloscope with high time resolution (about 2 ns) was used. Theoretically predicted multi-mode generation in a rather high Q-factor resonator was observed experimentally via the modulation of the output RF-power due to beating of longitudinal modes. Conversely the absence of such modulations in configurations with optimal Q-factors confirms the single-mode operation in the high-efficiency regime.

FEM-amplifier experiment is under progress currently. A new scheme of RF-input based on the effect of microwave beams multiplication [4] is suggested. Preliminary results of the experiment are presented.

DYNAMICS OF SINGLE-MODE AND MULTIMODE OPERATING REGIMES IN BRAGG FEM-OSCILLATOR

Preliminary, dynamics of oscillation build-up in a FEM with a two-mirror Bragg resonator was studied theoretically. Time domain analysis taking into consideration the dispersion properties of the Bragg reflectors was used. For a low and moderate Q-factor resonator the dependence of the output RF signal with respect to time indicates a two stage transient process. At the first stage large oscillations of efficiency and output signal occur (Fig.1a).

Such oscillations are caused by excitation of all longitudinal modes disposed at the zone of Bragg reflection. Later at the second stage one of the modes grows and suppresses other modes due to a nonlinear mode competition mechanism. This results in a single mode being established (Fig.1a) and, consequently, stationary single frequency operation.

Increasing the reflectivity of the Bragg mirrors above the optimal value led to lower electron efficiency and an increase in the width of the radiation spectrum. In this case the excitation of several longitudinal resonator modes takes place (Fig.1b), and the modulation of the output signal in the final stage of evolution is caused by beating between these modes.

An experimental study of the FEM was performed on the linac LIU-3000 (JINR, Dubna) which generated electron energies of 0.8 MeV and a 200 A beam current pulse, of duration ~200 ns, at a repetition rate up to 1 Hz. The helical wiggler of period 6 cm and amplitude of the transverse magnetic field of up to 3.5 kG was used to drive the electron transverse oscillations. The wiggler was immersed in a uniform axial magnetic field generated by a solenoid. The strength of this field could be varied from −7 to 7 kG.

In the oscillator a two-mirror Bragg resonator was used to provide a selective feedback circle. The resonator was designed for $TE_{1,1}$ operating mode with three possible reflections within Bragg reflectors: into the backward waves $TE_{1,1}$, $TM_{1,1}$ and $TM_{1,2}$ at the frequencies near 29 GHz, 31 GHz and 38 GHz respectively. The results of calculations were confirmed by "cold" microwave measurements. The maximum reflection was realised in the 38 GHz zone and minimum reflection in the 29 GHz zone. The number of high-Q-factor longitudinal modes for every reflection zone varied from 3 to 7 when the length of regular cavity section between 30 -70 cm and lengths of the reflectors between 3 - 16 cm were changed.

In the experiments, radiation at the designed circularly polarized $TE_{1,1}$ wave and separate frequencies bands corresponding to all the feedback waves mentioned above were detected. Selection of the feedback regime was achieved by changing both the wiggler and guide fields. The highest radiation power as well as the narrowest bandwidths were realized at a frequency of 31 GHz ($TM_{1,1}$.backward wave) when a reversed guide field configuration was used. In this zone the reflection coefficients of the Bragg mirrors and, consequently, the Q-factors of the excited modes corresponded to the optimal calculated values. A maximum output power of 37 MW corresponding to a record FEM-oscillators efficiency of 26% was obtained.
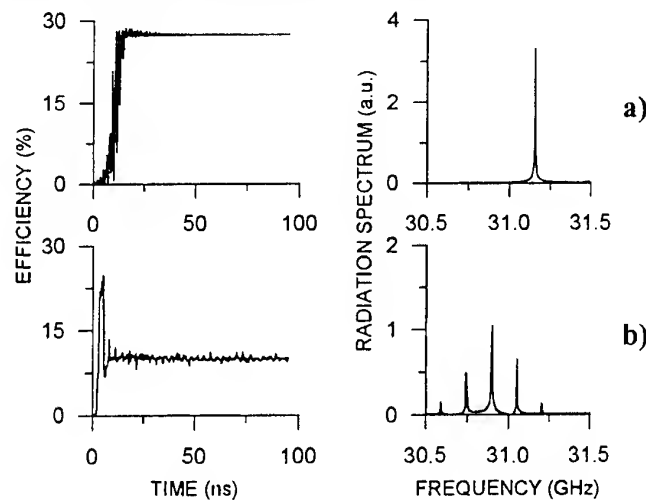
Fig.1 Computer simulation of excitation of the FEM-oscillator with two-mirror Bragg resonator: time dependence of efficiency and spectrum of radiation in the stationary regime ($t > 50$ ns)

a) optimal resonator configuration $l_{Br,up} = 16$ cm, $l_0 = 40$ cm, $l_{Br,down} = 3$ cm ($Q \approx 400$);

b) high-Q resonator $l_{Br,up} = 16$ cm, $l_0 = 85$ cm, $l_{Br,down} = 15$ cm ($Q \approx 2000$);

($E_{beam} = 0.8$ MeV, $I_{beam} = 150$ A, $B_0 = -2$ kG, $B_w = 1$ kG).

In the previous experiments [1] spectrum of the radiation was measured by means of a set of cut-off waveguide filters with an accuracy of 1.5%. Such frequency measurements did not allow us to prove single-mode operation of the FEM because the frequency difference between the longitudinal modes was comparable with the measurement precision. New investigations of a mode pattern in the oscillator were completed recently. The microwave output signal was recorded using high time resolution (about 2 ns) oscilloscope. For high efficiency operation with optimal (rather small) Q-factors no modulation of output signal was observed (Fig.2a). Conversely, according to theoretical predictions for the cavity configuration with a high Q factor multimode operation of the oscillator was detected by the modulation of the output signal due to beating of longitudinal modes. The oscillator efficiency in this configuration was ~5 to 10%. The beating patterns were measured for several resonator lengths in the frequency band of 31 and 38 GHz. It was noted that the period was higher for the 38 GHz zone as compared to the 31 GHz zone (6.0 ns for 31GHz fig (2b) and 7.5 ns for the 31 GHz fig (2c)). The difference in the period can be explained due to the distance between neighboring longitudinal modes being determined by the distance between the mirrors as well as the group velocities of both the forward and backward waves. The different frequency zones are distinguished by the different backward waves which provide the feedback cycle. For the backward $TM_{1,2}$ wave the group velocity is smaller than the $TM_{1,1}$ wave which resulted in a decrease in the frequency interval between different longitudinal resonator modes and an increase in the beating period.

a)   b)
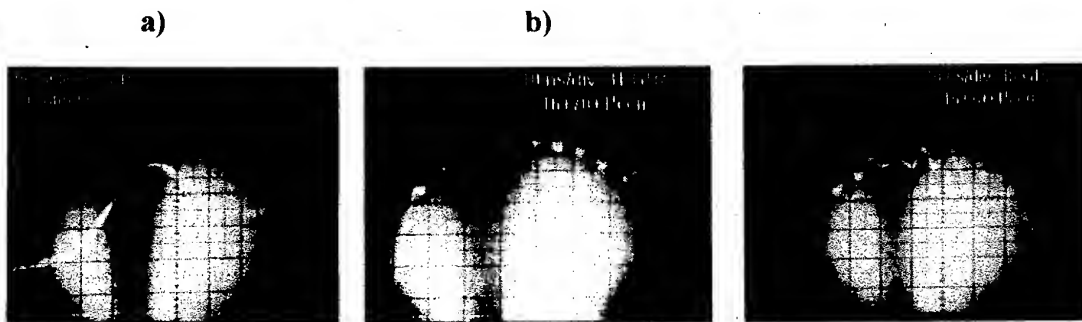
Fig.2 Typical oscilloscope traces (time scale 10 ns/div) of RF-power for different resonator configurations:

a) $f = 31\,\text{GHz}$, $l_{Br,up} = 16\,\text{cm}$, $l_0 = 40\,\text{cm}$, $l_{Br,down} = 4.5\,\text{cm}$ $(Q \approx 450)$;

b) $f = 31\,\text{GHz}$, $l_{Br,up} = 16\,\text{cm}$, $l_0 = 70\,\text{cm}$, $l_{Br,down} = 15\,\text{cm}$ $(Q \approx 1500)$;

c) $f = 38\,\text{GHz}$, $l_{Br,up} = 16\,\text{cm}$, $l_0 = 70\,\text{cm}$, $l_{Br,down} = 15\,\text{cm}$ $(Q \approx 3000)$.

FEM-AMPLIFIER WITH RF-INPUT BASED ON THE EFFECT OF MICROWAVE BEAMS MULTIPLICATION

Drawing of RF-input for the FEM-amplifier project is presented in Fig.3. The operating principle of the RF-input is based on the effect of microwave beams multiplication [4]. In accordance with this effect, a narrowly directed monochromatic wave beam with cross-section a, when injected into a wide waveguide with its cross-section $A > a$, excites such a set of eigenmodes with certain definite amplitudes and phases that at distance $L = A^2/p\lambda$ from the input of the wide waveguide the field looks like a set of p split wave beams with amplitude profiles identical to the injected beam. In principle, the new unit makes it possible to separate microwave and electron beams and to provides a high (up to 100%) transformation of the input signal into the operating wave of an oversized waveguide without any elements
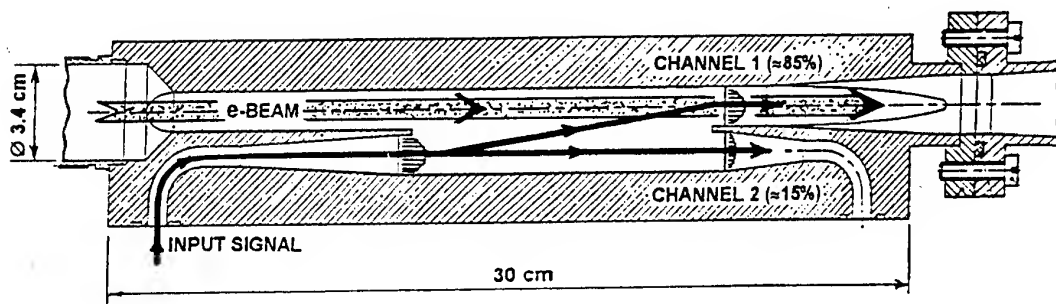
Fig.3 Scheme of the RF-input based on the effect of microwave beams multiplication.
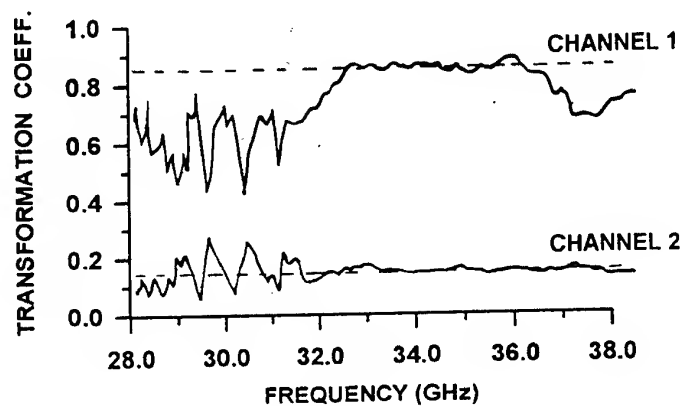
Fig.4 Results of «cold» microwave measurements of the RF-input: transformation coefficient versus frequency.

on electron beam aperture. Moreover, this high transformation is possible in rather wide (about 10%) frequency range.

For the project the RF-input was designed with a 85% input signal transformation into the operating $TE_{1,1}$ mode of a circular waveguide in the frequency region from 32 to 37 GHz. Results of "cold" microwave measurements are presented in Fig.4. Channel 1 corresponds to transformation into the interaction region and channel 2 (the rest 15% of the input signal) is designed to use for on-line control.

Experimental study of the amplifier on LIU-3000 is under progress now. Magnetron with the frequency of 36.4 GHz was used to drive the amplifier. At the present stage of the experiment amplification of 20 dB and output power of 5 MW were obtained when the beam of current of 110 A is utilized. We expect that at the next stage an improvement in the beam transportation through the new unit and the use of full beam current produced by the accelerator (about 180 – 200 A) will increase the amplification and output power.

References
1. Ginzburg N.S., Kaminsky A.A., Kaminsky A.K., Peskov N.Yu., Sedykh S.N., Sergeev A.P., Sergeev A.S., Proc. of 11th Int. Conf. on High Power Particle Beams, Prague, Czech Republic, 1996, vol.1, p.245.
2. Kaminsky A.A., Kaminsky A.K., Rubin S.B. Particle Accelerators. 1990, vol.33, p.189.
3. Conde M.E., Bekefi G. Phys. Rev. Lett., 1991, vol.67, no.22, p.3082.
4. Denisov G.G., Lukovnikov D.A., Shmelyov M.Yu., Proc. of SPIE, Edit. by J.R.Birch and T.J.Parker, 1993, vol.2104, pp.485-486.

FREE ELECTRON LASERS WITH SHEET ELECTRON BEAMS AND TWO-DIMENSIONAL PLANAR BRAGG RESONATORS

N.S. Ginzburg, N.Yu Peskov, A.S. Sergeev and I.V. Konoplev
Institute of Applied Physics RAS, 603600 Nizhny Novgorod, Russia

A.V. Arzhannikov and S.L. Sinitsky
Institute of Nuclear Physics RAS, 630090 Novosibirsk, Russia

The use of two-dimensional Bragg resonators of planar geometry, realizing two-dimensional distributed feedback, is considered as a method of producing spatially coherent radiation from a large sheet electron beam. Selective properties of a 2-D Bragg resonator are studied when the transverse sides of the resonator are open and also when they are closed. A time-domain analysis of the excitation of an open 2-D Bragg resonator by a sheet electron beam demonstrates that a single mode steady-state oscillation regime may be obtained for a sheet electron beam of width up to 1000 wavelengths. At the same time, even in a closed 2-D Bragg resonator a steady-state regime can be realized if the beam width does not exceed 50 - 100 wavelengths. Project of FEL with a 2-D Bragg resonator driven by a sheet electron beam based on the U-2 accelerator (INP RAS, Novosibirsk) is discussed.

INTRODUCTION

The project of gigawatt power level millimeter wave FEL driven by a large high-current sheet beam is developed during the last several years on the base of the U-2 accelerator (INP RAS, Novosibirsk) [1, 2]. The use of a beam of such geometry makes it possible to increase the total beam power and, correspondingly, the microwave power while still keeping the current and radiation density per unit transverse size constant. Indeed at the U-2 accelerator a microsecond relativistic sheet beam with electron energy of 1 MV, current per unit transverse size of 1 kA/cm, transverse size up to 140 cm and power level of tens of gigawatts was generated [3].

To provide a spatial coherence of the radiation in FEL driven by the large size beam the use of "two-dimensional" Bragg resonators was proposed [4]. Within these resonators mutual scattering of electromagnetic energy fluxes propagating in forward, backward and transverse directions relative to the direction of electron beam propagation takes place. The additional transverse electromagnetic energy fluxes synchronize radiation of the large size beam. In [5] a high selectivity of the open planar 2-D Bragg resonators was proved. Simulations of excitation of these resonators by sheet beams demonstrated the possibility to provide spatial coherent radiation up to the beam width of 10^2 - 10^3 wavelengths.

However, to design FEL with the open 2-D Bragg resonator one should solve a problem of output for the transverse e.m. fluxes. Actually, the transverse output of the radiation through the walls of beam transporting channel and the electron-optical system (solenoid) is a rather complicated problem. In principal, using some additional elements it is possible to turn these transverse fluxes and to provide a single-directed output of radiation. However, it seems more simple to restrict the resonator by two metal mirrors on transverse edges and to consider the "transversely closed" scheme of the FEL (fig. 1).

In the present report we study an influence of reflections for transverse e.m. fluxes (reflections provided by restricting metal mirrors or "parasitic" reflections from the side walls of the vacuum channel) on selective properties of the 2-D Bragg resonator. Project of super-power FEL operating in millimeter wavelength bang and driven by sheet relativistic electron beam that is formed by the accelerator U-2 is discussed.

SIMULATIONS OF "COLD" 2-D BRAGG RESONATOR

A planar 2-D Bragg resonator, constructed from two metal plates of width l_x, length l_z, distance between them a_0 (fig.1) and corrugated as

$$a = a_0 + a_1 \left[\cos(\overline{h}x - \overline{h}z) + \cos(\overline{h}x + \overline{h}z)\right] \tag{1}$$

($\overline{h} = \sqrt{2}\pi/d$, d is the corrugation period, a_1 is the corrugation depth) provides coupling and mutual scattering of four partial waves: $A_\pm$ propagating in $\pm z$ directions and $B_\pm$ propagating in $\pm x$ directions. We assume that the partial waves do not reflect from the end of the resonator in the longitudinal $\pm z$ directions, but there is a reflection R for the transverse energy fluxes from the transverse edges of the resonator.
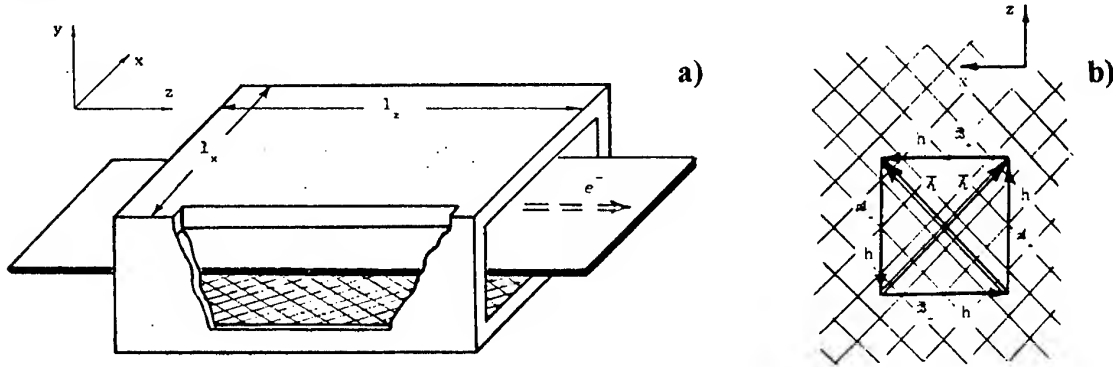
Fig.1 Schematic diagram of FEL-oscillator with closed planar 2-D Bragg resonator driven by sheet electron beam **(a)**, and diagram illustrating the scattering of the partial waves on the Bragg structure **(b)**.

Evolution of the resonator's spectrum versus the reflection coefficient R is shown in fig.2. This spectrum is obtained from simulation using a time-domain code for the partial waves scattering on the Bragg structure (1). This method allows one to separate the highest Q-factor modes presented in the spectrum. For $R \leq 0.2$ the spectrum of eigenfrequencies is close to the spectrum of the open resonator (Fig.2). The resonator retains high selectivity over the longitudinal and the transverse coordinates with the maximum Q-factor belonging to the
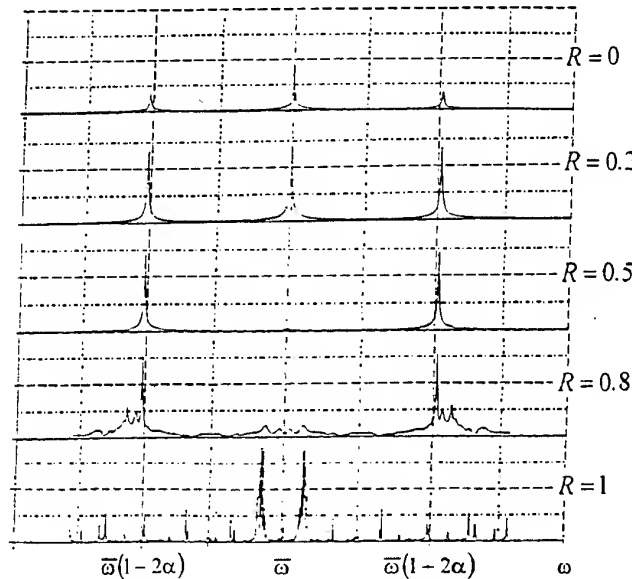
Fig.2 Evolution of the mode spectrum of the planar 2-D Bragg resonator versus side reflection coefficient R ($h\alpha l_x = h\alpha l_z = 9$).

eigenmode at the Bragg resonance frequency $\overline{\omega} = \overline{h}c$. The structure of synchronous to the electron beam partial wave A_+ for this eigenmode does not depend on the transverse coordinate. The Q-factor of this mode decreases with an increase of the reflection coefficient and at $0.3 < R < 0.8$ the eigenmodes with one field variation over both the transverse and longitudinal coordinates located at $\omega \approx \overline{\omega}(1 \pm 2\alpha)$ (where $\alpha = a_1/4a_0$ is the parameter describing coupling of the partial wave on the Bragg structure [4]) have the highest Q-factor.

At $R \approx 1$ a new set of eigenmodes having frequencies $\omega \approx \overline{\omega}\left(1 \pm \pi n/\overline{h}l_x\right)$ arises. Under the zero wave coupling condition ($\alpha = 0$) these eigenmodes are reduced to the eigenmodes of a two-mirror Fabry-Perot resonator formed by the metal side walls. The Q-factors of these modes decrease with the increase of wave coupling α (in contrast to the behaviour of modes located near $\omega \approx \overline{\omega}$ and $\omega \approx \overline{\omega}(1 \pm 2\alpha)$, which originate from scattering of the waves on the Bragg structure). At $\alpha \neq 0$ the Q-factors of the eigenmodes from all sets of modes are comparable to each other (fig.2) and, as a result, the selective properties of the "cold" resonator are impaired.

EXCITATION OF 2-D BRAGG RESONATOR BY SHEET ELECTRON BEAM

The simulations of excitation of the 2-D Bragg resonator were carried out for parameters of an electron beam close to the conditions of the experimens at the U-2 accelerator. The RF-field was presented in the form of four partial waves (propagating in the $\pm z$ and $\pm x$ directions) which were coupled on the Bragg gratings (1). The particles motion was described by a pendulum-like equation.

For the open 2-D Bragg resonator the dependencies of efficiency on time at the region of parameters, where the establishment of the stationary regime of generation takes place, are presented in the Fig.3. At the stationary regime spatial profiles of partial waves $A_\pm$ and $B_\pm$ are close to the profiles of corresponding waves for the most high-Q mode of "cold" resonator. The frequency of this mode as well as the oscillations frequency coincides with the Bragg frequency. Note, that transverse distribution of amplitude of synchronous wave A_+ does not depend on transverse coordinate x that provides equal energy extraction from all parts of the electron beam. It can be shown analytically that for open 2-D Bragg resonator a distribution of waves along longitudinal coordinate as well as efficiency do not change when the conditions $l_z = const$ and $\hat{\alpha}^2 l_x = const$ are satisfied. Such a scaling gives possibility to increase the width of the interaction space simultaneously decreasing the coupling parameter. Computer simulations confirms that under conditions close to the parameters of the experiment the synchronization regime is stable at least up to $l_x \leq 300\,cm$ (that correspond to $l_x/\lambda \approx 750$). However, the transitional time increases with increasing system's width (Fig.3a).

The numerical simulations of oscillation build-up in the resonator with small side reflections ($R \leq 0.2$) demonstrate the existence of a broad range of the systems parameters where the single-mode operation regime is established practically for any width of the resonator. In this case, similar to the open resonator, the fundamental mode at the Bragg frequency $\omega = \overline{\omega}$ with constant transverse distribution is excited by the beam.

For the high reflectivity from the transverse side walls ($R \approx 1$) the single mode operation regime is changed to self-modulation regime for large widths of the resonator $l_x \geq 80 \div 100\,cm$. These regimes are accompanied by excitation of several modes of the resonator, beating of which takes place (fig.3b). However, for $l_x \leq 50\,cm$ the single-mode operating regime may be realized even in the closed resonator ($R = 1$). The establishment of

the single-mode operating regime is caused by electronic selection of different modes (as opposed to electrodynamical mode selection in the open 2-D Bragg resonator). It should be noted that even small RF-losses for transverse e.m. fluxes (i.e. decrease in reflection from the transverse side walls) stabilize the single-mode operation of the FEL.
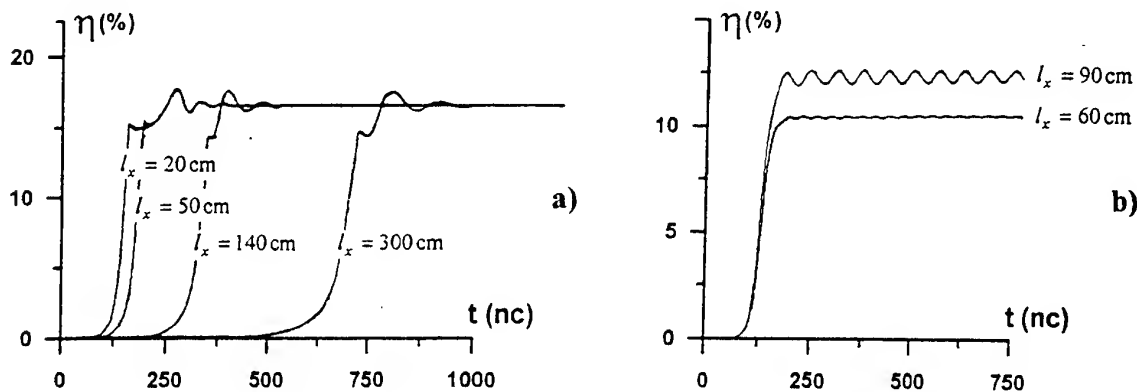
Fig.3 Oscillations build-up in FEL with open ($R = 0$, **a**) and closed ($R = 1$, **b**) planar 2-D Bragg resonator: time dependence of efficiency
($E_b = 1\text{MeV}$, $I_b = 200\,\text{A/cm}$, $\lambda = 4\,\text{mm}$, $d_w = 4\,\text{cm}$, $H_w = 0.1\text{T}$, $H_0 = 1\text{T}$, $l_z = 50\,\text{cm}$).

PROJECT OF POWERFUL FEL BASING ON THE U-2 ACCELERATOR

The theoretical analysis carried out has demonstrated the potential of 2-D Bragg resonators in obtaining high-power spatially-coherent radiation from a wide relativistic electron beam. The computer simulations discussed above were made for the project of 4 mm FEL with such a resonators on the base of high-current accelerator U-2 (1 MV / 1 kA/cm / 5 mcs). The wiggler of 4 cm period and amplitude of the transverse field up to 0.1 T is used to drive the oscillatory electron velocity $\beta_\perp \approx 0.2 \div 0.3$ at axial guide field strength about 1 T [2]. Following computer simulations, the use of an open 2-D Bragg resonator with a corrugation of period 3 mm and depth 0.4 mm would make it possible to realize a single mode-operation regime in the FEL. The transit time will be about 300 ns. With 15% efficiency the radiation power amounts to 20 GW. However this scheme of the FEL requires additional elements to output radiation which should have "parasitic" reflections for transverse e.m. fluxes not higher than 20%.

At the same time, for a sheet beam of width less than 50 cm ($l_x/\lambda \approx 100$) the simpler transversely closed resonator scheme may be used in the project. The transient time is expected to be shorter than 150 ns and the radiation power is calculated to be up to 5 GW.

References
[1] Arzhannikov A.V., Ginzburg N.S., Nikolaev V.S., Peskov N.Yu., Sergeev A.S., Sinitsky S.L., Zotkin R.P., Yushkov M.V., 14-th Int. FEL Conf., Kobe, Japan, 1992. p.214.
[2] Agafonov M.A., Arzhannikov A. V., Ginzburg N. S., Peskov N.Yu., Sinitsky S.L., Tarasov A.V., Proc. of 11th Int. Conf. on High Power Particle Beams. Prague. Czech Rep., 1996. v.1, p.213.
[3] Arzhannikov A.V., Bobylev V.B., Nikolaev V.S., Sinitsky S.L., Tarasov A.V., Proc. of 10th Int. Conf. on High Power Particle Beams. San Diego. USA, 1994. v.1. p.136.
[4] N.S.Ginzburg, N.Yu.Peskov, A.S.Sergeev, Optics Commun., 1993, v.96, p.254.
[5] N.S.Ginzburg, N.Yu.Peskov, A.S.Sergeev, A.V.Arzhannikov, S.L.Sinitsky, Nuclear Instr. and Meth. in Phys. Research A, 1995, vol.A358, p.189.

ON THE POSSIBILITY OF CONCRETE DESTRUCTION UNDER HIGH-POWER MICROWAVES GENERATED BY E-BEAM

A.V. Arzhannikov, V.A.Bychenkov*, J.Eibl***, P.V. Kalinin, G. Kessler**,
V.S. Koidan, G.V. Kovalenko*, Yu.N.Lazarev*, K.I. Mekler, P.V.Petrov*, A.V.Petrovtsev*

Budker Institute of Nuclear Physics, Novosibirsk, 630090, Russia
*Russian Federal Nuclear Center - All-Russian Institute of Technical Physics P.O.245
Snezhinsk, Chelyabinsk Region, 456770, Russia*
**Forschungszentrum Karlsruhe, P.O. Box 3640, Karlsruhe, D-76021, Germany
*** Institute fur Massivbau, University Karlsruhe, D-76128 Karlsruhe, Germany

INTRODUCTION

A potential cleaning method for polluted construction surfaces by high-power pulses of microwave radiation may be based on the destruction of a surface thin layer by an action of shock waves generated due to dissipation of the microwave energy there. When defining the possibility of concrete plane layer destruction by high-power microwave radiation flux it should be stressed that dry concrete being dielectric material conducts electromagnetic radiation rather well (specific resistance is more than 10^3 Ohm·m), but shock wave generation and fragments formation under its action occurs most intensively at local energy release. Obviously the prime problem is to create a small region in a material capable of under microwave pulse to generate a shock wave which has the ability to cause fragmentation on a sample surface. Such region should have increased conductivity which ensures the creation of the region with high energy density. The creation of such a region can be available, for example, by saturation of concrete surface with a well conductive salt solution, as it is known that concrete has water absorption from 4-8% /1/ up to 30 - 40% /2/ of its mass according to various publications. Current experiments show that the specific resistance of a concrete region has been accepted equal to 50 Ohm·m., and the skin length corresponding to 4 mm wavelength of electromagnetic radiation, is 1.2 cm.

MEASUREMENTS OF ABSORPTION DISTRIBUTION OF MICROWAVE ENERGY BY CONCRETE AND ITS COMPONENTS

In order to measure absorption of the microwave energy a special experimental device has been constructed. Schematic of this device is shown in Fig.1. Microwave radiation with a wavelength 4mm or 8mm is generated by a klystron generator KG, passes through a directional coupler DC, an attenuator Att and a standing-wave meter SWM. Than the radiation propagates through a tapered transition from 4mm (or 8mm) waveguide to 3 cm waveguide. In the 3cm waveguide an investigated sample S is placed. The length of the sample can be varied from one set of measurements to another during experimental investigations and as a result, the dependence of microwave power decrease on the increase of the thickness of the investigated matter has been experimentally obtained.
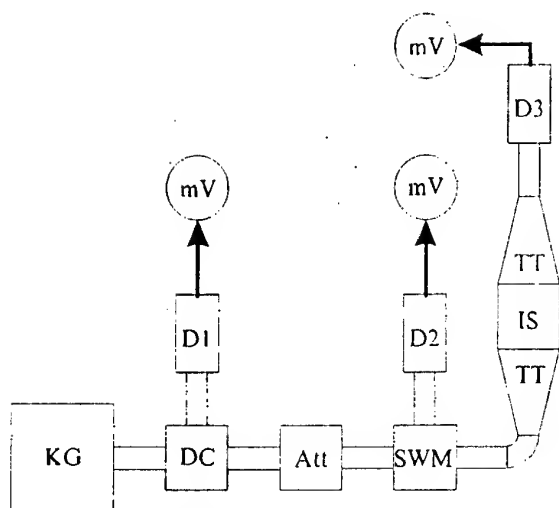
Fig.1. Schematic of the experimental device.
KG- Klystron Generator; DC- Directional Coupler; Att-Attenuator; SWM- Standing Wave Meter; TT- Tapered Transition from 4 (or 8) mm to 3cm; IS- Sample for Investigation; D1, D2, D3- Detectors of microwave radiation; mV- millivoltmeters.
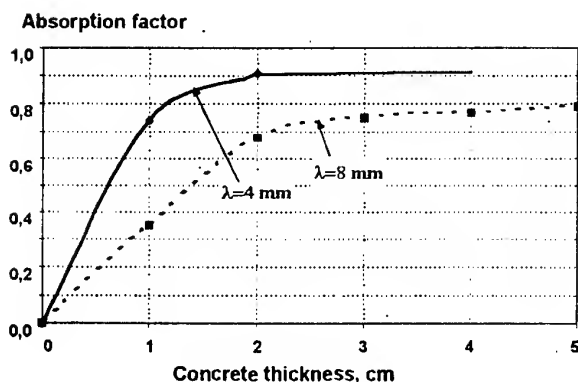
Fig.2. The absorption factor of microwaves with wavelength 4 mm and 8 mm by concrete.

Results of measurements for the samples made of concrete with a various thickness are presented in Fig.2. The samples were made of the concrete marked «200». Measurements of electrical properties of such samples were performed at the device in two weeks after their production. The absorption depth of the concrete for the wave with a wavelength λ=4mm is 1÷2 cm and the reflection coefficient for this wave is about 10%. For the wave with λ=8mm the absorption depth is about 2÷3 cm and the reflection coefficient is some more than 20%.

The absorption depth and the reflection coefficient for concrete components are of importance in analyzing the prospect of using the microwave radiation for destruction of the concrete wall surface. For this purpose the measurements of these parameters were carried out for dry cement and dry sand. We can report that both these components have (20-25)% reflection coefficient as for λ=4mm and for λ=8mm too. As to the absorption depth, this parameter is somewhat different for the cement samples and the sand ones. In the case of cement the depth is about 2 cm at λ=4mm and about 4 cm λ=8mm. For the sand samples the absorption depth is about 4 cm for both values of the wavelength.

NUMERICAL CALCULATIONS OF CONCRETE DESTRUCTION

Under intense energy release a concrete can be destroyed due to tension (fragmentation or shear destruction). Estimations of this possibility were carried out by using one-dimensional code VOLNA and two-dimensional one RAPID, the basic algorithms of which are described in /3,4/. In doing so elastic-plastic properties of materials and destruction simulation were carried out according to the approach given in /5/.

A plane concrete layer (z>0) with free boundaries was irradiated by a microwave beam with Gaussian profile of width r_0. The layer thickness was chosen sufficiently that the right boundary had no effect on obtained results.

Spatial-temporal distribution in cylindrical coordinate system of microwave energy absorbed by concrete was set as $\dfrac{dE(t,r,z)}{dtdzdr} = \dfrac{Q}{Tl}\exp(-\left(\dfrac{r}{r_0}\right)^2 - \dfrac{z}{l})\begin{cases}1, & 0 \le t \le T, \\ 0, & t > T.\end{cases}$ where the

characteristic decay constant l=1.2 cm corresponded to the specific resistance 50 Ohm·m, r_0=5 cm. The duration of microwave pulse T and energy flux density Q were varied in calculations.

Equation of state for concrete was defined as $P = C_{0c}^2 (\rho - \rho_{0c}) + (\gamma - 1)\rho E$. The initial concrete density coincided with «crystalline» density and was equal to $\rho_{00}=\rho_{0c}$=2.25 g/cm^3. According to the specified above tabulated data the parameters the equation of state were the following: acoustic velocity C_{0c}=2.4 km/s, Gruneisen coefficient γ=1.3.

The values of concrete dynamic strength characteristics were assumed to be equal to their static values specified above. The value of the shear strength Y was assumed to be constant and is equal to Y=0.02 GPa, and the value of the tensile strength (fragmentation strength) - σ_{ds}=-30 kg/cm^2=-0.003 GPa /5/.

The strength properties of the concrete fell sharply under shear destruction. The shear strength for such material was specified in relation to pressure:

$$Y = Y_0 + \beta P \frac{A - Y_0}{A - Y_0 + \beta P}, \quad Y_0=0, \ A=0.002 \ GPa, \ \beta=1.$$

In the absence of pressure it decreased to zero, and as the pressure increased it returned to the value equal to 0.1 of concrete strength. It was assumed that this material could not resist to tension (σ_{ds}=0). The concrete destroyed by tension was devoid of shear and tensile strength.

One-dimensional calculation results demonstrating a concrete state after irradiation are presented in. Fig. 3. It shows data for the stress tensor in the form of $\sigma_1(z)$ profiles at various times, illustrating wave distribution in the bulk of the concrete and its destruction. The destruction of the concrete is realized when the minimum value of released energy at which destruction (fragmentation) of the concrete under consideration occurs. It can be seen in Fig.3 that under the pulse duration T=1 μsec and the energy flux density $Q \cong 30$ J/cm^2 fragmentations occur at the time 4 μsec and the point z≈1.3 cm.

This value of the energy flux density Q needed for concrete destruction increases with the increasing of the pulse duration. The needed density becomes 80 J/cm^2 at τ=10 μsec and then higher than the limit of shear destructions 120 J/cm^2, which is in agreement with estimations made in quasistatic approximation (in this case both zones of fragmentation and shear destructions occur). The material destroyed in shear (owing to loss in strength) then undergoes fragmentation destruction.

More realistic two-dimensional calculations confirm the one-dimensional model. The two-dimensional calculations of final state of the concrete irradiated by the microwaves with τ=100 μsec and $Q \approx 120$ J/cm^2 are presented in Fig.4. For this case in the region of the most intense energy absorption the shear destruction is realized because the material has no time to change anisotropic type of stress state caused by irradiation. And hence the shear destructions zone is surrounded by the fragmentation zone which exceeds it in sizes approximately two times.

DISCUSSION OF OBTAINED RESULTS

Results of calculations and estimations show that for the concrete with the specific resistance about 50 Ohm·m fragmentation phenomenon occurs in the distruction thickness about 2 cm under the effect of high-power microwave radiation for the pulses with energy fluxes of 30 J/cm^2 at duration about 1 μsec, for 80 J/cm^2 at duration 10 μsec and for 120 J/cm^2 at duration about 100 μsec.
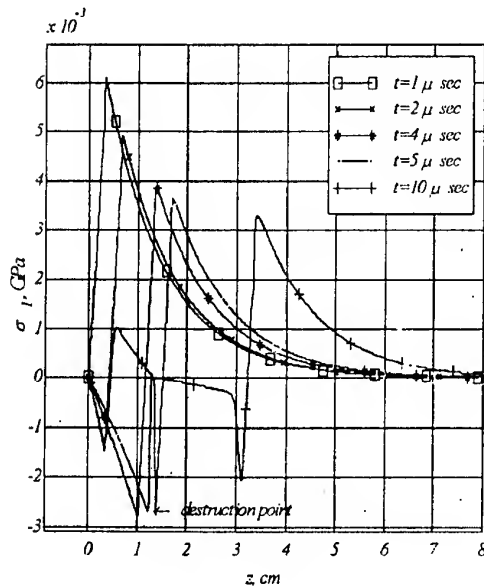
Fig.3. Stress profiles $\sigma_i(z)$ at different times $(Q \cong 30$ J/cm^2, pulse duration T=1μsec)

Fig4. State of concrete after microwaves irradiation at Q=120 J/cm^2, T=100 μsec

The experimental measurements show that the parameters of the region with increased conductivity have been chosen to correspond most closely to the real conductivity of wet concrete providing absorption of about 80% of electromagnetic energy falling on the irradiated surface.

On the basis of our investigations it is possible to formulate the first requirement on microwave generators at which one can perform experimental works on destruction of concrete surfaces: the power is 0.3÷1 GW and the pulse duration is 1-100 μsec. Such generators may be constructed on the base of high-current sheet beams (see /6/).

The work was partially supported by ISTC grant #531.

REFERENCES

[1] Jakobson Ja.M., Sovalov I.G., A brief handbook in concrete and reinforced concrete, Moscow, Stroiyizdat, 1974.

[2] Garboczi E.J., and Bentz D.P., Multi-scale picture of concrete and its transport properties: Introduction for non-cement researches, National Institute of Standards and Technology Internal Report 5900 (1996)

[3] Kuropatenko V.F., Kovalenko G.V., Kuznetsova V.I., Mihailova G.I., Sapozhnikova G.N. VOLNA complex of codes and inhomogeneous difference method of compressible media motion computations.VANT, ser. "Techniques and codes of numerical solution to mathematical physics problems", issue. 2, p. 9...25, 1989.

[4] Alekseeva T.N., Bychenkov V.A., Kuropatenko V.F., RAPID technique for two-dimensional adiabatic fluids of compressible media computations in Lagrangian variables with free points neightbourhood.VANT, ser. "Techniques and codes of numerical solution to mathematical physics problems", issue. 1, p. 14...21, 1988.

[5] Bychenkov V.A., Gadzhieva V.V., Kuropatenko V.F. Compressible media unsteady motion computation. Numerical methods of continuous medium mechanics, v. 3, p.3...17, 1972.

[6] Agafonov M.A, Arzhannikov A.V., Ginzburg N.S., Peskov N.Yu., Sinitsky S.L., Tarasov A.V. Powerful FEM-generator driven by microsecond sheet beam. Proc. of 11-th Intern. Conf. on High Power Particle Beams. Prague, 1996, v.1, pp.213-216.
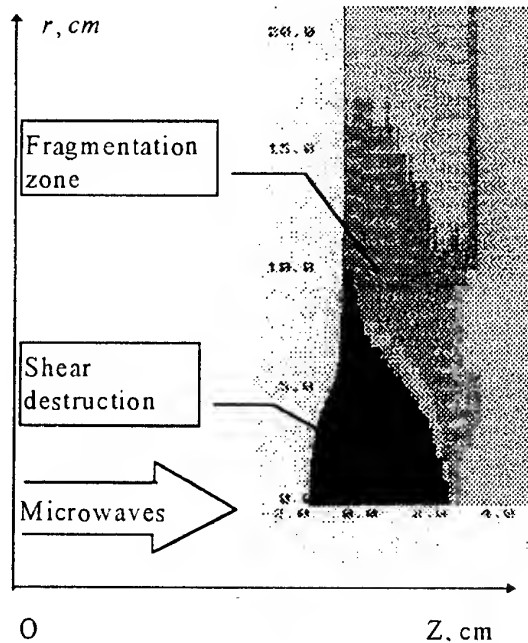
HIGH-POWER MICROWAVE GENERATION BY A PLASMA-LOADED BACKWARD-WAVE OSCILLATOR

Bao-Liang Qian, Chuan-Lu Li, Yong-Gui Liu, Hui-Huang Zhong,
Jian-De Zhang, Qi-Mei Tan, Jin-Liang Liu, Cun-Hua Liu,
Dong-Qun Chen, Xiang-Sheng Li, and Che-Bo Liu

*(Department of Applied Physics, National University of Defense Technology,
Changsha 410073, Hunan, P. R. CHINA)*

High-power microwave was measured at a frequency range from 9.5*GHz* to 13.4 *GHz* in a plasma-loaded backward-wave oscillator employing an annular relativistic electron beam with kinetic energy varying from 400 *keV* to 500 *keV* and current ranging from 1 *kA* to 3 *kA*. The relativistic electron beam, which was produced from a helium gas-loaded foilless diode, was injected into the helium gas-loaded rippled-wall waveguide of the backward-wave oscillator, generating the plasma in the waveguide and then the high-power microwave. The gas-loaded diode operated stably without encountering the closure problem in the helium gas pressure range (less than 100 *mTorr*) which was of interest to the operation of the backward-wave oscillator. An enhancement in the total microwave power emission over the vacuum case by a factor of up to 7 was found in the experiment, and the highest efficiency of electron beam to microwave radiation was estimated to be about 29%.

I. INTRODUCTION

The backward-wave oscillator (BWO) is one of the most successful examples utilizing relativistic electron beams to generate high-power microwave radiations. Many authors [1-10] have focused their attention on this device for more efficient operation at high-power levels, and important results have been obtained both experimentally and theoretically. In order to further enhance the output power of microwave and the conversion efficiency of electron beam to microwave radiation, some scientists [11-19] have introduced background plasmas into the BWO, and both theoretical and experimental results have demonstrated that the background plasma improves the beam-waveguide interaction dramatically.

The background plasma can be easily produced by the electron-beam-impact ionization of a low pressure neutral gas prefilled in the device[11-15]. In addition, one can also fill the device with plasma by the external injection[16-19]. In the case of the electron beam injection into a low pressure neutral background gas producing a plasma in the BWO, an anode foil was usually employed to separate the vacuum diode from the gas-loaded rippled-wall waveguide[11]. In this situation, the anode foil needs to be changed after each shot and the anode foil may lead to the degradation of the beam angular characteristics[20]. The goal of the

present experiment was to remove the anode foil and develop a helium gas-loaded foilless diode to investigate our plasma-filled BWO. The experiment presented the electron beam to microwave radiation conversion efficiency of 29% for the plasma-filled BWO in the frequency range from 9.5 *GHz* to 13.4 *GHz*.

For the production of a background plasma in the present experiment, the foilless diode and the rippled-wall waveguide of the BWO were both filled with a low pressure helium gas. Depending on the background gas pressure, an enhancement over the vacuum case by a factor of up to 7 in the total power emission was found in the experiment.

The remainder of this paper is organized as follows. In Sec. II, the description of the experiment is given. In Sec. III, the experimental results are presented and discussed. Conclusions are stated in Sec. IV.

II. EXPERIMENTAL SETUP

A schematic of our plasma-filled BWO is shown in Fig.1. The REB with duration of 40 *ns* was generated in a foilless diode in which a hollow cathode with inner diameter of 10 *mm* and outer diameter of 12 *mm* was employed. The voltage of the operating diode was in the range of 400 *keV* ~ 500 *keV*, and the beam current varied from 1 *kA* to 3 *kA*. The REB was then injected into the rippled-wall cylindrical waveguide of the BWO, whose radius $R(z)$ varies sinusoidally according to the relation

$$R(z) = R_0 + h\cos(k_0 z) , \qquad\qquad (1)$$

1. Cathode	2. Anode	3. Reflector	4. Rippled-wall waveguide	5. Magnetic coils
6. Smooth taper	7. Helium inlet	8. Receiving horn	9. Attenuator	10. X-band waveguide
11. Oriented coupler	12. Crystal detector	13. Dispersive line	14. Cable	15. Attenuator
	16. Crystal detector	17. Digitizing oscilloscope		
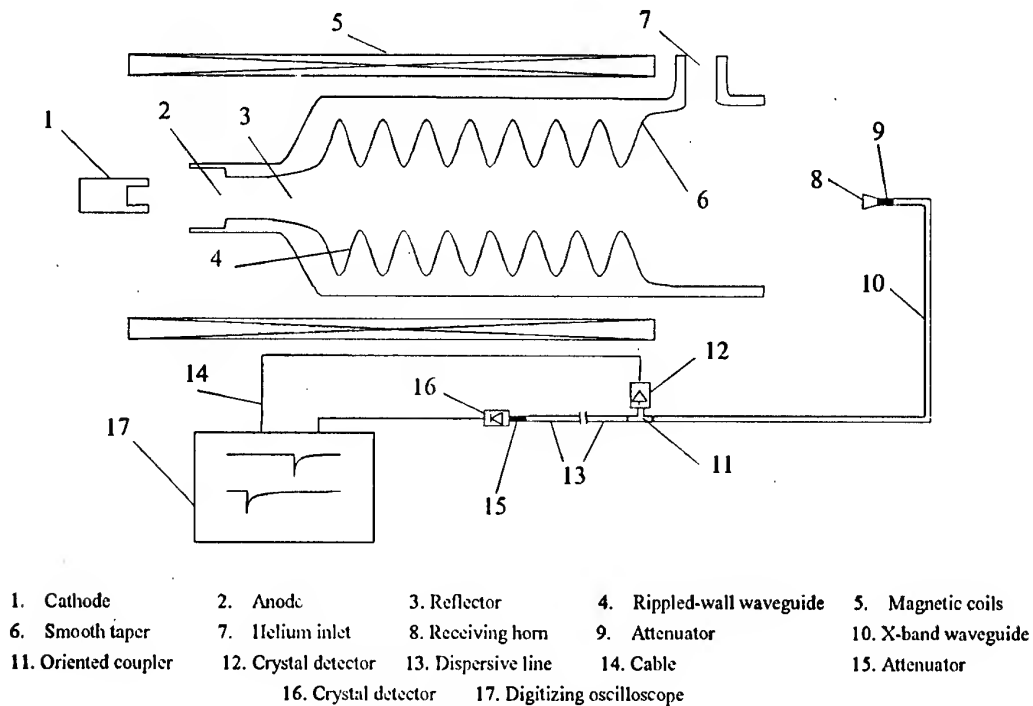
FIG. 1. Experimental setup

where R_0=1.45 *cm* is the average radius of the rippled-wall waveguide, *h*=0.2 *cm* represents

the ripple amplitude, $z_0=1.8$ *cm* denotes the ripple period, and $k_0=2\pi/z_0$ is the ripple wave number.

The voltage V_D of the diode was monitored by a voltage divider, the beam current I_B was collected using a Faraday cup, and the total current of the diode circuit was measured by a current divider. The entire system was immersed in an externally applied axial guide magnetic field of 7 *kG* ~18 *kG*. The guide magnetic field played an important role in the REB propagation, and exerted an obvious influence on the interaction occurred in the device.

We placed an rf receiving horn at the end of the BWO to receive the high-power microwave emitted from the BWO. For measuring the total power of the microwave, the calibrated crystal detector and attenuators were used directly, and the detected microwave signal was sent to a HP54502A digitizing oscilloscope. The frequency of the microwave was measured by a dispersive line of X-band, in which different frequency components were discriminated by their different group velocities. In the dispersive line technique, the received microwave signal propagated through an X-band rectangular waveguide and reached an oriented coupler which divided the microwave radiation into two beams. One beam traveled directly to a crystal detector, and the other turned to the dispersive line of X-band, then propagated to another crystal detector. Finally, the two detected microwave signals were both scanned and shown on one HP54502A digitizing oscilloscope. Thus, one can read the time difference of the propagation of the two microwave signals on the screen of the oscilloscope and determine the propagation time of the microwave in the dispersive line, which bears a relation to the group velocity of the microwave. It may be mentioned that the frequency of the microwave is a function of the group velocity of the microwave and one can determine the frequency easily.

1. Helium outlet   2. Cathode   3. Anode
4. Rippled-wall waveguide   5. Helium inlet   6. Output window
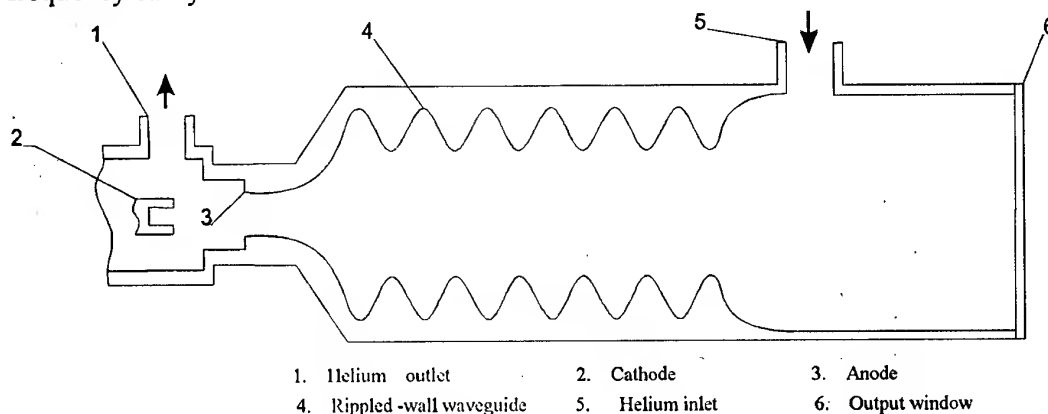
FIG. 2. The generation of plasma in the BWO in which the foilless diode and the rippled-wall waveguide were both filled with the helium gas.

A description of the plasma generation is shown in Fig.2. In general, the REB is produced from a vacuum diode maintained at about 10^{-5} *Torr*. In studying the plasma-filled BWO that used the technique of beam- impact ionization of a low pressure neutral gas [11],

one had to employ a diode with an anode foil separating the vacuum diode from the gas-loaded rippled-wall waveguide. In this case the anode foil bears the pressure difference of the diode region and the rippled-wall waveguide, and needs to be changed after each shot. In order to solve this difficulty, as shown in Fig.2, we have developed a helium gas-loaded foilless diode [21] that operated stably when the gas pressure was below 100 $mTorr$ in the presence of an axially applied guide magnetic field. The development of the gas-loaded foilless diode is of interest to the repetitive pulse operation of the plasma-loaded BWO.

III. EXPERIMENTAL RESULTS AND DISCUSSION

The introduction of a helium gas into the foilless diode will affect the generation of the REB. Figure 3 displays the experimental data for the diode operation voltage V_D versus the helium pressure P_{He} in the presence of an axially applied guide magnetic field B=11 kG, and figure 4 shows the experimental data of the beam current I_B versus the helium gas pressure P_{He} for B=11 kG. It can be seen from Figs.3 and 4 that the beam current increases substantially with the increase of the helium gas pressure and the diode operation voltage drops simultaneously, which implies a decrease in the diode impedance. In addition, the diode operated unstably and shorted in most of the shots when the helium gas pressure exceeded 100 $mTorr$ in the presence of an axially applied guide magnetic field.
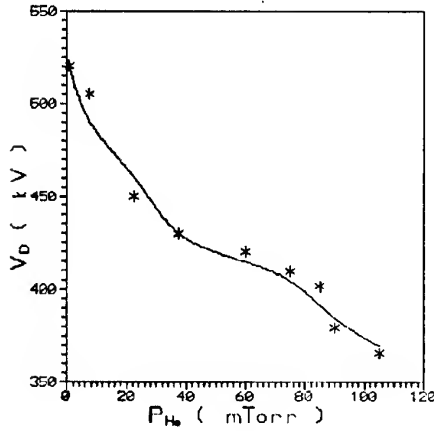
FIG.3. The operation voltage V_D versus the helium gas pressure P_{He} for guide magnetic field B= 11 kG
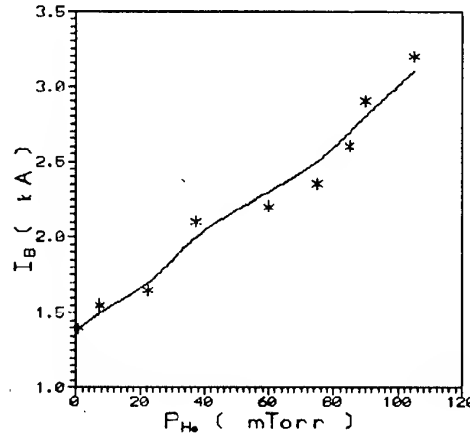
FIG.4. The beam current I_B versus the helium gas pressure for guide magnetic field B = 11 kG

The frequency is an important parameter describing the microwave. In the experiment, we measured the microwave frequency using the dispersive line which was built up by using the standard X-band rectangular waveguide. The microwave was propagated through the dispersive line in the TE_{01} mode, and the group velocity V_g can be expressed as

$$V_g = c \, [\, 1 - (f_c/f)^2 \,]^{1/2} \, , \tag{2}$$

where f_c is the cutoff frequency of the rectangular waveguide, f is the microwave frequency, and c denotes the speed of light in vacuum. In addition, the group velocity V_g can

be determined by

$$V_g = L / T \quad , \tag{3}$$

where L is the length of the dispersive line and T represents the propagation time of the microwave in the dispersive line. Thus, the microwave frequency can be obtained by using Eqs.(2) and (3).

The microwave frequency of the vacuum BWO was measured to be 8.7 GHz ~ 9.5 GHz when the diode voltage was varied from 400 kV to 500 kV. Employing the formulation of the theoretical models [5,7,10,19], one can calculate the frequency of TM$_{01}$ mode of the vacuum BWO and obtain a theoretical result of 9.1 GHz ~ 9.5 GHz, which resembles the experimental result. Therefore, we deduce that the operating mode of the high-power microwave in the rippled-wall waveguide is TM$_{01}$ mode.
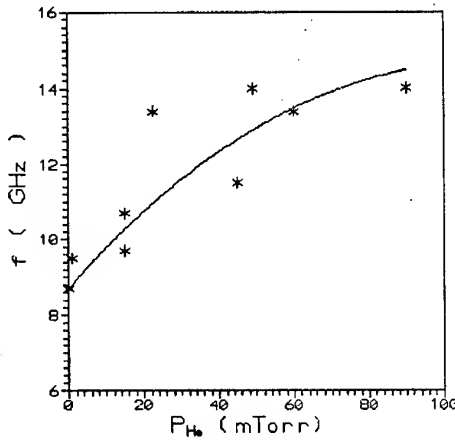
FIG. 5. The microwave frequency f versus the helium gas pressure P_{He}
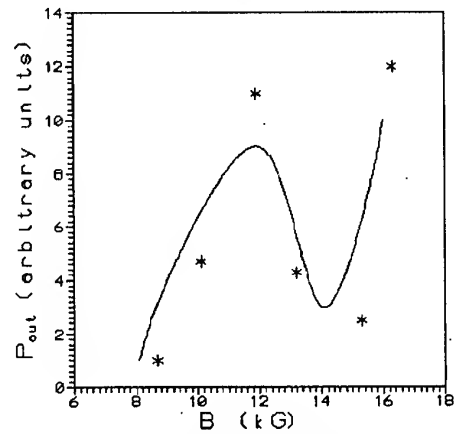
FIG. 6. The microwave peak power P_{out} versus the guide magnetic field B in the vacuum BWO case

In the case of the plasma-loaded BWO, the microwave frequency was found to be upshifted to 9.5 GHz ~ 13.4 GHz, which is identical with the previous experimental and theoretical results obtained by other scientists [12,17,18,19]. Figure 5 shows the experimental data of the microwave frequency versus the helium gas pressure P_{He}, and indicates an obvious influence of the background plasma on the frequency.

Figure 6 illustrates the experimental result of the total microwave power P_{total} versus the externally applied axial guide magnetic field B for the vacuum BWO. The experimental data imply that the externally applied guide magnetic field considerably affected the beam-waveguide interaction. It can be found in Fig.6 that the microwave power was low when the guide magnetic field was less than 8 kG, and that the microwave power peaked at B ~ 12 kG and B ~ 16 kG. We can also see from Fig.6 that the microwave power dropped rapidly when magnetic field B was around 14.5 kG , which means the cyclotron absorption of the electromagnetic wave due to the cyclotron mode existed in the magnetized REB [9]. For the vacuum BWO,

the maximum interaction efficiency of electron beam energy to microwave radiation was estimated to be about 6 %.

The introduction of a plasma into the BWO increases the total microwave power and the efficiency of converting the beam energy into electromagnetic radiation under the condition that the guide magnetic field and the helium gas pressure are maintained at certain values. Figure 7 gives the experimental data of the total microwave power as a function of the helium gas pressure for guide magnetic field $B \sim 11 \ kG$. As can be seen from Fig.7, the microwave power increased rapidly when the helium gas pressure was around 25 $mTorr$. In this case, the maximum microwave power was determined to be about 7 times larger than that of the vacuum case, and the interaction efficiency was estimated to be about 29%. Figure 8 shows the experimental data of the total microwave power versus the guide magnetic field for the helium gas pressure $P_{He} \sim 25 \ mTorr$. It can be seen from Fig.8 that the microwave power was increased considerably at certain values of the guide magnetic field, which resembles the experimental data given in Refs.[11] and [12]. Possible mechanism of the enhancement of the microwave power and the interaction efficiency in a plasma-loaded BWO can be found in Refs.[22-24]. It may be mentioned that the Trivelpiece-Gould modes, occurred in the plasma-loaded BWO, were not investigated in the present experiment. It has been shown that these modes are usually with low frequencies and low power levels compared with the X-band TM_{01} modes of the rippled-wall waveguide [12,18].
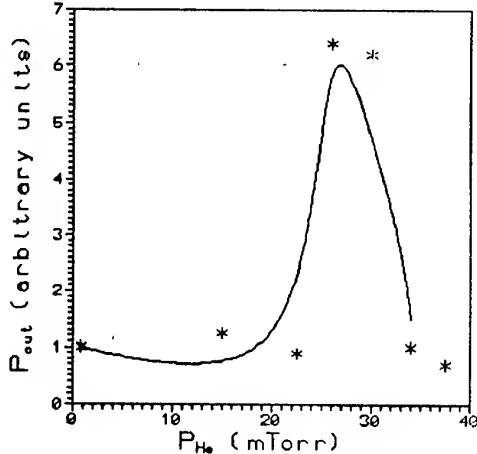
FIG. 7 . The peak microwave power P_{out} versus the helium gas pressure P_{He} for guide magnetic field $B\sim$ 11 kG
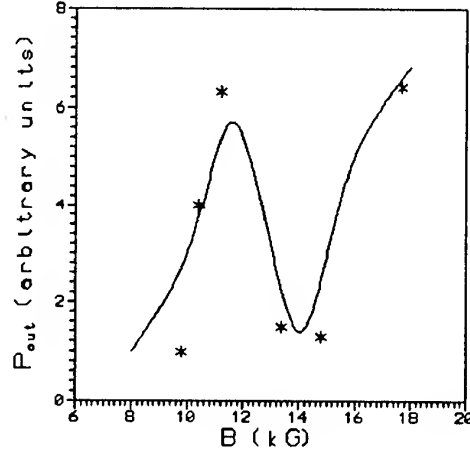
FIG. 8. The peak microwave power P_{out} versus the guide magnetic field B for helium gas pressure $P_{He} \sim$ 25 $mTorr$

IV. CONCLUSIONS

In conclusion, we have observed the high-power microwave radiation from a plasma-loaded BWO that employed a helium gas-loaded foilless diode. The entire system, including the foilless diode and the rippled-wall waveguide, was filled with the low pressure helium gas to

generate the background plasma in the BWO by the electron beam-impact ionization of the background gas. The gas-loaded foilless diode operated stably without encountering the closure problem when the helium gas pressure was below 100 *mTorr*, which is of interest to the repetitive pulse operation of the plasma-loaded BWO. The maximum interaction efficiency was about 29% for the plasma-loaded BWO, and an enhancement in the total microwave power emission over the vacuum case by a factor of up to 7 was found in the experiment. The microwave frequency of the vacuum BWO was in the range of 8.7 *GHz* ~ 9.5 *GHz*, while the microwave frequency of the plasma-loaded BWO was upshifted to the range of 9.5 *GHz* ~ 13.4 *GHz*. The operating mode in our device was determined to be TM_{01} mode.

ACKNOWLEDGMENT

REFERENCES

[1] Y. Carmel, J. Ivers, R.E. Kribel, and J. Nation, Phys. Rev. Lett. 33, 1278 (1974).

[2] L. S. Bogdankevich., M. V. Kuzelev, and A. A. Rukhadze, Zh. Tech. Fiz. 50, 233 (1980) [Sov. Phys. Tech. Phys. 25, 143 (1980)].

[3] Y. Carmel, V. L. Granatstein, and A. Gover, Phys. Rev. Lett. 51, 566 (1983).

[4] R. A. Kehs, A. Bromborsky, B. G. Ruth, S. E. Graybill, W. W. Destler, Y. Carmel, and M. C. Wang, IEEE Trans. Plasma Sci. PS-13, 559 (1985).

[5] J. A. Swegle, Phys. Fluids 28, 3696 (1985).

[6] J. A. Swegle, Phys. Fluids 30, 1201 (1987).

[7] B. Levush, T. Antonsen, Jr., A. Bromborsky, W. Lou, and Y. Carmel, IEEE Trans. Sci. PS-20, 1 (1992).

[8] B. Levush, T. Antonsen, Jr., A. Bromborsky, W. R. Lou, and Y. Carmel, Phys. Fluids B 4, 2293 (1992)

[9] A. Vlasov, G. Nusinovich, B. Levush, A. Bromborsky, W. Low, and Y. Carmel, Phys. Fluids B 5, 1625 (1993).

[10] J. A. Swegle, J. W. Poukey, and G. T. Leifeste, Phys. Fluids 28, 2882 (1985).

[11] K. Minami, W. R. Lou, W. W. Destler, R. A. Kehs, V. L. Granatstein, and Y. Carmel, Appl. Phys. Lett. 53, 559 (1988).

[12] X. Zhai, E. Garate, R. Prohaska, G. Benford, and A. Fisher, IEEE Trans. Plasma Sci. PS-21, 142 (1993).

[13] Yu. V. Tkach, Ya. B. Fainberg, I. I. Magda, N. I. Gaponenko, A. V. Skachek, S. S. Pushkarev, N. P. Gadetskii, and A. A. Belukha, Fiz. Plazmy 1, 81 (1975) [Sov. J. Plasma Phys. 1, 43 (1975)].

[14] Yu. V. Tkach, N. P. Gadetskii, Yu. P. Bliokh, E. A. Lemberg, M. G. Lyubarskii, V. V. Ermolenko, V. V. Dyatlova, S. I. Naisteter, I. I. Magda, S. S. Pushkarev, and G. V. Skacheck, Fiz. Plazmy 5, 1012 (1979) [Sov. J. Plasma Phys. 5, 566 (1979)].

[15] D. M. Geobel, J. M. Butler, R. W. Schumacher, J. Santoru, and R. L. Eisenhart, IEEE Trans. Plasma Sci. PS-22, 547 (1994).

[16] Y. Carmel, K. Minami, R. A. Kehs, W. W. Destler, V. L. Granatstein, D. A. Abe, and W. L. Lou, Phys. Rev. Lett. 62, 2389 (1989).

[17] Y. Carmel, K. Minami, W. Lou, R. A. Kehs, W. W. Destler, V. L. Granatstein, D. K. Abe, and J. Rodgers, IEEE Trans. Plasma Sci. PS-18, 497 (1990).

[18] Y. Carmel, W. R. Lou, T. M. Antonsen, Jr., J. Rodgers, B. Levush, W. W. Destler, and V. L. Granatstein, Phys. Fluids B4, 2286 (1992).

[19] K. Minami, Y. Carmel, V. L. Granatstein, W. W. Destler, W. Lou, D. K. Abe, R. A. Kehs, M. M. Ali, T. Hosokawa, K. Ogura, and T. Watanbe, IEEE Trans. Plasma Sci. PS-18, 537 (1990).

[20] V. S. Burmasov, I. V. Kandaurov, E. P. Kruglyakov, and O. I. Meshkov, IEEE Trans. Plasma Sci. PS-23, 952 (1995).

[21] Bao-Liang Qian, Chuan-Lu Li, Yong-Gui Liu, Jian-De Zhang, Qi-Mei Tan, Jin-Liang Liu, and Che-Bo Liu (unpublished).

[22] A. T. Lin and L.Chen, Phys. Rev. Lett. 63, 2808 (1989).

[23] M. Botton and A. Ron, Phys. Rev. Lett. 66, 2468 (1991).

[24] C. S. Liu and V. K. Tripathi, IEEE Trans. Plasma Sci. PS-21, 191 (1993).

RELATIVISTIC BWO WITH ELECTRON BEAM PRE-MODULATION

A. V. Gunin, S. D. Korovin, I. K. Kurkan, I. V. Pegel, V. V. Rostov, and E. M. Totmeninov

Institute of High Current Electronics, 634055, Tomsk, Russia

Abstract - The paper presents the results from theoretical and experimental studies of a backward wave oscillator with resonant reflector incorporated in electromagnetic system. The reflector serves simultaneously as a short modulating gap and this provides the selection of TM_{01} operating mode among parasitic transversal modes in extended approximately twice slow-wave structure. In course of experiment a 0.8 GW microwave power in X-band was obtained with the efficiency of 25%. The electron beam pre-modulation and the extension of BWO transversal size allowed for increasing its efficiency in a low magnetic field. A periodically-pulsed regime of BWO operation with 20% efficiency utilizing DC magnet with 0.6 T field was realized.

INTRODUCTION

The design of the relativistic BWO using a cut-off neck for reflection of the electromagnetic wave propagating backward to electron motion has gained acceptance since the first experiments [1,2]. Taking the lowest axisymmetric TM_{01} wave of a circular waveguide as the operating mode, the cut-off neck diameter should be $\sim 0.7\lambda$. Application of this element results in simplicity of the electrodynamic system but at the same time it limits the opportunities for increasing the generated pulse energy and reduction of magnetic field.

Obviously, the prospects of relativistic BWO as well as of other microwave devices based on high current electron beams are associated with the conversion to oversized electrodynamic system and solution of the parasitic mode discrimination problem. One of the approaches in this context is using high-order modes, for instance, TM_{02} or TE_{m1} ($m \gg 1$) [3]. This allows for employing the cyclotron selection by means of choosing the beam radius and magnetic field or the condition that the norm of the operating wave is lower than that of competitive ones.

The selecting element of suggested BWO design with TM_{01} operating wave is the resonant reflector similar to described in [4]. The diameter of the slow wave structure (SWS) is about 1.5λ. An efficient wave reflection from axisymmetric waveguide nonuniformity is provided by the presence of a high-order locked mode (in our case TM_{02}) having the same azimuthal index as the propagating one. The mechanism of this reflection for TE_{0n} waves was discussed in 1956 [5]. The wave reflection at a resonant frequency is similar to the reflection from an open circuit. This fact is clearly shown in the standing wave diagram in Fig. 1. The thin line corresponds to the standing wave extension to $z=0$. Actually, the equivalent circuit diagram is presented as a band-pass rejection filter (LC-resonant circuit) built in a transmission line gap.

Efficient electron beam modulation occurs in the reflector region at a resonant frequency caused by the z-component of resonant electric RF-field. This leads to the decrease of start current as the analogue conditions for the competitive waves are either not provided or not matched with the Cherenkov interaction band.
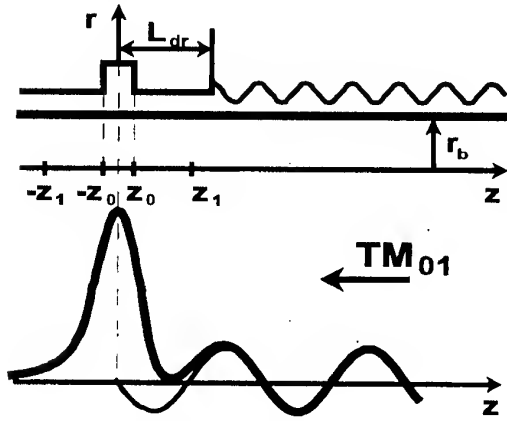
Fig. 1. BWO with resonant reflector and z-distribution of a standing wave of E_z field for $r=r_b$ under small corrugation amplitude approximation.

Consider the main electrodynamic properties of a resonator formed by axisymmetric nonuniformity having a rectangular profile with the radius b and width $L=2z_0$ (Fig. 1). The waveguides with radius a are considered matched at the edges. At least one oscillation of TM_{02} locked mode exists over the range of wavelengths $v_{02}/b<k<v_{02}/a$, where $k=2\pi/\lambda$ and $v_{02}=5.52$ is the second root of zero-order Bessel function $J_0(x)=0$. Under a zero diffraction losses approximation, the resonant frequencies are derived from the equation $\cos\xi=s\xi$ where $s=2/[k_{\perp2}L(1-a^2/b^2)^{1/2}]$, $\xi=L(k^2-k_{\perp2}^2)^{1/2}/2$, $k_{\perp2}=v_{02}/b$. If $s>1$, the only eigenmode exists. The resonant frequency shiftdown takes place in the presence of diffractive and ohmic losses. The ohmic losses are typically low and the corresponding factor $Q_{ohm}\sim a/\delta$ (where δ is the skin depth) therewith can be evaluated by $10^3\div10^4$.

Omitting the field distortion at the edges $z=\pm z_0$ derive the following expression for the diffractive quality factor

$$Q_d \cong \frac{J_1^2(v_{01})}{2J_0^2(k_{\perp2}a)} \cdot \frac{k_{//}b^2 \int_{-z_1}^{z_1}|f|^2 dz}{\left|\int_{-z_0}^{z_0} fe^{ik_{//}z}dz\right|^2} \quad,$$

where $f(z)$ is a function describing the longitudinal field distribution in the resonator, $f(0)=1$, $|f(\pm z_1)|<1$, $k_{//}$ is the longitudinal wave number of TM_{01} mode, and $v_{01}=2.405$. Operation near the limits $a/b\rightarrow1$, $L\rightarrow0$ and $L_{ef}\approx2\pi/k_{//}$ (L_{ef} is typical field distribution width, $L_{ef}\approx L$) where the Q-factor is indefinitely increasing is not recommended. Of practical interest is the case $Q_d<<Q_{Ohm}$ when the wave reflection factor at a resonant frequency close to unit: $R\approx1-Q_d/Q_{Ohm}$. The scattering matrix method was used to calculate the reflection factor as a function of frequency and the RF-field structure [4]. The reflector having $Q_d\approx7$ was taken for the experiment. The reflection coefficient was $|R|^2>0.9$ in the bandwidth of ~600 MHz with the center at 10.0 GHz.

In the presence of electron beam the frequency shift is much less than the reflection band. The maximum efficiency of electron beam modulation is reached at $kL_{ef}/\beta_{//}\approx\pi$ where $\beta_{//}=v_{//}/c$, $v_{//}$ - the electron velocity, c is the speed of light. If Q_e is the factor characterizing this mechanism of resonator energy losses then, at $L_{ef}\approx\beta_{//}\lambda/2$,

$$Q_e \approx \left[\frac{4I_b}{I_A k^2 b^2 \gamma_0^3 \beta_{//}} \frac{J_0^2(k_{\perp2}r_b)}{J_1^2(v_{02})}\right]^{-1}$$

where I_b is the beam current, $I_A\approx 17$ kA, and γ_0 is the relativistic particle mass-factor. For the experimental conditions, $Q_e^{min}\approx200$.
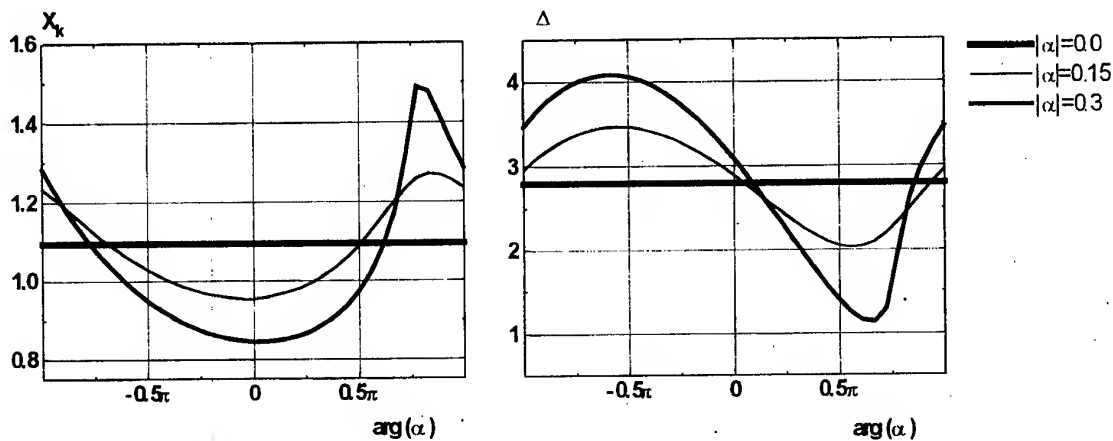
Fig. 2. Start length (X_k) and synchronism mismatch as functions of modulation phase in linear BWO approximation

Only the velocity modulation of particles was considered in the BWO boundary problem analysis. The electron beam pre-modulation at the input of corrugated slow-wave structure can be fully described by the complex parameter

$$\alpha = \frac{I^{1/3}k \int\limits_{-z_1}^{z_1} E_z(r_b, z) exp(ik\, z/\beta_{\parallel})dz}{2\gamma_0^2 E_{-1}(r_b)} \quad \text{where } I = \frac{\gamma_0^3 I_b c |E_{-1}(r_b)|^2}{\pi I_A k^2 P}.$$

In this case $E_z(r_b, z)$ is the modulating field, $E_{-1}(r_b)$ is the field of the (-1)-st SWS spatial harmonic, and P is the power of the TM_{01} wave. Playing an important part, the modulation phase $arg(\alpha)$ sets the initial phase of the RF-current. In accordance with the α definition the modulation phase is the phase difference between the fields $E_z(r_b, 0)$ and E_{-1}. Therefore, under real experimental conditions, there can be variations in its value through a choice of the initial phase of corrugated SWS sinusoidal profile or the L_{dr} value (see Fig. 1). In the case of $arg(\alpha) \cong 0$ the phase distribution of RF-current relative to decelerating field phases along z is slightly different from the distribution in the conventional BWO ($|\alpha|$=0) up to $|\alpha| \cong 1$ both in a linear interaction and nonlinear one. So, the values of energy exchange efficiencies appear to be closely allied. At the same time the optimum SWS length tends to decrease as $|\alpha|$ increases with the phase conserved. The cases when I<<1 therewith provide the generation efficiency to be even in increase. The relation between normalized SWS start length $X_k = kL_{st}I^{1/3}/2\gamma_0^2$ and the synchronism mismatch for the linear stage $\Delta = [2\gamma_0^2((k_d - k_{\parallel})/(k-1)-1]I^{1/3}$ (where $k_d = 2\pi/d$ and d is SWS period) are presented in Fig. 2 as a functions of $arg(\alpha)$. The behavior of the synchronism mismatch variation when shifting $arg(\alpha)$ from the efficiency optimum (also near zero) remains the same for non-linear interaction. This effect can be useful for oscillator operational mode adjustment, and in fact it is the most important feature of the BWO with electron beam pre-modulation.

Detailed optimization of the entire BWO system was made in numerical experiments employing the axisymmetric 2.5D version of the fully electromagnetic PIC-code KARAT [6]. These simulations delivered the main dependencies of microwave power and frequency and pulse rise time on the parameters of BWO electrodynamic system and electron beam. Most of these dependencies were then clearly observed in experiment.
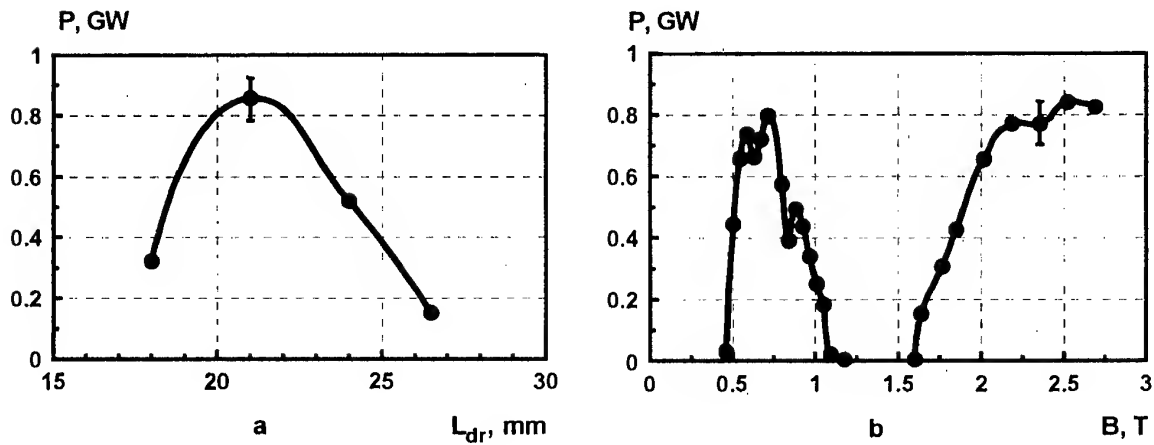
Fig. 3. Dependence of generated power as a function of resonator location (a) and guiding magnetic field (b)

EXPERIMENTAL RESULTS

All experiments were carried out in two stages using electron accelerators of SINUS type. In course of the first stage the magnetic system with the field strength of up to 2.7 T and pulse repetition rate of up to 0.1 p.p.s. was used. Fig. 3a shows the dependence on generated power as a function of L_{dr}. This dependence and the observed shift of measured frequency over the entire range of L_{dr} variation closely agree with the theoretical data. The microwave power at a maximum accelerator parameters (beam current I_b =5.5 kA, and accelerating voltage U=600 kV) was 0.8 GW that corresponds to 25% BWO efficiency. The experiments showed that an efficient generation can be obtained in a relatively low magnetic field of ~0.7T (Fig. 3b). From the practical point of view this result is important for BWO applications. This is why similar experiment was carried out at I_b =4.5kA, U=530kV in a repetitively-pulsed mode with the repetition rate of up to 100 p.p.s. A DC-magnet system having a 25 kW power consumption was providing static magnetic field. The microwave power of 0.5 GW with 10 GHz frequency and 10 ns pulse width was obtained. The typical time delay for microwave emission was 8 ns.

ACKNOWLEDGMENTS

REFERENCES

[1]   N. F. Kovalev, M. I. Petelin, M. D. Raizer et al., JETP Lett., vol. 18, pp. 138-140, 1973.
[2]   Y. Carmel, J. Ivers, R. E.Kribel, and J. Nation, Phys. Rev. Lett., vol.33, pp. 1278-1282. 1974.
[3]   E. B. Abubakirov, M. I. Fuchs, V. A. Gintsburg et al., Proc. Conf. "Beams'90", pp. 1105-1110, 1990.
[4]   G. G. Denisov, D. A. Lukovnikov, S. V. Samsonov, Int. J. Infr. and MM Waves, vol.16, N.4, pp.745-752, 1995.
[5]   A. P. King, E. A. Marcatili, Bell System Tech. J. vol.35, pp. 899-907, 1956.
[6]   V. P. Tarakanov. User's Manual for Code KARAT. - Springfield, VA: Berkeley Res. Assoc., 1994.

GRATING TRANSITION RADIATION
A NEW SOURCE OF MONOCHROMATIC LIGHT
USING RELATIVISTIC ELECTRONS

O. Haeberlé, P. Henri, P. Rullhusen

European Commission, Joint Research Centre,
Institute for Reference Materials and Measurements, Retieseweg, B 2440 Geel, Belgium

N. Maene

Vlaamse Instelling voor Technologisch Onderzoek, Boeretang 200, B 2400 Mol, Belgium

W. Mondelaers

Vakgroep Subatomaire en Stralingsfysica, University of Gent,
Proeftuinstraat 86, B 9000 Gent, Belgium

ABSTRACT

The production of quasi-monochromatic light by relativistic electrons impinging on the surface of an optical grating is investigated at electron energies between 3 and 120 MeV. In analogy to Smith-Purcell (SP) radiation generated by electrons travelling close and parallel to the grating surface the wavelength depends on the angle of observation. In addition, in grating transition radiation (GTR) the wavelength depends also on the angle of incidence of the electron. At a fixed wavelength the angular distribution is concentrated in hollow cones centered around the main directions of emission of the different orders of diffraction. These hollow cones are similar to the well-known distribution of transition radiation from flat surfaces (TR).

The experiments have been carried out at the Gent linear accelerator in the energy range 3-15 MeV and at the Geel linear accelerator at 20-120 MeV. Several gratings were used, ruled in SiC with 1800 lines/mm and 2000 l/mm and with different profiles. The angular distribution and polarization of GTR have been measured in zeroth and first diffracted order for several wavelengths between 400 and 700 nm. The intensity observed in zero order near specular reflection is compared to TR observed from a flat mirror of the same surface material.

We calculated the GTR intensity expanding the Coulomb field of the electron into plane waves. These waves are diffracted by the grating leading to a "grating problem" as in the case of SP radiation. The formalism converges towards TR in the limit of vanishing groove depths.

THEORETICAL MODEL

A virtual photon field is associated with the electric field of a relativistically moving electron charge. When the electron trajectory is parallel to a grating, the polarization components of this virtual photon field can be represented by Fourier integrals and the calculation of SP [1-4] is reduced to the solution of the so-called "grating problem" in optics [5]. For electron beams at finite incidence angles the application of this approach is not straightforward because a singularity appears where the electron hits the surface. For the calculation of optical transition radiation (OTR) from plane surfaces, however, the far-field approximation can be used and the reflectivity of the surface is obtained from the well-known Fresnel coefficients [6-7]. In the following we propose a general approach which contains both phenomena as limiting cases.

For simplicity, we restrict ourselves to electron trajectories perpendicular to the rulings of the grating. Fig.1 shows the main geometrical quantities. The notation is similar to the one used
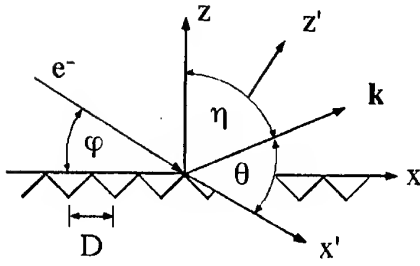
Figure 1. Geometry used in the description of GTR. x': direction of the electron; y=y': direction of the rulings; z: surface normal.

previously [3,4] in calculations of SP, to which we refer for further details. The incident electromagnetic field is written as a Fourier expansion in the (x',y',z',t) reference frame in which x' is the direction of the electron velocity and y' the direction of the grating rulings. As in the case of SP radiation, the x' and z' components of the Fourier transforms (FT) E^i and H^i can be expressed as functions of the y' components $E^i_{y'}$ and $H^i_{y'}$. Contrary to SP, however, it is not sufficient to consider only a FT in y' and t but in addition also in z'. After rotation by an angle φ into the (x,y,z,t) laboratory reference frame one obtains a decomposition of the incident field into plane waves of the form $E^i_y(\varphi,\beta,\sigma,\omega)\exp(iA^i)$, in which β,σ,ω are the Fourier components belonging to the y',z',t transformation, respectively, $A^i = \alpha_0 x' + \beta y' + \sigma z' = (\alpha_0\cos\varphi + \sigma\sin\varphi)x + \beta y + (-\alpha_0\sin\varphi + \sigma\cos\varphi)z$, and $\alpha_0 = kc/v$. Correspondingly, the reflected field is expanded into a Rayleigh series $\sum E^r_{y,n}(\varphi,\beta,\sigma,\omega)\exp(iB^r_n)$, with $B^r_n = \alpha_n x + \beta y + \gamma_n z$, $\alpha_n = \alpha_0\cos\varphi + \sigma\sin\varphi + 2\pi n/D$, $\gamma_n = (k^2 - \beta^2 - \alpha_n^2)^{1/2}$, D is the grating period, and $n = 0, \pm 1, \pm 2,...$ Propagative waves are those for which $\text{Im}(\gamma_n) = 0$. Such a propagative diffracted wave is emitted in order n and wavelength λ at angles (η,ζ) defined by $\alpha_n = k\sin\eta$, $\beta = k\cos\eta\sin\zeta$, $\gamma_n = k\cos\eta\cos\zeta$ and consists of a superposition of waves of different Fourier components σ. In the far field (i.e., at distances R with $kR \gg 1$) we may use the method of stationary phases (or Fraunhofer approximation) and evaluate the integral only at a so-called "critical point" [8]. At given observation angles (η,ζ) we obtain the following "diffraction law":

$$-\frac{n\lambda}{D} = \frac{c}{v}\cos\varphi - \sin\eta + \frac{\sigma}{k}\sin\varphi \qquad (1)$$

In the limit $\varphi \to 0$ Eq.1 becomes the well-known diffraction law for SP radiation. Since $v < c$ only negative orders of diffraction $n < 0$ can be observed in SP. At finite angles of incidence $\varphi > 0$ and for trajectories perpendicular to the rulings the GTR intensity for a certain wavelength λ and diffraction order n is concentrated around observation angles $\zeta = 0$ and η obtained from Eq.1 for $\sigma = 0$. Contrary to SP also positive orders of diffraction may be observable. In zero order the angular distribution is the same for all wavelengths and shows the well-known hollow cone from OTR centered at $\zeta = 0$, $\sin\eta = (c/v)\cos\varphi$. Fig.2 shows the GTR distribution calculated for 5 MeV electrons at an incidence angle $\varphi = 45°$. The 0-order contribution near specular reflection is the same as for OTR from a perfect conducting mirror. A similar angular distribution is obtained for the first diffraction order n=-1 (minimum at $\eta = -11°$) but with re-
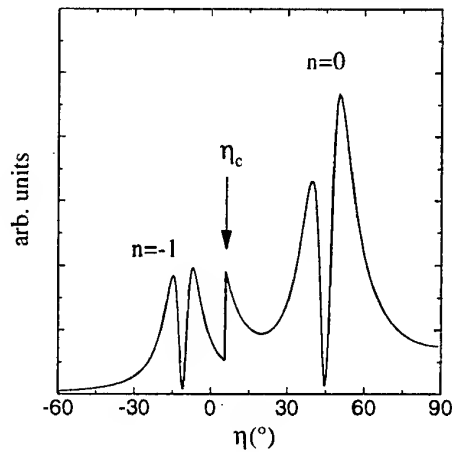
Figure 2. GTR intensity as a function of observation angle η at a fixed incidence angle $\varphi = 45°$ calculated for 5 MeV electrons and D=500 nm, $\lambda = 450$ nm. η_c: 0-order cutoff (see text).

duced intensity when the 0-order of diffraction for the same value of σ is also propagative (c.f. the sharp "cutoff" at $\eta=5.7°$). The bandwith $\Delta\lambda$ depends on two factors: the aperture $\Delta\eta$ (as for SP) and $\Delta(\sigma/k)\sin\varphi\approx\gamma^{-1}\sin\varphi$. At observation angles $\eta<\eta_c$ with $\sin\eta_c=1+n\lambda/D$ the 0-order for the same value of σ is forbidden by the diffraction law and GTR becomes a useful light source of rather small bandwith.

EXPERIMENTS

The experiments have been carried out at optical wavelengths using gratings ruled in a 100 μm SiC layer deposited on a 50x50x10 mm graphite block and aluminized on the surface. Different grating profiles were used: two lamellar gratings with either 1800 or 2000 lines/mm and a groove depth h/D=0.1, and two blazed gratings with 2000 lines/mm and blazing angles of 7.3° and 12.4°, respectively. The surface of 50x50 mm^2 was divided into two parts etched with
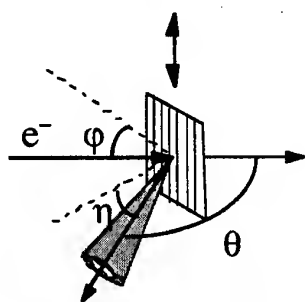
Figure 3. Experimental setup. The GTR intensity is observed at a fixed observation angle q to the electron beam rotating the grating around an axis perpendicular to the incidence plane

different profiles (case of the two blazed gratings) or only one half etched (case of the lamellar profiles) leaving the second half as a flat surface for conventional OTR measurements. The radiation emitted from the gratings was observed in constant-deviation geometry at two fixed observation angles of $\theta=90°$ and 120° to the electron beam, respectively. The radiators were mounted on a target holder and could be rotated around an axis perpendicular to the observation plane. Fig.3 describes the experimental setup. For the measurements we used an intensified camera, a linear polarization filter, and a set of interference filters with bandwidths of ±5 nm. Fig.4 shows the maximum of the intensity distribution at the grating surface as a function of the incidence angle φ, obtained using 5 MeV electrons and a $\lambda=450$ nm interference filter,

and observed at the two fixed observation angles θ given above. The data have been corrected for the known transmission of the filters and the objective as well as for the wavelength-dependent sensitivity of the camera. The solid lines are guides to the eye. The radiation emitted at small angles of incidence φ is largely monochromatic (n=-1) whereas the broad-band intensity (n=0) dominates near specular reflection.
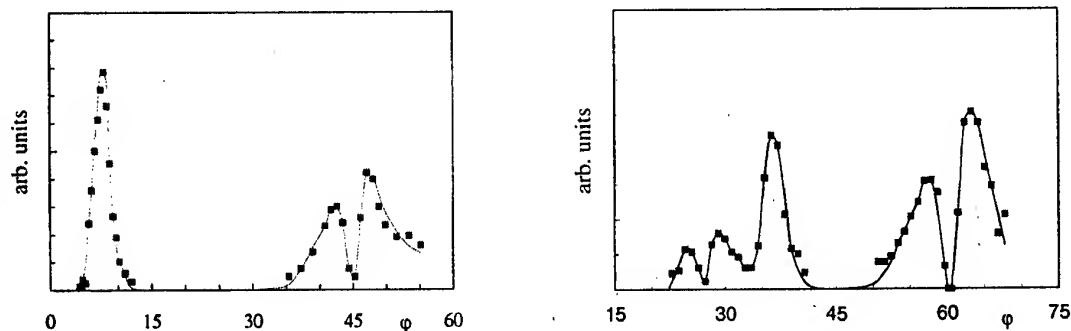
Figure 4. GTR from 5 MeV electrons observed at a wavelength of 450 nm and at fixed angles to the electron beam of $\theta=90°$ (left) and $\theta=120°$ (right)

No difference was observed between this 0-order GTR distribution and OTR from mirrors of the same surface material. Because of the diffraction law (1) no simple $\lambda(\eta)$ dependence as for SP can be established for GTR. There are, however, some characteristic angles at each wavelength, viz the minimum and the two maxima in the n=-1 distribution when the 0-order is evanescent, and the "cutoff" in the n=-1 intensity when the 0-order becomes propagative. Fig.5 depicts the observed cutoff angles for different wavelengths, observation angles and grating profiles in comparison to the values calculated from Eq.1.

The polarization of the radiation was measured for an observation angle $\zeta=0$ (i.e., observing in the incidence plane) and also for $\zeta=3.8°$. GTR emitted in 1st diffraction order n=-1 at small angles of incidence φ was always purely H-polarized (i.e. the H vector parallel to the rulings) as for SP at $\varphi=0$. The 0-order contribution near specular reflection, however, showed a polarization identical to that of OTR from the flat mirror.

The experiments have been repeated for several electron energies E=3-15 MeV at the Gent accelerator and E=20-110 MeV at Geel. At the low energies used in the Gent experiments the aperture of the optical system was always smaller than the typical opening angle $1/\gamma$ of the OTR and GTR distributions. The beam shape was defined by a set of collimators upstream of the electron beamline. In the Geel experiments the angular acceptance of the optical bench was larger than $1/\gamma$, thus integrating over large portions of the "lobes". No collimators in the electron beamline could be used and therefore the beam size varied with energy and was determined for each experiment using OTR from the flat mirrors. The 0-order GTR intensity increases with electron energy in the same way as OTR from flat surfaces. For a comparison of the n=-1 intensities with theory the reflection coefficients for the different grating profiles have to be calculated. We are planning to adapt our SP codes [3,4] to the GTR geometry. The observed intensities indicate that the n=-1 contribution does not change very much with electron energy.

Figure 5. Comparison of the 0-order cutoff-angles φ_c observed at 5 MeV to the values calculated from Eq.1

REFERENCES

[1]   S.J.Smith and E.M.Purcell, Phys. Rev. **92**, 1069 (1953)

[2]   P.M. van den Berg, J. Opt. Soc. Am. **63**, 1588 (1973)

[3]   O.Haeberlé, P.Rullhusen, J.-M.Salomé and N.Maene, Phys. Rev. E **49**, 3340 (1994)

[4]   O.Haeberlé, P.Rullhusen, J.-M.Salomé and N.Maene, Phys. Rev. E **55**, 4675 (1997)

[5]   R.Petit (Ed.) *Electromagnetic theory of gratings* (Springer Verlag, Berlin 1980)

[6]   L.Wartski, S.Roland, J.Lasalle, M.Bolore and G.Filipi, J.Appl.Phys. **46**, 3644 (1975)

[7]   M.L.Ter-Mikaelian, High-Energy Electromagnetic Processes in Condensed Media, Wiley 1972

[8]   M.Born and E.Wolf, *Principles of Optics,* Cambridge Univ.Press 1980

A GYRO-TWT WITH A WEAK SENSITIVITY
TO ELECTRON VELOCITY SPREAD

V.L. Bratman[1], A.W. Cross[2], G.G. Denisov[1], W. He[2], A.D.R. Phelps[2],
K. Ronald[2], S.V. Samsonov[1], C. Whyte[2]

[1]Institute of Applied Physics, Russian Academy of Sciences, 46 Ulyanov St.,
Nizhny Novgorod, 603600, Russia
[2] Department of Physics and Applied Physics, University of Strathclyde, 107 Rottenrow,
Glasgow, G4 0NG, U.K.

ABSTRACT

A new microwave system for a gyro-TWT in the form of a circular waveguide with a helically grooved inner surface is proposed and studied. The corrugation radically changes the wave dispersion in the region of small axial wavenumbers: at "nearly infinite" phase velocity the group velocity of the wave is finite and constant in a broad frequency band. According to the theory, this allows significant reduction in the sensitivity of the amplifier to the axial velocity spread and an increase in its efficiency and frequency bandwidth. The helical gyro-TWT is realized for the first time experimentally. In the regime of single-frequency amplification, the gyro-TWT operating at the second cyclotron harmonic with a 200 keV/25 A electron beam having a large axial velocity spread of 30% and moving in a relatively weak magnetic field of 2.2 kG yields in X-band the high output power of 1 MW, gain of 23 dB and efficiency of 20%.

INTRODUCTION

Gyro-TWT [1] is a known amplifier variety of a broad class of gyrodevices which operation is based on the stimulated cyclotron radiation of electrons moving along the helical trajectories in a homogeneous magnetostatic field $\vec{H}_0 = H_0 \vec{z}_0$. In the interaction region of a gyrodevice the cyclotron resonance between an operating electromagnetic wave and electrons occurs:

$$\omega - h v_{\parallel} \approx s \omega_H. \tag{1}$$

Here ω and h are the frequency and the axial wavenumber of the wave, $v_{\parallel}$ and $\omega_H = eH_0/mc\gamma$ are the axial velocity and the cyclotron frequency of the electrons, s is the cyclotron harmonic number. According to Eq.(1) a gyro-TWT has an important peculiarity, namely, the possibility of the resonant amplification of fast electromagnetic waves.

As a rule, a smooth cylindrical metal waveguide is used as a microwave system of a gyro-TWT. In order to increase the frequency bandwidth, one usually uses an operation regime of grazing incidence of the wave and beam dispersion characteristics when the axial electron velocity is close to the group velocity of the wave (Fig.1a). Correspondingly, gyro-TWTs with weakly relativistic electron beams operate at frequencies near cutoff which limits their frequency band and reduces their stability to gyrotron oscillation (see e.g.[2]). At the same time, gyro-TWTs driven by electron beams with relativistic particle axial velocity may have a

much broader frequency band, but due to operation with relatively high Doppler upshift (CARM-TWT regime), they are very sensitive to particle velocity spread (see e.g.[3]).

Thus, the spread in axial velocity and the unfavorable dispersion of a cylindrical waveguide significantly limit possibilities of the gyro-TWT. The most favorable wave dispersion for a gyro-TWT is that when the wave group velocity is constant and equal to the electron axial velocity in the region of close-to-zero axial wavenumber (Fig.1b). As shown in [4], a similar dispersion can be realized in an oversized circular waveguide with a special helical corrugation of its inner surface.

SOME THEORETICAL RESULTS FOR GYRO-TWT WITH A HELICALLY GROOVED CIRCULAR CYLINDRICAL WAVEGUIDE

The desired change of the dispersion has been achieved when the corrugation $r(\varphi,z) = r_0 + l\cos(\overline{m}\varphi + \overline{h}z)$ couples the two partial rotating waves of an oversized smooth waveguide with a radius of r_0: a near-cutoff mode (A) with a small axial wavenumber, $h_A \ll k$, where $k = \omega/c$, and a traveling wave (B) with a large axial wavenumber, $h_B \sim k$, providing their mutual resonant scattering. For this, axial wavenumbers and azimuthal indexes of the waves and the corrugation should satisfy the Bragg conditions

$$h_B \approx \overline{h}, \quad m_A - m_B = \overline{m} \qquad (1)$$

Here $\overline{m}$ and $\overline{h} = 2\pi/d$ are azimuthal and axial numbers of the corrugation, d is the corrugation period. The resonant coupling of the waves corresponds to the intersection of their dispersion curves or, more exactly for the considering situation, the intersection occurs between the mode A and the first spatial harmonic of the wave B (Fig.2). If the corrugation amplitude l is small compared with the wavelength, the field structure and dispersion characteristics of a helical waveguide can be calculated by means of the method of perturbation [5]. Then we find eigenwaves W_- and W_1 (Fig.2), which arise as a result of coupling the partial waves A and B. When parameters of the corrugation are properly chosen, the wave W_1 has the desirable dispersion. The frequency gap between W_1 and "spurious" waves $W_\pm$ in the region of "zero" axial wavenumbers is of the order of the coupling coefficient of the waves, σ, which is proportional to the relative amplitude of corrugation l/r_0 and depends also on the azimuthal and radial indexes of the partial waves. For a relatively small corrugation depth, when $\sigma \leq 0.1$, the method of perturbation provides a good agreement with "cold" experiments.

A stationary theory of a gyro-TWT with the helical waveguide reflecting its main principal properties [6] represents usual self-consistent gyrotron equations [7] combined with the coupled mode equations describing mutual scattering of partial modes A and B on the corrugation. For conditions of the cyclotron resonance (1) one can neglect the influence of mode B the electron motion. The axial structure of mode A obeys a second-order wave equation with a right-hand site including a high-frequency current term as well as a term responsible for scattering of mode B into mode A. A first-order equation for mode B describes its "cold" coupling with partial mode A. The numerical analysis confirms attractive features arising with the use of the helical waveguides for gyro-TWTs and demonstrates important advantages of the "helical" gyro-TWTs over the "smooth" ones in sensitivity to electron velocity spread, frequency bandwidth and stability to parasitic self-excitation [6] (Fig.3).

EXPERIMENT

At present we are carrying out three different experiments on the spiral gyro-TWTs with a weakly (80 keV) and moderately (200 keV and 300 keV) relativistic electron beams. Here we are reporting the first results on a 200 keV X-band amplifier. All the experiment have important common peculiarities. In order to significantly enhance mode selection, a thin beam of electrons gyrating around the axis of the system is used to drive the gyro-TWT. Such a beam can excite only corotating modes of a circular waveguide with the azimuthal index m equal to the cyclotron harmonic number s. In particular, we use the second-harmonic operation and the $TE_{2,1}$ mode as a near-cutoff partial mode A. The rotating $TE_{2,1}$ mode couples with the counter-rotating and forward-propagating $TE_{1,1}$ mode (partial mode B in Fig.1) on the corresponding 3-fold helical corrugation. For frequencies below cutoff of $TE_{2,1}$ mode the operating eigenwave W_1 totally transforms at end sections with increasing/decreasing amplitude of the corrugation into $TE_{1,1}$ mode of the smooth waveguide which simplifies input/output of RF power.

A 200 keV/25 A rectilinear electron beam with the diameter of 8 mm and flat-top duration of 50-100 ns was produced from a "cold" velvet cathode (Fig.4). A transverse velocity $\beta_1 = 0 \div 0.6$ was imparted to the electrons in a dc single-period bifilar spiral kicker. The electron velocities and their spreads were estimated experimentally investigating the tracks of the beam on a scintillator placed at different distances from the kicker. For the operating transverse velocity $\beta_\perp = 0.5 - 0.6$ a large spread in axial velocity exceeding 30% was measured.

Two magnetrons operating at fixed frequencies of 9.1 GHz and 9.4 GHz were used as sources of RF input signal for the amplifier. After a waveguide transmission line and a wave launcher maximum input power in the operating circular polarized wave amounted to 5-6 kW. The electron-wave interaction length was varied by changing position of a dc deflecting magnet (Fig.4) at fixed length (40 cm) of the helical waveguide. At present stage of the experiment the regime of saturated amplification was not achieved because the parasitic self-oscillation limited the electron transverse velocity (up to $\beta_\perp \approx 0.5$) and the interaction length. It had been proven that the amplifier oscillated at the operating mode at frequencies close to the operating ones because of not perfect matching of the microwave system.

In the regime of stable amplification for both operating frequencies of the magnetrons, 9.1 and 9.4 GHz, and fixed other parameters of the system the same output power of 1 MW and corresponding efficiency of 20% were measured. The maximum gain amounted to 23 dB. At the next stage of the experiment we intend to improve the matching of the microwave system and achieve saturated amplification with higher gain, power and efficiency.

[1] A.V. Gaponov, Izv. VUZov. Radiofizika. 2, 443 (1959).

[2] Q.S. Wang, D.B. McDermott, N.C. Luhmann. IEEE Trans.Plasma Sci. 24, 700 (1996).

[3] W.L. Menninger, B.G. Danly, R.J. Temkin. IEEE Trans. Plasma Sci. 24, 687 (1996).

[4] G.G. Denisov, S.J. Cooke. Digest 21st Int. Conf. Infrared Millimeter Waves, Berlin, Germany, July 1996, M. von Ortenberg and H.-U. Mueller, Eds., p.AT2.

[5] N.F. Kovalev, I.M. Orlova, M.I. Petelin. Izv. VUZov. Radiofizika. 11, 783 (1968).

[6] G.G. Denisov, V.L. Bratman, A.D.R. Phelps, and S.V. Samsonov. IEEE Trans. on Plasma Sci. 26, (to be published June 1998).

[7] V. L. Bratman, M. A. Moiseev, M. I. Petelin, and R. E. Erm, Izv. VUZov. Radiofizika, 16, 622 (1973).
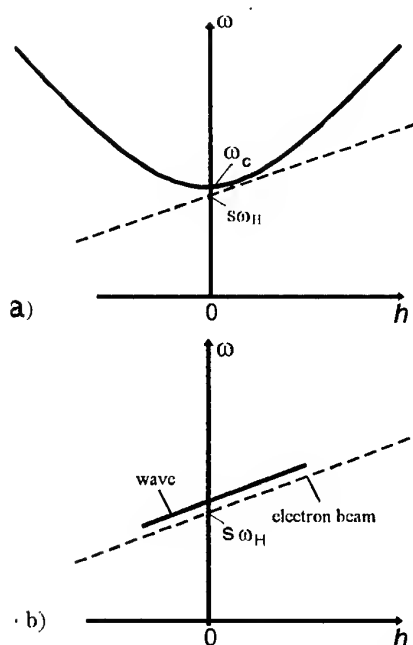
Fig.1. Usual (a) and desirable (b) dispersion of the waves for a gyro-TWT.
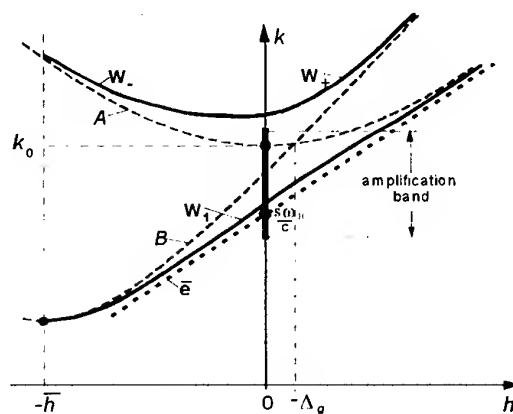
Fig.2. Dispersion diagram for a helical waveguide: A, B are the partial near-cutoff and traveling waves of a smooth waveguide, respectively, which are coupled due to helical corrugation of the inner surface, W_1 and $W_\perp$ are the operating and "spurious" eigenwaves of the helical gyro-TWT. $\bar{e}$ is an unperturbed electron cyclotron wave.
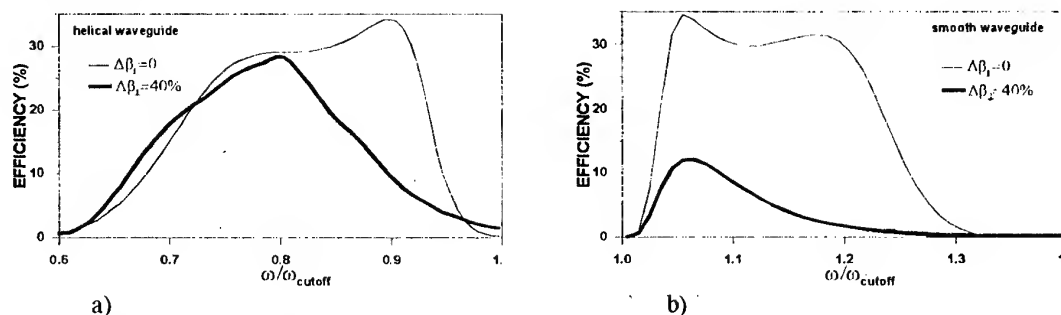
Fig.3. Results of simulations demonstrating advantages of a gyro-TWT with helical waveguide (a) over that with smooth waveguide (b) in sensitivity to electron velocity spread. Simulations made for a design of a second harmonic gyro-TWT driven by a 300 keV/80 A electron beam with velocity ratio $v_\perp/v_\parallel = 1.2$.
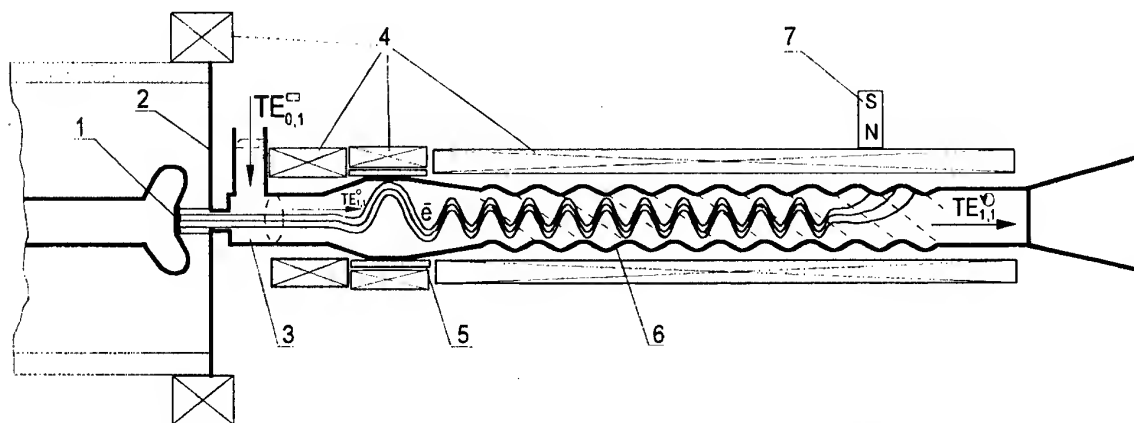
Fig.4. Schematic diagram of the gyro-TWT with a helical waveguide: 1 - velvet cold cathode; 2 - anode; 3 - wave launcher (converter of $TE_{0,1}$ mode of a rectangular waveguide into $TE_{1,1}$ mode of a circular waveguide); 4 - coils generating dc guiding magnetic field; 5 - kicker; 6 - operating helical waveguide; 7 - deflecting magnet.

NEW CATHODES FOR A RELATIVISTIC MAGNETRON

Y. M. Saveliev, S. N. Spark[*], B. A. Kerr[*], M. I. Harbour[*], S. C. Douglas[*] and W. Sibbett

University of St Andrews, School of Physics and Astronomy, North Haugh, St. Andrews, Fife, KY16 9SS, UK
[*]DERA, St. Andrews Road, Great Malvern, Worcs, WR14 3PS, UK

INTRODUCTION

Pulse shortening and the lower efficiency of relativistic magnetrons (RM) as compared to conventional magnetrons is a complex issue because of the range of physical mechanisms involved. In a given system, a particular set of mechanisms may be dominant. However, the expansion of plasma from explosive emission cathodes into an interaction space is the major factor that affects operation of every high power relativistic magnetron.

The straightforward way to reduce the plasma expansion rate is to increase the cathode plasma ion mass and this may be achieved by eliminating water vapour and organic deposits from the cathode surface [1,2]. This implies the necessity to handle the overall vacuum system in a way similar to that employed in sealed-tube manufacturing procedures. The latter is also an issue if special cathode materials, like CsI [2], are considered as high-current electron suppliers. These approaches lead inevitably to increased costs of the RMs and, most importantly, to a reduced flexibility in the overall system.

We believe that a viable alternative is to develop "smart" cathodes that are capable of controlling the plasma behaviour and, as a consequence, the operational characteristics of relativistic magnetrons.

EXPERIMENT

In this paper, we present experimental results obtained with several different cathodes tested in a high power RM system developed by Physics International [3]. This tuneable magnetron is of a rising-sun type and operates at frequencies in the
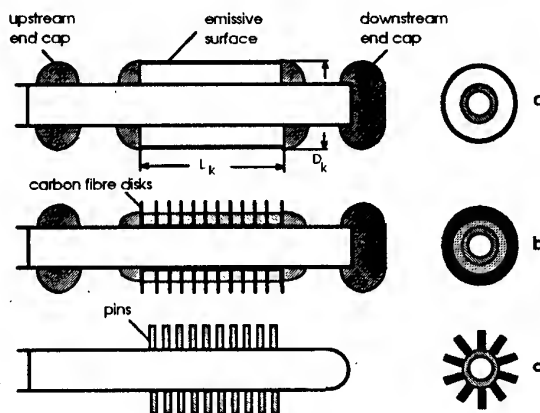
Fig.1   Relativistic magnetron cathodes.
a- "smooth" (velvet, carbon fabric and perforated stainless steel) cathodes;
b- disk cathode; c- pin cathode. All versions were tested with and without end caps.

1.1-1.3GHz range for a diode voltage U≤500kV and a total microwave power of P<1GW being extracted from the two separate arms.

The tested cathodes were (i) velvet cathode with an outer perforated stainless steel cylinder (2mm hole diameter, 47% open area) covering the velvet surface, see Fig.1a, (ii) carbon fabric cathode of the same geometry (Fig.1a), (iii) carbon fibre disk cathode (Fig.1b), and (iv) stainless steel multipin cathode (Fig.1c) of a design

similar to that reported in [4]. The first two cathodes are of "smooth" geometry and, taking into account good explosive emission characteristics of velvet and carbon fibres, thus ensure a uniform electron emission over all of the cathode surface. The disk cathode is somewhat intermediate between smooth and pin cathodes from a geometrical point of view. The emissive surface length L_k=110mm and diameter D_k=74mm were kept identical for all of the cathodes tested for comparison purposes despite the fact that the above value of D_k being optimal for one cathode was not necessarily optimal for the others. The provision was made to test all the cathodes with (Fig.1a,b) or without (Fig.1c) upstream and downstream end caps. The experiments were conducted at a moderate residual gas pressure of $\sim 10^{-5}$Torr and no special cathode conditioning was undertaken.

EXPERIMENTAL RESULTS

The cathodes with fitted end cap electrodes allow the relativistic magnetron to generate significantly more power in comparison to the use of cathodes without end caps. This is applicable to both smooth (Fig.2a) and pin cathodes (Fig.2b). The dependencies of the total microwave power P_μ on magnetic field B (Fig.2) are essentially the same at low B close to the Hull cut-off value, B_H. But at larger B values, the difference between the curves becomes appreciable. The maximum value of magnetic field above which the magnetron does not operate (experimental Buneman-Hartree threshold) shifts toward larger values of B when the cathode with end caps is employed. Accordingly, the magnetic field value B^* at which the microwave power reaches maximum also increases (Fig.3). The above features, which are inherent for both smooth and pin cathodes, find an explanation in the fact that the downstream current I_d is effectively suppressed by the end caps; see Fig.2c. As this current constitutes a
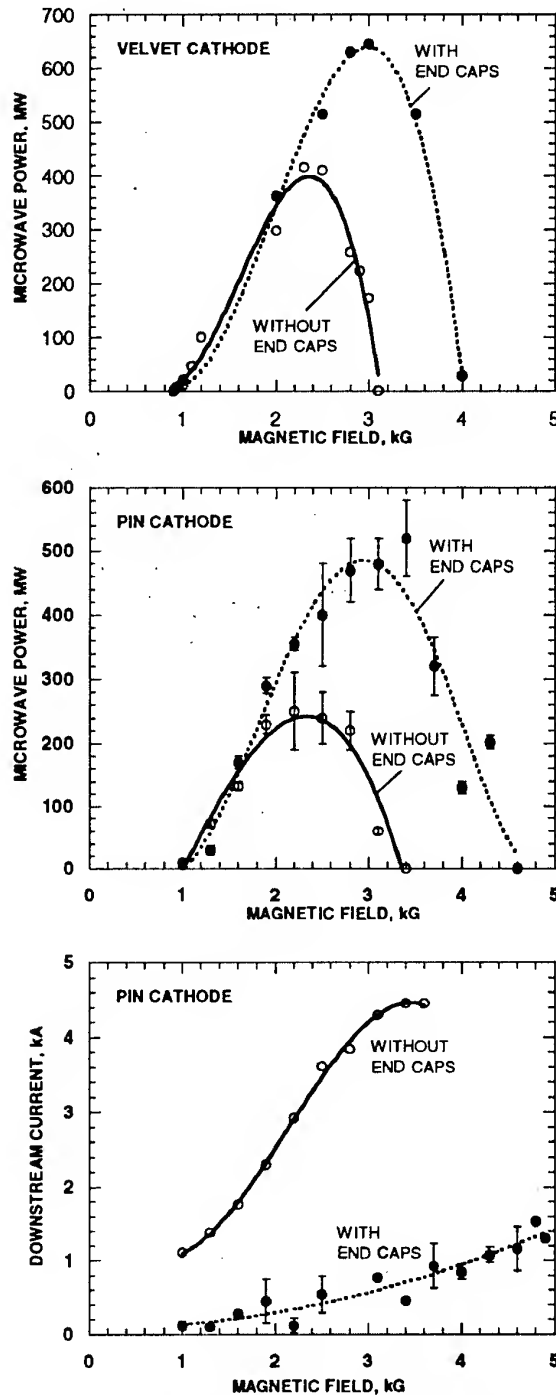
Fig.2 Plots of the microwave power (a,b) and the downstream electron current (c) vs the applied axial magnetic field. The curves were obtained when the cathodes with (dotted lines) and without (solid lines) end caps were employed.

significant fraction of the total diode current, it leads to an increase of the magnetron impedance, at least, at magnetic fields sufficiently larger than B_H.

-862-
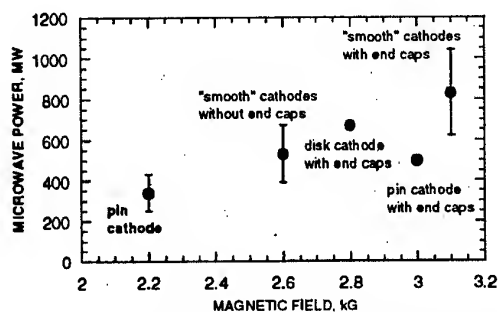
Fig.3 Peak output microwave power as a function of relevant magnetic field values for all cathodes tested.

Consequently, the diode voltage V_d also increases, provided the charging voltage of the pulsed power supply with 50Ω internal impedance is kept constant, and this increased effective diode voltage accounts for the larger microwave power generated by the magnetron. (The microwave power exhibits an approximately cubic dependence on the diode voltage [5]). This also leads to the shift towards higher B_{BH} because $B_{BH} \sim V_d$.
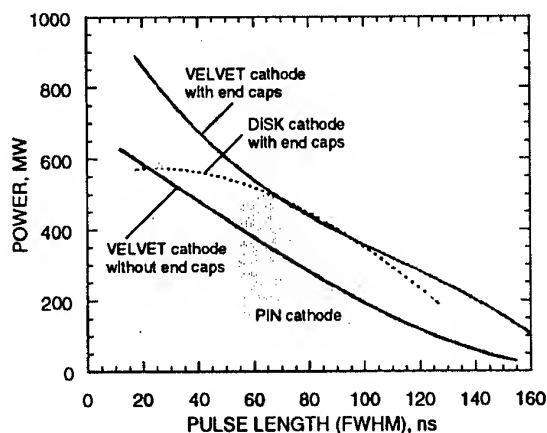
Fig.4 Microwave power vs pulse length. The curves are obtained by varying magnetic field at the constant charging voltage of the pulsed power supply.

At a low magnetic field and, accordingly, at a low microwave power, the microwave pulse duration $\tau_\mu \approx 150$ns and diminishes to ~20-30ns at $B \approx B^*$ where P_μ reaches its maximum. Significantly, τ_μ does not depend on whether the end caps are fitted to the cathode. Therefore, creation of the unwanted explosive emission plasma spots
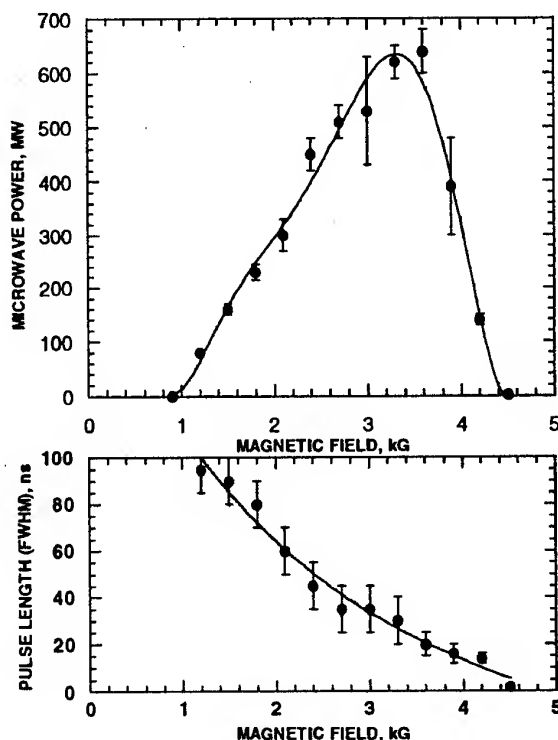
Fig.5 Plots of the microwave power (above) and FWHM pulse length (below) vs magnetic field obtained with the perforated stainless steel cathode.

on the electrode surfaces, if any, does not facilitate the pulse shortening.

By comparing the operation of the RM with pin and smooth cathodes, we can conclude that the latter allow generation of larger microwave power in the region of short τ_μ and longer τ_μ ($\geq 50\%$) at lower P_μ (Fig.4). In the intermediate region of P_μ and τ_μ (~300-400MW, 60-90ns), the magnetron characteristics obtained with smooth and pin cathodes are similar to each other. Remarkably, the $P_\mu(\tau_\mu)$ dependence obtained with the disk cathode represents features that are specific for both types of cathodes. This leads to a conclusion that the geometry of the cathode emission surface is an essential factor which determines the RM output power and, most importantly, the microwave pulse length.

Amongst all cathodes tested, the velvet cathode represents the most favourable option. After ~10^3 shots it still

operated satisfactorily despite an appreciable degree of deterioration of velvet fibres. (We believe that such a relatively long lifetime is the result of the incorporation of the perforated stainless steel cylinder covering the velvet surface into the cathode design). Nevertheless, the lifetime of ~10^3 shots would not be acceptable in practical applications where long periods between cathode replacements are required. We therefore tested a version of the cathode consisting of the perforated cylinder only. This cathode still has a large number of points with enhanced electric field (edges of the cylinder perforations) that are uniformly distributed along the cathode surface thus providing a more uniform plasma distribution than that associated with a plain metal cathode. This cathode exhibited slightly lower P_μ and τ_μ than the original velvet type (Fig.5), but the longer lifetime that is expected makes the perforated metal cathode a satisfactory alternative.

CONCLUSIONS

The cathode end caps were mostly abandoned after transition from conventional low voltage to relativistic magnetrons (with rare exceptions, for example, [6]). We have shown that the introduction of the end caps to the cathode intended for use in the relativistic magnetrons allow an increase of the overall (if not electronic) efficiency of the relativistic magnetron without compromising the pulse shortening.

The experimental results obtained with various cathode emissive surface geometries showed that such design features affect not only the microwave output power but also the pulse length. The more uniform cathode plasma production facilitates increase of the microwave pulse length.

REFERENCES

[1] J. Benford and G. Benford, IEEE Trans. on Plasma Sci., **25**, 311 (1997).
[2] D. Price and J. S. Levine, in *Digest of Int. Workshop on HPM generation and Pulse Shortening* (June 10-12 1997, Edinburgh, UK), p.127 (1997).
[3] J. S. Levine, B. D. Harteneck and H. D. Price, in *Intense Microwave Pulses III*, Proc. SPIE 2557, p.74 (1995).
[4] R. R. Smith, J. Benford, B. Harteneck and H. M. Sze, IEEE Trans. on Plasma Sci., **19**, 628 (1991).
[5] H-W. Chan, C. Chen and R. C. Davidson, J. Appl. Phys., **73**, 7053 (1993).
[6] T. A. Treado, R. A. Bolton, T. A. Hansen et al., IEEE Trans. on Plasma Sci., **20**, 351 (1992).

CYCLOTRON AUTORESONANCE MASER
IN THE REGIME OF TRAPPING
AND ADIABATIC DECELERATION OF ELECTRONS

V.L.Bratman[1], A.W.Cross[2], Yu.K.Kalynov[1],
A.D.R.Phelps[2], S.V.Samsonov[1], and A.V.Savilov[1]

[1] *Institute of Applied Physics, Russian Academy of Sciences*
46 Ulyanov St., Nizhny Novgorod, 603600, Russian Federation

[2] *University of Strathclyde, Dept. of Physics and Applied Physics*
John Anderson Building, 107 Rottenrow, Glasgow G4 0NG, Scotland, UK

ABSTRACT

A sectioned oscillator (twystron with the self-exciting input section) is studied as a method for realization of the regime of trapping and adiabatic deceleration of electrons in CARMs. It is shown that the achievement of almost total trapping of electron beam and, therefore, of a high electron efficiency, is possible when the first section is a Bragg cavity with the distributed feedback. Experimental realization of the CARM-twystron in the regime of trapping at the fundamental cyclotron harmonic with the wavelength of 8 mm, the electron beam current and voltage of 100 A and 500 kV respectively, and the estimated output RF power of 20 MW ith the efficiency of 40-50%, is being in the process.

INTRODUCTION

A natural method for efficiency enhancement of Free-Electron Lasers (FELs) is providing some mechanism of prolonged synchronism between electrons and the RF wave during the process of electron-wave energy exchange. For various types of FELs (in particular, for CARMs), one such mechanism is the well-known regime of trapping of electrons by the potential well formed by the RF wave, and of adiabatic deceleration of the trapped particles by smoothly profiling the parameters of the system (a similar regime was first proposed for TWTs [1]) [2-6]. According to the theory [1-6], this regime can provide a considerable increase in efficiency and a decrease in the sensitivity to spread in electron velocity, as compared with the "traditional" regime of compact electron bunching [7]. One should stress that just the realization of the regime of trapping allowed the achievement of a high electron efficiency for the first time in a FEL-amplifier experiment [8]. However, in auto-oscillators the realization of this regime is more complicated due to several reasons. Evidently, the main ones are difficulties in providing single-frequency operation, and in the excitation of the long, profiled system, especially for a relatively short electron pulse. In order to avoid these difficulties, one can develop the idea of sectioning (see e.g. [9]) and consider a FEL-oscillator of the twystron type with the microwave system consisting of the first, self-exciting section, being a relatively short cavity, and the second prolonged section, where trapping is provided [10].

SIMPLEST MODEL

In the simplest model of a sectioned FEL-oscillator [10] (Fig.1), the first, self-exciting, section is a relatively short segment of a waveguide with RF feedback, which is provided by very short reflectors at the input and output of this section, with the reflection coefficients

100% and R respectively. The RF field passes through the output reflector and comes into the second section, which consists of a long waveguide without RF feedback.

If electrons are close to the resonance with the RF-wave, then the main part of them is trapped by the potential well, which is formed by the RF field. On the phase plane with axes of electron energy and electron phase with respect to the wave, the trapped particles perform synchrotron oscillations inside the bucket with energy center, $\mathcal{E}_r$, corresponding to the exact cyclotron resonance of electrons with the wave (Fig.2 a). The first section is excited due to the "traditional" mechanism of compact electron bunching during the electron-wave interaction over a length of the order of the half-period of the electron synchrotron oscillation. The second section represents an amplifier. The input signals for this amplifier are both the RF wave, having passed through the output reflector of the first section, and perturbations in the electron density due to electron bunching inside the first section. In the second section, the resonant energy, $\mathcal{E}_r(z)$, decreases with the longitudinal coordinate (Fig.1) due to profiling the parameters of the system (for instance, profiling the guiding magnetic field in the CARM, or the undulator field in the ubitron). Energies of the trapped particles decrease with the decrease of $\mathcal{E}_r(z)$, energies of the other particles practically do not vary. For this regime, the electron efficiency of the CARM is limited by the trapping coefficient, K, being the share of particles which are trapped in the second section (Fig.2b):

$$\eta = K\eta_{s.p.} ,$$

where

$$\eta_{s.p.} = \frac{\beta_\perp^2}{2(1 - \beta_\| / \beta_{ph})(1 - \gamma_0^{-1})} ,$$

is the so-called single-particle electron efficiency [11], being the maximal possible share of the energy which is radiated in the CARM by a single particle when it loses all its transverse momentum. Here $\beta_{\perp,\|} = v_{\perp,\|} / c$ and $\beta_{ph} = v_{ph} / c$ are the initial transverse and longitudinal electron velocities and the RF wave phase velocity normalized by the speed of light, $\gamma_0 = \mathcal{E}_0 / mc^2$.

Fig.1. Schematic of the sectioned auto-oscillator with a self-exciting input section and a profiled output section.

Fig. 2. Distribution of electrons over the phase plane at the output of the first (a) and the second (b) sections.

According to calculations [10], for smooth profiling the trapping coefficient is defined basically by the parameters of the self-exciting section; namely, by the reflection coefficient at the output of the first section. If the power reflection coefficient is small enough, $R = 0.1 - 0.3$, then almost total trapping, $K = 0.9 - 0.95$, can be achieved in a very wide region of parameter

space. The increase of R leads to a significant decrease of the trapping coefficient because in this case the system contains a non-adiabatic factor. This is a fast change of the complex RF amplitude in the region of the transition from the first section into the second one, because in this region the strong reflection of the RF wave by the output reflector takes place. On the phase plane, this leads to a significant phase shift between the buckets corresponding to the output of the first section and the input of the second section (Fig. 2 a). As a result, a lot of electrons leave the bucket.

SELF-EXCITING SECTION WITH DISTRIBUTED FEEDBACK

This difficulty can be avoided by using a prolonged output reflector: the self-exciting section can be a cavity with the distributed feedback provided by two reflectors: a short input reflector, and a Bragg reflector with a length approximately equal to the total length of the section (Fig. 3). In this case, due to a smoother distribution of the RF field within the region of the transition, the shift in the phase of the bucket centers is not so fast as in the case of the short output reflector. This should provide more accurate trapping of electrons at the beginning of the second section.
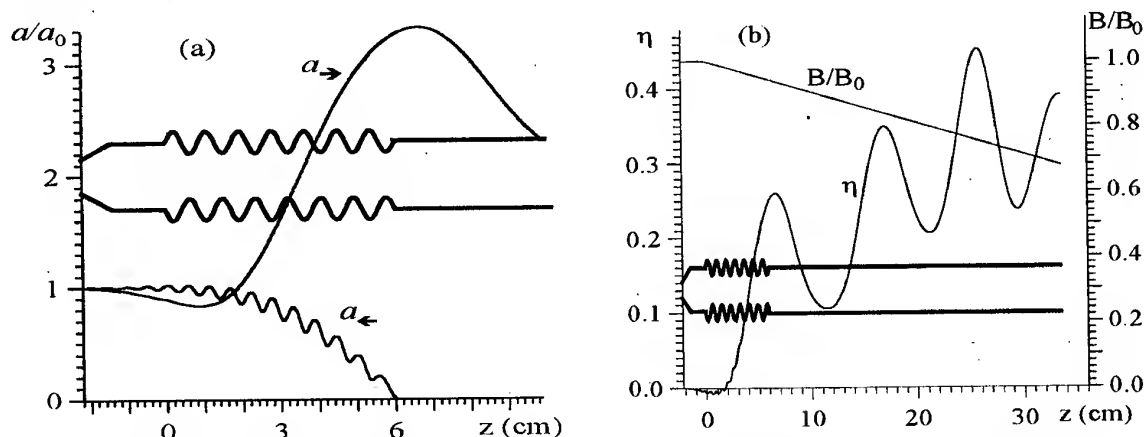
Fig. 3. Design and calculations for the CARM at the fundamental cyclotron resonance.
a - Longitudinal structures of the forward and backward waves
of the "hot" eigenmode inside the self-exciting section.
b - Electron efficiency and guiding magnetic field versus the longitudinal coordinate.
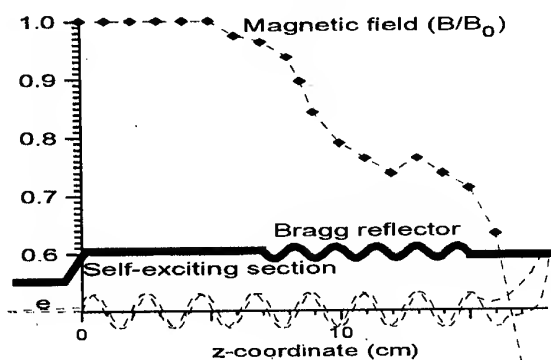
Fig. 4. Schematic of the preliminary experiment

The proposed scheme can be effectively used for various FELs, including ubitrons, CARMs and Cherenkov devices. As for the CARM, our goal is a significant enhancement of their efficiency in the experiments at the fundamental [12] and the second [13] cyclotron harmonics. As calculations show (Fig. 3), at the both harmonics a high electron efficiency (about of 40 - 50 %) can be achieved.

Advantages of the supposed scheme of the CARM were confirmed by a preliminary experiment under the realization of the CARM-twystron in the regime of trapping (the fundamental cyclotron harmonic, 8 mm wavelength, 100 A / 500 kV electron beam). The main disadvantage of this experiment were a quite bad quality of the electron beam (a large velocity

spread), as well as a non-ideal tapering of the magnetic field (Fig.4). However, even for a bad electron beam, the experiment demonstrated the possibility of a significant increase of the output power due to the use of the regime of trapping: the power of 5.2 MW (in stead of 3.6 MW obtained in this experiment for the traditional scheme of the oscillator) was achieved.

CONCLUSION

The scheme of the sectioned oscillator (twystron with self-exciting input section) is very attractive from the point of view of realization of the regime of trapping and adiabatic deceleration of particles in FELs (in particular, CARMs). It is shown that the achievement of almost total trapping of the electron beam and, therefore, of a high electron efficiency, is possible in such devices. If the self-exciting section is a waveguide, terminated by RF reflectors, then trapping is effective at relatively low Q for this section. The case, when the first section is a cavity with distributed feedback, proves to be more attractive. Due to a smoother distribution of the RF field within the region of the transition from the first section into the second one, trapping of electrons is more complete. Thus, in this case, effective trapping can be achieved at both low and high Q of the first section. It is demonstrated that the considered scheme can provide a high electron efficiency CARMs operating at both the fundamental and second cyclotron harmonics.

REFERENCES

|1| E.D.Belyavsky, Radiotekhnika i Electronika16 (1971) 208.
|2| N.M.Kroll, P.L.Morton, M.N.Rosenbluth, Phys. Quant. Electron. 7 (1980) 113.
|3| P.Sprangle, C.-M.Tang, W.N.Manheimer, Phys. Rev. Lett. A. 21 (1980) 302.
|4| N.S.Ginzburg, I.A.Man'kin, V.E.Polyak et al., Relativistic HF Electronics 5 (1988, Inst. of Appl. Phys., N.Novgorod, Russia) 37.
|5| V.L.Bratman, N.S.Ginzburg, A.V.Savilov, Relativistic HF Electronics 7 (1992, Institute of Appl. Phys., N.Novgorod, Russia) 22.
|6| G.S.Nusinovich, Phys. Fluids B 4 (1992) 1989.
|7| V.L.Bratman, N.S.Ginzburg, M.I.Petelin, Opt. Commun. 30 (1979) 409.
|8| T.Orzechowski, B.Anderson, J.Clark et al., Phys. Rev. Lett. 57 (1986) 2172.
|9| E.B.Abubakirov, A.V.Smorgonsky, Radiotekhnika i Electronika 35 (1990) 2644.
|10| A.V.Savilov, IEEE Trans. on Plasma Sci. 26 (1998) 36.
|11| V.L.Bratman, N.S.Ginzburg, G.S.Nusinovich, M.I.Petelin and P.S.Strelkov, Int. J. of Electronics 51 (1981) 541.
|12| V.L.Bratman, G.G.Denisov, B.D.Kol'chugin, S.V.Samsonov and A.B.Volkov, Phys. Rev. Lett. 75 (1995) 3102.
|13| S.J.Cooke, A.W.Cross, W.He and A.D.R.Phelps, Phys. Rev. Lett. 77 (1996) 4836.

RECENT RESULTS FROM A LONG PULSE, RELATIVISTIC VACUUM AND PLASMA-FILLED BACKWARD WAVE OSCILLATOR EXPERIMENT

E. Schamiloglu, F. Hegeler, C. Grabowski,* and D. Borovina
Department of Electrical and Computer Engineering, University of New Mexico,
Albuquerque, NM 87131, USA

ABSTRACT

The University of New Mexico (UNM) long pulse backward wave oscillator (BWO) experiment has been investigating three issues: i) the observation of axial mode switching during the course of microwave generation in vacuum, ii) the use of laser interferometry to correlate the evolution of wall plasma with pulse shortening during operation in vacuum, and iii) the effects of a controlled plasma prefill from a cathode-mounted plasma source on BWO output characteristics. Results-to-date from our investigations indicate that a cross-excitation instability is observed under certain operating conditions during vacuum operation. This instability depends on three parameters: i) the normalized slow wave structure length, ii) the ratio of electron beam current to start-oscillation current, and iii) the reflection coefficient at the downstream end of the electrodynamic system. Furthermore, a HeNe laser interferometer indicates that plasma appears in two phases during the course of vacuum operation. The initial low density phase I plasma is attributed to beam scrape-off from the cutoff neck region at the input to the electrodynamic system. A significantly higher phase II plasma is measured after the occurrence of pulse shortening, and the magnitude of this plasma is correlated with the radiated microwave power level. We believe this plasma is attributed to a catastrophic discharge occurring during very high power excitation. Finally, the intentional prefill of the slow wave structure with a preionized plasma emanating from the cathode is found to both enhance microwave generation efficiency, and quench the radiated power, depending on the density of the plasma prefill.

UNM LONG PULSE BWO CONFIGURATION

The basic experimental apparatus has been described previously [1, 2], and thus, is only briefly summarized here. A cross-sectional diagram of the BWO is shown in Fig. 1. A modified Physics International Pulserad 110A with a maximum storage capacity of 2.75 kJ is connected to a parallel L-C network and provides a voltage pulse of up to 500 kV with a FWHM pulse duration of 350 ns. An electron beam is emitted from an annular knife-edge graphite cathode, and is guided by a magnetic field of 2 T through the SWS into the beam dump. The generated microwaves are extracted from a conical horn antenna, 12.7 cm in diameter, covered with a 0.25 mm thick Mylar window to maintain
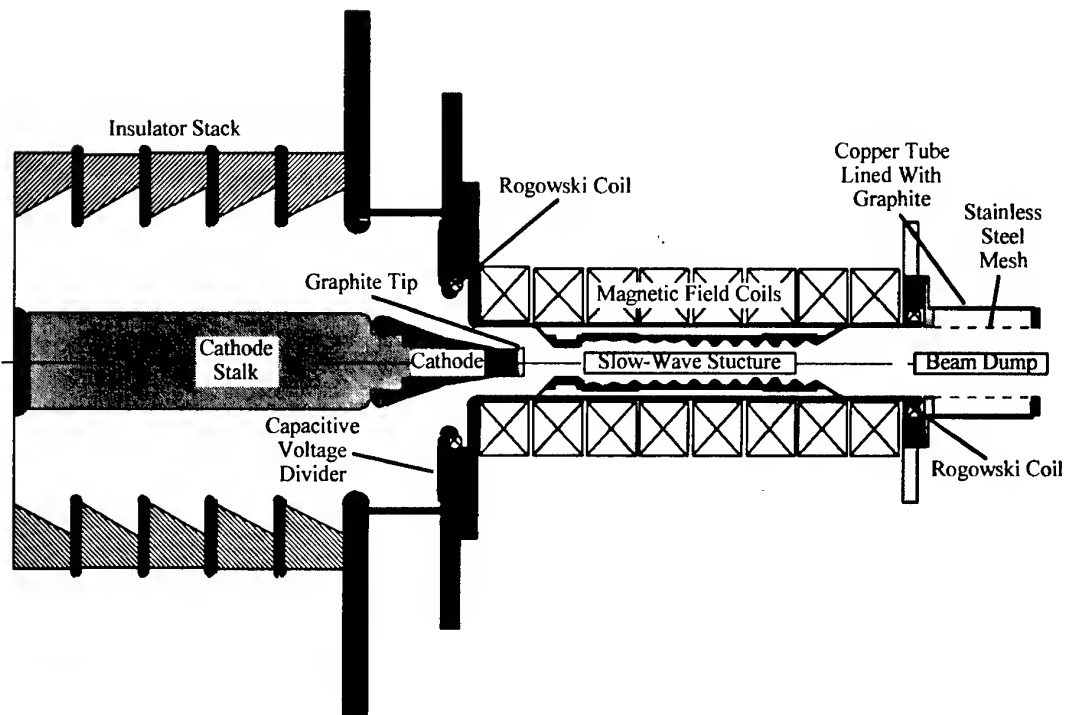
Figure 1. Cross-sectional diagram of the BWO.

the vacuum-to-air interface. The base pressure in the SWS region is on the order of $7 \cdot 10^{-5}$ Torr (10^{-2} Pa).

CROSS-EXCITATION INSTABILITY

Levush, *et al.* [3] presented results from nonlinear numerical simulations that show various aspects of BWO operation. The value of the resonance wave number determines whether the BWO operates in a steady, single frequency regime or in a multi-frequency regime characterized by instabilities that result from over-bunching of the electron beam. Furthermore, an additional regime exists where the start current and gain of one mode is modified by the presence of another saturated mode, enabling it to compete with the first. This regime is referred to by Levush and his colleagues as the "cross-excitation" instability regime. If the amplitudes of the two modes are approximately the same, the total power output and efficiency of the BWO are essentially unchanged, but no single-frequency equilibrium is achieved. If the second mode has a considerably larger amplitude, the first mode will be suppressed and a noticeable jump in efficiency, power output, and now frequency will occur as the second mode reaches saturation.

This cross-excitation instability or axial mode switching has been observed experimentally with the UNM long pulse BWO, and is presented in Fig. 2. As shown in the plot, the radiated power initially rises to 22 MW at an output frequency of 9.1 GHz. Approximately 5 ns after the peak power is reached, the power rapidly decreases as the second axial mode in the SWS begins to grow. This second mode results in considerably more efficient beam-to-microwave energy conversion, as the power quickly rises above 70 MW, eventually reaching a peak of 92 MW. The frequency also increases by several 100 MHz to about 9.4 - 9.5 GHz. The BWO runs in the single frequency regime when operated at a slightly lower or higher diode voltage.
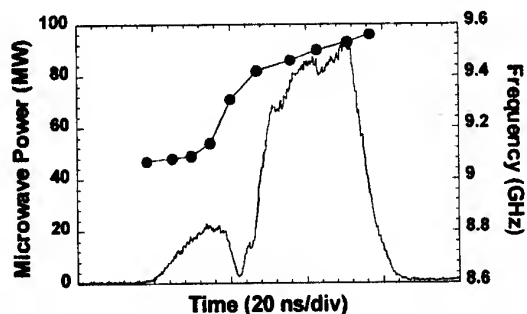
Fig. 2. Microwave power waveform and frequency measurements illustrating the "cross-excitation" instability. Diode voltage: 460 kV, average beam current: 1.5 kA, and B = 2 T.

LASER INTERFEROMETRY MEASUREMENTS

Although pulse shortening is observed across a wide class of high power microwave devices, its origin is not definitively understood. Many hypotheses suggest that the unintentional introduction of plasma into the interaction region near the walls of the SWS is one of several likely causes of pulse shortening in intense electron beam-driven devices. Here, laser interferometry is used for the first time to measure the line-integrated, temporally resolved plasma density between an intense, relativistic, annular electron beam and slow wave structure (SWS) walls for a variety of radiated microwave peak power levels.

In general, two phases of the line-integrated electron density have been measured using the interferometer. The initial or first phase is characterized by a linear increase in plasma density and can only be detected on a very sensitive scale. This plasma is first observed at a time corresponding to the onset of the electron beam current in the SWS, as shown in Fig. 3. The linear rise in line-integrated electron density continues until about 200 ns after the onset of electron beam current, at which point the second phase in the measurement begins, as indicated in Fig. 4. Note that this measurement is presented on a less sensitive amplitude scale, and a much

longer time scale than the measurement shown in Fig. 3. (The features in Fig. 3 are barely visible as the rising portion of the signal in Fig. 4.) At approximately $t = 200\,ns$, $<n_e L>$ increases dramatically until it reaches its maximum at about $t = 400\,ns$, as shown in Fig. 4. This enormous increase in plasma is measured after the termination of the microwave pulse. However, this can be attributed to plasma originating along the SWS wall and diffusing radially inward across the magnetic field lines into the path of the laser beam.
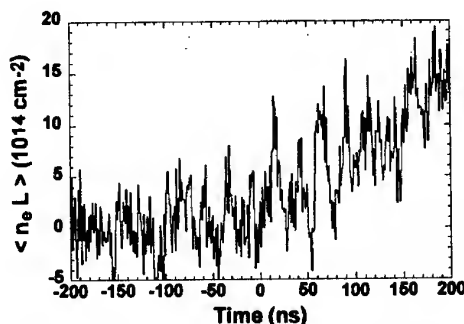
Fig. 3. Typical result of the early phase of the line-integrated plasma density (phase I plasma), with $t = 0$ corresponding to the start of the microwave signal.
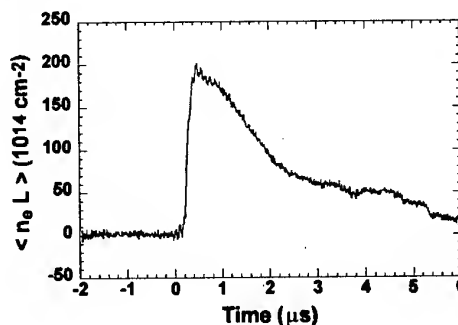
Fig. 4. Typical line-integrated plasma density signal on a longer time scale (showing the phase II plasma).

Fig. 5 presents a plot of the maximum line-integrated plasma density measured in phase II as a function of radiated microwave pulse duration. It is clearly seen that when the phase II plasma peak is greater, a decrease in the radiated microwave pulse

duration occurs. The same trend is also seen for the phase I plasma, which is about one order of magnitude smaller in amplitude than the phase II plasma.
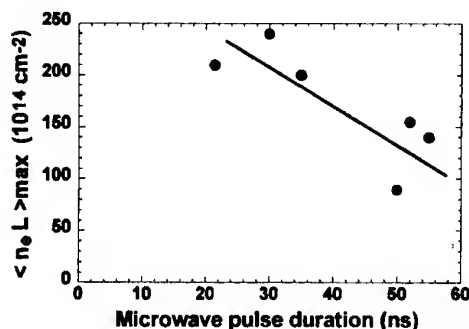
Fig. 5. Maximum line-integrated plasma density (measured around t = 400 ns) as a function of microwave pulse duration.

The measurements can be interpreted as follows. The electron beam scrapes along the wall of the cutoff neck and produces plasma that rapidly diffuses along the magnetic field lines into the SWS (the phase I plasma). We believe that the phase II plasma is probably the plasma following a catastrophic event, such as a microwave field-initiated breakdown in the SWS. A more detailed description of these measurements is given in reference [4].

PLASMA PREFILLED BWO

The intentional introduction of plasma into the SWS of a BWO has been shown to increase microwave power output and generation efficiency, as well as provide several other benefits. Researchers at Niigata University in Japan have performed a linear analysis that shows that the optimal plasma-filled BWO configuration is one in which the plasma is confined close to the axis of the SWS, while the electron beam driving the device is kept close to the walls [5]. At UNM, the plasma prefill source is uniquely mounted internal to the cathode structure of a high power BWO, providing

injection of the plasma directly on axis in the strong, uniform field region of the BWO. The plasma prefill has been found to both enhance and reduce the microwave generation efficiency, depending on the plasma density.

With a prefill plasma density on the order of 10^{11} cm^{-3}, an enhancement of about 30% in microwave generation efficiency has been observed compared with the vacuum case. At higher fill densities, though, the effect of the plasma was to quench the microwaves. Details of the novel plasma injection system and initial results summarizing its effects on microwave generation are presented in reference [6].

REFERENCES

[1] C. Grabowski, et al., "Pulse Shortening in High-Power Backward Wave Oscillators," Proceedings of the Society of Photo-Optical Instrumentation Engineers; Intense Microwave Pulses IV, SPIE, vol. 2843, pp. 251-259, 1996.

[2] C. Grabowski, J.M. Gahl, and E. Schamiloglu, "Electron Emission from Slow-Wave Structure Walls in a Long-Pulse, High-Power Backward Wave Oscillator," IEEE Trans. Plasma Sci., vol. 25, pp. 335-341, 1997.

[3] B. Levush, T.M. Antonsen, Jr., A. Bromborsky, W.R. Lou, and Y. Carmel, "Theory of Relativistic Backward-Wave Oscillators With End Reflectors," IEEE Trans. Plasma Sci., vol. 20, pp. 263-280, 1992.

[4] F. Hegeler, C. Grabowski, and E. Schamiloglu, "Electron Density Measurements During Microwave Generation in a High Power Backward Wave Oscillator," to appear in IEEE Trans. Plasma Sci., June 1998.

[5] M.M. Ali, et al., "Linear Analysis of a Localized Plasma-Loaded Backward Wave Oscillator Driven by an Annular Intense Relativistic Electron Beam," Journal of the Physical Society of Japan, vol. 60, pp. 2655-2664, 1991.

[6] C. Grabowski, J. M. Gahl, and E. Schamiloglu, "Initial Plasma-Filled Backward Wave Oscillator Experiments Using a Cathode-Mounted Plasma Prefill Source," to appear in IEEE Trans. Plasma Sci., June 1998.

COAXIAL CONFIGURATION FOR A HIGH-POWER RELATIVISTIC TRAVELING WAVE TUBE OPERATING IN THE LOWEST NON-AXISYMMETRIC WAVEGUIDE MODE

A. S. Shlapakovski

Institute of Nuclear Physics of Tomsk Polytechnical University
P. O. Box 25, Tomsk 634050, Russia

INTRODUCTION

Coaxial configuration of a drift space in which a high-current electron beam propagates interacting with an electromagnetic field was used as early as in the first experimental work on high-power microwave generation [1]. The space charge limiting current value is higher for a coaxial geometry so that this geometry seemed natural for beams of several tens kA current used in [1]. The same reason, along with the possibility to produce ultrahigh RF power at higher than L-band frequencies, argued the concept of the triaxial relativistic klystron [2]. Also for Cherenkov masers, the advantages of the coaxial configuration pointed out in [3, 4] were increased beam drive power and decreased electric field along a dielectric surface for a given RF power.

There is, however, a specific attractive feature of the coaxial configuration with an inner rod supporting slow wave propagation which was emphasized for the first time in [5]. It concerns original possibilities for the microwave input and output in a traveling wave tube (TWT) device. Indeed, a dielectric rod, or a ridged or corrugated metal rod, is a long ago known microwave transmission line and well developed surface wave antenna. The coaxial system can be considered as the section of such antenna where the feed signal is amplified due to Cherenkov interaction with a beam moving near the antenna surface. An outer conductor of the coaxial is necessary to provide a vacuum region for beam propagation and can also be used as the place of beam dumping. In fact, such a device would be the hybrid antenna-amplifier device, - a combination of a traveling wave tube and a surface wave antenna.

Usually, the operating mode of a rod antenna is the fundamental non-axisymmetric HE_{11} mode which has no cut-off frequency, whereas for traveling wave tubes, the typical operating mode is the lowest axisymmetric TM mode. The HE_{11} mode, however, has E_z component of electromagnetic field and, hence, can bunch an electron beam as well as the TM mode. In order to determine gain and bandwidth values achievable for the HE_{11} mode and make a comparison with the case of the symmetric TM mode, it is sufficient to derive a dispersion relation not assuming azimuthal symmetry for perturbations. From the numerical solution of a dispersion relation, one can obtain growth rates for any eigenmode with arbitrary azimuthal index.
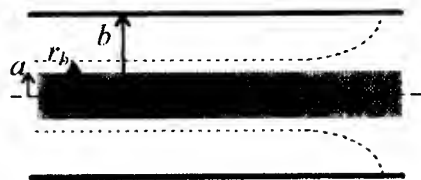
Fig.1. Configuration of the system.

In this work, such an investigation has been performed for the case of a circular waveguide with an inner dielectric rod and an annular beam between the rod and outer wall. The geometry is shown in Fig.1 where the dimensions are indicated. In fact, this system is a dielectric Cherenkov maser (DCM) of unusual configuration as in the traditional DCM, a beam propagates inside a hollow dielectric liner. The beam is assumed fully magnetized, monoenergetic, and infinitely thin.

DISPERSION RELATION

Azimuthally-depended rf fields are proportional to $\exp\{i(l\theta + kz - \omega t)\}$ where ω is the frequency, k is the longitudinal wavenumber, and l is the azimuthal index. Radial dependences of the longitudinal field components are given by Bessel and modified Bessel functions of lth order

$$E_z = A_E J_l(pr), \quad H_z = A_H J_l(pr), \qquad\qquad r < a$$

$$E_z = B_E I_l(qr) + C_E K_l(qr), \qquad\qquad a < r < r_b$$

$$E_z = D_E\left[K_l(qb)I_l(qr) - I_l(qb)K_l(qr)\right], \quad r_b < r < b \tag{1}$$

$$H_z = B_{II}\left[K_l'(qb)I_l(qr) - I_l'(qb)K_l(qr)\right], \quad a < r < b$$

where $p^2 = \varepsilon\omega^2/c^2 - k^2$, $q^2 = k^2 - \omega^2/c^2$, ε is the dielectric constant. The matching conditions at the dielectric surface for E_θ and H_θ components expressed through E_z and H_z are written as follows:

$$\frac{1}{p^2}\left(k\frac{l}{r}E_z + i\frac{\omega}{c}\frac{dH_z}{dr}\right)_{r=a-0} = -\frac{1}{q^2}\left(k\frac{l}{r}E_z + i\frac{\omega}{c}\frac{dH_z}{dr}\right)_{r=a+0}$$

$$\frac{1}{p^2}\left(i\varepsilon\frac{\omega}{c}\frac{dE_z}{dr} - k\frac{l}{r}H_z\right)_{r=a-0} = -\frac{1}{q^2}\left(i\frac{\omega}{c}\frac{dE_z}{dr} - k\frac{l}{r}H_z\right)_{r=a+0} \tag{2}$$

Using the one-dimensional linear fluid equations for the beam, one can obtain the condition for the jump of E_z derivative at the beam surface

$$\left\{\frac{dE_z}{dr}(r_b)\right\} = -\frac{2eI_b}{\gamma^3 mur_b}\frac{q^2 E_z(r_b)}{(\omega - ku)^2} \tag{3}$$

where I_b is the beam current, u is the beam velocity, and γ is Lorentz factor. Substitution of (2) and (3) into (1) and the matching conditions for E_z and H_z yield finally the following dispersion relation:

$$\left\{\left[p\frac{F_E'(qa,qb)}{F_E(qa,qb)} + \varepsilon q\frac{J_l'(pa)}{J_l(pa)}\right]\left[p\frac{F_H'(qa,qb)}{F_H(qa,qb)} + q\frac{J_l'(pa)}{J_l(pa)}\right] - \left[\frac{(\varepsilon-1)l\omega k}{cpqa}\right]^2\right\}(\omega - ku)^2 =$$

$$= \frac{2eI_b}{\gamma^3 mu}q^2\frac{F_E(qr_b,qb)}{F_E(qa,qb)}F_E(qa,qr_b)\left\{\left[\frac{(\varepsilon-1)l\omega k}{cpqa}\right]^2 - \right. \tag{4}$$

$$\left. - \left[p\frac{F_E'(qa,qr_b)}{F_E(qa,qr_b)} + \varepsilon q\frac{J_l'(pa)}{J_l(pa)}\right]\left[p\frac{F_H'(qa,qb)}{F_H(qa,qb)} + q\frac{J_l'(pa)}{J_l(pa)}\right]\right\}$$

where

$$F_E(x,y) = I_l(x)K_l(y) - I_l(y)K_l(x); \qquad F_E'(x,y) = I_l'(x)K_l(y) - I_l(y)K_l'(x);$$

$$F_H(x,y) = I_l(x)K_l'(y) - I_l'(y)K_l(x); \qquad F_H'(x,y) = I_l'(x)K_l'(y) - I_l'(y)K_l'(x).$$

NO-BEAM SYSTEM

In the no-beam case ($I_b = 0$), the solution of Eq. (4) are shown in Fig.2 for $l = 0$, 1, and 2 (solid curves). The a/b ratio has been taken to be 0.5 in order to compare the waveguide with the rod with traditional DCM configuration of the same a/b. From this comparison, the main significant difference of the system studied is clearly seen. Namely, at the phase velocities less
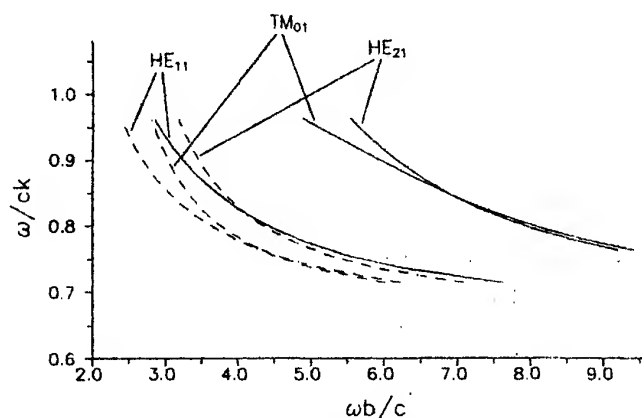
Fig.2. Phase velocity vs frequency for various waveguide modes. Solid curves - waveguide with dielectric rod, dashed curves - waveguide with hollow liner. $\varepsilon = 2.25$, $a/b \approx 0.5$.

than c, the lowest non-axisymmetric mode HE_{11} is quite well spaced by frequency from the nearest neighbours, TM_{01} and HE_{21} modes, whereas for the case of the liner loading the waveguide wall, the dispersion curves of the HE_{11} and TM_{01} modes are very close to each other.

Indeed, for a single dielectric rod, propagating surface waves are slow and all the modes have cut-off frequencies determined by the rod thickness except for the fundamental HE_{11} mode. If an outer wall is placed around rather far from a rod, the frequency ranges appear where modes are fast, and the HE_{11} mode has the cut-off frequency determined by the wall diameter; however, in the ranges where the phase velocities are less than c, there is no considerable changes. Therefore, the thinner rod, the larger spacing between the HE_{11} mode and others shown in Fig.2. It means that the scale of evanescence of the surface wave field in the vacuum region can be significantly greater for the HE_{11} mode so that it can dominate in the instability spectrum of the "hot" system if the beam moves at rather large distance from the rod. This is illustrated below.

RESULTS AND DISCUSSION

In Fig.3, the instability spectrum of the system obtained from the numerical solution of the dispersion relation (4) at various azimuthal indices is presented. The rod parameters are taken the same as in Fig.2, and the beam parameters are very typical for relativistic TWTs (taking into account the dc space charge potential depression, 1.7 kA beam current and $\gamma = 1.8$ at given radius correspond to the applied voltage of ~470 kV). The frequency corresponding to the HE_{11} mode spatial growth rate maximum falls to the X-band at the waveguide radius b of 2.0-2.5 cm that yields the beam-dielectric gap of 2.0-2.5 mm and the gain of 0.8-1.0 dB/cm. One can see, however, that the absolute peak of the growth rate falls to the HE_{21} mode and even for the HE_{31} mode, growth rates are the same as for the HE_{11} in spite of much higher frequency. This is explained by the specific radial dependence of the electromagnetic field transverse components. Indeed, for the HE_{11} mode, the power transmitted is distributed over the whole rod cross-section, whereas for other modes, it is concentrated, more or less, near the rod surface, so that the same power corresponds to the lower E_z component for the HE_{11} mode.

The situation is changed if one decrease

Fig.3. Spatial growth rate vs frequency for various modes. $\varepsilon = 2.25$, $a/b = 0.5$, $r_b/b = 0.6$, $\gamma = 1.8$, $I_b = 1.7$ kA.

Fig.4. The same plot as Fig.3 except for
$a/b = 0.3$ and $r_b/b = 0.4$ (solid curves),
$r_b/b = 0.5$ (dashed curves).

the rod radius and increase the distance between the beam and dielectric surface. In Fig.4, the instability spectrum is shown for the less ratio $a/b = 0.3$ and two different beam radii (for given beam energy and current, the applied voltage turns out to be of 521 kV for $r_b/b = 0.4$ and 494 kV for $r_b/b = 0.5$). In this case, the HE_{11} mode dominates, especially, for $r_b/b = 0.5$. The X-band frequency range for the HE_{11} mode would be, for instance, at $b = 3.5$ cm that corresponds to the gain values of 0.74 dB/cm for 3.5 mm beam-dielectric gap (solid curve) and 0.37 dB/cm for 7 mm gap (dashed curve).

The last figure for the gain seems to be rather small so that such a geometry providing the HE_{11} mode prevalence would be more acceptable for smaller waveguide radius and higher than X-band frequencies (for instance, 20 GHz). It should be noted, however, that high degree of the HE_{11} mode prevalence for X-band frequencies can be achieved with lower beam energies and larger dielectric constants of the rod. In Fig.5, the results of calculations are presented for $\varepsilon = 5$, and the taken beam parameters correspond to 265 kV accelerating voltage. Here, the frequency of the HE_{11} mode growth rate peaking would be of 10 GHz at $b = 2$ cm, and the gain would be 0.97 dB/cm at 4 mm beam-dielectric gap, quite acceptable values for a TWT device. The bandwidth in this case, though, is narrower than for the parameters of Fig.3 or Fig.4 (for the solid curve).

To make a conclusion, the linear theory has been developed for the coaxial configuration of a TWT without the assumption of axial symmetry for electromagnetic fields in the system. The lowest non-axisymmetric HE_{11} mode can be the prevaling mode in the instability spectrum. The gain and bandwidth values achievable in this case can be typical for usual relativistic TWTs at the very accessible electron beam parameters and reasonable geometries for the X-band frequencies and above. The configuration considered allows one to combine a traveling wave tube and a

Fig.5. The same plot as Fig.3. $\varepsilon = 5$, $a/b = 0.3$, $r_b/b = 0.5$, $\gamma = 1.4$, $I_b = 1$ kA.

surface wave radiating antenna in a single hybrid device. Such a device would be rather compact for high radiated power and, at the same time, would provide a wide range of possibilities for high-power microwave beam control.

The work was supported in part by the Russian Foundation for Basic Researches (Contract No. 98-02-17931).

[1] J. A. Nation. Appl. Phys. Lett., Vol. 17, no. 11, pp. 491-494, 1970.

[2] M. Friedman and V. Serlin. Proc. of SPIE. Ed., Howard E. Brandt. Vol. 1872, pp. 2-8, 1993.

[3] E. P. Garate, A. Fisher, and W. T. Main. IEEE Trans. Plasma Sci., Vol. 18, no. 5, pp. 831-836, 1990.

[4] T. J. Davis, L. Schachter, and J. A. Nation. IEEE Trans. Plasma Sci., Vol. 22, no. 5, pp. 504-510, 1994.

[5] A. S. Shlapakovskii. Proc. of SPIE. Ed., Howard E. Brandt. Vol. 2557, pp. 404-413, 1995.

EXCITATION OF BROADBAND OSCILLATIONS BY ELECTRON BEAM IN COAXIAL DISK LOADED TRANSMISSION LINE

E.A.Kornilov, P.I.Markov, I.N.Onishchenko, G.V.Sotnikov

Institute Plasma Electronics & New Methods Accelerations NSC Kharkov Institute of Physics and Technology, Akademicheskaya Str. 1, Kharkov, 310108, Ukraine

The excitation by an electron beam of UHF oscillations in coaxial slowing down transmision line with comb on internal and external cylinders is considered. The analytical and numerical analysis of the received dispersion equation is carried out. The dependence of the gain on energy of an electron beam is investigated. It is shown, that the dependence of the gain on frequency has a maximum nearby Cherenkov resonance of a beam with an eigen wave of structure, outside of a resonance the gain falls down under the linear law at reduction of frequency. The nonlinear theory of the UHF amplifier is constructed on the basis of the chosen slowing down structure. The maximal amplitude of a longitudinal electrical field, efficiency of interaction, optimum length of structure are determined.

1. INTRODUCTION

To begin with the pioneer work by Pierce [1], a study of the travelling wave tube (TWT) is being carried out during several decades. Notwithstanding the great successes in design and construction of the TWT, investigations of the physical processes which take place there are still in progress to date [2].

Coaxial slow-wave lines with disks on one (or both) of the conductors belong to the type of the structures that permit excitation by an electron beam with a fixed energy over a wide frequency range. Such corrugated structures [3] - and the helical ones as well - are characterized by the proper slow wave for which the dispersion law is close to the linear function and, in consequence of this, the coupling resistance weakly depends on the frequency in the principal pass band. Besides the mentioned advantage, the coaxial slow-wave structures make it possible to raise the electron beam currents essentially because the cross-section area becomes enlarged. This makes one to prefer the UHF devices based on such slow-wave systems to other ones where the beams with a persistent sectional density are used (e.g. a chain of coupled cavities [5]).

Investigation of the disk-loaded coaxial lines as the slow-wave structures for the powerful SHF devices in the microwave band is being performed for a long time. The dispersive characteristics are rather completely studied both theoretically [6,7] and experimentally [8]. The coupling resistance dependence on the frequency is examined by the methods of numerical simulation in the case of a given structure geometry. As it was suppose-d to apply the examined structures in the Cerenkov SHF devices with a low electron beam energy ($W_b < 8\,\text{keV}$), the authors of [7] have investigated the coupling coefficient dependencies only for the first. spatial harmonic.

It should be mentioned that the slow-wave systems in question can be used not only in the Cerenkov devices, but also in the powerful electron devices of the magnetron type [9,10].

2. LINEAR ANALISIS

The disk-loaded coaxial line in question is schematically demonstrated in Fig. 1. Cylindrically symmetric annular monoenergetic electron beam with the energy W_b and the current I_b is propagating along the structure axis. Being homogeneous over the cross-section, the beam completely fills the passage channel and it's placed into a

strong magnetic field, which allows to consider its motion to be one dimensional.

Let's suppose, that disturbances of all the quantities which are contained in the Maxwell equations have the form $\sim \exp(i\beta_0 z - i\omega t)$ where ω is the angular frequency and β_0 is the longitudinal wave number.
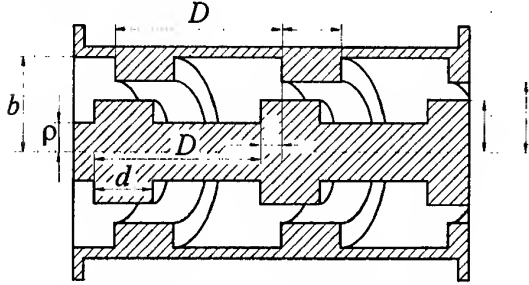
Fig. 1. The slow-wave structure geometry.

The dispersion equation (DE), which describes the electron beam interaction with the slow wave of the coaxial line in the linear approximation is obtained by the method of the partial areas [11, 3]. In result of applying of this method we obtain unknown DE:

$$\left\{ \frac{d}{D} \sum_{m=-\infty}^{\infty} \frac{k\varepsilon_{3m}}{k_{\perp m}} \psi_m^2 \frac{F_1(k_{\perp m},a,\sigma)}{F_0(k_{\perp m},a,\sigma)} - \frac{F_1(k,a,b)}{F_0(k,a,b)} \right\} \times$$

$$\left\{ \frac{d}{D} \sum_{m=-\infty}^{\infty} \frac{k\varepsilon_{3m}}{k_{\perp m}} \psi_m^2 \frac{F_1(k_{\perp m},\sigma,a)}{F_0(k_{\perp m},\sigma,a)} - \frac{F_1(k,\sigma,\rho)}{F_0(k,\sigma,\rho)} \right\} -$$

$$\frac{d^2}{D^2} \sum_{m=-\infty}^{\infty} \frac{k\varepsilon_{3m}}{k_{\perp m}} \psi_m^2 e^{im\phi_0} \frac{F_1(k_{\perp m},a,a)}{F_0(k_{\perp m},\sigma,a)} \times$$

$$\sum_{m=-\infty}^{\infty} \frac{k\varepsilon_{3m}}{k_{\perp m}} \psi_m^2 e^{-im\phi_0} \frac{F_1(k_{\perp m},\sigma,\sigma)}{F_0(k_{\perp m},a,\sigma)} = 0. \qquad (1)$$

In DE (1) the following meanings are used:

$F_n(q,x,y) = J_n(q,x)Y_0(q,y) - Y_n(q,x)J_0(q,y),$

$$\varepsilon_{3m} = 1 - \frac{\omega_b^2}{(\omega - \beta_m v_0)^2}, \quad \omega_b^2 = 4\pi \frac{I_b}{I_A} \frac{c^3}{S_e v_0},$$

$$k_{\perp m} = \sqrt{(k^2 - \beta_m^2)\varepsilon_{3m}}, \quad \beta_m = \beta_0 + \frac{2\pi m}{D},$$

$$k = \omega / c, \quad \varphi_0 = \frac{2\pi l}{D}, \quad \Psi_m = \frac{\sin(\beta_m d / 2)}{(\beta_m d / 2)},$$

Se is the beam cross-section area, v_0 is the beam velocity, $I_A = 17 \text{kA}$, $m = 0, \pm 1, \ldots$,

J_n, Y_n are the Bessel and Veber functions of the order n.

The results of the DE (1) numerical simulation are given in Fig. 2. The structure parameters are $b = 5.3 \text{cm}$, $a = 4.0 \text{cm}$, $\sigma = 3.5 \text{cm}$, $\rho = 1.9 \text{cm}$, $D = 0.7 \text{cm}$, $d = 0.5 \text{cm}$, $\phi_0 = 0$. The electron beam energy is $W_b = 35 \text{keV}$ and the beam current is $I_b = 10 \text{A}$.
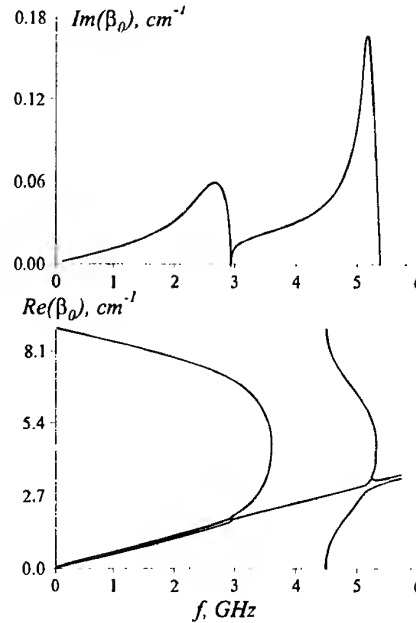
Fig.2

In Fig. 2 the plots are represented as the dependencies of the real $\text{Re}\,\beta_0$ and imaginary $\text{Im}\,\beta_0$ parts of the longitudinal wave number on the frequency $f = \omega / 2\pi$. Within the frequency interval $f = 0 \div 5.5 \text{GHz}$ the slow-wave structure has two transmission bands in the first LF band $f = 0 \div 3.6 \text{GHz}$ dispersion is analogous with the case of a helical slow-wave structure [4, 2], and the phase velocity is determined over the LF range (13). The second transmission band is that of high frequencies (HP) $f = 4.5 \div 5.5 \text{GHz}$. In the case examined by us for the LF transmission band the cutoff frequency is determined by the inner slow-wave structure where the disk height is larger. For the HF transmission band the upper cutoff frequency is given by an external corrugating.

This fact should be taken into account when a thin electron beams, which don't fill the passage channel completely, are used for excitation of natural oscillations in the structure. The beam must be placed tightly to the structure that determines the proper wave. It should be mentioned that both the transmission bands simultaneously exist only in the case of the slow-wave line with two corrugatings. If just one slow-wave structure is provided (either the external or the inner one), only the coaxial wave exists; its upper cutoff frequency is given by the cavity transverse sizes. The dependence of the imaginary part of the longitudinal wave number $Im\,\beta_0$ on the frequency is also characterised by two specific bands. Within the interval $f = 0 \div 3\,GHz$ the first of them sets amplification of the coaxial slow wave. The amplification coefficient dependence on the frequency is maximum in vicinity to the beam risonance with the structure proper wave: it linearly decreases towards he range, and. it abruptly comes to an end towards the HF range. The second maximum which is sharp and narrow, is given by the beam resonance with the structure proper wave which belongs to the next transmission band. The group velocity of this wave is essentially less than the group velocity of the coaxial slow wave. Therefore here the maximum amplification coefficient is almost in 3 times higher than in the first band. However, the resonance width is sufficiently smaller than in the first band.
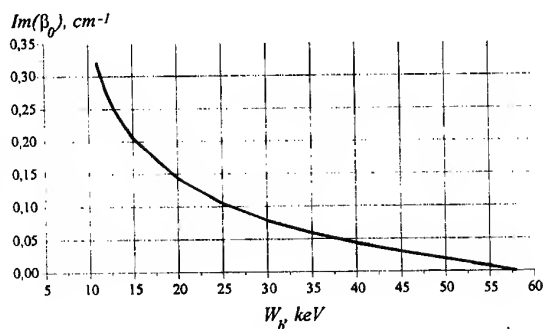
Fig.3

In Fig. 3 the dependences of the maximum amplification coefficient $Im\,\beta_0$ in the first transmission band are given as the functions of the electron beam energy. The dependence curve has a sharp maximum in vicinity to the electron beam energy $W_b \approx 10\,keV$, which corresponds to the beam resonance with the π-mode of the structure proper wave. Over the high energy range the maximum amplification coefficient almost linearly decreases with the energy increase. The dependence depicted in Fig. 3 qualitatively coincides with the dependence $Im\,\beta_0$ on the frequency in the high energy range when the beam energy is fixed, (Fig. 2), which confirms the resonance character of the interaction between, the electron beam and the structure proper waves in a wide frequency band.

3. NONLINEAR ANALISIS.

Describing the nonlinear stage of the interaction between the electron beam and the proper waves of the coaxial slow-wave structure, which are found in the previous section, let's use the nonlinear stationary theory [12] (the latter is applicable for calculations of the TWT). Let's neglect the spatial charge because the electron beam currents are light. With the help of the formalism [12] one gets the following equation for the longitudinal electric field amplitude overaged over the electron beam cross-section:

$$\frac{dE}{dz} + i(\beta_e - \beta_0)E = \beta_0^2 I_b R_{co}^0 I_0, \qquad (2)$$

where $I_0 = \dfrac{1}{\pi}\displaystyle\int_0^{\pi}\exp i\theta\,d\theta_0$, $\beta_0 = \omega/v_0$, β_0 is the longitudinal wave number of the structure proper wave in the beam absence, S_b is the electron beam cross-section, and R_{co}^0 is the coupling resistance at the zero spatial harmonic of the wave with which the beam interacts.

The coupling resistance is determined as:

$$R_{co}^0 = \frac{\int\limits_{S_b} E_{z,0}^2 \, dS}{\frac{c}{2\pi} S_b \beta_0^2 \sum\limits_{m=-\infty}^{\infty} \int\limits_{S_b} E_{r,m} H_{\varphi,m}^* \, dS}, \qquad (3)$$

where: $E_{z,m}$, $E_{r,m}$, $H_{\varphi,m}$ describe the m-th spatial harmonic of the electromagnetic field transverse distribution in the beam absence.

The equation for the longitudinal electric field must be supplemented with the equations of the beam particle motion:

$$\frac{dv(z)}{dz} = \frac{e}{mv(z)} \left(1 - \frac{v^2(z)}{c^2}\right)^{3/2} \mathrm{Re}\!\left(Ee^{-i\theta}\right),$$

$$\frac{d\theta}{dz} = \frac{\omega}{\beta_0 v(z)} - 1. \quad (4)$$

Fig.4

$f = 1.9 \div 3.0\,\mathrm{GHz}$. The amplitude first maximum dependence on the frequency corresponds to the amplification coefficient dependence on the frequency (Fig. 2). Hire the optimal structure length weakly varies on the frequency interval within the limits $60 \div 75\,\mathrm{cm}$.

Fig.5

The results of numerical simulation of the set of equations (3), (4) are presented in Fig. 4 and 5. The parameters of the structure and beam are the same as in the case of the linear theory illustrated in Fig. 2. The longitudinal electric field dependence given in Fig. 4. One can see that when the input signal level is $E_0 = 100\,\dfrac{V}{cm}$ the structure optimal length is $\approx 60\,\mathrm{cm}$ at the frequency $f \approx 2.4\,\mathrm{GHz}$. Interaction efficiency, which is defined as the ratio of the beam energy losses to the beam initial energy, is approximately equal to $\approx 27\%$.

In Fig. 5 a family of the longitudinal electric field dependences and the interaction efficiency on the distance is presented for various natural frequencies

4. REFERENCES.

1. Pirce D. Travelling-Wave Tubes. (Van Nostrand, New York, 1950).
2. Freud H.P., Zaidman E.G., Antonsen T.M. Phys.Plasmas. 1996. V.3, N 8. P.3145.
3. Marimanov R,G., Gyleiko V.G. RiE. 1956. V.1, N 2., p.1374, rus.
4. Silin R.A., Sazonov V.P. Zamedlyaushchie Sistemy. M: Sov.Radio, 1966, 632p.,rus.
5. Grigoryev A.D., Yankevich V.B. Rezonatory i Resonatornye Zamedlyaushchie Sistemy SVCh. M.: Radio i svyaz, 1984. 248p., rus.
6. Marimanov R,G., Gyleiko V.G. RiE. 1957. V.2, N 2., p.172, rus.
7. Stel'mach M.F., Ol'derogge E.B. RiE. 1959. V.4, N 6., p.980, rus.
8. Chirkin N.M. RiE. 1959. V.4, N 1., p.126, rus.
9. Kapitsa P.L. Echlektronika Bol'shych Mochnostey. M.: Izd. AN SSSR, 1962, p.3, rus.
10. Destler W.W. et al. J.Appl.Phys. 1983. V.54,N 7. P.4152.
11. Lopuchin I.M. Vozbusgdenie Electromagnitnyh Kolebaniy i Voln Elektromagnitnymi Polyami. M.: GITTL, 1953,rus.
12. Vainshtein L.A., Solntsev V.A. Lektsii po Sverh-vysokochastotnoy Echlektronike. M.: Sov.Radio, 1973, 400p., rus.

RELATIVISTIC CHERENKOV PLASMA MASER OF MICROSECOND PULSE DURATION

O.T. Loza, P.S. Strelkov, and I.E. Ivanov

General Physics Institute, Russian Academy of Sciences,
Vavilova str. 38, Moscow, 117942 Russia

The principle of operation of Cherenkov plasma maser (CPM) makes it possible to avoid the microwave pulse shortening, which is inherent to vacuum devices of relativistic high-current microwave electronics. A 800-ns microwave pulse with an energy of 21 J was obtained at a peak power level of 40 MW (the efficiency being 4%) in a broad (~ 100%) frequency band.

The microwave pulse duration in oscillators in which the microwave power is only several tens of megawatts is about several hundreds of nanoseconds. The microwave radiation terminates and does not resume although the REB still propagates through the electrodynamic system. This is the so-called microwave pulse shortening, which is governed by spontaneous plasma generation in different regions of the oscillator due to different reasons. The majority of these reasons may be eliminated, e.g., the method of production of a high-current REB with stable cross section during a microsecond from a field-emission cathode [1] is discussed at this conference. We proposed the mechanism [2] of pulse shortening, which may be briefly described as follows. First, powerful microwaves cause the electrons to emerge from a REB onto the SWS walls, and these electrons produce plasma on the wall surface. Second, the microwave field heats the plasma near the wall and initiates the discharge followed by a fast accumulation of the plasma.

In the first stage, the rate with which the plasma is generated is governed by the intensity of the electron flow onto the wall that, in turn, depends on the gap between the REB and the wall. It is desirable to make this gap as large as possible in order to prevent plasma creation, but there is one serious obstacle: the limiting vacuum current. Especially strong restrictions are imposed by the space charge on the gyrotrons and similar devices in which the transverse velocities of electrons are significant. A different restriction is imposed on Cherenkov devices (such as BWOs and TWTs): the REB must propagate near the wall, because it interacts with a slow microwave mode that drops exponentially from the wall toward the axis.

If the radial component E_r of the microwave electric field is nonzero near the wall, then the second stage of pulse shortening may occur, during which the plasma is further increased by the microwave discharge. This stage is especially dangerous for devices with corrugated walls (such as BWOs and TWTs), in which the discharge develops between the ripples of the wall surface along the magnetic field lines.

Hence, the above conditions, e.g., a sufficiently small gap between the REB and strong microwaves on the wall, are peculiar to all devices of vacuum high-current microwave electronics. At the same time, according to the above mechanism for plasma creation, these conditions contradict the requirement that the microwave generation be long-term. Nevertheless,

there exists a high-current microwave device that is free of these drawbacks: the plasma relativistic microwave oscillator [3], or CPM. The oscillator is based on Cherenkov excitation of a slow eigenmode of a plasma waveguide. The plasma wave with both phase and group velocities along the electron beam direction is amplified, a partial reflection from the ends of the plasma waveguide provide the feedback and the regime of self-oscillations.

In the present work, we make use of the advantages of plasma electronics and propose a new approach to the problem of microwave generation in the microsecond range.

EXPERIMENT
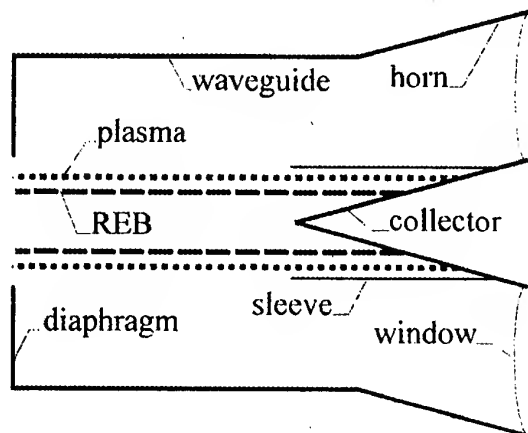
Fig. 1. Plasma microwave oscillator.

Fig. 1 shows a drawing of the device. An annular REB propagates through the diaphragm to the collector inside the prearranged annular-shaped plasma. The collector unit also plays the role of the inner electrode of the outlet coaxial horn through which the microwaves are emitted. The collector for both plasma and the beam is concealed in a metal sleeve that prevents the penetration of the plasma into the waveguide. The beam radius $R_b = 6$ mm, the plasma radius $R_p = 13$ mm, and the waveguide radius $R_w = 35$ mm. The length of the interaction region is 23 cm, and the distance between the collector and the entrance plane of the metal sleeve is 25 cm.

The value of the magnetic field was 1.7 T. The microwave peak power was about 40 MW with a beam current of 2 kA and an electron energy of 500 keV. This current was approximately equal to the vacuum limiting current in the drift tube.

If the plasma density is sufficient ($10^{12} \div 10^{13}$ cm^{-3}) to neutralize the space charge of the REB, the electron beam may propagate far from the waveguide walls. The radial profile of the absolute value of microwave field E_r is presented in Fig. 2. We can see that this field rapidly decreases as the radius increases from R_p to R_w and remains comparatively low in the near-the-wall region in which a plasma layer may arise. In the plasma column, the magnitude of the longitudinal component E_z of the microwave electric field is maximum (hence, in order that both plasma and REB could interact effectively, they should be close to each other), but the distance between the REB and the waveguide walls may be large.
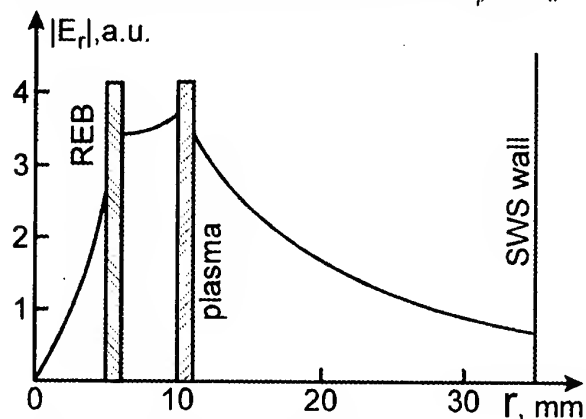
Along with these merits, the CPM, being compared with a vacuum device, has a number of drawbacks. First, the REB electrostatic field, which prevented the

Fig. 2. $|E_r|$ vs radius in CPM.

electron emission from the wall in the microwave fields, is screened now by the plasma and is absent near the wall. Second, an electrode is placed inside the waveguide. Although the collector plasma is concealed inside the metal sleeve, the microwave field on its surface and especially at its edge is strong (see Fig. 2) and may initiate a discharge.

The spectrum of microwaves was measured by a calorimetric spectrometer. The spectrum width is about 100%, and the mean frequency grows from 9 GHz to 15 GHz as the plasma density increases. The waveforms of the cathode voltage and of the microwave pulse are shown in Fig.3. Microwaves are emitted over 800 ns, and the radiation does not terminate abruptly, as it usually does in the case of microwave breakdown. The radiation pulse energy was measured with a broadband calorimeter [4] and, in the shot under consideration, was found to be 21 J, which value corresponds to the average microwave power ~ 25 MW (and, accordingly, the peak power ~ 40 MW) and the peak efficiency 4%. Although the microwave pulse shortening and an abrupt termination of the microwave radiation are absent in Fig. 3, the shape of the microwave pulse is far from rectangular: the microwave power increases during 300 ns, remains constant for about 300 ns, and, then, decreases during 200 ns. Such a behavior of the microwave generation may be attributed to different reasons.

Fig. 3. Waveforms of the microwave power (top) and of the cathode voltage(bottom).

The first reason stems specifically from the method by which an annular-shaped plasma was produced [5]. This plasma was generated by a special (600 eV, 1 ÷ 100 A) electron beam in xenon at a pressure of about $10^{-4} \div 10^{-3}$ Torr. Over almost 1 μs, the REB ionized xenon gas and, then, interacted effectively with the produced plasma because of a strong coupling of the plasma to the REB. Nevertheless, when the plasma gun was turned off, no microwaves were radiated if the pressure was $3 \cdot 10^{-4}$ Torr. With the plasma gun switched on, microwaves again appeared.

Another reason explaining why the trailing edge of the microwave pulse was comparatively steep (200 ns) is the influence of the collector plasma, whose velocity u_{cp} may be as high as 1 m/μs (in [6] one can find an experimental dependence of u_{cp} on the cathode potential; it is linear, and $u_{cp} = 40$ cm/μs for 200 kV and $u_{cp} = 80$ cm/μs for 300 kV). Even if the plasma moves at a velocity equal to only one half of this 1 m/μs, it has enough time to pass throughout the metal sleeve from the collector to the SWS during the first 500 ns and to begin to violate the operation of the microwave oscillator.

Finally, the operation efficiency of the CPM depends on the beam parameters, namely, the electron energy and the total current. In the course of microwave pulse, the diode voltage varied from about 300 kV to 500 kV, with the corresponding variation (by a factor of about two) of the beam current, which began and terminated when the voltage had approximately the same value.

CONCLUSION

In a high-current microwave oscillator driven by a REB, pulse shortening of microwave radiation is determined by the process of plasma formation in the device. Although there are many factors leading to the undesirable plasma formation, most of them can be successfully eliminated. Nevertheless, in a vacuum high-current microwave device, in which a REB propagates near the SWS surface because of its significant space charge, there is one mechanism for intense plasma accumulation that is difficult to overcome.

The proposed model of microwave pulse shortening is as follows. First, a strong microwave field causes the destruction of a REB, and a certain fraction of the beam electrons are ejected to the wall under the action of this field. The electron bombardment results in the formation of a plasma layer on the wall surface. Then, a microwave discharge develops, and the amount of plasma increases until the process of microwave radiation comes to an end.

In order to avoid microwave pulse shortening, we propose to use plasma microwave oscillators. In these devices, the space charge of an electron beam is neutralized by that of the plasma, so that the REB may propagate far from the waveguide surface. Besides, the microwave field on the wall is low, and the probability for the development of a microwave discharge on the wall is also low. Additionally, all the available means must be engaged to eliminate the influence of the plasma on the collector, cathode, etc. over the entire device.

The above experiments with a plasma microwave oscillator permitted us to generate microwave pulses with energy 21 J during 800 ns in a broad frequency band. The theory of CPM predicts that microwaves can also be generated in a narrow frequency band. In the first experiment with a plasma relativistic microwave amplifier [7] (which has the wave structure like in the CPM) the radiation spectra with the bandwidth of 2% was obtained, the results of our tentative experiments with the CPM (the bandwidth of ~ 10%) and numerical simulations show that the design of a narrow-band plasma relativistic microwave oscillator is also possible.

Therefore, our experiments demonstrated that the features of the Cherenkov plasma maser enable to eliminate the effect of microwave pulse shortening, and we think that this result is very encouraging.

REFERENCES

1. O.T.Loza and P.S.Strelkov "Generation of an annular REB of microsecond pulse duration and stabilized transverse dimensions in a diode with a field-emission cathode" Proc. of 11th Int. Conf. On High Power Particle Beams, June, 1998, Israel (Beams'98).
2. O.T.Loza, P.S.Strelkov, and S.N.Voronkov, *Plasma Phys. Rpts.*, vol. 20, #4, pp. 374-379, April, 1994.
3. M.V.Kuzelev, O.T.Loza, A.V.Ponomarev. *et al.*, *Sov. Phys. JETP*, vol. 82, #6, pp. 1102-1111, June, 1996.
4. A.G.Shkvarunets, *Instruments and Experimental Techniques*, vol. 39, #4, pp. 535-538, July-August, 1996.
5. O.T.Loza, A.V.Ponomarev, P.S.Strelkov, *et al.*, *Plasma Phys. Reports*, vol. 23, #3, pp. 201-208, 1997.
6. N.I.Zaitsev and G. S.Korablev, *Sov. J. Tech. Phys.*, vol. 27, #1, pp. 110-111, January, 1982.
7. A.V.Ponomarev, P.S.Strelkov, and A.G.Shkvarunets, *Plasma Phys. Reports*, vol. 24, #1, pp. 48-52, 1998.

ELECTRON BEAM MODULATION AND LEAKAGE CURRENTS DURING SELF-SUSTAINING SECONDARY EMISSION IN MAGNETRON GUNS*

A. V. Agafonov,
P. N. Lebedev Physical Institute of RAS,
Leninsky Prosp. 53, Moscow 117924, Russia,

V. M. Fedorov, <u>V. P. Tarakanov</u>,
High Energy Density Researh Center of RAS,
IVTAN, Izhorskaya 13/19, Moscow, 127412, Russia

ABSTRACT

Problems of magnetic insulation violation inside a vacuum coaxial diode with dense electron flow are considered from the point of view of the development as low-voltage as high-efficiency relativistic magnetrons with secondary emission cathode. The numerical model of nonstationary nonuniform secondary electron emission from a cathode was developed. The results of computer simulations of an electron clouds formation due to nonlinear azimuthal instability under the condition of strong nonuniform secondary self-sustaining emission are described. The existence of BKB-instability with transverse quasistationary leakage current of a few percents of Child-Langmuir current and rotating states of electron flow has been shown under conditions of conservation of full power and full momentum of the system. The transverse leakage current drops sharply when $B_0/B_{cr} \geq 1.3$ and longitudinal leakage current prevails. It is emphasised the dominant influence of a feedback due to nonuniform secondary emission on dynamics of electron beam modulation and on arising of a transverse leakage current to the anode across the external magnetic field. The instability arises due to an energy and a momentum exchange between particles and rotating crossed $E \times B$-fields. The BKB-instability exists as in potential as electromagnetic approximations. 2.5D-simulations have been performed in the range of magnetic insulation $B_0/B_{cr} \leq 1.3$ for the coaxial gun with parameters close to experimental one and for the guns with different types of azimuthal inhomogeneites. 3D-simulations are in progress.

INTRODUCTION

Well known, many high-power magnetrons employed high-current density electron emission from the primary low emission cathode due to the back-bombardment (BKB) secondary emission [1], [2], [3]. Comparison experiments [3] have demonstrated clearly that the secondary emission is produced by the BKB-instability at pre-cathode electron layer [4].

This paper reportes on computer simulations of an electron cloud formation inside a smooth-bore magnetron. Preliminary results were published in [5], [6]. The main calculations of the beam dynamics were carried out with PIC-code KARAT [7].

COMPUTER SIMULATION OF BACK-BOMBARDMENT INSTABILITY

Computer simulations have been performed using 2.5-D electromagnetic PIC code KARAT for the magnetron diode (MD) with parameters close to experimental [3], and with an external voltage source $V_0(t)$ connected to MD via an RL-circuit. The yield of secondary electrons from the cathode takes into account the dependence of the yield on the energy of electrons and the angle between the direction of electron velocity and the perpendicular to the cathode surface, and also the threshold of secondary emission.

The main parameters of MD are: radius of the anode $r_A = 0.53$ cm, radius of the cathode $r_K = 0.33$ cm; external longitudinal magnetic field $B_0 = 2.5$ kG ($B_0/B_{cr} \simeq 1.15$, $\omega_{ec}/2\pi = 7$ GHz, period of cyclotron rotation 0.14 ns); the voltage rise time to maximum value of $V_{0m} = 12$ kV is 2 ns; maximum emission current of the primary beam $I_{em} = 2$ A. For given voltage and geometry of MD the Child-Langmuir current through the MD without a magnetic field equals approximately $I_{CL} \simeq 200$ A (here and below currents and charge densities correspond to linear values per cm of length in the longitudinal direction). Electrotechnical parameters are $\tau_{L/R} = 0.25$ ns, $\tau_{RC} = 0.24$ ns, where C is the capacitance of MD. Drift velocity of electrons in crossed fields is $\bar{v}_{e\theta} = cE_0/B_0 = 2.4\times10^9$ cm/s, if the electric field is estimated as V_{AK}/d_{AK}.

Fig. 1 shows dynamics of store of primary N_{e0} and secondary N_{es} electrons and time
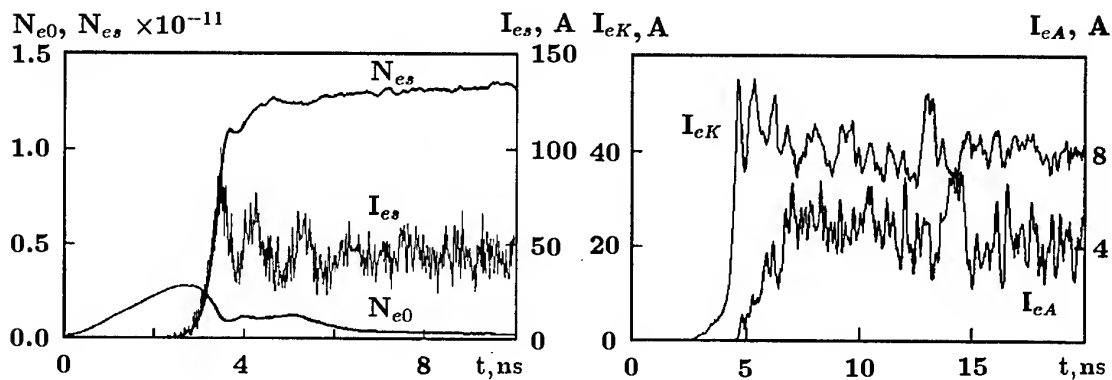
Fig. 1: Dynamics of store of primary N_{e0} and secondary N_{es} electrons and time behaviour of secondary emission current I_{es} (left) and time behaviour of leakage current I_{eA} and back-bombardment current I_{eK} (right).

behaviour of secondary emission current I_{es}. The time behaviour of leakage current I_{eA} and back-bombardment current I_{eK} are shown at the same figure.

Fig. 2 shows configurations of electron flows for various variants of emission of primary and secondary electrons at t = 10 ns. Under conditions of conservation of full energy and momentum a part of the electrons lose energy under the action of the field and drifts to larger radii towards the anode. Another part of the electrons increases its energy and returns to the cathode with an energy exceeding the threshold value for secondary emission. In view of indicated reasons, the emission of secondary electrons is nonuniform. This effect leads to an intensification of the cathode back-bombardment process and to fast and effective growth of secondary electrons inside MD. The secondary-emission current exceeds the primary-beam current by more then order of magnitude and subsequently exerts a determining action on the operation of the MD. The MD passes over to a condition
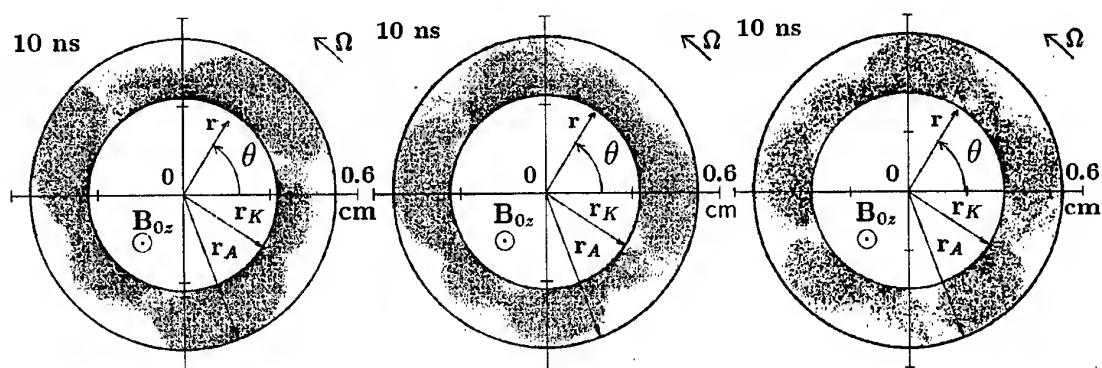
Fig. 2: Configurations of electron flows inside MD at $t = 10$ ns: left — a uniform emission of primary beam of 2 A from a secondary emission cathode; central — a uniform emission of primary beam of 2 A from a cathode having a 20° strip with no emission of secondary electrons; right — emission of primary beam of 2 A from a 30° strip at the cathode having a 60° strip with no emission of secondary electrons.

of self-sustaining emission and the primary beam could be switched off. After the transient process, a stable formation consisting of three main bunches is formed in this geometry. Electron clouds rotate as a whole with approximately constant angular frequency $\Omega \simeq 2\pi \times 10^9$ s^{-1}.

The nonuniformity of various types leads to the following main effects: broadening of the functions of distribution of electrons at the anode on energy and angle of incidence; formation of flows with non-regular azimuthal structure; change of the spectrum of field frequencies. However, integral characteristics of flow (total charge in the gap, leakage current of electrons at the anode) practically do not change, i.e., the system is stable relative to the initial conditions. Therefore, the main results are described for the case of homogeneous emission of primary beam from secondary emission cathode surface of an axisymmetrical MD.

In Fig. 3, the energy distributions of electrons reaching the anode (f_{eA}) and returning
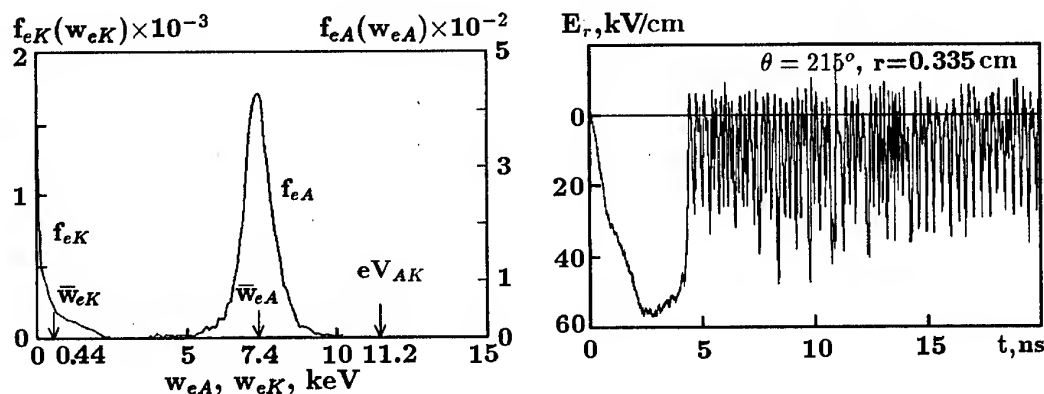
Fig. 3: Distribution functions of electrons for energy at the anode and the cathode (left) and time behaviour of radial electric field E_r near the emission surface (right).

back to the cathode (f_{eK}) are presented. The average energy of electrons reaching the anode equals $\bar{w}_{eA} = 7.4$ keV and at the cathode the average energy $\bar{w}_{eK} = 0.44$ keV. Thus, for the given conditions $\eta_{BKB} = (eV_{AK} - \bar{w}_{eA})/eV_{AK} = 34\%$ for power of back-

bombardment flow $P_{eK} \simeq 15$ kW and power of beam reaching the anode $P_{eA} \simeq 30$ kW. The radial electric field E_r near the emission surface (see Fig. 3) changes quasi-periodically its direction in time and provides for a feedback on deep electron beam modulation and on arising of a leakage current.

Fourier-spectra of the field shows the presence of several high harmonics of the main frequency of "BKB-noises" equals approximately $f_0 \simeq 0.5 \times f_{cc}$. The most irregular frequency spectrum is observed for noncoaxial MD (see Fig. 4).
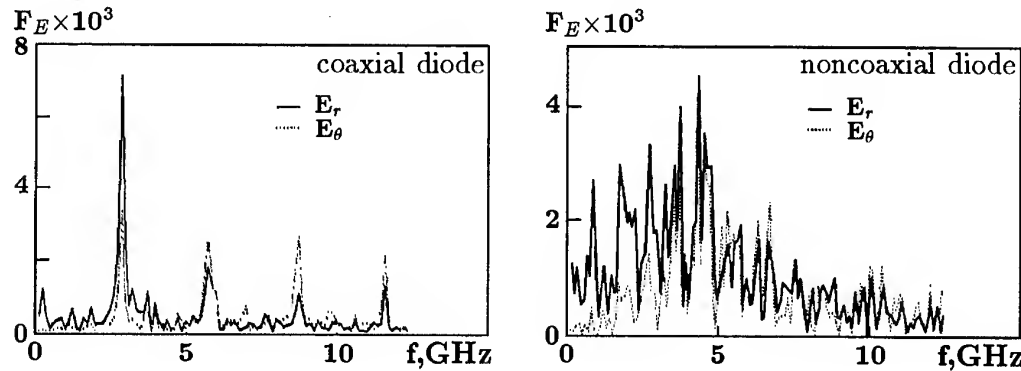
Fig. 4: Fourier-spectra of electrical field inside coaxial and noncoaxial MD

CONCLUSION

The selfconsistent picture of an electron flow formation inside secondary emission MD has been described. The existence of BKB-instability with transverse quasistationary leakage current of a few percents of Child-Langmuir current and rotating states of electron flow has been shown.

Both full energy and momentum of the system are conservated as following: a part of the electrons lose energy under the action of the field and drifts to larger radii towards the anode, another part of the electrons increases its energy and returns to the cathode with an energy exceeding the threshold value for secondary emission.

Under condition of weak magnetic insulation ($B_0/B_{cr} \sim 1.1$) the BKB-instability goes to large amplitudes. When $B_0/B_{cr} \geq 1.3$ a longitudinal leakage current prevails and the BKB-instability develops in pre-cathode layer.

REFERENCES

[1] Okress E. (ed.). Academic Press. N.Y., 1961.

[2] Treado T.A. et al. IEEE Trans. on Plasma Sci., 1992, v. 20, 351 − 359.

[3] Jepsen R.L. and Muller M.V. J. Appl. Phys. 1951, v. 22, 1196 - 1207.

[4] Fedorov V.M., Schmidt W., Westermann Th. Proc. of the 9th Intern. Conf. on High-Power Particle Beams. Washington, USA, 1992, v. 2, 747–755.

[5] Agafonov A.V., Fedorov V.M., Tarakanov V.P. Proc. of 1997 Particle Accelerator Conf. (PAC'97). Vancouver, Canada. 1997. Preprint FIAN, 1997, N 37.

[6] Agafonov A.V. et al. Proc. of the 11th Intern. Pulsed Power Conf. (PPC'97). Baltimore, USA, 1997. Preprint FIAN, 1997, N 46.

[7] Kotetashwily P.V., Rybak P.V., Tarakanov P.V. Institute of General Physics, Moscow, Preprint N 44, 1991.

EFFECT OF BEAM MODULATION ON A BROADBAND MM RADIATION FROM A STRONG BEAM-TURBULENT PLASMA

Hiroshi Yoshida, Masaru Masuzaki, Shintarou Ooyama, Ritoku Ando, and Keiichi Kamada

Department of Physics, Faculty of Science, Kanazawa University, Kanazawa 920-1192, Japan

ABSTRACT

High-power broadband millimeter-wave radiation is emitted from a plasma in a strong Langmuir turbulence state driven by an intense relativistic electron beam (1.4 MeV, 10 KA, and 30 ns). In order to ascertain that the radiation is due to interaction of modulated beam with caviton fields, the radiation and the beam modulation were measured with two spectrometers covering 18 to 140 GHz. The radiation spectrum had nearly flat spectrum up to about 40 GHz and declined steeply above it. The beam modulation is measured by two methods: observation of spectrum of waves excited in a waveguide pickup and observation of spectrum of synchrotron radiation. Both spectra were similar to the radiation spectrum. Discussion is given on the experimental results in connection with the collective Compton boosting model.

1. INTRODUCTION

Broadband electromagnetic-wave radiation is one of interesting phenomena in IREB-plasma interaction experiments [1-3]. The radiation has a broadband spectrum above the plasma frequency and disappears just after the electron beam passes through the plasma [1, 3]. For the broadband radiation, the plasma must be in a strong Langmuir turbulence state [4], in which creation, collapse, and burnout of cavitons are repeated [5]. Weatherall [6] showed that the spectrum of radiation emitted by a single electron interacting with caviton fields is broad up to the frequency corresponding to its passage time through a caviton. Benford and Weatherall [7, 8] proposed the collective Compton boosting model in which beam density fluctuation is taken into account in order to explain high-power of the radiation. In this model the radiation spectrum should depend on the beam density fluctuation.

To investigate the relation between radiation and beam modulation, we measured the radiation and beam modulation spectra. For determination of the k-spectrum of the beam modulation, we adopted two methods. One is to use a waveguide pickup using WR-42, and the other is to utilized synchrotron radiation. The measured ω-spectrum of the beam modulation was compared with the radiation spectrum. Also it was transformed to the k-spectrum using the relation $\omega = kv_0$, where v_0 is the beam velocity, from which we estimated the spatial beam distribution. We discuss these results in connection with the collective Compton boosting model.

2. EXPERIMENTAL SETUP

Major components of the system were a modified Pulserad 110A electron beam generator (1.4 MV, 27 kA, 30 ns) produced by Physics International, a drift chamber, and a plasma gun system. A diode of the beam generator consisted of a carbon cathode of 36 mm diameter and a titanium foil anode of 20 μm thick. The beam current injected into the drift chamber was around 10 kA with the anode-cathode distance of 30 mm. The stainless steel drift chamber had two observation ports at 175 mm downstream from the anode. An electromagnetic-wave absorber, Eccosorb AN73, was put on the inner wall of the chamber. The chamber

Figure 1. Experimental setup for the observation of the radiation.

was evacuated to the pressure less than 5 x 10^{-5} torr. A pair of rail-type plasma gun were installed opposite to each other at 100 mm downstream from the anode. The plasma density, n_p, at the observation ports was determined with a microwave interferometer and a triple probe. The density became maximum at $\tau = 12$ μs and then decreased, where τ is the delay time after the gun firing.

We prepared a three-channel filter-bank spectrometer for 18 GHz - 60 GHz and a three-channel filter-waveguide-combination spectrometer for 73 GHz - 140 GHz. The filter-bank spectrometer was consisted of directional couplers, variable attenuators, bandpass filters (BPFs), and detectors. The combination spectrometer included BPFs, variable attenuators, detectors, and wide-band amplifiers. Three filter units were prepared to change the observation frequency and bandwidth. These spectrometers were calibrated by Gunn oscillators.

The experimental setup for observation of the radiation spectrum is shown in Fig. 1. Horn antennas were attached in the observation ports. For measurement of the beam modulation the waveguide pickup illustrated in Figure 2 was devised. When the modulated beam passes across the waveguide through holes, it excites electromagnetic waves which couple with waveguide modes. We calculated the frequency response of this pickup for TE$_{n0}$ modes using Lorentz reciprocity theorem to correct the spectra obtained from the modulated beam. The pickup was placed at 175 mm downstream from the anode and the centers of the holes were adjusted to lie on the chamber axis.

Figure 3 shows the set up for the beam modulation measurement utilizing synchrotron radiation. An additional vacuum chamber was attached at the end of the chamber which discussed above. A titanium foil of 20 mm thickness was put at 600 mm downstream from the anode to prevent intrusion of the plasma and the radiation into this additional chamber. Bending magnets and horn antenna were set at 600 mm and 680 mm downstream from the anode, respectively.
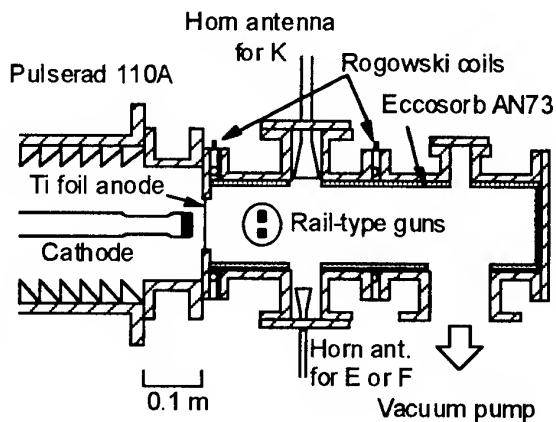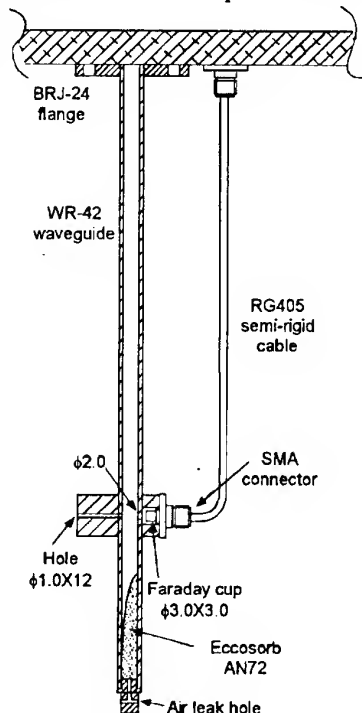
Figure 2. Waveguide pickup.
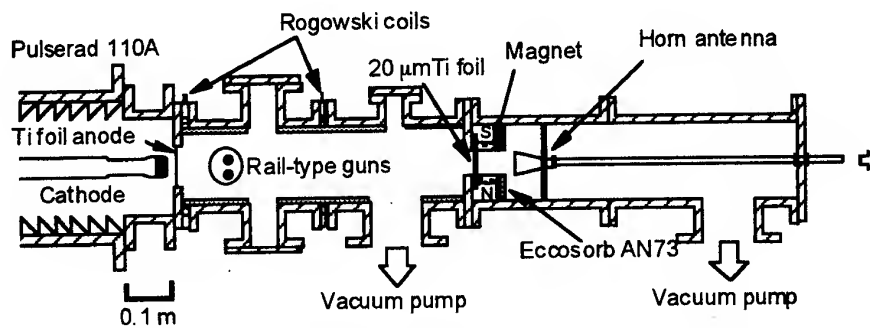
Figure 3. Experimental set up for the beam modulation measurement by synchrotron radiation.

3. RESULTS AND DISCUSSIONS

Figure 4 shows the radiation spectrum at $\tau = 30$ μs which corresponds to the plasma frequency of about 16 GHz. It has nearly flat part up to about 40 GHz and declines steeply with about 40 dB/Oct. at the higher frequency side. Figure 5 shows the measured frequency spectrum of the beam modulation at $\tau = 30$ μs. The power in U-band disappeared because, in this experiment, the lowest detection limit of the detector for the frequency range of 18 - 60 GHz was rather high. Figure 6 shows the synchrotron radiation spectrum. The obtained spectrum was compensated by the spectrum

Figure 4. Radiation spectrum

of synchrotron radiation by an electron. The spectra are also nearly flat up to 40 GHz and decline steeply above this frequency.

From these ω-spectra we obtain directly the k-spectrum of the beam modulation under the assumption of constant beam velocity. On the other hand the radiation spectrum is expressed as
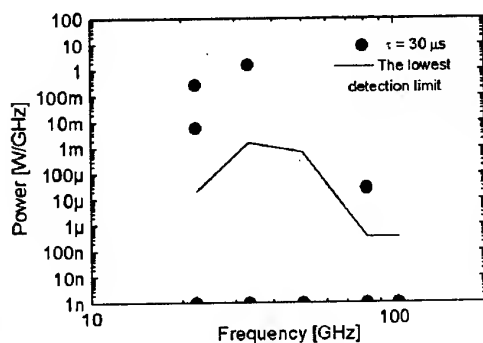
Figure 5. Modulation spectrum measured by waveguide pickup.
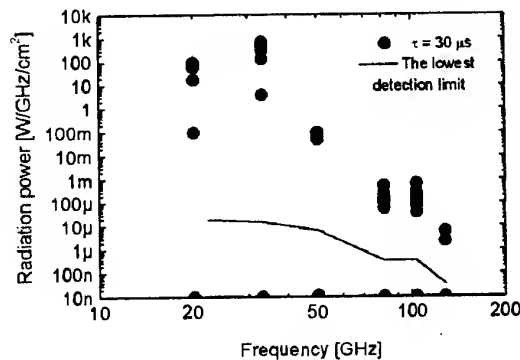
Figure 6. Modulation spectrum measured by synchrotron radiation.

the product of the radiation spectrum from single electron and the spectrum of the beam modulation. Since the radiation spectrum from a single electron in our observation range is estimated to be flat, we could compare directly both spectra. So we think that the k-spectrum of the beam modulation determines the radiation spectrum.

We tried to use the collective Compton boosting model in order to explain the observed spectra under the assumption that the caviton's dipole moments are parallel to the beam velocity. In this model following four spectral density functions are assumed for the fluctuation of the beam density: power law, delta function, exponential, and Gaussian. We calculated spectra using each spectral functions with our experimental parameters. The calculated spectrum using the Gaussian spectral function was similar to the measured spectrum in shape but the cutoff frequency of the latter was much less than the former. This difference comes from the difference in the spectral bandwidth in the spectral density function. In this model [7] this bandwidth is defined as $k_m = \gamma^2/D$, where γ is Lorentz factor, the characteristic length of caviton $D = 20 \lambda_d$, and λ_d is the Debye length. From this definition the cutoff frequency of the calculated spectrum becomes approximately several THz. On the other hand, the cutoff frequency of our experimental spectrum was several tens GHz. To estimate this bandwidth from the experimentally obtained spectrum, we fitted the spectrum to Gaussian and calculated the symmetric spatial beam distribution of Gaussian shape. The width of the spatial beam distribution was estimated to be 5 mm.

4. CONCLUDING REMARKS

To investigate the effect of the beam modulation on the radiation, the radiation and the beam modulation were measured with two spectrometers covering 18 to 140 GHz. The obtained radiation spectrum had nearly flat spectrum up to about 40 GHz and declined steeply above it. In order to measure the beam modulation a waveguide pickup was devised and synchrotron radiation was utilized. Spectra obtained by both methods agreed fairly well and were similar to the radiation spectrum. From observed spectra, we estimated the spatial beam distribution as Gaussian using $\omega = kv_0$ and its width as to be 5 mm. We do not know yet the mechanism of this beam bunching.

The authors would like to thank K. Natsume for his assistance in the experiments.

REFERENCES

[1] K. G. Kato, G. Benford, and D. Tzach, *Phys. Fluids*, **26**, pp. 3636-3649, 1983.

[2] M. S. DiCapua, J. F. Camacho, E. S. Fulkerson, and D. Meeker, *IEEE Trans. Plasma Sci.*, **16**, pp. 217-224, 1988.

[3] M. Masuzaki, H. Yoshida, R. Ando, K. Kamada, A. Ikeda, C. Y. Lee, and M. Kawada, in *Proc. of the 11th International Conference on High-Power Particle Beams*, Prague, Czech, 1996, **1**, pp. 339-342.

[4] M. Yoshikawa, M. Masuzaki, R. Ando, and K. Kamada, *J. Phys. Soc. Jpn.*, **65**, pp. 2081-2086, 1996.

[5] P. A. Robinson, and D. L. Newman, *Phys. Fluids B*, **2**, pp. 3120-3133, 1990.

[6] J. C. Weatherall, *Phys. Rev. Lett.*, **60**, pp. 1302-1305, 1988.

[7] G. Benford and J. C. Weatherall, *Phys. Fluids B*, **4**, pp. 4111-4120, 1992.

[8] J. C. Weatherall and G. Benford, *Astrophys. J.*, **378**, pp. 543-549, 1991.

THERMIONIC ELECTRON GUNS FOR HIGH-POWER TRANSIT-TYPE SOURCES OF MICROWAVE RADIATION

N.I. Zaitsev, E.V. Ilyakov, I.S. Kulagin, G.S. Korablyov, V.K. Lygin

*Institute of Applied Physics of the Russian Academy of Sciences,
46, Ulyanov St., Nizhny Novgorod, 603600, Russia*

High-power microwave sources are necessary for a number of important physical or technical applications, such as investigations on interaction of powerful electromagnetic radiation with plasma, acceleration of charged particles, time compression of electromagnetic pulses, energy transmission through space, radaring. Parameters of these sources should be as follows: output power 10–100 MW at pulse duration of 10 or more microseconds, operation both in the single-pulse regime and at the repetition rate of several kilohertz. The necessary power level has been achieved and used in high-current relativistic electronics for quite a long time. However, generation of multi-microsecond pulses of radiation in systems with field-emission cathodes seems problematic due to spatio-temporal instability of electron beams.

The solution of this problem is quite realisable by the use of classical thermionic cathodes. For this purpose, we developed a three-electrode electron-optic system of the magnetron-injection type with a strong magnetic guide, which formed a tubular flow of electrons 20 mm in diameter with energy of 350 keV, current of 400 A at pulse duration of 10 µs. Optimisation of geometry for the gun electrodes was carried out by means of computer simulation with the code "EPOS" [1]. Configuration of gun electrodes is shown in Fig. 1,a. The presence of an intermediate electrode makes it possible to change the beam current smoothly (to decrease it to about the order of maximum value), while the gun stays in the space-charge limitation regime. It permits us to minimize the influence of spotted emission on the parameters of the formed electron beam. Depending on the value of the cathode magnetic field, and on the first-anode voltage, this gun can form both a helical (for gyroresonance devices) and a rectilinear (for the Cherenkov and ubitron types of devices) electron beam. The main parameters of this gun are shown in the Table 1.

The mean value and spread of longitudinal velocities (at the rectilinear-beam formation) were measured by means of the retarding field method [2] in the scaling regime (accelerating voltage 11 kV). The ratio of the mean longitudinal velocity of electrons to the full one $\beta_{||}/\beta=0.99\pm0.1$ and its spread $\delta(\beta_{||}/\beta)=(2\pm1)\%$ were found with the use of the experimentally received function of collector current depending on the decelerating field. Integral characteristics of the full-scale electron beam were near to the calculated ones.

The barium-aluminate cathode with the operating temperature 1050 – 1150°C ensured its characteristics at the heater power 0.8 – 1 kW. These characteristics were invariable during more than 500 h of operation (at the vacuum $5\cdot10^{-7}$ Torr at the oil-free evacuation) and after ten unsealings of the vacuum volume.

This gun was successfully used in the experiments with models of microwave Cherenkov-type generators [3]. At the relativistic carcinotron of 3- and 6-centimeter wavelength the output power of 5 and 10 MW, respectively, was obtained at the pulse width that was equal to duration of the high-voltage pulse, that was 10 µs.

However, these guns are more sensitive to inhomogeneity of the emission current of the cathode, and need rather large magnitude of the guiding magnetic field (about 3 T in the operating space). Otherwise, destruction of the beam, discontinuance of its transport, and appearance of high-voltage breakdown are observed. To increase the beam current and
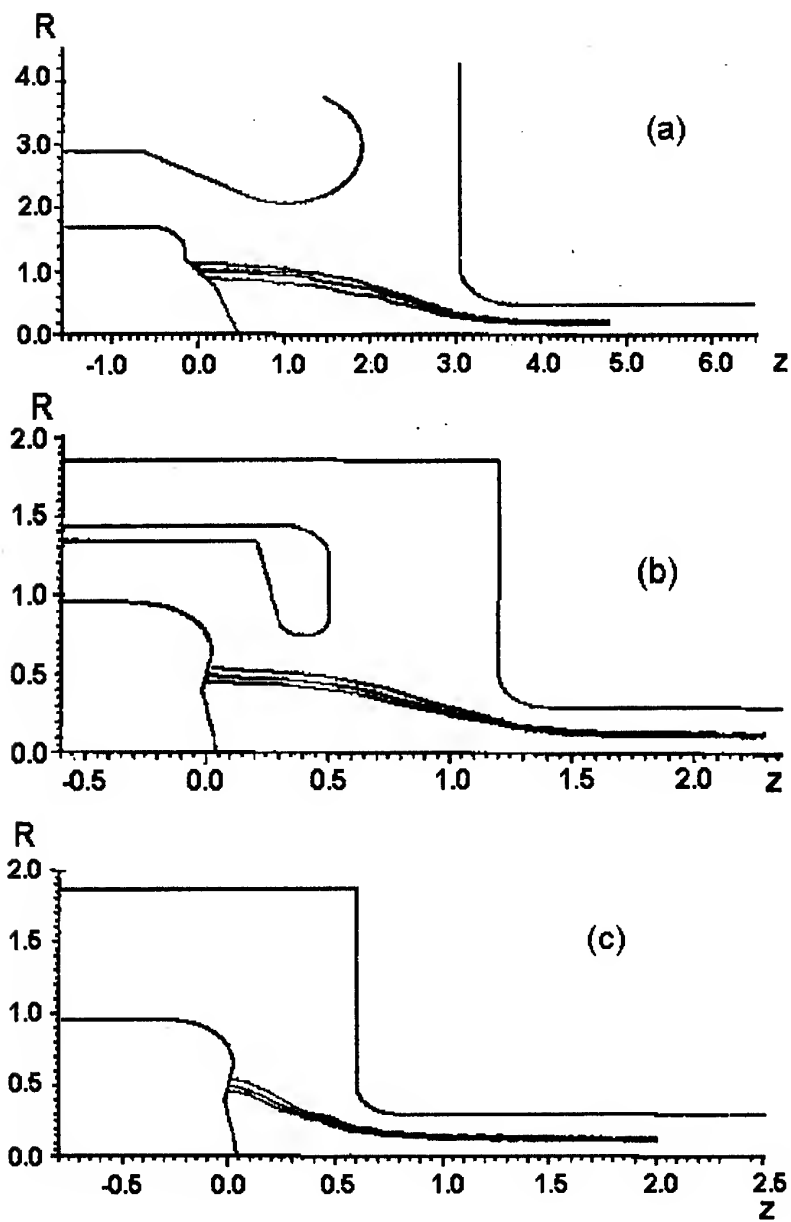
Fig. 1. Configuration of electrodes for the electron guns: (a) of magnetron-injection type (with the cathode diameter 100 mm); (b) and (c) are three- and two-electrode guns of quasi-planar configuration (both with the cathode diameter 160 mm)
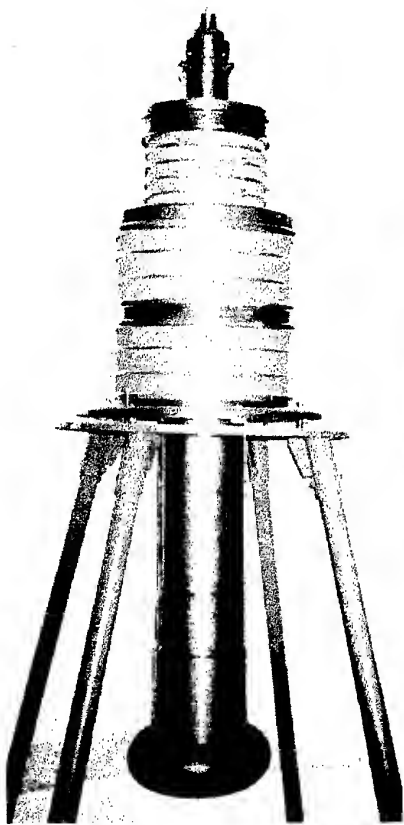
Fig. 3. Cathode

Fig. 2. Cathode unit with metal-ceramic sealed-off accelerating section
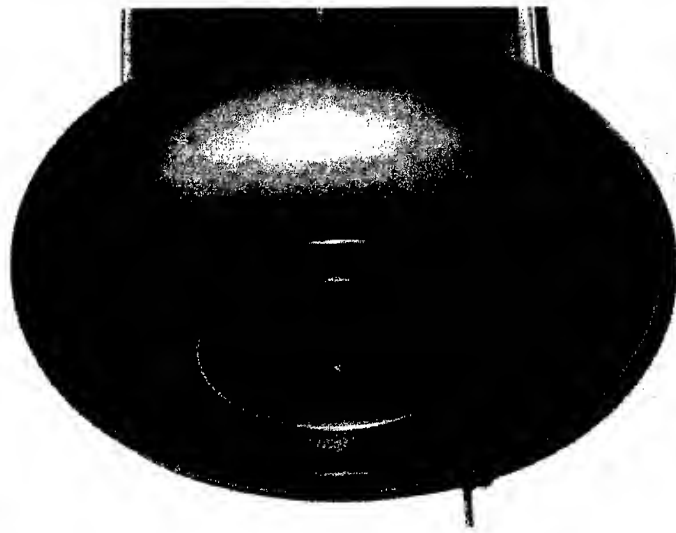
simultaneously to decrease the magnetic field, the electron gun with quasi-planar configuration of the electrodes and the enlarged radius of the emitter was designed. The possibility to use the reduced magnetic field (up to magnitude of ~1 T) was foreseen at the design stage. The diameter of the formed beam was 40 mm; thickness of the beam wall was 4 mm. The gun electrodes were optimised with the regard for the above-mentioned requirements and the available distribution of magnetic field. The numerical codes KARAT of V.P. Tarakanov and EPOS [1] were used for the optimisation. An electron-optical system (see Table 1), which provides formation of the beam with the current of 600 A, energy of electrons 300 kV, and the spread of longitudinal velocities less than 10 %, has been developed and manufactured basing on the proper calculations. Configuration of electrodes is shown in Fig. 1,c. A photo of the cathode unit with metal-ceramic sealed-off accelerating section and a photo of the cathode for this version of the gun are shown in Fig. 2 and Fig. 3. At higher electron energies (up to 500 keV) and beam currents (up to 1000 A) it is reasonable to use the three-electrode version of this gun (Fig. 1,b).

Table 1

	Magnetron-injection gun, helical beam	Magnetron-injection gun, rectilinear beam	Quasi-planar gun
Cathode voltage, kV	200	350	300/500
Cathode-intermediate anode voltage, kV	125	140	
Beam current, A	55	400	600/1000
Magnetic field in the drift channel, kOe	10	25	10
Mean diameter of the emitting belt, mm	100	100	160
Belt width, mm	4.7	15	15/20
Angle between the belt and the axis	50°	50°	80°
Diameter of the beam at the drift channel, mm	20	25	40
Relative longitudinal velocity of electrons $\beta_{||}$		0.81	0.76/0.86
Spread of the latter parameter $\delta\beta_{||}$		0.002	0.04
Relative transversal velocity of electrons $\beta_{\perp}$	0.5	0.05	0.1
Spread of the latter parameter $\delta\beta_{\perp}$	0.03	0.063	0.2

REFERENCES

1. Lygin V.K. et al. Elektronnaya Tekhn. Ser. 1. Elektronika SVCh, 1987, No.7, p.1605-1612 (in Russian).
2. Avdoshin E.G. et al. Izv. Vyssh. Ucheb. Zaved. Radiofizika, 1973, vol. 16, No. 4, p. 605-612 (in Russian).
3. Zaitsev N.I. et al. Instruments and Experimental Techniques, 1995, vol. 38, No 3, Part 2, p. 380-385.

PROBLEMS OF CATHODE DESIGN
AND BREAKDOWN AVOIDANCE RELEVANT
TO HIGH-POWER BROADBAND GAS-PLASMA-FILLED
MICROWAVE SOURCES

M.A. Zavjalov, V.I. Perevodchikov, A.L. Shapiro
All-Russian Electrotechnical Institute,
111250, Krasnokazarmennaya 12, Moscow, Russia

ABSTRACT

The main aspects of the problem of high-power broad-band gas-plasma-filled microwave device designed as sealed tube, including beam-plasma processes, gas-dynamic system, electron optical system and cathode ion protection, are discussed. Non-relativistic beam-plasma microwave amplifier has been created to operate at output power up to 20 kW, electron efficiency 30% and pass-band width up to 30%.

During the past decade there have substantial advances in non-relativistic plasma microwave electronics [1-3].

Non-relativistic Cherenkov type beam-plasma microwave amplifier based on hybrid slow-wave structure has been created to operate at output power up to 20 kW, electron efficiency 30% and pass-band width up to 30%. Hybrid slow-wave structure consist of chain of coupled cavities with plasma-filled transit channel. Cylindrical beam-plasma column ($\sim 10^{12}$ cm^{-3}) created by electron beam (3 A, 20 keV) as a result of beam-plasma discharge. Working gas pressure (H_2) in the region of slow wave structure is equal 7.10^{-4}-1.10^{-3} Torr. At the same time it is necessary to have gas pressure about 10^{-6} - 10^{-5} Torr in E-gun accelerating gap in order to avoid electrical breakdown. The gas-dynamic system for gas-plasma-filled microwave device designed as sealed tube has been developed. Original measures for cathode defence from ion bombardment and for coordination of electron-optical system and beam-plasma interaction region has been investigated.

Also, the main aspects of the problem of gas-plasma-filled microwave device performance which we want briefly to consider are:

- beam-plasma processes;
- gas-dynamic system;
- electron optical system and cathode-ion protection;
- electric strength of the electron gun.

In book [4] an attempt of systematizing and generalizing both useful and accompanying plasma phenomena in various kinds of high power electron guns and generated beams was given. At the definite conditions, when the plasma density generated in electron beam setup may be much higher than beam density, the principal processes responsible for the electron beam spreading and relaxation are the beam-plasma instabilities resulting from a collective particle interaction.

The plasma TWT is placed in magnetic field (0,25-0,3 T) satisfied the following conditions $\omega_b \ll \omega < \omega_p < \omega_c$, where ω_b is the electron beam frequency, ω_p is the plasma frequency and ω_c is the electron cyclotron frequency.

As can be seen from the articles [1-3] the output microwave radiation power of plasma TWT in the amplifier mode is increased 2-3 time at working gas pressure of $7.10^{-4} \div 1.10^{-3}$ Torr in comparison with quasi-vacuum regime at pressure of $1.10^{-6} \div 1.10^{-5}$ Torr. At the same time gas pressure more than 3.10^{-3} Torr leads to destruction of hybrid plasma slow wave structure and fall microwave radiation. Further rough estimations of system parameters are given.

In Table 1 three main beam states (two component quasi-neutral beam, three component «plasma beam» and beam-plasma discharge state) at different gas pressure P are presented. The first line of the Table 1 indicates the example of initial beam parameters. Here, n_b, n_i, n_e and n_o are densities of beam electrons, ions, plasma and neutral gas, accordingly; kT_e - plasma electron temperature, v_b - beam electron velocity; σ_i - atom ionization cross-section by electron impact; $\tau_i = 1/(n_o v_b \sigma_i)$ - ionization time; $\sigma_i v_b$ - gas ionization rate by beam electrons; $<\sigma_i v_e>$ - gas ionization rate by plasma electrons (ionization probability in unit time averaged over plasma electron velocities v_e); $n_b n_o \sigma_i v_b$ and $n_e n_o <\sigma_i v_e>$ - the ion production rates by beam and plasma electrons, accordingly.

Table 1

e V_{bo} = 20 keV, I_b = 4 A, d_b = 1 cm, n_b = 3.10^9 cm^{-3}		
Quasi-neutral E.B.	Plasma E.B.	E.B. plasma discharge (collective processes)
n_b, n_i	n_b, n_i, n_e	n_b, n_i, n_e
P~ 10^{-5} Torr	P~ 10^{-4} Torr	P~ 10^{-3} Torr
n_o ~ 3.10^{11} cm^{-3}	n_o ~ 3.10^{12} cm^{-3}	n_o ~ 3.10^{13} cm^{-3}
n_b~ n_i ~ 3.10^9 cm^{-3}	n_e ~ 10^9 - 10^{10} cm^{-3}	n_e ~ 10^{11} - 10^{12} cm^{-3}
-	kT_e ~ 4 eV	kT_e ~20 eV
τ_i ~ 20 mcs	τ_i ~ 2 mcs	τ_i ~ 0,2 mcs
$n_b n_o \sigma_i v_b$~10^{14}cm^{-3}s^{-1}	$n_b n_o \sigma_i v_b$~10^{15} cm^{-3}s^{-1}	$n_b n_o \sigma_i v_b$ ~10^{16} cm^{-3}s^{-1}
$\sigma_i v_b$ ~10^{-7} cm^3 s^{-1}	$\sigma_i v_b$ ~ 10^{-7} cm^3 s^{-1}	$\sigma_i v_b$ ~10^{-7} cm^3 s^{-1}
-	$n_e n_o <\sigma_i v_e>$~6.10^{12}cm^{-3}s^{-1}	$n_e n_o <\sigma_i v_e> \gg 10^{17}$ cm^{-3}s^{-1}
-	$<\sigma_i v_e>$~7.10^{-10}cm^{3}s^{-1}	$<\sigma_i v_e>$~4.10^{-8}cm^{3}s^{-1}
-	$\dfrac{n_o n_b \sigma_i v_b}{n_o n_e <\sigma_i v_e>} > 10^2$	$\dfrac{n_o n_e <\sigma_i v_e>}{n_o n_b \sigma_i v_b} > 10$

This situation was investigated on special experimental arrangement with use of electrical probe and non-contact X-ray diagnostics obtained information directly from interaction region (Fig.1) [4].

The gas-dynamic system of plasma microwave devices designed as a sealed tube contains hydrogen generators in the field of collector and an evacuating arrangment between E-gun and electrodynamic structure. Fig.2 shows schematic diagram of E-gun and vacuum pumping-out systems consisted of sorption part and magnetic-discharge pump. The electrodes of discharge pump form also ion-catcher which is used to partially protect cathode from ionic bombardment. Thermionic flat cathode with diameter 1 cm is made of W or LaB_6. Fig.3 shows calculation results of the gun electron-optical system.

Also, to avoid the problems of E-gun breakdown and cathode degradation during ion bombardment from the plasma generated by beam in slow wave structure region, the original vacuum pumping system is attached to E-gun. Plasma microwave device is normally operated without breakdowns of accelerating gap.

The variant of the gun with ion-protective annular cathode for new model of plasma microwave tube is developed. The examples of configurations of E-beam and synthesis electrodes are presented in Fig.4 (a) [5]. Fig.4 (b) shows potential distribution along curved axis of the beam.

It is necessary to say that perspective direction for high-power plasma tube application can be the use gas-discharge plasma cathode operated at working gas pressure. This project aims to develop plasma tube that can be used with bipolar electron-optical system and without needing complicated gas-dynamic array.

REFERENCES

1. V.I.Perevodchikov, M.A. Zavjalov, V.F.Martynov et al. BEAMS'92, p.183, Washington, 1992.
2. M.A.Zavjalov, L.A.Mitin, V.I.Perevodchikov et al. IEEE Transactions on Plasma Science, vol.22, №5, p.600, 1994.
3. G.I.Butskih, K.G.Gureev, M.A.Zavjalov et al. Radiotechnika i electronica, №9, pp.1681-1685, 1993 (in Russian).
4. M.A.Zavjalov, Yu.E.Kreindel, A.A.Novikov, L.P.Shanturin. Plasma Processes in Technological Electron Guns. Moscow, Energoatomizdat (1989) (in Russian).
5. P.I.Akimov, L.A.Neganova et al. Radiotechnika i electronica. Vol.41, №5, pp.619-626, 1996 (in Russian).
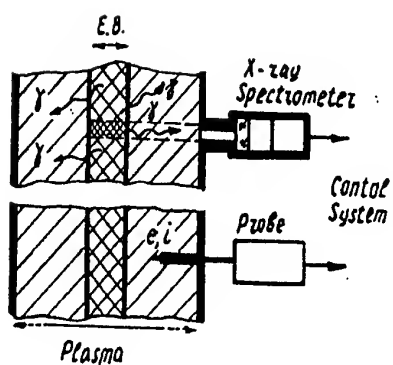
Fig.1
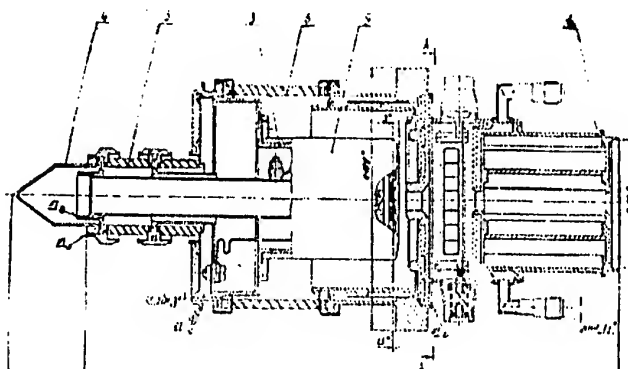
Fig.2
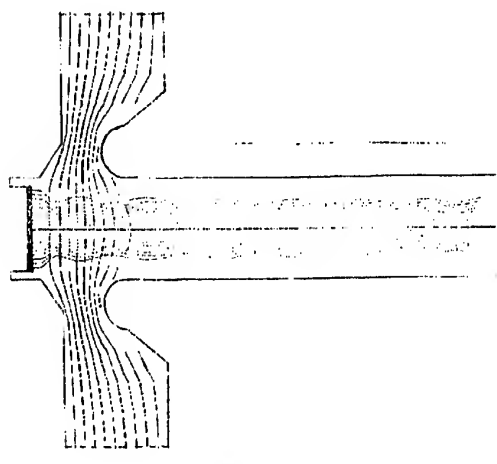
Fig.3
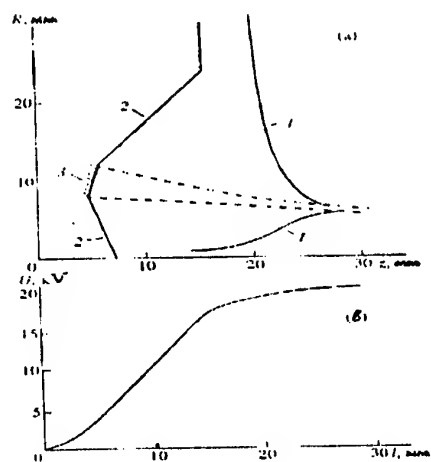
Fig.4

Fig.1 Schemes of X-ray and electrical probe diagnostics.

Fig.2 Schematics diagram of E-gun and vacuum pumping-out system.

Fig.3 Electron optical system of plasma TWT.

Fig.4 Synthesis of optical system with annular cathode. Configurations of beam and electrodes (a) and potential distribution along curves axis of beam (b).
1- anode forming electrodes, 2- cathode forming electrodes, 3- cathode.

GENERATION OF SUBNANOSECOND MICROWAVE PULSES BY INTENSE ELECTRON BUNCHES MOVING IN A PERIODIC BACKWARD WAVE STRUCTURE IN THE SUPERRADIATIVE REGIME.

N.S.Ginzburg, Yu.V.Novozhilova, I.V.Zotova, A.S.Sergeev, and N.Yu.Peskov,
Institute of Applied Physics, RAS, 603600, Nizhny Novgorod, Russia

A.D.R.Phelps, A.W.Cross, S.M.Wiggins, W.He and K.Ronald
University of Strathclyde, Glasgow, G4 0NG, UK

V.G.Shpak, M.I.Yalandin, S.A.Shunailov, and M.R.Ulmaskulov
Institute of Electrophysics, RAS, 620049, Ekaterinburg, Russia

V.P.Tarakanov
High Energy Research Centre, RAS, 127412, Moscow, Russia

The study of multifrequency dynamics of backward oscillators carried out in [1] showed that when injection electron current increases the steady state oscillations change for selfmodulation operation regime. It has been noticed that high amplitude spikes form at the initial stage of transient process under such conditions and the amplitude of these spikes substantially (2-3 times) exceeds the amplitude of steady state oscillations. However, only recently it was recognized [2] that this spike has the superradiative nature and its formation is related not so much with feedback mechanism but just with mutual influence of different part of electron beam caused by slippage of the wave with respect to the electrons. Under certain conditions (long interaction space and low current) the peak power associated with this spike grows as the square of the beam current, which indicates that electrons in the leading edge of the beam radiate coherently. Thus, if the electron pulse duration is restricted by the value sufficient for formation of the above mentioned superradiative spike it is possible to expect effective generation of high power ultrashort microwave pulses.

Taking into account the general interest in superradiance phenomena in ensembles of classical electrons which has attracted considerable attention in recent year [3,4] we tried to realise this emission as one of appearance of superradiance. The electron accelerator based on RADAN 303 modulator [5] equipped with an adjustable subnanosecond pulse sharpener [6] was used as a driver of intense subnanosecond electron bunches. When such bunches passing through the periodic slow-wave structure and interacted with backward propagating radiation generation of ultrashort subnanosecond megawatt level K_a band microwave pulses based on superradiance have been observed [4]. However, in these first experiments rather low guide magnetic fields up to 2T were used. This value of magnetic field was less than the cyclotron resonance value. At the same time it is known [7-9] from previous studies of long (5-30 nanoseconds) pulse relativistic BWO that as the magnetic field is varied BWOs have two operating ranges separated by the cyclotron absorption region. Cyclotron absorption arises when cyclotron resonance conditions are fulfilled for the fundamental harmonic the wave propagating in the periodic structure. Based on this experience it is reasonable to assume that for the short pulse injection regime for high guide magnetic fields the peak power of SR spikes should be several times higher as compare with those attained in the previous experiments. A superconducting magnet was used in a new series of experiments to generate a

longitudinal magnetic field with strengths of up to 10 T. Using a dc solenoid instead of the pulsed one used in the previous experiments permits us to operate in the burst-repetitive mode (25pps) to actually create a novel source of powerful subnanosecond K_a band radiation. In this paper results of the experimental investigation of superradiance of intense subnanosecond electron bunches moving through a periodic waveguide structure and interacting with a backward propagating wave are presented. These results are compare with first results of the numerical simulation of superradiation based on the particle-in-cell (PIC) code KARAT.

EXPERIMENTAL SET-UP.

A RADAN 303 compact accelerator with a subnanosecond slicer was used to inject typically 0.5-1.2 ns, 1-2 kA, 200-250 keV electron bunches [10]. These electron bunches were generated from a magnetically insulated coaxial diode, which utilised a cold, explosive emission cathode. A new design of cathode unit has been developed to provide the possibility of the smooth, precise adjustment of the accelerating gap to vary the electron current. The fast rising e-beam current and accelerating voltage pulses were measured using a Faraday cage strip line current probe and an inline capacitive voltage probe respectively, with both signals recorded using a 7GHz Tektronix 7250 transient digitising oscilloscope. High current electron pulses were transported throughout the interaction space in the form of corrugated waveguide of 6 cm of a total length in a longitudinal guiding magnetic field of up to 10 T created by a superconducting magnet. The period of corrugation of the slow wave structure was approximately 3.5 mm, the corrugation depth was 0.75 mm and had a mean radius of 3.75 mm. The mean electron bunch diameter varied between 4.8-5.2 mm. For measurement of the K_a-band radiation a hot-carrier germanium detector which had a transient characteristic of 200ps was used. The electron beam current and accelerating voltage probes possessed 200ps and 150ps transient characteristics respectively.

EXPERIMENTAL RESULTS.

Typical oscilloscope trace of microwave signal from an electron pulse passing through a periodical waveguide of total length 6 cm is presented in Fig.1. The observed microwave spikes have duration about 300 ps and the rise time of 200 ps. The dependence of peak power on the strength of guide magnetic field is shown in Fig.2. In this diagram it is clearly seen that there is a region of cyclotron absorption near the resonance magnetic field value 3.25 T and then two operating regimes with low 1.5-3 T and high >4 T magnetic fields. The previous experiments

Fig.1 Typical waveforms of superradiation microwave pulse recorded by germanium detector.

on the observation of SR in corrugated waveguide [4] were carried out only in the region of low magnetic fields. Implementing the strong guide magnetic field resulted in a drastic 4-5 times increase of peak power. The increase in power can be easily explained by the improvement in the quality of the electron beam, the decreasing gap between the beam and the

slow-wave structure as well as the decrease to 0.4mm of the transverse width of the electron bunch. Frequency measurements have been made using a set of cut-off waveguides filters showed that the main peak had a central oscillating frequency of approximately 38 GHz. The relative radiation spectrum bandwidth found from these measurements was about 5 %. The radiation had a polarisation corresponding to the TM_{01} mode. The measured radiation pattern also corresponded with good accuracy to the excitation of the TM_{01} mode. This measurement allowed the absolute peak power to be estimated by integrating the detected signal from the detector over its radial position. The peak power estimated by this method was about 60 MW. A rather high level of radiation power was indicated also by the illumination of a neon bulb panel when the radiation signal irradiated the panel at a distance of 30 cm from the output horn. The radiation pattern accurately corresponded to the excitation of the designed TM_{01} mode. One more important evidence of the high peak power was obtained from the observation of RF breakdown of ambient air for subnanosecond pulses in the focus of parabolic reflector as well as inside receiving concentrating conical horn. Estimation of the strength of electrical fields inside horn and comparison with the results of previous observations of breakdown from long nanosecond microwave pulses [9] demonstrates that the absolute power was not less then 60 MW. The calculations have shown that above peak power corresponds to 5% efficiency of the energy transformation from the e-bunch into microwave pulse. Besides it takes to note that the rate of microwave power rise time represents rather high value of 0.3-0.4 GW/ns.
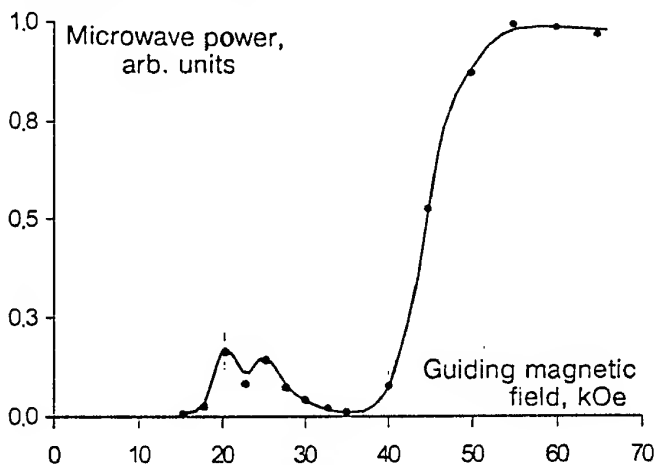
Fig.2 Peak microwave power as function of guide magnetic field.
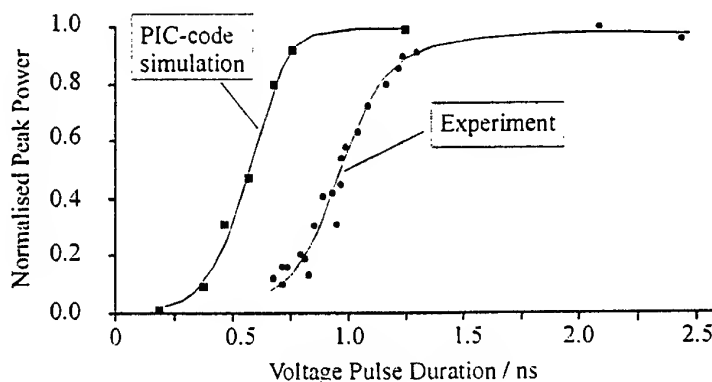
Fig.3 Superradiance peak power vs accelerating voltage pulse duration
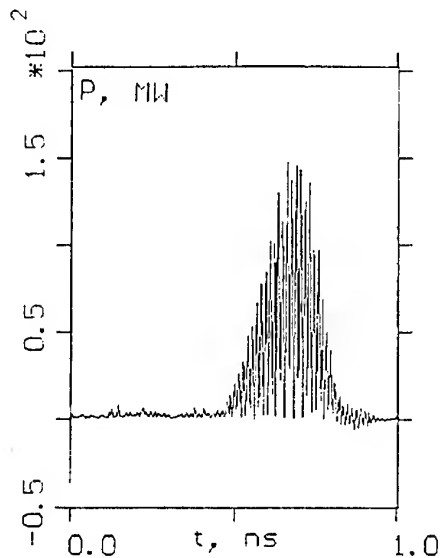
Fig.4 KARAT code simulation of SR pulse waveform

To study the dependence of peak power on the total bunch charge the accelerating pulse duration was varied while keeping the accelerating voltage amplitude constant. The dependence of peak power on pulse duration (actually bunch charge) is presented in Fig 3. This dependence is rather close to square law in some region of pulse duration. Note that for small pulse duration given interaction length 6 cm is not sufficient for formation of SR spikes. For long electron pulses saturation of grows of peak power obviously related with the fact that pulse became too long to provide coherent radiation from all over pulse length. Actually, subsequent microwave spikes emitted with increasing pulse duration. Note that experimental dependence is rather close to results of simulations based on PIC code KARAT. Microwave pulse shape, pulse width as well as absolute power found from simulations also in good agreements with experimental data. The simulated average peak power for the maximum injection current of 1.5 kA reached 70 MW (after averaging over the high frequency it should be half of the magnitude presented in Fig. 4).

The generated microwave pulses possess high stability and reproducibility. Alongside with capability of operation of RADAN 303 modulator in repetition rate mode and using for bunch transportation dc magnetic fields it gives possibility to generate microwave pulse with repetition frequency of 25 Hz.

REFERENCIES

[1] N.S.Ginzburg, S.P.Kuznetsov and T.M. Fedoseeva, Sov. Radiophysics and Electronics 21, 728 (1979).

[2] N.S.Ginzburg, Yu.V.Novozhilova and A.S.Sergeev, Sov. Tech. Phys. Lett. 22, 359 (1996).

[3] R. H. Bonifacio, B. W. J. McNeil and P. Pierini, Phys. Rev. A 40, 4467 (1989).

[4] N. S. Ginzburg *et al*. Nucl. Inst. and Meth. in Phys. Res. A393, 352 (1997).

[5] V.G.Shpak, S.A.Shunailov, M.I.Yalandin, A.N.Dyad'kov IET.- 1993.-V.36, №1.- P.106-111.

[6] G.A.Mesyats, V.G.Shpak, S.A.Shunailov, M.I.Yalandin Proc. of SPIE Inter. Symp.: Intense Microwave Pulses.-Los Angeles, CA, USA, 1994.- Vol.2154.-P.262-268.

[7] E.A.Abubakirov, N.S.Ginzburg, N. F.Kovalev and M.I.Fuchs, Radiotechnika I Eletronika 34, 1058, 1989

[8] C.D.Korovin *et al*. Pis'ma v ZhTF, 11, 1972 (1985).

[9] M.l.Yalandin, G.T.Smirnov, V.G.Shpak, S.A.Shunailov, Proc. 9th IEEE International Pulsed Power Conference.- Albuquerque, NM, USA, 1993.- P.388-391.

[10] M.I.Yalandin, V.G.Shpak, S.A.Shunailov, M.R.Ulmaskulov Proc. XVII th International Symposium on Discharges and Electrical Insulation in Vacuum.- Berkeley, CA, USA.- 1996.- Vol.2.- P.635-639.

BEAMS'98

12th INTERNATIONAL CONFERENCE ON HIGH-POWER PARTICLE BEAMS
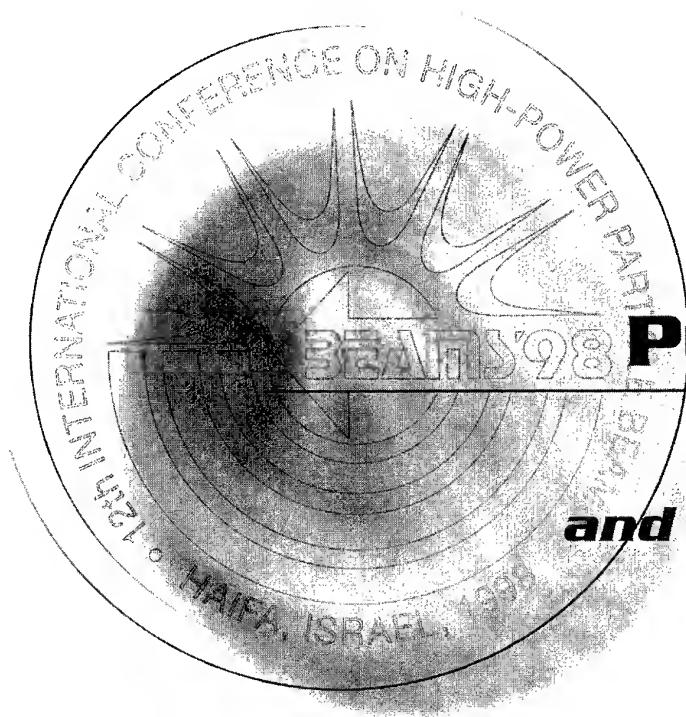
POSTERS

Ion Beams and Diodes, ICF

INVESTIGATION OF LARGE-AREA MULTIARC PULSED ION SOURCE PLASMA PARAMETERS

V. Engelko[2], H. Giese[1], B. Ljublin[2], S. Schalk[1]

1 - Forschungszentrum Karlsruhe, INR, Postfach 3640, D-76021 Karlsruhe, Germany
2 - Efremov Institute of Electrophysical Apparatus, 189631, St. Petersburg, Russia

Abstract - Using plasma probes of different geometry and spectroscopic methods, crucial plasma parameters like electron temperature, plasma density and plasma potential were measured on the multiarc large area ion source (MAIS). MAIS is a pulsed source of plane geometry and circular circumference, in which the ion emitting plasma is built up by synchroneous ignition of an array of 180 individual discharge units. The total current through all discharge units was varied in the range of 100 - 300 A. The pulse duration, was of the order of $\tau \approx 30$ μs, the applied acceleration voltage U = 10 - 20 kV. Plasma parameters assessed by these measurements were the following: electron temperature near the anode (extractor) grid - 10 - 30 eV, in the spark region ≥ 4 eV. The electron density n_e near the anode grid is in the range of $10^{11} cm^{-3}$ (depending on discharge current, the radial coordinate, and on the potential of the anode grid), in the spark region $\geq 5 \times 10^{13} cm^{-3}$. The plasma potential lies in the range of 50 - 70 V.

1. INTRODUCTION

In MAIS the ion - emitting plasma is built up by an array of individual discharge units homogeneously distributed over the surface of a common discharge electrode [1, 2]. The type of ions produced by MAIS can be controlled by the type of discharge employed. A proton beam is generated when a flash over discharge across a polyethylene(PE) surface is used. Metal or carbon ions are obtained when a vacuum arc discharge is used. Current density, homogeneity, pulse duration, and divergence of the ion beam being produced depend on parameters of the ion-emitting plasma. Obtaining of the information about these parameters was the aim of our measurements.

2. EXPERIMENTAL APPARATUS

The layout of the experimental facility is shown in Fig.1. Plasma parameters were measured by means of Langmuir probes and visible spectroscopy.

Under normal operating conditions, a high voltage pulse of positive polarity was applied to the anode discharge electrode and to the anode grid. This leads to flashover discharges between the body of the discharge electrode and the grounded individual needle electrodes (i.e. across the surface of the PE plugs),and results in the formation of a plasma layer from which, after its expansion to the anode grid, ions can be extracted.

During the probe measurements the anode grid was substituted by a metal plate with holes, through which the probes were inserted. A high voltage pulse of negative polarity was applied to the needle electrodes.

The anode discharge electrode was grounded. This modification of the electrical circuit allowed to arrange the probes under ground potential without perturbation of the plasma production process. Nine probes were mounted along the diameter of a metal plate. Four probes had a cylindrical geometry with collecting area of $0.08 cm^2$. Five probes had a flat geometry with collecting area of $0.33 cm^2$. The
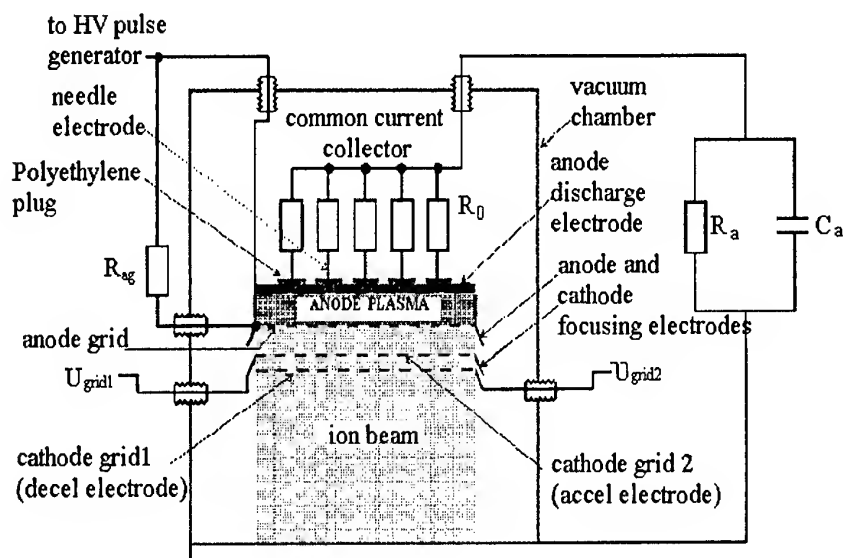
Fig.1 Schematic of the large area multiarc ion beam source MAIS

information about plasma parameters in the spark regions was obtained with the help of visible spectroscopy. The integral spectrum was recorded using KODAK-3600 film in the range of 230 - 600 nm. The chronological behavior of the spectral lines intensity was analyzed by the monochromator, photomultiplyer and oscilloscope. The measurements were performed under different amplitudes of the high-voltage pulse U.

3. EXPERIMENTAL RESULTS

3.1 Probe measurements
In Fig. 2 the oscillogramms of the discharge
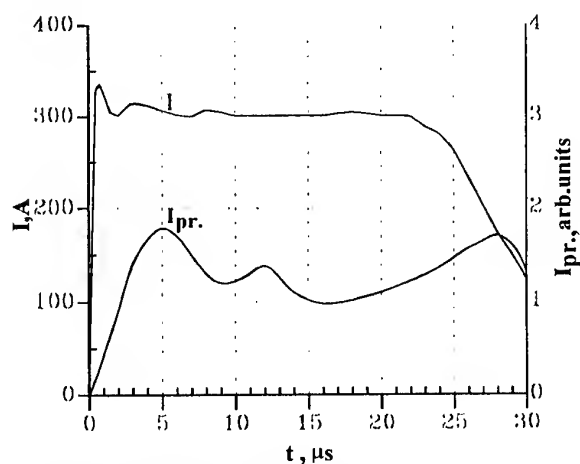
Fig.2 Discharge current and ion saturated probe current oscillogramms

current and of the ion saturation current to the probe (representing the temporal behavior of the plasma density) are shown. One can see that the plasma density reaches its quasistationary value within 5 μs. Such a behavior is in good agreement with the model of the plasma formation described in [2]. Examples of typical PC are given in Fig.3.
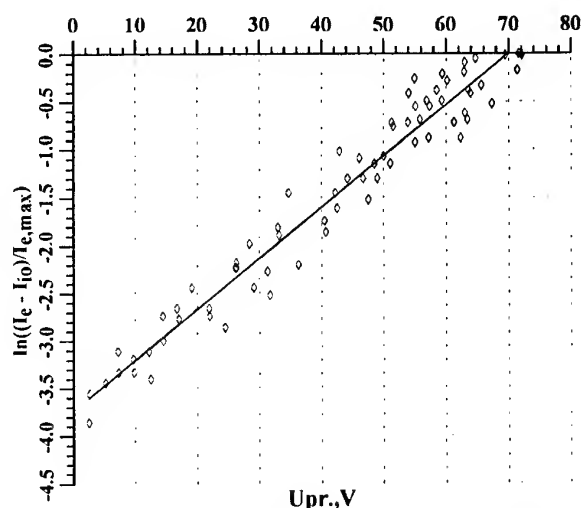
Fig.3 The probe U-I-characteristic for t=11μs from the beginning of the pulse

Here each point represents an average value over 5 shots. One can see that dependence $\ln(I_e)$ on U_{pr} (I_e - electron current to the probe, U_{pr} - probe potential) is practically linear. It

means, that the plasma electrons have a Maxwellian energy distribution and this dependence can be used for determination of the plasma electron temperature T_e.

The measurements yielded the following results:

-the electron temperature changes in time in the range of 10 to 20 eV. In the middle part of the pulse, the most probable value of T_e is 20 eV;

-the plasma density, determined by the ion saturation current, is in the range of 10^{11} cm^{-3}. It depends on time, discharge current, radial coordinate, and on the potential of the anode grid. The latter can be controlled by means of the resistor R_{ag} inserted between this grid and the discharge electrode. When $R_{ag} = 0$ the anode grid potential is equal to the potential of the discharge electrode. When $R_{ag} = 1.5$ kΩ the anode grid adopts floating potential.

In Fig. 4 the radial distribution of the plasma density is shown ($R_{ag} = 1.5$ kΩ , U = 14.5 kV). It has Gaussian shape caused by plasma recombination on the wall of the insulator situated between the anode grid and the discharge electrode.
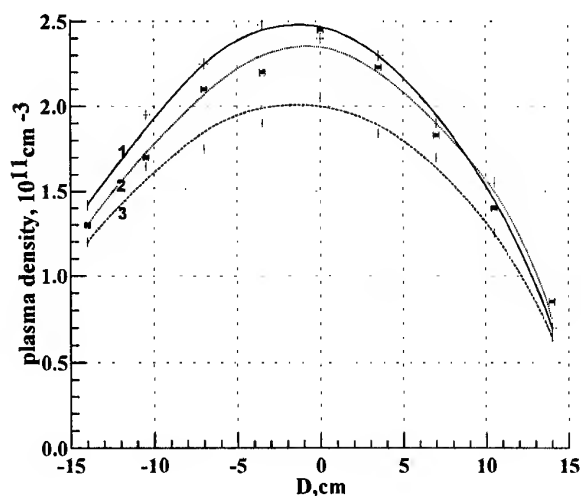
Fig.4 Radial distribution of the plasma density.
1 - 11μs, 2- 16μs, 3 - 21μs after start of current pulse

In the case of $R_{ag} = 0$ the plasma density was found to be about two times smaller then in the case of $R_{ag} = 1.5$ kΩ. Therefore, the difference

in the magnitude of the ion current for $R_{ag} = 0$ and 1.5 kΩ observed in [2] can be explained by difference in the values of the plasma density in these two cases.

The plasma density becomes proportional to the discharge current when it exceeds a certain value, which is apparently necessary for ignition of the majority of the discharge units.

The plasma floating potential changes in time in the range of + 40 $\div$-50 V. In the middle of the pulse its typical value lies in the range between -20 and -50 V. The plasma potential relative to the discharge electrode is in the range of +50 $\div$ +70 V and depends on R_{ag}. For $R_{ag} = 1.5$ kΩ the plasma potential is less then for $R_{ag} = 0$.

3.2 Spectroscopy measurements

The spectroscopy measurements revealed that the typical spectrum of the plasma in the spark region contains lines of hydrogen H_α, H_β, H_γ.and the carbon ion lines CII. The half width of the H_β line was found to be 0.05 - 0.055 nm and exceeds the apparatus resolution (0.025 nm). The broadening of this line is caused only by the Stark effect, since the influence of the Doppler effect on neutral atoms is negligible. Estimations show, that the observed broadening of the H_β line corresponds to a plasma density exceeding $5\times10^{13}cm^{-3}$ [3]. The half-widths of the carbon ion lines at 426.7 nm and 391 nm corresponded to the apparatus resolution. The absence of the broadening of the CII lines allows to conclude that the temperature of the carbon ions does not exceed 1 - 2 eV.

In Fig.5 an example of the oscillogramms of the chronological behavior of the spectral lines H_β and CII and of the discharge current is given. The analysis of the oscillogramms shows, that the rate of hydrogen ionization in the range of the sparks is high when the current through the spark exceeds 2.5 - 3 A.

The decrease of the CII line intensity 10μs after pulse beginning suggests the existence of C^{+2} ions in the discharge in this time period. It is known that the composition of a plasma allows to draw conclusions concerning the elec-

tron temperature [4]. To assess this parameter it is of vital importance to use an adequate model of the ionization state. In our case the determination of the ionization state proves a difficult task since the plasma discussed here is both, of inhomogeneious and non-stationary. We are therefore limited to relative rough estimations of the ionization state, using a non-stationary Corona model [4, 5].With such a model one finds an electron temperature T_e in the spark region > 4 eV. The density of the hydrogen atoms at the beginning of the discharge is $6 \times 10^{14} cm^{-3}$. The estimations confirm that in the source plasma the unexcited double ionized carbon ions can also exist.
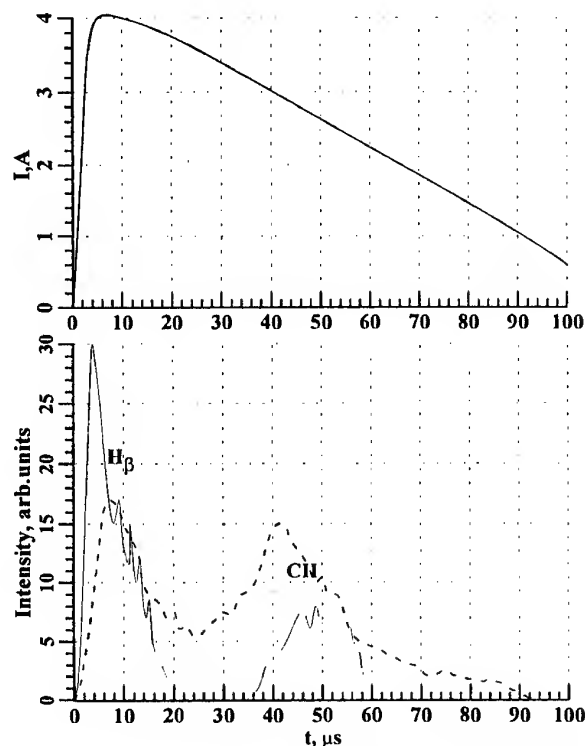
Fig. 5 Chronological behavior of the spectral lines intensity in the spark region

4. CONCLUSIONS

The parameters of the plasma produced in the multiarc pulsed ion source MAIS were measured with the help of Langmuir probes and visible spectroscopy. It was found that in the spark region, the plasma electron density exceeds $5 \times 10^{13} cm^{-3}$, the electron temperature is in the range $T_e \geq 4$ eV. The rate of the hydro-

gen ionization is rather high when the spark current exceeds 2.5 - 3A. Apart from protons, the plasma contains single and, probably, double - ionized carbon ions. The electron temperature of the expanded plasma is in the range of 10 - 20 eV, the plasma density is of the order of $10^{11} cm^{-3}$, the plasma potential $V_p = 50 \div 70$ V. The plasma density and potential are sensitive to the potential of the anode grid. When the grid is under plasma floating potential, the plasma density is about two times higher and the potential is lower than in the case where the potential of the grid corresponds to the potential of the discharge electrode The radial distribution of the plasma density has the Gaussian shape.

REFERENCES

1. V. Engelko et al., "Formation of an intense proton beam of microsecond duration" in Proc.11th Int. Conf. High Power Particle Beams, Prague, Czech. Rep., vol. 1, 1996, pp. 95 - 100.
2. V. Engelko et al., " Large - area multiarc ion beam source "MAIS" in IEEE Transactions on plasma science, vol. 25, No. 4, August 1997,pp. 722 - 728.
3. Plasma Diagnostics. Edited by W. Lochte-Holtgreven. North-Holland publishing company, Amsterdam, 1968.
4. Plasma diagnostic techniques. Edited by R. Huddelstone and S. Leonard. Academic Press, New York - London, 1965.
5. L. Vainshtein, I. Sobelman, E. Yukov. Excitation of atoms and broadening of the spectral lines (in Russian). Moskow, Nauka. 1979.

THE EFFECT OF THE PLASMA POTENTIAL ON CHARACTERISTICS OF BEAMS FORMED BY ELECTROSTATIC ION OPTICS

N.V. Gavrilov, D.R. Emlin, V.V. Bersenev
Institute of Electrophysics RAS,34 Komsomolskaya Str., Yekaterinburg, 620049, Russia

ABSTRACT

In glow-discharge based plasma emission structures the potential difference $\Delta\phi$ between plasma and the screen electrode of the ion optics may equal 0 -1 kV depending on the electrode system. This paper presents results of computer simulation and experimental study of the formation of argon ion beams having the energy of 0.5 - 50 keV and the current density of 1 - 10 mA/cm^2 at various $\Delta\phi$ values. It is shown that large $\Delta\phi$, which are typical of hollow-cathode discharges, have an effect upon the efficiency of the ion extraction from plasma, require a higher accelerating electric field strength and/or cause a drop in the maximum density of the beam current. Extraction of ions and formation of high-perveance low-divergent beams are impaired due to a presence of thick layer of space charge, which affects the shape of the plasma boundary in apertures of the ion optics.

INTRODUCTION

A high ion current density j and its uniform distribution j(r) over the beam cross-section are the main requirements imposed on sources of broad beams (BB's) used for surface modification of materials. These characteristics of BB's generated by multi-aperture ion optical systems (IOS) depend not only on the density and spatial homogeneity of plasma, but also on the conditions of formation and propagation of the beams (angular divergence and the IOS-collector distance). The divergence angle θ of the beams formed in separate apertures of the IOS should be a minimum, but sufficient to provide overlapping of the beams and a uniform distribution j(r). If the angle θ increases with j, the initially homogeneous beam may transform on its drift length into a beam with a profile j(r) similar to the Gaussian one.

The beam formation conditions depend on the potential difference $\Delta\phi$ between plasma and the screen electrode of the IOS. In glow-discharge based plasma emission structures [1] ion emitting plasma is produced in chambers whose walls may carry cathodic or anodic potential depending on the electrode system. The surface area of the screen electrode of the IOS generating BB's is, as a rule, comparable with the total surface area of the chamber walls. Therefore the electrode potential may prove to be adjustable on a limited scale so as to avoid impairment of the discharge operation conditions. For example, the increase in the potential at elements coming in contact with a plasma of the hollow-cathode discharge was followed by rise of loss rate of fast electrons and the increase in the voltage and gas pressure required for the stable discharge operation. In these type of plasma-emission structures a layer of space charge appears between plasma and the screen electrode. The potential drop $\Delta\phi$ across this layer may reach ~1 kV and the layer may be 1-10 mm long depending on the plasma density. The space charge layer affects the shape of the plasma boundary and conditions of the ion beam formation. This paper presents results of computer simulation and experimental study of formation of argon ion beams having the energy eU = 0.5 -50 keV and the current density of 1-10 mA/cm^2 in systems employing a glow-discharge based plasma emitter of ions.

COMPUTER SIMULATION

We simulated conditions of formation of ion beams in a single-aperture accelerating-decelerating IOS with the hole diameter d ~ 3-15 mm, the accelerating gap length l ~2-20 mm and the electrode thickness h ~ 1-3 mm. Two energy intervals were taken: several keV and several tens of keV. The ion emitter was argon plasma with the single-charged ion density n ~ 10^{10}-10^{12} 1/cm^3 and the electron temperature of 5-10 eV. The no-loss conditions of the beam at the IOS electrodes were determined, the angle θ of the beam divergence was calculated, the current density distribution j(r) at any preset cross-section of the beam was found. The relationship between the flow of ions to the IOS screen electrode and the beam current was estimated. The calculations were made for $\Delta\phi = 0$ and $\Delta\phi = 0.5$-1 kV.

When $\Delta\phi$=0, the beam behavior corresponded to the relationship θ=0.29S(1-2.14 P/P$_0$) [2], where S = d/l, P is the working perveance, and P$_0$ is the maximum perveance for a plane diode. Figure 1 shows the angle θ of a low-energy beam at the exit of an accelerating-decelerating IOS as a function of the ratio between the net (determining the beam energy) and total (at the accelerating gap) voltages U$_n$/U$_t$, with the ion emission current density j = 2 mA/cm^2 being constant. Calculations were performed for three versions of the IOS, which had the same hole diameter d = 4 mm, but differed by the gap length l and, correspondingly, values of the voltage U$_t$, which were chosen so as to correspond to the optimal perveance P ~ 1/2 P$_0$. Minimum values of the angle θ over a wide range of U$_n$/U$_t$ were obtained at an optimal working perveance P for minimum S (largest l). To reduce the loss of the beam at the IOS electrodes at the same current density j during simulation of the IOS with $\Delta\phi$ = 0.5-1 kV, the gap length l had to be decreased at least by a factor of two. A high strength of the field in the accelerating gap of this IOS suggests that the highest attainable level of beam current density is lower than in systems with $\Delta\phi$ = 0.

In a high-voltage IOS with U = 30-50 kV and j = 1-30 mA/cm^2 the presence of the layer does not hinder formation of well-focused beams. Figure 2 shows the current density j and the angle θ as a function of the plasma density n for an IOS with d=10 mm and l=15 mm. The increase in n was followed by displacement of the plasma boundary, redistribution of the flow of ions from plasma at the periphery of the IOS apertures, the decrease in the beam current, and alteration of the angle θ. The efficiency of the ion extraction from plasma and the angular divergence of the beam depended on the combination of the parameters j, $\Delta\phi$, eU and l, and the screen electrode thickness.
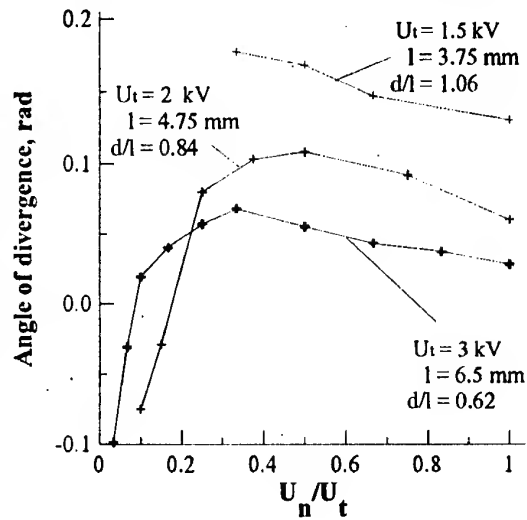
Fig. 1. Ion optics simulation results for j = 2 mA/cm^2, d = 4 mm.
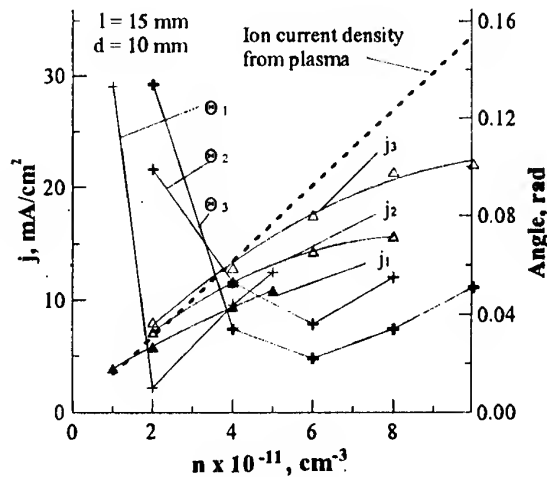
Fig. 2. Ion optics simulation results for U = 30 (1), 40 (2), 50 (3) kV.

EXPERIMENTAL STUDY

a) Formation of high-energy ion beams

The ion source based on a hollow-cathode discharge in a magnetic field [3] was used in the experiments. The ion optics of the source was replaced by a single-aperture three-electrode IOS (d = 1 = 10 mm). The beam profile at the distance of 300 mm from the IOS was measured using a probe in the form of a wire 0.5 mm in diameter, which moved in a slit 2 mm wide. Figure 3 shows the angle θ as a function of the accelerating voltage for different values of the current density of ions from plasma: j = 4 (1), 6.7 (2) and 10 (3) mA/cm^2. The angle of the beam divergence θ was evaluated from the ratio between the width at the half-height of the beam profile and the drift length of the beam. As is seen from Fig. 3, the presence of the cathodic layer does not impede achievement of small θ. The working subintervals of the IOS voltage providing formation of uniform BB's are located on both sides of the minimum in the dependence $\theta(U)$. These subintervals have a small width (<10 kV). The subinterval on the right-hand branch is narrower, but this regime ensures a better extraction of ions from plasma (see Fig. 2). A change in the density j or the gap length l is accompanied by displacement of the IOS working range on the energy scale.

Fig. 3. Beam divergence for j = 4 (1), 6.7 (2), 10 (3) mA/cm^2.

b) Formation of low-energy ion beams

Ions were extracted from plasma produced in the anodic chamber of the discharge system and therefore the potential of the screen electrode could be adjusted between anodic and cathodic values. In the case of a multi-aperture IOS, the discharge operation conditions and the density of plasma generated under the two regimes differed little thanks to a large total surface area of the apertures and the effect of the accelerating field. Figures 4 and 5 show the U_n/U_t dependencies of the beam current I_1 and currents in the circuits of the accelerating (I_2) and output (I_3) electrodes of an accelerating-decelerating IOS forming a beam of argon ions with the constant energy eU_n = 1 keV. The dependencies were taken at the floating (Fig. 4, $\Delta\phi \sim$ 60 V) and cathodic (Fig. 5, $\Delta\phi \sim$ 1 kV) potentials across the screen electrode and at a constant discharge current. In both cases a maximum beam current was achieved at the maximum strength of the accelerating field corresponding to U_n/U_t = 0.3. The half-angle of divergence, which was estimated from the profile width of the beam formed by a single aperture of the IOS, was 3-4° at the emission current density of 1-1.5 mA/cm^2. However, the gap length had to be decreased from 5 to 3 mm in the system with the cathodic potential (Fig. 5) in order to obtain comparable parameters. Given the same gap length l=5 mm, the current loss in the electrode circuits of the IOS with $\Delta\phi \sim$ 1 kV was much greater than the beam current.
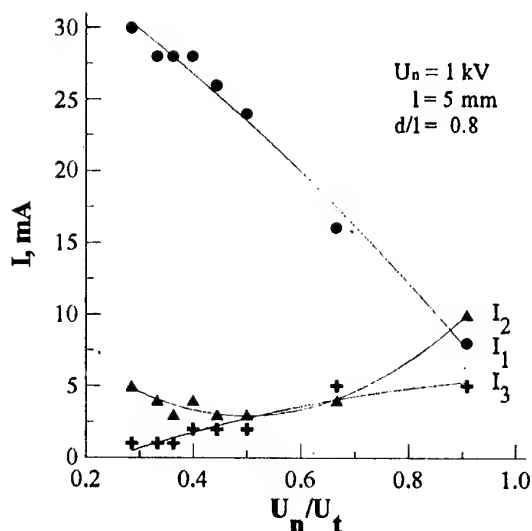
Fig. 4. Low energy ion beam
formation ($\Delta\phi = 60$ V).
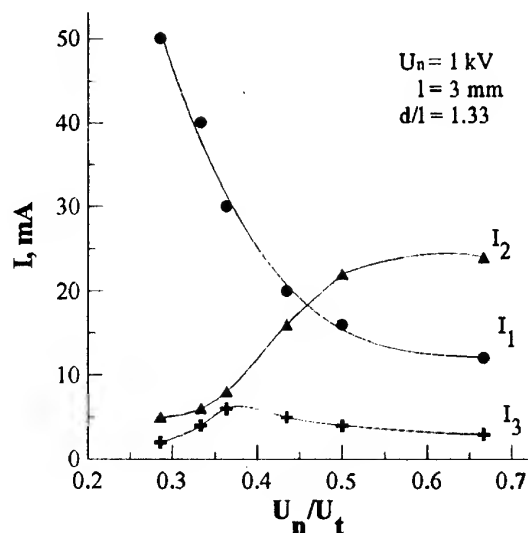
Fig. 5. Low energy ion beam
formation ($\Delta\phi = 1$ kV).

CONCLUSIONS

1. A considerable potential difference ($\Delta\phi = 0.5$-1 kV) between hollow-cathode glow-discharge plasma and the screen electrode of the ion optics greatly affects extraction of ions from plasma, the maximum current density and angular divergence of the ion beam.

2. In high-voltage (U ~ 50 kV) ion optics (IOS) a layer of a positive space charge at the screen electrode of the IOS mainly affects extraction of ions from plasma. The efficiency of the ion extraction also depends on the plasma density, the U value, and geometrical dimensions of the IOS elementary cell.

3. In low-voltage (U ~ 1 kV) IOS the presence of this layer causes an increase in the angle θ of the beam divergence and limits the maximum beam current density j. To form a beam with preset θ and j, the field strength in the accelerating gap should be increased as compared to the system with $\Delta\phi = 0$.

ACKNOWLEDGMENTS

REFERENCES

[1] N.V. Gavrilov, G.A. Mesyats, G.V. Radkovskii, and V.V. Bersenev. Surface and Coating Technology, 96, No. 1, pp. 81-88 (1997).

[2] J.R Coupland, T.S.Green, D.R.Hammond, A.C.Riviere. Rev. Sci. Instrum., 44, No. 9, 1258-1270 (1973).

[3] N.V. Gavrilov, G.A. Mesyats, S.P. Nikulin, G.V. Radkovskii, A. Elkind, A.J. Perry, and J.R. Treglio. J. Vac. Sci. Technol. A, 14, p. 1050-1055 (1996).

MAGNETICALLY INSULATED ION DIODE IN PLASMA OPTICAL MODE

A. Goncharov, I. Litovko, I. Protsenko

Institute of Physics NASU, prospekt Nauki, Kiev-39, 252650, Ukraine

Introduction

Magnetically insulated diode gap in the plasma optical mode (MDG) is a special case of the one-dimensional DG with magnetized electrons and free ions. The conception of such DG is based on simplest physical models of many devices, e.g. accelerator with a closed drift of electrons (ACD), ion magnetron, magnetically insulated pulse diode etc. These models have their specific features depending on the type and destination of the device. The first simplest model of the stationary ACD [1] set as a basis for further investigations. There were supposed space charge of an accelerated ion beam is compensated by electrons created in the DG volume by shock ionization of the low pressure gas by electrons themselves, which than go away to the anode due to permanent mobility along the DG in the strong electric field, caused by rigid collisions with atoms of a gas. Within the framework of this model it was found in [1] for the regime of quasi-neutrality the self-consistent stationary distributions of the potential along the DG, providing acceleration of the ion beam without restrictions on a density, in other words, the conditions were found for which the parameter $\alpha = j_b / j_{bl}$ $(j_{bl} = \frac{1}{9\pi}(2e/M)^{1/2}\varphi_0^{3/2}/d^2$ is a Langmuir current in the DG with a length d and voltage φ_0) has no upper limit. At the same time, the stationary regime for this method of compensation of an accelerating DG is accompanied by slow (proportional to the time of space ionization of low pressure gas atoms) increasing of the ion beam current.

Progress in generation and formation of power ion beams with short duration ($\tau \leq 1\mu s$) and current densities exceeding the Langmuir limit in tens times increases an interest to the analysis of a physical nature of these effects. In the works carried out in this connection it was proposed [2] and developed [3,4] a stationary one-dimensional model of Larmor electron circles starting from the cathode and forcing out to the anode by their space charge an applied electric field of MDG. Within the framework of this model essential increasing of the parameter α up to values $\alpha \gg 1$ is noticeable only for magnitudes of a homogeneous magnetic field close to the critical one $H* = \frac{1}{d}\sqrt{\frac{2m_e\varphi_0 c^2}{e}}$, since for H→H* electron orbits tend to fill the whole volume of the DG. However, for magnitudes of the magnetic field H≥2H* α~1 with the help of this model it is not possible to account for the experimental data accumulated in the course of investigations of the magnetically insulated pulse diodes [5].

Directional shifts of electrons along the DG (electron current leakage onto the anode) for insulated magnetic fields H≫H* serve as a base for creation of stationary state models [5], in which dynamics of the electron component is described under assumption of existence of the anomalous diffusion transfer mechanisms. That is why, in the numerical experiment [5] the directional to the anode polarized electron drift was created by introduction of the model electric field of the turbulent oscillations. In the pulse relativistic diode $\left(e\varphi_0 > m_e c^2\right)$ with a strongly marked effect of electron diamagnetic, which deforms essentially applied fields EH, there were obtained current densities of non-magnetized hydrogen ions, exceeding the Langmuir limit by the factor more than order.

For the case when relativistic and diamagnetic effects are negligible, the applied
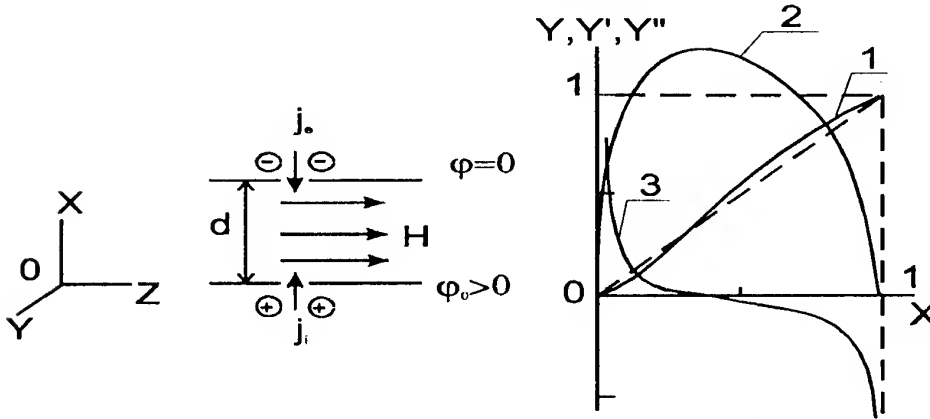
Fig. 1.   **Fig. 2.**

magnetic field H>>H*, the accelerating magnetically insulated diode gap become analogous to a certain extent to the part of the plasma optical system. We call it an elementary plasma optical cell, in which a voltage $\varphi_0=\varphi_1-\varphi_2$ applied to external electrodes is fixed by magnetic field strength lines $\mathbf{H} \| Oz$ (fig. 1) with a distance between them x=d.

MDG in plasma optical mode

In the plasma optical mode of the MDG model it is essential an assumption of correctness of the Ohm law for the electron current, due to which a behavior of electrons is self-consistent with the electric field of the one-dimensional DG. For basing of this assumption it is enough to introduce an anomalous cross mobility supposing that electron gas state is turbulent in the crossed EH fields. Stationary electric field distributions and maximum ion and electron currents passed through the system we will find from the smooth and monotonous solutions of the Poisson equation under assumption that there are no reflected particles.

For the case of accelerating DG (initial velocity at the entrance $V_b=0$) it is followed by the creation of a double layer with maximum E field exceeding the vacuum field by a factor of 1.24. The limiting density of the passing beam is 3.24 times higher than the Langmuir limit. On the fig. 2 it is presented non-dimensional distributions of the potential (1), electric field (2) and space charge (3), following from the equation for the limiting current $Y' = \gamma \sqrt{\sqrt{Y} - X}$, which is justified for Y(0)=0, Y(1)=1, Y'(0)=0, Y'(1)=0 only in the point $\gamma^* = 2,395$. It is seen, that maximum electric field in the created double layer is realized in the region of quasi-neutrality for the values X≈0,3÷0,4 and it increases rapidly when going from the DG boundaries. Thus, an approximation based on the assumption that electron current on the anode is connected with mobility can be applied even for currents close to the limiting ones virtually in the whole volume.

It is shown in [6] that in the additional accelerating MDG with the input ion beam velocity $V_0 >> (2e\varphi_0/M)^{1/2}$ the quasineutral regimes with $E \approx const$ without restrictions on current density of the passing ion beam can be achieved.

For the such MDG the dissipate instability of short wave oscillations (kd>>1, k is a wave vector, $k \| V_b$), caused by damping on the electrons with finite mobility in crossed EH fields [6], plays the main role in deviation of stationary states. The stationary E-field is of essential

role in the dynamics of the disturbed component of the passing ion beam. Investigations of an effect of non-disturbed parameters $n_b^{\circ}(X)$, $V_b(X)$, $n_e^{\circ}(X)$ changes in the stationary field $E^{\circ}(X)$ on the space evolution of the disturbed beam current density show that the higher initial density and velocity the more effective growth of initial perturbations. This can lead to deformations of the stationary potential distribution and beam current breaks.
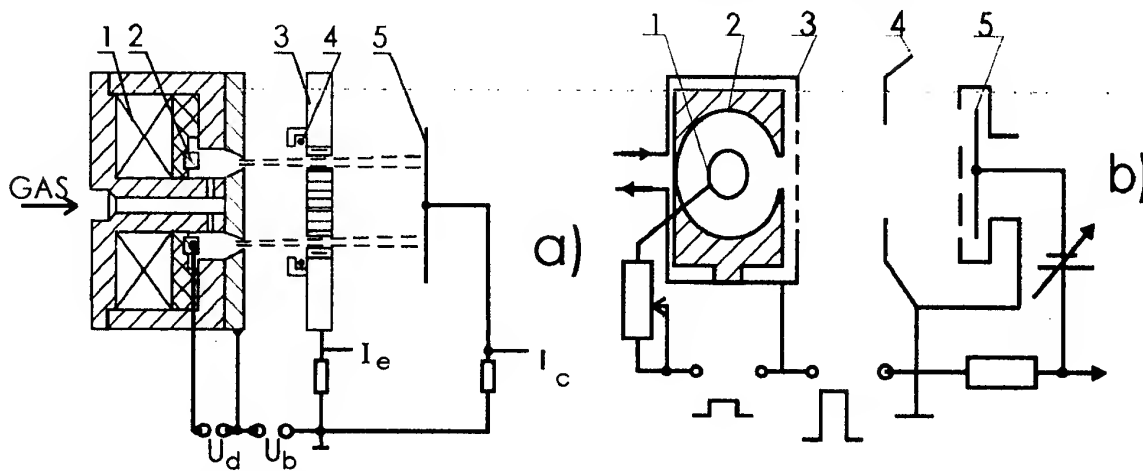
Fig. 3. a) ACD type source: 1-coil, 2-anode, 3-extractor, 4-emitter of electrons, 5-collector; b) a scheme of the setup with a reverse gas-magnetron type source: 1-anode, 2-cathode, 3-cathode loop, 4-extractor, 5-collector.

To compare results of the theoretical analysis of stationary and non-stationary states, experiments have been carried out. As a hydrogen ion emitter, the effective ACD-type source was applied [fig.3(a)]. The insulated H-field in the volume of the accelerating DG was created by the plain coil (extractor). The experiments show that introduction of the H-field on the DG increases its capacity and improves electric stability during the time less than the time of development of self-maintained discharge in the crossed EH field. The maximum amplitude of ion current pulses on the collector I_c ($\tau \leq 30\mu s$) is determined by correlation of high voltage pulses U_b <20kV, magnetic field $H \leq 0.3T$, gap length d=1cm, and also by presence of thermoemission from the extractor plain.
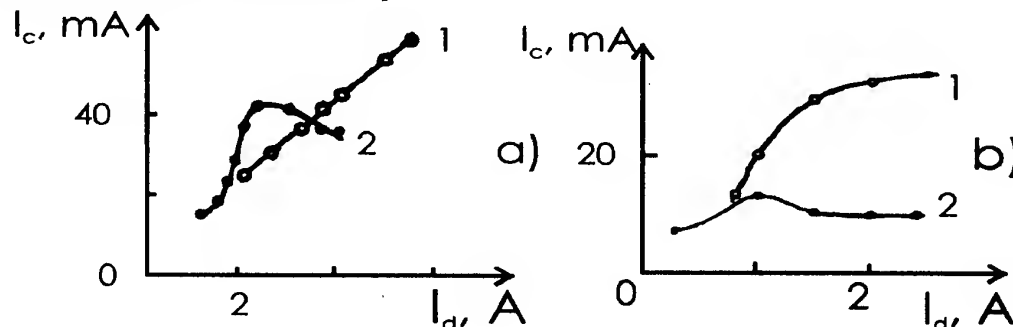
Fig. 4. Dependency I_c vs I_d: (a)—U_b=15 kV, d=4 mm; (b)—U_b=3 kV, d=8 mm; H: 1-0,2T, 2-0 (a,b)

Maximum amplitude of the non-compensated electron current fall down for H=H* and trends smoothly toward the null for H>> H*. Noise modulation of the current signal increases sharply (up to 100%); this testifies to mechanisms of anomalous cross mobility of electrons. It is possible to estimate correctly the capacity of MDG with magnetized electrons by comparison of dependency of I_c on I_d in the source with an analogous depende 2 when there are no electrons in the gap. Such experiments shown that sufficient quantity ot compensated electror 0 ıds to growth of the electric field in the MDG, keeping of the emission boundary

with more dense plasma and, hence, formation of the beam with a density increased by the factor three (fig. 4).
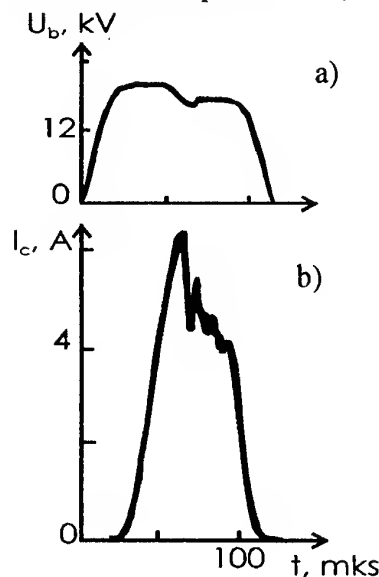
In the additional accelerating MDG, where stationary states do not restrict the limiting density of the passing beam, the restrictions can arise as a result of development of collective processes. Experimental investigations of the ion beam passing through the accelerating MDG with magnetized electrons were carried out using one of source modifications of reverse gas-magnetron type [fig. 3(b)]. An accelerating voltage pulse ($\tau \approx 100\mu s$, $U_b \leq 25kV$) was applied between the extractor (a frame 1X1 cm) and the source cathode unit with a slit ($d \leq 1cm$) for hydrogen ion beam injection into the MDG. For magnetic insulation of the DG it was used a magnetic field ($H \leq 0.25T$) created by pulse of current, passing through the cathode coil. The collector who was 1 cm behind the extractor measured the current and density of the beam.

Fig. 5. Oscillograms for high-voltage pulse -a).; total beam current - b)

Experiments show secondary electrons from the extractor are of importance for enhancement of the source's ion emission and beam passing through the gap. The measurements of potential distribution in the gap show that ion beam is accelerated mostly in the narrow layers in the vicinity of electrodes ($\leq 1mm$). This creates favorable conditions for developments of beam dissipate instability on electrons in the DG. Experiments show (see oscillograms fig. 5) that passing of the ion beam through the gap can be unstable. With a growth of I_d current it is observed increasing of current onto the collector which is followed by current break. When decreasing accelerating voltage one can observe analogous breaks. At that deformations of collector current pulse correlate with current changes on the extractor. Beam current instability can be explained qualitatively on the base of carried analysis. It is important to note accelerating MDG in accordance with calculations can operate currents exceeding essentially the Langmuir limit. Current density of hydrogen ions on the extractor (about 6 A/cm^2) achieved in the course of experiments exceeds the Langmuir density of the uncompensated ion beam by the factor more than order.

Conclusion

Thus, in this work it is proposed and experimentally investigated the model of magnetically insulated diode gap in the plasma optical mode. It is shown, that use of such MDG can provide unique parameters of the ion beam (current ~6A, current density - 6A/cm^2 for pulse duration about 100μs and energy 20keV) at the exit from the extractor.

References:
[1] Jarinov A.V. Popov Yu.S. Zh. Tekh. Fiz. 37, №2, 1967
[2] Sudan R.N., Lovelace R.Y. Phys. Rev. Let. 31, #19, 1973
[3] Antonsen T.M. Ott E. Phys. Fluids, 19, #1, 1976
[4] Bergeron K.D. Appl. Phys. Let., 28, #6,1976
[5] Poukley I.M., Humphries S., Lockner Jr. and Flow T.R. - Phys. Fluids, 25,8,1982
[6] Goncharov A., Protsenko I., Ukr., Fiz. Zh. 36, 11,1991

EFFECTS OF AXIAL CURRENT IN AN EXTRACTION GEOMETRY APPLIED-B ION DIODE*

J.B. Greenly, D. Sinars, B.R. Kusse
Laboratory of Plasma Studies, Cornell University, Ithaca, NY 14853 USA

A new diode voltage monitor has been developed for the COBRA (2.5 MV, 120 kA, 40 ns) accelerator. It consists of a magnetically-insulated transmission line (MITL) connected on axis across the extraction geometry, applied-B ion diode gap. The monitor is connected at the cathode (ground) side of the diode, passes through the 3.1 m long hollow anode electrode of the COBRA four-stage linear inductive voltage adder, and then terminates. The COBRA MITL, ion diode, and monitor are shown in Figure 1. The current in the MITL wave traveling from the diode is used to calculate the voltage at the diode.
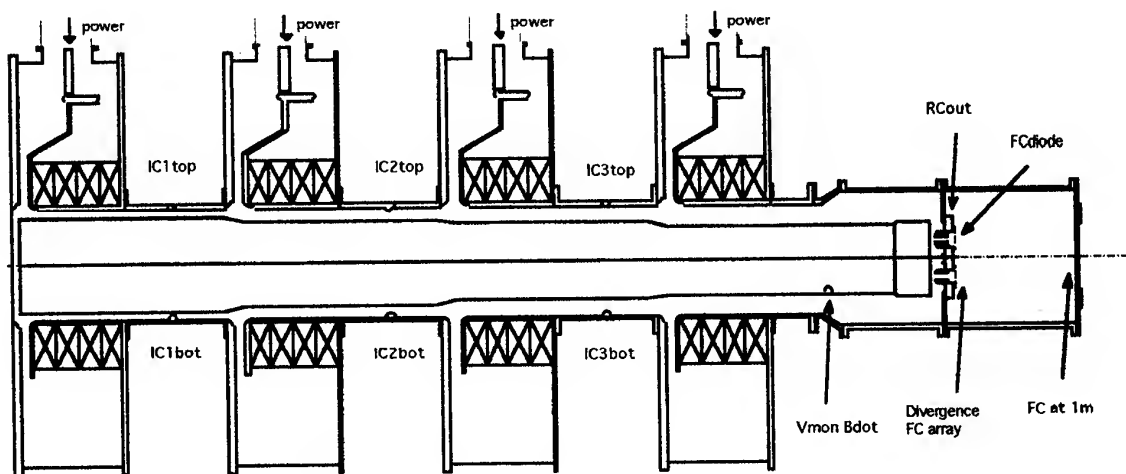
Figure 1. The COBRA linear inductive voltage adder, with the voltage monitor MITL internal to the anode stalk (in positive polarity), connected to the cathode on the diode axis.

Several different monitor configurations have been studied. Both 105 ohm and 260 ohm vacuum impedances have been used, with the MITL monitor terminated in either a short circuit or an open circuit connection. In the open circuit case the monitor was terminated using a 60 cm long axial polyacetal rod. To measure the monitor current Bdot loops were placed at 45 cm and 280 cm from the diode. The 45 cm location is used to infer the diode voltage, and the other location provides further information for understanding the transmission line characteristics of the monitor. With the shorted termination, the reflected wave arrives back at the diode after two transit times of the monitor (about 22 ns), which doubles the monitor current and further reduces available diode current. The wave is partially transmitted and partially reflected from the complex diode geometry. This complexity makes it difficult to unfold the diode voltage. The most useful voltage monitor configuration is the open termination at the far end. It is observed that this termination eliminates the first reflection of the forward-going wave. As predicted by MITL theory, as long as the impedance of the termination is higher than the self-limited impedance of the MITL, the vacuum electron flow is lost at the termination and there is no reflected wave. The Bdot signals at 45 cm are clearly interpretable as simple forward-going waves for about 35 ns. After this time a high-frequency component appears on the Bdot whose origin is not understood. The inferred voltage is unreliable after this time.

Figure 2 shows Bdot signals for the shorted and open cases, as well as an integrated trace showing the current doubling of the reflected wave in the shorted case.

Figure 2 shows an unfolded voltage waveform from the open 260 ohm monitor. The Bdot waveform is integrated to get the MITL current. This needs to be multiplied by the effective MITL impedance to find the voltage. For the waveform shown, the effective MITL impedance used was 175 ohms. Time-of flight measurements of beam ions over 1 m from the diode were used to determine the voltage at one point on the waveform, and this point was used to scale the monitor waveform to actual voltage, thus determining the effective MITL impedance. Further analysis will be done to compare the Bdot measurements at all locations to theory.
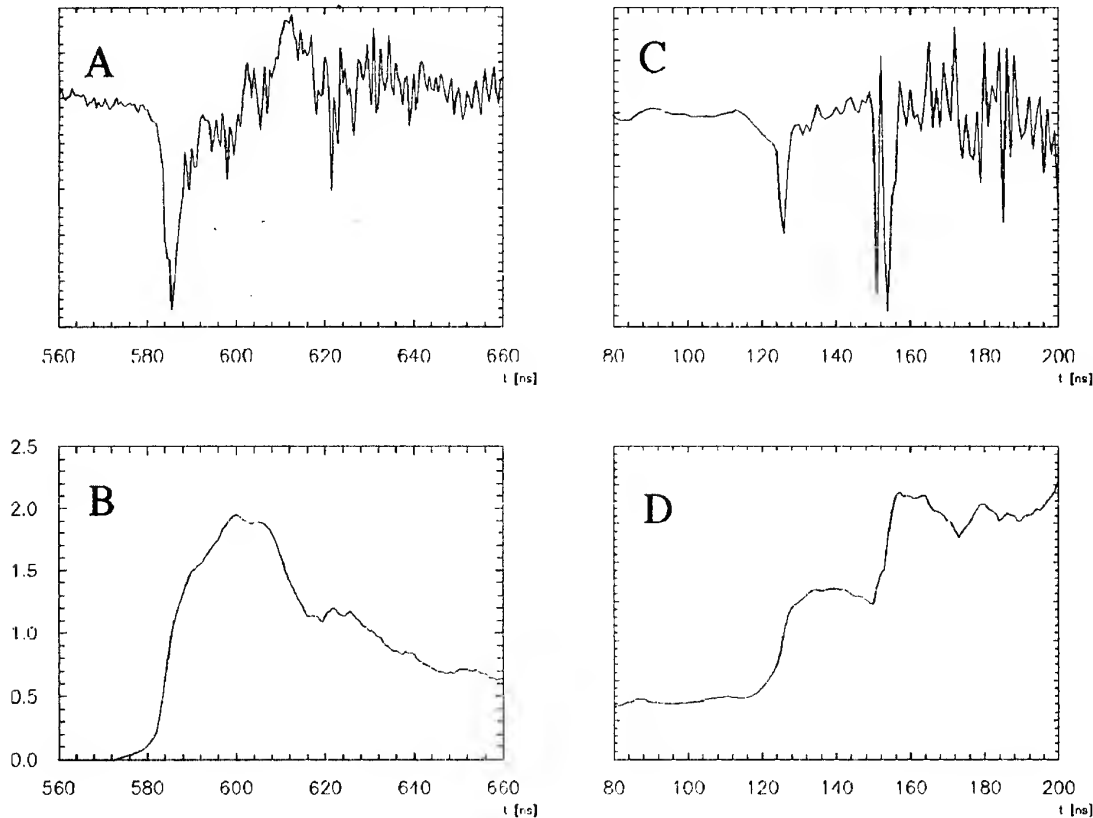
Figure 2. A) A signal from a Bdot voltage monitor at z = 45 cm, open termination. B) Voltage waveform (in MV) derived from the integral of trace (A). C) A signal from the Bdot voltage monitor with shorted termination. D) The integral of trace (C) showing the effect of the reflected wave. The current nearly doubles as the reflected wave arrives after 150 ns.

The on-axis MITL monitor conducts 15- 60 kA depending on the impedance configuration used. It thus imposes a controlled and variable azimuthal magnetic field in addition to the radial applied insulating field in the diode accelerating gap. Compared to operation without the line on axis, the addition of this azimuthal field greatly changes the operation of the diode: it reduces the ion current density in the gap by up to factor of two, it reduces the electron loss current in the gap by more than a factor two, and it decreases the time-integrated microdivergence of the ion beam from the diode by up to 50%.

Table 1 lists the currents in the diode: the ion and electron currents, and the axial (monitor) current, as well as the results from a time-integrated microdivergence diagnostic, for several different values of axial current and diode insulating field.

	12 mm gap V/Vcrit ≈ 2.0		12 mm gap V/Vcrit ≈ 1.5		10 mm gap V/Vcrit ≈ 1.5		10 mm gap V/Vcrit ≈ 2.0
I axial kA	none	45	none	15	none	15	15
I total kA	85	90	105	95	120	110	105
I electron kA	25	10	35	20	45	40	25
I ion kA	60	35	70	60	75	55	65
Divergence mrad HWHM	50 ± 10	30 ± 10	48 ± 5	31 ± 3	45 ± 5	42 ± 3	32 ± 3

Table 1. Peak currents and time-integrated microdivergence for various diode conditions, with and without axial current. The time-integrated divergence is in the radial direction and includes all radial beam sweeping, so is an upper limit on the actual divergence.

The larger monitor current clearly has stronger effects, but at the expense of using more of the available current. Clearly, the presence of the axial current acts to limit the enhancement of ion current density in the gap giving lower ion current. However, this reduction in enhancement is accompanied by a reduction in the electron loss current of the diode, so that the gap efficiency (ratio of ion to ion plus electron current) is actually increased with the axial current. The improvement in time-integrated microdivergence is clear, but the question remains how this relates to useful beam brightness and achievable focused power density.

The first time-integrated diagnostic used a set of three azimuthal slits at different radii to produce collimated beamlets, which impinged upon two identical targets at 30 and 60 mm distances. The targets were ink on stainless steel, which gave a reproducible ablation of the ink without melt of the stainless at about 1 J/cm^2. The ink was less than 8 mm thick, far below the range of 2 McV protons, so the ablation threshold is rather insensitive to ink thickness or ion energy. The widths of the ablated regions at the two distances were fitted by a gaussian to infer the time-integrated divergence of the beamlets. A new diagnostic has recently been developed to give time-resolved information. It consists of an azimuthal slit viewed at a distance of 61 mm by a linear array of five miniature faraday cups with 2 mm spacing and 0.5 mm apertures. The cups are magnetically insulated by a samarium-cobalt permanent magnet. The five cup signals are fitted to a gaussian every 0.4 ns to quantify the instantaneous microdivergence at those times. The current density at the slit is also found using the cup signals, allowing the determination of the instantaneous beam brightness at the slit (in current density over microdivergence squared). Figure 3 shows early results from this diagnostic for a shot with 15 kA axial current and a second shot without an axial current. The qualitative features of these plots are universal for all diode conditions. As the ion current rises, the divergence is relatively low and the brightness steadily grows. At or after peak current, however, the divergence grows and brightness decreases rapidly. Quantitative comparisons of cases with and without axial current will be reported in the near future.

With Axial Current

Without Axial Current

Faraday Cup Position in mm
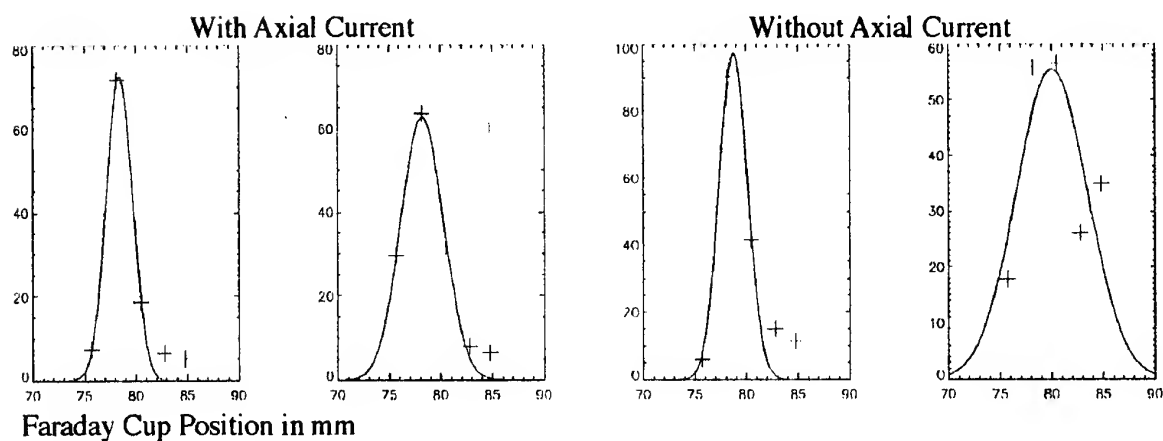
Figure 3. Data from the time-resolved microdivergence diagnostic. Two shots are shown, both with a 10 mm gap and Vcrit/V of about 1.9. The plots above are data from the Faraday cup array for these two shots, with fitted Gaussians, and were taken just before and just after peak power, respectively. Below, the first shot, indicated with square points and a solid line, had 15 kA of axial current. The second shot, indicated with diamond points and a dashed line, had no axial current. The plot below shows the time history of measured microdivergence and brightness for the two shots. Arrows indicate the forward direction of time. The plot for the shot without axial current terminates earlier in time because the data become very non-Gaussian late in the pulse.

Angular Divergence in mrad

Brightness in Amps/cm^{2}mrad^2
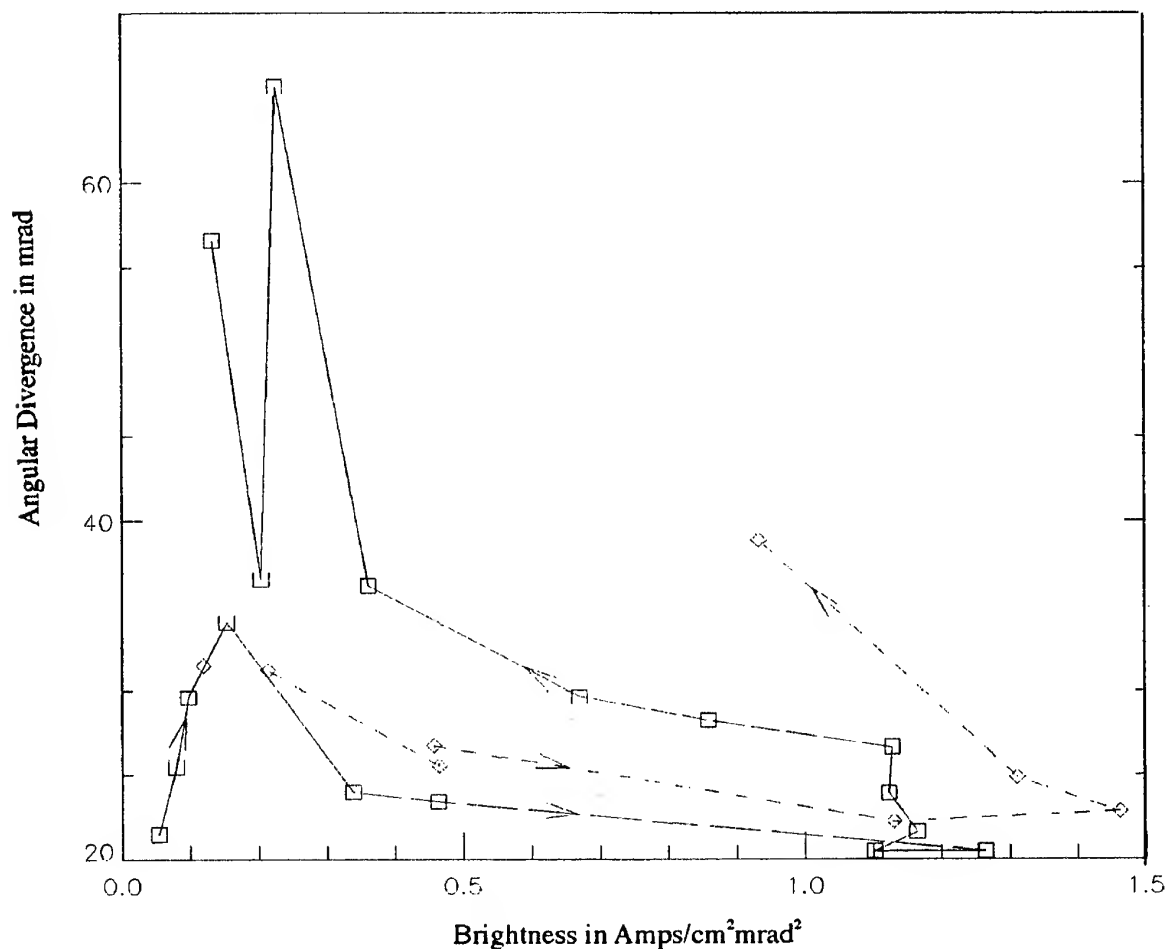
IMPROVEMENT OF BEAM DIVERGENCE BY EMISSION PROFILES WITH BETTER HOMOGENEITY

P. Hoppé[a] M. P. Desjarlais[b], H. Bluhm[a], L. Buth[a], D. Rusch[a], O. Stoltz[a], W. Väth[a]

[a] Forschungszentrum Karlsruhe, Institut für Neutronenphysik und Reaktortechnik, P. O. Box 3640, D-76021 Karlsruhe, Germany
[b] Sandia National Laboratories, P. O. Box 5800, Albuquerque, New Mexico 87185, USA

Abstract

Ion beam divergence is influenced by the emission profile of the beam; inhomogeneities can stimulate the transition from the stabilizing diocrotron mode to the detrimental high divergence ion mode. Applied fields for homogeneous beam emission profiles, which differed in strength and tilt, were designed for the KALIF B_{appl} diode. Experiments were performed on KALIF with these fields. They resulted in the lowest divergences ever measured with this diode. This proves, that the beam emission profile is a controllable key variable to improve the focusing properties of the beam.

Introduction

One of the primary limitations for the maximum power density P_{max} achievable in the focus of light ion diodes continues to be unacceptably high beam divergence Θ, defined as the half angle of the emission cone of a beamlet accelerated in the diode. For extractor type ion diodes P_{max} is related to the beam brightness $B=JV/(\pi\Theta^2)$. In this equation V is the acceleration voltage and J the ion current density. Simulations have shown that the beam divergence can be reduced by improving the uniformity of the ion current density [1]. This diode type supports two large amplitude instabilities: the diocroton mode (high frequency, low divergence) and the ion mode or transit-time instability (low frequency, high divergence). Extraction diodes, with their 1/r dependence of the applied magnetic field, are especially susceptable to a radial skewing of the ion current density, which can stimulate the transition from the benign and stabilizing diocrotron mode to the detrimental high divergence ion mode under conditions that would otherwise favor lower divergence [2]. Experiments were performed with the B_{appl} proton diode on the KALIF accelerator [3] with the main goal to investigate the influence of various applied magnetic field configurations on the emission profile of the beam and on beam divergence.

Field calculations

The ion beam current density J_i of an extractor type diode (r,z geometrie) is $J_i=\chi(r)J_{cl}d^2(r)/g^2(r)$ with the enhancement χ depending on the electron distribution in the acceleration gap with the geometrical gap width d_0 and the Child -Langmuir current J_{cl}. The term $d(r)/g(r)$ -describing the diamagnetic compression- goes to infinity as the diode voltage V approaches the saturation voltage
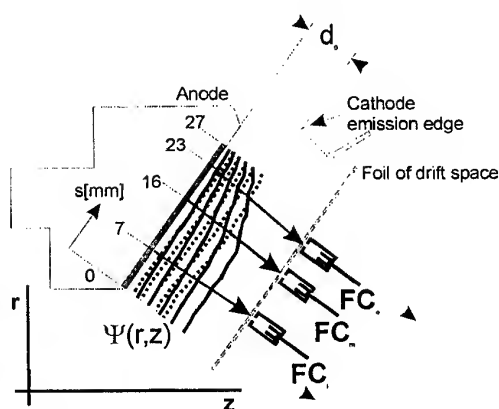
Fig.1: Calculated stream lines (SF:solid, DF: dotted)
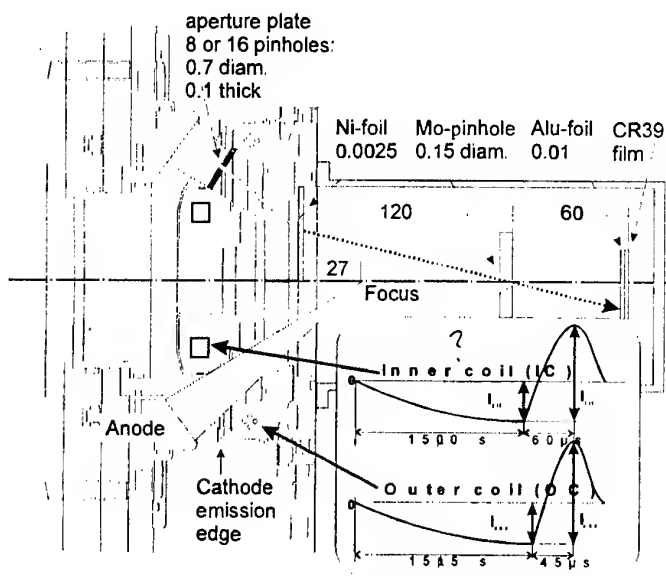
Fig.2: B$_{appl}$ ion-diode with shadow box diagnostic.
Dimensions are in mm, times in μs

V*~1/r. Hence the current density peaks for larger radii. 'Tilting' the applied magnetic field may compensate for these radial variations in current density. However, the amount of tilt required for uniform emission depends on V and the unknown electron distribution in the gap and must therefore be investigated experimentally. This diode model was added to the magnetic diffusion code ATHETA [4] used for the calculation of the fields of the KALIF B$_{appl}$ diode under emission conditions, i.e the magnetic fields in the diode are due to externally supplied currents through the inner and outer field coils (the applied field) and the self fields due to the non-neutralized beam in the acceleration gap (Fig.1).

Applied fields which differed in tilt and strength were achieved by seperating the inner from the outer coil and connecting them to independent power supplies (double feed design, DF) (Fig.2). In standart type single feed coils (SF), the inner and outer coil are connected in series to a common supply. For the DF coils, the required compensation of the diffusion of the fast insulating field (currents I$_{FIC}$, I$_{FOC}$) into the anode is achieved by slow currents with opposite polarity (I$_{SIC}$, I$_{SOC}$). The KALIF pulse is fired at the time both currents reach their maximum.
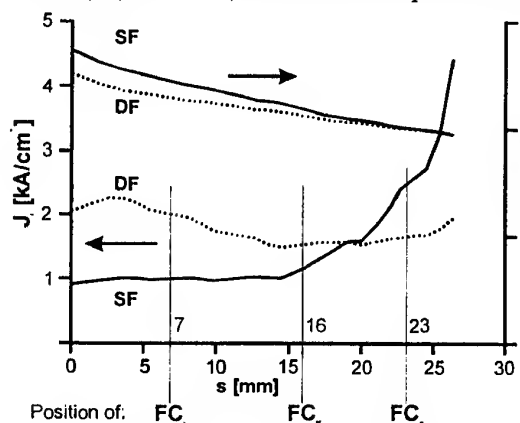
Fig.3: Calculated V$_{crit}$ and current emission profile J$_i$ for a single feed- (SF, solid) and a double feed (DF, dotted) coil

For the SF arrangement, the calculated stream lines Ψ show a strong radial dependence in contrast to the DF case (Fig.1). Consequently, the calculated current density for the DF case is much more uniform (Fig.3). This should be observable in the FC measurements.

Diagnostics

The main beam diagnostics consisted of magnetically insulated Faraday cups (FC) and a pin hole camera. The maximum tolerable pinhole diameter in the front plate of the FC's (Tungsten, 0.2mm thick) was just 0.2mm due to the high expected current densities up to 6kA/cm^2. In each experiment a set of 6 FC's was placed on 3 radial (inner, middle, out) and 2 azimuthal positions. The signals of the cups were routinely recorded with a bandwidth of 500MHz, 2 channels with a bandwidth of 4.5GHz were available. The upper frequency limit for the cups itself was estimated to be at least 2GHz.

The time integrated beam focusing properties were achieved from track patterns on a CR39 film placed in a pin hole camera, covered by a 10μm thick Al-foil (Fig.2). Beamlets (6 or 12) were cut out of the main ion beam by 0.7mm diameter holes in a stainless steel aperture plate,

placed 5mm downstream of the 1.5μm thick Mylar foil closing the drift space. The interaction of the beamlets with a 2.5μm thick Ni foil produced Rutherford scattered protons which in turn impact on the CR39 film. The higher energy impact patterns on the film (*filtered with a* 10μm Al-foil) were determined with an automatic track counting system [5].
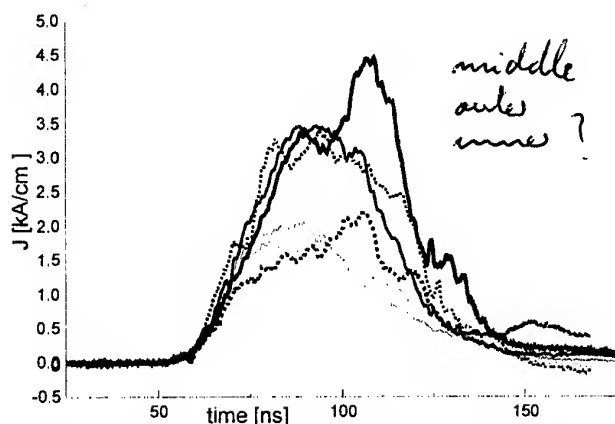
Fig.4: Radial current density emission profile: SF (solid) compared to DF (dotted)

middle outer inner ?
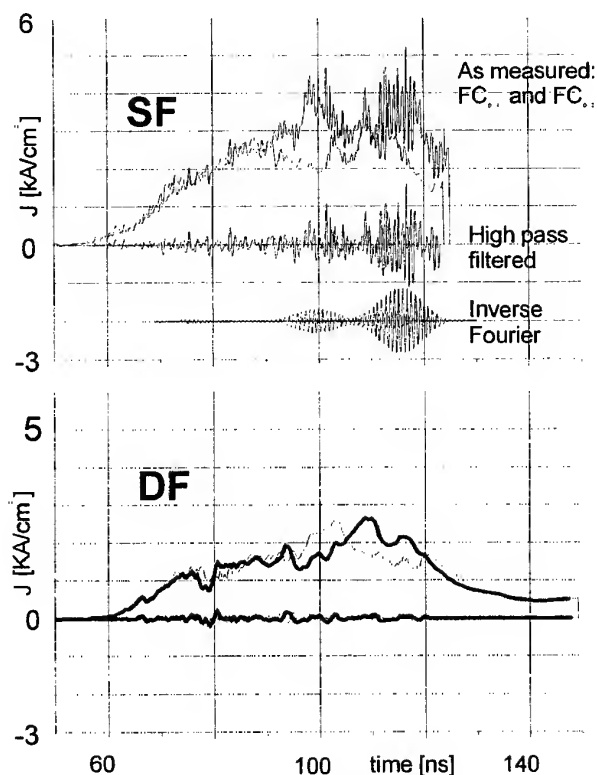
Fig.5: Frequency analysis of 2 FC signals placed on the same radius (out) and recorded with 4.5GHz SF: up, DF: down

Results

The signals of the Faraday-cups showed that the beam emission in SF and DF experiments started independently from the radius at the same time and with the same slope (Fig.4). In SF experiments the emission from the inner radii starts to saturate about 25ns after current onset while the middle and outer areas continue rising up to about 3.5kA/cm². In contrast to the inner and middle areas, emission from outside starts increasing again and reaches up to 4.5kA/cm². The corresponding signals measured in DF experiments showed improved beam homogeneity: they extended over a longer time period but with reduced current densities, showed less time dependent structures and less radial differences. This emission structure for both, SF and DF experiments, fits well to the calculated stream lines (Fig.1) and the calculated current densities (Fig.3). Compared to SF experiments, the fluctuations in the signals of the FC's in DF experiments were found strongly reduced. The frequency spectra of SF experiments showed strong contributions in the range around 1.3GHz which could not be observed in DF experiments. Phase shift relations between FC signals, which might be caused by azimuthally propagating current fluctuations procuced by instabilities, were identified for SF experiments only. If these correlated signal fluctuations from 1.2 to 1.3GHz are due to the ion mode instability the inverse fourier transforms give the time of the occurence of this instability. It starts first at about current maximum, then decreases and reaches a second maximum at late times. The
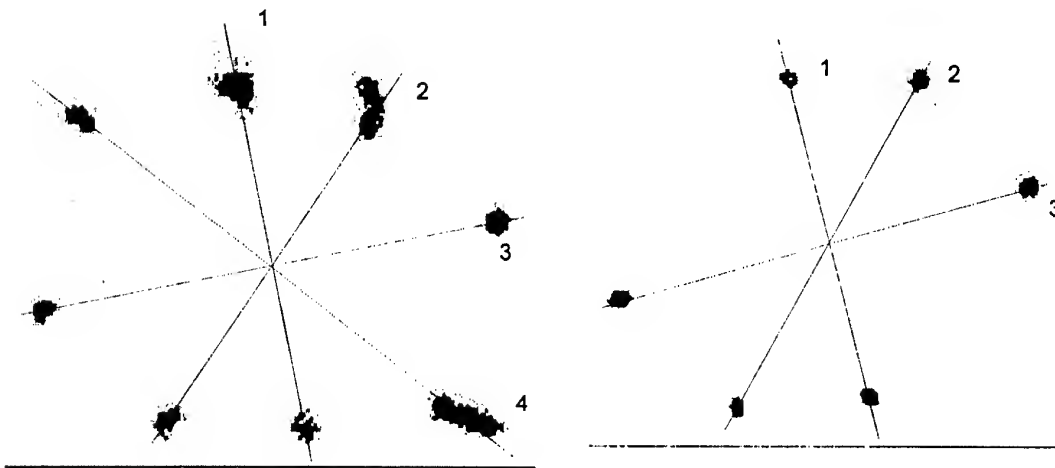
Fig.6: Patterns on the CR39 films from a SF-(left) and a DF experiment (right).
The transition from dark to light shows the 50% level for each spot

transit time of the signal fluctuations in this frequency range is around 2ns for a distance of 28mm between the outer FC's. This corresponds to a velocity of xcm/ms or c/20. However, the statistical basis for these numbers must be considered as rather limited.

The analysis of theCR39 images showed for all DF experiments performed so far a reduction of the spot size and hence less beam divergence. The best result was a divergence of 16mrad (average over all beamlets spots in one experiment) compared to 26mrad achieved in SF-experiments (Fig.6). Since their influence proved to be negligible, these divergence numbers were achieved without using any pinhole correction factor.

Summary

The experimental results achieved so far are in excellent agreement with the predictions; the magnetic beam profiles designed for uniform current substantially improved the radial homogeneity of the ion current, dramatically reduced the amplitude of the fluctuations attributed to the ion mode instability, resulted in the lowest beam divergences yet measured on KALIF (17mrad vs. 26mrad) and finally produced considerably less damage on the diode hardware. The 'optimum' field profile was probably yet not achieved because -due to problems with the field coils- only a part of the considered parameter settings could be investigated. Therefore these experiments should be continued. However, the results achieved so far showed, that the ion beam current density profile is one controllable key variable in ion diode performance.

References

[1] S. A. Slutz, Phys. Fluids B **4** (8) August 1992

[2] M. P. Desjarlais et al., in Proc. of the 11th Int. Conf. on High-Power Particle Beams, Prague, Czech Rep., June 1996, p.101-110

[3] H. Bluhm et al., in Proc. of the 10th Int. Conf. on High-Power Particle Beams, San Diego, USA, June 1994, p.77-82

[4] J. P. Quintenz et al., Laser Part. Beams **12**, 283 (1994)

[5] H. Guth et al., FZKA Bericht 5523, Forschungszentrum Karlsruhe (1995)

DEVELOPMENT OF LONG PULSE
ION INDUCTION LINAC

K.Horioka, M.Nakajima, D.Hashimoto, M.Watanabe,

M.Yoshida[1], J.Hasegawa[1], M.Ogawa[1],

K.Takayama[2], J.Kishiro[2], S.Maebara[3], M.Shiho[3] and S.Kawasaki[4]

Department of Energy Sciences, Tokyo Institute of Technology
Nagatsuta 4259, Midori-ku, Yokohama 226, Japan
Research Laboratory for Nuclear Reactors,[1] Tokyo Institute of Technology,
O-okayama 2-12-1, Meguro-ku, Tokyo 152, Japan
National Laboratory for High Energy Physics (KEK)[2], Tsukuba 305, Japan
Japan Atomic Energy Research Institute (JAERI)[3], Ibaraki 311-02, Japan
Department of Physics, Saitama University[4], Urawa 338, Japan

Important issues for development of high power ion induction accelerator are discussed based on some experimental results. For cost effective magnetic core selection, B-H characteristics of various ferromagnetic materials were evaluated as a function of magnetization rate. To stabilize the fluctuation of ion flux from a grid-controlled vacuum arc ion source, a laser triggering was utilized. It can supply stable ion flux up-to 10's μ-sec level. For high current and long pulse ion injection of A(ampere)-μ sec level, a plasma-gun-type injector was also developed. A laser produced plasma is scheduled to be tested as a high flux point ion source of sub-μ sec pulse level.

1. Introduction

For induction linac approach to Heavy Ion Fusion (HIF)[1,2], an ion source which can supply more than 10^{15} ions per pulse is of crucial importance. To avoid space charge blow up, the beam pulse should be longitudinally compressed from pulse length τ of a few μ sec-A(Ampere) level to $\sim$10nsec through an order of 10^3 induction module units[3,4,5]. For cost effective core size, we should utilize full flux swing of the magnetic materials, then (dB/dt) τ =2Bs. Therefore we need precise voltage modulation for the longitudinal compression of the beams and the magnetic cores must accept a wide range of operating parameters[6,7]. This means we have to know precise B-H characteristics of the magnetic materials especially at high magnetization rate.

2. Magnetization Characteristics of Laminated Ferromagnetic Materials at High Magnetization Rate

In conventional induction linac approach for HIF, the expected operational range of dB/dt of the magnetic cores extends from 0.1T/μ sec at low-β injector stage to more than 10T/μ sec at the final stage. From the point view of construction cost and cost effective core size, finding the compact, low cost, and low loss magnetic materials is essential. In order to evaluate suitable magnetic cores at each acceleration stage, we investigated B-H

Material	Elements	Core.No.	d(μm)
Silicon Iron	Fe-(3%)Si	GT100	100
	Fe-(3%)Si	GT 50	50
	Fe-(6.5%)Si	EX 10	100
	Fe-(6.5%)Si	EX 05	50
Amorphous	ACO-5H(Co)	NGT975-1	20
	FT-1AH(Fe)	NGT975-4	20
Finemet	FT-1H	NGT975-7	20
	FT-1H	NGT975-10	12

Table-1 Ferro-magnetic materials tested in this study
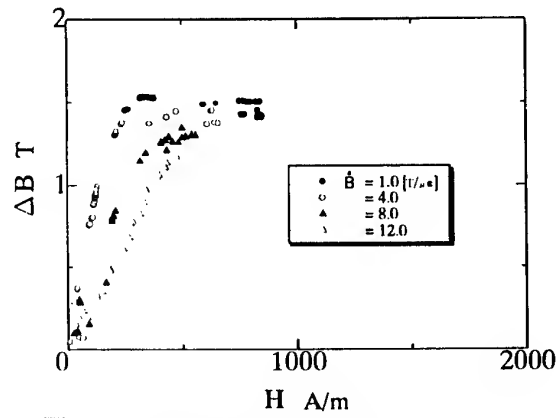
Fig.1 Typical magnetization curves for laminated material (NGT 975-10)

characteristics of various laminated materials over a wide range of magnetization rate. Table-1 shows the ferromagnetic materials tested in this study. Typical magnetization curves for Finemet of 12 μ m thickness are shown in Fig.1, with magnetization rate [T/μ sec] as a parameter. Although the magnetization levels were vastly different, qualitative behavior of those magnetic materials was very similar. As had been pointed out in ref[8], the magnetization curves of laminated core materials could be normalized by d^2/ρ at high magnetization rate[11].

3. Development of Long-Pulse and High-Flux Ion Injectors

If the plasma source of density ni and electron temperature Te is stationary, the extractable ion current is limited by the Bohm current $J_B=0.4en_i(2kTe/m_i)^{1/2}$. So to maintain the ion emission surface at proper position, the extraction curent strictly match the plasma flux J_B for a few μ-sec time duration. One way to avoid this difficulty is to extend the cross sectional area of the ion source by a grid-controlled structure [9,10]. Another way is to use a drifting plasma. If the source plasma has drift velocity of v_d, it can upgrade the current limit to the flux of drifting plasma as $J_i=en_iv_d$. Although the plasma pre-fills the acceleration gap, which recovers to normal high impedance mode after a transient gap opening phase[11]. With plasma injection and pre-filled configuration, we can expect to get high flux, stable ion beams.

3-1 Laser Triggered Grid-Controlled Vacuum Arc Ion Source

Conventional vacuum arc ion sources generally use surface flashover triggering[9]. They have intrinsic fluctuation caused by the uncertainty of initiation and movement of cathode arc spots. The flashover trigger contaminates the cathode surface [10] and spoils a reliable operation.

To overcome these difficulty, a laser triggering was tested. A schematic diagram of the laser triggered vacuum arc ion source is shown in Fig.2. A frequency doubled YAG laser
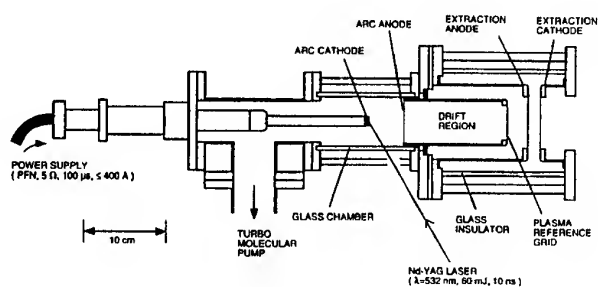
Fig.2 Schematic of laser triggered vacuum arc ion source
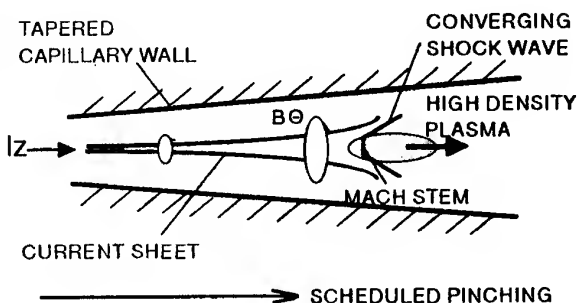
Fig.3 Concept of electro-magnetically accelerated point plasma source

of 60mJ-10nsec level (Continuum Model NY-60B) is used as the triggering source. The 2 ω-laser irradiates the cathode surface at 65 degrees with respect to the normal. The laser triggering could improve the initial positioning and triggering probability of the arc spot, and was almost free from the contamination problem on the cathode surface[10].

3-2 Point Plasma Injectors

In order to overcome the Bohm current limit, we should accelerate the ion source plasma as fast as possible. We tested the tapered capillary Z-discharge for compression and acceleration of the bulk plasma[12]. A schematic of the electro-magnetically accelerated point ion source is shown in Fig.3. In the tapered capillary, a converging current sheet sequentially
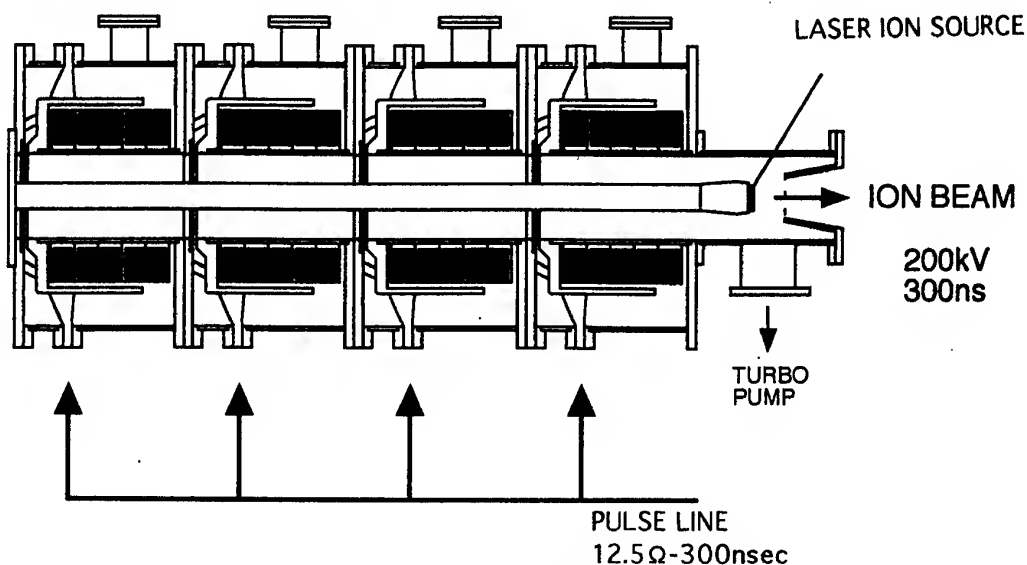
Fig.4 Schematic diagram of 4-module induction accelerator

compresses and accelerates the plasma. After that, it expands as a drifting Maxwellian from the point source. For more reliable operation, we are going to test a laser plasma as the high flux point source.

3-3 Development of a 4-module Induction Unit

We are developing a 4-module, long-pulse ion induction accelerator at TIT. The accelerator has 4 inductive acceleration units. Each unit is composed of a ferrite core of 2×10^{-2} volt-sec and a coaxial water line of 12.5 ohm-300nsec. Here our emphasis is placed on the development of high current, low emittance and reliable ion injector; especially on the laser source, and a realistic scheme for the ion beam transport at low-β region is the next step issue.

4. Concluding Remarks

Various magnetic materials were investigated as a function of magnetization rate. The results indicated that all of the magnetization curves of laminated materials at high magnetization rates could be explained by the saturation domain model. Although low cost materials with high magnetic saturation induction are associated with high magnetic losses due to induced eddy currents, we should select proper magnetic materials with minimum cost and size depending on the acceleration stage.

The laser triggering could improve the positioning of the cathode arc spot and dramatically reduced the contamination problem of conventional vacuum arc ion sources. For high flux and low emittance ion source, a scheme which use electro-magnetically accelerated or laser produced point-expanding plasma was proposed. We are going to start the acceleration experiments, using a 4-unit long pulse induction accelerator, from this summer.

References

[1] A.Faltens and D.Keefe, Proc. Linear Accelerator Conf., **LA-9234-C**, p.205 (1981)

[2] R.O.Bangerter, Nuovo Cimento, **106**, (11), p.1445 (1993)

[3] C.H.Kim and L.Smith, Particle Accelerators, **18**, p.101 (1985)

[4] S.Kawasaki, Y.Kubota, A.Miyahara and K.Yamamoto;
IEEE Trans. Plasma Sci., **NS-30**, (4), p.3016 (1983)

[5] T.J.Fessenden, Proc. IEEE Particle Accelerator Conf., **1**, p.586 (1991)

[6] E.P.Lee, J.Hovingh, AIP Conf. Proc.**249**, p.1714 (1992)

[7] D. D.Ho, S.T.Brandon and E.P.Lee, Particle Accelerators, **35**, p.15 (1991)

[8] S. Humphries, Jr., et. al., J. Appl. Phys., **59**, p.1790 (1985)

[9] D.W.Rutkowski, D.W.Hewell, and S.Humphries,Jr., IEEE Trans. Plasma Sci., **19**, 5, p.782 (1991)

[10] J. Hasegawa, K.Horioka and M.Nakajima, Jap. J. Appl. Phys., **37** (6) (1998)

[11] K.Horioka, J.Hasegawa, M.Nakajima, M.Ogawa et. al., Nucl. Instr. Meth.A, (1998)

[12] K.Horioka, M.Nakajima, T.Aizawa and M.Tsuchida, AIP Conf. Proc. **409**, p.311 (1997)

CHARGE COMPENSATION AND ACCELERATION OF A THICK-WALLED HIGH-CURRENT ION BEAM IN INDUCTION LINAC

N.G.Belova, V.I.Karas'*, O.N.Shulika*

*Institute of Physics & Technology Russian Academy of Sciences,
25-A Krasikov St., Moscow, 117879, Russia
* National Scientific Center «Kharkov Institute of Physics & Technology»,
1 Academicheskaya St., Kharkov, 310108, Ukraine*

1. At present, several methods of obtaining high-current ion beam, which are based on the use of induction accelerators and are applied to inertial controlled fusion (ICF) research, are being considered [1-3]. To date, kiloampere ion beams with energies of several hundred keV have been produced in high-current linear induction accelerators (linac) with collective focusing [4-6]. The power of HHCIBs for ICF purposes must be several orders greater, with rather stringent requirements on beam brightness. Therefore, when developing a driver for ICF on the basis of a high-current linac, it is necessary to investigate a number of important physical problems: (1) the formation of high-current beams in injector; (2) the provision of efficient magnetic insulation for accelerating gaps; (3) charge compensation of the ion beam in the transport channel and in the magneto-insulated accelerating gaps; (4) effective acceleration and stability of the ion beam in accelerating channel; and (5) transport, focusing, and space-time compression of HHCIBs.

In linac, the conventional way of charge and current compensation [7, 8] is inefficient. In [9, 10], a new mechanism for the neutralization of HHCIBs in axially symmetric magneto-insulated gaps was proposed. Its physical meaning is that a specially injected compensating electron beam drifts through the cusp due to self-consistent azimuthal magnetic field and an electric field caused by a small radial separation of ion and electron beams.

During the last six years, we carried out systematic investigations of the dynamics of relativistic electron and nonrelativistic ion beam propagation in both an electric field and an axisymmetric nonuniform magnetic field. In [11-13], the investigation results of the acceleration, and the charge and current compensation of HHCIBs in one and two linac cusps are reported. These results have shown that both in the presence and in the absence of an accelerating electric field, the following effects take place: (1) charge and current compensation of HHCIB in the accelerating gaps; (2) stability of the ion beam during times that substantially exceed the inverse ion Langmuir and Larmor frequencies.

The performed numerical simulations have also shown that a required charge neutralization of the ion beam is only achieved within accelerating gaps of linac. In the drift space between two accelerating gaps the current and charge compensation of the ion beam proved to be insufficient because of a substantial difference in the electron and ion velocities acquired up to the time of the transit of the beams through the drift gap. As a result, the positive potential of the self-consistent field in the drift space leads to the spread and deceleration of the ion beam and, consequently, to the degradation of the beam brightness. The positive space charge in the drift gap can be compensated by injecting thermal electrons into it. In [14-16], several ways of the cold electron injections for the space charge suppression of HHCIBs in the drift gap of a linac were investigated. It was shown that a preliminary injection of cold electrons permits to eliminate broadening and decelerating an ion beam in the drift gap and to provide its additional focusing.

Decreased to minimum of the negative influence of the self-consistent fields we will try to

optimize the process of the ion beam acceleration.

In this work, the investigation directed to: (1) reaching of the optimal relation between the external electric field parameters and the compensating electron beam parameters; (2) defining of the optimal thickness of annular beam at which the ion beam is effectively accelerated and at a time is remaining compensated and not losing a stability.

2. To describe the collisionless plasma dynamics of beams the set of relativistic Vlasov's equations for the distribution functions of particles $f_s(\vec{P}, \vec{R}, t)$) in the axisymmetric $(\partial/\partial\theta = 0)$ cylindrical geometry $\vec{R} = (r, z)$ has been used for the investigation of the transient and stationary processes in linac (here $\vec{P}$ momentum). The self-consistent electric $\vec{E}(r, z)$ and magnetic $\vec{B}(r, z)$ fields including in Vlasov's equations are determined by the Maxwell's equations, the right hands of which are defined as the zeroth and first moments of the distribution functions.

From the set of Vlasov's equations can be obtained the set of the dynamic equations for the particles. The Maxwell's equations using the Lorentz gauge $\left(\operatorname{div}\vec{A} + \dfrac{1}{c}\dfrac{\partial\Phi}{\partial t} = 0 \right)$ can be reduced to the wave equations for the scalar $\Phi(r, z)$ and vector $\vec{A}(r, z)$ potentials.

The units of measurement using in the treatment are determined by relations: $[v] = c$, $[q] = e$, $[r, z] = c/\omega_{pe}$, $[t] = \omega_{pe}^{-1}$, $[n] = n_{0e}$, $[m] = m_0$, $[\Phi, \vec{A}] = m_0 c^2/e$, $[\vec{J}] = e n_{0e}$, $[\vec{T}_{ce}] = m_0 c^2$, $[P_0] = [\psi] = c^2/\omega_{pe}$, $[E, B] = \sqrt{4\pi n_{0e}\varepsilon_{ch}}$, where $\vec{u} = \gamma\vec{v}$, $\vec{v} = \{\dot{r}, r\dot{\theta}, \dot{z}\}$, $\psi = \gamma r^2\dot{\theta} = P_\theta - \dfrac{q}{m}rA_\theta$, ($P_\theta$ is the dimensionless generalized particle momentum), $\gamma = \sqrt{1 + u_r^2 + (\psi/r)^2 + u_z^2}$ is the relativistic factor, $\omega_{pe} = \sqrt{4\pi n_{0e} e^2/m_0}$ is the electron plasma frequency, n_{0e}, m_0, e are the initial density, rest mass and charge of the electrons respectively, T_{ce} is the temperature of cold electrons. The initial velocity of a given sort (s) of particles is defined by the boundary conditions for the distribution functions at $z = 0$: $f_s(m_s\vec{u}, \vec{R}, t) = \delta(u_r)\delta(u_z - u_{0s})\delta(u_\theta)$ for $r_{min} \le r \le r_{max}$ and $u_z > 0$. Here r_{min} and r_{max} are the minimum and maximum beams radii respectively which define the initial r-coordinates of particles, $u_{0s} = v_s/\sqrt{1 - v_s^2}$, v_s is a beams velocity. At $(r = 0, r = r_L)$ the reflection regime is set. The particles exit free from the simulation region at $z = z_L$. At the initial time the particles are absent in modeling region.

The set of equations and the initial and boundary conditions for the potentials and distribution functions are described in detail in [15].

The configuration of the external magnetic field is defined by the expression $A_\theta = -B_0/k\, I_1(kr)\cos(kz)$, where $I_1(kr)$ is the first order modified Bessel function, B_0 is the amplitude of magnetic field, and $k = K\pi/z_L$, K is total number of cusps.

The discrete model, which is developed for the study of both relativistic and nonrelativistic axisymmetric plasma configuration, is realized as 2.5-dimensional axisymmetric numerical code. The calculations were carried out using Pentium-133.

In simulation of the thick-walled high-current ion beam acceleration in linac for searching the optimal relation between the parameters of the accelerating electric field and the compensating electron beam energy the potential difference across the accelerating gap and the energy of the relativistic electron beam were varied. Hollow magnetized relativistic electron beam (Larmor radius r_{Le} is substantially smaller than the size of the cusp L_z and the chamber radius

r_L) and high-current unmagnetized ion beam (Larmor radius r_{Li} is more greater L_z and r_L) were injected along z-axis. In all cases the beam current densities were equal to $q_e n_{0e} V_e = q_i n_{0i} V_i$. The ion beam velocity was $V_i = 0.285$. The minimum and maximum beams
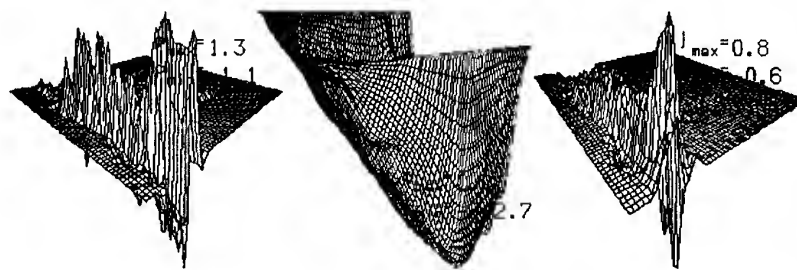
Fig. 1. Distribution of the total charge density $\rho(r,z)$, the scalar potential $\Phi(r,z)$ and the total axial current densities $j_z(r,z)$ at $t = 440\omega_{pe}^{-1}$ for the case with additional electron injection into drift gap and thick-wall ion beam.

radii were $r_{min}=30$ and $r_{max}=37.5$. The size of one cusp and radius of the chamber were $L_z=78.5$ and $r_L=157.5$ respectively. The amplitude of the external field was $B_0 = 1.76$. The mass ratio was $m_i/m_e = 100$, $m_e = 20m_0$. The number of particles in the cell was

$N_e = 64$, $N_i = 180$. The number of the nodes was equal to $(J_z \times J_r) = (64 \times 64)$. The time step was varied within the range $0.025 - 0.05\omega_{pe}^{-1}$ for solving the equations of motion and $0.0125 - 0.025\omega_{pe}^{-1}$ when solving the wave equations. The parameters of the electron and ion beams have satisfied the condition of the electron beam transport together the ion beam through the magnetoinsulated accelerating gap ($v_e = 0.8 \div 0.85$). The preliminary injection of the thermal electrons with the Maxwellian distribution function with the temperature $T_{ce} = 0.002$ into drift gap was used. The calculations were continued in during about ten reciprocal Langmuir ion frequency.

Further (below) the results of three cases distinguished by the potential difference across one cusp are discussed. Fig.1 illustrates the distribution of the total charge densities $\rho(r,z)$, the scalar potential $\Phi(r,z)$ and the total axial current densities $j_z(r,z)$. The distributions presented in fig.1 show that the applied external electric field, which accelerates ions and retards electrons, does not prevent the electron beam drift through the accelerating gaps. From the functions $j_z(r,z)$ it is clearly seen that not only the charge but also the current compensation of the ion beam occur. The distribution functions $f(v)$ of the electron and ion beams illustrate that the ion beam generally retains monoenergetic shape, because its spread in v_z and v_r does not exceed 10%. The electron beam spread in the velocities is nearly 100%, but this does not prevent the charge compensation of the ion beam by electrons.

The preliminary injection of the thermal electrons into the drift gap upgrades the characteristics of HHCIB as shown in fig.2 in which the time dependencies of the mean ion beam velocities for the case without the thermal injection (*), and with one for two cases of the potential difference (◊), and (+) are presented.

As a result of increasing the difference potential across the accelerating gap up to $\Delta\Phi = 30.0$ (the electron beam velocity $v_e=0.8$, $\gamma \approx 1.7$) in variant (c) the kinetic energy of electron beam was $\varepsilon_{eb} = (\gamma - 1)m_e c^2 < e\Delta\Phi/2$. This case has demonstrated that the electrons localize mainly in the first part of the cusp. The ion beam is accelerated at first and then one is
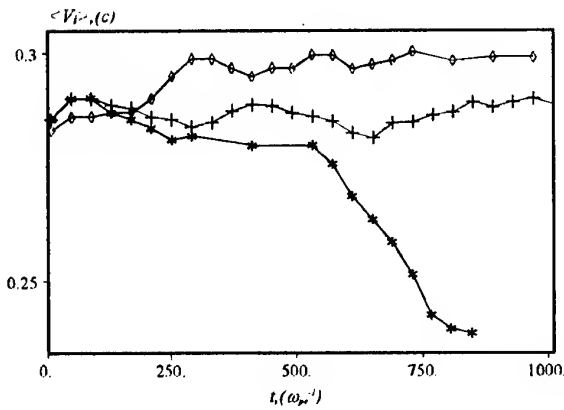
Fig. 2. Distribution of the mean ion velocity $\langle V_i(t) \rangle$ versus time: (*) - without thermal injection into accelerating gap; (+) - with injection and without accelerating field; (◊) - with injection and accelerating field.

decelerated as seen in fig.2 (+). The thermal electrons can not neutralized the space charge and current of the ion beam.

More optimal relation between the potential difference $\Delta\Phi = 15.0$ and the electron beam energy was at the parameters $v_e = 0.85$, $\gamma \approx 1.9$. The kinetic energy of electron beam $\varepsilon_{eb} \approx 18.0$ was sufficient to overcome the potential difference. As a results the ion beam is accelerated and then its velocity is a constant $\langle v_i \rangle \approx 30.0$ in all time of simulation (fig.2.◊). Fig.1 illustrates that the self-consistent field of the positive charge is suppressed, and an additional focusing of ion beam by the negative space charge of the thermal electrons occur also. As a result the better characteristics of the ion beam can be produced in linac.

3. Results of the 2.5-dimensional numerical simulation of the hollow high-current ion beam (HHCIB) dynamics in two magnet-isolated accelerating gaps separated by the drift gap are presented. The previous study has shown that the good charge and current compensations of the ion beam by the specially injected in accelerating gap electron beam and the thermal electron injection into drift gap of the induction linac occur. With the aim of increasing the ion beam acceleration rate in the two cusps linac we have studied the optimal correlation between an accelerating electric field and an electron beam energy. We obtained the restriction on the wall thickness of annular HHCIB which ensure the following: (1) charge- and current compensation is homogeneous on the ion beam cross-section; (2) a penetration depth of the accelerating electric field is considerably greater than the beam wall thickness.

[1] A.I. Fattens, and D. Keeffe, *Proc. Lin. Accel. Conf.*, Santa Fe, LA-9234c, 205 (1981).

[2] R.O. Bangerter, Part. Accel. **37-38**, 3 (1992).

[3] S.A. Slutz, P. Primm, T. Renk et.al. Final Report, SAND97-0344 UC-414, March 1997.

[4] V.A. Kiyashko, Yu.E. Kolyada, E.A. Kornilov, Ya.B. Fainberg, Pis'ma Zh. Tekhn. Fiz. 3, 1257 (1977).

[5] S.Jr. Humphries, Nucl. Fusion **20**, 1549 (1980).

[6] I.S. Roth, J.D. Ivers, J.A. Nation *Proc. VI Int. conf. on high power particle beams*, Kobe, 1986.

[7] W. Peter, N. Rostoker, Phys. Fluids **25**, 730 (1982);

[8] W. Peter, A. Ron, N. Rostoker, Phys. Fluids **22**, 1471 (1979).

[9] V.I. Karas', V.V. Mukhin, V.E. Novikov, A.M. Naboka, Fiz. Plazmy **13**, 494 (1987).

[10] V.I. Karas', V.A. Kiyashko, E.A. Kornilov, Ya.B. Fainberg, Nuclear Instruments and Methods in Physics Research A278, 245 (1989).

[11] N.G. Belova, V.I. Karas', Yu.S. Sigov, Fiz. Plazmy **16**, 209 (1990).

[12] N.G. Belova, V.I. Karas', Part. Accel. 37-38, 225 (1992).

[13] N.G. Belova, V.I. Karaa', *Proc.IEEE Part.Accel. Conf.* (Washington DC, V.I, 1993).

[14] V.I. Karas', N.G. Belova, *Proc. X Int. Conf. on High Power Particle Beams BEAMS'94* (San Diego, 1994).

[15] N.G. Belova, V.I. Karas', Plasma Physics Reports **21**, 1005 (1995).

[16] N.G. Belova, V.I. Karas', Plasma Physics Reports **23**, 328 (1997).

DETAILED MODELING OF KALIF BEAM-TARGET EXPERIMENTS

H. Marten[1], K. Baumung[1], H.-J. Bluhm[1], P. Hoppé[1], G. Meisel[1]
and
J.J. MacFarlane[2], P. Wang[2]

[1] *Forschungszentrum Karlsruhe GmbH, INR, Postfach 3640, D-76021 Karlsruhe, FRG*
[2] *PRISM Computational Sciences, P.O. Box 260181, Madison, WI 53726-0181*

Abstract. The Karlsruhe Light Ion Facility KALIF generates proton pulses of typically 50 ns duration with proton energies up to 1.7 MeV and currents between 0.2 and 0.4 MA. The protons are focussed on thin Aluminum foils thus generating specific energy densities of a few MJ/g, pressures of up to 60 GPa and temperatures of about 20 eV in the targets. Time resolved velocity measurements are used to study the hydrodynamic response of ablatively accelerated foils, and plasma temperatures are determined from K_α emission spectroscopy. We compare radiation hydrodynamic models and synthetic K_α spectra with the measurements in order to deduce details about the beam history of the KALIF diodes.

1. Introduction

In foil acceleration experiments performed at KALIF Aluminum foils with initial thicknesses larger than the proton range are irradiated with intense proton beams. A dense plasma forms in the proton energy deposition zone and the corresponding ablation pressure accelerates the remaining solid and cold part. The rear surface velocity of these foils is recorded with a space and time resolving laser-Doppler velocimeter.

In a different experiment subrange targets are completely evaporated by the proton beam thus forming an almost homogeneously expanding plasma. In this plasma K-shell electrons are removed by direct impact of beam particles. As the K-shell vacancies are spontaneously filled by L-shell electrons, K_α lines are observed in emission, the satellite structure of which is related to the degree of collisional ionization and can be used for temperature estimates.

In the following we present a comparison of measured and calculated target velocities for the selfmagnetically insulated B_Θ diode (Section 2) and for the applied B diode (Section 3) currently used at KALIF. The computations are based on 1 D radiation hydrodynamic models with the code KATACO [1] taking into account realistic beam angle and energy distributions of the protons along the KALIF beam history. The state of Aluminum is described by the wide range equation of state given in [2], and radiation transport is treated in the diffusion approximation with LTE opacities provided by the code EOSOPC [3] for 100 frequency groups. K_α spectra are computed in a postprocessing step to be described in Section 4.

2. Foil acceleration experiments with the B_Θ diode

Fig. 1 shows experimental results (symbols) and computational simulations (solid lines) of foil acceleration experiments with Al foils of 33, 50 and 75 μm initial thickness performed with the B_Θ diode. Once the protons start to deposit their energy and heat the target, the corresponding plasma pressure drives a compression wave into the remaining solid part. At the rear surface of the foil the compression wave is reflected as a release wave running back into the target, the release wave is reflected at the ablation plasma bounday as a compression wave, and so
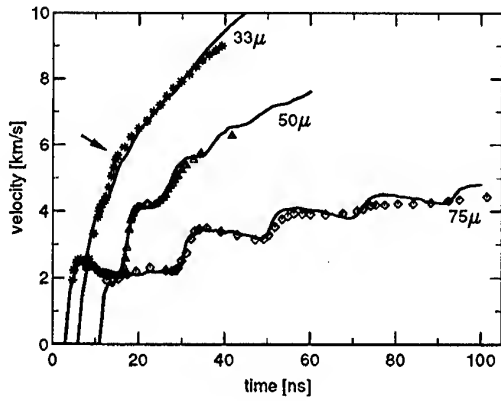
Figure 1: Measured (symbols) and computed (solid lines) rear surface velocities of Aluminum foils with 33, 50 and 75 μm initial thickness during irradiation with the B⊖ proton beam
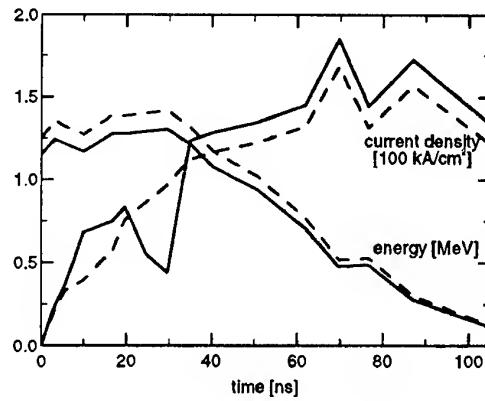
Figure 2: Dashed: Experimentally determined time history of the B⊖ proton beam at the target. Solid lines exemplarily show the beam parameters used for the simulation of the 50 μm foil in Fig. 1

on. These wave reverberations lead to a stepwise increase of the target velocity whenever the compression wave reaches the rear surface.

The average beam history of the B⊖ diode derived from electrical signals is shown by dashed lines in Fig. 2. Solid curves exemplarily demonstrate the modifications necessary to simulate the 50 μm foil of Fig. 1. The models take into account a distribution of proton impact angles between 20° and 40° with respect to the target normal due to the ballistic focusing of the diode as well as a Gaussian distribution of proton energies with a FWHM of 20 % of the average value. According to recent measurements with a magnetic energy analyzer the average proton energy has been reduced by 8 %. The proton current density has been increased by 10 % accordingly to keep the experimentally determined peak power density of $0.15 (\pm 0.05)$ TW/cm². The ion current density was slightly increased additionally between 5 and 15 ns of the pulse in order to get a correct height of the first two velocity plateaus. Furthermore, we introduced a local current minimum at about 30 ns which leads to an early decoupling between the beam energy input and the accelerated foil. This decoupling is visible as a kink in all experimental velocity data, it is the more pronounced the smaller the accelerated mass is (see e.g. the arrow at $t = 14$ ns for the 33 μm foil in Fig. 1). Such a current minimum could be caused by a parasitic load similar to that found in the B_{appl} diode (see next section). Qualitatively the same modifications of beam parameters had to be introduced in all three models of Fig. 1.

3. Foil acceleration experiments with the B_{appl} diode

The beam parameters used in simulations for the B_{appl} diode are given in Fig. 3. As for the B⊖ diode the models account for a distribution of proton impact angles (here between 30° and 42°) as well as for a Gaussian distribution of proton energies (FWHM = 20 % of the average value). The average kinetic energy of the protons in Fig. 3 is taken from the electrical diode voltage without modifications. Curve fc is an average current density derived from Faraday cup measurements inside the diode. The current falloff is caused by the development of some "parasitic load". Curves A to D were given the same early current development as fc; they model different assumptions about the onset time of the parasitic load and its further development.
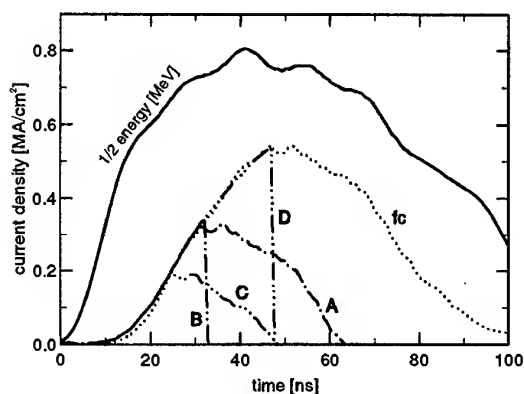
Figure 3: Average proton energies and proton current densities used to simulate different experiments with the B_{appl} diode (see text)
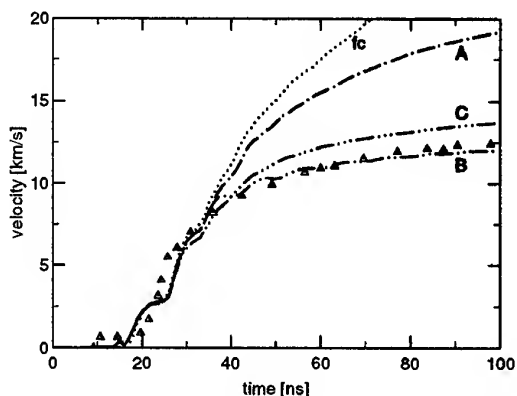
Figure 4: Computed rear surface velocities of a 50 μm Al foil for the beam models of Fig. 3 The triangles are measured velocities for shot #3360

Fig. 4 compares measured (symbols) and computed (lines) rear surface velocities of a 50 μm Al foil. The results of the calculations mainly differ at times later than 35 ns. The target velocities are found to depend on both, the peak proton flux (compare models **A** & **C**) and on the slope after peak current (**A** & **B**). Model **B** gives the best fit to the measurements, **fc** is far off the experimental results at late times. We also tried to model the target acceleration with the Faraday current density multiplied by a factor of 0.5. However, such beam models can completely be ruled out because they produce too small target velocities between 20 and 40 ns.

4. K_α satellite spectroscopy with the B_{appl} diode

For the computation of K_α spectra the target surface is devided into four concentric regions with radii of 2.4, 3.84, 5.76 and 9.6 mm (0.3, 0.48, 0.72 and 1.2 times the measured FWHM of the spacial beam profile). For each of these regions radiation hydrodynamic simulations of 6 μm thick Al foils are performed with 88.4, 64.6, 36.3 and 8.6 % of the current densities shown in Fig. 3. The resultant temperature and density profiles at different times together with the respective proton fluxes are then fed into the Non-LTE radiation transport code NLTERT [4] to calculate time dependent emission spectra. Finally, the spectra of the four regions are space integrated over an observational slit of 1 mm width, time integrated over the whole KALIF pulse and broadened to account for an experimental resolution of 500.

The experimental spectra mostly show 3 components as in Fig. 5c). The intensity ratio of the two stronger components (Al IV to Al I-III) is about 0.3; it is well reproduced from shot to shot. The intensity ratio Al V to Al I-III varies widely between 0.05 and 0.2 in the same experiments. The Al VI satellite is very weak and only rarely observed.

Comparing the computed with the observed spectra in Fig. 5 it is again obvious that current **fc** is not consistent with the experiments since the satellites Al VI and Al VII were never observed with a relative intensity as given in Fig. 5b. The same is true for current curve **D**. **B** and **C** result in almost the same spectra; they have a very weak but still observable Al V component. The spectrum calculated for current **A** is close to the "strongest" observed spectra. Altogether, the actually observed spectra all lie between the spectra calculated with models **A** and **B** (or **C**). The peak temperatures for models **A** and **B** (or **C**) are 20 eV and 13 eV, respectively.
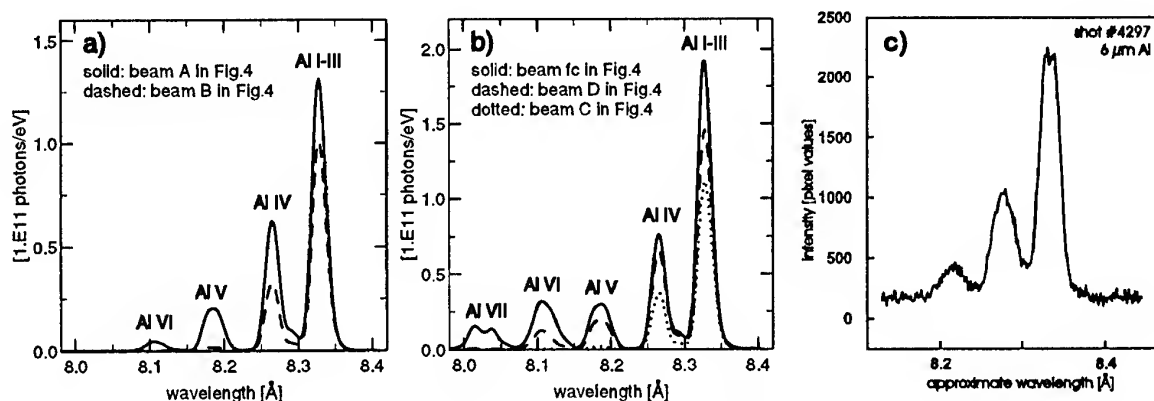
Figure 5: a) and b) are computed K_α spectra of a 6 μm Al foil with beam parameters given in Fig. 3. c) is a typical observed K_α spectrum

5. Conclusions

Two types of target experiments quite different in nature have been performed with the B_{appl} diode. A comparison of the experimental results and of the simulations nevertheless leads to similar conclusions for both types of experiments. Both experiments allow us to exclude certain current developments in the diode such as, e.g., **fc** and **D**. The acceleration experiments can distinguish between curves **C** and **B** because the voltage and thus the proton range keeps increasing all time during the proton flux, the K_α spectra vary considerably between current curves **B** and **A** or **C** and **A**. Both types of experiments can serve as a sensitive means to determine the onset of the parasitic load and the following current decay. The calculations show that velocities in excess of 20 km/s and plasma temperatures above 30 eV were obtained if curve **fc** could be realized, which requires to delay the parasitic load by about 15 ns.

In the case of the B_Θ diode only small modifications of the beam parameters for each individual experiment lead to a satisfactory agreement between measured and computed target velocities. A comparison of individual experiments with simulations for average beam profiles or even of individual experiments among each other is limited by the shot to shot variation of the KALIF diodes. In this respect a simultaneous measurement of target velocities and K_α spectra together with beam parameters during individual KALIF shots would significantly improve the analysis of the experiments.

References

[1]   Goel B., Höbel W., Würz H., Numerical Simulation of Radiation Transport on Supercomputers. in: H. Küsters (ed.) Proc. of the Joint Internat. Conf. on Mathematical Methods and Supercomputing in Nuclear Applications, Karlsruhe, Germany, April 19-23, 1993 Vol. 2, p.63

[2]   Lomonosov I.V., Fortov V.E., Kishchenko K.V., Levashov P.R., Multi-Phase Wide-Range Equation of State for Metals. 8th International Workshop on Atomic Physics for Ion-Driven Fusion, Heidelberg, Germany, September 22-23, 1997

[3]   Wang P., 1993, EOSOPC – A code for computing the equations of state and opacities of plasma with detailed atomic model. Internal Report Forschungszentrum Karlsruhe, 1993

[4]   MacFarlane J.J., NLTERT – A code for computing radiative properties of Non-LTE plasmas. Fusion Power Associates Report, FPA-93-6, Madison, 1993

ION EMISSION FROM PLASMA IN THE PRESENCE OF CHARGE TRANSFER

S. P. Nikulin,

Institute of Electrophysics, Russian Academy of Sciences
Komsomol'skaya 34, Ekaterinburg, 620049, Russia

Usually particles do not collide in the accelerating gap of ion sources, because the gas pressure in the gap should be low to provide a high electric strength. However, the gas discharge systems of the sources may allow for such gas conditions that the ion free path becomes comparable with dimensions of the systems. This is due to the pressure differential between the accelerating and gas-discharge systems of the sources and also to the fact that dimensions of the gas-discharge chambers may by far exceed the length of the accelerating gaps. Given these conditions, the relationships derived for the collision-less regime cannot be used to evaluate the ion current flowing from the discharge system to the accelerating gap. These relationships need be refined allowing for charge transfer. The goal of this study was to ascertain how collisions affect the value of the ion emission current over the pressure interval where the collision-less mode of the ion motion (the ion velocity is determined by the potential difference passed) is replaced by motion in a strong electric field (the ion velocity is proportional to the square root of the electric field intensity).

Let us consider the problem in terms of the plane geometry and assume that the gas-discharge plasma is located between two plane-parallel plates spaced 2d from one another. Assume that electrons are distributed by the Boltzmann law:

$$n_e = n_0 \, exp\left(\frac{e\varphi}{kT}\right) \quad (1)$$

where n_e is the electron concentration; n_0 the concentration at the center of the system; e the electron charge; φ the potential; k the Boltzmann constant; T the electron temperature. If the condition that the energy accumulated by an ion on the free path is much higher than the thermal energy of the gas atoms is fulfilled, the ion concentration is determined by the following relationship [1]

$$n_i(x) = \int_0^x \frac{(G(\xi) + C(\xi)) \, exp(-\frac{x-\xi}{\lambda}) d\xi}{\sqrt{2e(\varphi(\xi) - \varphi(x))/M}} \quad (2)$$

where λ is the mean free path before the charge transfer; G the number of ions generated per unit time in a unit volume as a result of ionization; C the number of ions generated per unit time in a unit volume as a result of the charge transfer. C and G are connected by the following relationship:

$$C(x) = \frac{j(x)}{e\lambda} = \frac{1}{\lambda} \int_0^x G(\xi) d\xi \quad (3)$$

where $j(x)$ is the ion current density at the point x. The concentrations of ions and electrons are equal:

$$n_e = n_i = n, \quad (4)$$

while the quasineutrality is disturbed at a negligibly small distance from the electrodes, i.e. when $x \approx d$. At this point the potential and concentration derivatives turn to infinity.

We shall consider two situations: first, assume that ionization is uniform

$$G = const \quad (5)$$

and, second, ionization is due to plasma electrons,

$$G = v_i n_e(x),$$ (6)

where v_i is the ionization frequency.

In the collision-less mode ($\lambda >> d$) the system of equations (1), (2) and (4) is simplified and the density of the ion current leaving the plasma is related to the plasma parameters by the following expression [2]:

$$j = 0.344 e n_0 \sqrt{\frac{2kT}{M}}$$ (7)

which holds for both cases in question.

At a high collision rate ($\lambda << d$) it is also possible to simplify the said system of equations and solve the problem analytically. Neglect G in (2) as compared to C. Considering that the exponent quickly tends to zero as the point ξ is removed farther apart from x, replace $C(\xi)$ by $C(x)$ and take it outside the integration sign. Expanding $\varphi(\xi)$ into the series in the denominator:

$$\varphi(\xi) = \varphi(x) + \varphi'(x)(\xi-x)$$ (8)

and taking into account that

$$\int_0^x \frac{exp(-t)}{\sqrt{t}} dt \approx \sqrt{\pi},$$ (9)

when x is large, we have

$$n_i(x) = \sqrt{\frac{\pi M}{2e\lambda}} \frac{j(x)}{e\sqrt{-\varphi'(x)}}$$ (10)

One can see from this relationship that the simplification procedure is equivalent to the use of assumption that ions move under mobility conditions in strong fields

$$v = \sqrt{\frac{2e\lambda E}{\pi M}}$$ (11).

where $E = - d\varphi / dx$. This case ($v \sim \sqrt{E}$) has been considered in [2] at $G = const$, but with different number coefficient in (11).

When $G = const$, the solution of the system of equations (1), (4) and (10) gives the following expression for the potential:

$$\varphi = \frac{kT}{2e} ln\left(1 - \left(\frac{x}{d}\right)^3 \right)$$ (12)

and the density of the ion emission current from the plasma is related to the value of λ/d and plasma parameters as

$$j = j(d) = \sqrt{\frac{3}{2\pi} \frac{\lambda}{d}} e n_0 \sqrt{\frac{2kT}{M}}$$ (13)

If $G(x) \sim n(x)$, the coordinate and potential are connected by the following relationship:

$$\frac{x}{d} = \frac{3}{\pi}\left[\frac{\sqrt{3}}{6} ln\frac{(1+t)^2}{1-t+t^2} + \frac{2t-1}{arctg \sqrt{3}} + \frac{\pi}{6} \right],$$ (14)

where

$$t = \left[exp\left(-\frac{3e\varphi}{kT} \right) - 1 \right]^{1/3} = \left[\left(\frac{n_0}{n}\right)^3 - 1 \right]^{1/3}$$ (15)

and the ion emission current density is determined by the next formula

$$j = \sqrt{\frac{2}{3\sqrt{3}}\frac{\lambda}{d}}en_0\sqrt{\frac{2kT}{M}}\qquad(16)$$

Now let us consider a general case. To this end, introduce the dimensionless variable

$$\eta = -\frac{e\varphi}{kT}\qquad(17)$$

and the parameters

$$j_0 = en_0\sqrt{\frac{2kT}{M}},\qquad(18)$$

$$a = \frac{j}{j_0}\qquad(19)$$

and rewrite (2) as

$$j_0 exp\left(-\eta\right) = exp\left(-\frac{x}{\lambda}\right)\int_0^x \frac{(G(\xi)+C(\xi))exp(\frac{\xi}{\lambda})d\xi}{\sqrt{\eta(x)-\eta(\xi)}}\qquad(20)$$

Multiplying by $d\eta/dx$ and integrating for dx from 0 to y, we obtain, after certain manipulations, an integral equation for the potential:

$$\eta(y) = -\ln(1-\frac{a}{j}\int_0^y (C(\xi)+G(\zeta))exp\left(\frac{\xi}{\lambda}\right)2\left[exp\left(-\frac{y}{\lambda}\right)\sqrt{\eta(y)-\eta(\xi)} + \right.$$

$$\left. +\int_\xi^y \sqrt{\eta(x)-\eta(\xi)}\,exp\left(-\frac{x}{\lambda}\right)\frac{dx}{\lambda}\right]d\xi.\qquad(21)$$

Now let us derive an equation for the coefficient a. Multiplying (20) by $exp\left(\frac{x}{\lambda}\right)\frac{d\eta}{dx}\frac{1}{\sqrt{\eta(y)-\eta(x)}}$ and integrating for dx from 0 to y, we have

$$\int_0^y exp\left(\frac{x}{\lambda}\right)\frac{d\eta}{dx}\frac{j_0 exp(-\eta)dx}{\sqrt{\eta(y)-\eta(x)}} = \pi j(y)exp\left(\frac{y}{\lambda}\right).\qquad(22)$$

When $x\approx d$, the derivative $d\eta/dx \to \infty$ and, correspondingly, $dj/d\eta = 0$. Then after some transfomations we have

$$a = \frac{1}{\pi}\left(\frac{exp\left(\frac{d}{\lambda}\right)}{\sqrt{\eta_0}}+\int_0^d \frac{exp\left(-\eta-\frac{d}{\lambda}+\frac{x}{\lambda}\right)dx}{\lambda\sqrt{\eta_0-\eta}}\right),\qquad(23)$$

where $\eta_0 \equiv \eta(d)$.

The system of equations (22) and (23) was solved by the successive approximation method. The potential distribution in the gap and the coefficient a were calculated for the parameter λ/d ranging from 0.05 to infinity. The calculations showed that the potential fall across the plasma increases (Fig.1) and the ion emission current drops (Fig.2) with decreasing λ/d. At large and small λ/d the calculation results coincide with the limiting cases discussed above.

Note that the calculated density of the ion emission current is well described by simple approximation relationships over the whole range of the λ/d values from 0.05 to infinity. In the

first case ($G(x) \sim const$) the density of the ion emission current may be estimated by the expression

$$j = \frac{0.344}{\sqrt{1+0.25d/\lambda}} n_0 \sqrt{\frac{2kT}{M}}$$

(24)

while in the second case ($G(x) \sim n(x)$) by

$$j = \frac{0.344}{\sqrt{1+0.31d/\lambda}} n_0 \sqrt{\frac{2kT}{M}}$$

(25)
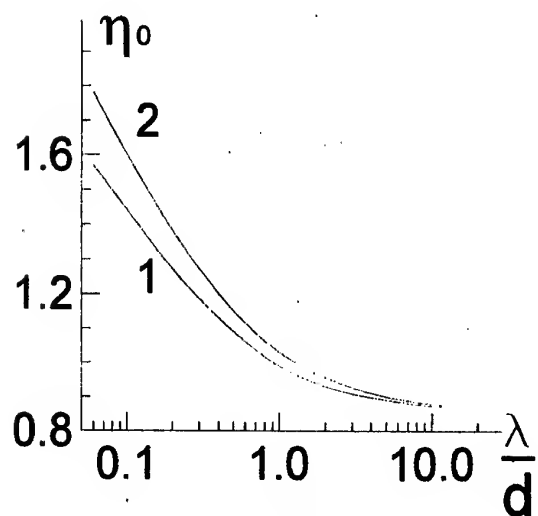
Fig.1
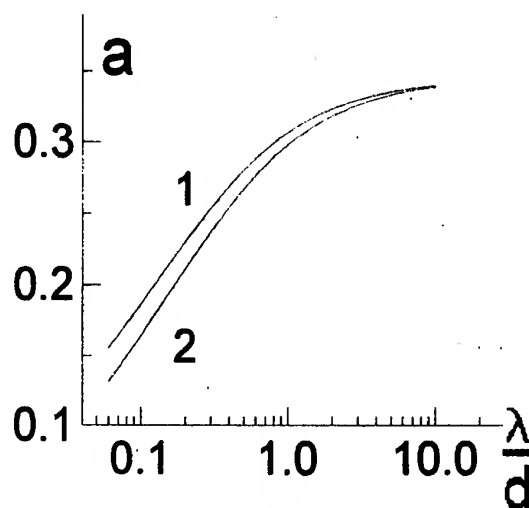
Fig.2

REFERENCES

[1] B.M. Smirnov. The Physics of Weakly Ionized Gases. Moscow, Nauka, 1985, 424 p.
[2] L. Tonks and I. Langmuir // Phys. Rev., vol. 34, 1929, pp. 876-922.

Beam-Plasma Interaction Experiments between Low-Energy Heavy Ions and Laser Plasmas

M. Ogawa, U. Neuner, K. Nishigori, A. Sakumi, H. Kobayashi,
M.Takizawa, K. Horioka and Y. Oguri

*Research Laboratory for Nuclear Reactors, Tokyo Institute of Technology,
2-12-1 Ohokayama, Meguro-ku, Tokyo 152-8550 Japan*

ABSTRACT

Interaction of ≈ 0.2 MeV/u oxygen ions with plasmas has been studied using laser plasma targets. We have observed high charge stripping at an early rise time of CO_2 laser and enhanced energy loss in LiH plasma.

INTRODUCTION

It is a key issue to study an energy deposit rate of heavy-ion driver beams in a fuel pellet for heavy-ion inertial confinement fusion. Stopping power of projectile ions is expressed as $-dE/dX \propto (Z_{eff})^2$ where Z_{eff} is equilibrium charge state of the projectiles. The equilibrium charge state Z_{eff} in the plasma with electron density of $n_e < 10^{19} cm^{-3}$ is larger than in cold matter. Theory [1] predicts that the charge state Z_{eff} turns to decrease for the denser plasma of $n_e > 10^{19} cm^{-3}$ where dielectronic recombination plays a significant role. On the other hand, the stopping power depends strongly on projectile ion energy in the range of 0.1 to 1 MeV/u. So it is interesting to measure the interaction experiments for the dense plasma near $n_e = 10^{19} cm^{-3}$ and also for the projectile energy of E < 1 MeV/u. So far interaction experiments [2-7] have been conducted using both discharge plasmas and laser plasmas. For the low-energy heavy ions, the laser plasma targets are suitable for the interaction experiments because they are free from the magnetic field which deflects the ion trajectory. We have developed two types of laser plasma targets by means of a CO_2 laser and a Nd glass laser. We report the present status of the interaction experiments performed by using low-energy oxygen ions.

EXPERIMENT

Heavy ions are generated by the NEC 1.7 MV tandem accelerator.Two interaction chambers are installed on separate beam lines. One plasma target is formed by irradiating a polyethylene plate with a TEA CO_2 laser of 5 J/pulse energy. An experimental setup with the CO_2 laser is schematically depicted in Fig.1. Fig.2 shows a time profile of the CO_2 laser. The laser light is focused on a planar target with a spot size of 0.5 mm x 9 mm. The surface of laser irradiation target is refreshed by rotating the planar plate. The electron density of the plasma is diagnosed via the Stark broadening of hydrogen lines. Fig.3 shows a time evolution of electron density. The density of ablating plasma ranges from 10^{18} to 10^{17} cm^{-3} for a period of 1 μs at a distance of 0.5 mm from the polyethylene surface. So areal density of free electrons is the order of 10^{17} cm^{-2}. The projectile ions are collimated with an aperture of 1 ϕ at a distance of 0.5 mm from the polyethylene surface. A typical beam current of 2.4 MeV O^{2+} is ~ 10 nA on the plasma target. The outgoing ions are analyzed by a dipole magnet and then are detected with aluminum coated plastic scintillators simultaneously for different charge states. A carbon foil of 20μgcm^{-2} is used as a reference material.
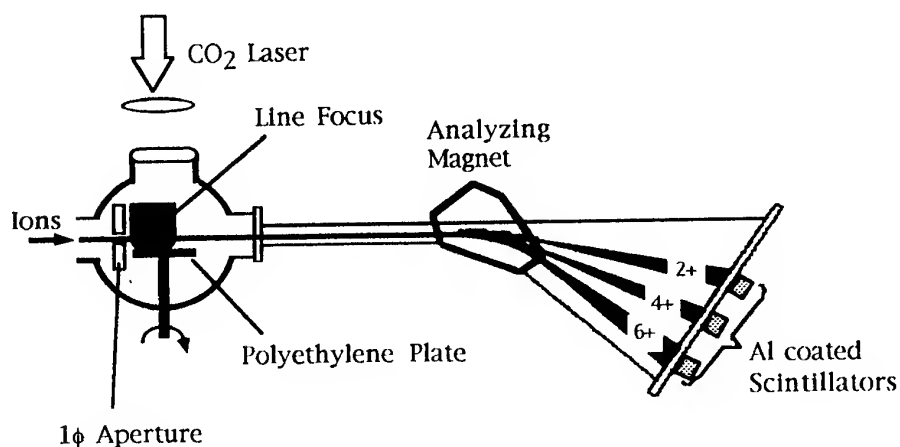
Fig.1 Schematic view of experimental setup

Another plasma target is produced by irradiating a LIH pellet of 50 to 100 μm in diameter with a Nd glass laser of 3J/pulse energy and of Δt = 30 ns pulse width. The laser irradiation forms a spherically expanding plasma. Mach Zehnder interferometry reveals the electron density decreasing gradually with radius for a period of 60 to 140 ns as indicated in Fig.4. The spherically symmetric expansion of the plasma is verified by observation with a high speed framing camera. According to these measurements the LiH plasma is suitable for the interaction experiments when the projectile-beam size is defined close to 1 mm. Several optical measurements are performed to derive the plasma temperature.
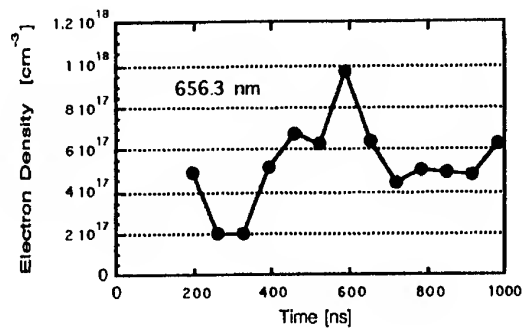
Fig.3 Electron density of polyethylene plasma
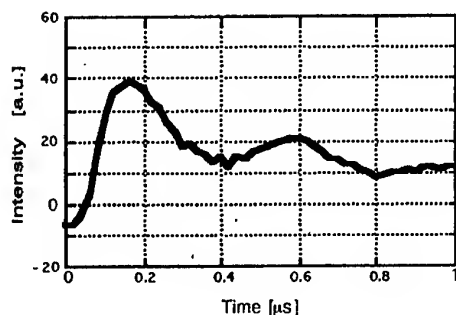
Fig.2 Time profile of CO_2 laser
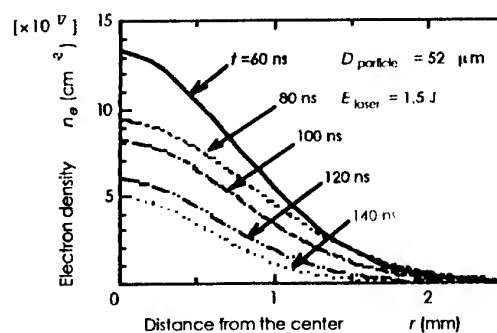
Fig.4 Electron density distribution of LiH plasma

RESULTS AND DISCUSSION

Fig.5 shows a time evolution of charge states of oxygen ions observed after the interaction with the polyethylene plasma. In this figure the flight time of the ions is subtracted to adjust the time scale to the laser. The yield of 6+ state has a peak near $t = 50$ ns on an early phase of the fast component of the CO_2 laser. In contrast with the 6+ case, the yield of 4+ state reaches to its first maximum around $t = 250$ ns and then to its second slow maximum at $t = 600$ ns. Two peaks of the 4+ yield coincide with two components of the CO_2 laser appearing at 160 ns and at 600 ns (Fig.2). The relative yield ratio of I^{6+}/I^{4+} at the peak of 6+ yield is 3.4 which is two orders of magnitude larger than the value of 0.04 reported [8] for a carbon foil. The high yield ratio is a clear evidence of the enhanced charge stripping of the plasma.
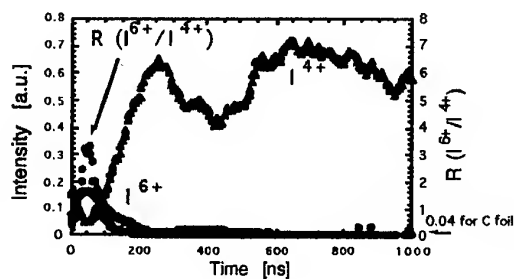
Fig.5 Yields of 4+ and 6+ states and their ratio in polyethylene plasma

Fig.6 indicates the energy losses of the oxygen ions in the plasma measured for the charge states of 4+ and 6+ where the time scale is corrected by flight time of ≈ 250 ns. Both energy loss curves reveal the same profiles within the experimental errors. The high charge-stripping yield of 6+ state is not reflected in these energy-loss profiles. The curves peak around $t = 100$ ns and $t = 500$ ns which correspond to the fast and slow components of the CO_2 laser as shown in Fig.2. We interpret the similar energy-loss profile as following; the charge state of either

4+ or 6+ is determined when the ions exit the plasma target although the effective charge Z_{eff} inside the plasma, independent of the charge state of the outgoing ions, governs the energy loss.
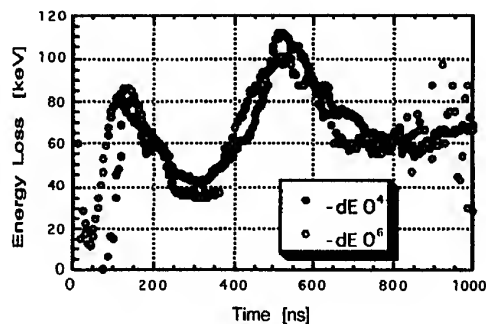
Fig.6 Energy loss of oxygen ions in polyethylene plasma

Preliminary evaluation of the stopping power for the 4+ ions in the polyethylene plasma is shown in Fig.7, where the target density is derived by assuming that two third and one third of free electrons are shared by hydrogen and carbon atoms, respectively. This estimate includes the errors of about 50%. A peak seen at $t = 300$ ns corresponds to the valleys both in Fig. 3 and Fig.6. So we conclude that this peak is spurious and caused by some unknown sources. Other data points are slightly above but close to the stopping power in the cold polyethylene [9]. This situation is the same for the case of 6+ ions. So the present observation can be explained as following; the carbon atoms are mostly ionized to only 1+ state in the polyethylene plasma, and the C^+ ions having five bound electrons behave like neutral atoms.

The stopping power observed for the LiH plasma with the 3.6 MeV oxygen ions is compared with a curve for the cold LiH [9] in Fig.8. The data point is obtained at $t = 60$ ns after the Nd laser irradiation. This case indicates a clear enhancement of energy loss in the plasma. The large stopping power is understood in terms of larger Coulomb logarithm and higher equilibrium charge state in the plasma.

-945-

CONCLUSION

We have observed enhanced charge stripping of oxygen ions in polyethylene plasma at an early rise time of CO_2 laser. Enhancement of stopping power has been measured clearly for LiH plasma but only slightly for polyethylene plasma.
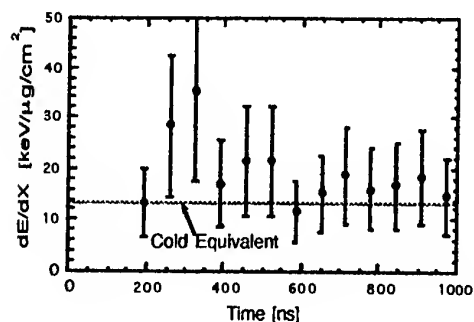
Fig.7 Stopping power observed for O^{4+}
ions in polyethylene plasma
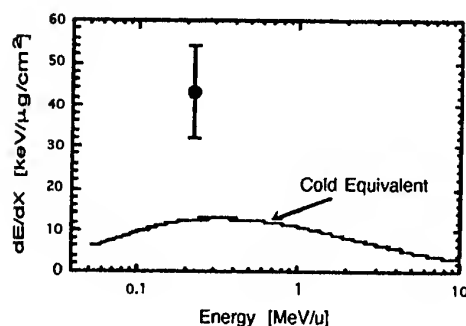
Fig.8 Stopping power of 3.6 MeV
oxygen ions in LiH plasma observed
at t = 60 ns

[1] T.Peter et.al., Phys.Rev. A43 (1991) 1998-2030

[2] D.H.H.Hoffmann et.al., Nucl. Instr. and Meth. B90 (1994) 1-9

[3] J.Jacoby et.al., Phys.Rev.Lett. 74 (1995) 1550-1553

[4] C.Couillaud et.al., Phys.Rev. E49 (1994) 1545-1562

[5] M.Chabot et.al., Phys.Rev. E51 (1995) 3504-3510

[6] M.Ogawa et.al., Fusion Engineering and Design in press (1998)

[7] U.Neuner et.al., Nucl. Instr. and Meth. in press (1998)

[8] K.Shima et.al., Atomic Data and Nuclear Data Tables 51 (1992) 173-241

[9] J.F.Ziegler, Handbook of Stopping Cross-sections for Energetic Ions in All Elements, and TRIM86

EXPERIMENTAL RESEARCH ON ION EJECTION FROM PREVIOUSLY CREATED EXPLOSION-EMITTED PLASMA IN MAGNETIC INSULATED DIODES.

M.S.Opekounov, G.E.Remnev, I.I.Grushin

Nuclear Physics Institute at Tomsk Polytechnic University, Tomsk

Our work is dedicated to research on dense plasma generation using explosive electron emission with desired plasma composition directly in the diode [1,2]. The first (negative) high-voltage pulse being applied to the potential electrode of the diode (subsequently called anode) serves for plasma formation. The second (positive) pulse serves for the acceleration. These pulses are produced by nanosecond generator and considered as one shot. During delay between these two pulses the plasma spreads from anode to cathode. So when the accelerating voltage pulse arrives the plasma in the anode-cathode gap already exists.

The first experiments were carried out on high-current electron accelerator "TONUS", which was upgraded for ion beam generation. The results of these experiments have formed the research branch on development of dual high-voltage pulses generators and diode systems working in a two-pulse mode.

Our further studies on operation conditions of various diode systems (the diodes with pinching of an electron beam, reflective triode, magnetic insulated diodes) have been carried out on "TONUS", "Loutch", "Temp", "Muk-M" accelerators [3,4,5,6]. These studies have revealed a number of advantages of strip magnetic insulated diode systems with the closed electron flow's drift. Such systems operate in a two-pulse mode and are used for the generation of heavy ion beams. One of above advantages is that the transverse magnetic field in the diode slows down the plasma flow from one electrode to another. This feature allows to vary the delay between pulses in rather wide range and makes it possible to choose the optimum diode operation mode. The second advantage is that the magnetic field provides a faster plasma flow along the field. Plasma spreads upon a potential electrode's surface, what leads to the formation of homogeneous plasma emission boundary and increases the efficiency of an ion ejection. Third advantage is that there is no electron dumping onto the anode's working area, that reduces the anode erosion and increases the anode lifetime and stability of ion flow's parameters. The target degeneration due to erosion products is also reduced. And the last feature is that there is a possibility of generation of homogeneous large-area ion beams with sufficient power density (10^6-10^8 W/cm^2) for practical use [7].
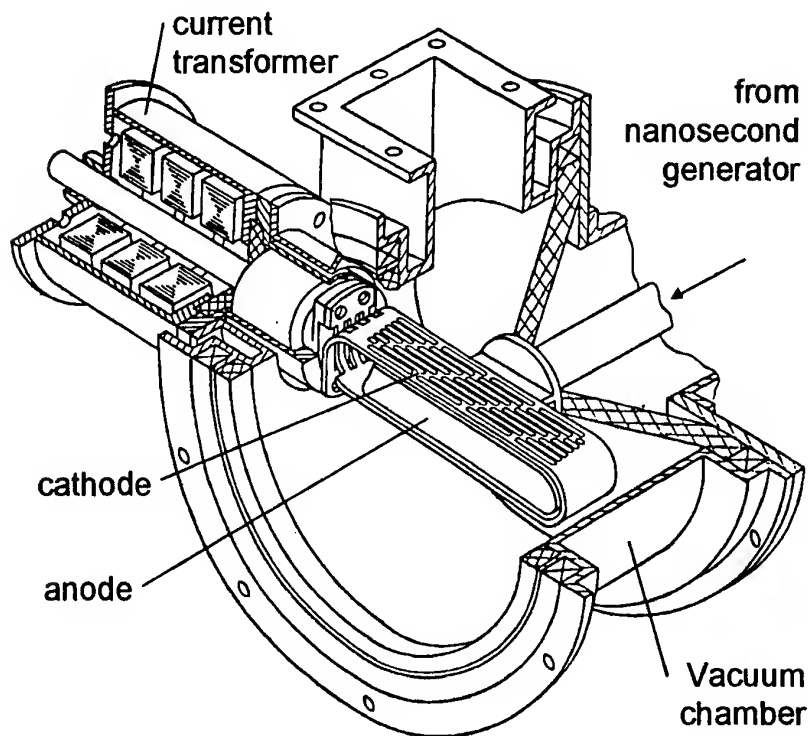
Fig. 1. "Muk-M" accelerator. Magnetic insulated diode with closed electron flow's drift.

The discussed below experiments were carried out on the "Muk-M" accelerator [6,7]. The amplitudes of plasma-generating and accelerating voltage pulses on the diode were varied in a range from 50 to 150 kV. The duration of voltage pulses was varied from 20 up to 200 ns, the duration of front of the plasma-generating pulse in all cases did not exceed 10 ns. The delay between voltage pulses had been changed from 50 up to 300 ns.

The studies of plasma generation and current removal from plasma were carried out for both graphite and aluminum potential electrodes. The geometry and design of the diode system is shown at the fig. 1. The cathode is designed [6] as a flattened strip coil with open side connected to the current transformer and provides the electron flow closure along coil's inner surface all over the anode-cathode gap cross-section. The holes (slots) in cathode's body are designated to pass the ion beam so the total cathode transparency on the side of beam removal is about 60%. The cathode is made from copper (in some experiments the stainless steel was used as cathode material) and encloses the anode as shown in fig. 1. The transformer operates as a source of an insulation current.

The anode of magnetic insulated diode is made from aluminum. Anode width is 45 mm and the length is 200 mm. The width of cathode is equal to anode one, its thickness is 4 mm. For improved plasma generation the anode has the special prepared surface. Currently this
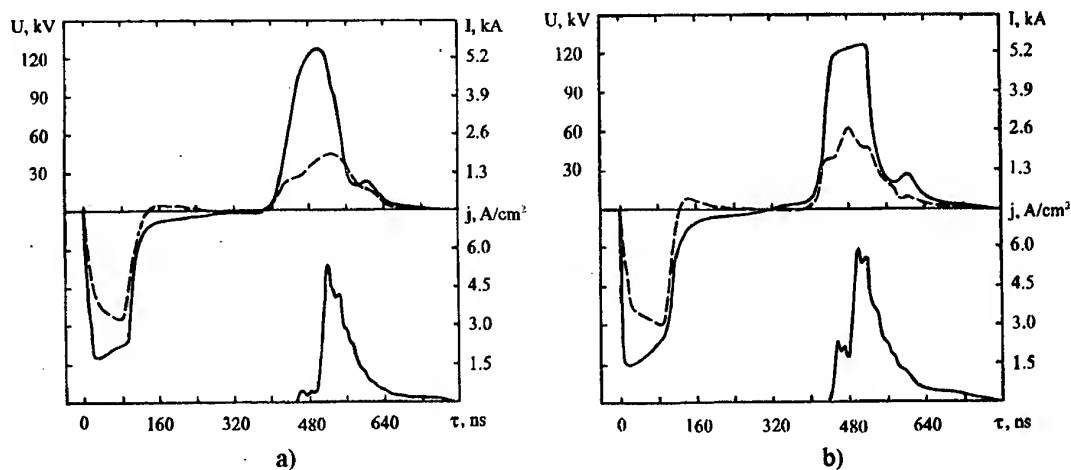
Fig.2   Voltage, total diode current and ion current density oscillograms for graphite (a) and aluminum (b) anode insertions.

surface is prepared on upper side of the anode as shown on fig.1. The surface is cultivated with ledges of rectangular cross-section of 2x2 mm and height of 5 mm. The width of intervals between ledges is 2 mm. Ledge dimensions and width of interledge intervals are estimated from the condition $h < 2 \cdot v_{pl} \cdot (t_1 + t_d)$, where v_{pl} is plasma velocity transverse to magnetic field direction, t_1 and t_d - durations of the first voltage pulse and of the delay, respectively. Thus the homogeneity of plasma emission boundary is provided. The cross-section of ejected ion flow is about 45x200 mm^2 (or 90x200 mm^2).

It is possible to install the coverings (insertions) made from various materials on the side of the beam removal. These insertions have also cultivated surface and define therefore the composition of accelerated ion flow. The anode insertions have dimensions of 45x200 mm^2 (in some experiments dimensions were enlarged up to 90x200 mm^2).

The density of the ejected ion current is measured by the Faraday cup, while the total diode current and diode voltage are measured by Rogovsky coil and active voltage divider respectively. The determination of the mass and energy spectra of accelerated ion flows is performed using Thomson spectrometer with CR-39 as a solid-state track detector [8, 9]. The oscillograms of the voltage, total diode current and ion current density at 40 mm far from the cathode are shown at the fig.2 for graphite and aluminum anode coverings.

The results of our studies are as follows:

- The plasma generation on a potential electrode in magnetic insulated diodes occurs only if voltage pulse duration is longer than 30 ns;

- During the action of an accelerating voltage pulse there are no additional plasma generation in the diode or it is negligible;

- The amount of charge ejected from plasma depends weakly on plasma generating voltage pulse duration, on delay between plasma generating and accelerating pulses and on accelerating voltage pulse duration.

The large-area (>100 cm^2) carbon and aluminum ion beams with total current of several kiloampers are produced in such diode systems. The beam composition depends on potential electrode material and depends weakly on the shot frequency in the range from 0.1 up to 5 Hz. The relative percentage of light elements (hydrogen, carbon or nitrogen ions) in the beam is less than 20%. The homogeneity of the ion flow over its cross-section at 10 mm distance from cathode is not worse than 20%.

Authors are grateful to Dr. V.M.Matvienko for his valuable remarks on this paper.

References

1. Mesyats G.A., Generirovaniye moshnykh nanosekundnykh impulsov. (The generation of nanosecond power pulses), Moscow, Sov. Radio, 1974, 255 (in russian).

2. Logachev E.I., Remnev G.E., Usov Yu.P. // Pisma v Zh.Tekh. Fis. 1980, t.6, v.22, s.1404–1406. (in russian).

3. Isakov I.F., Logachev E.I., Lopatin V.S. et al. / Generation of Heavy Ion Plasma // Proc. XI Int. Simp. Jn Discharges and Electrical Insulation in Vacuum. Berlin, 1984, p.413–416.

4. Isakov I.F., Logachev E.I., Lopatin V.S. et al. / Pulsed ion beams generated from dense plasma in streak MID. // Proc. 6 Int. Conf. On High Power Particle Beams. Kobe, Japan. BEAMS'86, 1986, p.77–80.

5. Isakov I.F., Kolodii V.N., Opekounov M.S. et al. Sources of High Power Ion Beams for Technological Applications. // Vacuum, 1991, vol.42, no.1/2, p.159–162.

6. G.E.Remnev, M.S.Opekounov, V.V.Vasil'ev et al. A high-current ion accelerator for short-pulse ion implantation // Instrum. and Experim. Techniques, vol.40, no.5, 1997, pp.727-731. Translated from Pribory i Tekhnika Eksperimenta, no.5, 1997, pp.152-156.

7. G.E.Remnev, I.F.Isakov, M.S.Opekounov et al. High-power ion beam sources for industrial application. // Surface & Coatings Technology 96, 1997, p.103-109.

8. M.S.Opekounov, G.E.Remnev, A.N.Grishin et al. / CR-39 Nuclear track detector application for the diagnostics of low energy high power ion beams // Radiation Measurements, 1995, vol.25, no.1-4, pp.739-740.

9. M.S.Opekounov, S.A.Pechenkin, G.E.Remnev et al. / CR-39 Nuclear Track Detector Application for the Diagnostics of Low Energy High Power Ion Beams // Proc. 11 Int. Conf. On High Power Particle Beams. Prague, Czech Republic, BEAMS'96, 1996, vol.2, pp.1068-1070.

Intense ion beam generation in an anomalous glow discharge with non-metallic liquid anode

I.M.Roife, Yu.A.Vasilevskaya, E.G.Yankin
D.V.Efremov Institute of Electrophysical Apparatus, 189631, Metallostroy,
S.-Petersburg, Russia, e-mail rim@niiefa.spb.su

A new type of an effective and compact ion source [1], [2], [3] has been developed in the D.V.Efremov Institute in the last few years. Conducted researches have shown that such type of the source provide currents of tens mA operating in the long stationary mode, since it is easily scaled. It permits to consider opportunities of industrial use of similar ion sources. The main feature of the source is use of a liquid with rather high pressure of residual vapours in the anode. Similar sources of ions with a liquid metall anode (LMS), which work in deep vacuum [6], are known.

Going from liquid metall emitters to liquid dielectric with higher pressure of residual vapours (such as mineral oils, alcohol, benzene), we managed to receive considerably larger currents of Ampere scale. The operating conditions corresponded to lower vacuum of 10^{-2} - 10^{-3} Torr. Thus, if in an LMS practically there are no discharge effects, here they should already play appreciable, if not determining role. It is production of discharge plasma of high enough concentration that determines opportunities of high currents generation.

Sources of ions with liquid dielectric in the anode emitter are characterized with the plasma production directly at the surface of the emitter in addition to concentration of the electrical field (as it takes place in an LMS) fig. 1.

A preliminary concentration of the field in the anode emitter is provided by the insertion of needle current inputs moistened with the anode liquid.

For maintenance of uniformity of work of the extended emitter, the idea of a multypoint current input with special ballast resistors [7] installed separately in each current input was used. On fig.3 such a source is schematically shown, with the help of which were managed to obtain rather satisfactory characteristics of the source operation (stability of work in time, uniformity of the beam in space).

In similar sources bunches of fibres of a carbon fabric with the diameter ~ $10\,\mu$. were used as current inputs.

A module of the source contains a high-voltage input of the anode voltage to a metal, pumping chamber pumped by a forevacuum pump to a pressure 10^{-2} - 10^{-3} Torr. At the end of the voltage input there are elements for fastening the needle current input placed inside an insulating volume from plexglass filled with a dielectric liquid (forvacuum oil). Point of the current input extends less than 1 mm beyond the oil surface. Current input in a considered design version of the source made fabricated from Wolfram wire.

Extractor, as well as the whole other volume, is under ground potential and has an aperture of 2 mm in diameter for the beam extraction. The needle point - extractor distance is in the limits $5 \div 10$ mm. Collector can be installed in any place of the ion drift tube. The high-voltage input work both in the mode of the source start-up up to 10 kV and in the stationary mode up to 1 kV. The source module source current is 5 mA (in the stationary mode).

The major parameter is the electrical field magnitude. In tested design version of the source, the emitter-extractor gap is in the limits from several mms up to 10 mm. The potential difference of at the moment of voltage switch on is from 7 kV (for the stationary mode) up to 15 kV (for the pulse mode). Thus, scale of an average electric field in the accelerating interval is about 10^4 V/cm. It is enough to form a, so-called, "Taylor cone" on the surface of the liquid

emitter, which provides rather high concentration of the electric field on the emitter. So for vacuum oil of BM-6 type (in the majority of cases used in this work) the surface tension force is T ~ 30 din/cm, the density is ρ < 1 g/cm^3. In this case a critical field necessary for formation of Taylor cones is provided [4, 5].

It should be noted, that in contrast to LMS (where, because of large T and ρ magnitudes, large fields are needed) in the considered sources the potential difference on the accelerating gape decreases in the process of operation.
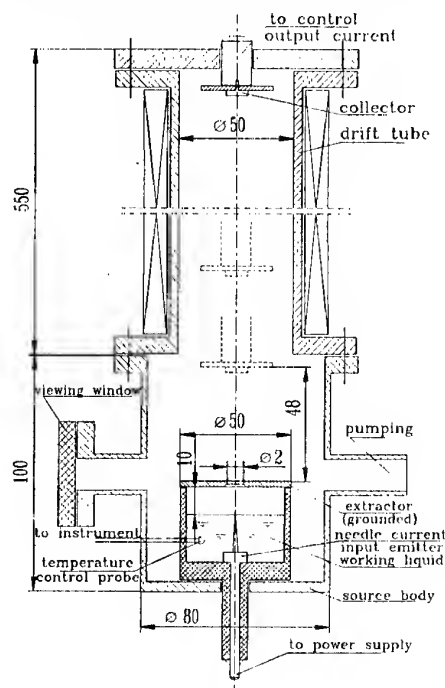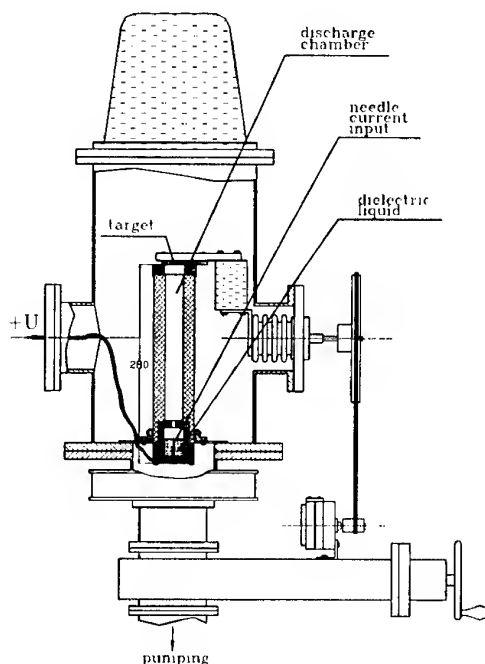
Fig. 1.   Fig. 2.

As was shown in [1], the source operates in the glowing discharge mode. The current-voltage characteristic of the discharge corresponds to that of anomalous glowing discharge. The feature of the discharge is the fact, that the potential drop is concentrated in a small area near the point current input of the emitter.

The evaluation of the electric field strength close to the needle current input in view of additional effect from the "Taylor cone" being formed (on the surface of the liquid moistening the needle point) shows that it can reach a magnitude of $\geq 10^5$ V/cm. At such fields an energy ~ 1 keV (appropriate to the voltage drop in the discharge) can be obtained by single-ionized ions at a distance of $\leq 10^{-2}$ cm.

Thus, in this discharge the main voltage drop is on the anode and energetic particles are ions, unlike a common discharge, these energy is transmited to electrons in the area of the cathode drop.

For studying the generated ion beam energy distribution additional collimation of the beam was done and proper vacuum conditions were provided in the space drift, where the electrostatic analyzer was placed.

Measurements have shown, that the average energy of the beam corresponds to the magnitude of the potential difference on the emitter-extractor gap.

When a source similar to that shown on fig. 1, operated in the stationary mode, a series of spectrometric measurements of observed glow both in the emitter-extractor gap and in the drift space was conducted. These measurement have shown following:

In drift space of the beam the spectrometer fixes glow of a large number of lines, corresponding both to ionized components of carbon-hydrogen liquid - ions of hydrogen and carbon and to a large number of various impurities in the residual gas, including ions of a number of metals - iron, copper, aluminium and others, being structural elements of the installation.

In the emitter-extractor gap, glow of only one lines - H_α is fixed. This paradox can be explained by the fact that the recombination intensity(it is known that glow there is the result of recombination) is inversely proportional to the relative ion mass (for a threefold impact) or root square of this value (for recombination on a surface). Thus, recombination, as the most probable process for light ions as though "cleans" the beam of lighter ions of hydrogen. Extracted in the drift space the beam of remaining carbon ions intensively interacts with the residual gas and surface of structural elements of the vacuum chamber. It is apparently the ions generated as a result of this interaction which "dieing" (i.e. in the process of recombination), give the wide spectrum of lines observed in the drift space.
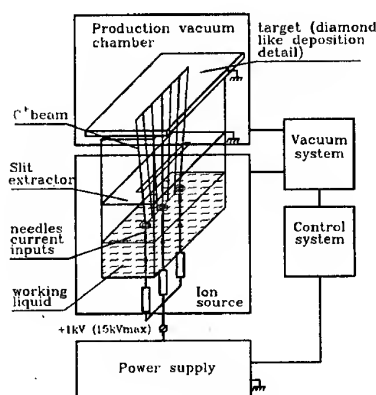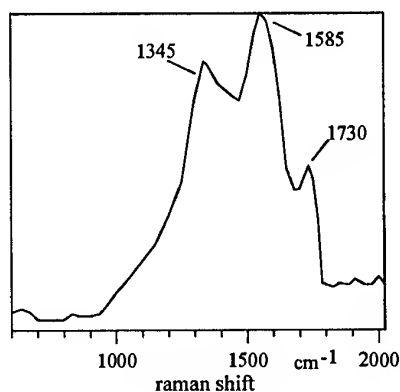
Fig. 3.   Fig. 4.

We shall consider now results of the mass - analysis on the ion beam on the exit from the source, where the vacuum oil was used as a liquid dielectric. For this purpose a known method of the electromagnetic mass-analysis was applied. A source, similar in a design to one shown on fig.1, additionally collimated and under proper vacuum ($\sim 10^{-6}$ Torr) in the drift channel was investigated. In the beam drift channel diagnostic electromagnetic system was installed.

The reliability of the results is confirmed by the fact that they are obtained after processing of a large number of measurements. Measurements in each experimental point were done not less than 100 times.

The conclusion from the conducted mass - analysis is that the main component generated by the source is the beam of singly ionized carbon. Certainly, a fraction of hydrogen ions and ,for example, singly ionized CH_4^+ can be present in the beam.

While optimizing the single point module mode of the source, the optimum (as a result of variations) magnitude of current ~5 mA was obtained. An appropriate flow of singly ionized ions per second is ~ 10^{17}. This current and corresponding flow of particles is generated in a rather small zone near the point of the current input. First of all, it can visually judge about small sizes of the area when the ion beam is generated. Conducted evaluations have shown, that linear sizes of this zone are ~ 10^{-2} cm, i.e. its volume is ~ 10^{-6} cm^3. It is obvious that the maintenance of a rather large flow of substance (in more acceptable units it is a flow of ~ 10^{23} particles per sec, crossing a cubic centimeter of volume in the point area) is not sufficient the "quiet" mechanism of thermal diffusion of molecules of the working liquid

vapour. The decreasing substance should be intensively replenished due to such a process as boiling of liquid, as well as processes close to explosive ones.

For determination of spatual uniformity of an extended ion beam, in particular, for an annular ring continuous emitter, experiments with collectors, made as a series of concentrating ring lamellas (for determination of radial uniformity in radius) and as sectoral lamellas (for determination of uniformity in corner) were conducted. The experiments were conducted in the pulsed mode. The results were unsatisfactory that, obviously, was determined by "walking" of the emission zone.

Positive results are obtained for the multipoint version shown on fig.3.

A multipoint ring current input with ballast resistors was made. Current input made as bunches of a carbon fabric 10 number were placed with regular intervals around a circle with a diameter of 3 cm. The experiments also conducted in the pulsed mode have shown rather high uniformity of the collector current distribution. Spread of the current density did not fall outside the limits of 10 %.

These results are the basis for choice (if generation of an extended beam of a multipoint current input with separate ballast resistor in each current input is needed).

Tests of variants current input have shown that the best results on stability and durability (when working in the stationary modes of an hour scale) are give by point current inputs from Wolfram wire. The stability and reliability of their work is increased for thinner points. With the help of electrolytic etching of a Wolfram wire in alkali of K or Na we manages to produce points with radius of less than $10\,\mu$, which were applied for improvement of modes of the working module of the source.

When developing the source such liquids as various alcohols, benzene, oil and others were tested. Attempts unfortunately, (unsuccessful because of violent boiling) to use water were done. The most proper for work appeared to be oil for vacuum pumps. This is determined both as it is combination of purely carbon-hydrogen compounds without an other impurities and also its temperature at which the pressure of its residual vapours provides steady operation of the source in limits convenient for operation. This also concerns the data on viscosity.

As illustration of practical use of the carbon ion source, a single-module installation (with a movable target) for diamond-like film deposition is shown in fig. 2.

On fig.4 a characteristic Raman shift spectrogram for our film is given. The maximum observed in the area of the line 1350 cm^{-1} testifies that the film has a mycrocrystal graphite phase amorphous diamond-like structure.

References

[1] I.Roife, Pisma v ZhTF, v.16, N 16, p.p. 1-4, 1990, (in russian).

[2] I.Roife, Proc. VIII Int. Conf. HPPB (Beams' 90). V2, 952-957,1990.

[3] I.Roife, Plasma Devices and Operations, v2, 103-110, 1992.

[4] G.I.Taylor, Proc. Roy. Soc. (London) A280, 303-397, 1964.

[5] L.Tonks, Phys. Rev., v48, 562-568, 1935.

[6] R.Gomer, Appl. Phys., 19, 365-375, 1979.

[7] M.A.Vasilevsky, I.M.Roife, V.I.Engelko, ZhTF, v.51, N 6, p.p. 1183-1194, 1981 (in russian).

[8] Roife I.M.,Yankin E.G., Vasilevskaya Y.A., Suetin N.V., VI Eur. Conf. DLRM, abstr. p. 11.009, Barcelone, 1995.

A HIGH-CURRENT ION SOURCE BASED ON A HOLLOW-CATHODE GLOW DISCHARGE WITH E-BEAM INJECTION

E.M. Oks[1,2], A.V. Vizir[1], and G.Yu. Yushkov[1]

[1]*Institute of High-Current Electronics, Siberian Division, RAS,*
4 Akademichesky Ave., Tomsk 634055 Russia
[2]*State University of Control System and Radioelectronics,*
40 Lenin St., Tomsk, 634050 Russia

I. INTRODUCTION

The hollow-cathode glow discharge is harnessed for generation of gas-discharge plasma [1] and production of charged-particle beams [2] at operating pressures of 10^{-3}–10^{-1} Torr. However, the use of this type of discharge as a plasma emitter in wide-aperture gaseous ion sources calls for its operation at a pressure of 10^{-4} Torr or less [3]. External injection of extra electrons into the cathode cavity [4] provides a reduction of its lowest limiting operating pressure to below 10^{-4} Torr. At this pressure the electric strength of the acceleration gap is sufficient to extract an ion beam of energy several tens of kiloelectronvolts, and the scattering and resonance charge exchange of accelerated ions at residual gas atoms affect the parameters of the beam in this transportation toward a target only slightly [4]. The paper is devoted to an investigation of the mass-charge composition of an ion beam extracted from the plasma of this type of high-current discharge.

II. EXPERIMENTAL ARRANGEMENT

An ion beam is extracted from the plasma of the main discharge operating inside hollow cathode *1* of diameter 12 cm (Fig. 1). A tungsten rod 0.7 mm in diameter serves as anode *2* for this discharge. Extra electrons are injected from the plasma of another, auxiliary glow discharge initiated between other hollow cathode *3* and electrode *1* which serves as an anode
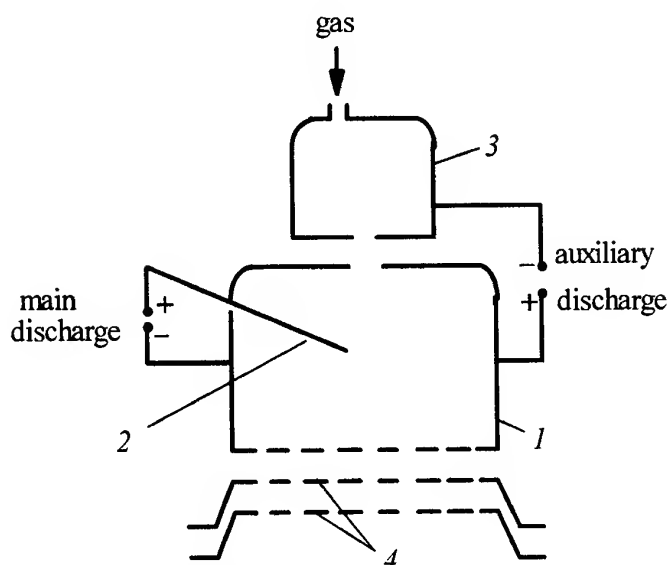
Fig. 1. Schematic of the ion source electrodes.

for this discharge. Electron injection occurs through coaxial holes made in electrodes *1* and *3*. To stabilize the emission boundary of the auxiliary discharge plasma, the hole in electrode *1* is covered with a high-transparency fine metal grid. The hole dimensions were optimized to allow electrons with a current making up to 80% of the current of the auxiliary discharge that generates these electrons to be extracted and injected into the cathode cavity of the main discharge. The injected electrons are accelerated in the cathode layer of the main discharge and, chaotically oscillating between the cavity walls, ionize the

working gas until thermalize or get on the discharge anode. The working gas is fed into the cathode region of the auxiliary discharge. Owing to the plasma drop at the holes, the pressures in the auxiliary discharge region and in the main discharge region differ at least by an order of magnitude. At the same time, the pressure difference at the multiaperture electrodes of the acceleration system is insignificant since the net surface area of the holes in the emission electrode is rather large. Used as working gases were argon, nitrogen, oxygen, and methane.

Both continuous and pulsed operation of the discharge was investigated. For the pulsed mode, the discharge power supply provides pulses of duration 300 μs and current up to 50 A. The discharge currents are switched by a trigger pulsed voltage applied is used. The auxiliary discharge current and the main discharge current are measured in the auxiliary cathode circuit and in the anode circuit, respectively.

Ions are extracted with the use of accel-decel multiaperture ion-optical system *4* whose electrodes are made of copper. For diagnosing the beam composition a time-of-flight spectrometer [5] is used. The ion source and the spectrometer are installed in a vacuum chamber with cryogenic evacuation which provides a residual pressure of 10^{-7} Torr.

III. EXPERIMENTAL RESULTS

Electron injection results in an abrupt decrease in the operating voltage of the main discharge, V_{md}. As can be seen from the plots of the discharge operating voltage as a function of the auxiliary discharge-to-main discharge current ratio, given in Fig. 2, electron injection shifts the plots toward the lower voltages; with that, the amount of shift is determined by this ratio and, hence, by the injected electron current. With the discharge operating voltage kept constant, injection of extra electrons allows the discharge to be initiated at lower pressures.

The current-voltage characteristic of the pulsed discharge is a rising curve (Fig. 3). The discharge operating voltage decreases with increasing operating pressure and injected electron current.

The minimum discharge operating voltage realized in the experiment was 50 V. In measuring the dependencies of the beam component contents on operating voltage (Fig. 4), the current onto the main discharge dc current was 1 A. At a voltage over 200 V the content of Ar^{2+} ions is 5% and is in fact invariable with voltage. The content of Al^{+} ions decreases
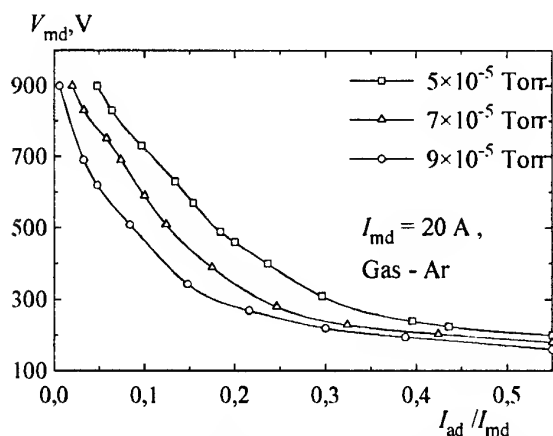
Fig. 2. Main discharge operating voltage versus auxiliary discharge current to main discharge current ratio.
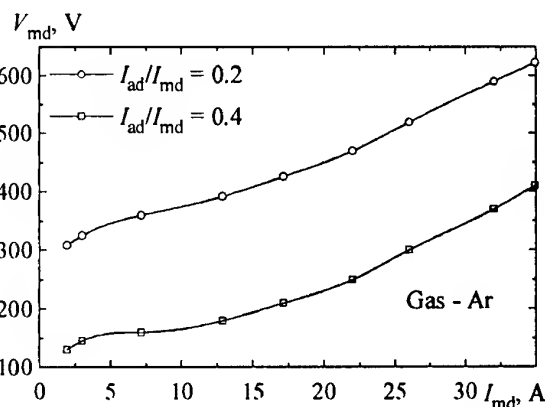
Fig. 3. Main discharge operating voltage versus current.
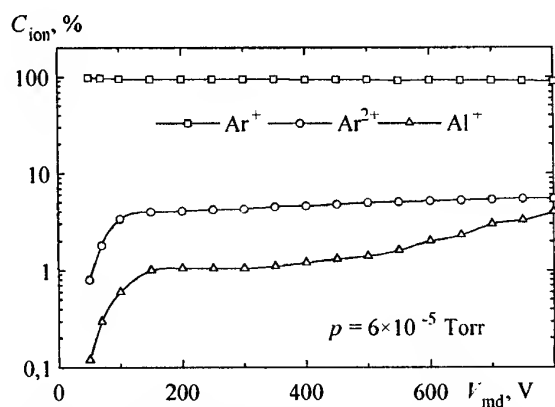
Fig. 4. Compositon of ion beam versus main discharge operating voltage.
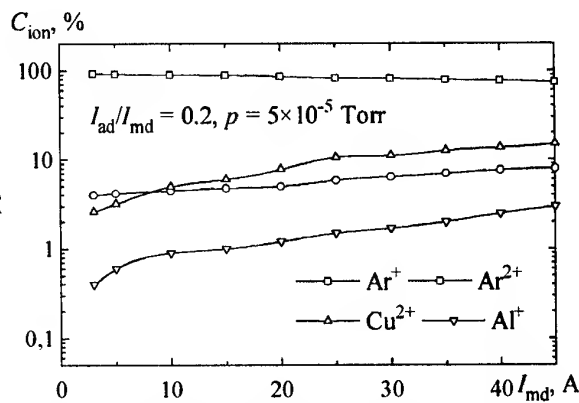
Fig. 5. Composiiton of ion beam versus main discharge current.

gradually with decreasing voltage. For voltages below 100 V, an abrupt decrease in Ar^{2+} content is observed, and the content of Al^+ ions at the lowest achieved discharge operating voltage is not over 0.15%.

Increasing main discharge current, I_{md}, leads to a change in beam composition (Fig. 5). With an increase in I_{md} the content of Ar^{2+} ions as well as the contents of the Al^+ and Cu^+ ions of respective sputtered metals increase. The fraction of metallic ions increases at a higher rate than the fraction of Ar^{2+} ions and reaches 18% at a current of 45 A. In measuring these functions, the discharge operating voltage was increased from 380 V at $I_{md} = 2$ A to 700 V at $I_{md} = 45$ A. At maximum currents, lines of Al^{3+} ions appear in the spectrum, their content in the beam being 0.4%.

With nitrogen used as a working gas, the same tendency for a change in the mass-charge composition f the beam with increasing discharge current is observed. At a low discharge current the ion beam consists of N_2^+ and N^+ ions as well as of metallic ions. As the current is increased from 1.5 to 25 A, the content of N^+ ions increases from 12 to 25%, and N^{3+} ions (up to 0.5%) appear. With that, the metallic fraction of the ion beam increases from 1.4 to 14%. Similar dependencies are observed for discharges operating in oxygen and methane.

IV. DISCUSSION

Injection of extra electrons is equivalent to an enhancement of the emissive power of the cathode. In glow discharges, the coefficient of secondary ion-electron emission is $\gamma < 0.1$ electron/ion. Therefore, a comparatively small fraction of extra electrons is suffice to change substantially the parameters of the main discharge. The discharge operating voltage decreases on injection of electrons since, first, a high discharge voltage is not necessary to provide emission from the cathode and, second, when ionizing electrons are great in number, their energy may be decreased. Injection of additional ionizing electrons makes possible a reduction of the minimum operating pressure.

The effect of the decrease in discharge operating voltage due to injection of extra electrons on the content of metallic ions in the beam is accounted for by the decrease in the coefficient of the sputtering of the cathode material caused by ion bombardment with decreasing V_{md}. Evidently, the abrupt decrease in Ar^{2+} content at voltages below 200 V is related to the fact that the double ionization potential and cross section are shifted toward the higher energies. The Ar^+-to-Ar^{2+} content ratio at voltages over 200 V approximately corresponds to the probability ratio for single and double ionization.

When comparing the parameters of a pulsed discharge corresponding to the initial portion of its current-voltage characteristic with the parameters of a dc discharge, it appears that the latter calls for a higher gas pressure for its operation than the former one, other parameters being the same. A possible explanation of this fact may be the desorption of the gas atoms adsorbed by the cathode surface during the interpulse period under the action of an ion flow onto the cathode and, as a consequence, a short-time elevation of pressure in the discharge chamber.

The dependence of the beam composition on discharge current suggests that at a high current the discharge plasma density becomes comparable to the gas atom density. The increase in Ar^{2+} content with discharge current is evidence of stepwise ionization occurring in the discharge chamber, which is process depending on plasma density and, hence, on discharge current. The increase in Ar^{2+} in this case cannot be explained only by the increase in discharge operating voltage accompanying the discharge current rise since the plot in Fig. 4 shows that the Ar^{2+} fraction depends on this voltage only in the range $V_{md} < 200$ V.

On the contrary, the mare rapid increase in the content of metallic ions in the beam is due to not only the effect of current on the increase in the amount of sputtered atoms, but also due to the dependence of the coefficient of sputtering of the cathode material on ion energy. The prevalence of the copper ion content over the aluminum ion content in the beam can be accounted for by the higher sputtering coefficient for copper [7] and by the fact that the copper electrode is in the close vicinity of the emission region.

Estimation of the plasma density at the maximum discharge current (45 A) by the well-known Bohm formula for the current onto the main discharge cathode yields 10^{12} cm^{-3}. Even if we take into account that the pressure almost doubles as a result of the gas desorption occurring during the discharge pulse, we obtain that the plasma-to-neutral density ratio reaches 0.4.

Thus, injection of electrons into the cathode cavity of a glow discharge results in a decreased discharge operating voltage and in a lower minimum operating pressure necessary for the discharge to occur. A decrease in the operating voltage of a hollow-cathode glow discharge decreases the percentage of metallic ions in the gaseous ion beam. For a hollow-cathode glow discharge, a high-current pulsed mode has been realized that, along with the benefit from the decrease in operating pressure, has made it possible to obtain the working gas 40% ionized.

REFERENCES

[1] Moskalev B.I. *Hollow Cathode Discharge*. Energiya, Moscow, 1969 (in Russian).
[2] *Plasma Emitter Electron Sources*. Ed. by E.Yu. Kreindel. Nauka, Novosibirsk, 1983 (in Russian).
[3] A.T. Forrester, *Large Ion Beam*. Wiley, 1988.
[4] E.M. Oks, A.V. Vizir, and G.Yu. Yushkov, Rev. Sci. Instrum., Vol. 69, 1998, pp. 853-855.
[5] I.G. Brown, J.E. Galvin, R.A. MacGill, and R.T. Wright, Rev. Sci. Instrum., Vol. 58, 1987, pp. 1589-1592.
[6] A.S. Metel, Sov. Phys. – Tech. Phys., Vol. 29, 1984, pp. 141-144.
[7] N.V. Pleshivtsev, *Cathode Sputtering*. Atomizdat, Moscow, 1968 (in Russian).

BEAMS'98

12th INTERNATIONAL CONFERENCE ON HIGH-POWER PARTICLE BEAMS

POSTERS

Beam-Matter Interaction and Industrial Applications

Vol. II

INVESTIGATION OF THE EFFECT OF HIGH-ENERGY ELECTRON BEAM IRRADIATION ON THE PROCESS OF FORMATION OF INTERMETALLIC PHASES IN Mo-Ni SYSTEM

G.G. Bondarenko, V.A. Belov, A.N. Tikhonov, E.M. Slyusarenko, M.M. Yakunkin

Moscow State Institute of Electronics and Mathematics (Technical University)
Bolshoy Tryokhsvyatitelskiy per., 3/12, Moscow, 109028, Russian Federation
E-mail: niipmt@cea.ru

At present stage of development of material research the principal attention is attracted the physic-chemical systems with a high degree of unequilibrity; such as amorphous alloys, compositive materials, thin-film multilayer materials etc. These systems possessed unique properties only in states remote on equilibrium are unstable. The spontaneous processes develop continuously in these systems, which transform ones in states more like to equilibrium.

In the overwhelming majority these processes are carried out in solid-phase materials by diffusion mechanism. However, in last time [1, 2] it was found out that analogous migration of atoms in materials was possible without thermal activation under high-energy electron irradiation (E ≥ 1 MeV). Apparently, for the first time this effect was found under investigation of radiation resistance of alloys [3, 4]. In [3, 4] anomalously high mobility of atoms and the formation of new phases was detected under irradiation. After that the direct evidences of this effect were received in investigations of the electron-stimulated mass transport in flaky systems [5–10].

For the results of these works we can let following comments:

1. In [5] it was found out that under influence with electron beams with energy E ≥ 1 MeV on two-layer specimens both migration of atoms from irradiated layer and reverse one occured.

2. According to [6] it is followed that electron irradiation increase both diffusion mobility of atoms and activation energy. This circumstance cause a certain suprise since majority of known mechanisms of electron-stimulated mass transport depends on the non-thermal character of atom migration.

3. According to [7] it is followed that this effect is barier character. It is shown at electron energy of $E > E_b$ individual for each materials.

4. The influence of "electron wind" on the process of electron-stimulated mass transport, apparently, is not considerable because of small value of scattering of relativistic electrons by ions of cristalline lattice [11].

5. In [8] the amorphization of intermetallic compounds under high-energy electron-beam irradiation was considered. It was shown that not only except electron energy but the irradiation temperature, and relative atomic sizes were important factors for the amorphization of intermetallic compounds.

However, behaviour of flaky systems for greatest times, when homogenization of initial systems takes place, is not considered in these works. It is considered that final states must coincide to equilibrium ones. That point of view is based by the assumption that electron beam do not essentialy change the energetic bonds in crystals but may cause a formation of supplementary defects facilitating the atom migration.

However, in [9] under electron irradiation of two-layer Cu(0.1 mm)-W specimen the formation of diffusion zone ~8–10 μm in which the copper concentration reached 10–15 % was observed from side of copper. Since these metals is unsoluble in each other then it

may be supposed that stationary states of the irradiated systems for greatest times do not coincide with equilibrium ones.

In this connection it is necessary to note that the intermediate states of system investigated in the irradiation experiments may be described if there are known initial non-equilibrium state, final equilibrium or stationary state of system, and kinetic equation describing regularity of change of system parameters under its transition to final state. For flaky materials that formulation is highly actual since for these materials the fulfilment of all conditions is really.

The principle problem which arise for that description is that if the final states of system under high-energy electron irradiation are equilibrium or stationary (quasiequilibrium). We note that existance of these quasiequilibrium states is not contradict to general thermodinamical principles, since both equilibrium and quasiequilibrium states correspond to condition of continuity of the chemical potential change on the phase boundary of flaky system. In this connection the aim of our work was to investigate an interaction of elements on the boundary of flaky systems for the greatest time under high-energy electron irradiation at the temperatures sufficient for formation of final states, to comparise these states with known equilibrium ones.

PROCEDURE AND DEVICES

The UELV-10-10 linear accelerator (electron energy $-$ 8$\div$12 MeV, maximum current density of beam $-$ 15 μA/cm^2, mean power of beam $-$ 10 kW) was used for irradiation of specimens. Irradiation was carried out in vacuum $\sim$10^{-6} torr. The specimens fixed in special thermostated device allowing to change the temperature of the specimens in the range of 600$\div$1800 K. The temperature was controled by the uncontacted method with two-spectral pirometer.

The specimens of flaky systems were prepared with use of high-pure metals: electrolitical Ni and Mo, V after fourple zone refining. The flaky systems were produced by deposition of metals on substrate of electroconductive composits in the evaporater of magnetron type. Thickness of layers for the different materials was from 50 to 200 μm and was chosen so in order to quasiequilibrium diffusion zone on an interface had a time to form.

In order to find the final states of flaky systems after irradiation a new kinetic methods have been created. This method is based on superposition of diffusion zones. In this method it is possible the use of pure metals as individual layers for production of final states.

In the method (fig. 1) after dissolution of the layers of the finite thickness the diffusion zones formed on its boundary are re-covered and the scanning of the diffusion path on the plane of the isothermal cross-section of state system diagram is beginning.

In order to draw izothermal cross-section of the state system diagram the irradiation of specimens was carried out at fixed temperature for the different expositions. After each exposition the phase composition and the distribution of elements is defined in formed diffusion zone. For investigations a set of methods of physic-chemical analysis was used, including optical and scanning electron microscopy, X-ray phase analysis and micro X-ray spectral analysis. The information about structure of diffusion zone after each subsequent exposition was compared with the one received after the preceding exposition and with the results received on the controlling unirradiated specimen producted in too conditins.
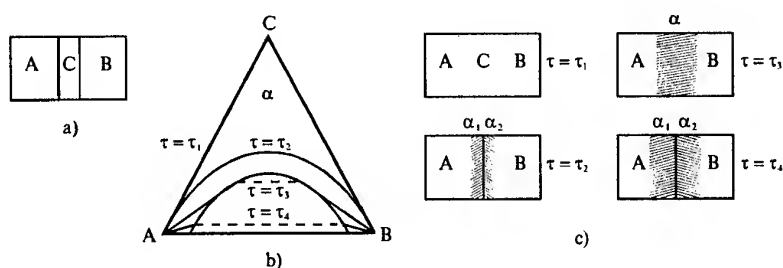
Figure 1. Form of the specimens, diffusion pathes and structure of the diffusion zones in method of superposition of diffusion zones.

THE RESULTS OF EXPERIMENTS

In this work the behaviour of the irradiated Mo-Ni diffusive pair for the different cross-sections of state diagram in range of 1000–1700 K was investigated. According to the equilibrium state diagram, apart from solid solutions on the base of Ni and Mo three phases are formed. Phase of MoNi is formed by peritectic reaction at 1635 K. Phases of MoNi$_2$ and MoNi$_3$ are formed by peritectoidic reactions at 1183 K and 1148 K. For example, under interaction of Ni and Mo in equilibrium conditions at temperature 1300 K the following structures must be formed: a) solid solution on the base of Ni, containing ~23 % at. Mo; b) MoNi phase containing ~55 % at. Mo; c) solid solution on the base of Mo, containing ~2 % at. Ni.

However, during irradiation the concentration contents of Ni and Mo at this temperature changes markedly. The contents of Ni in phase of MoNi increases to 52 % and concentration of Ni in solid solution on the base of Mo at an interface increases in 3–4 times. Contents of Ni in solid solution on the base of Ni also increases to ~85 %, and the limitary concentration exceeds equilibrium one. The concentration profiles of Ni in the transition zone of Mo-Ni diffusive pair under izothermal annealing at 1300 K for 100 hourses and under irradiation (electron energy – 12 MeV, integral dose – 5·10^8 electrons/cm^2) is presented on fig. 2a,b accordingly. Investigation of the other izothermal cross-sections allowed to detect removal of the temperatures of formation of MoNi$_2$ and MoNi$_3$ phases to the values of more high temperatures. They are 1244 K and 1206 K accordingly. By this, apart from common acceleration of mass transport across the interface its amorphization with formation of supersatured regions in relation to equilibrium compositions determined equilibrium state diagram was observed by the electron-graphic method.

For study of influence of irradiation on chemical compatibility a series of izothermal cross-section of the state diagram of Ni-Mo-V in the triple system was studied at too irradiation conditions. Mo and V are incompatible with Ni but there is a wide range of two-phase equilibrity between BCC solid soluton on the base of Mo and FCC solid solution on the base of Ni. If we shall be able to select the parameters of irradiation in order to diffusion path passed across two-phase region then a problem of the chemical compatibility this class of materials may be solved.

The investigation of the izotherms of this system in absence of irradiation (fig. 3a) have shown that V with Ni forms σ-phase which in three-system is able to form three-phase equilibrity of σ+β+γ. In Ni-Mo-V system both δ-phase of Mo-Ni system and σ-phase of Ni-V system have a small stability. In result we observed a wide region of two-phase equilibrity of β+γ, limited the triple phase equilibrities with the phases of σ and δ. Investigation of this system in conditions of irradiation showed that in the range of

concentrations of 30–65 % at. V the formation of layers of intermetallic compounds on the interface was not observed (fig. 3b). The strenght of binding of the layers after irradiation is on the level of the strenght of Ni. In the alloy with V concentration less 20 % the layer of δ-phase of Mo-Ni system was formed, and in the alloy with V concentration more 60 % the layer of σ-phase of Ni-V system was formed. Irradiation allows to reach the chemical compatibility of Ni-V alloys with Mo at V concentration of ~28–67% (fig. 3).
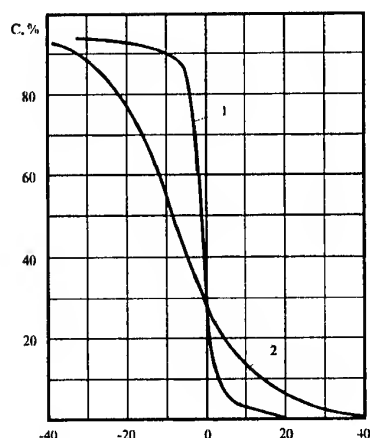
Figure 2. Concentration profiles of Ni in the transition zone of Mo-Ni diffusive pair:
1) annealing without irradiation;
2) annealing under irradiation.
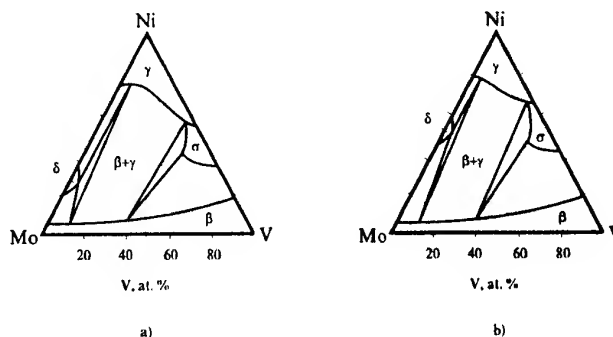
Figure 3. Izothermal cross-section on the state diagram of Mo-Ni-V system at temperature of 1300 K:
a) without irradiation;
b) under irradiation.

REFERENCES

[1] Shlenov Yu.V.,Yakunkin M.M. // J. Advanced Materials, 1996, № 4, p. 5–10.
[2] Vada T., In: Proceeding of 6th symposium on Ion source and ion-assisted technology, Pergamon Press, Tokio, 1982, p. 433–437.
[3] Bystrov L.N., Ivanov L.I., Ustinovtshikov V.M., Phizika i Chimia obrabotki materialov (in Russian), 1977, № 6, p. 25–29.
[4] Krishan K., Ray S.K., J. Nucl. Mater., 1975, № 3, p. 285–289.
[5] Mori H., Fujita H., Ultramicroscopy, 1991, 39, № 1–4, p.355–361.
[6] Zhang Y.G., Iones J.P., J. Nucl. Mater., 1989, 165, № 3, p. 252–257.
[7] Pritulov A.M., et al, Pis'ma ZhTF (in Russian), 1989, 15, № 12, p. 82–83.
[8] Bondarenko G.G., Bystrov L.N., Tikhonov A.N., et al, Phizika i Chimia obrabotki materialov (in Russian), 1988 № 4, p. 31–36.
[9] Bondarenko G.G., Tikhonov A.N., Shlenov Yu.V., Yakunkin M.M.// BEAMS'96, 1996, Prague, 2, p. 840–843.
[10] Belov V.A., Bondarenko G.G., Tikhonov A.N., Shlenov Yu.V.,Yakunkin M.M. // Book of Abstracts of the IV Sino-Russian Symposium "Advanced Materials and Processes." Beijing, China./ Printing Hourse of General Reseach Institute for Nonferrous Metals. Beijing, 1997, p. 148.
[11] Emtsev V.V., et al, Fiz. Tekhn. Poluprovodnikov (in Russian), 1992, 26, № 1, p. 22–24.

STIMULATED CONDENSATION OF NONSATURATED VAPORS: A NEW EFFECT IN THE NONEQUILIBRIUM PLASMA AND ITS APPLICATION FOR AIR CLEANING

S.P. Bugaev[1], A.V. Kozyrev[1], V.A. Kuvshinov[2], and N.S. Sochugov[1]

[1]*Institute of High-Current Electronics Russian Academy of Sciences Siberian Division, 4 Akademichesky Av., Tomsk, 634055, Russia*
[2]*Institute of Petroleum Chemistry Russian Academy of Sciences Siberian Division, 3 Akademichesky Av., Tomsk, 634055, Russia*

ABSTRACT

The phenomenon of stimulated condensation of nonsaturated vapors of organic compounds observed in recombining nonequilibrium plasma of atmospheric pressure pulsed discharges has been studied experimentally. It has been found that an aerosol is produced even at a partial pressure of vapors making up only 0.1–10% of the saturation pressure. The results of an investigation of aerosol characteristics are presented. It has been demonstrated that the harnessing of this phenomenon increases substantially the efficiency of the process of scrubbing air from organic impurity vapors.

INTRODUCTION

The dominant role of charged particles in processes of heterogeneous generation of drops was first noticed by C.T.R. Wilson [1]. The principle of operation of the Wilson chamber is based on condensation of supersaturated vapors. It is known that, even in a nonsaturated vapor, charges always generate drops (or clusters) whose characteristic size is on the nanometer scale [2].

In the literature there are data on the formation of aerosols in various plasmachemical processes. Thus, *Bogdanov* [3] reports on measurements of the mass characteristics of the aerosol formed on radiolysis of gaseous hydrocarbons under the action of an electron beam. *Paur* and co-workers [4] reports on the plasmachemical scrubbing of air from organic solvent vapors. It is proposed to harness the phenomenon of aerosol formation under the action of an electron beam for increasing the efficiency of the scrubbing process. It has been shown [4] that the detected aerosol particles consist of partially oxidized and polymerized molecules of the original organic impurity. In our opinion, a phase transition with the formation of an aerosol occurs in many plasmachemical processes where nonequilibrium low-temperature plasma is present. At the same time, the mechanism for the formation of aerosol particles and the particle parameters has not been studied at all. This paper presents results of our study performed in this line.

EXPERIMENTAL

The high-voltage nanosecond pulse generator [5] was used in the experiment. A schematic diagram of the setup is given in Fig. 1. The electric circuit of the setup operates as follows: Resonance charging of the capacitors C_1–C_{17} is performed from a single-phase ac supply line through the transformer T_2. As the spark gap $SG2$ operates, pulsed charging of the

double pulse-forming line (*1*) occurs. Closure of the spark gap *SG*1 results in application of a pulsed voltage of amplitude up to 150 kV to the electrode (*2*). The voltage pulse duration is 5 ns and is determined by the dimensions of the double pulse-forming line. Pulsed corona discharge is initiated between the high-voltage electrode (*2*) and the grounded case (*3*). The pulse repetition rate is 33, 50 or 100 Hz. The power absorbed by the discharge could be varied from 3 to 30 W. There have been used two constructions of high-voltage electrodes.

Wire high-voltage electrode consists of 0.2 mm in diameter and 130 mm in length wires, and knife electrode consists of one 0.2 mm thick stainless steel disk.

Gas (air, argon, nitrogen) with a controllable content of organic-liquid vapors is fed through the inlet pipe (*4*), goes through the discharge zone, enters the measuring chamber (*5*), and then is removed through the outlet pipe (*6*). The gas

Fig.1. Schematic diagram of the setup

flow rate is up to 900 l/h. The vapor content is varied in the range of 0.4–3 g/m^3. The formation of an aerosol could be watched and photographed owing to the transparent walls of the measuring chamber. The concentration of aerosol particles and the particle size were measured by nephelometer, which was connected to the outlet pipe (6).
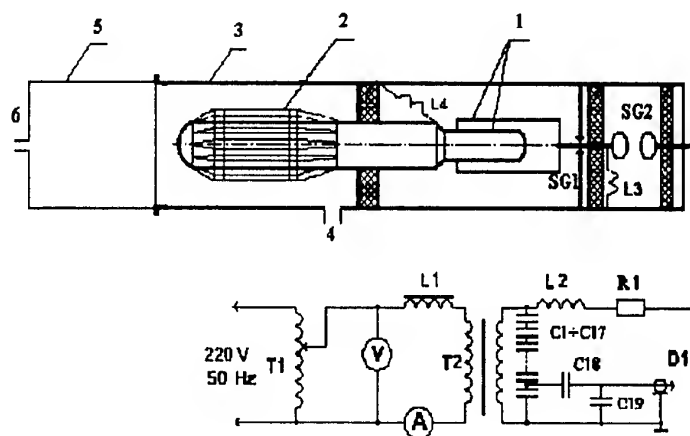
RESULTS AND DISCUSSION

The formation of an aerosol with the particle size ranging from 0.05 to 0.5 μm from nonsaturated vapors of linear (C$_5$–C$_8$) and aromatic (styrene, xylene) hydrocarbons was detected for various carrier gases (air, argon, nitrogen), but measurements were performed in the main for the air–styrene and argon-styrene mixtures. Volume and mass concentration of aerosol were varied in the range of 10^7 – 10^8 cm^{-3} and 0.1- 2 g/m^3, respectively. The characteristics of aerosol depended on resident time of gas – vapor mixture in the discharge zone, discharge power, and geometry of discharge zone, vapor mass concentration in original gas.

It is found that aerosol has electrical charge. The charge state of the aerosol was determined from measurements of its conductivity. With this purpose, a plane-parallel electrode system with the electrode separation $d = 1$ cm and the effective area of current extraction $S \approx 250$ cm^2 was placed in the diagnostic chamber. Gas containing charged aerosol particles was passed through the system. Measuring the current for a given electric field between the electrode makes it possible to find the conductivity of the medium and to estimate the charge density. Voltage-current characteristics of the aerosol medium for different concentrations of the impurities are given in Fig. 2. The air flow rate in the course of measurements was 700 l/h. It can be found from the values of current saturation that charge density in the aerosol is varied from 10^{6}cm^{-3} for iso-propanole (lower curve) up to $1.5 \cdot 10^7$cm^{-3} for styrene (upper curve).

Fig.2. Current - voltage characteristics of the aerosols.

The mechanism for the concentration of vapors can be represented in the following simplified form. The plasma ions generated by the pulsed corona discharge serve as condensation centers for microdrops with a characteristic size of some fractions of a nanometer. Later the drops grow in size due to their coalescence as a result of thermal motion and under the action of mutual Coulomb attraction.

Estimates have shown that with the characteristic drop radius $R \approx 10$ nm the most efficient coalescence of drops is due to their thermal motion. Neglecting the process of drop evaporation, we can obtain an estimate of the average drop radius R as a function of time t, since the formation of primary seeds:
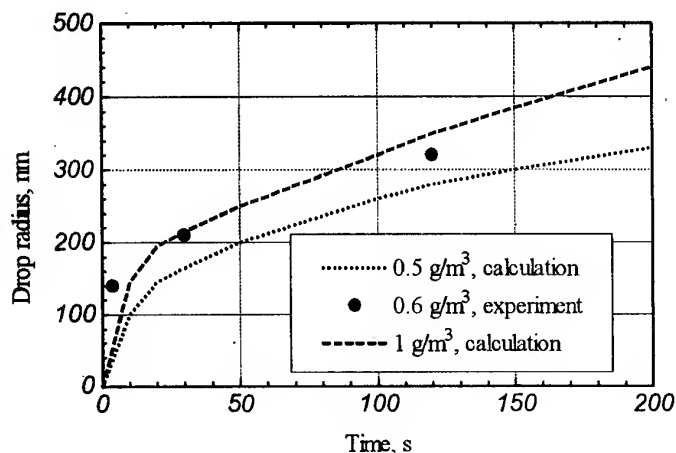
Fig.3. The average drop radius as a function of time

$R \approx [5(\rho_0/\rho_1)t(3kT/2\rho_1)^{1/2}]^{2/5}$. The results of calculations of average drops radius for two mass concentration of aerosol as a function of time are presented in Fig.3. There are experimental points at the same figure, which have been obtained in experiments with argon-styrene mixture. Knife high-voltage electrode was used. Argon flow rate was 250 l/h. Discharge power was equal to 3 W.

HARNESSING OF THE PHENOMENON OF STIMULATED CONDENSATION

We have realized on the laboratory scale the air scrubbing process based entirely on the effect of stimulated condensation. This process was realized with the use of the same technique (Fig. 1). A water scrubber was used for removal of aerosol from the air. The principle of the cleaning process was as follow. The air with organic impurities is ionized with the use of a pulsed corona discharge in an ionization chamber. The ions of the nonequilibrium low-temperature plasma produced become primary condensation centers for the impurity molecules. In the process of recombination of the plasma, the drops increase in size and a stable charged aerosol is formed. The air containing aerosol particles enters a water scrubber where it is scrubbed from the condensed impurity. The high efficiency of the condensation scrubbing has been demonstrated in an experiment described below. The main goal of the experiment was to compare the energies to be expended for the removal of one impurity molecule by the method of oxidation in a discharge and by the method of condensation scrubbing. Experimentation with the system described was performed in three modes:

Mode I: The high–voltage pulse generator is on and the scrubber is on. With that, styrene vapor is partially oxidized in the discharge and condensed with the formation of an aerosol and removal of aerosol particles in the scrubber.

Mode II : The high–voltage pulse generator is on, while the scrubber is off. With that, partial oxidation of styrene and its condensation occur as well, but the condensed drops are not removed from the gas and evaporate.

Mode III : The generator is off, while the scrubber is on. In this mode, absorption removal of styrene being in the vapor phase is accomplished.

The results of the experiment are given in Table 1. From the data presented in Table 1 it can be concluded that the highest scrubbing efficiency is achieved in Mode I. The removal of condensed styrene drops in the scrubber decreases substantially the energy required to remove one molecule of styrene. The best results we obtained were 13 eV per molecule, which is significantly lower than the energies typically consumed in plasmachemical oxidation facilities.

Table 1 Characteristics of different air scrubbing modes.

Conditions of the process	Mode I	Mode II	Mode III
Air flow rate, m^3/h	0.6	0.6	0.6
Air temperature, ^0C	20	20	20
Styrene content in the original air, g/m^3	2.16	2.16	1
Electrical power absorbed by the discharge, W	7.5	7.5	0
Water flow rate in the scrubber, l/h	30	0	30
Styrene content in the treated air, g/m^3	0.09	0.98	0.5
Efficiency of air scrubbing, %	96	54.6	50
Energy input, eV/molecule	13	23	-

SUMMARY

1. The low-temperature nonequilibrium plasma produced by a pulsed electrical discharge serves as an efficient aerosol generator even if the partial pressure of the condensing material vapor is much lower than the saturation pressure.

2. Stimulated condensation, taken into account and used purposefully, increases substantially the energy efficiency of the process of air scrubbing from low-concentrated organic vapors.

3. The air cleaning method suggested makes it possible to decrease the energy expenditure for cleaning in comparison with plasmachemical and catalytic ones. The advantage of the method becomes apparent at an initial concentration of the impurity less than 1 g/m^3.

REFERENCES

1. Wilson CTR. Phil. Trans. Roy. Soc., 1897, 189 : 265 .
2. N.N. Das Gupta, S.K. Ghosh, Reviews of Modern Physics, 1946, 18 (2) : 225
3. V.S. Bogdanov, Dokl. AN SSSR, 1961, 136 (1) : 121
4. H.–R. Paur, H. Matzing, K.J. Woletz, Aerosol Sci. 1991, 22 (1) : 509
5. S.P. Bugaev, V.B. Zorin, B.M. Kovalchuk, V.A. Kuvshinov, N.S. Sochugov, P.A. Khryapov, Proc. of 10-th IEEE Int. Pulsed Power Conf., Albuquerque, New Mexico, 1995 : 1206.

AN APPLICATION OF BARRIER DISCHARGE FOR METHANE OXIDATIVE CONVERSION WITH STIMULATED CONDENSATION OF INCOMPLETE OXIDATION PRODUCT

S.P. Bugaev[1], A.V. Kozyrev[1], V.A. Kuvshinov[2], and N.S. Sochugov[1]

[1]Institute of High-Current Electronics Russian Academy of Sciences
Siberian Division, 4 Akademichesky Av., Tomsk, 634055, Russia
[2]Institute of Petroleum Chemistry Russian Academy of Sciences
Siberian Division, 3 Akademichesky Av., Tomsk, 634055, Russia

INTRODUCTION

Rational use of methane constituting the major portion of natural gas has been the subject of investigation for many research groups throughout the world. Some studies have been devoted to the plasmachemical conversion of methane-oxygen mixtures into methanol [1, 2]. *Okasaki* and co-workers [2] have found evidence for the possibility of the production of methanol at comparatively low energies consumed; however, the degree of conversion achieved was not over a few percent. At the same time, an increase in the degree of conversion is accompanied by a fast rise in the fraction of profound oxidation products – carbon oxides [1, 2].

This course of events could be avoided if intermediate incomplete oxidation products could be removed from the reaction zone. It is known that radiolysis of gaseous hydrocarbons is accompanied, under certain conditions, by the formation of an aerosol consisting of condensing reaction products [3]. This process can be used for removal the desired conversion products from the active zone of the reactor. The present study has been devoted to the conversion of light hydrocarbons mixed with oxygen in a plasmachemical reactor where condensation of intermediate products stimulated by an electrical discharge has been accomplished.

EXPERIMENTAL EQUIPMENT AND PROCEDURE
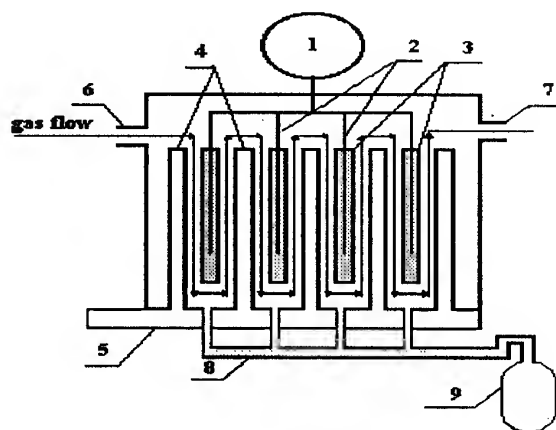
Fig. 1 Schematic diagram of the plasmachemical barrier– discharge reactor.

The schematic diagram of the setup is given in Fig. 1. The discharge was initiated with the use of a high - voltage pulse generator (1) producing high-voltage pulses. The pulse waveform was similar to that of one wave of harmonic oscillations. The most important parameters of the system are given in Table 1. The plasmachemical reactor consisted of twenty discharge cells joined in series for the passage of gas. The voltage pulse was applied to high–voltage electrodes (2) covered with a dielectric barriers (3). The

parameter	value
Power input	0.6 kW
Amplitude of high– voltage pulses	up to 15 kV
Pulse repetition frequency	1 kHz
Pulse duration	70 μs
Electrode area	0.8 m^2
Gas flow rate	up to 200 l/h
Temperature of cooled electrodes	15 °C
Conversion yield	up to 40 %

Table 1. Parameters of equipment

grounded electrodes (4) were cooled to 10—15 ^{0}C with a water– cooling system (5).

Natural gas consisting of methane (up to 90 wt. %) and the lowest alkanes C_2 - C_4 (about 10 wt. %) was used in the experiment. The natural gas mixed with oxygen (30 vol. %) was supplied to the reactor through an inlet pipe (6). The gas passed sequentially through all sections of the reactor and was removed through the outlet pipe (7). The reaction of oxidation of hydrocarbon proceeds in the reactor on initiation of a discharge. The products of incomplete oxidation are condensed on the plasma ions, which prevent them from further oxidation. The resulting aerosol consisting of the reaction products diffuses toward the cooled metal electrode and precipitates on its surface. The condensate film is removed from the active zone of the reactor under the action of the gravity force. The condensate is collected, with the help of a pipe system (8), in a receiver (9).

EXPERIMENTAL RESULTS

Harnessing the stimulated phase transition of reaction products directly in the discharge zone has made it possible to increase the degree of conversion of the gas mixture to 40 % with no increase in the yield of complete oxidation products. The contents of the reaction products determined by a chromatographic method are given in Table 2. The main useful reaction products are formic acid and methanol. It can be seen also that, 96 % of the condensable reaction products are in the liquid phase. The partial pressure of the methanol vapor is an order of magnitude lower than the equilibrium pressure of the vapor above the water solution. Other substances presented in the condensed phase, such as formic acid, methylformate, and ethanol, have not been detected in the gas phase, or their contents have been measured to be a few fractions of a percent. The efficiency of the conversion of carbon into incomplete oxidation products has made up about 60 %. It should be noted that the cost of formic acid is higher than the cost of methanol by an order of magnitude. In view of this, the plasmachemical technologies for the production of formic acid appear to have considerable promise. The noticeable content of methylformate ($HCOOCH_3$) in the condensate is due to the chemical reaction between methanol and formic acid proceeding even in the condensed phase. The presence of ethanol

Product	Found in condensate, wt.%	Found in gas, wt.%
water	36.5	1.9
formic acid	21.6	below 0.2
methanol	8.7	1.2
methylformate	3.7	0.4
acetic acid	1.2	below 0.2
acetaldehyde	0.6	below 0.2
ethanol	0.6	below 0.2
formaldehyde	below 0.2	0.5
carbon monoxide	below 0.2	11.6
carbon dioxide	below 0.2	10.4
ethylene	below 0.2	0.5
Total, %	72.9	26.7

Table 2. Composition of the conversion products found in the condensate and effluent gas

(C_2H_5OH) and acetic acid (CH_3COOH) is accounted for by the presence of C_2 - C_4 hydrocarbons in the original gas.
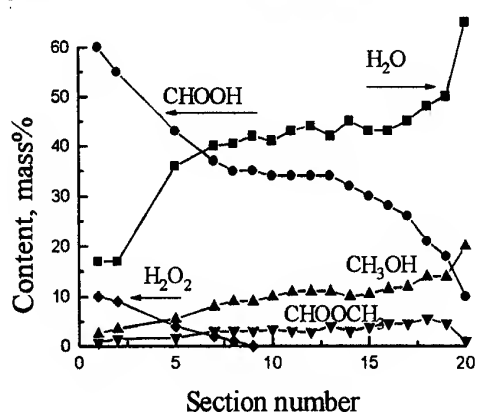
Fig. 2. Content (mass%) of various components in the condensate sampled from various sections of the reactor.

The data of the analysis of the composition of the condensate taken from various sections of the reactor are given in Fig. 2. The condensate formed in the first sections of the reactor consists of mainly formic acid plus water and hydrogen peroxide. Hydrogen peroxide has the lowest pressure of saturated vapor among these substances. Therefore, it can be supposed that the primary centers of condensation are nuclei consisting predominantly of H_2O_2 molecules. The formation of these nuclei in the first sections of the reactor promotes the heterogenic chemical reactions taking place on the surface of aerosol drops. This physicochemical process has the result that many of the reactions involved go from the gaseous phase to the condensed phase, and in the 5th to 10th sections the condensate formation rate is observed to rapidly increase.

The influence of electrophysical factors on the process efficiency was investigated in a plasmachemical reactor with a maximum electrode area of 200 cm^2. The repetition rate of the voltage pulses was varied from 100 Hz to 2 kHz and the average electric power released in the discharge was varied from 5 to 40 W.
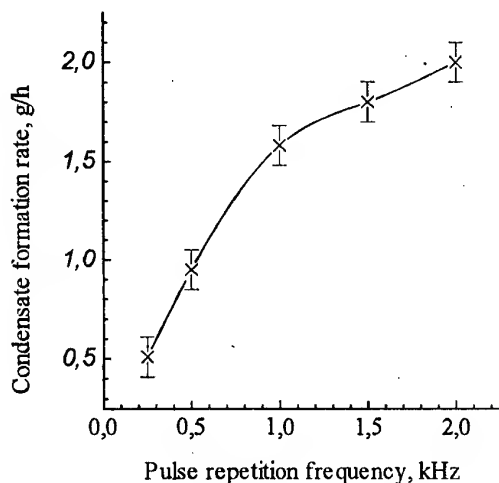
Fig.3. Condensate formation rate as a function of pulse repetition frequency

The curve given in Fig. 3 was obtained for a gas mixture containing 25 % of oxygen and for a reactor with an electrode area of 160 cm^2. The pulse energy was fixed at 35 mJ. The volumetric degree of conversion was 25 % and it was maintained constant by varying the flow rate of the gas mixture at the reactor inlet. The electrode temperature was 10 °C.

The curve given in Fig. 3 has two nearly linear sections with a kink at a pulse repetition frequency of 1 kHz. The reduced slope of the curve at high frequencies may be an indication of either an elevated average temperature of the gas in the reactor or be a characteristic of the aerosol formation time. The increase in the gas temperature due to the increase in discharge power with increasing pulse repetition frequency should decrease the degree of saturation of the vapor and the condensation rate. The same effect will be observed if the condensation of newly formed products has no time to complete within the interval between successive discharge pulses. In this case a new portion of energy is expended for decomposition and further oxidation of the incomplete oxidation products already formed but yet to be transformed into the condensed phase. If we adhere to the later viewpoint, we can estimate the characteristic time for condensation and heterophase death of radicals to be 1 ms.
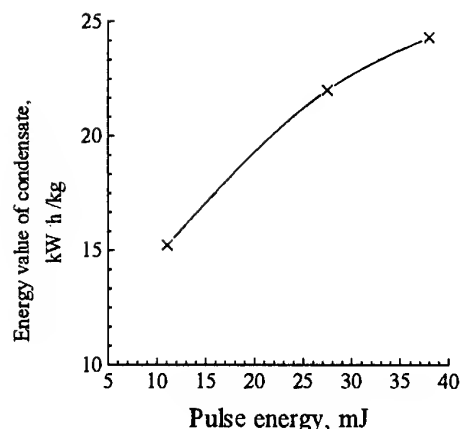
Fig.4. Energy value of the condensate as a function of pulse energy.

The energy absorbed by the gas in a single pulse affected substantially the energy efficiency of the process. Fig. 4 presents the energy value of the condensate as a function of the pulse energy. The experiment was performed with a gas mixture containing 30 % of oxygen. The pulse repetition frequency was 1 kHz. The pulse energy was varied by varying the parameters of the power supply circuit of the discharge.

As can be seen from Fig. 4, the energy efficiency increases when electric energy is supplied to the gas by small portions. The minimum energy value of the condensate achieved in this experiment was 15 kW.h/kg. The energy value of the chemical products produced, with no regard of the water incorporated into the condensate, was on a level of 32 kW·h/kg.

SUMMARY

1. A plasmachemical process of the oxidative conversion of natural gas has been realized in a barrier-discharge reactor.

2. The recombining chemically active plasma generated in the reactor favors the condensation of oxygen-containing substances even if the partial pressure of their vapor is significantly lower than the pressure of the saturated vapor. This phenomenon can be called a "stimulated condensation".

3. The formation of a metastable condensed phase makes it possible to remove a significant part of the incomplete oxidation products from the gas-phase reaction zone thus preventing them from further oxidation.

4. The operating modes of the reactor have been revealed where the principal useful reaction product is formic acid. The energetic value for its production is about 30 kW·h/kg.

REFERENCES

[1] S.S. Shepelev, H.D. Gesser, and N.R. Hunter, Plasma Chem. and Plasma Process, 13, 479 (1993).
[2] K. Okasaki, T. Nozaki, Y. Uemitsu, and K. Hijikata, Proc. ISPC-12, Minneapolis, USA, Vol. 2, 581 (1995).
[3] V.S. Bogdanov, Dokl. AN SSSR, 136, No. 1 (1961).

DEPOSITION OF A-C:H FILMS ON LARGE-AREA PLANE DIELECTRIC SUBSTRATES BY MEANS OF PULSED SURFACE DISCHARGE AT ATMOSPHERIC PRESSURE

S.P.Bugaev, K.V.Oskomov, N.S.Sochugov

High Current Electronics Institute, 4 Akademichesky Ave., Tomsk, 634055, Russia

ABSTRACT

A new-developed method for deposition of amorphous hydrogenated diamond-like carbon (a-C:H) films on plate dielectric substrates by means of pulsed surface (gliding) discharge at atmospheric pressure is presented here. It was found that films properties are influenced mainly by pulse volume energy density and, in less extent, by average surface power density of discharge, with optimum at about 75 J/cm^3 and 2-3 W/cm^2 correspondingly. Diamond-like films deposited from methane under these conditions are similar to those obtained by traditional low-pressure (p <10 Torr) methods of chemical vapour deposition, but the equipment for a-C:H film deposition in the surface discharges is much simpler and cheaper than the vacuum systems with various types of plasma generator conventionally used for this purpose. To demonstrate technological potential of the proposed method set-up for deposition of a-C:H films on flat dielectric substrates of 20X50 cm^2 was created.

INTRODUCTION

In spite of unique combination of properties and rich variety of deposition methods, technological application of amorphous hydrogenated carbon (a-C:H) diamond-like films (e.g. as protective and hard transparent coatings on soft large-area plastic components) is still limited, mainly because of low productivity and high cost of existing equipment. Therefore it is necessary to increase an efficiency of a-C:H films producing without sufficient reduction of their quality. Using of atmospheric pressure electric discharges (such as barrier and surface (gliding) pulsed discharges) for this purpose is promising. These techniques do not require complicated vacuum equipment and also provide fast deposition of a-C:H films on large-area low-melting-point substrates. However, no data are now available on the structure and properties of carbon coatings deposited with the use of the plasma of such atmospheric-pressure discharge. To obtain a-C:H films using surface (gliding) discharge and to investigate their properties was just the goal of the work under discussion. Another purpose was demonstration of technological potential of the proposed method to coat large-scale substrates by a-C:H films with sufficient growth rate.

EXPERIMENTAL

The pulsed surface (gliding) discharge was realized in system of two parallel 4-8 cm-long electrodes, separated with distance of 0.5-2 cm and situated on a dielectric plate (Fig.1). This discharge gap was subjected by bipolar voltage pulses with duration and amplitude of 50 μs and 18 kV correspondingly and with repetition frequency of 1 kHz. As a result, surface discharge, consisting of statistically and spatially homogeneously distributed single breakdowns
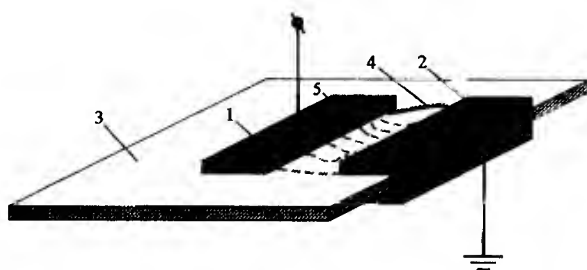
Fig.1 Schematic of pulsed surface (gliding) discharge:

1- high-voltage electrode; 2-grounded/initiating electrode; 3- dielectric plate (substrate);4- single spark breakdown; 5- discharge region.

was initiated between electrodes. Using methane as a source gas, substrate surface between the electrodes was homogeneously covered by a-C:H film deposited under atmospheric pressure.

To determine pulsed volume energy density and average surface power density, oscillograms obtained by means of high-speed oscilloscope, and photographs of sparks were analyzed. Similar method was used in [1,2]. These characteristics were easily influenced by parameters of the discharge circuit of pulse voltage generator, such as its capacitance, inductance and resistance. Average surface power of this discharge, besides the parameters mentioned above, was governed by voltage pulses repetition rate. To determine hydrogen to carbon atomic ratio (H/C), diamond-like to graphite-like carbon bonds ratio (sp^3/sp^2) and hydrocarbon groups percentage ($CH_3:CH_2:CH$) in the films we used an original precise technique based on IR spectroscopy analysis [3]. Such properties of the films as their hardness, thickness, refractive index, absorption in visible and IR range and density were determined by means of standard techniques and equipment.

RESULTS AND DISCUSSION

The density of pulse energy delivered in single spark discharge during 20-40 nanoseconds was up to 200 J/cm^3. It's worth to note that this value is close enough to [1,2], where under similar conditions this parameter for single spark in nitrogen was varied from 50 till 500 J/cm^3. Such unequilibrium conditions (rapid heating and quenching), caused by high density of the delivered energy, must lead to occurrence of metastable carbon phases on substrate [4]. It was found that films' properties are influenced mainly by pulse energy density and, in less extent, by average surface power density of discharge. The dependence of growth rate on pulse energy density (Fig.2) has unmonotonous character with maximum at about 75 J/cm^3, which corresponds to the growth rate of 110 μm/h. Most probably, existence of this maximum is connected with competitive deposition and etching processes, occurring in the discharge. Namely, as pulsed volume energy density reaches approximately 70-80 J/cm^3, etching of as-deposited film becomes sufficient. Sharp increase of absorption coefficient and decrease of hydrogen content in films (Fig.2,3), as well as increase of refractive index (Fig.3) indicate preferential etching of hydrogen from the films.

To illustrate crucial role of the pulsed energy density, points for a-C:H films deposited in a barrier discharge from methane were indicated on Fig.2,3. In this case pulsed energy density is 10 mJ/cm^3, growth rate is about 3 μm per hour and the films have polymer-like properties: H/C ratio is 1.6, microhardness is about 0.2 GPa, refractive index is 1.57 and average absorption coefficient in a visible range is $5*10^3$ m^{-1}. In contrast, a-C:H films deposited with pulse energy density of 75 J/cm^3 and had the following main properties H/C=0.7-0.8, sp^3/sp^2=3.5, $CH_3:CH_2:CH$ =22%:25%:53%, microhardness is up to 5-10 GPa, refractive index is 1.71-1.83 and average absorption coefficient in visible range is $4*10^4$-$1.8*10^5$ m^{-1}, density is 1.3 g/cm^3. Optically, the films were yellow-transparent and had high integral transparency in the visible (up to 80% for 5 μm-thick film) and IR ranges (up to 98% for 5 μm-thick film). Set of the

parameters mentioned above allows characterizing these films as a-C:H diamond-like ones, similar to those obtained by traditional vacuum CVD methods [5,6].

As for voltage pulses repetition rate, it was found that for the range between 500 Hz and 2 kHz film's growth rate is proportional to this parameter. When repetition rate exceeded 2 kHz the discharge transformed into pulsed arc stage and lost its homogeneousity. For repetition rate less than 500 Hz films became less homogeneous and, therefore, had worse optical properties. In our opinion it connected with thermodynamic processes on the surface, i.e. with existence of minimum surface power density able to supply thermal surface diffusion of growth species (in our experiments this value was determined as 1 W/cm^2). Though, this hypothesis requires further experimental and theoretical confirmations. Thus, optimum parameters for a-C:H films deposition process are pulsed volume energy density of 75 J/cm^3 and average surface power density of 2-3 W/cm^3.
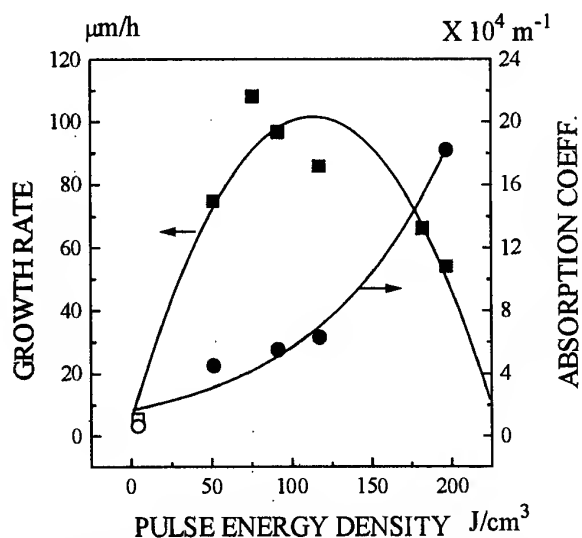
Fig.2 Dependences of growth rate (solid squares) and absorption coefficient (solid circles) on pulse energy density for a-C:H films deposited from methane by pulsed surface (gliding) discharge. Data for barrier discharge are indicated by open square and circle correspondingly.
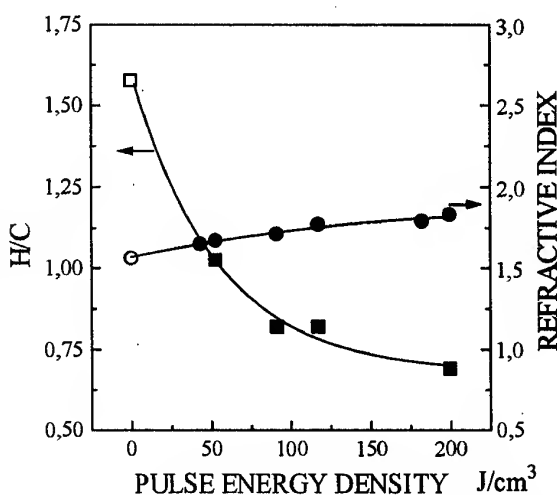
Fig.3 Dependences of H/C ratio (solid squares) and refractive index (solid circles) on pulse energy density for a-C:H films deposited from methane by pulsed surface (gliding) discharge. Data for barrier discharge are indicated by open square and circle correspondingly.

To prove a possibility of technological application of gliding discharge, the set-up for deposition of a-C:H films on flat dielectric substrates of 20X50 cm^2 was created (fig.4). In vacuum-tight chamber (*1*) with gas inlet and outlet were situated 24 discharge gaps (*2*), each of them was consisting of high voltage and grounded parallel electrodes. All the electrodes were mounted at the distance of 0.1-0.5 mm above a substrate to be coated (*3*). The substrate could be scanned under the electrodes by means of scanning mechanism (*4*). A metal plate, situated under the substrate was used as grounded initiating electrode (*5*). For the discharge initiation we used high-voltage pulse generator with output power of 750 W. Accordingly to optimum parameters listed before, it is necessary to distribute power of the generator between 20-30 discharge gaps of 5X1.5 cm^2 (here 5 cm is length of high-voltage and grounded parallel electrodes and 1.5 cm is distance between them). Simultaneous initiation of the discharge in all

gaps (G1-G24) was provided by voltage branching throw inductances L1-L24 (fig.5). Value of the capacitances (C1-C24) determines energy, delivered in sparks. In this
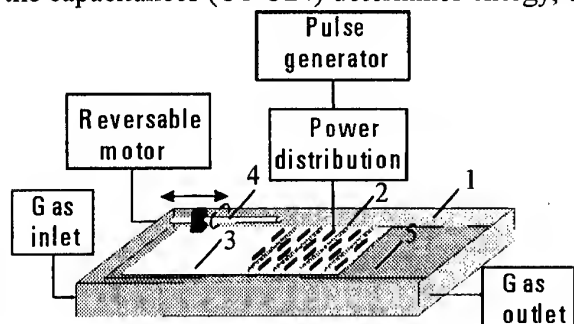
Fig.4 Schematic of set-up for a-C:H deposition on large-scale flat dielelectric substrate (20X 50cm²) by means of pulsed surface (gliding) discharge.
1-vacuum-tight chamber; 2-discharge gaps;
3-substrate; 4-substrate scanning mechanism;
5-grounded initiating electrode.
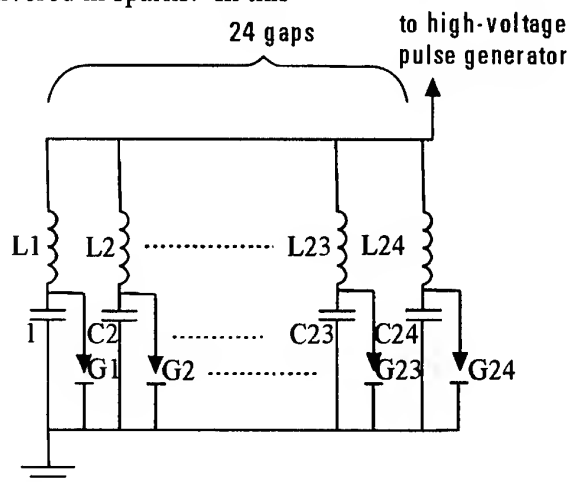
Fig.5 Schematic of block of high-voltage pulse generator power distribution between 24 gaps..

construction all the gaps (G1-G24) are equivalent concerning a breakdown probability, thus, breakdowns occur in all of them during each voltage pulse. Having L1-L24=0.1 mH and C1-C24=100 pF we attain optimum pulsed volume energy density in all sparks (75 J/cm^3) and optimum average surface power density in all gaps (2-3 W/cm^2). This set-up allows us to coat flat dielectric substrates of 20X50cm^2 by a-C:H films with growth rate of 20 μm per hour. The films' properties are similar to those described before (in case of one discharge gap and without substrate moving). Although sufficient reduction of the growth rate have been observed (because of sufficient increase of coated area), this productivity is acceptable for the most of technological regimes. Thus this set-up allows to deposit protecting transparent a-C:H films by means of gliding discharge under atmospheric pressure.

CONCLUSION

A possibility of deposition of amorphous hydrogenated diamond-like carbon (a-C:H) films from methane on flat dielectric substrates by means of pulsed surface (gliding) discharge under atmospheric pressure was investigated. It was found that films' properties are easily influenced by pulse energy density and, in less extent, by average surface power density of discharge. The specific nature of this discharge makes it possible to deposit protective a-C:H films with high transparency on plane large-scale dielectric substrates, including roll polymer materials (mylar, polyethylene).

REFERENCES

[1]. Kozyrev A.V., Korolev Yu.D., Tinchurin K.A., Fizika Plazmy, 1988, 14(8), p.1003-1007.
[2]. Baranov V.Yu., Borisov V.M., et.al. "Investigation of gliding discharge" (preprint), Kurchatov Nuclear Power Institute, Moscow, 1981.
[3]. Bugaev S.P., Korotaev A.D., Oskomov K.V., Sochugov N.S., Surf.and Coat.Technol., 1997, 96, p.123-128.
[4]. Jogender S. J.Appl. Phys., 1993, 73 (9), p.4351- 4356.
[5]. Jacob W., Unger M. Appl. Phys. Lett., 1995, 68 (1), p.475-477.
[6]. Dishler B., Bubenzer A., Koidl P. Appl. Phys. Lett., 1983, 42(8), p.636-638.

MEDICAL EQUIPMENT STERILIZATION
USING SUPERHIGH DOSE RATE X-RAY IRRADIATION

N. U. Barinov, G. I. Dolgachev, D.D. Maslennikov, M. S. Nitishinsky,
A. G. Ushakov, L. P. Zakatov, O. A. Zinoviev

*Applied Physics Dept., Russian Research Center Kurchatov Institute,
Moscow, 123182, Russia,*

Abstract

The results of sterilization tests made at the RS-20 generator of Bremsstrahlung for sterilizing purpose are reported. The measurements were done under different conditions in the area of 10-30 kGy dose levels at 1 MGy/s peak dose rate range for various microorganisms. The immediately irradiated volume was 0.036 of cubic meter with average dose rate at 1 kGy/hour provided in the center of the volume. The Bremsstrahlung was created by 2.0 MeV 10 kA 100 ns pulsed e-beam directed toward the target at 2 Hz. The tests were compared with those made simultaneously at continuos radionucleic radiation source using Co-60 isotope providing same dose values. It was found that full sterilization effect at RS-20 using 1 MGy/s peak dose rate takes 2-5 times lesser dose against radionucleic source and increases total efficiency of the system. Total dose decrease down to 5-12 kGy allows to reduce radiation loads on the equipment and broadens the area of sterilizing application.

X-RAY STERILIZATION

X-ray sterilization is used for commercial applications. Some data illustrating the use of x-rays for medical-biological purposes are reported in the Table 1 and reviews [1,2]. X-ray sterilizers may be radionucleic as *Co60* or *Cs137* and accelerator based. For large-scale industrial applications requiring electron beam or x-ray treatment, accelerators may be preferable due to economical reasons and radiation safe exploitation as well. They do not require large amount of renewed radionucleic material, its transportation, storing and wastes utilization. X-ray source on a base of 5 MeV 500 kW accelerator will economically effective from the viewpoint of direct and energy costs than corresponding radionucleic irradiator [3].

TABLE 1
Industrial technologies used accelerators containing sterilization/decontamination

Technology description	Irradiation	Energy. MeV	Dose, kGy	Beam Power, kW
Medical eq-t sterilization	e-beam, x-rays	1-10	20-30	5-20
Foodstuffs pasteurization	x-rays	0.5-3	1-3	5-100
Waste water decontamination	e-beam	0.5-10	0.5-15	50-500
Grain disinsection	e-beam	1	0.5-1	30
Gas flues decontamination	e-beam	0,2-1	10-15	100

Effectiveness of accelerator energy utilizing for x-ray production is substantially lesser than for electron beam. Efficiency in electron beam for most effective accelerator concepts is near 40% with 5-10 MeV and 50-70% at 2 MeV. But one can not use electron beam for volume sterilization due to low electron beam penetration

into the substance. In x-ray radiators electron beam creates Bremsstrahlung in the heavy targets with efficiency 10-15% at 10 MeV and 2-3% at 3-4 MeV [4]. Despite that, a use of x-ray generated in accelerators may be economically effective.

TABLE 2
Technical data for the most developed world commercial accelerator concepts

Name	Manufact.	Acc. voltage, MV	Beam power, kW	Beam eff., %	Av. current, mA	Peak power GW/s (pulse duration, ns)	# of machines
DYNAMITRON, [5]	Radiation Dynamics, USA	5	200	65	65	-	4
RHODOTRON, [6]	IBA, Belgium	10	200	50	40	-	7
RHEPP II [7]	SNL, USA	2,5	350	50	140	80 (70 ns)	1
Nissin HV [8]	JAERI, Japan	5	150	-	30	-	n/a
Electron [1]	Efremov,Ru	2	100	80	10	-	3
SINUS 7 [9]	HCEI,Ru	2	300	65	160	40 (40 ns)	1
ILU [1]	NFI, Ru	4	40	27	10	-	5
RS-20 [10]	Kurchatov, Ru	2,5	20	25	8	100(100 ns)	2
RS-200 [11]	Kurchatov, Ru	5	200	50	80	400 (100 ns)	design

REPETITIVE HIGH POWER STERILIZER USING POS TECHNOLOGY

In 1990-1997 a new type of x-ray generators based on repetitive POS technology has been developed in the Kurchatov Institute. The new system was capable of producing at the output both 2 MeV electron beam and intensive Bremsstrahlung irradiation in a Tungsten target from 10-20 kA 100 ns electron beam [10,11] . The systems being developed possess high peak dose rate 1 MGy/s in x-ray mode and 100 ns pulse duration. The pulses are repeated with a frequency of 2 Hz until the sterilizing effect is obtained. The results were simultaneously compared with those obtained at *Co60* facilities for same types and of biological cultures and same average power. The authors have also resolved a row of technical problems concerning life-time increasing of facility up to 10 million shots, high power flow converter creation etc.

EXPERIMENTAL LAYOUT

The output of the generator consists of *ss* flange with *ss* 0.8 mm foil 45 cm diameter order to provide minimum losses for the Bremsstrahlung radiation coming from the Tungsten converter. An effective area of irradiation was 50x50x50 cm^3. The dose absorbed in the center of the foil in the air was 0.1 Gy/pulse with a peak dose rate 1 MGy/s. Dose drops 40% after 50 cm length. For better uniformity test samples were rotated. For a typical irradiating sample - a box sized at 40x30x30 cm^3 a non-uniformity is better than 17%. Dosimetry measurements were made using thermoluminescent detectors and spectrophotometer methods as well basing on the effect of optical density change of liquids irradiated. For in-situ dose monitoring while treating a special dosimeter was developed together with calibrated dose rate indicator.

Sterilization degree is usually measured by a ratio of revived microorganisms to their initial quantity. Sterilization is full if this ratio is not greater than 10^{-6}, i.e. <0.0001%. According to the rules of radiation treatment tests are held using specially selected test samples reflecting different radiation strength. 8 cultures were chosen and

attested including both spores and microorganisms. 100% death of microorganisms was determined on standard cambric tests with microbe loading.

For a comparative estimate of treatment efficiency at RS-20 and *Co60* facility test samples imitating medical equipment for polymer materials were used. Test samples were manufactured from the polyamide, polyethylene of high and low pressure. They were infested with a suspension of vegetative and spore forms of microorganisms with a density at 10^6 per unit. Infested and dried in thermostat for moisture absence the tests were placed into the packages hermetically sealed for a subsequent treatment. After the treatment the test were sown in aseptic conditions into the liquid feeding media and were termostated under 37° C. Preliminary estimate has been done after 48-72 hours , final - after 14 days.

EXPERIMENTAL RESULTS

Experimental results are reported in Table 3. They demonstrate that sterilization effectiveness is 2-5 times higher than at *Co60* facility [12]. The volume density of tested samples was 0,2 g/cm³ with 10-35 cm thickness. Subsequent experiments used medical syringes packages, metallic, plactic and wood materials. RS-20 section of the Table 3 reports the maximum lethal doses ever been obtained for RS-20 experiments on sterilization.

TABLE 3
A comparative efficiency of test samples sterilization

№	Name	X-ray irradiation at *Co60* facility							
		Dose, kGy							
		1	3	5	10	15	20	25	30
1	Micrococcus radiodurans	+	+	+	+	+	+	-	-
2	Micrococcus radiodurans (M-1)	+	+	+	+	+	-	-	-
3	Micrococcus radiodurans (M-2)	+	+	+	+	+	-	-	-
4	St. aureus 906	-	-	-	-	-	-	-	-
5	E. coli 1257	-	-	-	-	-	-	-	-
6	B. cereus 96	+	+	+	+	-	-	-	-
7	B. subtilis 20	+	+	+	+	+	-	-	-
8	Mucobacterium B$_5$	+	+	+	-	-	-	-	-

№	Name	RS-20 Bremsstrahlung radiation							
		Dose, kGy							
		1	3	5	10	15	20	25	30
1	Micrococcus radiodurans	+	+	+	-	-	-	-	-
2	Micrococcus radiodurans (M-1)	+	+	-	-	-	-	-	-
3	Micrococcus radiodurans (M-2)	+	+	-	-	-	-	-	-
4	St. aureus 906	-	-	-	-	-	-	-	-
5	E. coli 1257	-	-	-	-	-	-	-	-
6	B. cereus 96	+	-	-	-	-	-	-	-
7	B. subtilis 20	+	+	-	-	-	-	-	-
8	Mucobacterium B$_5$	+	-	-	-	-	-	-	-

CONCLUSION

Considering sterilization results obtained one can suggest that killing sterilization dose for microorganisms is sensitive also to peak dose power absorbed by biology material and drops 2-5 times at 1 MGy/s. The authors plan to continue this research to determine a killing dose as a function of peak dose rate using electron beam facility at GGy/s range for a case of surface treatment.

The measurements were done for various substances and equipment used in medical industry: plastic, metal etc. X-ray irradiation from RS-20 facility penetrates deep and allows radiation treatment of complicated objects from composite materials. Thus, the overall productivity of the system may be increased 2-5 times as high at 2-3 MeV due to effect of high dose rate. This makes further development of RS-20 type accelerator to 5 MV and 500 kW more optimistic comparing with existing commercial x-ray systems.

Fig. 1. A general view of RS-20 X-ray sterilizer.
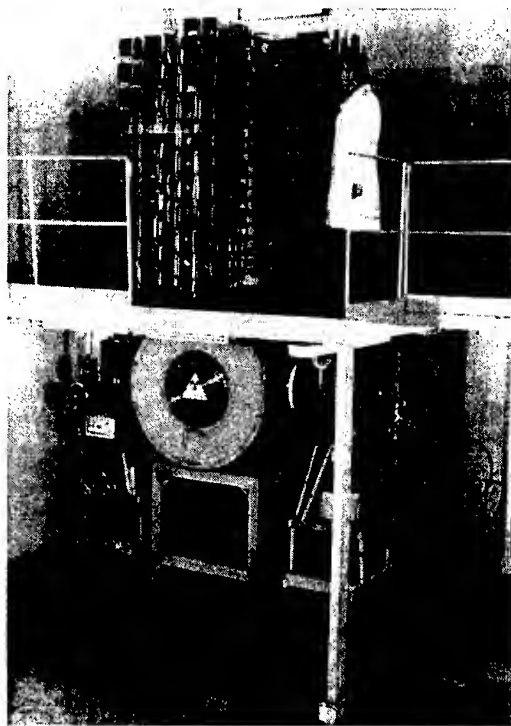
REFERENCES

[1]. Abramyan E.A. // Sov. Industrial electron accelerators, Moscow, Energoatomizdat Publishers, 1986.
[2]. Neau E.L. // IEEE Transactions on plasma Science, 1994, V. 22, I.1, P.2.
[3]. M.R. Cleland and G.M. PAGEAU // Nucl. Inst. and Meth. in Phys. Res. B24/25 (1987) 967-972.
[4]. J.A. Halbleib and T. W.L. Sanford // Sandia Report SAND83-2572 UC-28, Sept. 1985.
[5]. Tompson C.C. and Cleland M.R. // Nuclear Instrum. And Meth. In Phys. Research, 1989, B40/41 , P. 1137-1141.
[6]. Defrise D.,et al. // Radiat. Phys. Chem., 1995, V. 46, No. 4-6, P. 473-476
[7]. Neau E.L. // Proc. 1995 Particle Accelerator Conf., 1-5 May 1995, V.2, P. 1188-1192.
[8]. Y.Hoshi, I. Sakamoto, M. Takehisa et al. // Nucl. instruments and methods in Physics Research, 1994, A 353, P. 6-9.
[9]. N.M. Bykov et al. // IX Symp. on High current Electronics, June 21-30 1992, Tomsk, Russia, Conf. Records, P.79-80.
[10]. Barinov N.U., Belenki G.S., Dolgachev G.I. et al. // IEEE Transact. on Plasma Science, 1995, V. 23. N.6, P. 945-948.
[11]. Dolgachev G. I. , Zakatov L.P., Ushakov A. G. // Proc. 11th IEEE International Pulsed Power Conference June 29- July 2, 1997, P2-65. Book of Abst. P.355.
[12]. Dolgachev G. I. , Zakatov L.P., Zinoviev O.A. et al. Patent of the Russian Federation, Bulletin of Inventions, 1997, N 10.

AIR INJECTED HIGH POWER REPETITIVE ELECTRON BEAM FOR RADIATION TREATMENT

G. I. Dolgachev, M. S. Nitishinsky and A. G. Ushakov

*Applied Physics Dept., Russian Research Center Kurchatov Institute,
Moscow, 123182, Russia,*

Abstract

Repetitive POS technology recently developed in the Kurchatov Institute may be applicable for various technology uses. Together with existing 2-3 MV 10-50 kW x-ray systems a new facility operating in electron beam mode was recently developed for radiation sterilization applications. This compact system possesses 0.5-1 kJ/shot in electron beam of 0.5-0.8 MeV depending on the initial Marx charging voltage and may repetitively perform at 1 Hz frequency. Electron beam creates 1-10 kGy/shot in a surface layers of irradiated substances with dose rate at 5 GGy/s.

INTRODUCTION

Microsecond Repetitive Plasma Opening Switch technology allows to compress Marx generator electric power to high levels and to obtain repetitive electron beam pulses and x-ray bursts in diode load. Both energy storage and pulse compression systems could be designed relatively compact and inexpensive to meet requirements of commercial use. In early experiments RPOS X-ray generator (RS-20) had demonstrated 2-5 times higher sterilizing effect over existing *Co60* technology. It produced X-ray Bremsstrahlung pulse from 2.5 MeV 20 kA 100 ns electron beam with a dose rate of 1 MGy/s [1-4]. The new machine operating in electron beam mode also contains RPOS technology and can expand dose rates to 1-10 GGy/s. Doses are absorbed by thin surface layer (~ 1 mm) of tested material irradiated with 0.5-0.8 MeV 10 kA repetitive electron beam. The electron beam accelerator was developed in order to estimate the effect of full sterilization/pasteurization dose reduction as a function of dose rate. The electron beam measured dose is 0.5 kGy in 1 shot in 6-10 cm diameter circle layer placed 10 cm behind the output foil surface.

The generator may be applicable in commercial uses where 1-10 kJ sub-MV electron beam is required. Suggested applications may lay in radiation chemistry experiments for liquid and gaseous hazardous substances and chemical weapons destruction, surface hardening etc.

Table 1. Comparative parameters of RPOS x-ray and e-beam generators

	Parameter		RS-20 and modifications	5 MV concept	E-beam generator
1	Year of creation		1991-1995	1997	1997
2	Power consumption	kW	60-100	400	30
3	Marx voltage	MV	0.8	1.8	0.18
4	Repetition rate	Hz	1-4	1-5	1
5	Energy stored in 1 pulse	kJ	16	128	3.2
6	Drive current amplitude	kA	70-80	200	120
7	Electron beam energy	MeV	2.5±0.5	5.0±0.5	0.7±0.2
8	Voltage multiplication		3	2.5-3	3.5-4

9	Electron beam current	kA	20	100	10
10	Beam peak power	TW	0.04-0.05	0.5	0.01
11	Average beam power	kW	8-20	50-300	0.5-1

GENERATOR PARAMETERS AND SET-UP

Fig. 1 illustrates the generator set-up. At the beginning of pulse compression air Marx generator forms a high-voltage pulse of 180 kV, 120 kA, 3 kJ and 1 µs going through the air vacuum polyethylene interface to the vacuum coaxial line containing RPOS unit with 24 plasma injectors and diode. The air Marx design was used for machine simplicity. The geometry of air-vacuum interface was chosen to obtain 10% uniformity of electric field distribution of the vacuum surface of the insulator. The insulator had enough electrical strength to allow 200 kV microsecond voltage pulses from the Marx generator and 700 kV, 100 ns pulses from the RPOS. Electrical strength of the vacuum part surface is near 50 kV/cm. RPOS opens in the maximum of drive current generating 100 ns 600-800 kV pulse transferring 10-20% of the total current to the diode load. RPOS unit material study at previous RPOS systems allows 10^7 shots (or GGy range lifetime) with water cooling of heated elements. The system uses 100 kA drive current and does not require additional magnetic field coils to provide sharp switching (as it was used at RS-20) and gives voltage multiplication from 170 to near 700 kV - 3,5-4 times as high. The electron beam diode was placed download the RPOS with a set of anode grids to prevent plasma reclosure of the diode gap. The lifetime of anode foil used in experiments was 100-1000 shots, using pirolized carbon layer placed before the thin foil [5], and was over than 1000 shots with grid sets preventing plasma incidence on the carbon protection layer and *Ti* foil (Fig. 2).

RPOS DESIGN AND PERFORMANCE

24 plasma guns are operated in parallel and used feeding from 10 kV 6.4 µF capacitor each gap. Plasma injectors create not only plasma but gas fractions utilized for the main discharge in RPOS during a conduction phase. Thus, RPOS performance was not much sensitive to the vacuum conditions up to 10^{-4} torr. RPOS operation frequency was limited with 1 Hz due to low power supply, electron beam injection window life-time and capacitors exploitation conditions, but was tested at 10 Hz separately from the machine.

Typical wavewforms of electric signal characterizing RPOS performance are given at Fig 3. Accuracy of RPOS power transmission into the load is near 20% in current amplitude and 20 ns in diode current beginning. RPOS parameters were chosen on a base of emphirical conditions we have used in early POS/RPOS design. We consider RPOS to be working in "erosion" regime with a self magnetic filed insulation of the switch gap at a final stage. A detailed regime of RPOS operation is determined by a combination of voltage, current, conduction time, geometry and load impedance.

ELECTRON BEAM PARAMETERS

Electron beam is injected into the air through the output window. It consists of pirolized carbon layer with thin (10-30 µm) Titanium film. The diode design includes a pirolized graphite cathode, sets of anode rods for plasma catching and 8-15 cm output window diameter with a foil. Diode current was 10 kA with 100-300 A/cm² current

density. Pulse duration was 100-150 ns. Pulses were repeated with 1 Hz frequency. Electron beam energy was estimated as 300-500 keV using electron beam sensitive film changing optical density covered with a sets of aluminum foil masks with different effective thickness from 50 to 250 μm with a step of 50 μm (Fig. 1-a). Axial uniformity of electron beam was measured using film changing their optical properties under the beam irradiation. Total current switched to the diode was measured using coaxial ohmic current monitor in the outer surface of the vacuum coaxial line.

This electron accelerator is proposed for medical sterilization experiments with high dose rates and could be considered as inexpensive "desktop" example of RPOS technology for electron surface treatment. Further development of this concept lays in increasing of repetition rate to 10 Hz making sufficient average beam power and improvement of low energy ions protection for increase of output film life.

References

[1]. V. M. Babykin et al. // Proc. 9th Int. Conf. on High-Power Particle Beams (BEAMS' 92), Washington DC, 1992, V.1, P. 512 - 517
[2]. N. U. Barinov et al. // Proc. 10th Int. Conf. on High-Power Particle Beams BEAMS' 94, San Diego, CA, 1994, Vl. 1, P. 21-24.
[3]. N. U. Barinov et al. // IEEE Transact. on Plasma Science, 1995, V. 23, N.6, P. 945-948.
[4]. G.I. Dolgachev et al. // 11th IEEE International Pulsed Power Conference June 29- July 2, 1997, Proc., P2-65 (Book of Abst. P. 355).
[5]. G.I. Dolgachev et al. // Patent of the Russian Federation #2101888 of 24/09/1996 , Bulletin of Inventions 1, 1998, P. 40 .
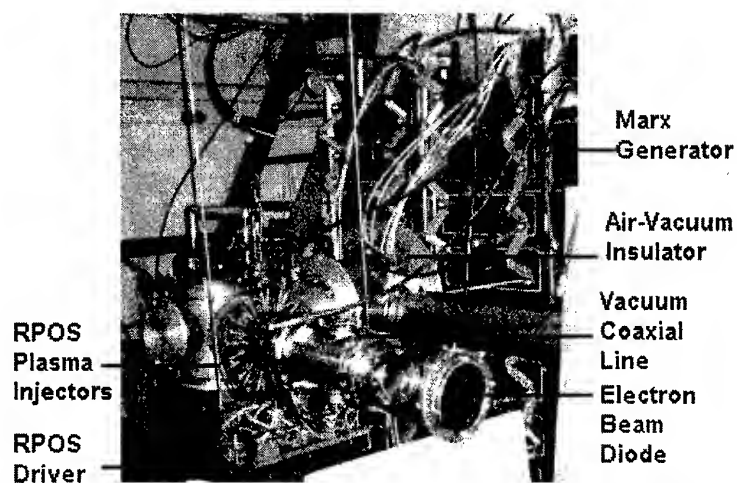
Fig.1. Electron beam facility photograph (up) together with schematic layout (down).

Fig.1-a. Sensitive film changing optical density after irradiating with 500 keV electron beam. The film was protected with *Al* foil ((6-i)*50) μm, where i=1÷5 (see above). 6 is non-protected layer of the film.
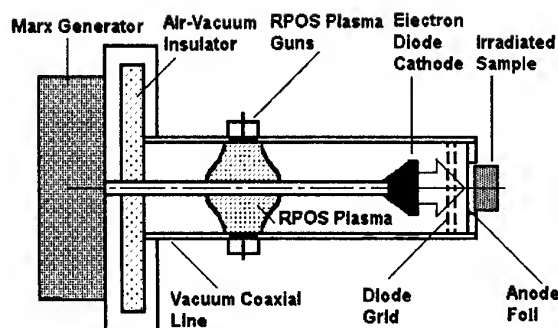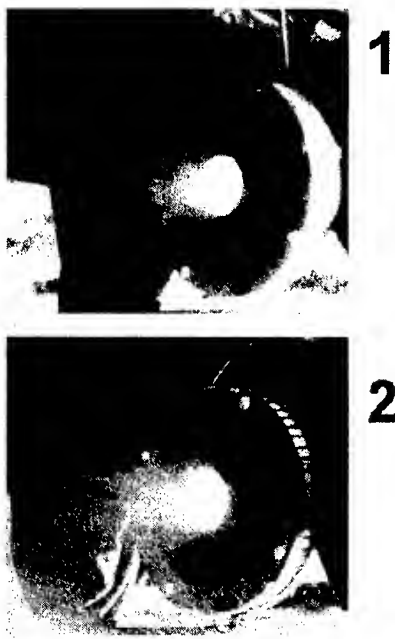
Fig.2. Time-integrated photograph of electron beam injected in the open air through *Ti* 50 μm foil. (1) - 200 kV beam, (2) - 700 kV beam. Pulse duration 100-150 ns. Output diameter - 8 cm.
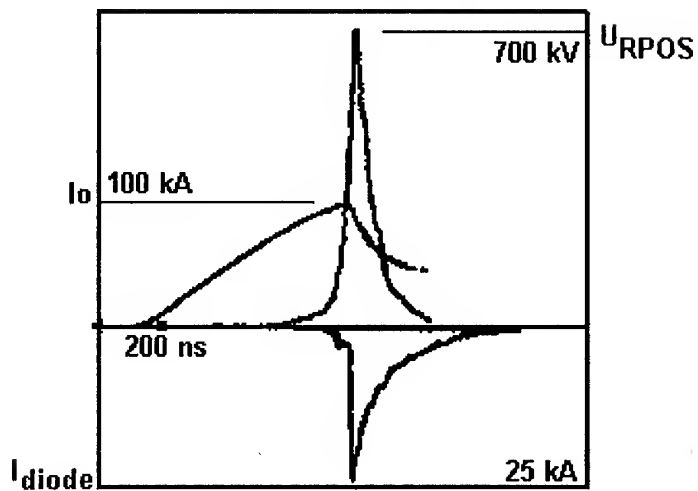
Fig. 3. Typical signals from voltage current monitors U_{RPOS} - voltage at RPOS during the swithcing, I_0 - total drive current of the generator, I_{Diode} - electrone diode diode current.
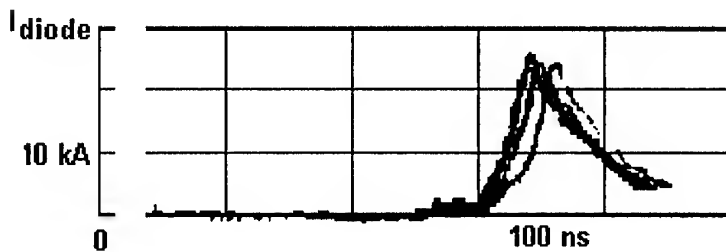
Electron diode current shapes taken from 5 consequental shots measured by ohmic shunt illustrate RPOS performance accuracy.

CHARACTERIZATION AND PERFORMANCE OF A HIGH-CURRENT-DENSITY ION IMPLANTER WITH A MAGNETIZED HOLLOW-CATHODE PLASMA SOURCE

Zoran Falkenstein, Donald J. Rej, and Nikolai Gavrilov[‡]

Los Alamos National Laboratory, P.O. Box 1663, Los Alamos, NM 87545, USA
[‡] Institute of Electrophysics, Ural Division of the RAS, 620049 Yekaterinburg, Russia

ABSTRACT

In a current collaboration between the Institute of Electrophysics (IEP) and the Los Alamos National Laboratory (LANL), the IEP is developing an industrial scalable, high-power, large-area ion source for the surface modification of materials.

The principle set-up of the ion beam source as well as some electrical characteristics (gas discharge current and the extracted ion beam current) are presented for a Lab-scale prototype. The first results of some surface modification experiments are given, which have been performed with the Lab-scale prototype at LANL.

The plasma source of the ion beam source can be described as a pulsed glow discharge with a cold, hollow-cathode in a weak magnetic field. Extraction and focusing of positive ions by an acceleration and an ion-optical plate system renders the generation of a homogeneous, large-area ion beam with an averaged total ion current of up to 50 mA at acceleration voltages of up to 50 kV. By using a cold-cathode also reactive gases can be used in the discharge.

Measurements of the ion current densities as function of the radial position within the beam are presented for various discharge parameters result in a fairly homogeneous ion beam over a large-area cross section of ca. 100 cm^2. Results on surface modification by ion implantation of nitrogen into aluminum and chromium are presented. Finally, a comparison of the calculated ion dose (from measurements of the ion current density) with the retained ion doses (determined by RBS of the implanted samples) is given.

INTRODUCTION

By increasing the dimensions of hollow-cathode discharge arrangements (> 10 cm) and the use of a weak magnetic field (ca. 1 mT), hollow-cathode glow discharges can be operated in a high-current discharge mode (1 to 10 A) at low gas pressures (< 0.1 mTorr). Under these conditions, the voltage applied across the discharge gap is concentrated in the cathodic layer of a space charge, the cathode cavity being filled by the discharge plasma having the anodic potential. The resultant high spatial uniformity of the plasma density makes it possible to use this type of the glow discharge for the generation of broad gas ion beams.

This type of ion source has a simple design and is reliable in service. The cold cathode discharge ensures a long-term operation of the ion source under elevated gas pressures, even in reactive gas media. These features and the ability to generate high-current ion beams make this source ideal for industrial applications. To increase the discharge stability, to widen the range of the average beam current and to improve the broad beam uniformity, a pulsed-repetitive mode of the discharge operation and the beam generation is used.

EXPERIMENTAL SETUP

The experimental set-up is shown schematically in Figure 1. The gas discharge system consists of a hollow-cathode (150-mm diameter, 150-mm length) and a rod anode (3-mm diameter, 100-mm length). A DC magnetic coil is positioned axially around the grounded vacuum chamber of the source, producing a magnetic field on axis up to $0 - 2.4$ mT.
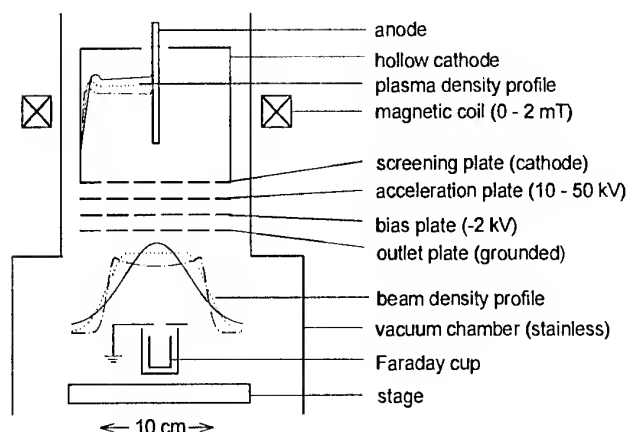
anode
hollow cathode
plasma density profile
magnetic coil (0 - 2 mT)

screening plate (cathode)
acceleration plate (10 - 50 kV)
bias plate (-2 kV)
outlet plate (grounded)

beam density profile
vacuum chamber (stainless)
Faraday cup
stage

← 10 cm →

Figure 1 *Schematic drawing of the ion beam source and the Faraday cup used. For all experiments, the acceleration gap length (distance from acceleration plate to bias plate) was 12.5 mm.*

In Figure 1 the radial plasma density throughout the discharge gap is indicated for different values of the magnetic field. To render the extraction of ions from the discharge plasma, the end plate of the hollow-cathode contains 160 holes (8 mm in diameter), uniformly placed over a 100-mm diameter. A broad ion beam is formed by a three-electrode electrostatic optics. The first screen electrode is at the cathode end, to which a high accelerating potential with respect to the grounded outlet plate of the ion optics is applied. A negative bias voltage of about - 2 kV is applied to the second electrode of the ion optics to repel secondary electrons from the beam plasma. The distance between the positive and negative high-voltage electrode plate is 12.5 mm, which is the acceleration gap length. The radial beam profile is indicated in Figure 1 for different plasma density profiles of the glow discharge and conditions of the beam formation.

The ion source is mounted on a vacuum chamber which is evacuated by a turbomolecular pump (pumping rate of 800 l/min). Processing gases (N_2, O_2, Ar, C_2H_2) are regulated using flow controllers, and are fed into the cathode cavity. Gas flows of $20 - 40$ sccm at a gas pressure of $(4 - 7) \times 10^{-4}$ Torr in the vacuum chamber can be realized.

The gas discharge is operated in a pulsed-repetitive mode with a mean pulsed discharge current of up to 5 A, pulse durations of 500 µs and pulse repetition rates in the range of 50 to 200 Hz. The average beam current is regulated within 10–50 mA. The D.C. accelerating voltage is operated between 10–50 kV.

A movable Faraday cup was used to measure the beam current density and its radial profile. It consists of a biased tube (diameter of 10 mm and length of 40 mm) with a bottom plate and is enclosed in a ceramic shield. A bias voltage of – 40 V was determined as best compromise for electron/ion attraction, enabling to estimate the ion beam current density. A grounded diaphragm is placed on the top of the ceramics shielding, enabling charge collection through the 0.5-cm² wide opening. In all experiments the cup was placed at a distance of 34 cm beyond the grounded outlet plate of the ion optics. Square plate specimen (10×10 mm², 1-mm thickness) of Al and Cr were placed on the stage were implanted with a nitrogen beam. The implanted specimen were then removed from the vacuum chamber and analyzed with Rutherford Backscattering Spectrometry (RBS) to determine the implant dose and depth profile.

RESULTS AND DISCUSSION

The radial profiles of the ion current density for a 25-kV nitrogen beam and for true different values of the magnetic field strength are given in Figure 2. The shape of the beam profile depends on three factors: first, the radial distribution of the plasma density in the glow discharge near the first electrode of the ion optics (which is itself a function of the magnetic field); second, on the divergence of the ion rays formed in each aperture of the ion optics (which is a function of the discharge current, the accelerating voltage and the length of the accelerating gap); and third, on the distance between the ion optics and the stage. To avoid any local non-uniformity of the ion beam density (due to the structure of the multi-aperture ion optics) it is necessary to ensure some overlap of single ion rays, which can be realized at a definite value of angle divergence of each ray. However, the angular divergence has to be limited because at large beam divergence angles and large values of beam propagation lengths, the beam profile transforms into strongly non-uniform (Gaussian) radial beam profiles. The uniform beam area at the beam collector plane will always be smaller than the area of the opening of the ion optics (which has a diameter of 10 cm).
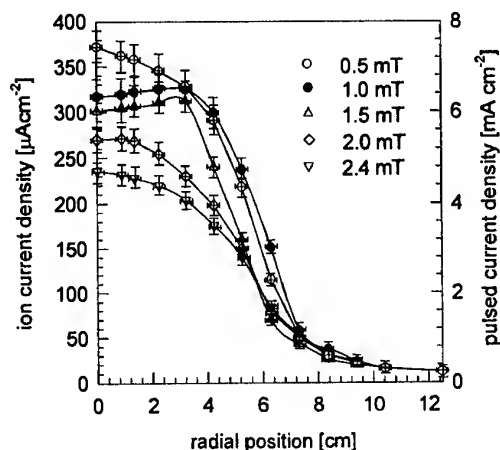
Figure 2   *Ion current density as function of the radial position within the beam at various magnetic field strengths (100 Hz, 25 kV, -40 V bias).*

In Figure 2 it can be seen that uniform (90 % of peak value) average ion beam current density of 300 μA cm^{-2} can be obtained over a diameter of ca. 9 cm at 1 mT. An increase of the magnetic field above 2 mT leads to a non-uniform beam current density profile which may be due to the simultaneous decrease of the discharge and beam current, leading to the increase of the beam divergence angle. Similar results were obtained for a constant magnetic field of 1 mT, where the optimal acceleration voltage is found at 25 kV. (These values are optimal for the acceleration gap length of 12.5 mm, which was held constant at all experiments. By changing the acceleration distance, uniform ion beams at different acceleration voltages can be adjusted.) Consequently, all further experiments for this study were performed at the optimal conditions of 25 kV acceleration voltage at 1 mT.
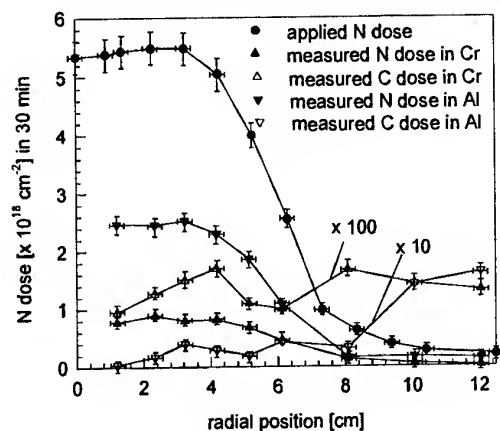
The radial profiles of the ion dose (assuming an ion dose composing of 50 % N$^+$ and 50 % N$_2$$^+$ [1]) and the retained dose in Cr and Al (quantified by RBS), generated with a constant dose rate of ca. 1 x 10^{17} N cm^{-2} min^{-1} are shown in Figure 3. Here, the samples were irradiated with an ion beam at optimal condition to beam uniformity (acceleration gap length 12.5 mm, 25 kV, 1 mT) with an irradiation time of 30 minutes.

Figure 3   *Applied ion doses and measured retained doses in Al and Cr as function of the radial position within the beam (100 Hz, 25 kV, 18 mA, 1 mT).*

It can be seen that the radial profile of the retained N doses corresponds to the radial profile of the applied ion dose, and that the retained doses are always substantially smaller than the applied doses. This is due to the fact that the sputter limit of the materials is reached at 'low' doses (1.7×10^{17} cm^{-2} for Cr [2] and 3×10^{17} cm^{-2} for Al [2]). The presence of carbon is associated to contamination of the vacuum with hydrocarbons from the pump. The retained C dose within a few % of the N dose is a result in balance of deposition, sputtering and recoil implantation of C-containing species.

The effect of quickly reaching the sputter limit can also be seen in Figure 4 for a constant N dose rate of ca. 1.7×10^{17} cm^{-2} min^{-1}. Now it can be seen that the retained doses are 1 - 10 times smaller than the applied ion doses, indicated by different treatment regimes. In phase I (0 – 3 min.) nitrogen accumulates nearly linearly with time and reaches an equilibrium state in phase II (3 – 8 min.). Here, ion sputtering equals the incoming ion dose (sputter limit of the materials). Because the retained doses do not reach and stay at the sputter limit in phase III, it can be concluded that here diffusion is strongly promoted. Increase of the temperature of the irradiated samples leads to an increase of the retained doses and penetration depths (ca. 200 nm from RBS spectra) with irradiation time, which would not be achievable by implantation of nitrogen at 25 keV at low sample temperatures (penetration length ca. 50 nm [3]).

Figure 6   *Applied ion doses and measured retained doses in Al and Cr as function of the irradiation time (100 Hz, 25 kV, 18 mA, 1 mT, -40 V).*

SUMMARY AND CONCLUSIONS

The beam current density of a high-current-density ion beam source is optimized in uniformity at 25 kV accelerating voltage and a magnetic field of 1 mT (at an acceleration gap length of 12.5 mm). Typical results of retained doses of N in Al and Cr are presented, confirming beam uniformity and showing (by RBS measurements) deep penetration into the material (range ca. 200 nm), due to diffusion. It is shown that the sputter limit is reached in very short times (2-5 minutes), enabling high-throughput surface processing.

ACKNOWLEDGEMENTS

[1] N.V. Gavrilov, G.A. Mesyats, G.V. Radkovski and V.V. Bersenev, Surf. Coat. Technol. **96** (1997), 81– 88
[2] Simulations have been performed with *PC PROFILE CODE*
[3] Simulations have been performed with *TRIM*

FAST SILICON DIODES OBTAINED BY ELECTRON BEAMS

Elena Iliescu [1], V. Banu [2], A. Niculescu[1]

[1] *National Institute for Laser, Plasma and Radiation Physics, Electron Accelerators Lab., Bucharest-Magurele, P.O.Box MG-36, Romania, e-mail: eiliescu@roifa.ifa.ro*
[2] *Baneasa S.A., 32 Erou Iancu Nicolae Str.,RO-72996 Bucharest, Romania*

Abstract: The manufacture of semiconductor devices is one of the beneficiaries of electron accelerators. One method of controlling the device turnoff time is the irradiation of the device body. The paper relates to irradiation of chips, wafers and fast diodes to improve their electrical characteristics. The electron linear accelerator ALIN-7 was used to irradiate at room temperature and high temperature silicon diodes manufactured by Baneasa S.A. The influence of 7 Mev electron irradiation upon the main electrical characteristics has been examined for different absorbed doses and different irradiation temperatures. The dependence of the minority carrier lifetime, reverse recovery time and forward voltage on the radiation dose and the percentage distribution of the reverse recovery time for the irradiated diodes are presented. Some experimental facts related to electron irradiated or gold doped silicon *pn* junctions are presented. After junctions' irradiation, the reverse recovery time decreases more than order of magnitude but the reverse current increase is not more than twice near room temperature.

1. INTRODUCTION

Some applications of semiconductor diodes require that they switch from a conductive to a nonconductive state more rapidly. The reverse recovery time (the time required for the current to reach the usually value in reverse bias after instantaneous switching from a specified forward current condition to a specified reverse bias condition) of a high speed switching diode is determined primarily by the recombination rate and consequently by the minority carriers lifetime in the junction region.

To reduce the reverse recovery time of a diode several methods are usually used: gold or platinum can be diffused into the device body, or the device body can be irradiated. Electron irradiation is preferably used as a suitable radiation source because of availability and inexpensiveness. Most preferably, the irradiation is of an energy level of about 1.5 to 12MeV [1]. Functionally, these two methods are similar since both create recombination centres that stimulate carrier recombination, thus depleting the semiconductor device of mobile minority carriers more rapidly. However, these methods also affect other device characteristics. For example, the diffusion generally increases the leakage current through the *pn* junction of the device and is costly. Irradiation typically increases the semiconductor device's forward voltage drop. In order to reduce that increase, after irradiation follows an annealing step of the devices. It is preferred that the anneal be conducted at a temperature between 250^0C and 350^0C for a time between 3 and 120 hours [1]. There will be some increase of the recovery time due to the anneal, but not up to its original high value. The irradiate-anneal cycle may be carried out more than once. A problem that occurs when practicing the irradiate and anneal sequence is that an excessive amount of energy and time, and thus money, are consumed in the device manufacture.

It has been found that for a given reverse recovery time, a device irradiated at an elevated temperature shows a lower forward voltage drop than would be obtained if the device was irradiated at room temperature[2-4]. So, elevated temperature irradiation provides results equivalent to room temperature irradiation and a long elevated temperature anneal in a time

less than that required for room temperature irradiation alone. The elevated temperature irradiation provides results equivalent to room temperature irradiation and a long elevated temperature anneal in a time equal to or less than that required for room temperature irradiation alone.

The energy levels introduced by the electron irradiation cause an increase in the recombination rate, and the irradiation effects on the silicon semiconductor device can be given by a simple equation [1,2]:

$$1/\tau = 1/\tau_0 + KD \qquad (1)$$

where τ and τ_0 are the post- and pre-irradiation minority carrier lifetimes, K is an irradiation efficiency factor, and D is the radiation dose.

2. EXPERIMENTAL PROCEDURE AND RESULTS

ALIN-7, a 7 MeV electron linear accelerator from the National Institute for Lasers, Plasma and Radiation Physics, was used to irradiate chips, wafers and complete packaged diodes from the standard production of Baneasa S.A.-factory 2300, to obtain fast devices. ALIN-7 has the following parameters: energy 7 MeV, average beam current $7\mu A$, pulse width 2.5 μs, pulse repetition rate 150 Hz, electron radiation dose $4 \cdot 10^3$ Gy/min at 1 m. Figure 1 shows the irradiation efficiency factor K versus irradiation temperature for ALIN-7.

Fig.1 The irradiation efficiency factor K versus irradiation temperature for ALIN-7

Table 1 presents the main electrical characteristics (I_F - continuous forward current, V_{RRM} - repetitive peak reverse voltage, V_F - forward voltage, t_{rr} - reverse recovery time, I_R - reverse current at T_a -ambient temperature) of these diodes in accordance with the data sheets.

Table 1. The main electrical characteristics of the investigated devices

diode type	I_F (A)	V_{RRM} (V)	V_F (V)	t_{rr} (ns)	$I_R(\mu A)$ $T_a=25^0C$	$I_R(\mu A)$ $T_a=100^0C$
6DRR	6	500	1.25	≤ 600	15	1000
BAX157	0.4	400	0.97	≤ 400	5	100

The diodes were obtained by cutting 2 inches diameter and 220 μm thickness wafers. The sizes of obtained chips are 2.5 x 2.5 mm^2 for 6DRR1 and 1.25 x 1.25 mm^2 for BAX157. The starting material was n-type silicon by resistivity 25 - 30 Ωcm. The irradiations were made at different temperatures (25^0 C, 175^0C, 250^0C). The influence of 7 MeV electron irradiation upon the main electrical characteristics (minority carrier's lifetime, reverse recovery time, forward voltage) has been examined for different absorbed doses. The percentage distribution

and the variance of the reverse recovery time has been calculated. The measurements were performed before irradiation and after irradiation. Figure 2 presents the reverse recovery time dependence on the irradiation temperature and dose for the diodes type BAX157 . Each data point is an average of a large number (300) of rectifiers fabricated using identical processing..

Figure 2.
The dependence of t_{rr} on the irradiation dose and irradiation temperature for diodes BAX157

Figure 3
The pre- and post-irradiation reverse recovery time distribution for 6DRR1 chips

Figure 3 shows the pre- and post-irradiation reverse recovery time distribution for 6DRR chips. For these chips the irradiation was done at 250^0 C temperature at a dose of 25 kGy. This dose was calculated with the relationship (1). Figure 4 shows the pre- and post-irradiation reverse current for 6DRR chips. Table 2 presents the results.

Figure 4. The pre- and post-irradiation reverse current for 6DRR1 chips

Table 2. The main electrical characteristics of the irradiated diodes (mean values)

diode	t_{rr}		t_{rr} variance		I_R at T_a =100⁰C V_R =400 V		I_R variance		V_F (V)	
type	before irrad. (ms)	after irrad. (ns)	before irrad. (ms)	after irrad. (ns)	before irrad. (mA)	after irrad. (mA)	before irrad. (mA)	after irrad. (mA)	before irrad.	after irrad.
6DRR	65.1	136.16	14.47	17.73	23.59	59.49	7.61	14.9	0.98	1.113
BAX157	53.4	115.39	10.21	12.57	2.17	4.81	6.51	13.05	0.82	0.97

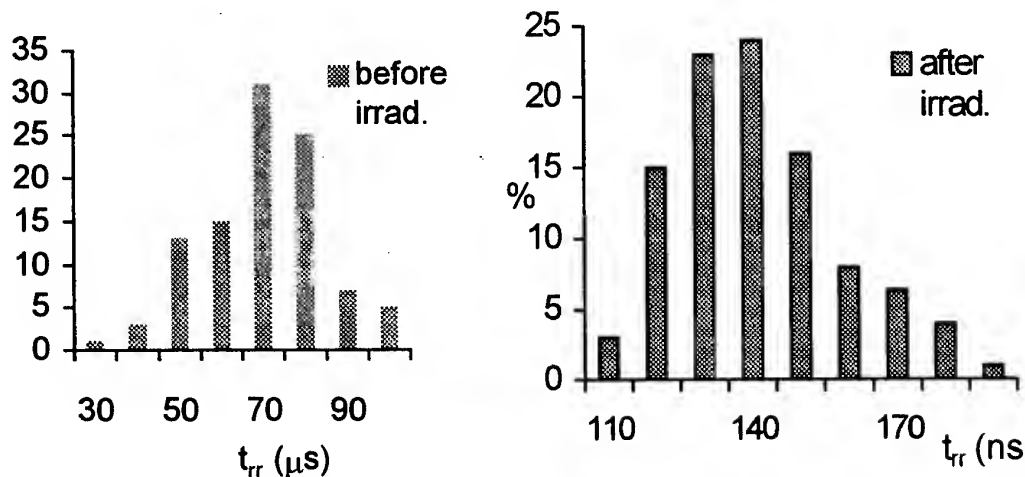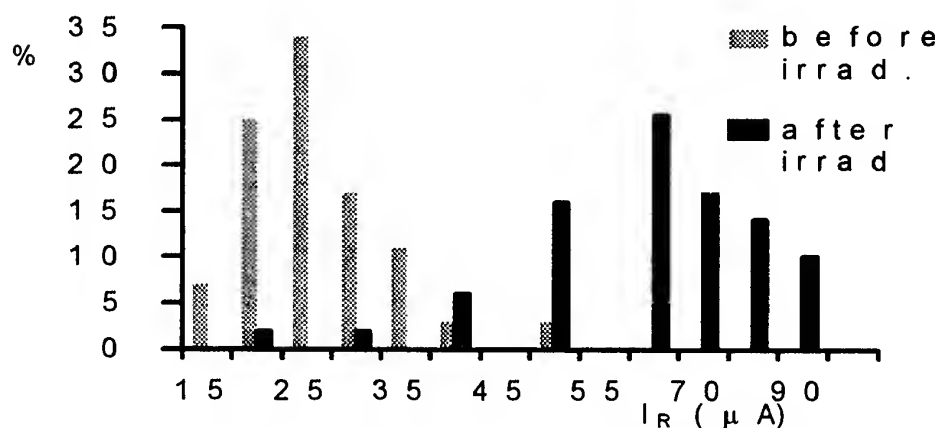Large area silicon n^+pp^+ mesa passivated rectifier structures (ϕ = 9.5 mm) with a breakdown voltage in the range of 140-2000 V were irradiated too. Before irradiation a reverse recovery time, t_{rr}, more than 30 µs has been measured for structures having a breakdown voltage greater than 1000 V. After the room temperature irradiation with a dose of 10 kGy, values less than 2-2.5 µs have been found for t_{rr} and a slight increase of reverse leakage current (no more than two times) has been observed. No change in the breakdown voltage value has occured excepting a softer knee of the current-voltage characteristic. I_R has increased with more than one order of magnitude at higher instantaneous T_j values (200-300⁰C). After at least 5-8 hours annealing time at T = 300-320⁰C of an irradiated structure, an increase of t_{rr} up to a half of the preirradiation value occurs. This is accompanied by a significant reduction of I_R which near room temperature may reach values less than the preirradiation ones.

3. CONCLUSION

The electron irradiation of the silicon diodes is an attractive alternative technology for the lifetime control. This technology has the advantage of being a clean, simple process with greater control and uniformity than is achieved by gold or platinum diffusion.

4. REFERENCES

[1] K.Tarneja, J.Bartko, U.S. Patent 3,888,701 (1975)

[2] Y.S.E.Sun, U.S. Patent, 4,043,836 (1977)

[3]Elena Iliescu, V. Banu, Gh. Dinoiu, Rom. Journal of Phys. 37 (1992), pp. 901-906

[4] Elena Iliescu, V. Banu, Nucl. Instr. and Meth. in Phys. Research B 113 (1996), pp. 103-105

SIMULATION OF THERMOELASTIC EFFECTS IN THE ION TREATMENT OF METALS

I.Amirkhanov, V.Fedyanin, Kh.Kholmurodov, I.Puzynin and V.Samoilov

Laboratory of Computing Techniques and Automation, Joint Institute for Nuclear Research, Dubna, Moscow region, 141980, Russia

We investigate thermo-elastic processes in metal materials exposed to high intensity ions and electrons. The dynamics of the stress and heat-transport has been obtained numerically. We have observed that the temporary evolution of the stress leads to formation of a localized structure. This may, in turn, explain the structural-phase changes of the surface treated, which are observed from the experiments.

1. INTRODUCTION

As is known [1-3], one of the effective methods of materials synthesis for modern technologies is the electron and ion surface treatment in a pulse explosion regime. Energy deposition in a thin surface layer by the high-power electron and ion beams may lead to a completely new structure on the surface, which may possess practically interesting physical and chemical properties [2,4,5]. Another important aspect of electron and ion irradiation of materials is transformation of such material parameters, which present great interest in metallurgy. For example, ion and electron irradiation of metalls may change the metalls hardening, fatigue, corrosion resistance and essentially increase their strength [2,6-8].

The electron and ion beam surface treatment may results in such dynamical processes as thermo-elastic strengths or shock waves [1-4]. The science of thermo-elastic phenomena, in spite of its large olds (see, for example, [9-11]), is, nevertheless, rather a little known area. Especially, one can easily observe this if we consider the problems of the electron and ion surface modification [2]. One of the causes here is by the our veiws a weak dependency among the deformation and temperature fields [10,12]. However, the interaction of high-power electron and ion beams with metals or alloys is enabling one to produce the thermo-elastic strengths in all irradiated medium [2,8], not on microlevel only. Shock waves or thermo-elastic effects, which are generated in the materials treated, may, consequently, become the essential factors to be taked into account in the analysis of new nontrivial structures on the surface. The aim of the present work is to study the thermo-elastic processes, which arise in the sample of metallic films exposed to high-power pulsed ion irradiation.

2. THE MODEL

Analysis of thermo-elastic processes is carried out on the basis of the following system of equations, which gives us a nonlinear coupling of the deformation and temperature fields [9]:

$$\rho_0 \frac{\partial^2 \vec{u}}{\partial t^2} = \mu \nabla^2 \vec{u} + (\lambda + \mu) grad \, div \vec{u} - \eta_0 grad T, \tag{1}$$

$$c\rho_0 \frac{\partial T}{\partial t} = \lambda_0 \nabla^2 T - \eta_0 T \frac{\partial}{\partial t} div \vec{u} + Q. \tag{2}$$

Here $\vec{u}$ is the shift (deformation) vector; T is the temperature; λ and μ are the Lame constants; $\eta_0 = (2\mu + 3\lambda)\alpha_T$; c is the specific heat of the material; ρ_0 is the mass density; λ_0 is the thermal conductivity; α_T is the coefficient of the thermal linear extension; Q is the source term including beam deposition from the pulse in the unit volume and unit time.

In the present work we restrict ourselves by the investigation of thermo-elastic effects, which arise in the ion bombardment of metallic samples, in one dimension only. This approach is rather not motivated by any computational or mathematical difficulties, though the system under consideration is essentially nonlinear and its analysis demands a serious attention. Simulation of heat transfer processes by one-dimensional heat equations shows the applicability of the approach to described adequately heat dynamics in metallic materials exposed to the high-power pulsed ions (see, for example, [1,2,13,14]). The analysis of propagation of temperature feilds [1,14] gives a good agreement between the one-dimensional model and the experimental one. Thus, to study thermo-elastic effects in metallic samples of a thickness of l_0, we have the following system of equations:

$$\frac{\partial^2 \sigma_x}{\partial t^2} = v_s^2 \frac{\partial^2 \sigma_x}{\partial x^2} - \alpha \frac{\partial^2 T}{\partial t^2}, \tag{3}$$

$$(c\rho + g_0 T)\frac{\partial T}{\partial t} = \kappa_0 \frac{\partial^2 T}{\partial x^2} - \beta T \frac{\partial \sigma_x}{\partial t} + q, \tag{4}$$

$$\sigma_x(x,0) = \frac{\partial \sigma_x(x,0)}{\partial t} = 0, \quad \sigma_x(0,t) = \sigma_x(1,t) = 0, \tag{5}$$

$$T(x,0) = T_0, \qquad \frac{\partial T(0,t)}{\partial x} = \frac{\partial T(1,t)}{\partial x} = 0. \tag{6}$$

In the eqs.(3) – (6) $\sigma \equiv \sigma_x(x,t)$; $T \equiv T(x,t)$; $q \equiv q(x,t)$ is the source function; and v_s^2, κ_0, α, β, g_0 are constant quantities ($v_s^2 = \frac{E\tau^2}{\rho_0 l_0^2}$, $\alpha = \frac{E\alpha_T T_0}{\sigma_0}$, $\kappa_0 = \frac{\lambda_0 \tau}{c_0 \rho_0 l_0^2}$, $\beta = \frac{\alpha_T \sigma_0}{c_0 \rho_0}$, $g_0 = \frac{E\alpha_T^2 T_0}{c_0 \rho_0}$). All quantities in the formulas of (3) – (6) are reduced, for the convenience of analysis, to dimensionless forms. The temperature of the sample (metallic films) is normed on the initial (normal) ones, $T \equiv \frac{T(x,t)}{T_0}$ ($T_0 = 293$ K), as regards the amplitude of strengths for $\sigma_x \equiv \frac{\sigma_x(x,t)}{\sigma_0}$, we use the well-known experimental data or the published data of numerical calculations ($\sigma_0 = 2.2 \cdot 10^6$ Pa) [2,13].

The system of eqs.(3) – (6) is expressed in terms of strengths, where we use the following connection between the strengths σ_x, deformation u and temperature T of the sample:

$$\sigma_x = E\frac{\partial u}{\partial x} - E\alpha_T(T - T_0).$$

The function of $q(x,t)$ that describes thermal sources, is defined by the following expressions:

$$q(x,t) = \frac{E_0 j(t)}{zeR_0} \cdot \frac{\tau}{c_0 \rho_0 T_0}, \quad \text{at} \quad t \le 1, \quad x \le r_0,$$

and

$$q(x,t) = 0, \qquad \text{at} \quad t > 1, \quad x > r_0,$$

where $x \equiv \frac{x}{l_0}$, $t \equiv \frac{t}{\tau}$, $r_0 \equiv \frac{R_0}{l_0}$, τ is the source action time; E_0, $j(t) = const = \frac{j_{max}}{2}$, ze, R_0 are initial energy, current density, charge and mean ion free pass, respectively.

3. RESULTS

We have numerically calculated the thermo-elastic strengths in the sample of iron in the nanosecond pulsed irradiation by carbon ions. The results of numerical solutions of eqs.(3)–(6) are presented in Fig.1. The spatial and temporary profiles in Fig.1 show us the dynamics of thermo-elastic strengths up to the moment of $t \equiv \frac{t}{\tau} > 1$. It is worth to note that the moment of $t = \tau$, during of which the target is irradiated, separates a threshold of the "structural"–deformational changes of the material. Under the influence of pulsed beams at $t \leq \tau$ in the iron sample the waves of small amplitude elastic strengths are generated. The strengths profile of $\sigma(x, t)$, which is formed after the source is switched off, is a single pulse of the shock waves type. Here we observe generations of large amplitude elastic strengths in the sample. The amplitude of these waves is directly proportional to intensity of irradiation and it increases with the increasing of energy E_0 and density of ion current of j. As regards to the velocity of strengths pulses, it is does not depend on j.

The existing solutions [9-12], obtained in the framework of thermo-elasticity theory (on a basis of the model we are considered), show a weak coupling of the temperature and the strengths fields. A dynamical effect here is the generation of elastic strengths in a solid body by fast heating [10,12]. The numerical results presented in Fig.1, show that the large amplitude strengths form in a regime of "fast cooling" (i.e., after the switching off the beams sources at $t > \tau$). From Fig.1 we can also see that a maximum of strengths pulses is directly proportional to the product of $q_0 \cdot R_0$, viz., the product of the amplitude of thermal sources $q(x, t)$ and R_0–depth of a beams penetrations. The forms of elastic strengths depend more strongly on the form of the source. However, one has to expect that by simulating of the forms of thermal sources in a practically interesting manner, one may obtain suitable forms of the strengths.

4. REFERENCES

[1] Stinnett R.W. et.al. Thermal surface treatment using intense, pulsed ion beams.//Proc. Materials Research Society Symp.: Materials Synthesis and Processing Using Ion Beams. V.316. P.521-532. Boston. 1994.

[2] Didenko A.N., Ligachev A.E., Kurakin I.B. The interaction of charged beams with the metalls and alloys surfaces. M.: Energoatomizdat, 1978. (in Russian)

[3] Korenev S.A. Pulse explosion ion vacuum condensation. Preprint of JINR. P12-89-615. 1989. (in Russian)

[4] Anisimov S.I., Imas Ya.A., Romanov G.S., Khodiko Yu.V. Action of high-power radiation on metals. M.: Nauka, 1970. (in Russian)

[5] Bikovskiy Yu.A., Nevolin V.N., Fominskiy V.Yu. Ion and laser implantation of metallic materials. M.: Energoatomizdat, 1991. (in Russian)

[6] Zel'dovich Ya.B., Raizer Yu.P. Physics of shock waves and high-temperature hydro-dynamic proccesses. M.: Nauka, 1966. (in Russian)

[7] Korenev S.A., Ligachev A.E., Meshkov I.N., Perevodchikov V.I. 1st Int. Symp. "Beam technologies (BT'95). Dubna. Russia. 1995.

[8] Balakin A.N., Isakov M.G., Kastchenko A.P., Meshkov I.N., Strokovsky G.S. The electron beam treatment of heat-zinced steel. 1st Int. Symp. "Beam technologies" (BT'95). Dubna. Russia. 1995.

[9] Nowacki W. Problems of thermoelasticity. M.: Izd-vo AN SSSR. 1962. (in Russian)

[10] Kovalenko A.D. Introduction to thermoelasticity. Kiev: Naukova Dumka. 1965.(in Russian)

[11] Landau L.D., Lifshits E.M. Theory of elasticity. M.: Nauka. 1987. (in Russian)

[12] Nowacki W. Theory of elasticity. M.: Mir. 1975

[13] Gann V.V., Zhukov A.I., Blazhevich S.V. // Problems of atom sciences and technics. Chapter: Physics of radiation damages and radiation materi 1983. v.4(27). pp. 75-78.

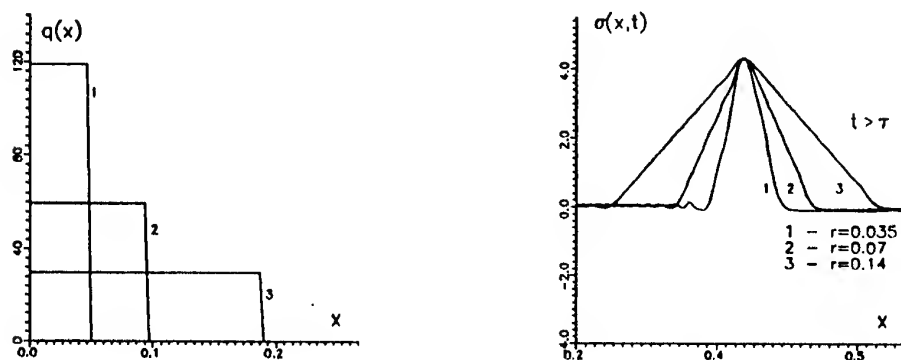[14] Davis H.A. et.al.//Annual Report of Los Alamos National Laboratory. 1995.

Fig. 1.

Modification of polyurethane endoprostetics surface
by pulse ion beam

[1]V. Begishev, [2]N. Gavrilov, [2]G.Mesyats, [3]Yu. Klyachkin, [4]I. Kondyurina, [1]I. Osorgina,
[3]A. Kondyurin

[1]*Natural - Scientific Institute, Perm State University, Perm, Russia*
[2]*Institute of Electrophysics, Russian Academy of Science, Ekaterinburg, Russia*
[3]*Institute of Technical Chemistry, Russian Academy of Science, Perm, Russia,*
kond@icmm.perm.su
[4]*21a M.Ribalko st., Apt.17, Perm 614101, Russia*

Implantation of any artificial prosthetics to an organism causes a foreign body reaction. Intensity of reaction depends on nature of the implanted material. Determination of foreign prosthetics material and initiation of reaction takes place on molecular level during interaction of body cells with prosthetics surface. In addition, a polymer surface layer is able to be destroyed under the organism medium action. On the other side, the usage of a carbon material as endoprosthetics induces the low reaction intensity of an organism [1]. So, the carbon coating of polymer endoprosthetics surface is preferred for decreasing of negative reaction of an organism.

Formation of carbon coating is possible by methods of vacuum deposition. But in this case the adhesion problem of carbon coating and polymer substrate appears. Similar problem appears in the case of chemical methods for carbon coating formation. More simple method for carbon coating on polymer substrate can be realized with the ion beam treatment. As it is well known, the ion beam treatment of polyethylene, polypropylene, polyimide and other polymers leads to carbon layer formation on polymer surface due to destruction processes in polymer surface layer under the action of the ion beam [2]. Therefore, this carbon layer has a good joint with polymer substrate.

In this paper, the influence of white rats organism medium on polymer endoprosthetics treated by ion beam is discussed. Medical polyurethane based on polyether, diisocyanate and diamin as films with 400 μ thick have been studied. Ion beam treatment was performed on the pulse ion source "Pulsar" (Institute of Electrophysics). The source generated the nitrogen ion beam with square of 100 cm^2, pulse current density of 5 mA/cm^2, pulse duration was 0.3 mS, frequency repetition was 1 Hz. Ion energy was 20 keV. Vacuum was created by oil vacuum pumps, the initial vacuum being $3 \cdot 10^{-3}$ Pa and vacuum under operating regime of the source being $5 \cdot 10^{-2}$ Pa. Polyurethane films were treated with dose from 10^{14} to 10^{16} ions/cm^2.

The polyurethane films were implanted to white rats for a 6 month period. The treated films aged in rat organisms and nearest to prosthetic tissues were studied by different spectral and histological methods. IR ATR spectra were recorded by using an UR-20 and Specord M-82 spectrometers (Carl Zeiss Jena, Germany) with ATR accessory on KRS-5 crystal (trapezium, 45^0 incident angle, 25 reflection number). Microphotographs of polyurethane surface were made with using of microscope MBS-10 (LOMO, Russia) with Zenit accessory.

The action of living organism tissue on polyurethane is the attack of organism active ferments to polyurethane prosthetic surface [3]. In the condition of active medium the hydrolysis of polyurethane leading to destruction of macromolecules and formation of low-weight products exists. At this case, durability of polyurethane film decreases and prosthetic loses its functional ability. Besides that, some products of reaction liberated into organism medium can have cancerogenic activity to organism [4]. Medical polyurethane has decreased

ability to hydrolysis. But hydrolysis of surface layer of this polyurethane exists with low speed of process [5].
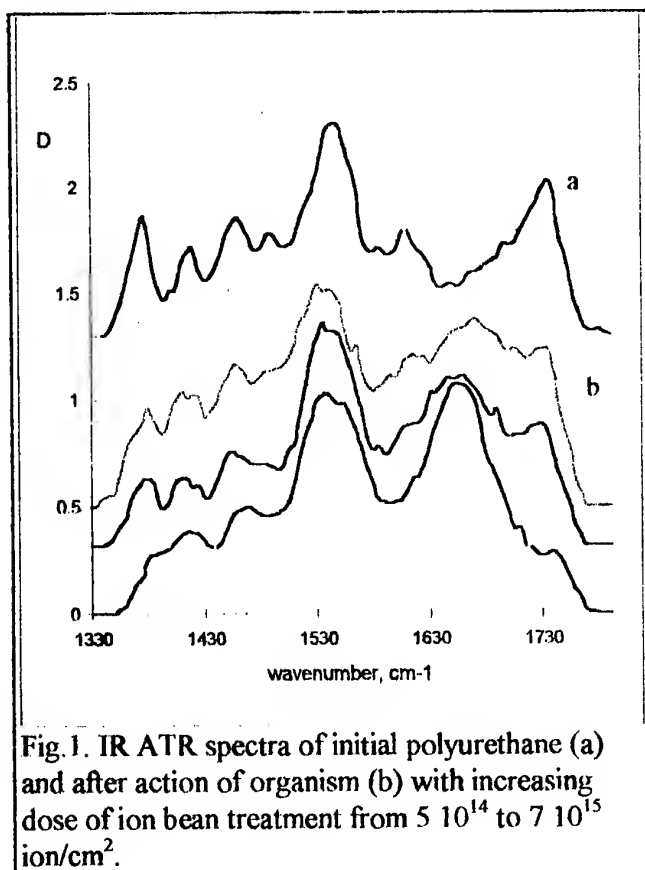

Fig.1. IR ATR spectra of initial polyurethane (a) and after action of organism (b) with increasing dose of ion bean treatment from $5 \cdot 10^{14}$ to $7 \cdot 10^{15}$ ion/cm^2.

Changes of polyurethane structure at hydrolysis in organism medium are observed in IR ATR spectra of polyurethane film surface as decreasing of spectral line intensity attributed to piece of macromolecules destructed in hydrolysis reaction. For the studied polyurethane, this piece of macromolecule is urethane fragment as the reminder of a toluenediisocyanate molecule. Hydrolysis reaction leads to formation of the second amine group and hydroxyl group with liberation of toluenediamine to organism medium. Decreasing of toluenediisocyanate reminder concentration were analyzed by 1375, 1415, 1490 and 1608 cm^{-1} lines intensity (Fig.1). Besides that, reaction of formation of guanidine group is observed by disappearing of carboxylic line in IR ATR spectra and appearing of intensive $v(C=N)$ line at 1665 cm^{-1}.

The ion beam treatment leads to carbon coating formation on polyurethane film surface. In differential IR ATR spectra the wide complex band of C=C groups vibrations in different positions and of C-O groups vibration appears (Fig.2). Similar changes of spectra were observed for polyethylene after the ion beam treatment [6]. Taking into consideration great difference between extinction coefficients of $v(C=C)$ and $v(C=O)$ lines in IR spectra, one can conclude that carbon layer is formed mainly consisting of a wide number of not saturated C=C bonds in different conjugations. The silvery shade of polyurethane surface which can be observed after the ion beam treatment characteristic of graphite covering, confirms it.
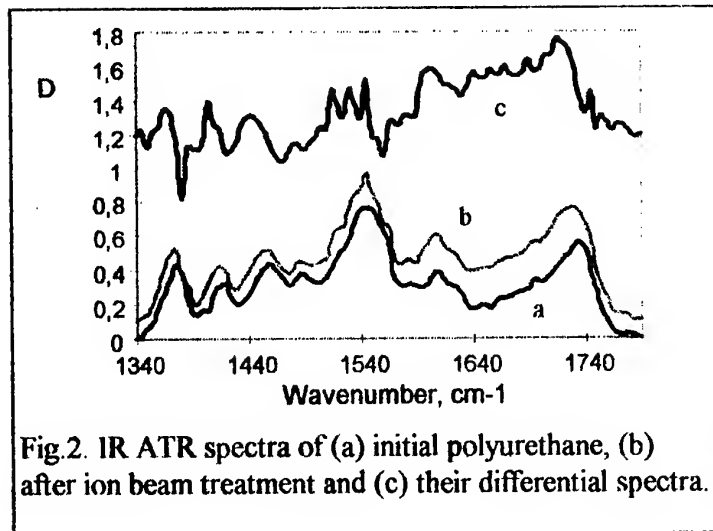

Fig.2. IR ATR spectra of (a) initial polyurethane, (b) after ion beam treatment and (c) their differential spectra.

Our observation of polyurethane surface with the help of microscope shows, that after the ion beam treatment polyurethane surface becomes covered by cracks (Fig.3). Cracks formation is explained by significant difference of stiffness of carbon covering and initial polyurethane. The carbon layer has thickness near the projected range of ion, which is about 757 Å in our experiments, so weak deformation of polyurethane film

leads to breaking of carbon covering and crack formation. Depth of cracks increases with the increase of a treatment dose.
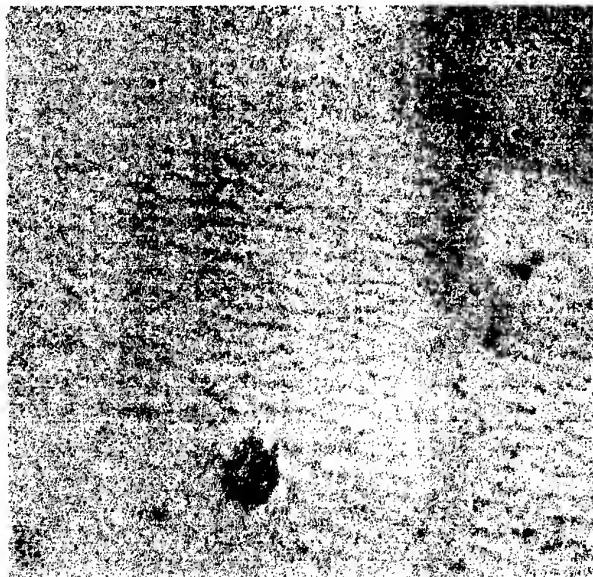
The organism action on polyurethane samples after the ion beam treatment changes IR ATR spectra too. But intensity of these changes is weaker and depends on a treatment dose (Fig.1). The weakest spectral changes in comparison with the spectra of initial polyurethane are observed for samples with the lowest ion beam treatment dose. In the other words, low doses of ion beam treatment leading to thin carbon covering formation are more effective for the delay of hydrolysis processes. The analysis of stability of 1490 cm^{-1} line intensity in spectra of treated polyurethane showed that the hydrolysis processes at $5 \cdot 10^{14}$ ions/cm^2 treatment dose are delayed 4 times as compared with untreated samples of polyurethane.
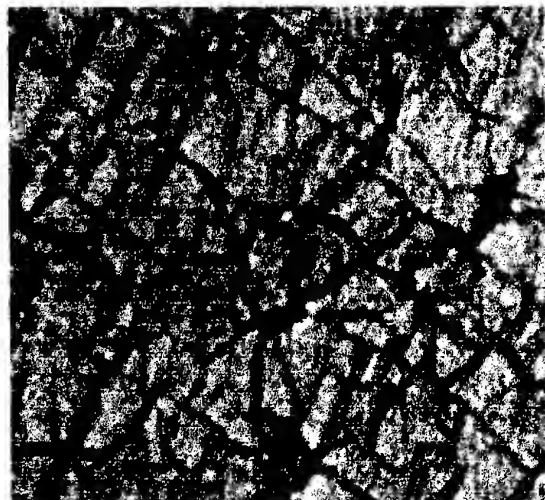
With the further increase of ion beam treated dose, the formation of thick carbon covering leads to formation of deeper cracks on polyurethane surface and hydrolysis of polyurethane under the action of organism medium takes place at these cracks. This is well observed by microphotographs of polyurethane surface after ion beam treatment at high dose and action of organism (Fig.3).

So, at low doses the ion beam treatment of polyurethane leads to carbon covering formation and can be the method for protection of polyurethane in organism medium.

Fig.3. Microphotographs of polyurethane surface: after $5 \cdot 10^{14}$ ion/cm^2, after $7 \cdot 10^{15}$ ion/cm^2, after $7 \cdot 10^{15}$ ion/cm^2 and organism action

References

|1| D.S.Borkos. Ceramics international, 9 (1), 3 (1983).

|2| L.Calcagno, G.Compagnini and G.Foti. Nucl. Instr. and Meth., B65, 413 (1992).

|3| T.E.Lipatova, G.A.Phakadze. Polymers in endoprostetics, Naukova Dumka, Kiev, 1983 (in Russian).

|4| W.J.Rea, Chemical Sensitivity, vol.1, Lewis publishers, Boca Raton, 1992.

|5| I.V.Osorgina, S.A.Plaksin, A.V.Kondyurin. V.P.Begishev, M.V.Subbotin. Posters, 3rd Int. Conf. "Modern approaches to the development of effective dressings, suture materials and polymer implants", May 26-27, 1998, A.V.Vishnevsky Institute of surgery, Moscow, p.254.

|6| G.A.Mesyats, Yu.S.Klyachkin, N.V.Gavrilov, V.N.Mizgulin, R.M.Yakushev, A.V.Kondyurin, Vacuum, 47 (9), 1085 (1996).

USING HIGH-CURRENT NANOSECOND ELECTRON BEAMS TO STERILIZE BONE MEAL

Yu. A. Kotov and S. Yu. Sokovnin

Institute of Electrophysics, Russian Academy of Sciences,
34 Komsomolskaya St., 620049 Ekaterinburg, Russia

and

P.V. Kolotov

Open Joint Stock Company "Ekaterinburg Meat Factory",
15 Titov St., 620085 Ekaterinburg, Russia

Abstract

On the basis of the URT-0.2 repetitive nanosecond electron accelerator (accelerating voltage up to 200 kV, FWHM pulse duration t_{pulse} = 34 ns, pulse repetition rate up to f = 200 pps, beam cross-sectional area 220 x 30 mm^2, pulsed current density 0.3 A/cm^2), we have developed a technology and a setup for radiochemical sterilization of bone meal (proteic feed additive with a bulk density of about 1 g/cm^2) while it is produced. With the accelerator operating at the highest pulse repetition rate, the output of the line ranges up to ~ 225 kg/h. The estimated cost of sterilization amounts to ~ \$0.034 per kilogram.

Introduction

In the production of bone meal from waste at the meat factory, the possibility always exists of the meal being biologically contaminated with pathogenic microorganisms, most frequently salmonella group microbes. And since this bone meal is used as a protein feed additive in industrial poultry farming, the likelihood arises that poultry may be infected through it. This may give rise both an an epidemic among animals and to poisoning of people, consumers of poultry meat or eggs. Continuous microbiological monitoring is therefore effected in the production of bone meal. Contaminated lots that are detected undergo further sterilization, entailing substantial energy losses and appreciable economic losses.

The purpose of the present work was to explore the possibility of sterilizing bone meal while it is produced and to develop a flow process chart for such sterilization.

Complete exposure to radiation of a bone meal layer about 5 mm thick (with a bulk density of about 1.2 g/cm^3) calls for using electrons with an energy upwards of 1 MeV. This is unacceptable because the cost of such a radiation source and organizing the radiation protection of personnel against the source is so high that it will make irradiation commercially inexpedient.

We therefore explored the possibility of employing the radiochemical sterilization technology [1]. The idea of radiochemical sterilization boils down to what follows. To sterilize tightly packed products, we use both the radiation of the electron beam itself and the radiation that arises within the packet when the sterilizing toxic chemical

substance is irradiated. The simplest and cheapest way is to use the ozone that forms when the oxygen of the air is irradiated.

Although most efficient for surface sterilization, this technology may well be applied because the site most likely to be contaminated with microorganisms is the porous surface of the bone meal, where the electrons and the ozone can penetrate. The geometry of "hermetically sealed items", the gist of which boils down to increasing the time of contact with the ozone, may be implemented in a different way.

Experimental

In the experiments performed, we made use of a URT-0.2 nanosecond repetitive electron accelerator [2] with an accelerating voltage of 200 kV, with an FWHM pulse duration of 34 ns, with a pulse repetition rate of 250 pps, and with an electron beam cross-sectional area of 220 x 30 mm^2 for a pulsed current density of 0.3 A/cm^3.

The irradiation geometry is given in Fig. 1. Bone meal (1) was delivered by a conveyer (7) at a rate of 1 cm/s. The thickness of the bone meal layer was restricted to 5 mm by means of a reflector (2). The electron beam (3) coming from the accelerator (4) was directed from above. To increase the bone meal - ozone contact time and to protect the personnel from the ozone and the braking radiation, a casing (5) was used in which a small rarefaction was maintained by means of ventilation (6).
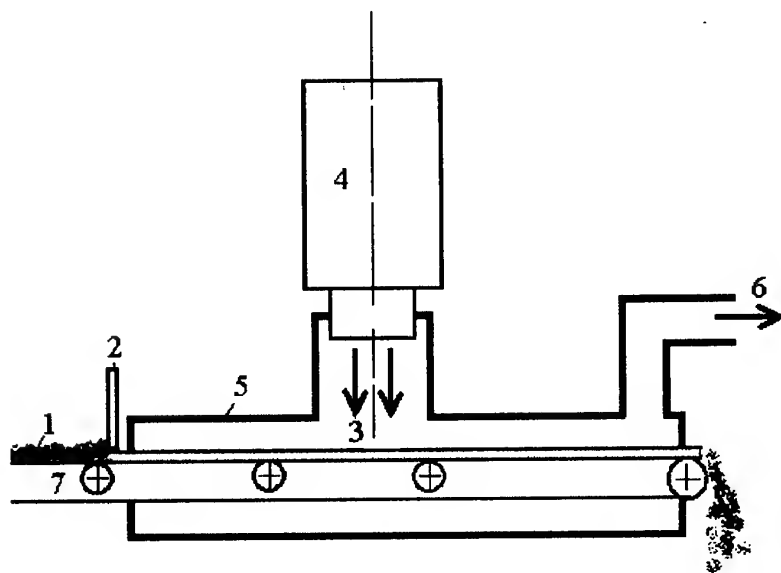

Fig. 1. The irradiation geometry.

The test samples consisted of bone meal discarded on account of microbiological indexes. Before and after irradiation, the samples (a batch weighed around 1 kg) were inspected by the Bacteriological Laboratory of the JSC "Ekaterinburg Meat Factory". In the course of experiments, the operating frequency of the accelerator was varied. Experimental results are presented in Table 1.

Table 1. Experimental results.

Run	Batch No.	Pulse repetition rate of accelerator, pps	Detected in samples prior to irradiation	Detected in samples subsequent to irradiation
1	803	10	S. derby	S. derby
	644	50	S. derby	Not found
	759	100	S. mission	Not found
2	814	25	S. mission	S. mission
	716	50	S. mission	Not found
	797	100	S. derby	Not found

Conclusions

It is found that the URT-0.2 nanosecond repetitive electron accelerator may provide a basis for developing a process flow route for the radiochemical sterilization of bone meal as it is produced.

With the accelerator operating at a maximal pulse repetition rate, the line will produce 225 kg per hour, with the estimated cost amounting to 0.2 ruble/kg ($0.034/kg). This is economically expedient since bone meal costs about 2.5 ruble/kg ($0.42/kg), while the thermal sterilization being replaced costs 0.65 ruble/kg ($0.11/kg).

References

[1]. Y. A. Kotov and S.Y. Sokovnin, Using high-current nanosecond electron beams for radiochemical sterilization), DAN, 1997, Vol. 355, No. 3, pp 424-426.
[2]. Y.A. Kotov and S.Y. Sokovnin, The URT-0.2 nanosecond repetitive electron accelerator, PTE, 1997, No. 4, pp 84-86.

ION IRRADIATION OF CARBON FIBRES

N.V.Gavrilov[a], D.R.Emlin[a], A.E.Ligachev[a], G.A.Mesyats[a]

E.A.Ligacheva[b], L.V.Galyaeva[b]

[a] *Institute of Electrophysics RAS, Russia*

[b] *Moscow Aviation and Technology Institute, Russia*

Introduction

To realize the excellent mechanical properties of carbon fibres in composite materials, it is necessary to have a good adhesion between fibre and matrix. A good adhesion depends on following properties: morphology a chemical composition of near surface layer of fibre. Surface treatment is in common for changes of physico-chemical properties of surface carbon fibres. But this properties can be changed although by application of particle beams.

The aim of the present work is to study changes of surface and volume physico-chemical properties of carbon fibres after ion irradiation. Ion irradiation of a foreign species can lead to the production of new compounds in near-surface layer of carbon fibre, but the displacement damage caused by energetic ions also lead to structural transitions of surface layer.

Experimental

For ion irradiation C^+ and N^+-ions was selected because C^+-ions are not interacted, but N^+-ions are interacted with carbon fibres: it's possible chemical reaction between atoms of carbon fibres and N^+-ions. In addition mass of C^+ and N^+-ions are closely spaced and after interaction of carbon fibre these ions are formed damage structure in carbon fibre single type.

N^+ and C^+ ion beams with ion energies 30 keV are used for the treatment of carbon fibres. Ion source was used to generate broad (~150 cm^2) ion beam with 5 mA/cm^2 current density. Pulse-periodic mode of treatment was used with pulse duration of 1 ms and pulse repetiton rates 50 s^{-1}. The ion beam are perpendicular of axis of fibre. The specimen's temperature during ion irradiation changes from 40-50^{0}C at doses (10^{14}-10^{15} cm^{-2}) up to 700-900^{0}C at high doses (10^{18} -10^{19} cm^{-2}).
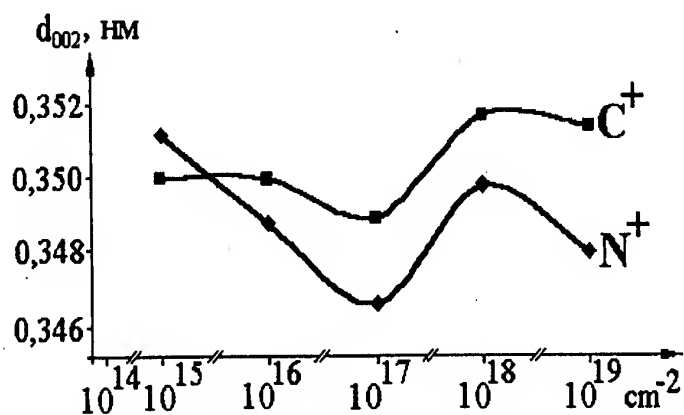
Fig. 1. Evolution of the interplaner distance d_{002} of carbon fibre after C^+ and N^+-ion irradiation as a function of the fluence
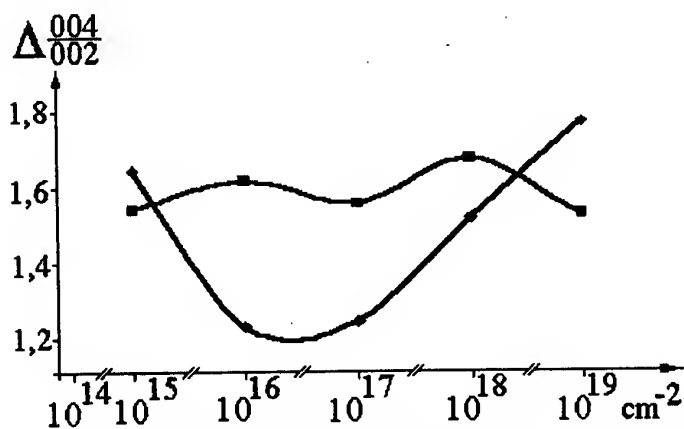

Fig.2. Ratio of width X-ray diffraction patterns from planes 004 and 002, $\Delta(004/002)$, of carbon fibre after C^+ and N^+-ion irradiation as a function of fluence
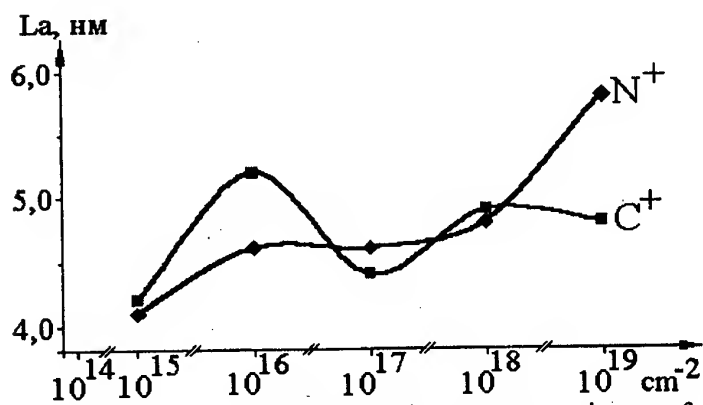

Fig. 3. Evolution of apparent sizes of crystallites along the axis "a" L_a of carbon fibre as a function of fluence

Scanning electron microscopy (SEM) was used to investigate the sample surfaces after ion irradiation.

The structure of ion irradiation fibre was studied by X-ray diffraction (CuK_α) from 10^0 to 150^0 without any rotation of the specimen.

Fibres were tested for ultimate strength and static Yong's modulus, before and after ion irradiation, using an Instron machine.

Surface wetting of fibres by organic liquid (epoxy resin) has been studied too, because a value of contact angle depends on the structure of fiber's surface.

Results

X-ray diffraction results showed: in the fluence range 10^{15}-10^{17} cm^{-2} interplaner distance d_{002} is decreased and minimum d_{002} being observed at a fluence of 10^{17}cm^{-2} (for C^+ and N^+-ion irradiation); in the fluence range 10^{17}-10^{19} cm^{-2} d_{002} is increased (fig.1). Internal stress of carbon fibre, characterized by $\Delta(004/002)$, ratio of width X-ray diffraction patterns from planes 004 and 002,
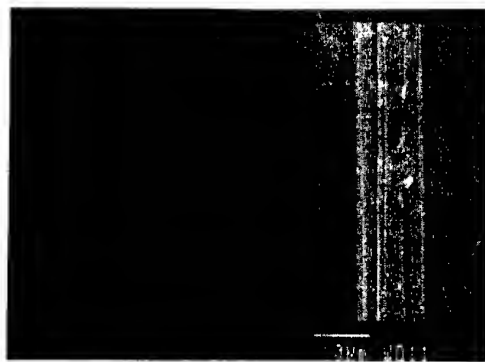
a – nonirradiation carbon fibres
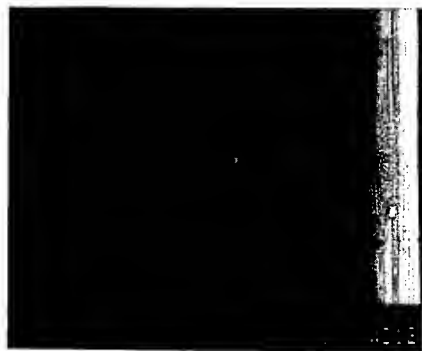
b – C^+, 10^{19} cm^{-2}
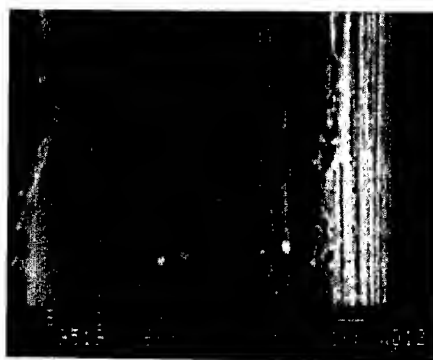
c – C^+, 10^{19} cm^{-2}

d – N^+, 10^{18} cm^{-2}

e – N^+, 10^{19} cm^{-2}

Fig. 4. Surface of carbon fibres before (a) and after (b-e) ion irradiation

after N^+-ion irradiation (10^{15}-$5 \cdot 10^{16}$ cm^{-2}) is decreased half again than that of the nonirradiated fibre.

Internal stress is minimum at a fluence $5 \cdot 10^{16}$ N^+/cm^2 (fig. 2). Internal stress of carbon fibre after C^+-ion irradiation (10^{15}-10^{19} cm^{-2}) is essentially independent of ion fluence (fig. 2). L_a-parameter of carbon fibre – evolution of apparent size of the crystallites along the axis "a" – is increased by 15-20% with changing fluence of C^+ and N^+ from 10^{15} to 10^{19} cm^{-2} (fig. 3).

Special interest is surface topography of carbon fibre after ion irradiation. SEM observation showed the smooth surface of unirradiated carbon fibres (fig. 4a). The irradiated near surface layers of carbon fibres are consist of alternating lengthwise (fig. 4b) and transverse (fig. 4c) riders and valleies after N^+-ion irradiation (fig. 4d) fibre can be conceived of as disk pack (fig. 4e). But after C^+-ion irradiation the surface fibre is consist of ridges and valleies which are set out in parallel of axis fibre. It is likely than this structure of near surface learn of carbon fibre after C^+ and particulary N^+-ion irradiation is formed as the result of C^+ and N^+ sputtering of surface fibre and chemical reaction between N^+ and surface's atoms of carbon fibre.

After ion irradiation σ_B and wetting angle of surface fibre Θ are changed too. In the fluence range 10^{14}-10^{19} C^+/cm^{-2} minimum σ_B being observed at a fluence of $5 \cdot 10^{16}$ cm^{-2}; however Θ is maximum (43^0 in this fluence range) at 10^{16} cm^{-2}. After N^+-ion irradiation (10^{14}-10^{19} cm^{-2}) σ_B is increased and it's maximum at 10^{17} cm^{-2}; Θ is not essentially changed with ion fluence.

Conclusion

It has been stated, that C^+ and N^+-ion irradiation is modification of surface carbon fibre. The parameter structure of carbon fibre (d_{002} and L_a) is changed too. Now we have not a clear knowledge of changing mechanism of surface's and bulk structure of carbon fibre and this properties will be investigation at a later time.

OXIDE SCALE GROWTH ON MCrAlY COATINGS AFTER PULSED ELECTRON BEAM TREATMENT

G. Müller, G. Schumacher, D. Strauß, F. Zimmermann
Forschungszentrum Karlsruhe, INR, Postfach 3640, D-76021 Karlsruhe, Germany

V. I. Engelko
Efremov Institute of Electrophysical Apparatus, 189631, St. Petersburg, Russia

ABSTRACT

The pulsed electron beam treatment method was applied to the surface of LPPS-MCrAlY coatings to improve the oxide scale behavior. Such protective coatings are used in advanced stationary and aero gas turbines to increase the corrosion resistance of air foils at high temperature

The electron beam generated by the GESA facility has a diameter of about 10 cm and sufficient power density to melt a surface layer of about 20 µm of this area by just one electron beam pulse. Cooling rates are around 10^6 K/s and result in a nanometer grained single phase structure of the surface layer, that solidifies directionally. The high roughness of the as sprayed surface is reduced by the GESA process from $R_A = 5$ µm to 1.5 µm.

The oxidation behavior of treated coatings at 950 °C in air was examined. During oxidation a single phase α-alumina scale developed on the treated surface with a considerably lower growth rate as compared to the untreated coatings. Therefore, it is expected that electron beam treatment improves the oxidation resistance of MCrAlY coatings and their suitability as a bond coat for EBPVD thermal barrier coatings.

INTRODUCTION

In advanced stationary and aero gas turbines, inlet temperatures have been dramatically increased in the past decade. Therefore the main corrosion mechanism limiting the blade life time is due to oxidation. Structure and adherence of the thermally grown oxide (TGO) scale on MCrAlY coatings are the key issues for their oxidation resistance and bonding properties for electron beam deposited thermal barrier coatings (EBPVD-TBC). The TGO should consist of dense α-alumina to act as an effective barrier against migrating oxygen and to avoid stresses that could be initiated by development of transient alumina phases or chromium oxide and spinels [1,2]

with different physical properties.

Low diffusivity of oxygen will lead to slow oxide scale growth. This is desirable because the scale failure due to cracking and spallation depends strongly on oxide thickness [3, 4]. Experiments with FeCrAl-based ODS alloys indicated that an increased scale growth rate leads to an earlier onset of the enhanced oxidation and scale cracking [5].

The surface treatment was conducted with the pulsed electron beam facility GESA [6,7] developed for the surface treatment of materials and the optimization of large area electron beam properties e.g. the homogeneity. Quick melting and rapid solidification due to heat conduction into the bulk produces nanocrystalline structures within the treated sur-

face area. The nanocrystalline structure should lead to modified oxide nucleation and growth especially at the beginning of the oxidation process before substantial grain growth in the restructured alloy occurs.

EXPERIMENTAL

The specimens, consisting of Inconel 738 rods and plates, were coated by low pressure plasma sprayed (LPPS) commercial MCrAlY, with Co-32Ni-21Cr-8Al-0,5Y in wt.% by Plasmatechnik AG, Switzerland. The coating thickness was 200 μm, which is one order of magnitude larger than the electron penetration depth applied in the experiments.
Oxidation of coated specimens was conducted in a tube furnace at a constant temperature of 950 °C in air. Samples of electron beam treated and just polished specimens were analyzed after 100, 200, 400, 600, 800 and 1400 hours heat treatment.

RESULTS AND DISCUSSION

After the large area pulsed electron beam treatment, the irradiated surface of the MCrAlY coating has a rapidly solidified surface layer of about 20 μm depth. Fig. 1 is the micrograph of the cross section of an irradiated specimen which shows the surface layer, in which no grains are visible (top) and the unaffected MCrAlY structure with an average grain size of about 2 - 10 μm (below). The modified layer was resistant to etching, while the multi-phase structure shows strong interaction of the etching agent with the β- and γ-phases. Furthermore, the surface roughness caused by the LPPS process is reduced significantly from R_A = 5 μm to R_A = 1.5 μm. To compare the oxide scale growth kinetics on polished coatings with and without pulsed electron beam treatment, a stationary oxidation at 950 °C in air was carried out.
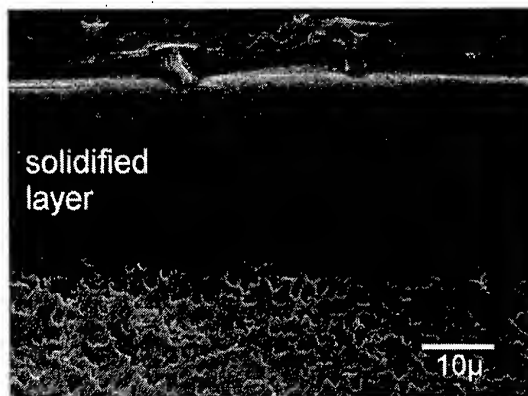

Fig. 1: Metallographic cross-section of MCrAlY treated by a single 40 μs electron pulse

The XRD analysis (Fig. 2b) of the treated samples shows a directionally solidified $\gamma_{(200)}$-phase that remains stable during the oxide scale growth.
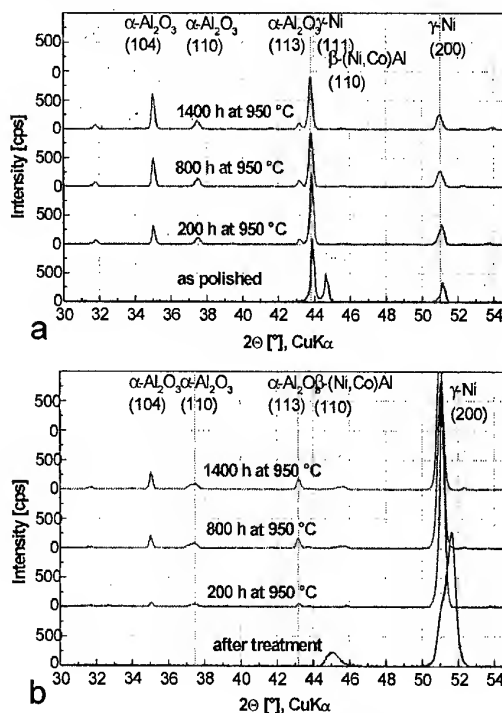

Fig. 2: XRD after isothermal oxidation at 950 °C in air, comparison of polished (a) and treated (b) samples

The polished, not treated sample (Fig. 2a) exhibits the expected ratio between the γ and the β-peaks of the original two phase alloy structure.
Already after 200 h the x-rays do not penetrate the β-depletion zone and no diffraction peaks of the β-phase are detected. A quick growing alumina-layer forms from which only α-Al$_2$O$_3$ x-ray patterns reach a noticeable intensity. The development of the α-

Al$_2$O$_3$ peaks hints at a much slower growth rate of the oxide scale of the treated specimen (Fig. 2b) in comparison to the oxide on the specimen that was not treated (Fig. 2a). Integration of all the α-Al$_2$O$_3$-peak counts shows the remarkable difference between treated and untreated specimens in (Fig. 3).
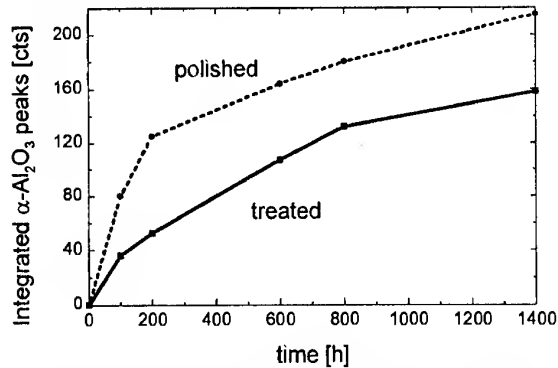

Fig. 3: XRD counts as a measure of the α-alumina scale growth as a function of exposure to air at 950°C

The samples treated by the pulsed electron beam obviously form an oxide layer with better oxygen barrier properties and thus slower oxide scale growth. This is illustrated in Fig. 4 that shows a much smaller oxide scale thickness and β-depleted zone width in case of the electron beam treated than the one in the untreated specimen coating after 1400 h at 950 °C in air.

The oxide surface of the coating, which was polished, shows after 1400 h oxidation a very different morphology compared to the electron beam treated coating. Blade structures typical for Θ-Al$_2$O$_3$ appear on the polished surface although the XRD indicates only an α-alumina crystal structure (Fig. 5a, b).

The oxide scale of the treated surface,(Fig. 5c, d) appears to be composed of typical α-alumina crystals. It seems to be obvious that the oxide scale on that surface forms a much better oxidation barrier. Moreover, the blade like structure on the untreated surface tends to spallation, the onset of which can be seen in Fig. 5a. After 1400 h extended spallation areas were observed that did not appear on the treated surface.

The blades are supposed to grow by grain boundary diffusion to the surface in the polished non treated coating, in which the grains are in the 2 - 10 μm size range, and by outward diffusion of aluminum [1,8].

Similar structures were observed in experiments with FeCrAl based ODS-[3] and with Ni-Cr-Al-Ti-Si-alloys [9] at 900 °C that did not appear at 1100 °C. The scale morphology at 900 °C was explained by possible Θ-Al$_2$O$_3$ formation that can occur at the lower temperatures. Since we could avoid the blade like structure by restructuring of the surface layer to very fine grains, one could assume that grain boundary diffusion within the coating alloy, that is dominant at lower temperatures contributes to the blade formation. Grains are not visible in the solidified melt region after electron beam treatment (Fig. 1). Nevertheless, a small broad β-peak appears in Fig. 2b that may indicate the onset of β-precipitation with very small grains. These conditions do not favor blade like structures. It can be expected that the oxide scale that grows on an electron beam treated, instead of a polished, surface makes up a better basis for EBPVD-TBC's for three reasons: lower oxide growth rate, better surface morphology and less tendency for scale spallation.
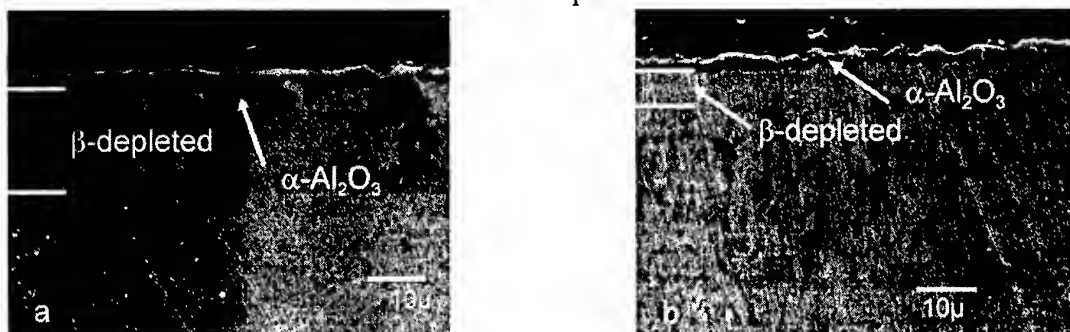

Fig. 4: Comparison of oxide thickness and β-depletion after 1400h oxidation of a polished (a) and an electron beam treated sample (b)
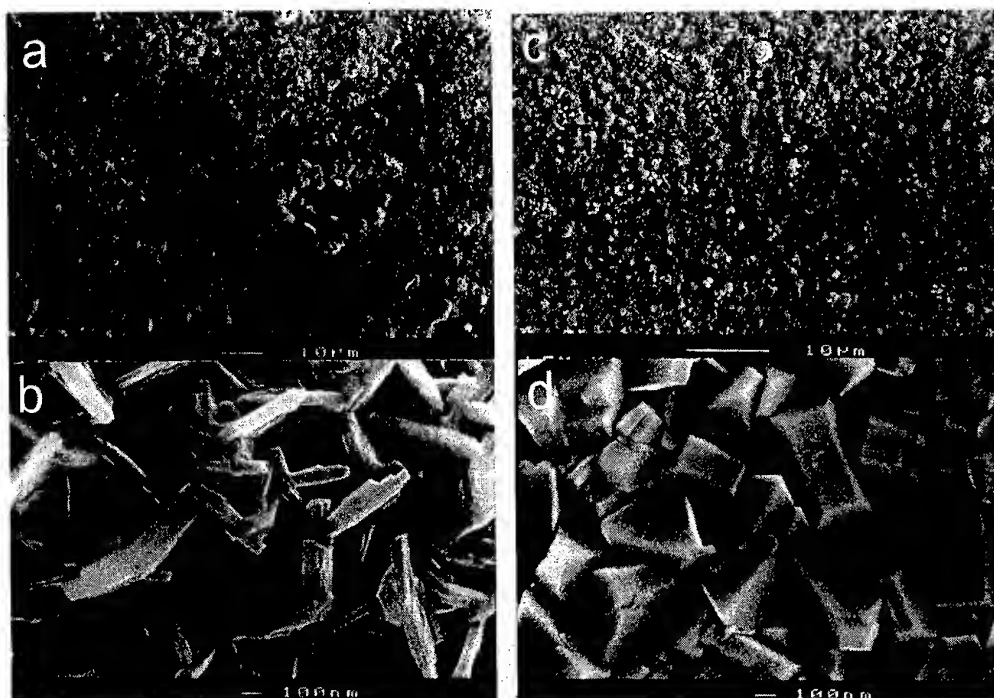
Fig. 5: Surface morphology afer 200h oxidation at 950 °C in air of polished (a, b) and electron beam treated (c, d) samples

CONCLUSIONS

Restructuring of the surface layer of an MCrAlY coating by the pulsed electron beam resulted in positive effects on the oxide scale growth during exposure to air at 950 °C. These effects include a smaller scale growth rate and formation of regular α-alumina grains as opposed to the higher growth rate, and blade like grains on the surface not treated by the electron beam.

It is expected that the electron beam treatment provides much better conditions for formation of oxide scales as an oxygen diffusion barrier and as a basis for deposition of EBPVD-TBC's. Experiments with TBC's on electron beam treated coatings are presently being carried out.

1. P.T. Moseley, K.R. Heyde, B.A. Bellamy and G. Tappin, Corr. Sci., 24, 1984, 547

2. N. Czech, V. Kolarik, W.J. Quadakkers, W. Stamm, Surf. Eng., 13(3), 1977, 384

3. F. Starr, Mat. at High Temp., 13(4) ,1995, 185

4. H.E. Evans, M.P. Taylor, Surf. Coat. Technol., 94-95, 1997, 27

5. W. J. Quadakkers, K. Schmitz, H. Grübner and E.Wallura, Mat. at High Temp., 10 (1), 1992, 23

6. G. Müller, G. Schumacher, D. Strauß, V. Engelko, A. Andreev, O. Kamarov, K. Shigalichin, Proc.11th Int. Conf. High Power Part. Beams, Prague, 1996, 267

7. G. Müller, G. Schumacher, D. Strauß, V. Engelko, A. Andreev, and V. Kavaljov, Proc.11th Int. Conf. High Power Part. Beams, Prague, 1996, 809

8. G.C. Rybicki, J.L. Smialek, Oxid. of Met., 31(3/4), 1989, 275

9. C. Leyens, K. Fritscher, M. Peters, W.A. Kaysser, Surf. Coat. Technol., 94-95, 1997, 155

REMOVAL OF NOx BY PULSE INTENSE ELECTRON BEAM IRRADIATION

Yoshiro NAKAGAWA and Hiroshi KAWAUCHI

Department of Electrical Engineering, Faculty of Engineering, Osaka City University,
Osaka 558 JAPAN

Abstract

Fundamental research on removal of NOx from the mixture gas by irradiation using the pulse intense electron beam, which have energy of $\leq$ 160 keV, beam current of 140 A, current density of 2 A/cm^2, pulse width of 700 ns and electron beam power of 12.6±0.4 J/pulse at standard conditions, was performed. When NO(=200 ppm)/N$_2$ was processed, NO was decomposed to N$_2$ and O$_2$ with the efficiency for the beam power of 220~300 nmol/J. Oxidization of NO to NO$_2$ was accelerated by the beam irradiation in the gas mixture of NO(=160ppm)/O$_2$ (20 %)/N$_2$(80%). By introducing equal amount of NH$_3$ or CH$_4$ to NO into this gas mixture, NOx decreased at 8th shot of beam irradiation when NO was completely converted to NO$_2$. NOx removal from NO(=200 ppm)/N$_2$ gas in various gas cell and NO(=2000 ppm)/N$_2$ gas were investigated. The removal ratio in single shot was largest(30%) at the high current electron beam transported and compressed by external magnetic field but the removal efficiency was largest(650~860 nmol/J) at large volume gas cell without magnetic field. The efficiency increased to 1100 nmol/J for high NO concentration gas treatment.

1. Introduction

The gas discharge process and the continuous current electron beam dry scrubbing process have been developing to be an alternative of existent wet pollutant control technologies.[1] On the other hand, the intense pulse electron beam generated by the pulse power technology is expected to be an another excellent method for pollutant removal because of its lower accelerator cost and effective chemical reaction compared with the gas discharge or the continuous current electron beam system.[2-5] At present, detailed investigations on the possibility of pollutant decomposition by the pulse intense electron beam processing should be required. In this paper, several basic results of removal of NOx by the pulse high current density electron beam irradiation were presented.

2. NOx removal experiment in N$_2$ and model flue gas

2.1 Experimental setup and procedure

In Fig. 1, the experimental setup for pulse intense electron beam processing of a gaseous mixture of NO is shown. High-energy electron beams were extracted from the diode and injected into the gas cell through the 20μm titanium foil. Mixed gas was prepared introducing several gases into the gas cell. The concentration of NOx(= NO+NO$_2$) and NO were measured using the NOx-O$_2$ gas analyzer (Shimadzu Co.,Ltd., NOA-7000) before and after beam injection. The electron beam power in one pulse ;P$_e$ was measured by the calorimeter and estimated by P$_e$ =∫ V$_e$×I$_e$ dt. V$_e$(~160keV) was approximately equal to the measured diode
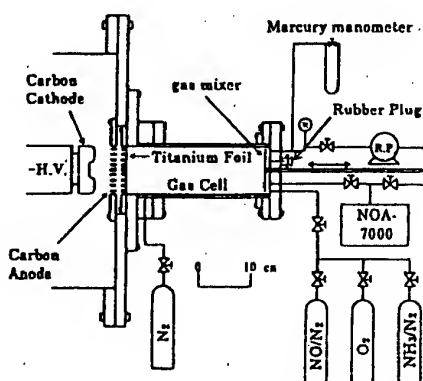
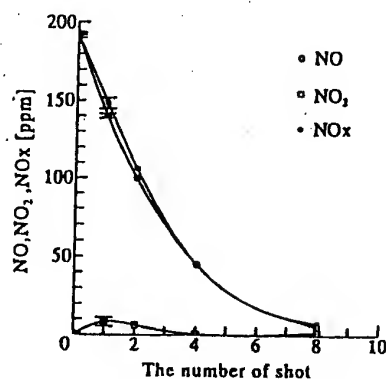Fig.1.Schematic diagram of experimental setup 1.

Fig.2.Change of NO,NO$_2$ and NOx.

voltage ;Vd and the electron beam current ;I$_e$(~140A) measured by the Faraday cup. The most probable values of the electron beam power was 12.6 ± 0.4J for the capacitor charging voltage of ± 50kV in the Marx generator.

2.2 Change of NO, NO$_2$, NOx and NOx removal efficiency

The NO(=200 ppm)/N$_2$ gas was irradiated by the pulse intense electron beam and change of concentrations of NO, NO$_2$ and NOx according to increase of the shot number was shown in Fig.2. Through many dominant reactions, NO was decomposed to N$_2$ and O$_2$ by N radicals produced by the electron beam. NOx removal ratio was about 20 % for the first shot and increased to 95 % after 8 successive shots. The NOx removal efficiency was 220 – 300 nmol/J, which was comparable to the efficiency for the low current density, continuous electron beam and 4 to 7 times larger than that for the electrical gas discharge processing.[3] The efficiency was 4 times higher compared with the decomposition efficiency of Freon by a similar pulse electron beam performed by one of the authors.[4]

2.3 Electron beam power dependence of NOx removal from NO(=200ppm)/N$_2$ gas

The removal ratio increases proportional to the increase of capacitor charging voltage in the Marx generator. As shown in Fig.3, the removed amount increased linearly with the increase of the beam power from 4.4 to 14.7J and the efficiency was almost constant or slightly decreasing at large power. It is possible that the efficiency is limited due to longer electron range compared with the length of the gas cell at large electron beam power.
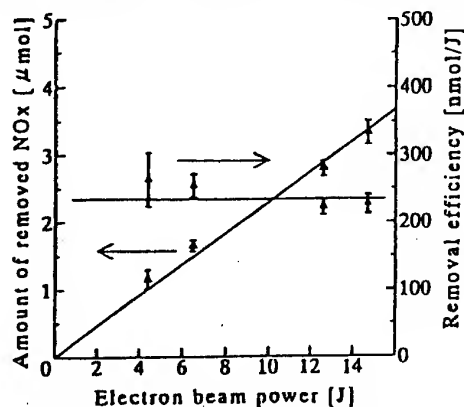

Fig.3.The amount of removed NOx and the removal efficiency as a function of the electron beam power.

However, it is probable that the electron beam power dependence corresponds to the result, which dose rate does not affect removal efficiency, obtained after detailed theoretical and model considerations of the continuous electron beam dry scrubbing process in the mixture gas.

2.4 Pulse electron beam irradiation on NO(=160ppm)/O$_2$(20 %)/N$_2$(80%) gas

The oxidization of NO was accelerated by the pulse electron beam irradiation but NOx was not decreased. In this case, the

-1013-

reduction of NO by nitrogen radical was lower grade reaction compared with the oxidization of NO through production of O radicals by the electron beam because its G-value for the reaction was larger than that for the production of N radicals. At 4th shot, the oxidization of NO to NO_2 was completed and the oxidization efficiency of NO was estimated to be 153nmol/J.

2.5 Addition of NH_3 or CH_4 to NO(=107 ppm)/O_2(20 %)/N_2 (80%) gas

In Fig.4, the change of NO, NO_2 and NOx according to the increase of the shot number was

Fig.4.Change of NO,NO_2 and NOx in the gas added of NH_3 to NO(107ppm)/O_2(20%)/N_2(80%).

shown, when NH_3 in equal amount of NO was added to the NO/N_2 gas with 20 % of O_2. The concentration of NO measured before the electron beam injection became smaller than the calculated value (107 ppm) due to insertion of the absorber of NH_3 between the gas cell and the analyzer. After oxidization of NO to NO_2 rapidly occurred, NOx =NO_2 started to decrease at 4th shot. NOx was 13 % of the initial concentration at 8th shot. In this process, the NO was removed from gas phase as particles of nitric acid (HNO_3) or aerosol particles of ammonium nitrate (NH_4NO_3) through many chemical reactions. These were including the generation of OH radicals from the dissociation of water (H_2O) in the gases. When equal amount of CH_4 was introduced instead of NH_3, NOx removal required more beam shot. Consequently, removal efficiency(90 nmol/J) at 8th shot was almost equal to that in NH_3 addition.

3.NOx removal from NO(=200ppm)/N_2 gas in various gas cell and NO(=2000ppm)/N_2 gas

In Fig.5, the setup for NOx removal experiment by high current electron beam transported and compressed by external magnetic field is shown. The pulse electron beam generated by the diode was transported and compressed by the magnetic field of 1T at maximum. Beam current density increased up to 17 A/cm^2. Electron beam power was 7.1±0.4J/pulse with magnetic field and 3.7±0.2J/pulse without magnetic field. In Fig.6, NOx removal ratio in various gas cell as a function of the number of pulse electron beam shot was shown. (A);Removal ratio of NOx in the gas cell of 49cm length and volume of 1.6 l shown in Fig.5. (B);in the same gas cell of 29cm length. (C);in the straight tube of 9.7cm inner dia. 49cm length and the volume of 3.7 l. (D); in the same gas cell of straight tube without magnetic field. (E); in the gas cell of 31cm inner dia., 30cm length and the volume of 23 l without magnetic field. The removal ratio by single pulse irradiation was as largest as 30% at (B). Beam shot number necessary for 50% removal ratio were (A);3, (B);2, (C);8, (D);11 and (E);more than 20. In Fig.7, removal
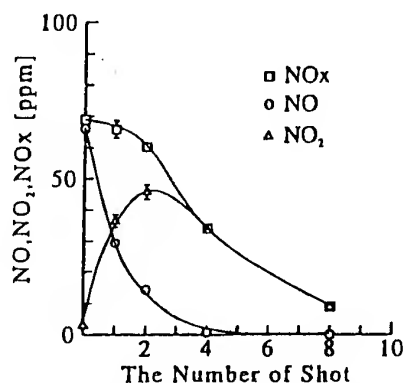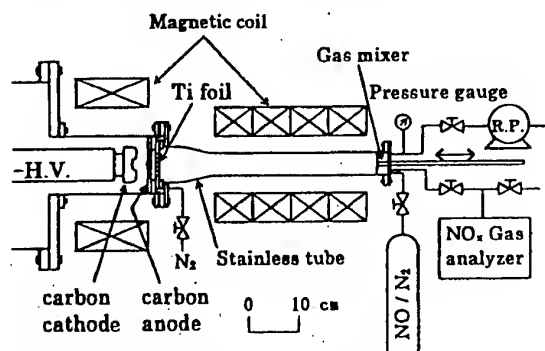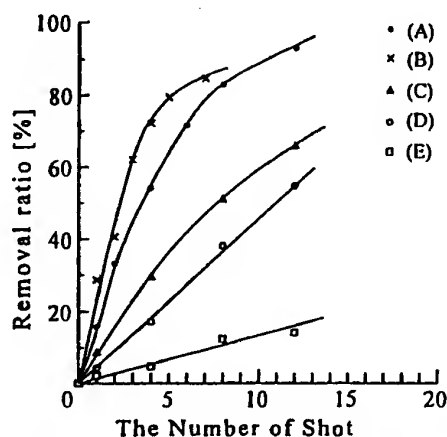

Fig.5.Schematic diagram of experimental setup 2.

Fig.6.Removal ratio of NOx in various gas cell.
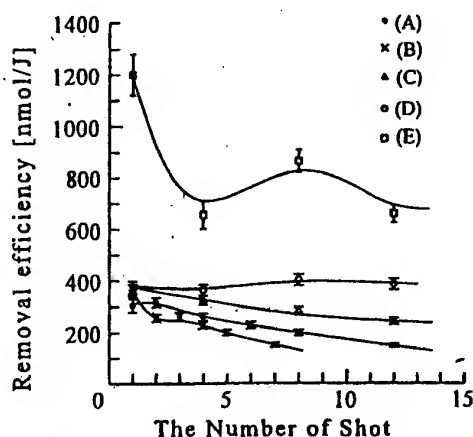

Fig.7.Removal efficiency of NOx in various gas cell.

efficiencies of NOx in various gas cell were compared. Magnetic field energy was not take into account in the calculation of the efficiency. At the first shot, the efficiency for (A), (B), (C) and (D) is almost equal and those were $310 - 380$ nmol/J. At the 7th shot, the efficiency decreased to 150 nmol/J for smallest gas cell (B) due to the decreased concentration of NO. For the largest gas cell(E), the efficiency at the first shot was 1200 nmol/J and 650–860 nmol/J at 4 to 12 shot which was more than twice of those in other gas cell. This result may be caused from DeNOx by some other effects peculiar to the pulse electron beam injection than low density electron beam irradiation. When $NO(=2000$ ppm$)/N_2$ was irradiated by the pulse electron beam in (D), the efficiency at 6th shot increased to 1100 nmol/J at removal ratio of 8%. This indicates that the pulse high current beam efficiently decomposes the high NO concentration gas due to high density radical production. Achieved maximum removal efficiency was about two times larger than that for continuous, low current density electron beam and over ten times larger than that for gas discharge processing.

4. Discussion and conclusion

The pulse electron beam irradiation of 3 shots with 700 ns pulse width removed about 50 % of NOx in the gas cell of 1.7 l. If the electron beam was injected by a pulse repetition rate of 5 kHz, extremely high speed flue gas in a limited volume could be treated by this processing. By addition of NH_3 or CH_4 to the model flue gas, NOx was removed by the OH radical produced by the electron beam. Removal efficiency to the electron beam power increased in large volume gas cell and in the gas of high concentration of NO.

References

1) J.Chang, P.C.Paul, C.Looy, K.Nagai, T.Yoshioka, S.Aoki and A.Maezawa: IEEE Trans. Ind. Appl. 32(1996)131.

2)G.A.Mesyats and Yu.N.Novoselov: Proc. 10th Int. Conf. High Power Particle Beams, San Siego, 1994(National Technical Information Service, Springfield, 1994) p.207.

3) B.M.Penetrante: Proc. 11th IEEE Pulsed Power Conference, Baltimore Maryland, June 29-July 2, 1997. [to be published]

4)Y.Nakagawa, S.Adachi, A.Kohchi and J.Nagasawa: Jpn. J. Appl. Phys. 34(1995)L793.

5) Y.Nakagawa and-H. Kawauchi: Jpn. J. Appl. Phys. 37(1998)L91.

PULSED ELECTRON BEAMS FOR REMOVAL OF CS$_2$ FROM AIR

Yu.N.Novoselov, G.V.Denisov, and A.I.Suslov

Institute of Electrophysics Ural Division of the Russian Academy of Sciences
34 Komsomolskaya St., Ekaterinburg, 620049, Russia.

Carbon bisulfide as a toxic impurity is present in large amounts in the gaseous waste produced by a number of industries, specifically in the production of viscose. One of the ways to lower the carbon bisulfide content of waste gases is by treating these with pulsed electron beams. As shown in Ref. [1], removing CS$_2$ from air exposed to microsecond-duration electron beams is possible with low expenditures of energy, less than the bond breaking energy of this molecule. In the present communication, we furnish results of experimental studies on the removal, by use of pulsed electron beams, of the carbon bilsulphide impurity from a gas mixture simulating the composition of actual industrial wastes.

The experiments were performed with two setups, which comprised electron accelerators generating pulses in the nanosecond and microsecond time range. For nanosecond-range investigations, a compact RADAN accelerator was used, which generated a 180 keV electron beam with a current density of 800 A/cm^2 and had a pulse duration of 3 ns and a pulse repetition rate of 10 s^{-1}. A 10-cm^3 tank was exposed to radiation. The other setup employed a plasma-cathod electron accelerator producing a radially divergent beam with the parameters: beam cross-section of 1.44 m^2, electron energy of 300 keV, beam current behind output foil of 10A, pulse duration of 48 μs. The tank irradiated had a volume of 170 l. With the mixture excited by the nanosecond beam, a single pulse injected into the gas an energy of $3 \cdot 10^{-4}$ J/cm^3. The energy introduced into the gas from the microsecond beam was on the order of 10^{-4} J/cm^3.

We explored model gas mixtures with the constituents in different concentrations: 89 - 99 % N$_2$, 0.1 - 10 % O$_2$, and up to 1% CS$_2$. The mixtures were prepared in a special mixer; the composition of the mixture and of the carbon bilsulphide degradation products was analyzed by gas chromotography on a detector, in terms of thermal conductivity. From experimental findings, we determined the number of removed molecules [ΔCS$_2$] and also the expenditures of energy ε (eV/molecule) to decompose a carbon bisulfide molecule: ε = WN/(e [ΔCS$_2$]). Here W is the energy inserted into the gas in a single pulse, N the number of pulses in a single radiation pulse train, and e the electron charge.
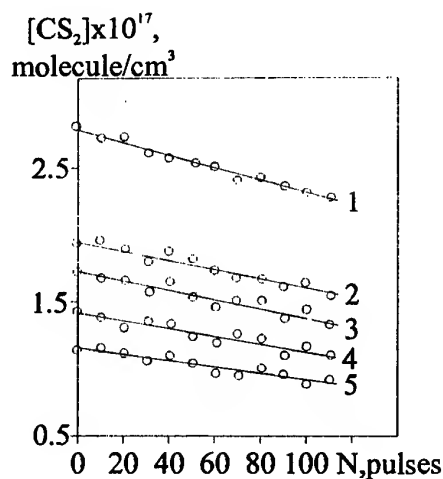
Fig. 1 Variation of carbon bisulfide concentration as a function of the number of pulses at different initial concentrations, [CS$_2$] 10^{17}, mol/cm^3: 1-2,8; 2-1,86; 3-1,63; 4-1,42; 5-1,16.
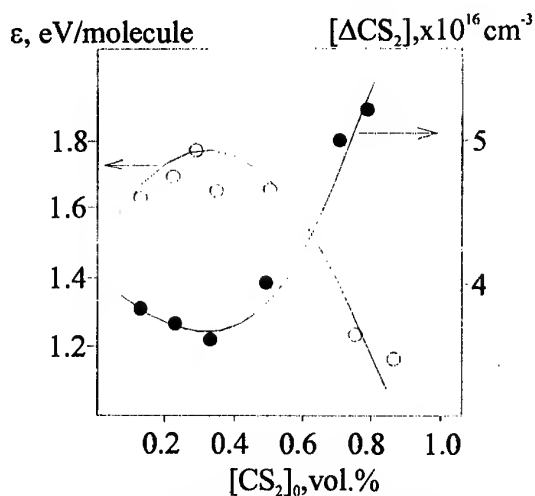
Fig. 2 Expenditures of energy, ε, and the number of removed molecules [ΔCS$_2$] versus the initial carbon bisulfide concentration.

In Fig. 1 we show the CS$_2$ concentration of the model mixture versus the number of radiation pulses. As can be seen, the decrease in impurity concentration depends linearly on the number of discharge pulses, i.e., on the quantity of energy injected into the gas. Significantly, decreasing the impurity content in the microsecond discharge is efficient when a much smaller amount of energy is introduced.

For the microsecond mixture irradiation mode, we have made plots of ε and [ΔCS$_2$] versus the initial concentration [CS$_2$]$_0$ (Fig. 2). In the interval [CS$_2$]$_0$ (0,8 - 2,7) 10^{17} cm^{-3} the number of removed molecules varies from 3.7 10^{17} cm^{-3} to 5.25 10^{17} cm^{-3}, the expenditures of energy range between 1.8 and 1.2 eV/molecule, values that are substantially lower than the dissociation energy of CS$_2$, which is equal to 7.6 eV.

When carrying out the experiments, the degradation products of carbon bisulfide were determined. In the microsecond mode, we detected sulphur dioxide SO$_2$ as the oxidation product of carbon bisulfide. We found that after the mixture had been exposed to a microsecond electron beam, the lateral surfaces and bottom of the plasmochemical reactor were covered with a yellow-colored condensed solid phase, while the upper horizontal surface of the reactor was covered with a dark-brown viscous liquid. An elementary analysis suggests that this compound corresponds to the general composition (-CS-)$_n$ and that its state of aggregation probably depends on molecular mass when the low-molecular compound sublimes and condenses as a liquid on the top of the reactor, whereas the the compound with a

greater number n precipitates as a solid powder.

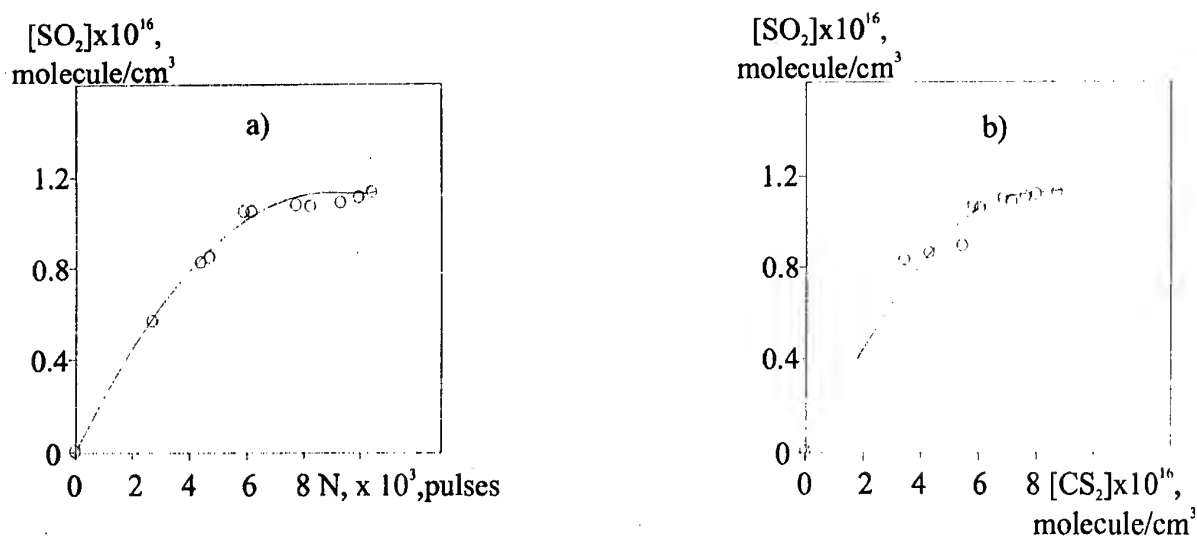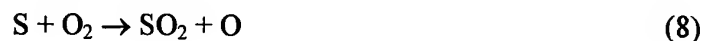[SO$_2$]x10^{16},
molecule/cm^3

Fig. 3 SO$_2$ concentration versus the number of pulses (a) and versus the number of removed carbon bisulfide molecules [$\triangle$CS$_2$] (b).

In the nanosecond mode, the principal carbon bisulfide oxidation product is sulphur dioxide SO$_2$. The dependence of SO$_2$ concentration on the number of radiation pulses in the nanosecond mode is given in Fig. 3a. A comparison with Fig. 1 shows that as the CS$_2$ content is decreased there is an increase in sulphur dioxide concentration. However, this increase is not a linear function of the number of irradiation pulses. Given in Fig. 3b, curve 3, is the dependence of sulphur dioxide SO$_2$ concentration on the number of carbon bisulfide molecules, Δ[CS$_2$], removed from the mixture; this dependence is not not a linear one, either. It is seen that with increasing Δ[CS$_2$] the concentration of sulphur dioxide molecules first increases and then stabilizes at approximately the same level.

The destruction of CS$_2$ with small expenditures of energy may result from the realization of a chain mechanism of carbon bisulfide oxidation similar to that observed in chemical CO lasers [2]. The chain reaction is initiated by the oxygen atoms that arise in the ionized mixture as the O$_2$ molecule dissociates. It may be that the initiation of a chain mechanism in our case comes from the dissociative sticking of plasma thermal electrons to carbon bisulfide and oxygen:

$$CS_2 + e \rightarrow CS + S^- \qquad (1)$$

$$O_2 + e \rightarrow O + O^- \qquad (2)$$

The concentration of free radicals to maintain the chain mechanism is increased owing to the following processes [3]:

$$CS_2 + S^- \rightarrow CS + S_2^- \qquad (3)$$

$$CS_2 + O \rightarrow CS + SO \qquad (4)$$

$$SO + O_2 \rightarrow SO_2 + O \qquad (5)$$

$$CS + O_2 \rightarrow COS + O \qquad (6)$$

$$O + S_2 \rightarrow SO + S \qquad (7)$$

$$S + O_2 \rightarrow SO_2 + O \qquad (8)$$

In the microsecond pulse mode, the product of reactions (1), (3), and (4), viz., CS, which arises during the decomposition of CS_2, probably forms a polymer of composition $((-CS-)_n$, that differs from it in the state of aggregation of the condensed phase, according to the degree of polymerization. When the mixture is exposed to a nanosecond beam, the polemerization process is virtually absent, and the final product precipitates as sulphur dioxide.

Developing a model to describe the processes of degradation of CS_2 in the plasma produced by pulsed electron beams is the subject of further research. However, the data that have been obtained permit the following conclusions to be drawn. The degradation of CS_2 in air by the action of a pulsed electron beam occurs with low expenditures of enrgy, $\sim (1,2 - 1,8)$ eV/molecule. Possibly, a probable cause for this is the realization of a chain mechanism of carbon bisulfide oxidation. Depending on the electron beam parameters, the major CS_2 decomposition product is either a polymer of composition $(-CS-)_n$ or the SO_2 gas. The mixture irradiation regime under which the end product is a polymer in the form of powder may turn out to hold much promise for commercial applications by virtue of high efficiency in removing solid decomposition products of carbon bisulfide and because the technology of trapping these products is largely simplified.

REFERENCES

[1]. G.V.Denisov, D.L.Kuznetsov, Yu.Novoselov, 1997, High Energy Chemistry. Vol.31, 427-8.

[2]. Krishnakumar E., Nagesha K., 1992, J. Phys. B: At. Mol. Opt. Phys. Vol.25, 1645-1660.

[3]. Handbook of chemical. Edited by R.W.F. Gross, J.F.Bott. 1976, The Aerospace Corporation Los Angeles, California

THE REMOVAL OF VOLATILE ORGANIC COMPOUNDS FROM AIR BY PULSED ELECTRON BEAMS

I.E. Filatov and Yu. N. Novoselov

Institute of Electrophysics Ural Division of the Russian Academy of Sciences
34 Komsomolskaya St., Ekaterinburg, 620049, Russia.

Many organic synthesis processes are accompanied by ventilation emissions of exhaust air contaminated with the vapor of volatile organic compounds (VOCs). Recent investigations have shown the efficiency of using electron beams to remove the vapor of VOCs from exhaust air. The use of pulsed electron beams for these purposes has not been adequately explored yet.

The goal of the present work was to study the processes of removal of VOCs from the air by means of a 3-ns electron beam. Subjects of inquiry included acrolein, styrene and benzene, i.e., the most common toxic VOCs present in emissions by various enterprises synthesizing organic compounds, producing plastic materials, etc.

To conduct experiments, a RADAN-303 electron accelerator was used, which provided an electron energy of 180 keV, an output current density of 800 A/cm^2, a pulse duration of 3 ns, an output window cross-sectional area of 1 cm^2, and a pulse repetition rate of 10 pps. The model mixture was placed in a 3000-cm^3 chamber; the electron path was restricted by a target disposed at a distance of 1.0 cm. In a single radiation pulse a total of 4.2 mJ were injected into the gas (90 percent of that energy was embraced by a truncated cone about 4 cm^3 in volume). With the help of a built-in high-efficiency fan, a flowrate of 0.5 m/s was modeled in the chamber. As it mixed uniformly with the rest of the volume the air being treated was again directed through the cycle for further treatment. The scheme that we employ here models a multistage cleaning process.

The reaction chamber was filled with a nitrogen-oxygen (80:20) mixture that contained VOC vapor in an amount on the order of ~100 to 1000 ppm (parts per million). Prior to treatment and subsequent to making a train of 1500 pulses, an air sample was taken from the volume investigated; the VOC content was evaluated by the chromatographic method.

The error in determining the VOC content did not exceed 7 percent in the 100-1000 ppm

range and 15 percent in the 10-100 ppm range.

In Fig. 1 we present typical curves showing variations in the concentration of acrolein (1), styrene (2), and benzene (3) as a function of the number of pulses for different initial concentrations (n_i). Note the exponential behavior of the curves.
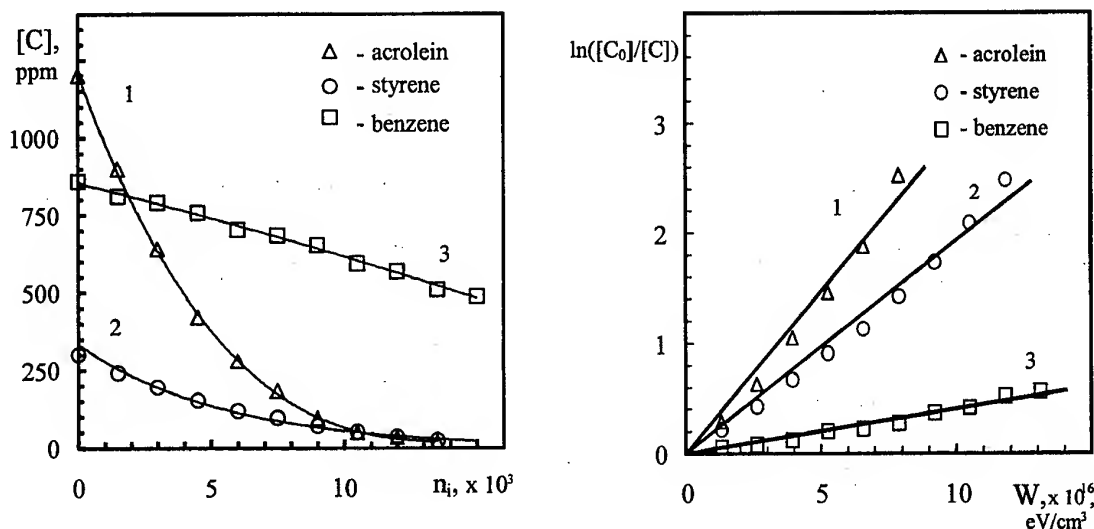

Fig 1. Variations of VOCs concentration ([C], ppm) as a function of a number of e-beam radiation pulses (n_i).

Fig 2. Dependencies of $\ln([C_0]/[C])$ (were[C_0] and [C]– initial and running VOCs concentrations respectively) from injected energy (W, eV/cm^3).

In Fig. 2 the same dependencies are plotted in other coordinates: the X-axis shows the amount of energy injected into the gas, W in eV/cm^3; the Y-axis gives the logarithm of the ratio of the initial to the running concentration. From the linear dependencies shown in the figure, it follows that the removal of the VOCs under study gives a good fit to the exponential behavior of concentration when the latter is varied by 90 percent.

This may be explained by the first macrokinetic order of the VOC removal process, for which the equation reads as

$$d[C]/dn_i = - K\ [C] \qquad\qquad (1)$$

where [C] is the running concentration of VOCs, n_i - the number of radiation pulses, and K a

constant of the corresponding dimension.

Inasmuch as $W = K_1 n_i$, where W is injected energy, the values of $K_a = 1/K_1$ can be calculated from the slope of the plots, using the least squares method: $\ln([C_0]/[C]) = W/K_a$. The constants K_a specify the efficiency of removing VOCs from the air and have the physical meaning of the energy that should be injected in unit volume of air for the concentration of VOCs to be decreased by a factor of $e = 2{,}718$. In curves 1 to 3, the values of K_a are equal to $3.45 \cdot 10^{16}$, $5.2 \cdot 10^{16}$, and $25 \cdot 10^{16}$ eV/cm^3 for acrolein, styrene, and benzene, respectively. These constants can be conveniently used for evaluating the energy contributions to the destruction of a single molecule (ε) with different degrees of cleaning and with different initial concentrations. Thus ε in the dimension [eV/molecule] is satisfactorily approximated by an equation that can be analytically derived from Eq. (1) and is therefore applicable to all processes of this kind, i.e., processes that involve treatment by a train of pulses.

Namely,

$$\varepsilon = K_a \ln(1-\eta)^{-1} / ([C_0] \eta) \qquad (2)$$

where $[C_0]$ is the initial concentration of VOCs in [mol/cm^3];
$\eta = ([C_0]-[C])/[C_0]$ - degree of cleaning

With the initial VOC content of 1000 ppm and with the degree of cleaning $\eta = 0.9$, the ε values as calculated by formula (2) are equal to 3.27, 4.9, and 24 eV/molecule for acrolein, styrene and benzene, respectively. These values differ by no more than 10-15 percent from those measured directly.

The efficiency of removing VOCs depends largely on the presence of reactive groups in organic substrate. The low values of energy contributions (ε) to remove a single VOC molecule may be attributed to the fact that the singlet oxygen generated in the air by the electron beam participates in the VOC oxidation process. Also, it is quite probable that the chain mechanism of VOC oxidation may take place.

The outward regularities that we have found do not suffice to ascertain the actual VOC transformation mechanism; however, knowledge of these regularities is indispensable in simulating VOC removal processes by computational methods. Apart from this, equations of the type (2) permit us to systematize factors that affect the efficiency of removing VOCs from the air, and such systematization helps develop commercial facilities.

NANOMETER-SIZED YSZ POWDERS PRODUCTION
BY MEANS OF TARGET EVAPORATION
USING HIGH-EFFICIENT PULSED-REPETITIVE CO2-LASER

V.V. Osipov, Y.A. Kotov, M.G. lvanov, O.M. Samatov, S.Y. Sokovnin and P.B. Smirnov

Institute of Electrophysics, Ural Division of Russian Academy of Sciences
34, Komsomolskaya st., 620049 Ekaterinburg, Russia
e-mail: osipov@ief.intec.ru

1. ABSTRACT

Our paper reports about YSZ powders production by successive evaporation and crystallization in the gas stream. In the laser applied the original method of active medium excitation was used. Efficiency of the laser constructed on the basis of this method reached 22% and specific power output ~1 W/cm^3. Pulsed regime is proved to be more efficient for active medium excitation and target evaporation then continuous one. Targets made from coarse YSZ powder with a Y_2O_3 content of 10.15 mol. % were evaporated and crystallized in a stream of cleaned air. Cubic-structure YSZ particles were obtained which had a shape close to spherical. Particle size distribution was close to a lognormal distribution with dg = 10 nm and $\sigma = 1.75$. Specific surface of the powder was up to 70 m^2/g, while the Y_2O_3 content reduced to 9.8 mol. %.

2. LASER PARAMETERS OPTIMIZATION

The competitiveness of the evaporation-condensation method for the production of ceramic nanopowders via heating the target by a CO_2 laser beam has recently been demonstrated by German researchers [1-3]. Also, the same authors have shown that usage of pulsed lasers permits a reduction in power consumption and in the size of the particles produced [3], although the maximum absolute magnitude of output, over 100 g/h, has been demonstrated for only the mode of continuous laser radiation. Understanding that this method holds much promise for the production of nanometer-sized powders of complicated chemical compositions and that it's optimizing is a challenge, we have decided to explore the potentialities of the method by in using pulsed CO_2 laser [4].

Schematic of the laser is shown on Fig.1. For the optimal excitation pulsed combined discharge was used. The electrical circuit of excitation used permitted separation of power supply sources without current limiting elements. Plasma in the discharge gap is produced by short time (~10^{-7} s) self-sustained discharge. Main part of the energy (95-97%) is pumped during non-self-sustained discharge when the recombination of plasma takes place (time ~10^{-4} s). Non-self-sustained discharge voltage was chosen under the condition of optimal energy pumping to the upper laser level.

The discharge volume was 1000 cm^3 and gas flow velocity was 50 m/s. Pulses of discharge might be single or united into bursts. The discharge length along optical axis was 80 cm, distance between electrodes - 4 cm. We used stable resonator consisting of spherical
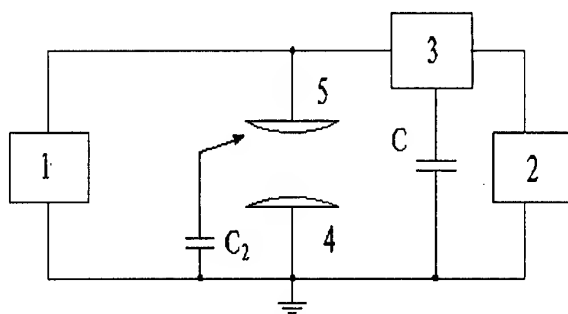
Fig. 1.

1 – pulsed high voltage generator,
2 – DC voltage source,
3 – separation element,
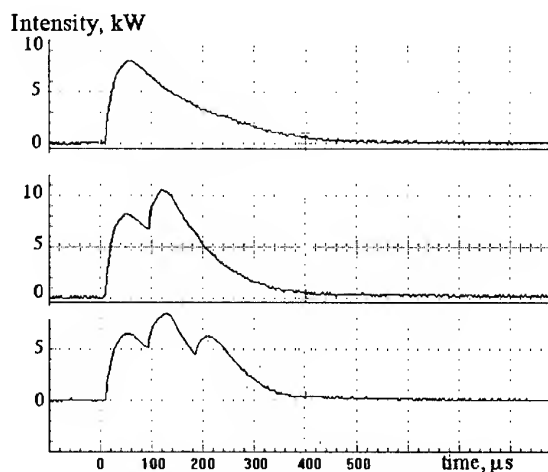4,5 – electrodes
C_2 – pre-ionisation capacitors

Fig.2. Output intensity profiles
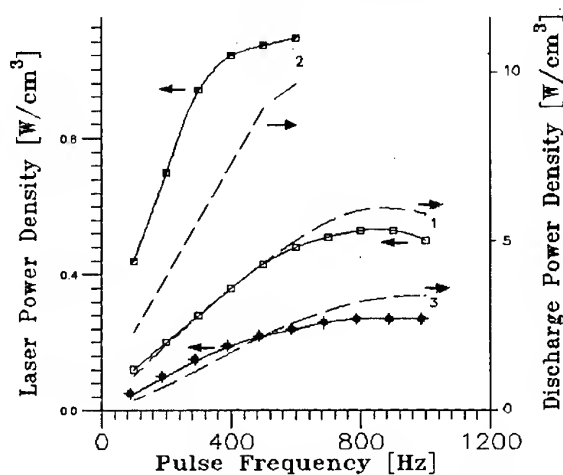for the different length of burst

Fig.3. Discharge and laser power densities
as the functions of the pulse frequency:
1 - CO_2:N_2:He=1:2:4, Pressure 90 Torr
2 - CO_2:N_2:He:H_2=3:10:26:3, 90 Torr
3 - CO_2:N_2=1:3, 40 Torr

copper mirror (focus length - 10 m, reflection - 98%) and plane ZnSe coupler (reflection - 80%). The distance between mirrors was 1.4 m. Burst frequency might be changed from 10 to 1000 Hz, number of pulses in burst - from 1 to 7 and time between pulses in the burst - from 50 to 200 μs. For the number of discharges in burst from 1 to 3, the length of output radiation pulse was almost constant (Fig.2). Only the shape of output pulse changed.

Generation characteristics of combined discharge-excited laser were investigated. The input power and output power densities as a functions of pulse repetition frequency are shown on Fig.3. In the range of low frequencies (up to400÷ 500 Hz) the input power is proportional to the pulse repetition frequency, so the irradiated power is also proportional to it. At the higher frequencies the saturation and then decrease of the input and output power take place (curve 1). Though the pulsed self-sustained discharge was stable up to 3÷4 kHz It seems to be connected with intensive energy dissipation processes, taking place in the cathode layer and hence, with the instabilities development in the cathode region. The calculations show that under such experimental conditions the cathode layer width was almost equal to the thickness of Prandtle layer. The gas flows slower in the border layer near the electrodes, so it was necessary to change the gas between electrodes more then once in order to remove old mixture entirely.

Moreover, acoustic processes take place. As the current between the electrodes appears, two shock waves goes back and forward along the gas flow. They are amplified inside the sustained discharge zone. So the pause between pulses is necessary to remove all inhomogenities appeared in gas. The difference in peaks of output power for the mixtures with and without H_2 (~600 and ~900 Hz) is obviously caused by heating the gas because of

greater pumped power, which is achieved at the lower frequencies for the mixtures containing hydrogen.

For the ratio $CO_2/(CO_2+N_2)$ higher then 0.15, specific output power decreases with the increase of CO_2 pressure. This fall is explained by lower energy input into the active media due to increase of attachment rate, which reduces the current pulse length.

The investigation of long-time working regimes were done for gas mixtures containing CO. It is possible in such mixtures to save the starting composition by CO_2 regeneration ($CO+O \rightarrow CO_2$), which compensates CO_2 dissociation. We have found a mixture $CO_2:CO:N_2:He = 1:1.5:10:20$, total pressure 60 Torr which provides the output power falling less then 10% after 4 hours of operation.

In the experiments mixture $CO_2:N_2:He=1:4:8$ at the 80 Torr pressure was found to be optimal. The efficiency 22% (or 28% without cathode fall) was obtained for this mixture on the first shot. But for this mixture efficiency decreased faster during the work because of CO_2 dissociation.

Laser characteristics used for performing this experiment are shown below:

Average radiation power	$P_{av} = 600$ W
FWHM of radiation pulse	$t_u = 180$ μs
Number of pulses in burst	2
Pulse shape	close to rectangular
Pulse repetition rate	$f = 400$ pps
Efficiency of converting power drain to radiation	$\eta = 7.5\%$
Diameter of laser beam at outlet mirror	$D_b = 35$ mm
Diameter of focal spot on target	$D_f = 0.45$ mm
Mean radiation intensity on target surface	$I = 3.77 \times 10^5$ W/cm^2
Blowing-through of laser chamber	transverse
Gas mixture	$CO_2:CO:N_2:He = 1:1,5:10:20$, total pressure 60 Torr

Gas mixture exchanged every 4 hours of continuous operation.

3. POWDER PRODUCTION

The experimental setup schematic is given in Fig. 4. The target 2 was rotated and displaced linearly by a special drive 1 in the horizontal plane so that the velocity of motion of the laser beam traveling over its surface remained constant and the evaporation of the target surface was uniform. As the target wore out it was displaced in the axial direction in such a way that its surface remained in the plane of the focal spot. The target used was a 60 mm dia. and 17 mm high pellet compacted from 10-YSZ powder (ZrO_2 stabilized with 10.15 mol % of Y_2O_3) with specific surface Ss = 6.1 m^2/g.

The target was compacted into a stainless steel cup and placed on the supporting table of the drive 1. The air-tight evaporation chamber 3 was blown through with air cleaned from mechanical impurities, which was forced by a fan 4. The particles produced were transferred by the air and trapped by a cyclone 5 and an electric filter 6. The consumption of air was 40 l/min, the air was emitted into the atmosphere via a mechanical filter 7. The laser beam was focused on the target by a lens 8 with a focal distance of 100 mm. The conditions above permitted to produce powders with an output of 15 g/h and specific area Ss = 65-75 m^2/g. The powder produced was used in conducting compacting and 200 nm in size cannot be sedimented from the suspension. sintering experiments [5]. These investigations have shown that the powders sinter at a temperature of 1100 °C and the ceramics has a density up to 98% of the theoretical density. The powder contains up to 3 wt. % of particles with sizes of 200 nm

and more. Particles under 200 nm in size cannot be sedimented from the suspension. These coarse particles represent chiefly spheres up to 1 μm in diameter, but there are also shapeless particles about 10 μm in size. A distribution constructed from the photos indicates that more than 98% of the particles are less than 40 nm in size.

X-ray diffraction and electron diffraction analyses have shown that the powder has a cubic crystal structure. A TG analysis has shown that the moisture and sorbed-gas content was 0.25% wt. % for raw-material powder and ~ 2.75 wt. % for the powder produced. This moisture and the gases are completely removed at about 900 °C. Y_2O_3 content has decreased to 9.8 molar percent, i.e., by 0.35 molar
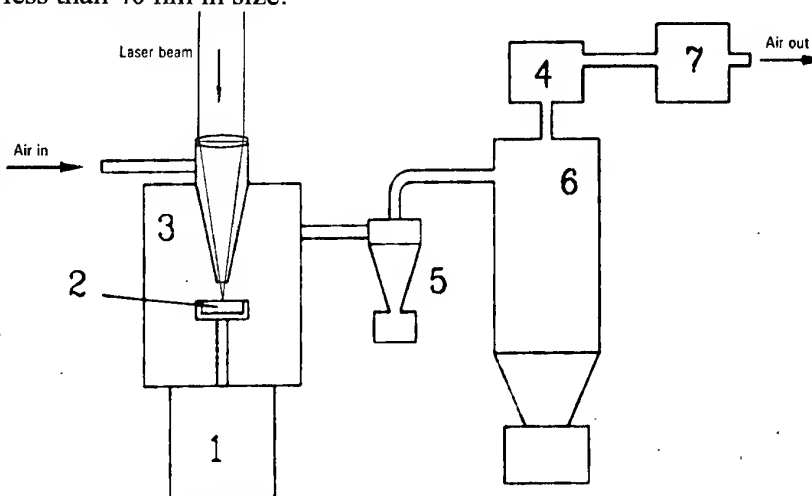
Fig.4. Experimental setup for powders production

percent, in the powder production process The authors of Ref. [2] observed a still greater decrease in Y_2O_3 content, on the order of 0.6-07 mol %, and attributed this to the evaporation temperature difference of Y_2O_3 and ZrO_2. In our experiments, the powder that remains in the target cup has a partially molten surface film about 100 μm thick. An X-ray diffraction analysis of the film material has shown that the Y_2O_3 content of the film has increased by approximately a factor of 1.5 as compared with the Y_2O_3 content in the initial composition of the raw material. That is, the hypothesis made in Ref. [2] has been confirmed.

A comparison of the output that we have obtained for $P_{av} = 600$ W and $I \sim 3.8 \times 10^5$ W/cm^2 with the data [3] shows that with P_{av} being equal and with the pulse durations being close to each other in magnitude, our conditions ensure an output that is a factor of 2 or 3 higher. Apparently, this can be ascribed to the difference in pulse shape and to the frequency of radiation pulses. Utilizing a CO_2 laser with a pulse shape close to rectangular to evaporate powder targets has enabled us to substantially increase the output in producing ultra fine ceramic powders of complicated compositions with typical particle size on the order of 15 nm.

4. REFERENCES

[1] Mueller, E., Oestreich, Ch., Popp, U., Staupendahl, G., and Hennenberg, K.-H. Kona - Powder and Particle, 1995, 13, 79.

[2] Mueller, E., Oestreich, Ch., Popp, U. Michel, G., Staupendahl, G., and Hennenberg, K.-H., Proceed. Fourth Euro. Ceram. Confer. (Ed. C. Galassi), Italy, 1995, 1, 219.

[3] Michel, G., Staupendahl, G., Eberhardt, G., Mueller, E. and Oestreich, Ch. Proceed. 5th Euro Ceram. Confer, France, Key Engineering Materials, 1997, 132-136, 161.

[4] Osipov, V.V., Ivanov, M.G. and Lisenkov. V.V., Optika atmosfery i okeana, 1997, 10, 11, 1266. (in Russian).

[5] Ivanov, V.V., Report at 4th Russian Conference «Physics and Chemistry of Ultradisperse (Nano) Materials». Obninsk, Russia, 1998 (to be published).

PRODUCTION OF LOW-ENERGY HIGH-CURRENT ELECTRON BEAMS IN A REFLECTED-DISCHARGE PLASMA-ANODE GUN

G.E. Ozur, D.I. Proskurovsky, and V.M. Gaponenko

High-Current Electronics Institute SD RAS,
4 Akademicheskii Ave., Tomsk, 634055, Russia

Abstract. The present work is an extension of our earlier research on the generation of low-energy (up to 30 keV), high-current (up to 40 kA) electron beams of microsecond duration in a plasma-anode gun operating based on a low-pressure pulsed reflected discharge.

Low-energy (10-30 keV), high-current electron beams (LEHCEBs) are widely applied for modification of surface layers of various materials [1].The most promising LEHCEB sources are guns with a plasma anode and an explosive-emission cathode [2] which have some advantages over vacuum-diode-based guns. Preliminary filling the diode and the beam drift space with plasma makes it possible to increase abruptly the electric field at the cathode and the electron flow perveance compared to the corresponding parameters of a vacuum diode and to improve substantially the uniformity of the energy density distribution over the beam cross section. Earlier [2] we used as anode plasma (AP) sources the vacuum arcs initiated by breakdowns over the surface of a dielectric. However, this method for the production of a plasma anode has some disadvantages conditioned by the erosion character of the AP generation.

To overcome these disadvantages, we have developed an electron gun where the anode plasma is produced by a pulsed reflected (Penning) discharge [3, 4]. A schematic diagram of the system is given in Fig. 1. The Penning discharge cathodes are the beam collector and the explosive emission cathode of the electron gun. The diameter of the explosive-emission cathode is 6 cm. The anode is made as a ring of inner diameter 7 cm and width 1 cm. The cathode-anode separation is 6 cm. A sectioned solenoid creates a uniform guide magnetic field of strength up to 3 kOe. The chamber is stationarily filled with a gas (Ar) to a pressure $p=(3\text{-}9)\times10^{-4}$ Torr.

CHARACTERISTICS OF REFLECTED DISCHARGE

The discharge was initiated by applying a 4-kV voltage pulse to the anode. The discharge current was limited by a ballast resistor. The discharge current amplitude was varied from 4 to 300 A.

A peculiarity of the reflected discharge (RD) under study is its asymmetry related to the presence of a resistor of resistance $R_1=25$ Ω and an inductor of inductance L=60 μH in the discharge circuit (see Fig. 1). This causes a misbalance in the current share between the cathode and the collector (the discharge current is almost completely closed onto the collector). This misbalance might result in an unstable operation of the discharge because of a deterioration of the conditions for electron oscillations. However, measurements of the ion current density onto the cathode have shown that the plasma density is the same at the cathode and at the collector, and the discharge operation is stable.

For a conventional Penning discharge being a glow in character, the operating voltage V_p is 400-500 V [5] for a similar range of gas pressures. The CSs present in the RD reduces V_p to
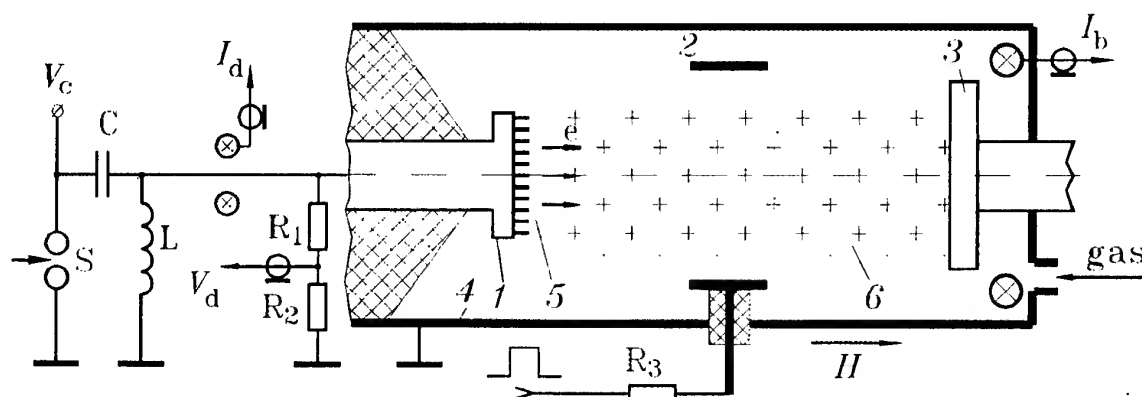
Fig. 1: Schematic of the electron gun: *1*- cathode; *2*- anode; *3*- collector; *4*- chamber; *5*- cathode plasma; *6*- anode plasma; *7,8*- Rogowski coils; C (3 μF)- capacitive energy store; S- gas spark gap; L (60 μH)- charge inductor, R_1, R_2- resistive voltage divider, and R_3- ballast resistor.

200-250 V. Probe measurements have shown that the plasma potential and the electron temperature in the discharge column are φ_{pl}=80-90 V and T_e=5-7 eV, respectively.

Examination of the oscillograms of the ion current density onto collector has shown that the average ion current density, except in the peripheral region, is j_i=0.05-0.15 A/cm^2 in 10-12 μs after the initiation of the discharge (Fig. 2). This corresponds to the plasma density $n_p \simeq$ (3-9) ×10^{12} cm^{-3}. An increase in discharge current leads in the main to an increase in the fraction of the current flowing through the CSs. As the discharge current is increased from 4 to 300 A, the ion current density increases from 0.03 A/cm^2 to only 0.15 A/cm^2.

Observation of the dynamics of CSs has shown that they originate in the near-axis discharge region within the falltime of the anode voltage, and in a few microseconds they all go into the peripheral region of the discharge. Even if a CS was force ignited in the near-axis region at the collector, it ceased to operate as the ignition pulse is completed.

In our opinion, the CSs dynamics is determined by the following: As a CS appears, a significant portion of uncompensated negative space charge is injected into the discharge column. Since the runaway of the electrons injected into the near-axis region of the discharge is strongly hindered by the external magnetic field ($j_a \sim H^{-2}$ [6]), only those CSs that appear on the collector within a radius equal to the radius of the anode will operate unhindered. This is also confirmed by the fact that the erosion traces appearing on the collector in the course of operation of CSs are localized within a radius equal to the inner radius of the anode.
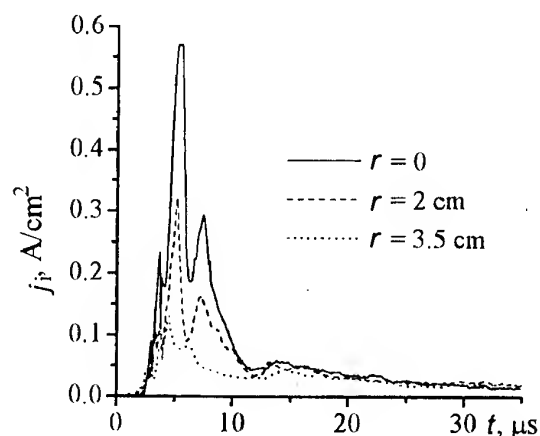
Fig. 2. Waveforms of the ion current density, j_i, onto collector taken at different radii, *r*. p=6 ×10^{-4} Torr, discharge current- 125 A and *H*=3 kOe.

GENERATION OF AN LEHCEB

The beam formation has been realized by the following way. About 25 μs after the initiation of a reflected discharge, an accelerating voltage pulse of risetime ≤ 10^{-8} s was

applied to the cathode. The plasma density $n_p \simeq 5\times10^{12}$ cm^{-3} with the RD current equal to 34 A turned out sufficient for effective initiation of explosive emission at the cathode with the accelerating voltage peaked at 20-25 kV. Once explosive electron emission had been initiated, an electron beam was formed in the double layer between the cathode and anode plasmas. Thus, the plasma-filled diode was a "direct-discharge" system with a high fall potential in the near-cathode region and a rather long plasma column.

To elucidate the mechanism for the current passage in a system like this, we studied the behavior of the waveforms of the accelerating voltage (V_d) and of the beam current onto collector (I_b) as functions of anode-collector distance, l. Figure 3 presents typical V_d and I_b waveforms for l=3, 9, and 25 cm. An analysis has shown that a waveform of I_b can be subdivided into four characteristic portions which reflect (I) the initial current rise stage, (II) the quasi-stationary stage, (III) the fast current rise stage, and (IV) the current fall stage. Let us consider successively each of these stages.
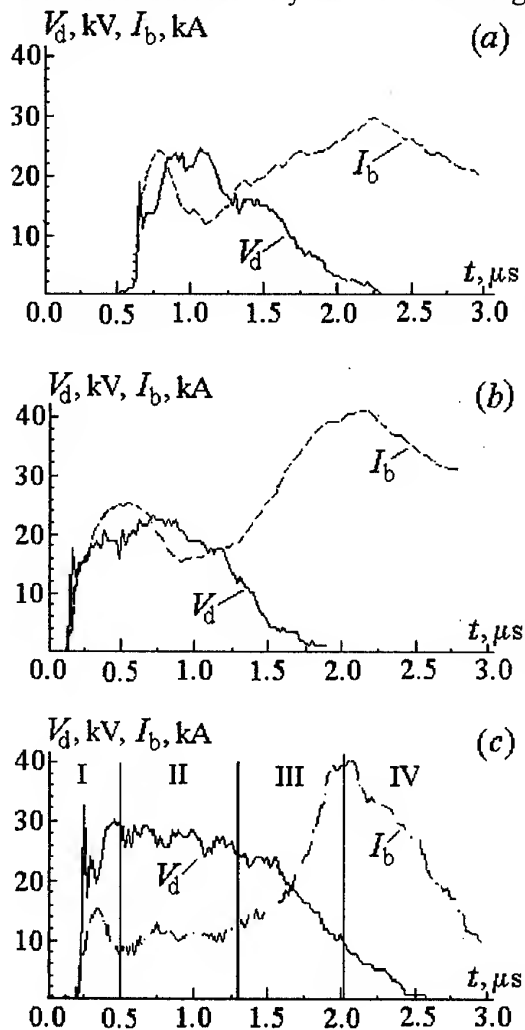
Fig. 3. Typical waveforms of accelerating voltage and beam current onto collector: l= 3 (*a*), 9 (*b*), and 25 cm (*c*); p=6×10^{-4} Torr, H= 1.5 kOe, pulse generator charge voltage - 32 kV.

At stage I ($t \le 500$ ns) the dynamics of the beam current is determined in the main by the nonstationary processes in the DL which are related to the fact that the discharge voltage pulse risetime ($\simeq$ 10 ns) is shorter than the time required for an ion to travel through the DL ($\simeq$ 40-50 ns). In this case, the electron current density in the DL rapidly increases to a value being much above the Langmuir limit for a bipolar flow [7]. The DL gradually expands, and the current density decreases to the value determined by the Langmuir law. The current sometimes falls more rapidly due to erosion of the anode plasma, like this occurs in plasma erosion opening switches. As the current rises, a collector plasma is formed from desorption products, and both the anode and collector plasmas are accelerated toward the cathode under the action of the inductive fall voltage across the plasma column, V_L. This fall voltage reaches 1-5 kV. A change in distance l results in a change in the initial ion density in the AP (and, hence, in beam current) since increasing l decreases the degree of ionization of the working gas for an the RD current remained unchanged. As a result, the beam current decreases with increasing l.

At stage II ($t \simeq 0.5$-1.5 µs), the current slowly increases which, in our opinion, is provided by an additional ionization of the working gas by the beam electrons and by the plasma electrons that acquire sufficient energy under the action of the vortex field in the plasma. Estimates show that the ion production rate in our case roughly corresponds to the observed beam current rise at stage II. The duration of stage II decreases with decreasing l.

At stage III the current rise rate increases owing to the ions coming into the DL from the collector plasma, accelerated at stages I and II. Estimates show that for large values of l, the dominant role in the increase in the ion current density in the DL should be played by H^1 ions, being the fastest ones. (When the chamber is evacuated with an oil-vapor pump, hydrocarbon films, being a source of protons, are always present on the collector surface). According to our data [8], the ion-emissive power of the collector plasma is higher than that of the AP, which just provides the increased current rise rate at stage III. The time interval from the beginning of the pulse to the current maximum increases with l.

At stage IV the current onto collector falls gradually. The current pulse duration is substantially longer than that of the accelerating voltage due to the plasma decay current.

Thus, the most important factors that dominate the evolution of the beam current are the nonsteady-state character of the DL at the initial stage of the beam formation, the inductive voltage fall across the plasma column, and the dynamics and properties of the collector plasma. Of special interest is the fact that we have been able to transport a beam with a current of up to 40 kA, which is almost three orders of magnitude greater than the Pierce current for electrons with energies of up to 30 keV, over a distance of up to 27 cm. It should also be noted that the total beam energy (as well as the energy density) decreases with l only slightly (Fig. 4), since the decrease in current is compensated by an increase in electron energy and by a lengthening of the voltage pulse.

Fig.4. Total beam pulse energy measured by calorimeter versus distance l.

ACKNOWLEDGEMENT

The authors are grateful to A.S. Myagkov for his help in conducting experiments.

REFERENCES

[1] *D.I. Proskurovsky, V.P. Rotshtein, and G.E. Ozur*: Proc. of the 11th Int. Conf. on High Power Particle Beams, v.1, pp.259-262, Prague, Czech Republic, June, 1996.

[2] D.S. *Nazarov, G.E. Ozur, and D.I. Proskurovsky*: Izv. Vyssh. Uchebn. Zaved. Fizika, 1994, No. 3, pp. 100-114.

[3] *G.E. Ozur, D.I. Proskurovsky, and D.S. Nazarov*: Proc. of the 11th Int. Conf. on High Power Particle Beams, v. 1, pp. 359-362, Prague, Czech Republic, June, 1996.

[4] *D.S. Nazarov, G.E. Ozur, and D.I. Proskurovsky*: Proc. of the 11th IEEE Int. Pulsed Power Conf., Baltimore, USA, 1997, pp.1335-1340.

[5] *Yu.E. Kreindel'*: "Plasma Sources of Electrons" (Russian). Moscow, Atomizdat, 1977, 144 p.

[6] *V.L. Granovsky*: "Electrical Current in Gas", Moscow, "Nauka", 1971, 544 p.

[7] *M.Yu. Kreindel', E.A. Litvinov, G.E. Ozur, D.I. Proskurovsky*: Fizika plazmy (Russian), 1991, v.17, No.12, pp.1425-1439.

[8] *D.S. Nazarov, G.E. Ozur, and D.I. Proskurovsky*: Proc. of the 10th Int. Conf. on High Power Particle Beams (BEAMS'94), San Diego, USA, 1994, pp.653-655.

POWER SUPPLY OF A STREAMER CORONA USING FITCH PULSE GENERATOR SWITCHED BY THYRATRONS

V.D.Bochkov, V.M.Djagilev, V.G.Ushich[1],
A.Z.Ponizovskiy, L.Z.Ponizovskiy, V.Ya.Starobinsky[2],
G.Harris, S.P.Kryutchkov, A.P.Shvedchikov[3]

[1]Research Institute of Gas-Discharge Devices - "Plasma", 24, Tsiolkovskiy str., Ryazan, 390023, Russia

[2] SEDB "Horizont", 8, 2nd Donskoy Proezd, Moscow, 117071, Russia

[3] Pulsatron Tech. Ltd., 9200 Sunset Blvd.-Suite 404 Los Angeles, CA 90069 USA

ABSTRACT

This report gives the description of an industrial pilot installation "PULSATECH™" generating a pulsed corona discharge for use in technical applications. The power supply of the corona is based on the use of a three-stage Fitch pulsed voltage generator (FPG) with hydrogen-filled thyratrons as switching elements. The installation can be used for cleaning hazardous off-gases of power plants and industrial objects, as well as in some exotic fields of application such as destruction of the chemical weapon stocks.

Comparative data on the operation of the two types of gas-discharge switches - thyratron with heated cathode and thyratron with cold cathode (pseudo-spark switchboard - PSS) with a rated voltage of 50 kV are also reported. Operating time attained for the PSS of Russian design and fabrication in testing modes of operation, allows to expect a service life in real modes of operation up to 3-7 thousand hours.

INDUSTRIAL PILOT INSTALLATION "PULSATECH™"

Now many countries are developing technologies for cleaning off-gases of power plants and industrial enterprises based on the use of pulsed corona discharge. Off-gases cleaning from harmful organic and inorganic admixtures can be performed by directing the off-gas flow in the electrofilter through a zone of pulsed corona discharge yielding ions and radicals of gas molecules which enter into radiation chemical reactions with contaminant molecules. These reactions result in transformation (conversion) of gaseous admixtures in aerosols or solid products. Table 1 gives some of our results on cleaning air and off-gases from ecologically harmful admixtures using pulsed corona devices.

Table 1

Contaminant		Cleaning rate, %	Power consumption, W-h/m³	Final products
Kind	Concentration, vol.%			
Sulfur dioxide, SO_2	0.02-4.0	60-90	5-7	Sulfuric acid
Nitrogen oxides, NO_x	0.05-0.6	70-95	3-5	Nitric acid
Phenol	0.01	99	25	Hydroquinon
Styrene	0.01	99	15	Polystyrene
Benzene	0.04	75	50	Hydroquinon
Ammonia	0.01	95	20	Ammomium nitrate

The main difficulty of industrial realization of the pulsed corona devices is the requirement of

an inexpensive and durable power supply of pulsed corona discharge capable to generate during a long time voltage pulses with required parameters. Using the results of experiments and results of computer simulation [1] we have developed and put into operation an inexpensive and quite industrially realizable pulsed corona device on the base of a 3-stage pulsed voltage Fitch generator (FPG) with maximum use of standard high-voltage equipment and thyratrons as a switchboard. A device of this type has been installed and tested at the US Department of Energy's former test bed facility in Butte, Montana, now – MSE Tech. Appl. The basic circuit diagram of this installation (Fig.1) is protected by Russian and USA patents [2] and is known as "PULSATECH™" device.

FPG involves: a high voltage power source B, three capacitor modules C_1-C_3, charging induc-tances L_1, L_2, a series diode D and thyratron S. FPG output is directly connected to the coronating electrode of the electrostatic precipitator EF. The heating current supply for hydrogen reservoir (and in the case of heated cathode thyratron also for cathode filament) under high voltage consists of two transformers T_1, T_2 with balancing capacitors C_4-C_7 and separating inductance coils L_3, L_4. The thyratron trigging system involves a control block E and a pulse transformer T_3. The device is also supplied with systems for measurement of output voltage U_d and current I_p.

Fig.1. Schematic diagram of the pulsed corona cleaning device "PULSATECH™"

The device functions as follows. By charging the capacitors charging vector polarity of odd capacitors is initially opposite to that of even capacitor thus the voltage applied to the coronating electrode is equal to charging voltage U_z. The thyratron trigging results in forming a closed oscillatory circuit involving even capacitor C_2, plasma beam inside the thyratron and geometrical inductance of wiring L_d. The oscillation half-period $\tau/2 = \pi \sqrt{Ld \cdot C2}$. After this time the charging vector of the even capacitor is completely revolted to the opposite direction and the vectors of all three capacitors are added thus a voltage pulse with amplitude $U \approx 3U_z$ is applied to the space between coronating and grounded electrodes of the EF producing streamer corona. Typical oscillogram of the FPG output is shown in Fig.2. The corona enables chemical reactions resulting in conversion of admixtures into liquid and/or solid products and the DC voltage constantly applied to the EF removes these products from the gas flow.

Fig.2. Typical oscillogram of generator output U - voltage, – current W - power U™

Main technical characteristics of the "PULSATECH™" device are as follows:

charging DC voltage U_z=40 kV, pulse amplitude U=80–110 kV (depending on the EF design), stage capacitance C_{1-3} =6 nF, pulse duration τ=300 ns, frequency of pulse repetition 100 Hz, power 10 kW, electrical efficiency 70%.

THE SWITCHING DEVICE

The most critical component of a pulse power supply is the switching device. In most cases in powerful installations operating in nanosecond range of pulse duration thyratrons are used as switchboards due to their high efficiency and large overloading ability. However classical thyratrons where the heated cathode is the main source of emission have the maximal total operating resource 10^5 C. This means that the durability of a thyratron is at maximum some hundreds hours, while an operating time of 3-8 thousand hours or $(1-4)*10^7$ C is required.

New type of switching devices - the thyratrons with the cold cathode (or pseudospark switches - PSS), combine the best features of thyratrons, spark discharges and thyristors. They are capable to switch energy storing devices to a low-impedance load satisfying practically all requirements by low power consumption, small dimensions and weight. Their additional important characteristics are relatively low cost and absence of high current heating circuits. However, known PSS as a matter of fact are thyratrons with grounded grid (GGT) whose triggering is caused by superdense glow discharge from hollow cold cathode rather than by arc discharge from the heated cathode. In this connection their durability approximately corresponds to that of GGT, but does not exceed this parameter for classical thyratrons.

There are four main factors limiting service life of thyratrons.

1. Intense erosion of the cathode resulting in destruction of its emission-active layer in thyratrons with the heated cathode, and in GGT - in increase of the sizes of apertures in the cathode (grid);

2. Decrease of electrical strength of the device;

3. Destruction of the anode by electronic bombardment caused by so-called starting losses;

4. Change of working pressure, due to gas absorption and poisoning of the generator of hydrogen by gases emitted from electrodes during service life.

The nanosecond modes of operation, in particular in Fitch generators, are especially heavy for switchboards. Thyratrons with heated cathode and existing PSS fail mainly due to the 1-st factor.

PSS developed in Russia [3,4,5] have essential differences in the design of cathode-trigger assembly which makes it possible for them to operate in the circuits with grounded cathode characteristic of classical thyratrons. This results in a drastic, by several orders of magnitude, increase of service life due to following reasons.

• The main emitting electrode is removed outside the high-voltage gap. In existing devices erosion at current densities near to apertures characteristic of PSS (10^4 A/cm^2) results in fast increase of interelectrode distance and failure of the device due to decrease of breakdown voltage, according to the Paschen law;

• The emitting surface of the main emitting electrode increases thus lowering the current load by distributing the current over greater surface.

Practically the failure of such devices in nanosecond mode of operation is caused by the 3-d factor - destruction of the anode rather than by the 1-st one. This process is especially accelerated (after 10^7-10^8 pulses) if the thyratron operates at reduced working gas pressure. One of the ways for resolving this problem is the use of a shared hollow anode design. In this case anode as well as cathode (grid) is made of two parts sharing functions of a high-voltage

electrode determining electrical strength and of a current-receiving electrode mainly subjected to erosion. The design of the pseudospark switch TP2-10k/50 with two high voltage gaps is shown in Fig.3. The device has the coaxial two-chamber cathode (C) with the auxiliary anode placed inside it (Aux A) and shared anode having two parts - potential (PA) and collector (A) ones.
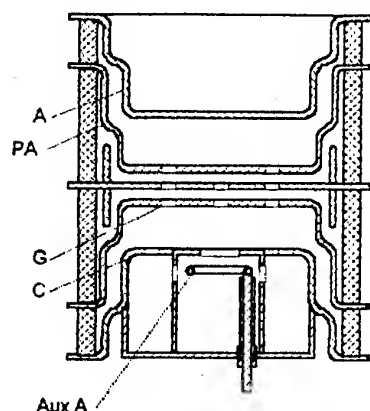

Fig.3. The TP2-10k/50 thyratron design

The auxiliary anode can serve as an electrode of the preparatory discharge, and by use of the device in the high-frequency circuits also as a blocking electrode. In the variant of operating circuit using PSS shown in Fig.1. the connection of the anode through the resistor R_2 provides reception of the basic current unfocused in the drift space inside the anode chamber by the surface of the collector (A). At the same time the potential anode subjected to the action of high voltage is not exposed to erosion thus providing increase of the device lifetime.

The device has high time stability ($t_{delay} < 100$ ns, jitter about 1 ns) and small time of discharge formation (5-10 ns), allowing to it to work in fast operation circuits.

Last results of testing allow to expect the durability of such PSS to be more than 5 thousand hours in modes of operation characteristic of nanosecond power sources of a streamer corona.

REFERENCES

[1].A.Z.Ponizovskii, A.A.Abramov, V.A.Goncharov, S.G.Gosteev, L.Z.Ponizovskii, V.A.Potapov, K.V.Suvorov, A.P.Shvedchikov, "Optimizing the Parameters of Electrophysical Equipment for Air Purification", Russian Electrical Engineering (Elektrotekhnika), 1993, Vol.64, № 3, pp.77-84, Allerton Press. Inc.

[2].L.Z.Ponizovsky, A.Z.Ponizovsky, V.A.Potapov, A.P.Shvedchikov, "High Voltage Electrical Apparatus for Removing Ecologically Noxious Substances from Gases", US Patent № 5,542,967, Aug. 6, 1996.

[3].V.D. Bochkov, V.M. Djagilev, Yu. D. Korolev, V.G. Ushich, I.A. Shemjakin, "Cold cathode Gas-Discharge device", Russian patent 2089003, Oct. 1995.

[4].O.B.Frants, Yu. D. Korolev, I.A. Shemyakin, V.D. Bochkov, C. Bickes, K. Frank, M. Schlaug, " Discharge initiation modes in a pseudospark switch with a trigger unite based on an auxiliary glow discharge ", Proc. 3rd Intern. Conference on Electrical Contacts, Arcs, Apparatus and Their Applications, Xi'an, (Jiaotong University), China, May 19-22 1997

[5].C. Bickes, V.D. Bochkov, K. Frank, O.B.Frants, V.G.Geiman, D.H.H.Hoffmann, Yu. D Korolev, U.Prucker, M. Schlaug, I.A. Shemyakin, J.Urban, "Development of sealed-off pseudospark switches for pulsed power", Proc. XIIth Intern. Conference on Gas Discharges and Their Applications, Greifswald, Germany, 1997. Vol.1. pp.218-221.

APPLICATION OF THE PULSED ELECTRON-BEAM TREATMENT OF ELECTRODE SURFACES FOR INCREASING THE ELECTRIC STRENGTH OF VACUUM GAPS

A.V. Batrakov, D.H. McDaniel[*], S.D. Korovin, G.E. Ozur, S.A. Popov,
D.I. Proskurovsky, and V.P. Rotshtein

Institute of High Current Electronics, RAS, Tomsk 634055, Russia
[*]*Sandia National Laboratories, Albuquerque, NM 87185-1194, USA*

Abstract. A method for preliminary treatment of electrodes with a low-energy, high-current electron beam of microsecond duration is proposed. This method, combined with subsequent conditioning of the vacuum gap by pulsed discharges, makes it possible to achieve high values of the breakdown electric field. Projected uses of the method for increasing the electric strength of high-power electrodynamic systems are described.

1. Introduction

A major concern in developing high-power electrodynamic systems is to provide high pulsed electric strength of the vacuum insulation. Thus, e.g., in systems intended for production of hot plasmas, a need arises to use constructional elements that locally violate the regime of magnetic self-insulation [1]. It is in these regions with enhanced electric fields that breakdown occurs, which leads to appreciable energy losses. Another example refers to the production of super-high-power pulsed microwaves. Thus, increasing the power and duration of microwave pulses generated with the help of high-power pulsed electron beams can be limited by the explosive electron emission and breakdown occurring in the electrodynamic structures [2].

It should be noted that the operating electric fields attained by now are far from the physical limit ($\leq 3 \times 10^7$ V/cm) determined by the tunnel emission of electrons from the cathode. The difference is related to the fact that the surface of an electrode is not perfectly smooth and clean; it contains local regions (micropoints or foreign inclusions) showing high emission activity.

A number of techniques for electrode preparation developed by now are focused on the elimination of emitting regions and on the enhancement of the electric strength of the vacuum insulation [3,4]. These techniques, as a rule, give no way for solving the problems concerned with the best smoothing of the surface and simultaneous efficient cleaning of the surface layers from impurities and contaminants and are rather labor-consuming and costly. This has stimulated us to develop a more perfect technique for preparation of electrode surfaces.

2. The essence of the method

In 1990 we proposed and then developed [5,6] a new method for enhancement of the electric strength of a vacuum insulation. It is based on preliminary treatment of the electrode surfaces with a low-energy, high-current electron beam (LEHCEB) of microsecond duration. In the process of surface treatment with an LEHCEB (1 – 3 µs, 20 – 30 kV, 5 – 15 J/cm^2), the surface layer of thickness up to several micrometers is molten and the surface is heated to a temperature at which noticeable evaporation takes place. As the beam pulse ends, directed superfast crystallization of the molten metal takes place which leads to a transfer of impurities to the surface and their evaporation and to the formation of more homogeneous structures. This effect is enhanced substantially upon treatment of the surface by a series of 10 to 50 pulses (cyclic treatment). In such treatment, a whole set of problems are solved: the surface is smoothed; foreign inclusions, impurities, and gases are removed from the surface layer; a material layer uniform in properties is formed; owing to the fine-grained structure, the residual impurities are dispersed over a very large area of the intergrain boundaries and their influence sharply decreases; the possibility for target production

of surface structures by mixing specially deposited layers with the base appears.

The paper presents the results of a study of the effect of LEHCEB treatment of electrodes on the pulsed electric strength of vacuum gaps with stainless-steel electrodes. Also discussed are the prospects for using this technology for finish treatment of parts of high-power electrodynamic systems.

3. Experimental

This experiment was carried out for stainless-steel electrodes in pure vacuum conditions with the use of rectangular voltage pulses of amplitude 250 kV and duration 30 – 100 ns [6]. The electric field at the electrode surface was calculated by solving numerically the Laplacian equation. When the vacuum gap spacing was varied from 1 to 10 mm, the effective area of the cathode (the area at which the electric field is over 90% of its maximum value) varied from 0.1 to 2 cm^2.

Figure 1 presents typical conditioning curves. Curves *I* and *II* have been obtained
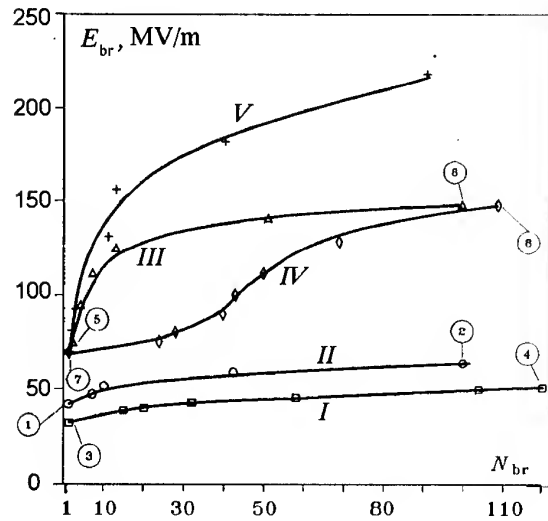
Fig. 1: Typical breakdown conditioning curves for vacuum gaps with electrochemically polished (*I*, *II*) and LEHCEB-irradiated (*III*, *IV*, *V*) electrodes. Pulse duration: *I – IV* – 100 ns, *V* – 40 ns.

for vacuum gaps with electrochemically polished electrodes and curves *III* and *IV*

for vacuum gaps with LEHCEB-irradiated electrodes. With that, curve *III* has been obtained for electrodes having been kept in air for two hours after irradiation and curve *IV* has been taken three days after irradiation.

Prior to the beginning of conditioning and after its completion, prebreakdown current-voltage characteristics were measured. The characteristics of prebreakdown currents were measured with the use of a high-sensitivity dc current amplifier and a low-jitter dc voltage source. These characteristics were processed using the Fowler-Nordheim equation for field emission. This processing makes it possible to find the parameters of the local efficient emission centers on the cathode surface that are responsible for the emission activity of the cathode, namely, the factor of electric field enhancement, β, and the emission area, S_e [3,4]. The results of processing of these characteristics are given in Table 1. An analysis of these data allows

Table 1: Results of processing of the Fowler-Nordheim plots. The plot numbers correspond to the respectively numbered points of the plots in Fig. 1.

No.	1	2	3	4
β	245	348	1060	340
$lg(S_e)$, (cm^2)	-10.2	-10.0	-10.3	-10.0
No.	5	6	7	9
β	180	53	160	53
$lg(S_e)$, (cm^2)	-10.2	-6.7	-10.0	-6.4

the conclusion that after LEHCEB irradiation, the first-breakdown electric field, E^1_{br}, had increased about twice. In the process of breakdown conditioning of the vacuum gaps with irradiated electrodes, the electric field E_{br} increased to a much greater degree than for the case with unirradiated electrodes. These data are in agreement with the results of processing of the respective Fowler-Nordheim plots. The LEHCEB treatment of electrodes followed by conditioning efficiently cleans the cathode surface and reduces the prebreakdown currents. Comparing curves *III* and *IV*, it can be stated that the keeping of irradiated electrodes in air has a detrimental effect only on the dynamics of the increase in electric strength in the pro-

cess of breakdown conditioning. With that, the first-breakdown electric field E^1_{br} remains on the same level. This effects of the keeping of irradiated electrodes in air can be accounted for by the fact that a thicker oxide layer is formed on the electrode surface in a longer time.

The experiments have demonstrated that the LEHCEB surface treatment of electrodes reduces the density of emission centers by a factor of five to ten. It follows that the smaller the electrode area, the more substantial effect of preliminary electron beam treatment on the electric strength of the vacuum insulation should be expected. This shows up in the dependence of E_{br} on S_{eff}. Figure 2 shows this dependence (plot 1) for vacuum gaps with electrodes pre-irradiated with an LEHCEB. Given for comparison are similar dependencies obtained in pure vacuum conditions after prolonged conditioning of the gaps by breakdowns. It can be seen that, despite the ``area effect" taking place, the high efficiency of the proposed method for surface treatment of electrodes is evident.

Fig. 3: Schematic diagram of a part of the wave lines - diode joint in the Saturn system. 1 - regions of the surface of the wave line cathode electrodes where the mode of magnetic self-insulation is realized and 2 - regions where breakdowns of vacuum gaps occur, leading to substantial energy losses.

Fig. 2: Dependence E_{br} on S_{eff} for vacuum gaps with stainless-steel electrodes (1) pre-irradiated with an LEHCEB and similar dependencies for gaps with stainless-steel (2) and copper (3) electrodes, obtained in pure vacuum conditions after prolonged breakdown conditioning of the gaps [7], given for comparison.

4. Electron-beam treatment of the Saturn system parts

Figure 3 shows schematically a fragment of the wave lines-to-diode joint of the Saturn system. During the passage of a high current, magnetic self-insulation takes place at the cathodes of the vacuum lines. These cathode regions are marked "1". However, the lines have construction holes (regions marked "2") where the mode of magnetic self-insulation is not realized. This results in breakdown of the vacuum gaps and in significant energy losses. Thus, the principal concern is to suppress the emission activity of the cathodes at the ends of these construction holes.

A conceptual solution of this problem is illustrated by Fig. 4. It is suggested to treat the hole ends with the use of a new version [8] of an available LEHCEB source [5,6]. An advantage of the new source over the former one is the absence of the generator of erosion (carbon) anode plasma and of the graphite cathode that contaminated the surface layer of the material under treatment. Used as anode plasma is the plasma generated by a Penning cell whose cathodes are a wire-array explosive-emission cathode (3) and the part under treatment (1) and whose anode is the cylinder (9) enclosing the electron beam aperture. The working material for the plasma is inert gas (argon) fed into the Penning cell. This, together with the oil-

free evacuation system to be used, will make the conditions for surface treatment much more pure. The magnetic field necessary for the operation of a Penning discharge is utilized simultaneously to form and to transport the beam. Preliminary testing of this LEHCEB source [8] has demonstrated that it can be used successfully for surface treatment of electrodes.
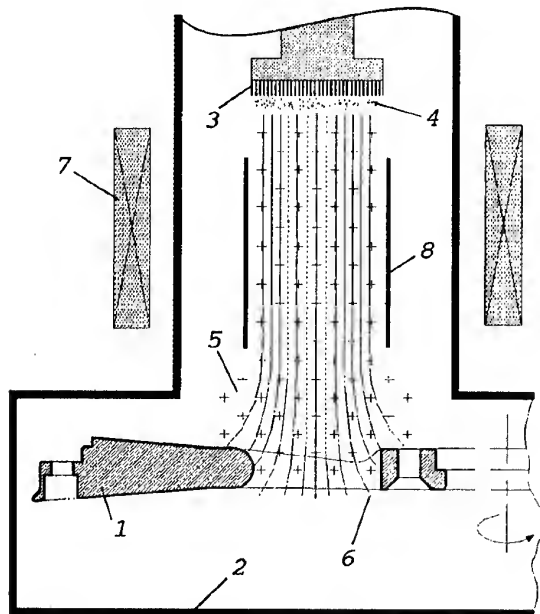
Fig. 4: Arrangement that will allow treatment of the ends of the wave-line cathode electrodes of the Saturn system. *1* - piece under treatment; *2* - vacuum chamber; *3* - multipoint wire cathode; *4* - cathode plasma; *5* - anode plasma of the Penning discharge in argon; *6* - trajectories of the beam electrons; *7* - solenoids creating a guide magnetic field, and *8* - anode of the Penning cell.

5. Electron-beam treatment of the parts of a high-power relativistic BWO

Figure 5 presents a schematic diagram of a one-mode relativistic BWO. To preclude explosive electron emission, it is intended to treat with an electron beam the slow-down system components at the surfaces of which the UHF electric fields may reach $10^5 - 10^6$ V/cm at a radiation pulsed power of $\sim 10^9$ W. Moreover, to improve the conditions for the formation of a high-current electron beam, at low magnetic fields included, electron-beam treatment of the

cathode holder will be performed. It is expected that the BWO will be operated with an electron beam of duration 40 ns and electron energy 1.5 MeV.
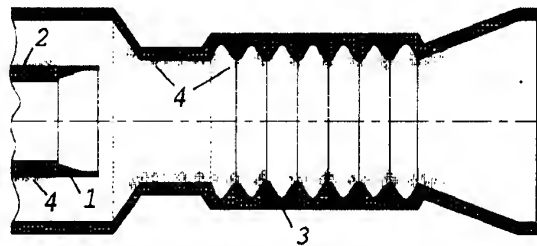
Fig. 5: Schematic diagram of a relativistic BWO. *1* - cathode, *2* - cathode holder, *3* - slow-down system components, and *4* - regions where breakdowns of vacuum gaps occur.

Acknowledgments

References

[1] W.A. Stygar et. al., Proc. 11th IEEE Int. Pulsed Power Conf., Baltimore, USA, 1997, pp. 591-596.

[2] G.A. Mesyats. Proc. of the Course and Workshop on High Power Microwave Generation and Applications, Varenna, Italy, 1991, pp. 345-363.

[3] R.V.Latham, *High Voltage Vacuum Insulation*, London: Academic Press, 1981.

[4] G.A. Mesyats and D.I. Proskurovsky, *Pulsed Electrical Discharge in Vacuum*, Berlin: Springer - Verlag, 1989.

[5] A.V. Batrakov, A.B. Markov, G.E. Ozur, D.I. Proskurovsky, and V.P. Rotstein, IEEE Trans. on Dielectrics and Electr. Insul., 1995, vol. 2, No. 2, pp. 237-242.

[6] A.V. Batrakov, D.S. Nazarov, G.E. Ozur, S.A. Popov, D.I. Proskurovsky, and V.P. Rotshtein, IEEE Trans. on Dielectrics and Electr. Insul., 1997, Vol. 4, pp. 857-862.

[7] M. Okawa et. al., IEEE Trans. on Electr. Insul., v. 23, No. 1, 1988, pp. 77-81.

[8] D.S. Nazarov, G.E. Ozur, and D.I. Proskurovsky, Proc. 11th IEEE Int. Pulsed Power Conf., Baltimore, USA, 1997, pp. 1335-1340.

TECHNOLOGICAL APPLICATIONS OF INDUSTRIAL
ELECTRON ACCELERATORS of ELV SERIES.

A.F.Vaisman, M.G.Golkovski, A.I.Korchagin, N.K.Kuksanov,

A.V.Lavruhin, S.E.Petrov, R.A.Salimov, S.N.Fadeev.

The State Research Centre of Russian Federation

The Budker Institute of Nuclear Physics

Ac. Lavrentyev av. 11, 630090 Novosibirsk, Russia.

From 1983 in our Institute is functioned a technological group for investigation of new application of powerful electron beam (EB) in atmosphere. For this purpose is used industrial accelerator ELV-6 and was designed set of installations and plants. The technologies have been carried out in co-operation with other firms and organisations. The energy range of electrons 1..1.5 MeV corresponds the penetration depth of electrons in the different materials 0.5...6 mm that is convenient for applications. EB extraction into atmosphere is done through the foil window with maximal power density of EB 80 W/cm² or through the system of diaphragms with holes about 1 mm diameter. In the last case EB specific power can achieved 1 MW/cm². Device for beam extraction through the diaphragms contains magnetic lenses and is used when high concentration of power in the beam is needed. After outputting end of the device it can be equipped by magnets for scanning in two mutually perpendicular directions. In this case, the beam is deflected in air.

Our Institute develops both low and high temperature EB technologies. One of the most promising low temperature applications of electron beam technology for environmental ones are flue gas purification and waste water treatment [1]. The delivered for this purpose ELV-type accelerators operate in follow countries: Russia - 5, Poland - 2, Japan - 2, Korea - 1. There were some full scale (several hundreds kW of accelerators power in each) projects in our country for waste water treatment (Voronezh, Pervomaisk, Petrodvorets, Kirishi) but all of them are not realised now. The most promoted project in Russia now is in Angarsk city (Angarskpetrosyntez). Here are delivered 2 accelerators (80

and 40 kW) with maximum energy up to 2.0 and 1.5 MeV correspondingly. Now this installation is under construction and will start at the end of this year.

The Electron Beam process is used for example to clean the flue gas from SO_2 and NO_x [2]. The estimation of the required dose for the efficient SO_2 (95%) and NO_x (80%) removal shows that 1 MW electron beam power would be sufficient for 100 MW generator of a powerful electric station. ELV-accelerators which are produced by BINP are widely used in investigation for this problems.

Waste water treatment is very actual too. The electron beam treatment of drinkable and waste water offers an universal efficient and ecologically acceptable possibility of water purification and disinfecting. The treatment of organic compounds (ethylene glycol and phenol), PVA, and dye by irradiation of an electron beam was studied in the BINP in cooperation with other scientific institutes. Besides that due to a vital problem of purification of waste water containing heavy metals ions the special investigation have been performed. Decrease in concentration of heavy metals in solution takes place practically in all the cases. The most high effect was observed for decreasing Cr(VI).

In Russia a line of surfactant waste water purification operates in Voronezh (Fig.1).
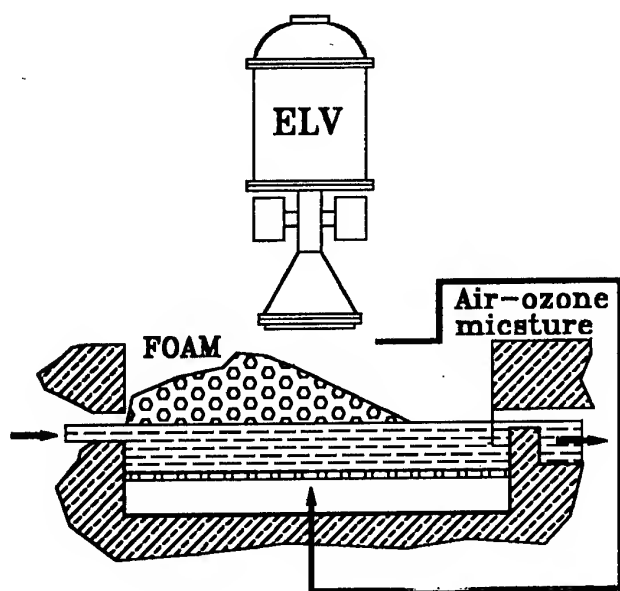
Fig.1. Irradiation of surfactant waste water.

The technological line is equipped with two ELV accelerators, 40 kW each. The line output is 10000 cubic meters per day. Here is combined electron beam and biological method of purification from biologically strong surface-active substance (nekal).

EB is used for gels production from water solutions as well [3]. The process consist of the irradiation of initial 3-5% water solution of polyethylenoxide. For irradiation as rule used conveyer with width of water layer 5 mm. Absorbed dose is 50-120 kGy. Aquagels widely used as medium for medicine preparation, cosmetics, as sealing medium for ultra high frequency investigation in medicine and so on.

Number of investigations were carry out on polymerisation of lacquer coat of different materials.

The technology of medicine sterilisation by using of X-ray converter of EB was developed [4]. In the converter used water-cooling tantalum target. One of the main advantage of this technology is that there is no heating of medicine during the sterilisation so active components of medicine did not destroyed. This converter make available high uniformity of volume absorbed radiation dose distribution. The uniformity of absorbed dose have the great important due of narrow range of dose when both medicine activity stay high enough and demand sterilise provided.

High temperature radiation technologies are attractive due to the heating source purity, volume heat inputting, practically unlimited EB specific power and combination of radiation and thermal action of it on material. In the field of this technologies promising results have been achieved in manufacturing wide class of ceramic materials by melting and sintering methods. This ceramics is complex oxide materials and intend as insulator, conductor, construction and heat insulation ceramics. They based on Ti, Cr, Zr compounds, ZrO_2 and so on. The abrasive materials of ZrO_2 - Al_2O_3 system were synthesised also. Special conveyer type plant with water cooling walls was designed for production of ceramic materials by melting of initial components. Quick cooling of molten faze in the plant is often used as drops into water. The similar equipment was used for production ammonia synthesis catalyst by melting of natural magnetite [5]. That technology was brought in the Institute of Nitrogen Industry in Moscow.

The whole set of investigations was made on EB manufacturing of various types of cements by sintering of initial components [6]. For this purpose was developed special stack type plant with water cooling walls and uniformly deposition of powder on the wide sintering zone under the beam. The top position of sintering zone stay stationary due to descending bottom of the sinters material.

The Investigation on manufacturing of pure ultra-dispersion nanometre range powders from gas phase was made. For this purpose a plant with accompany the beam in magnetic field for conserving of high specific power and preventing an overheating a wall of reactor is used.

The regimes of steel hardening was developed for various machinery parts [7]. Steel hardening is water-free process (self-hardening) and is produced without melting of surface (Fig.2).
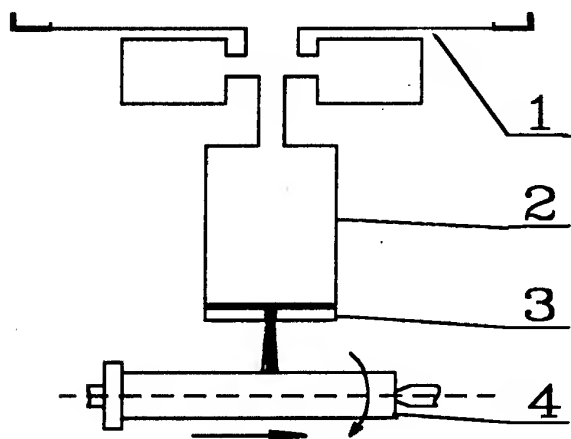
Fig.2. The scheme of hardening the roll detail: 1 - accelerator, 2- concentrated beam, 3 - EB declining device, 4 - treated detail.

The depth of hardened layer varies from 0.2 to 2 mm and the process productivity achieved 200 cm²/s. The whole diapason of carbon steels, cast irons, and a great number of alloy steels of martencite class is exposed to hardening [8]. The splitting of initial corn of austenite took place for number of alloy steels, that secures high complex of surface layer properties [9]. Hardening can be final operation, because of preserving the initial surface finish class as a result of high speed of process and because of a warpage usually accompanying hardening can be negligible. The computer simulation of temperature conditions during the hardening was made and shows the good agreement with experimental dates.

Concentrated EB can be effective for powder surfacing on the metal parts from different materials [10]. The hardening powder is applied on the surface of metal part and is melted by EB together with the surface layer of initial part. The EB penetration depth is about 1 mm and the depth of melted layer can be regulated from 1 to 5 mm. The essential

features of process are the following: high productivity up to 20 cm²/s or up to 40 kg of powder per hour and low specific expenses of energy during the process.

Besides above-mentioned our technology group get some promising results in production of fullerens by evaporation of carbon in helium atmosphere (fig. 3) and purification of metals by evaporation method and destruction by incineration of high-toxic and difficulty-distracted compounds (Fig. 4).

Fig. 4

Production of fullerens by evaporation
of carbon in helium atmosphere.

Fig.5.

Destraction by incineration of high-
toxical and difficulty - destructed
compounds.

REFERENCES.

1. R.A.Salimov,   N.K.Kuksanov,   B.M.Korabelnikov,   P.I.Nemytov,   S.E.Petrov,
    V.V.Prudnicov, S.N.Fadeev, M.E.Veis. Environmental Application of High Power
    Electron Accelerators of ELV Series. The Third International Conference on Advanced
    Oxidation technologies for Water and Air Remediation. Cincinnati, Ohio, USA.
    October, 1996.

2. А.Л. Файнштейн., Н.К. Куксанов., Б.М. Корабельников., И.Н. Мешков., В.В.
    Прудников. и др. Опытно-экспериментальная установка электронно-лучевой
    очистки дымовых газов от оксидов серы и азота производительностью до 100000
    м3/час на Славянской ГРЭС. 8-е совещание по применнению ускорителей
    заряженных частиц в народном хозяйстве. Тезисы докладов, Санкт-Петербург,
    1995, Москва, ЦНИИАТОМИНФОРМ, 1995 (Russian).

3. *R.I. Salganik, A.M. Gonchar, A.V. Troitsky*, Patent: (19)RU (11) 2026349 (13) C1 (51) 6C12N 11/4, Russia, res. from 24.07.89.

4. *R.I.Salganik, A.M. Gonchar. A.V. Troitsky*, Patent: application number PST/US 93/03542 USA from 20.04.92, publication number WO 93/20838.

5. В.В. Коваль, А.В. Кондратьев, Калистратова, А.И. Мищенко. Применение радиационно-термического метода в технологии приготовления катализатора синтеза амиака. Журнал Всесоюзного Химического Общества, т.36, 1991, №2, стр. 212-213.

6. *I.G. Abramson, A.F. Vaisman, R.M. Kapralova, N.G. Fadeyeva*, Development of Radiation- Thermal Technology of Cement Manufacturing. 9th International Congress of the Chemistry of Cement. New Delhi, India, 1992. Communication papers, vol. 11, p. 171-176.

7. *V.A.Neronov, V.P.Zinovieva, V.P.Larionov, N.P.Bolotina, T.V.Argunova, M.G. Golkovski, A.F.Vaisman and A.M.Matsievsky*. Examples of Electron Beam and Laser Radiation Application in the Processes of Surface Hardening, Coating Melting and Refractory Compound Sintering. High-temperature Dust-laden Jets in Plasma Technology. Proceedings of the International Workshop, 6-8 September 1988, Novosibirsk, USSR. Utrecht, The Netherlands: VSP, 1989, p. 367-379.

8. *Dongwoo Suh, Sunghak Lee, Yangmo Koo, Byungil Jean and M. Golkovski*. Microstructural Study of a High Speed Steel Roll Irradiated by Accelerated Electron beam. J. of the Korean Inst. of Met. & Mater. Vol. 33, No. 8, (1995).

9. *E.V. Konopleva, M.G. Golkovski, O.V. Abramov, A.F. Vaisman*. Modification of Surface Layer Structure of Low Carbon Alloy Steel by Electron beam in atmosphere. Metals, No 4, 1990, Moskow, USSR.

10. *И.М. Полетика, М.Д. Борисов, Г.В. Краев, В.Г. Дураков, А.Ф. Вайсман, М.Г. Голковский*. Особенности формирования структуры и свойств поверхностного слоя стали при электроннолучевом легировании. Металловедение и Термическая Обработка Металлов. ,1997, N 1, С. 17-23.

USING X-RAY RADIATION TO ERASE INFORMATION FROM A CMOS PROGRAMMABLE READ-ONLY MEMORY

Yu.A. Kotov, S.Yu. Sokovnin, V.A. Skotnikov

Institute of Electrophysics, Russian Academy of Sciences
34 Komsomolskaya St., Ekaterinburg, Russia, 620049

Abstract

We have investigated the possibility of the use of the X-rays to erase CMOS programmable digital ICs (PDIC). In the experiment were used microcontrollers IC Z86 (Zilog) and 87C196KR (Intel).

Repetitive pulsed electron accelerator URT-0,5 was used as a X-rays generator. It had produced 7,6 Gy per minute (50 pps) at 5cm from the anode on the axis, where the chips were placed. The maximum doze rate was 6,36 kGy/sec. The absorbed dose was measured using a LiF- detectors.

Tested chips with special program in its memory were irradiated until the information has been erased. A periodic control the chip memory during the irradiation was performed. It has been found experimentally that CMOS PROM become free after irradiation with a doze about 380 Gy, if it was wrapped up with 10-µm thick Al foil. The foil only connected chip pins. It is possible to make this erasing procedure with the same chip more than twice. Irradiation erased chips was successfully tested in the working device.

Introduction

In designing electronic devices, extensive use is currently made of programmable digital ICs (PDIC)), specifically microcontrollers. PDICs make it possible to develop new devices by programming their internal memory - a way that is simpler, faster and less expensive than the conventional method. The software and hardware sets available permit the functions of both the PDIC itself and of the electronic device being created to be computer simulated before writing the program in the internal memory of the PDIC. This has recently enabled manufacturers to abandon using costly ultraviolet-transparent windows above PDIC chips. Those windows allowed a repeated use of PDICs by erasing the internal memory with the ultraviolet light.

However, computer simulation cannot be complete and does not rule out possible errors; apart from this, it often becomes necessary to introduce some alterations when developing new devices. But reprogramming expensive enough PDICs today is not possible.

For this reason, we have made an attempt to erase the internal memory of PDICs by using the braking radiation of a pulsed high-current electron beam. It is known that radiation, including bresmsstrahlung radiation, enjoys uses in testing the quality of semiconductor ICs and in modifying their properties [1]. The effect of ionizing radiation on the materials and structure of semiconductors has been much studied [2]. However, we have not found in the literature the proposed use of radiation.

Experimental

The experiments were performed on Zilog series Z86 microcontrollers and Intel 87C196KR chips. The radiation source used was a 0.5 MeV URT-0.5 accelerator [5] operating in the braking radiation mode at a pulse repetition rate of 50 pps and producing at a distance of 0.5 cm from the target, where the chips were placed, the average power of the absorbed dose of 7.64 Gy/min, with the maximum pulsed power of the absorbed dose of 6.36 kGy/s.

Testing and writing was effected for:
- Zilog series Z86 microcontrollers, with the company's programmer ommulator;
- Intel 87C196KR microcontrollers, with the programmer "Sterkh-710", NPO "BOND", Berdsk.

Preliminarily certified PDICs with a written test (all units) or working program were irradiated until completely erased. During radiation, the PDICs underwent periodic testing. On exposure to radiation, the PDICs were tested for the possibility of writing both test programs and working programs with subsequent operation in a real device.

Our findings are as follows:
- A realiable erasure of information from all PDICs (ten pieces of each type were used) took place with an exposure time of 50 minutes (absorption dose of about 380 Gy).
- At half the dose, most of the information was erased, except for several bits.
- Erasure is possible only provided that the PDIC is wrapped in an aluminum foil so that all IC contacts are reliably interconnected.
- All PDICs were ready for reuse after the first erasure; 80 percent, after the second erasure; 50 percent of the chips withstood four cycles.

The test PDICs were made on the basis of the CMOS technology. The available data on the radiation resistance of Intel 8080A CPU microprocessors [2], made by the same technology, suggest that with an absorbed dose of 100 Gy, 9 out 10 microchips remain serviceable. These data may account for the fact that failures of PDICs increase in number as the number of irradiation cycles is increased.

Information in the PDIC memory element built on the CMOS technology is written by applying a certain negative critical voltage. Significantly, a charge arises at the silicon nitride - silicon dioxide interface and a high logical level "1" is set up, whereas when a positive critical voltage is applied a low logical level "0" is set up [4]. Thus, erasing information from the PDIC calls for increasing the magnitude of the charge to the logical "0". The charge dispersal mechanism may be both superficial and spatial. With the X-radiation intensity exceeding 10^2 Gy/s, as in our case, the injected current density becomes commensurate with the bulk current density, 10^{-7} A/cm2 [2]. Support for the decisive role of leakage currents comes from the need to electrically connect PDIC leadouts, as the memory element circuit built around CMOS transistors [4] presupposes the absence of connections between writing, reading, address, supply, and ground buses. And that complicates the path for the current to be dispersed without the interconnection of the busbars.

However, our intensities do not suffice (10^6 Gy/s threshold) for the development of a photovoltaic effect, which resides in the voltage drop varying across the under-the-gate dielectric and, therefore, in a threshold voltage shift [2].

To test the mechanism of erasure, we exposed 87C196LC PDICs PDICs to irradiation with 60Co isotopes, with a gamma radiation intensity of about 102 Gy/min.

With an absorbed dose of 500 Gy, information was reliably erased from the PDICs. This confirms the determining role of leakage currents in the radiation-induced erasure of information from PDICs.

Conclusion

Thus the possibility of using photon radiation to erase infromation from the internal memory of PDICs may be considered as an established fact. The URT-0.5 accelerator permits up to 30 Z86 or 15 87C196KR to be irradiated concurrently. The energy consumption for radiation-induced erasure does not exceed 3 kW h. Considering that operating the accelerator for one hour costs about $15, the estimated cost of radiation-induced erasure will amount to about $0.5 for Z86 PDICs and to $1 for 87C196KR. This value is a factor of 10 to 30 lower than the cost of PDICs and may be largely reduced by rational use of radiation, for example by stacking PDIC in several layers.

References

[1]. Radiation methods in solid-state electronics, V.S. Vavilov, B.M. Gorin, N.S. Danilin et al., Radio i Svyaz', 1990, 184 p. (in Russian)

[2]. V.S. Pershenkov, V.D. Popov, and A.V. Shalnov, Surface radiation effects in IC elements, M.: Energoatomizdat, 1988, 256 p. (in Russian)

[3].Y.A. Kotov and S. Y. Sokovnin, URT-0.5 Accelerator for Commercial Applications, to be published in these Conference Proceedings.

[4]. S.V. Yakubovsky ... et al., Analog and Digital Integrated Circuits. Reference Manual. M.: Radio i Svyaz', 1984, 432 p. (in Russian)

FOIL ACCELERATION BY HIGH DENSITY ABLATION PLASMA BY INTENSE PULSED ION BEAM

Nob. Harada*, H. Shinkai, W. Jiang and K. Yatsui

Laboratory of Beam Technology, *Dept. of Electrical Engineering
Nagaoka University of Technology,
1603-1 Kamitomioka, Nagaoka 940-2188, Japan

ABSTRACT

We studied on foil acceleration driven by a reaction of high density ablation plasma produced by irradiation of an intense pulsed light ion beam (LIB) on a solid foil target. Two kinds of diodes were used; 1) magnetically insulated diode (MID) with energy density on a target is 300J/cm^2 and 2) two-dimensional focused spherically shaped plasma focus diode (SPFD) with 4kJ/cm^2. We measured foil velocity up to ~3.3km/s for the case of SPFD and evaluated ablation plasma pressure was ~5GPa, which were in good agreement with simple numerical analysis. Significant increase in hardness of the aluminum target was also observed. We were much interested in further studies on acceleration process, comparison of precise numerical simulation, improvement of material properties of a foil target and interaction between a highly accelerated flyer and other target materials.

INTRODUCTION

Recently studies on interaction between thin foil target and intense pulsed light ion beam (LIB), where the equation of state, dynamics of the beam interaction with condensed target, and properties of solids and plasma at high-energy densities have been investigated.[1,2] Precise velocity measurements of foil target have also reported.[3] We, at the Laboratory of Beam Technology of Nagaoka University of Technology, have started to study on an acceleration process of a solid foil target by ablation plasma produced by irradiation of an LIB.

The main objectives of the present paper are to introduce experimental configuration, measurements of a foil target velocity, and evaluation of ablation plasma pressure.

PRINCIPLE AND EXPERIMENTAL ARRANGEMENT

Basic principle of the present foil acceleration is shown in Fig. 1. Intense pulsed LIB is produced by MID or SPFD, whose schematic cross sectional views are shown in Fig. 2 and Fig. 3. It is irradiated on a solid foil target and its energy is deposited within the depth so-called the range. Energy of LIB is so intense that a part of a solid target turns into ablation plasma instantaneously. While high
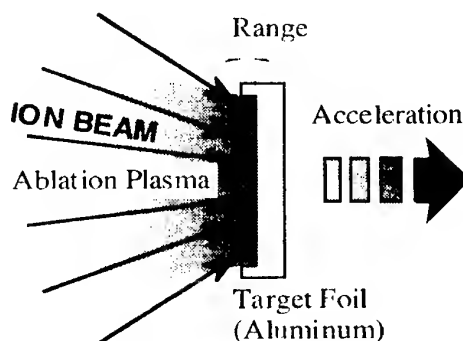
Fig.1 Basic principle of foil acceleration by high density ablation plasma.
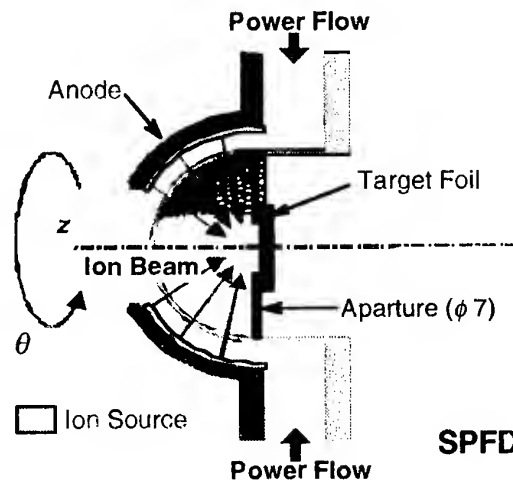
Fig.2 Schematic cross sectional view of the Two-dimensional focused spherically shaped plasma focus diode (SPFD).
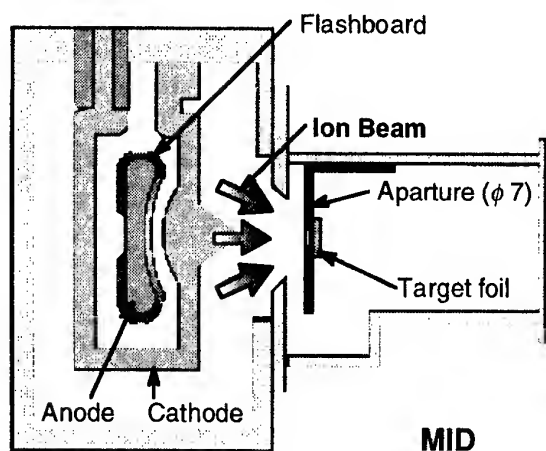
Fig.3 Schematic cross sectional view of the magnetically insulated diode (MID).

Ions, energy	H^+, 1.2MeV
Ion Source	Nitrocellulose Alkyd Resin
Composition	$(C_{12}H_{15}O_{19})n$ $(C_{11}H_{10}O_6)n$
Composition Ratio	C:H:O:N=33:34:32:4
Beam Energy Density	SPFD: $4kJ/cm^2$ MID: $100J/cm^2$
Foil Configuration	10mmx10mm
Thickness (mass)	$50\mu m$ (13.5mg), $100\mu m$ (27mg)
Foil material , mass	Al, Cu

pressure and high temperature ablation plasma then expands backward, the residual solid target is accelerated forward due to a reaction of the ablation plasma. Experimental conditions are summarized in Table 1. Species of LIB is mainly proton. Energy densities are $4kJ/cm^2$ for SPFD and $100J/cm^2$ for MID. Materials of a solid target foil are aluminum and copper with thickness of $50\mu m$ and $100\mu m$.

VELOCITY MEASUREMENT

Outline of velocity measurement and expected oscilloscope trace are shown in Fig.4. The aluminum target foil accelerated by ablation plasma reaches to the detector electrodes and make the circuit short.

Oscilloscope trace must rise after some delay of t' (s) which is required for the target foil to fly the distance of d (m), as shown in Fig.4. Therefore, averaged target foil velocity $\bar{v}$ over t' can be given by the following relation.

$$\bar{v} = d/t' \tag{1}$$

Typical measured trace for the case of SPFD ion source is shown in Fig.5. At t=0, LIB reaches to the target foil. Although noticeable noise is superposed on measured signal, delay time can be determined with sufficient accuracy. In this case shown in Fig.5, obtained delay time and distance d are $0.6\mu s$ and 2×10^{-3}m, respectively. Measured average velocity is 3.3km/s. Conversion

Fig.4 Outline of velocity measurement and expected oscilloscope trace.

Fig.5 Typical measured trace for the case of d=2mm using SPFD.
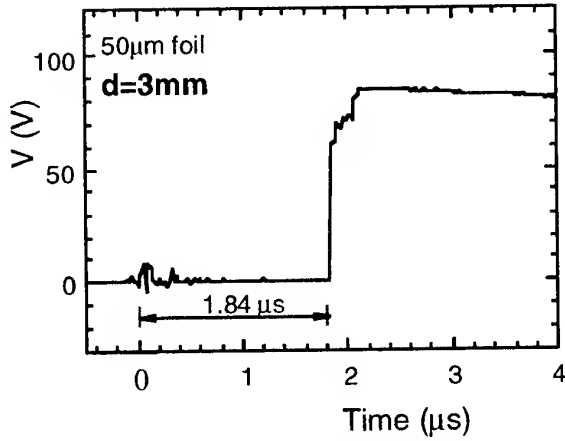
Fig.6 Typical measured trace for the case of d=3mm using MID.
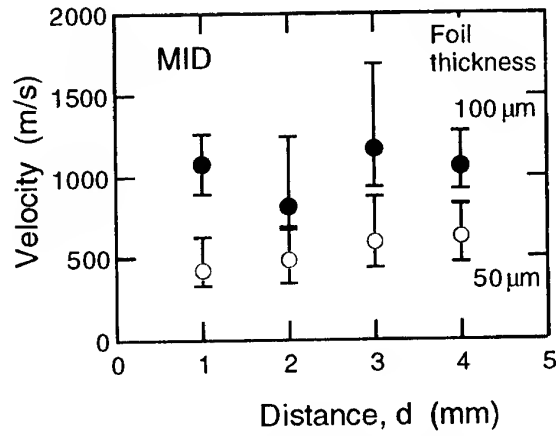
Fig.7 Measured velocity for various distance using MID.

efficiency, which is defined by kinetic energy of foil flyer divided by deposited energy of LIB on the target foil, can be estimated as ~ 4%. Typical result using MID is shown in Fig.6. It can be seen that accuracy of t' (s) measurement can be much improved due to minor modification of measurement system. Measured velocity in this case is 1.63km/s. Measured velocities for the case of MID are summarized in Fig.7. We have to note that uncertainty of measured velocity is not due to error in measurement but to a bit poor reproducibility of experiments. Velocities reached are 1.6km/s for the foil thickness of 50μm and 0.8km/s for 100μm. Conversion efficiencies are 9% for 100μm and 17% for 50μm. Further it must be noted that foil flyer may be accelerated within the distance of 1mm. This may be quite reasonable because the duration time of pulsed ion beam is about 60ns.

PRESSURE EVALUATION

In order to evaluate the pressure of ablation plasma, we assume that the foil is accelerated up to measured velocity with constant acceleration over the delay time t' as is shown in Fig.8. Then acceleration of the foil can be written as:

$$\alpha = 2 \cdot \bar{v}/t'^2 \qquad (2)$$

The pressure of ablation plasma, P can be evaluated by

$$P = \alpha \cdot m/A \qquad (3)$$

where m and A denote mass of the foil flyer and cross sectional area. Let us evaluate ablation plasma pressure for the case of maximum foil velocity has obtained with

Fig.8 Assumption of constant acceleration motion for evaluation of ablation plasma pressure.

SPFD. In this case, measured delay time t' and distance d are 0.33μs and 1×10^{-3}m, respectively. Then assumed constant acceleration α is calculated as 1.8×10^{10}m/s^2 and ablation plasma pressure is evaluated to be about 5GPa using mass of the foil target of 27mg and cross sectional area of 1×10^{-4}m^2. Of course, we have to note that these values are averaged ones over the period of t' sec., and the actual acceleration must be much higher. So the actual

maximum ablation plasma pressure is expected to be quite higher, too. We are preparing time-resolved optical velocity measurement for detailed studies on acceleration process and for precise information of ablation plasma pressure.

FOIL OBSERVATION

We observe accelerated foil target after an experiment. Typical photographs of them before and after a shot is shown in Fig.8. From the photograph of after the shot, central part is almost removed due to the collision with electrodes for velocity measurement. We found significant increase in hardness of the aluminum target. Studies on improvement of surface hardness by an irradiation of high power pulsed ion beam have been reported.[4,5] We are now preparing to measure surface hardness of irradiated foil target. We have strong interest in improvement of material properties and interaction between a highly accelerated flyer and other target materials.

Aluminum target foil

(a) before shot   (b) after shot
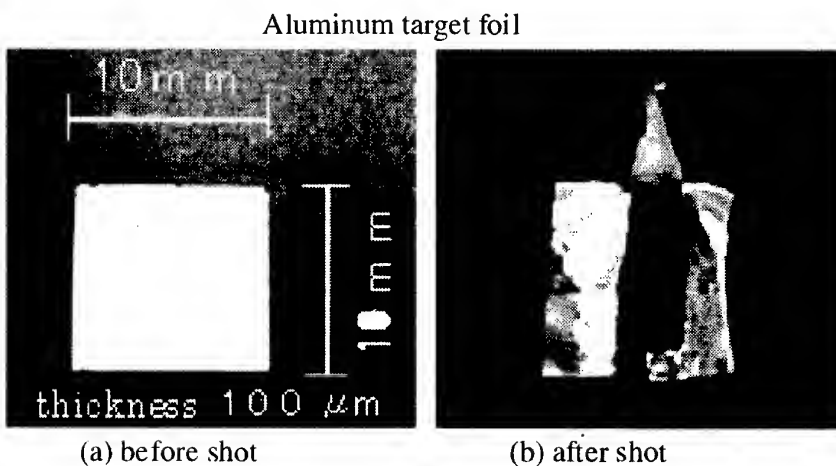
Fig.8 Photographs of aluminum target foil before and after shot.

CONCLUDING REMARKS

The first experiments of foil acceleration by a reaction of high density ablation plasma produced by irradiation of an intense pulsed LIB on a solid foil target. were introduced. Two kinds of diodes were used; (1) magnetically insulated diode (MID) with energy density on a target is 100J/cm^2 and (2) spherical plasma focus diode (SPFD) with ~4kJ/cm^2.

Measurements of a foil velocity and evaluation of ablation plasma pressure were carried out. Measured foil velocity was up to ~3.3km/s for the case of SPFD with higher energy deposition and evaluated ablation pressure was ~5GPa, which were in good agreement with simple numerical consideration. This value was evaluated under the assumption of constant acceleration. Actual maximum ablation plasma pressure, therefore, was expected to be quite higher.

Significant increase in hardness of the aluminum target was also observed. We would like to proceed to next steps of further studies on acceleration process, comparison of precise numerical simulation, improvement of material properties of a target and interaction between a highly accelerated flyer and other target materials.

REFERENCES

[1] K. Baumung, et al., Laser and Particle Beams, Vol.14, No.2, pp.181-209, 1996.

[2] B. Goel and O.Yu. Vorobiev, Laser and Particle Beams, Vol.14, No.4, pp.637-653, 1996.

[3] V.E. Fortov, et al., IEEE Trans. on Plasma Science, Vol.25, No.4, pp.729-732, 1997.

[4] A.D. Pogrebnjak, et al., Phys. Lett. A, Vol.141, No.3,4, pp.204-206, 1989.

[5] A.D. Pogrebnjak, Phys. Stat. Sol. (a), Vol.117, No.17, pp.17-51, 1990.

NANOSIZE POWDER PRODUCTION BY PULSED WIRE DISCHARGE

W. Jiang and K. Yatsui
Laboratory of Beam Technology, Nagaoka University of Technology
Nagaoka, Niigata 940-2188, Japan

Abstract   Pulsed wire discharge has been successfully applied to nanosize powder production.   In the demonstration experiments, the discharge was carried out with the peak current of ~ 10 kA, the pulse length of ~ 20 μs, and the pulse energy of ~ 80 J.   Nanosize powders of metals, metal oxides, and metal nitrides have been synthesized by pulsed discharge of metal wires in argon, oxygen or nitrogen.   The typical powder production rate was ~ 5 mg/pulse.   The results of surface-area measurement have given the average powder sizes in the range of 20 ~ 70 nm, depending on the material of the powders.

1. INTRODUCTION

Nanosize powders are solid particles with typical size in the range of 1 to 100 nm. Materials of this size have very large specific surface area.   As a result, nanosize powders have many special physical and chemical properties that can not be obtained with the bulk material.   For this reason, nanosize powders are of many interesting applications in material processing for electronics, magnetics, and optics.   They are also applicable as catalysts and pigments.

Fine particles with dimensions less than 1 μm are difficult to obtain by mechanical method. Instead, they are usually produced in the process of uniform solidification of a supersaturated vapor in an ambient gas.   There are two different kinds of process that may lead to the supersaturated vapor necessary for powder production, the chemical process and the physical process.   In the chemical process, the expected vapor is produced by appropriate chemical reactions between gases.   In the physical process, on the other hand, the vapor is produced by heating (evaporation).   The physical process may get rid of the unexpected products of the chemical reactions, resulting in higher purity of the produced powders, although the chemical process is advantageous in having higher powder production rate.

High-power pulsed lasers or pulsed particle beams can be used to evaporate almost any kind of matter.   Experiments have proved that nanosize powders can be produced by using a pulsed laser or a pulsed light-ion beam [1,2].   In this paper, we report a new technique which applies pulsed wire discharge to material evaporation, as a physical process, for nanosize powder production.   The basic principle is illustrated in Fig. 1.   A pulsed current is driven through a solid wire which is located in an ambient gas (Fig. 1a).   The current deposits electrical energy in the wire due to its finite resistance.   This deposited energy melts, evaporates and ionizes the wire material resulting in a plasma that expands into the ambient gas (Fig. 1b).   This high temperature plasma gradually cools due to its interaction with the gas, giving rise to a high temperature vapor of the wire material that condense uniformly in the ambient gas (Fig. 1c).   In addition, as in the other physical processes, the evaporated metal vapor produced by pulsed wire discharge may react with the ambient gas resulting in ceramic powders.

We have carried out demonstration experiment to show the practicability of powder production by pulsed wire discharge.   The experimental results have shown that nanosize

(a)	(b)	(c)
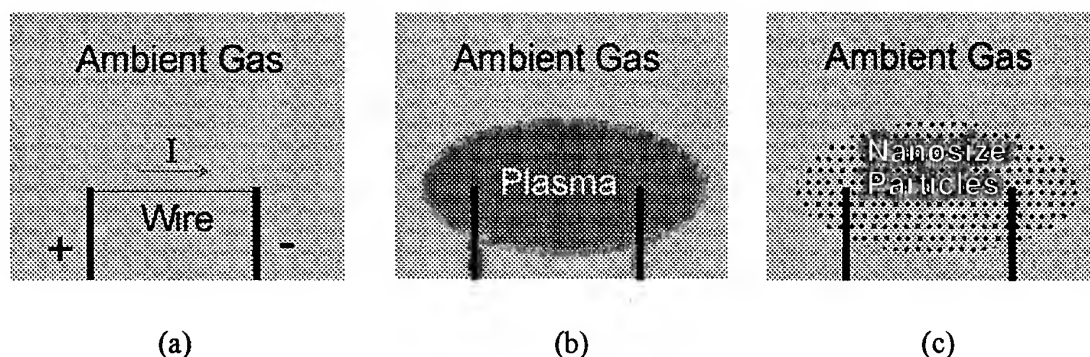
Fig. 1   Principle of nanosize-particle production by pulsed wire discharge.

powders of metals as well as many kinds of oxide and nitride can be synthesized by pulsed discharge of metal wires in the ambient gas of argon, oxygen or nitrogen [3].

Table I   Typical parameters of the experiment

Circuit	Capacitance	10 μF
	Charging voltage	4 kV
	Half cycle	~ 12 μs
Wire	Material	Al, Ti, Fe, Ni, Cu, Zr, Mo, Pd, Sn, Ta, Pb
	Diameter	0.2 mm
	Length	25 mm
Ambient Gas	Species	Ar, O$_2$, N$_2$
	Pressure	400 Torr

2. EXPERIMENTAL SETUP

Figure 2 schematically shows the arrangement of the experiment.   The wire is located in a chamber filled with the ambient gas.   The discharge is driven by a simple circuit consisting of a capacitor and a gap switch.   After discharges, the powders floating in the ambient gas are collected by pumping the gas through a filter.

Typical experimental condition is summarized in Table I.
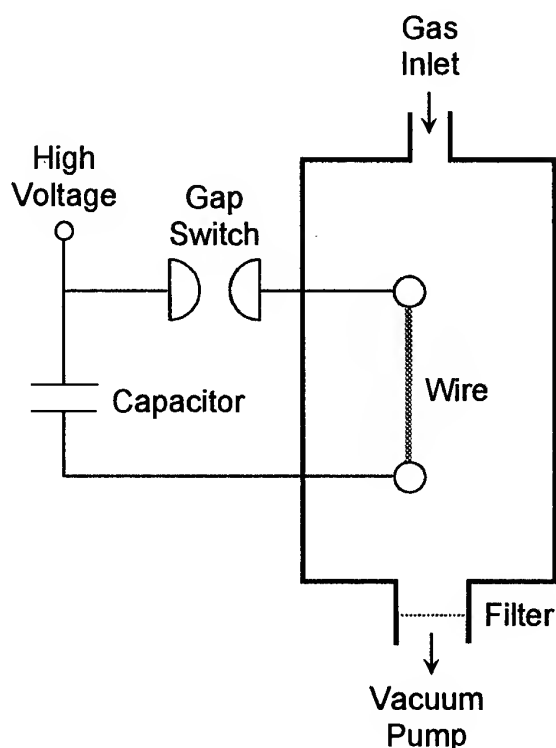
Fig. 2   Experimental setup.
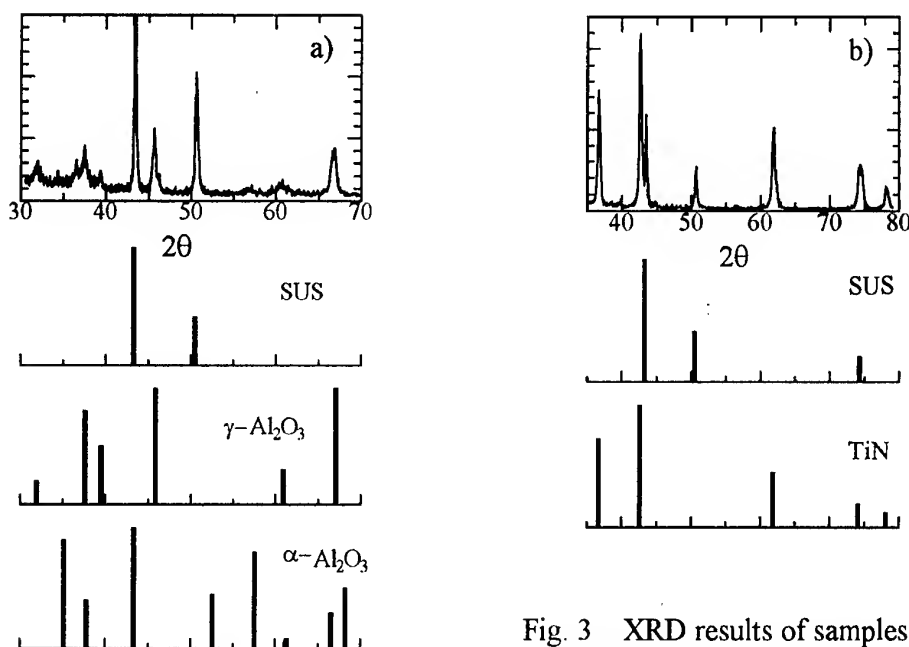
Fig. 3 XRD results of samples obtained with a) Al wire in O_2 and b) Ti wire in N_2.

3. POWDER CHARACTERIZATION

The powders obtained on the filter are analyzed by using X-ray diffraction (XRD) for evaluation of crystalline structure and surface-area measurement for estimation of average particle size.

Table II   Nanosize powders obtained by pulsed wire discharge.

Wire	Ambient Gas (400 Torr)	Nanosize Particles	Specific Surface Area (m^2/g)	Average Particle Size (nm)
Ti	O_2	TiO_2	40.1	35.3
Fe	O_2	Fe_2O_3	26.9	42.9
Cu	O_2	$CuO+Cu_2O$	16.1	62.1
Zr	O_2	ZrO_2	30.4	35.6
Mo	O_2	MoO_2+MoO_3	26.0	49.1
Ti	N_2	TiN	52.0	21.2
Fe	N_2	Fe	15.7	48.7
Mo	N_2	Mo	15.9	41.9
Pd	N_2	Pd	30.0	16.4
Al	Ar	Al	28.9	77.0
Cu	Ar	Cu	10.8	62.2

Figure 3 shows the XRD results of the samples obtained with a) aluminum wires in oxygen and b) titanium wires in nitrogen. The solid lines of Fig. 3 show the measured XRD characteristics of the samples that are compared with the JCPDS powder diffraction data. The SUS peaks are caused by the stainless steel holder under the samples. The crystalline structures of the two samples are clearly same with that of γ-alumina and titanium nitride, respectively.

By changing the material of the wire and the species of the ambient gas, many kinds of powders have been produced that are identified by XRD analysis. Some of the results are shown in Table II. The average particle size was calculated from the specific surface-area for each sample. In the calculation, it was assumed that all particles are spherical.

In order to see the dependence of the average particle size on the gas pressure, powder production experiments with titanium wires were carried out under different nitrogen pressures. The results of surface area measurement and the calculated average particle size are shown in Fig. 4. All samples obtained are identified as pure TiN by the XRD analysis. It is seen that the average particle size varies from 13 to 27 nm as the pressure is increased from 100 to 600 Torr.
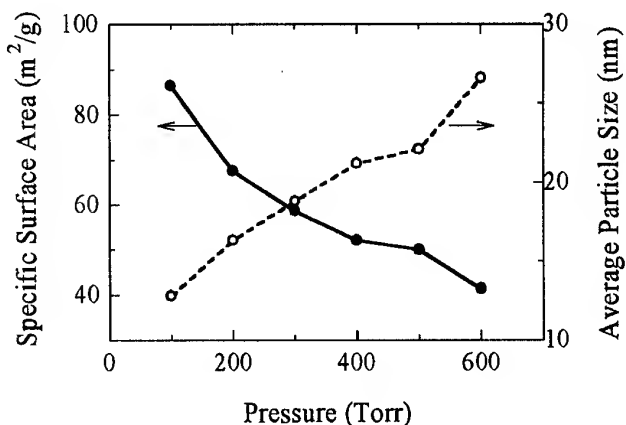
Fig. 4   Dependence of specific surface area and average particle size on N_2 pressure.

4. CONCLUSIONS

We have carried out demonstration experiments of nanosize powder synthesis by pulsed wire discharge and have obtained the following conclusions.

1) Powders with average particle size on the order of 10 nm of metals, metal oxides, and metal nitrides are successfully synthesized. All these powders are obtained by evaporating metal wires in Ar , O_2, or N_2.

2) The average particle size of TiN powders varies from 13 to 27 nm when the pressure of the nitrogen gas is increased from 100 to 600 Torr, indicating the possibility of average powder size controll by the pressure of the ambient gas.

In our experiment, the powder production rate was about 5 mg/pulse with the pulse energy of 80 J. Therefore, if this is done with a repetition rate of 10 Hz, we can obtain powder production rate of 180 g/h with electricity consumption of 800 W. This result clearly offers new commercial application of the pulsed wire discharge to nanosize powder production because it is more efficient and more economic than other physical processes.

REFERENCES

[1] W. Jiang, M. Hirai, K. Yatsui, in this proceedings.
[2] K. Yatsui, C. Grigoriu, H. Kubo, K. Masugata, and Y. Shimotori, Appl. Phys. Lett., 67, 1214 (1995).
[3] W. Jiang, K. Yatsui, Proc. 11th IEEE Int'l Pulsed Power Conf., I, 214 (1997).

SYNTHESIS OF AlN NANOSIZE POWDERS BY PULSED LASER ABLATION

Weihua Jiang, M. Hirai, and K. Yatsui

Laboratory of Beam Technology, Nagaoka University of Technology
Nagaoka, Niigata 940-2188, Japan

Abstract   We report production of AlN nanosize powders by using pulsed laser ablation.   A Nd:YAG laser (1.06 μm, 320 mJ, 7 ns, 10 Hz) was used to ablate the Al or AlN target in nitrogen gas of 10 ~ 500 Torr.   The characteristics of the powders were analyzed by transmission electron microscope, x-ray diffraction, transmission electron diffraction and specific surface area measurement.

1. INTRODUCTION

Nanosize powders are particles with diameter in the range of 1 ~ 100 nm.   The nanosize powders of many kinds of material have specific magnetic, optical, chemistry and sintering properties.   These properties have made the nanosize powders very interesting materials for applications in magnetic media, catalysts, gas sensors, and other industrial fields.

Nanosize powders can be produced by using chemical method.   With the chemical method, the nanosize powders can be produced in large amount but with poor purity.   It has been realized that the purity of nanosize powders produced by the chemical method can hardly be improved due to its reliance on chemical reactions.   In recent years, physical methods, such as pulsed laser ablation [1] and pulsed ion beam ablation [2], are developed for production of high purity nanosize powders.

Figure 1 shows the principle of nanosize powder production by using the pulsed laser ablation.   When the high power laser beam is irradiation on the target surface, a small part of the target material close to the surface is heated to high temperature due to very fast energy deposition of the laser beam.   It is vaporized, ionized and expands into the surrounding space.   If the surrounding space is filled with gas, the ablated material cools and reacts with the gas molecules.   The uniform solidification of the material results in nanosize powders.

In this paper, we report our recent results of AlN nanosize powder production by using pulsed laser ablation. Either aluminum metal or aluminum nitride ceramics was used as the target.   The obtained powders were analyzed by using x-ray diffraction (XRD) and transmission electron diffraction (TED) for crystalline characterization, as well as transmission electronic microscopy (TEM) and specific surface area
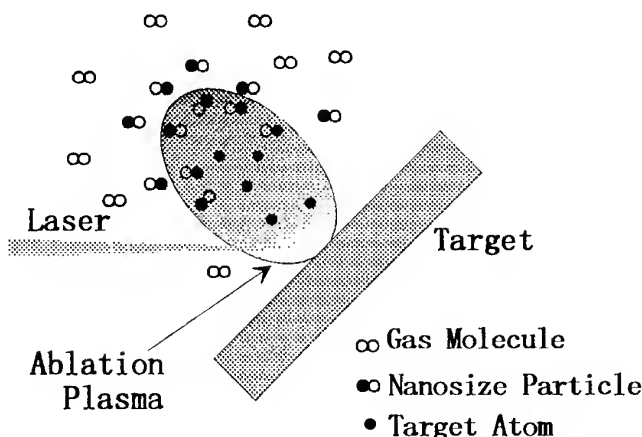
Fig. 1   Principle of nanosize powder production by pulsed laser ablation.
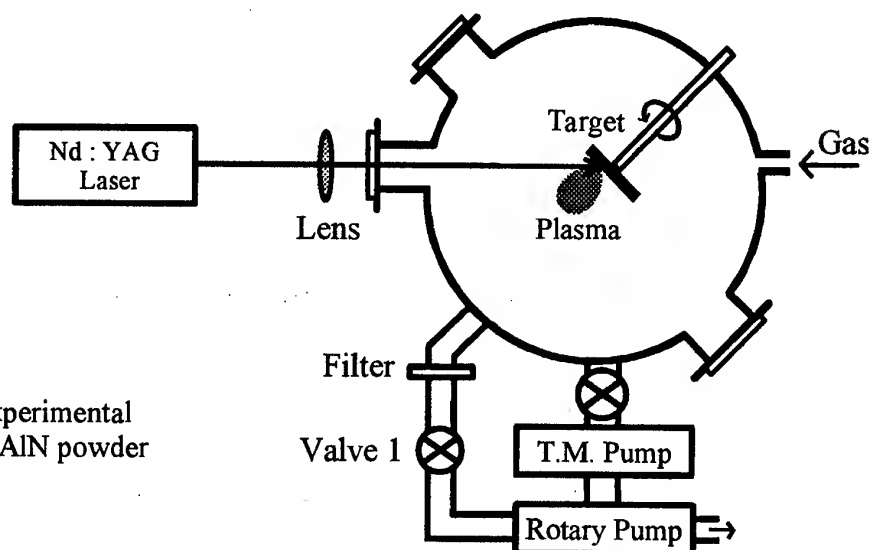
Fig. 2 Experimental setup for AlN powder synthesis.

measurement for particle size.

2. EXPERIMENTAL SETUP

Figure 2 shows the experimental setup. A Q-switched Nd:YAG laser (1.06 μm, 7 ns, 10 Hz) was used to ablate the target with an angle of 45 degree to the target surface. Nitrogen was used as the ambient gas. The pressure was varied from 10 to 500 Torr. Throughout the experiments, the ambient was flowing with the speed of 1Nl/min and the target was being rotated to avoid concentrated damage. At the outlet of the gas flow, there
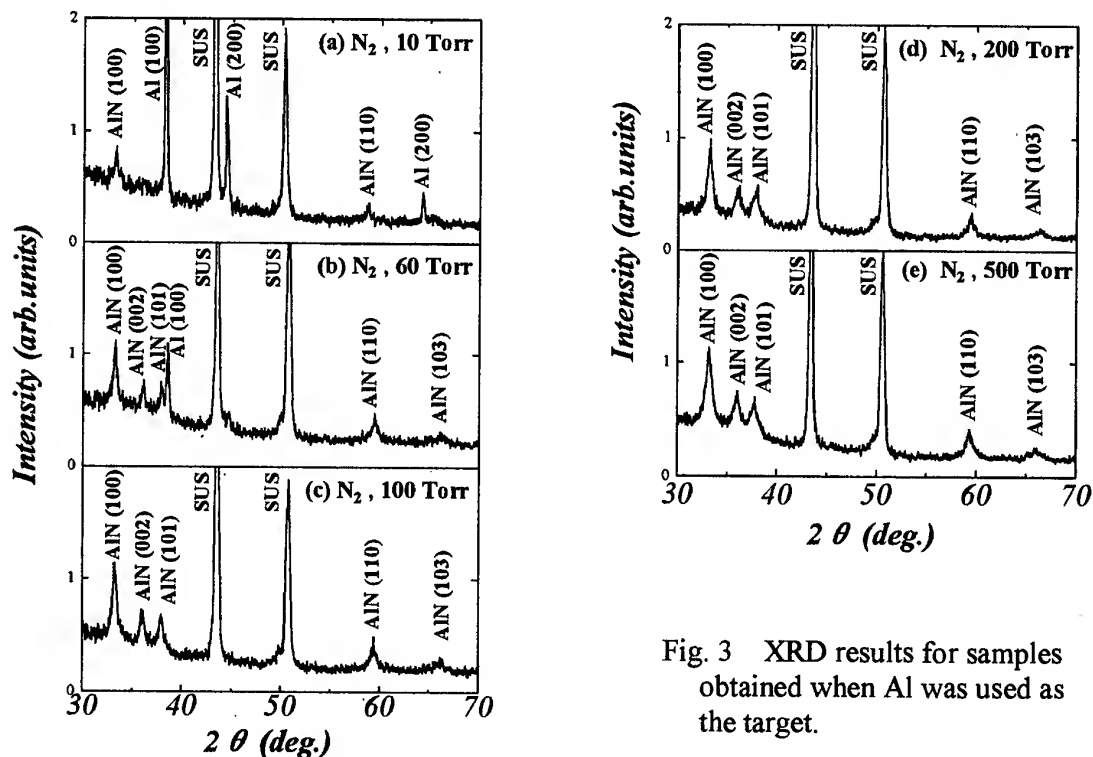
Fig. 3 XRD results for samples obtained when Al was used as the target.

is a nylon filter where the produced powders were collected.

3. EXPERIMENTAL RESULTS

3.1 Al Target

Figure 3 shows the results of XRD for powder samples when aluminum was used as the target. In Fig. 3, the deflection peaks of SUS (stainless steel) are caused by the steel mesh that was used as the supporter of the particles in XRD analysis. We see from Fig. 3 that, with nitrogen pressure lower than 60 Torr, the produced particles are Al or mixture of Al and AlN. When the pressure is higher than 100 Torr, however, the produced particles are pure AlN. Therefore, 100 Torr seems to be the minimum pressure, under our experimental condition, for the ablated aluminum material to be completely nitrified.

Figure 4 shows the TEM photograph of the particles obtained with nitrogen pressure of 200 Torr. It is seen from Fig. 4 that the particles are around 10 nm in diameter. Some particles are seen to be hexagon which is consistent with the hexagonal structure of the AlN crystal. Figure 5 shows the TED pattern of the particles shown in Fig. 4. The diffraction rings of AlN are clearly identified.

Figure 6 shows the particle size distribution obtained from Fig. 4. All particles are smaller than 25 nm and the average particle size is ~ 11 nm.

3.2 AlN Target

The results of Fig. 3 have shown that, when the nitrogen pressure is increased, the produced particles changes from Al, to mixture of Al and AlN, and then pure AlN. However, in order to see the dependence of the particle size on the pressure of the ambient gas, we need to compare the samples of the same material. For this reason, we used aluminum nitride ceramics as the target.
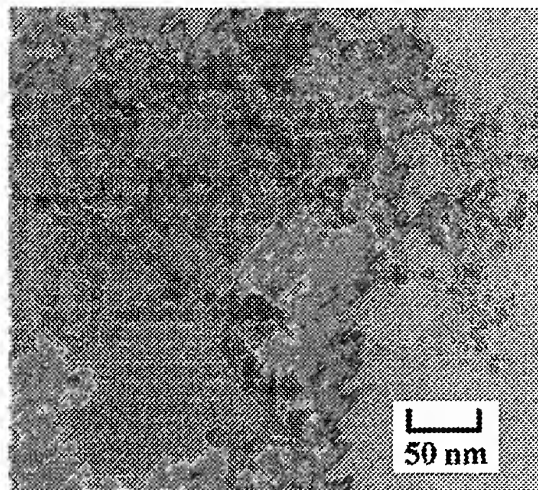
Fig. 4　TEM photograph of AlN powders obtained by using Al target.
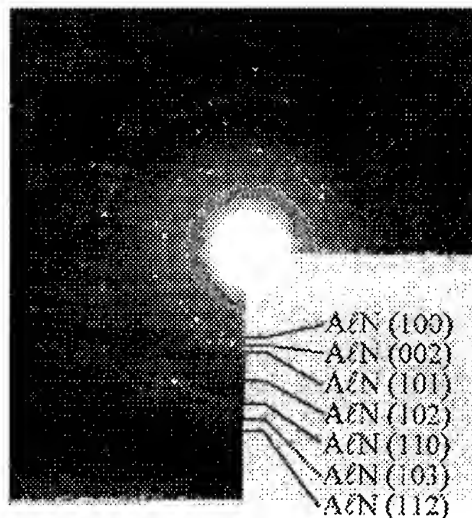
Fig. 5　TED patterns of the sample shown in Fig. 4.

Except the difference in target material, all experimental parameters are the same as that described above. The XRD results for the samples obtained in nitrogen pressure range of 10 ~ 500 Torr have shown that all are pure AlN.

For each sample, the specific surface area was measured by using BET (Brunauer-Emmett-Teller) method. The average particle size was estimated from the specific surface area and the results are shown in Fig. 7. It is seen from Fig. 7 that, when the nitrogen pressure is increased, the average particle size of AlN increase as the pressure is lower than ~ 100 Torr and decreases as the pressure is high than 100 Torr.

4. CONCLUSIONS

The nanosize powders of AlN were produced by using pulsed laser ablation with either Al or AlN target. From the analytical results by XRD, TEM, TED and surface area measurement, we have obtained the following conclusions.

1) When Al was used as the target, the obtained particles are either pure Al, mixture of Al and AlN, or pure AlN, depending on the pressure of nitrogen used as ambient gas. Under our experimental condition, the minimum pressure for obtaining pure AlN particles is ~ 100 Torr. The average particle size obtained at 200 Torr is ~ 11 nm.

2) When AlN was used as the target, all samples obtained with different N_2 pressures are AlN. The average particle size increases with the pressure as the it is lower than 100 Torr and decreases as the pressure is higher than 100 Torr.

REFERENCE

[1] A. Matsunawa and S. Katayama : Transaction of JWRI, **19**, 137 (1990).
[2] K. Yatsui, C. Grigoriu, H. Kubo, K. Masugata and Y. Shimotori : Appl. Phys. Lett., **67**, 1214 (1995).
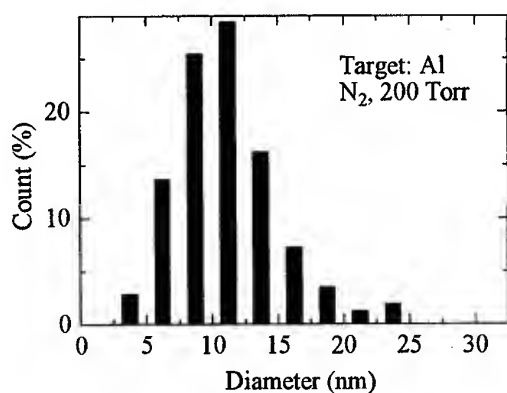
Fig. 6 Particle size distribution obtained from Fig. 4.
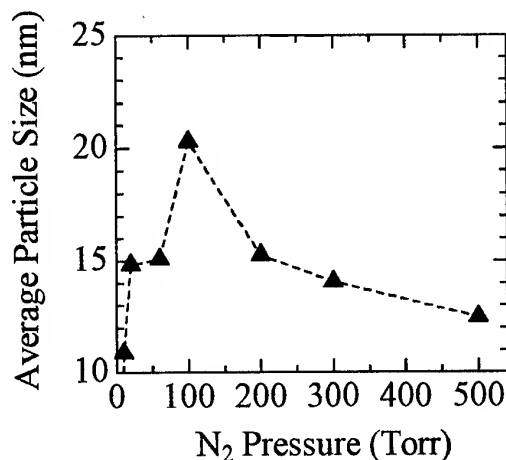
Fig. 7 Dependence of the average particle size on the N_2 pressure when AlN was used as the target.

BEAMS STATISTICS

Meir Markovits

Rafael, Dept.24, Haifa, Israel

Following Jiri Ullschmied's 1996 example, some BEAMS conferences statistics are presented below, with details regarding BEAMS'98.

The 12th International Conference on High Power Particle Beams was held in Haifa, Israel from June 7 to June 12, 1998. Previous BEAMS Conferences were held in Albuquerque, USA (1975), Ithaca ,USA (1977), Novosibirsk, Russia (1979), Palaiseau, France (1981), San Francisco, USA (1983), Kobe, Japan (1986), Karlsruhe, Germany (1988), Novosibirsk, Russia (1990), Washington, DC, USA (1992), San Diego, USA (1994) and Prague, Czech Republic (1996). The Haifa, Israel, BEAMS'98 Conference will be followed by BEAMS'2000 in Nagaoka, Japan.

BEAMS'98 was attended by 273 participants from 19 countries:

Russia – 80, Israel – 64, USA – 58, Japan – 17, France – 9, Czech Republic – 8, Germany – 8, China – 7, Ukraine – 6, Poland – 3, Belgium – 2, Singapore – 2, United Kingdom – 2, Yugoslavia – 2, Brazil – 1, Chile – 1, Holland – 1, Italy – 1, and Romania – 1. Compared to the attendance list of the previous six BEAMS conferences (based on Jiri Ullschmied's 1996 table), our 1998 "total less host country" number of participants was surpassed only at BEAMS'96, (see table below).

BEAMS STATISTICS (1986 - 1998)

	Japan	Germany	Russia + (other FSU)	USA	France	Israel	Others	Total	Total less host country
1986 .Kobe	155	5	17	77	8	5	14	281	126
1988 Karlsruhe	19	75	16	99	21	8	21	259	184
1990 Novosibirsk	14	10	149	52	6	0	13	244	95
1992 Washington,DC	15	10	64 (+1)	286	13	12	22	423	137
1994 San Diego	19	13	56 (+2)	173	10	12	16	295	122
1996 Prague	17	25	105 (+8)	60	19	12	63 (38 from Cz. Rep.)	309	271
1998 Haifa	17	8	80 (+6)	58	9	62	31	271	209
2000 Nagaoka									

505 paper abstracts were submitted to BEAMS'98 program committee, out of which 472 papers were accepted for presentation, and about 460 were included in the abstracts book. At the conference, 347 papers were presented at poster sessions, and 56 papers were orally presented. To our disappointment, only 240 papers in final full format were submitted for inclusion in the Proceedings. Following numerous appeals to the presenting authors and several extensions of the submission deadline, we have decided not to include in the proceedings, those abstracts for which presenting authors did not submit full papers, even after extensions of the deadline.

BEAMS'98

12th INTERNATIONAL CONFERENCE
ON HIGH-POWER PARTICLE BEAMS
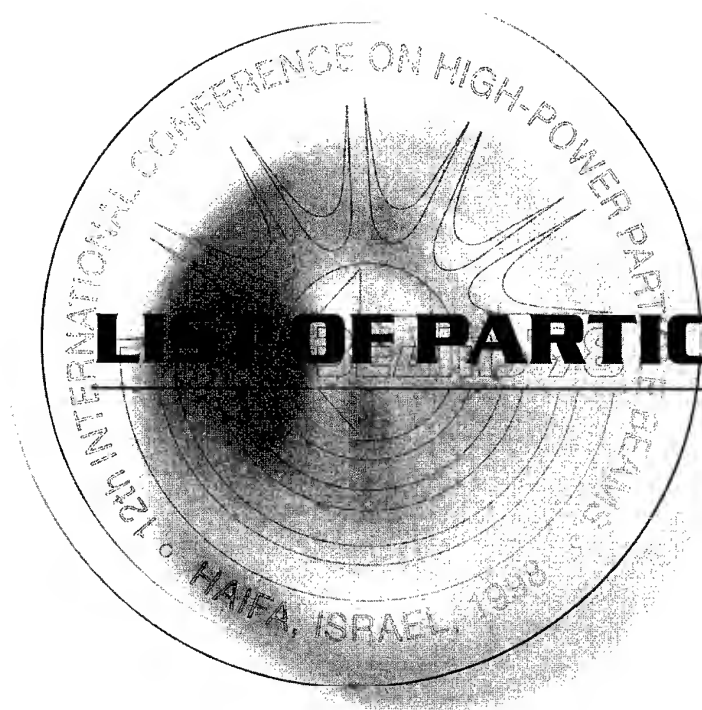
LIST OF PARTICIPANTS

Vol. II

LIST OF PARTICIPANTS (by ABC)

AGEE Forrest J. , Dr.

Air Force Office of Scientific Research, 110 Duncan Ave., Suite C232, Bolling AFB DC 20332-8050
USA
Phone: (505) 846 2824 **Fax:** (505) 846 1278
Email Address: ageef@plk.af.mil

ANDO Ritoku, Prof.

Kanazawa University, Faculty of Science, Kanazawa Ishikawa 920-1192
JAPAN
Phone: 76 264 5670 **Fax:** 76 264 5739
Email Address: ando@plasma.s.kanazawa-u.ac.jp

ARAD Ron, Mr.

Department of Particle Physics, Weizmann Institute of Science, P.O. Box 26, Rehovot 76100,
ISRAEL
Phone: 8 934 2211 **Fax:** 8 934 3491
Email Address: fnmaron@weizmann.weizmann.ac.il

ARANCHUK Leonid, Dr.

Ecole Polytechnique, 91128 PARIS
FRANCE

ARJONA Melany, Ms.

Institute for Plasma Research, University of Maryland, College Park MD 20742
USA
Phone: 301 405 4972 **Fax:** 301 314 9437
Email Address: mrarjona@eng.umd.edu

ARZHANNIKOV Andrei V., Prof.

Budker Institute of Nuclear Physics, SD RAS, Lavrentyev Avenue 11, Novosibirsk 630090,
RUSSIA
Phone: 7 (3832) 359 912 **Fax:** 73832 352 163
Email Address: a.v.arzhannikov@inp.nsk.su

ATCHISON Walter L., Mr.

Los Alamos National Laboratory, Plasma Physics, MS-B259, P.O. Box 6331, Los Alamos NM 87545
USA
Phone: 505-665-9384 **Fax:** 505-665-7725
Email Address: wla@lanl.gov

BAILEY James E., Dr.

Diagnostics and Target Experiment, Sandia National Lab., P.O. Box 5800, Albuquerque NM 87185-1186
USA
Phone: (505) 845-7203 **Fax:** (505) 284-4135
Email Address: jebaile@sandia.gov

BAKSHT Rina B., Dr.

High Current Electronics Institute, SD RAS, 4, Akademicheski Avenue, Tomsk 634055,
RUSSIA
Phone: (3822) 259 133 **Fax:** (3822) 258 677
Email Address: baksht@hcei.tomsk.su

BARAK Gad, Dr.

RAFAEL, P.O. Box 2250, Haifa 31021
ISRAEL

BARNEA Gideon, Dr.

RAFAEL, P.O. Box 2250, Haifa 31021
ISRAEL

BARONOVA Elena O., Ms.

RRC Kurchatov Institute, Nuclear Fusion Institute, Kurchatov Sq. 1, Moscow 123182
RUSSIA
Fax: 095--9430073
Email Address: baronova@qq.nfi.kiae.su

BASHAN Avraham, Mr.

RAFAEL, P.O. Box 2250, Haifa 31021
ISRAEL

BAUER Walter H., Dr.

INR, Forschungszentrum Karlsruhe, Postfach 3640, D-76021 Karlsruhe 1,
GERMANY
Phone: 49 (7247) 82 3869 **Fax:** 49 (7247) 82 2823
Email Address: bauer@inr.kfk.de

BEN-AMAR Andrei, Dr.

Lasers Department, NRC-Negev, P.O. Box 9001, Omer 84965
ISRAEL

BEN-KISH Amit, Mr.

Phys. Dep., Technion Haifa 32000
ISRAEL

BENFORD James N., Dr.

Principal, Microwave Sciences, Inc., 1041 Los Arabis Lane, Lafayette CA 94549
USA
Phone: 925 283 8454 **Fax:** 925 283 8487
Email Address: jbenford@earthlink.net

BLAUGRUND Abraham E., Prof.

Dept. of Nuclear Physics, Weizmann Institute of Science, P.O. Box 26, Rehovot 76100
ISRAEL
Phone: 8 943458 **Fax:** 8 934 4182
Email Address: fnbla@weizmann.weizmann.ac.il

BLIOKH Yury, Dr.

Institute of Plasma Electronics, national Sc. Center "KhPhTI", 1 Akademicheskaja, Kharkov 310108
UKRAINE
Phone: 572 404 474 **Fax:** 0572 353 564
Email Address: invest@folio.kharkov.ua

BLUHM Hansjoachim, Dr.

INR, Forschungszentrum Karlsruhe, JNR, Postfach 3640, D-76021 Karlsruhe 1,
GERMANY
Phone: 72 47 82 24 38 **Fax:** 72 47 82 28 23
Email Address: bluhm@inr.fzk.de

BOBROV Emanuel S., Dr.

BWX Technologies, NNFD, P.O. Box 785, Lynchburg VA 24505
USA
Email Address: emanuel.bobrov@mcdermott.com

LIST OF PARTICIPANTS [by ABC] - cont'd.

BOGATU I.N., Dr.

Weizman Institute of Science , Dept. of Particle Physics,
Plasma Laboratory, Rehovot 76100
ISRAEL
Phone: 8 934 2211 **Fax:** 8 934 4106
Email Address: bogatu@plasma-gate.weizman.ac.il

BONDARENKO Gennadi G., Prof.

Moscow State Inst. of Electronics and Mathematics,
Bolshoi Vuzovskiy Per. 3/12, Moscow 109028
RUSSIA
Phone: 095 135 4436 **Fax:** 095 916 2807
Email Address: root@onti.miem.msk.su

BOTTON Moti, Dr.

RAFAEL, P.O. Box 2250, Haifa 31021
ISRAEL
Phone: 04 879 5191 **Fax:** 04 879 5315
Email Address: motib@rafael.co.il

BRATMAN Vladimir L., Prof.

Institute of Applied Physics, RAS, 46, Ulyanov St.,
Nizhnyi Novgorod 603600,
RUSSIA
Phone: 8312 384 552 **Fax:** 8312 362 061
Email Address: bratman@appl.sci-nnov.ru

BRUNSTEIN Michael, Dr.

Applied Materials, Atidim Industrial Park, Building 2,
PO Box 58152, Tel Aviv
ISRAEL

BUGAEV Sergei P., Prof.

High Current Electronics Instititute , 4 Akademichesky
Avenue, Tomsk 634055
RUSSIA
Phone: 3822 258 544 **Fax:** 3822 259 410
Email Address: bugaev@hcei.tomsk.su

BURDOVITSIN Viktor V.A., Dr.

40, Lenin Street, Tomsk University of Control Systems,
Tomsk 634050
RUSSIA
Phone: 3822414712
Email Address: fizik@fet.tasur.edu.ru

BURTSEV Vladimir A., Prof.

Efremov Institute of Electrophysical Apparatus,
Metallostroy, Sovetskii-1, St. Petersburg 189631,
RUSSIA
Phone: 7 (812) 265 5610 **Fax:** 7 (812) 463 9812
Email Address: burtsev@niiefa.spb.su

CARMEL Yuval, Dr.

University of Maryland, Institute for Plasma Research,
College Park MD 20742
USA
Phone: 301 405 4976 **Fax:** 301 314 9437
Email Address: carmel@plasma.umd.edu

CHARNIA Alexander L., Dr.

All-Russian Electrotechnical Institute (VEI),
Krasnokazarmennaya 12, Moscow 111250
RUSSIA
Phone: 7-095-3619228, (095) 361 9453
Fax: 7-095-3625114, (095) 362 5617 or 5114
Email Address: kozlov@dir.vei.msk.su

CHERETZ Dr, Prof.

Weizmann Institute of Science, Faculty of Physics,
P.O. Box 26, Rehovot 76100
ISRAEL

CHERKASSKY Valery V.S., Dr.

Novosibirsk State University, Novosibirsk 630090
RUSSIA
Phone: 383 2 397805 **Fax:** 383 2 397101
Email Address: cherk@phys.nsu.ru

CHERNYAVSKY Igor .A., Dr.

High Current Electronics Institute RAS, 4
Akademichesky Ave, Tomsk 634055
RUSSIA
Email Address: koshelev@lhfe.hcei.tomsk.su

CHOI Peter, D

Ecole Polytechnique, Laboratoire PMI, F-91128
Palaiseau,
FRANCE
Phone: 33 (1) 6933 3416 **Fax:** 33 (1) 6933 3023
Email Address: pchoi@lpmi.polytechnique.fr

CHORNY Valentin Vasyuljevych, Dr.

PO Box 2096, 310108 Kharkov Ukraine, Ukraine
310108, Ukraine 310108
RUSSIA
Phone: 380572 35-27-22
Email Address:
valentin.v.chorny@pht.univer.kharkov.ua

CHUVATIN Alexander, Dr

Laboratoire de Physique, Des Milieux Ionises, Ecole
Polytechnique, F-91128 Palaiseau,
FRANCE
Phone: (1) 69 33 36 60 **Fax:** (1) 69 33 30 23
Email Address: chuvatin@lpmi.polytechnique.fr

COLEMAN Philip, Dr.

Maxwell Technologies, Inc., 888 Balboa Avenue,
SanDiego California 92123
USA
Phone: 619 496 4139 **Fax:** 619 576 7659
Email Address: coleman@maxwell.com

COOK Daniel L., Dr.

Director, Sandia National Laboratories, Org. 9500, P.O.
Box 5800, MS 1190, Albuquerque, NM 87185-1190,
USA
Phone: (505) 845 7447 **Fax:** (505) 845 7464
Email Address: dlcook@sandia.gov

LIST OF PARTICIPANTS (by ABC) - contd.

COOPERSTEIN Gerald, Dr.

Code 6770, Plasma Physics Division, Naval Research Laboratory, 4555 Overlook Ave., S.W., Washington, DC 20375-5346, Washington DC
USA
Phone: 202 767 2290 **Fax:** 202 767 0436
Email Address: cooperstein@ppd.nrl.navy.mil

DAN'KO Sergei A., Dr.

Russian Res. Centre "Kurchatov Institute", Kurchatov Sq., 1, Moscow 123182,
RUSSIA
Phone: 7 (095) 196 9672 **Fax:** 7 (095) 196 9874

DAVIS Harold A., Dr.

Los Alamos National Laboratory, Physics Division, MS E526, Los Alamos NM 87545
USA
Phone: 505 667 8373 **Fax:** 505 665 8296
Email Address: davis@lanl.gov

DEMIDOV Vasilii A., Mr.

Russian Federal Nuclear Center - VNIIEF, Pr. Mira, 37, Sarov 607190
RUSSIA
Phone: 831-30-4-55-84 **Fax:** 831-30-4-53-84
Email Address: selemir@ntc1.vniief.ru

DEMIN Anatoly, Dr.

Russian Federal Nuclear Center (VNIIEF), Pr. Mira 37, Sarov (Arzamas-16), Nizhnyi Novgorod Reg. 607 190,
RUSSIA
Phone: 7 (83130) 457 38 **Fax:** 7 (83130) 545 65
Email Address: vcher_1763@rfnc.nnov.su

DEUTSCH Alon, Mr.

RAFAEL, P.O. Box 2250, Haifa 31021
ISRAEL

DIAMANT Stela, Dr.

Applied Material, Atidim Ind. Park, Bldg. 2
ISRAEL
Email Address: stela_diamant@amat.com

DIDENKO Andrei N., Prof.

32a Leninsky, Prosp., Moscow 117334
RUSSIA
Phone: 095 938 52 49 **Fax:** 095 938 18 44
Email Address: didenko@ras.phys.msu.su

DING Bonan, Prof.

Southwest Institute of Fluid Physics, POBox 523, Chengdu Sichuan 610003
CHINA

DING Wu, Prof.

Institute of Applied Physics & Computational Math., No. 6 Huayuan Road, Hai-Dian Dist, Beijing 100088
CHINA
Phone: 10 6201 4411-3136 **Fax:** 10 6201 0108
Email Address: jsls@mail.japcm.ac.cn

DIYANKOV Oleg V., Dr.

Russian Federal Nuclear Center - VNIITF, P.O. Box 245, Snezhinsk, Chelyabinsk Reg. 456 770,
RUSSIA
Phone: 7 (35172) 3 2993 **Fax:** 7 (35172) 3 0979
Email Address: ovd@dep26.ch70.chel.su

DOLGACHEV George I., Dr.

Applied Physics Division, Russian Res. Centre "Kurchatov Institute", Kurchatov Sq., 1, Moscow 123182,
RUSSIA
Phone: 7 (095) 196 9185 **Fax:** 7 (095) 196 9874
Email Address: potap@potap.msk.su

DUBINOV Alexander E., Mr.

Russian Federal Nuclear Center - VNIIEF, Pr. Mira, 37, Sarov 607190
RUSSIA
Phone: 831-30-45144 **Fax:** 831-30-4-53-84
Email Address: dubinov@ntc.vniief.ru

DUMITRESCU Carmen N., Dr.

Ecole Polytechnique, LPMI, 91128 Palaiseau
FRANCE

DUNAEVSKY Alexander, Mr.

Technion-Israel Institute of Technology, Dept Physics, Haifa 32000
ISRAEL
Phone: 04 829 3666 **Fax:** 04 822 6641
Email Address: fnkrasik@physics.technion.ac.il

EFIMOV Sergey, Dr.

Dept. of Electrical Engineering-Physic. Eclectronics, Faculty of Engineering, FEL - group, Tel Aviv University, Ramat Aviv 69978
ISRAEL
Fax: 36423508
Email Address: efimov@post.tau.ac.il

EICHENBAUM Arie, Mr.

Electronic Eng. Phys., Tel Aviv University, Ramat Aviv, Tel Aviv 69978
ISRAEL
Phone: 3 640 8246 / 677 3724 **Fax:** 3 642 3508
Email Address: eichenbm@eng.tau.ac.il

ENGELKO Vladimir I., Dr.

D.V. Efremov Institute of Electrophysical Apparatus, 1 Sovetski Prospect, St. Petersburg Metallostroy 189631
RUSSIA
Phone: 812 462 7845 **Fax:** 812 314 3360
Email Address: engelko@sirius.niiefa.spb.su

ESHHAR Shmuel , Dr.

Department 23, RAFAEL, P.O. Box 2250, Haifa 31021,
ISRAEL
Phone: 972-4-795100 **Fax:** 972-4-795315

Laboratoire de Physique des Milieux Ionises, Ecole
Polytechnique, B.P. 27, F-91128 Palaiseau,
FRANCE
Phone: 33 (1) 6933 3259 **Fax:** 33 (1) 6933 3023
Email Address: etlicher@lpmi.polytechnique.fr

LBNL MS 47-112, 1 Cyclotron Road, Berkeley CA
94720
USA
Phone: 510 486 7325 **Fax:** 510 486-5392
Email Address: s_eylon@lbl.gov

Los Alamos National Laboratory, P.O. Box 1663, MS
B259, Los Alamos NM 87545
USA
Phone: (505) 667 2806 **Fax:** (505) 665 7725
Email Address: rjf@lanl.gov

531 Rim Road, Los Alamos NM 87544
USA

Ecole Polytechnique, 91128 Palaiseau
FRANCE
Phone: 56 (2) 686 4365 **Fax:** 56 (2) 686 4365
Email Address: mfavre@lascar.puc.cl

High Energy Density Research Center, Institute for
High Temperatures, RAS (IVTAN), Izhorskaya 13/19,
Moscow 127412,
RUSSIA
Phone: 7 (095) 485 7988
Email Address: karat@tarak.msk.su

Dept. of Physics, Technion Israel Institute of Technology,
Haifa 32000,
ISRAEL
Phone: 04-8293869 **Fax:** 972-4-221514

Code 6790, Naval Research Laboratory, 4555 Overlook
Ave., S.W., Washington, DC 20375-5000,
USA
Phone: (202) 767 3708 **Fax:** (202) 767 3950

Director of Research & Development, Prudence
Software Ltd, PO Box 45125, Jerusalem 91450
ISRAEL
Phone: 2 586 0769 **Fax:** 2 587 0015
Email Address: fomel@jsi.co.il

Academician, Chairman of, Institute of Chemical
Physics, Russia Academy of Science, 14th Institutskii
Prospect, Chernogolovka, Moscow 142432
RUSSIA
Phone: 095 913 2322 **Fax:** 095 913 2322
Email Address: fortov@ficp.ac.ru

Haefely Trench, Power Capacitors, 16 rue du General
Cassagnou, B.P. 70, St. Louis F-68302 Cedex
FRANCE
Phone: 89-70-23-23
Fax: 41-61-3155913, 89-67-26-63

Ithpp, Drele, 46500 Thegra
FRANCE

Sciences Cteh, 52 Golomb st., Holon 58102
ISRAEL
Phone: 972-8-342651 **Fax:** 972-8-344106
Email Address: fnfrucht@weizmann.weizmann.ac.il

Institute of Electrophysics, UD RAS, Komsomolskaya
34, Ekaterinburg, Ekaterinburg 620 049
RUSSIA
Phone: 3432 499 185 **Fax:** 3432 745051
Email Address: pulsar@ief.intec.ru

Institute of Applied Physics, RAS, 46, Ulyanov St.,
Nizhnyi Novgorod 603600,
RUSSIA
Phone: 7 (8312) 384 552 **Fax:** 7(8312)362 061
Email Address: ginzburg@appl.sci-nnov.ru

ASO National Laboratories, 20 Science Park Drive,
Singapore 118230
SINGAPORE
Phone: +65-871-2059 **Fax:** +65-775-9011

Advanced Power Technologies, Inc, APTI, Suite #850,
1250 Twenty-Fourth Street, NW, Washington D.C.
20037
USA
Phone: 202-223-8808 **Fax:** 202-223-1377
Email Address: farris@apti.com

RAFAEL, Dept. 24, P.O. Box 2250, Haifa 31021,
ISRAEL
Email Address: fngomber@weizmann.weizmann.ac.il

LIST OF PARTICIPANTS [by ABC] - contd.

GONCHAROV Alexey Anton, Dr.

Institute of Physics National Academy of Science of Ukraine, 46 Prospect Nauki, Kiev 252650
UKRAINE
Phone: 44 265 7824 **Fax:** 44 265 7824
Email Address: gonchar@iop.kiev.ua

GORDEEV Alexander V., Dr.

Institute of Nuclear Fusion, Russian Res. Centre "Kurchatov Institute", Kurchatov Sq., 1, Moscow 123182,
RUSSIA
Phone: (095) 196 7345 **Fax:** (095) 196 9874
Email Address: gordeev@tapdki.ips.ras.ru or otd4@expd.vniief.ru

GOVER Abraham, Prof.

Fac. of Engineering, Tel Aviv University, P.O. Box 39040, Tel Aviv 69978,
ISRAEL

GOYER John R., Dr.

Maxwell Technologies, Inc, 8888 Balboa Avenue, San Diego CA 92123
USA
Phone: 619 496 4106 **Fax:** 619 576 7659
Email Address: lgoyer@maxwell.com

GRABOVSKI Evgeniy V., Dr.

TRINITI, Troitsk Inst. for Innov. & Thermonucl. Investigation, Centralnaya St. 3-19, Troitsk, Moscow Region 142092,
RUSSIA
Phone: 7 (095) 334 5614 **Fax:** 7 (095) 334 5614
Email Address: angara@fly.triniti.troitsk.ru

GRABOVSKI Theodore C.

WEIZMANN INSTITUTE, REHOVOT 76100
ISRAEL
Phone: 505 277 1303 **Fax:** 505 277 1439

GREGORIAN Lev, Mr.

Department of Particle Physics, Weizmann Institute of Science, P.O. Box 26, Rehovot 76100,
ISRAEL
Phone: 8 934 2677 **Fax:** 8 394 3491
Email Address: fngregor@plasma-gate.weizmann.ac.il

GRUN Jacob, Dr.

Naval Research Laboratory, Code 6795, 4555 Overlook Ave., Washington DC 20375
USA
Phone: 11 202 7679117 **Fax:** 11 202 7673869

HARADA Nobuhiro, Mr.

Nagaoka University of Technology, Dept. of Electrical Engineering, 1603-1 Kamitomioka, Nagaoka-city, Niigata 940-21,
JAPAN
Phone: 81 (258) 46 6000 **Fax:** 81 (258) 46 6506
Email Address: nob@voscc.nagaokaut.ac.jp

HASEGAWA Daisuke , Mr.

Dept. of Physics, Faculty of Science, Kanazawa University, Kakuma-Machi, Kanazawa 920-1192
JAPAN
Phone: 76 264 5917 **Fax:** 76 264 5739
Email Address: daisuke@plasma.s.kanazawa-u.ac.jp

HAWKINS Houston T., Dr.

Los Alamos National Laboratory, Nonproliferation & International Security Division, P.O.Box 1663 MS F650, Los Alamos NM 87545
USA
Phone: 505 6651259 **Fax:** 505 6654109

HE Guorong, Prof.

Southwest Institute of Fluid Physics, POBox 523, Chengdu Sichuan 610003
CHINA

HINSHELWOOD David D., Dr.

c/o Code 6773, Naval Research Laboratory, 4555 Overlook Ave., S.W., Washington DC 20375-5000
USA
Phone: 202 767 8486 **Fax:** (202) 767 2012
Email Address: ddh@suzie.nrl.navy.mil

HOPPE Peter F.W., Dr.

Forschungszentrum Karlsruhe, INR Dept., Bau 630, Zi 207, D-76021 Karlsruhe
GERMANY
Phone: 7247 824674 **Fax:** 7247 822823
Email Address: hoppe@inr.fzk.de

HORIOKA Kazuhiko, Prof.

Deptartment of Energy Sciences, Tokyo Institute of Technology, 4259 Nagatsuta, Midori-ku Yokohama 226
JAPAN
Phone: 45 924 5661 **Fax:** 45 921 1318
Email Address: khorioka@es.titech.ac.jp

HOTTA Eiki, Prof.

Dept. of Energy Sciences, Tokyo Institute of Technology, Nagatsuta, midori-ku, Yokohama 226-8502
JAPAN
Phone: 3-3726-111 **Fax:** 3-3729-139
Email Address: ehotta@hotta.es.titech.ac.jp

HUIHUANG Zhong, Prof.

National University of Defence Technology, Dept. of Applied Phys., changsha hunan 410073
CHINA

ILIESCU Elena, Dr.

Institute for Atomic Physics, Nat'l Inst for Laser, Plasma & Radiation Physics, Electron Accelerators Laboratory, PO Box MG-36, Bucharest-Magurele
ROMANIA
Fax: 423 1791
Email Address: eiliescu@roifa.ifa.ro

BEAMS'98

IMASAKA Kimitoshi, M.

Kyushu University, Dept. of Electrical and Electronic
Systems Engineering, Graduate School of Information
Science and Electrical Engineering, 6-10-1 Hakozaki
Higashi-ku, Fukuoka 812
JAPAN
Phone: 92 642 3894 **Fax:** 92 642 3964
Email Address: imasaka@ees.kyushu-u.ac.jp

JAKUBOWSKI Lech, Dr.

THE ANDRZEJ SOLTAN INSTITUTE FOR NUCLEAR
STUDIES, 05-400 OTWOCK-SWIERK N., PL-
WARSAW
POLAND
Phone: (48)22 779 8678 **Fax:** (48) 22 779 3481
Email Address: jakubows@cx1.cyf.gov.pl

JERBY Eli, Dr.

Faculty of Engineering, Dept. of Physical Elec, Tel Aviv
University, Ramat Aviv 69978
ISRAEL
Phone: 03 966 5408 **Fax:** 03 642 3508
Email Address: jerby@tavivm.ac.il

JUNGWIRTH Karel, Dr.

Pulsed Plasma Systems Dept., Institute of Plasma
Physics AS CR, Za Slovankou 3, P.O. Box 17, CZ-182
00 Prague 8
CZECH REPUBLIC
Phone: 2 2424 0536 **Fax:** 2 2422 0944
Email Address: jungwirt@ipp.cas.cz

KALININ Yuri G., Dr.

Institute of Nuclear Fusion, Russian Res. Centre
"Kurchatov Institute", Kurchatov Sq., 1, Moscow
123182,
RUSSIA
Phone: 7 (095) 196 9672 **Fax:** 7 (095) 196 9874

KALYNOV Yuri K., Mr.

Institute of Applied Physics, RAS, 46, Ulyanov St.,
Nizhnyi Novgorod, 603600,
RUSSIA
Phone: 7 (8312) 384347 **Fax:** 7 (8312) 362 061
Email Address: kalynov@appl.sci-nnov.ru

KAMADA Keiichi, Dr.

Kanazawa University, Faculty of Science, Kakuma-
Machi, Kanazawa Ishikawa 920-1192
JAPAN
Phone: 76 264 5671 **Fax:** 76 264 5739
Email Address: kkamada@plasma.s.kanazawa-u.ac.jp

KARAS Vyacheslav I. I., Prof.

Kharkiv Institute of Physics and Technology,
Akademicheskaya 1, Kharkov 310108
UKRAINE
Phone: 57-2404794 **Fax:** 57-2351738

KIRICHENKO Khristofor, Dr.

Laboratory of Computing Techniques and Automation,
Joint Institute For Nuclear Research, Dubna Moscow
141980
RUSSIA
Phone: 9621 64808 **Fax:** 9621 65145
Email Address: mirzo@lcta6.jinr.dubna.su

KNYAZEV Boris A., Prof.

Novosibirsk State University, Dept. of General Physics,
2 Pirogova St., Novosibirsk 630090
RUSSIA
Phone: 383 2 35 0770 **Fax:** 383 2 39 7101
Email Address: knyazev@phys.nsu.ru

KOIDAN Vasily S., Dr.

Budker Institute of Nuclear Physics, SD RAS,
Lavrentyev Avenue 11, Novosibirsk 630090,
RUSSIA
Phone: 7 (3832) 359 589 **Fax:** 7 (3832) 352 163
Email Address: koidan@inp.nsk.su

KOLACEK K., Dr.

Institute of Plasma Physics, Academy of Sciences of
the Czech Republic, Za Slovankou 3, P.O.Box 17,
18200 Pague 8, Czech Republic, CZ-
CZECH REPUBLIC

KORMILITSIN Victor P., Dr.

Head of Division, Russian Federal Nuclear Center
(VNIIEF), Pr. Mira 37, Sarov (Arzamas-16), Nizhnyi
Novgorod Reg. 607 190,
RUSSIA
Phone: 83130 457 38 **Fax:** 83130 45738
Email Address: vkor@elph.vniief.ru

KORJENEVSKI Sergei, Mr.

Institute of Electrophysics, 34 Komsomolskaya,
Ekaterinburg 620219
RUSSIA

KORNILITSYN Alexei, Dr.

Russian Federal Nuclear Center (VNIITF), P.O. Box
245, Snezhinsk, Chelyabinsk Reg. 456 770,
RUSSIA
Phone: 7 (35172) 329 93 **Fax:** 7 (35172) 309 79
Email Address: ovd@dep26.ch70.chel.su

KORNILOV Eugene A., Dr.

NSC Kharkov Institute of Physics and Technology,
Akademicheskaya St. 1, Kharkov 310108,
UKRAINE
Phone: 7 (057) 235 1993 **Fax:** 7 (057) 235 1738
Email Address: kfti@kfti.kharkov.ua

KOROVIN Sergei D., Prof.

High Current Electronics Institute, SD RAS, 4,
Akademicheski Avenue, Tomsk 634055,
RUSSIA
Phone: 7 (3822) 258 706 **Fax:** 7 (3822) 259 134
Email Address: korovin@hcei.tomsk.su

KOSHELEV Vladimir I., Prof.

High Current Electronics Institute, 4 Akademichesky
Avenue, Tomsk 634055
RUSSIA
Phone: (3822) 258 915 **Fax:** (3822) 259 410
Email Address: koshelev@hcei.tomsk.su

KRASA Joseph, Dr.

Institute of Physics, Acad. Sci., CR, Na Slovance 2,
18040 Prague 8
CZECH REPUBLIC
Phone: 2 82 12 27 858 45 69
Email Address: krasa@fzu.cz

KRASIK Yakov E., Dr.

Technion-Israel Institute of Technology , Dept of
Physics, Haifa 32000
ISRAEL
Phone: 04 829 3666 **Fax:** 04 822 6641
Email Address: fnkrasik@physics.technion.ac.il

KRAVARIK Josef, Dr.

Dept. of Physics, Fac.of Elect. Engin., , Czech Technical
University, Technicka 2, Prague 6, Dejvice, 16627
CZECH REPUBLIC
Phone:
420-2-24353336+420-2-24352331, 42 (2) 2435 3336
Fax: 42 (2) 311 1786
Email Address: kubes@feld.cvut.cz

KRISTIANSEN Magne M., Prof.

Texas Tech. University, Electrical Engineering Dept.,
Lubbock TX 79409-3102
USA
Phone: (806) 742 2224 **Fax:** (806) 742 1281
Email Address: nukrs@ttacsl.ttu.edu

KROUPP Eyal, Mr.

Weizmann Institute of Science, Dept of Physics, Herzl
Street, Rehovot 76100
ISRAEL

KUBES Pavel, Dr.

Dept. of Physics, Fac.of Elect. Engin., Czech Technical
University, Technicka 2, Prague 6, Dejvice, 16627
CZECH REPUBLIC
Phone: 420-2-24352330, (422) 2435 2330
Fax: 420-2-24352331, (422) 311 1786
Email Address: kubes@feld.cvut.cz

KUFTIN Andrei N., Dr.

Institute of Applied Physics, RAS, 46, Ulyanov St.,
Nizhnyi Novgorod 603600,
RUSSIA
Phone: 8312 366 141 **Fax:** 8312 362 061
Email Address: manuilov@appl.sci-nnov.ru

KUPERSZTYCH Joseph, Dr.

Service S.R.S.I.M., C.E.A.- C.E. de Saclay, Batiment
462, F-91191 Gif-sur-Yvette,
FRANCE
Phone: 1 69 08 65 56 **Fax:**1 69 08 84 46
Email Address: jkupersztych@cea.fr

KUROPATKIN Yurii P., Dr.

Russian Federal Nuclear Center (VNIIEF), Pr. Mira 37,
Sarov (Arzamas-16), Nizhnyi Novgorod Reg. 607 190,
RUSSIA
Phone: 7 (83130) 546 38 **Fax:** 7 (83130) 545 65
Email Address: popkov_3001@spd.rfnc.nnov.su

KUSHNIR Volodimir A., Dr.

KIPT, 1 Academicheskaja Street, Kharkov UA-310108
UKRAINE
Phone: 57 235 6286 **Fax:** 57 235 3731
Email Address: kushnir@nik.kharkov.ua

KUSSE Bruce R., Dr.

LPS, Cornell University, 369 Upson Hall, Ithaca, NY
14853,
USA
Phone: (607) 255 4127 **Fax:** (607) 255 3004
Email Address: kusse@lps.cornell.edu

KUZYAEV Anatoliy I., Dr.

All-Russian Research Institute of Experimental Physics,
Pr. Mira 37, Sarov (Arzamas-16), Nizhnyi Novgorod
Reg. 607 190,
RUSSIA
Phone: 7 (83130) 457 38 **Fax:**7 (83130) 545 65
Email Address: aik@elph.vniief.ru

LAWRENCE George P., Dr.

Los Alamos National laboratory, Mail Stop H816, Los
Alamos NM 87545
USA
Phone: 505 667 9349 **Fax:** 505 667 7344
Email Address: glawrence@lanl.gov

LAWSON Wesley G., Prof.

University of Maryland, Electrical Engineering Dept.,
College Park, MD 20742,
USA
Phone:(301) 405 4972 **Fax:** (301) 314 9437
Email Address: lawson@eng.umd.edu

LEIBOVITCH Hayim, Dr.

RAFAEL, P.O. Box 2250, Haifa 31021
ISRAEL

LEOPOLD Yochanan, Dr.

RAFAEL, P.O. Box 2250, Haifa 31021
ISRAEL

LEVI Niv

IDF,
ISRAEL

BEAMS'98

LEVINE Jerrold L., Dr.
Primex Physics International, 2700 Merced Street, San
Leandro CA 94577-0599
USA
Fax: 510 577 7108

LEVUSH Baruch, Dr.
Code 6841, Naval Research Laboratory, 4555 Overlook
Ave. S.W., Washington DC 20375-5347
USA
Phone: 202 767 0037 **Fax:** 202 767 1280
Email Address: levush@mmace.nrl.navy.mil

LIGACHEV Alexandr E., Prof.
Institute of Electrophysics, UD RAS, Komsomolskaya
34, Ekaterinburg 634 049
RUSSIA
Phone: 095 938 2211 **Fax:** 095 938 2211
Email Address: game405@glasnet.ru

LISITSYN Igor V., Dr.
Kumamoto University, Dept. of Elec. & Comp.
Engineering, Kurokami 2-39-1, , Kumamoto 860
JAPAN
Phone: 81-96-342-3618 **Fax:** 81-96-342-3630
Email Address: lisitsyn@eecs.kumamoto-u.ac.jp

LONCAR Boris, Mr.
Faculty of Technology and Metallurgy, University of
Belgrade, Karnegijeva 4, Belgrade 11000 Serbia
YUGOSLAVIA
Phone: 381-11-3370398 11 337 0387
Fax: 381-11-3370387 11 337 0387
Email Address: 11 337 0398

LOUKSHA Oleg.I., Dr.
Dept. of Physical Electronics, St. Petersburg State
Tech. University, Polytechnicheskaya 29, St. Petersburg
195 251,
RUSSIA
Phone: 7 (812) 552 7954 **Fax:** 7 (812) 552 7954
Email Address: sominski@phtf.hop.stu.neva.ru

LUDMIRSKY Ariold, Dr.
NRC Soreq, Plasma Group, Yavne 81800,
ISRAEL
Phone: 972 (8) 943 4753 **Fax:** 972 (8) 943 4775
Email Address: ariold@ndc.soreq.gov.il

MALY Benny, Mr.
Faculty of Electrical Engineering, Technion, Technion
City, Haifa 32000
ISRAEL
Fax: 04 832 3041
Email Address: maly@techunix.technion.ac.il

MANDELBAUM Benjamin, Mr.
RAFAEL, Dept. 21, P.O. Box 2250, Haifa 31021,
ISRAEL
Phone: 972 (4) 795 233 **Fax:** 972 (4) 792 212

MARKOVITS Meir, Dr.
RAFAEL, P.O. Box 2250, Dept. 24, Haifa 31021
ISRAEL
Phone: 972 (4) 879 2563 **Fax:** 972 (4) 879 5289
Email Address: meirm@rafael.co.il

MARON Yitzhak, Prof.
Weizmann Institute of Science, Faculty of Physics,
P.O. Box 26, Rehovot 76100
ISRAEL
Phone: 972 (8) 934 4055 **Fax:** 972 (8) 466 966
Email Address: fnmaron@weizmann.weizmann.ac.il

MARTEN Holger, Dr.
Forschungszentrum Karlsruhe, INR, Postfach 3640,
D-76021 Karlsruhe
GERMANY
Phone: 07247 822444 **Fax:** 07247 823824
Email Address: holger.marten@inr.gzk.de

MASUGATA Katsumi, Prof.
Dept. of Electric and Electronic System Engineering,
Faculty of Engineering, Toyama University, 3190
Gofuku, Toyama 930-8555
JAPAN
Phone: 764 91 2848 764 45 6714
Email Address: masugata@nagaokaut.ac.jp

MASUZAKI Masumi, Prof.
Department of Physics, Kanazawa University, Faculty
of Science, Kakuma-Machi, Kanazawa Ishikawa 920-
1192
JAPAN
Phone: 76 264 5672 **Fax:** 76 264 5739
Email Address: masuzaki@plasma.s.kanazawa-u.ac.jp

MEHLHORN Thomas A., Dr.
Sandia National Laboratories, Org. 1207, P.O. Box
5800, MS 1187, Albuquerque, NM 87185-1187,
USA
Phone: (505) 845 7266 **Fax:** (505) 845 7890
Email Address: tamehlh@sandia.gov

MEIER Gert O., Dr.
INR, Forschungszentrum Karlsruhe, Postfach 3640,
D-76021 Karlsruhe 1, KARLSRUHE
GERMANY
Phone: (7247) 82 3437 **Fax:** (7247) 82 2823
Email Address: bauer@inr.fzk.de

MELAMUD Efraim, Mr.
Rafael, P.O. Box 2250, Haifa 31021
ISRAEL

MENDEL JR. Clifford W., Dr.
High Energy Plasma Physics Division 9573, Sandia
National Laboratories, P.O. Box 5800, Albuquerque,
NM 87185-1194, ALBUQUERQUE
USA
Phone: (505) 845-7245 **Fax:** (505) 845-7864
Email Address: cwmende@sandia.gov

LIST OF PARTICIPANTS (by ABC) – contd.

MESYATS Gennadi A., Prof.

Institute of Electrophysics, UD RAS, Komsomolskaya 34, Ekaterinburg 620 049,
RUSSIA
Phone: 7 (3432) 440 223 **Fax:** 7 (3432) 444 133
Email Address: gregory@ami.e-burg.su

MICHIZONO Shin-Ichiro, Mr.

JAPAN

MILLER R. Bruce, Dr.

Titan, P.O. Box 9254, Albuquerque NM 87119-9254
USA

MOROZOV Ivan V., Dr.

Head of Laboratory, All-Russian Research Institute of Experimental Physics, Pr. Mira 37, Sarov (Arzamas-16), Nizhnyi Novgorod Reg. 607 190,
RUSSIA
Phone: 7 (831) 304 5738 **Fax:** 7 (831) 304 54738
Email Address: vcher_1763@rfnc.nnov.su

MOSCHELLA John J., Dr.

Hy-Tech Research Corp., 104 Centre Court, Radford VA 24141
USA
Phone: 540 639-4019 **Fax:** 540 639 4027
Email Address: johnmhtr@aol.com

MROZ Waldemar, Dr.

Institute of Optoelectronics, MUT, 01-489 Warsaw 49, 2 Kaliski Street, PL-
POLAND
Phone: 48-2-685-96-12 **Fax:** 48-2-666-8950
Email Address: lastech@wat.waw.pl

MUELLER Georg, Dr.

INR, Forschungszentrum Karlsruhe 3NR, Hermann-von-Helmholzplatz - 1, D-76344 Eggenstejn-Leopolds Hafen
GERMANY
Phone: 7247 824 302 **Fax:** 7247 824 874
Email Address: mueller@inr.fzk.de

MURRAY Oren K., Mr.

USA Air Force, 3550 Aberdeen Ave., Kirtland AFB NM 87117-5776
USA
Phone: 505 8464345 **Fax:** 505 7464374
Email Address: towne@pik.af.mil

NAKAGAWA Yoshiro, Prof.

Osaka City University
Dept. of Electrical Engineering
3-3-138 Sugimoto-cho, Sumiyoshi-ku,, Osaka 558-0022
JAPAN

NATION John A., Prof.

325 Rhodes Hall, Cornell University, Ithaca NY 14850
USA
Phone: 6072558703 **Fax:** 6072553004
Email Address: jnation@lps.cornell.edu

NAVON Itamar, Dr.

RAFAEL, P.O. Box 2250, Haifa 31021
ISRAEL
Phone: 4 879 2975 **Fax:** 4 877 2972

NEMIROVSKY Roni, Mr.

75 Einstein ST., Haifa 34602
ISRAEL
Phone: 4-834-0490
Email Address: roni@physics.technion.ac.il

NIKULIN Sergei P., Dr.

Institute of Electrophysics, UK RAS, Komsomolskaya 34, Ekaterinburg 620 049
RUSSIA
Phone: 3432 499 392 **Fax:** 3432 445051
Email Address:nikulin@ief.intec.ru

NIU Keishiro K., Prof.

Teikyo Heisei University, Dept. of Information System, 2289-23 Ohtani, Uruido, Ichihara Chiba 210-01
JAPAN

NOVAKOVIC Ljiljana, Dr.

VINCA Institute of Nuclear Sciences, Laboratory of Radiation Chemistry and Physics, PO Box 522, 11001 Belgrade
YUGOSLAVIA
Phone: 11 453 986 **Fax:** 11 344 0100
Email Address: bratmil@rt270.vin.bg.ac.yu

NOVOSELOV Yuri N., Dr.

Institute of Electrophysics, UD RAS, Komsomolskaya 34, Ekaterinburg 620 049,
RUSSIA
Phone: 7 (3432) 441 853 **Fax:** 7 (3432) 445051
Email Address: nov@ief.e-burg.su

NUSINOVICH Gregory S., Dr.

University of Maryland, Institute for Plasma Research, College Park MD 20742
USA
Phone: 301 405 4917 **Fax:** 301 314 9437
Email Address: gregoryn@glue.umd.edu

OGAWA Masao, Prof.

Tokyo Institute of Technology, Research Laboratory for Nuclear Reactors, 2-12-1 Ohokayama, Meguro-Ku Dept., Tokyo 152
JAPAN
Phone: 3 5734 3294 **Fax:** 3 5734 3295
Email Address: mogawa@nr.titech.ac.jp

OLEJNIK Georgiy M., Dr.

TRINITI, Troitsk Inst. for Innov. & Thermonucl. Investigation, reg. "B", 3-159, Troitsk, Moscow Region 142092,
RUSSIA
Phone: 7 (095) 334 5614 **Fax:** 7 (095) 334 5614
Email Address: angara@fly.triniti.troitsk.ru

ONISHCHENKO Ivan N., Prof.

NSC Kharkov Institute of Physics and Technology,
Dept. of Plasma Electronics, Academic Str. 1,
KHARKOV 310108
UKRAINE
Phone: 0572 356140 **Fax:** 0572 353564
Email Address: onish@kipt.kharkov.ua

OPEKUNOV Mikhail S., Dr.

Institute of Nuclear Physics of Tomsk PTU, Prospekt
Lenin 2A, P.O. Box 25, Tomsk 634 050,
RUSSIA
Phone: 7 (3822) 440 097 **Fax:** 7 (3822) 440 812
Email Address:mike@ephc.npi.tpu.ru

OX Efim, Prof.

High Current Electronics Institute , 4 Academichesky
ave., Tomsk 634055
RUSSIA
Phone: 3822 258 776 **Fax:** 3822 259 410
Email Address: oks@hcei.tomsk.su

PARKS Donald, Dr.

Maxwell Technologies, Inc., 8888 Balboa Avenue, San
Diego California
USA
Phone:(619) 576 7802 **Fax:** (619) 576 7659
Email Address: parks@maxwell.com

PASSOW Cord A.H., Dr.

Lill Eva-Maria
Kolberger Str. 28c, 76139 Karlsruhe,
GERMANY
Phone: 0721-689524

PEGUEL Igor V., Dr.

Institute of High Current Electronics, 4 Akademickesky
Ave., Tomsk 634055
RUSSIA
Phone: 3822 259 652 **Fax:** 3822-259-134
Email Address: pegel@lfeup2.hcei.tomsk.su

PEREIRA Nino R., Dr.

Berkeley Research, PO Box 852, Springfield VA 22150
USA
Phone: 703 750 3434 **Fax:** 703 750 3106
Email Address: pereira@bra4a.nrl.navy.mil

PERELSTEIN Elkuno, Prof.

Moskovskaya St. 12, app. 251, Dubna Moscow 141980
RUSSIA
Phone: 96 21 650 54 **Fax:** 96 21 666 66
Email Address: perel@nu.jinr.ru

PEREVODCHIKOV Vladimir I., Prof.

Deputy Director, All-Russian Electrotechnical Institute
(VEI), Krasnokazarmennaya 12, Moscow 111250
RUSSIA
Phone: 7-095-3625114 7 (095) 361 9453
Fax: 7-095-3625114 7 (095) 362 5617 or 5114
Email Address: kozlov@dir.vei.msk.su

PETCHERSKI Oleg, Prof.

D.V. Efremov Institute of Electrophysical Apparatus, 1
Sovetski Prospect, St Petersburg 189631
RUSSIA
Phone: 812 462 7845
Fax: 812 314 3360
Email Address: petcherski@sirius.niiefa.spb.su

PETRUKHIN Alexander A., Dr.

Head of Department, All-Russian Research Institute
of Experimental Physics, Pr. Mira 37, Sarov (Arzamas-
16), Nizhnyi Novgorod Reg. 607 190,
RUSSIA
Phone: 7 (83130) 457 38 **Fax:** 7 (83130) 54 565
Email Address: apetr@elph.vniief.ru

PIFFL Vojtech, Dr.

Institute of Plasma Physics AS CR, Za Slovankon
3,CZ-18221 Prague 8
CZECH REPUBLIC
Email Address: piffl@ipp.cas.cz

PONIZOVSKI Lazar Z., Dr.

State Experimental Design Bureau (SEDB) "Horizont",
8, 2nd Donoskoy pr., Moscow 117071
RUSSIA
Phone: 095 955 4079
Email Address: pac@ponizl.msk.ru

POSTAN Aaron, Dr.

Rafael,P.O. Box 2250, Haifa 31021
ISRAEL

PROSKUROVSKY Dmitry, Prof.

High Current Electronics Institute, SD RAS, 4,
Akademicheski Avenue, Tomsk 634055,
RUSSIA
Phone: 3822 259 709 **Fax:** 3822 259 410
Email Address: pdi@lve.hcei.tomsk.su

QIAN Bao-Liang, Dr.

Department of Applied Physics, Changsha Institute of
Technology, Changsha, Hunan 410073,
CHINA
Phone: 731 4434601 83206 **Fax:** 731 4448307

QUINTENZ Jeffery P., Dr.

Sandia National Laboratories, Org. 9502 MS 1191,
P.O. Box 5800, Albuquerque NM 87185-1191
USA
Phone: (505) 845 7245 **Fax:** (505) 845 7464
Email Address: jpquint@sandia.gov

RALCHENKO Yuri V., Dr.

Weizmann Institute of Science, Physics Dep., Rehovot
76100
ISRAEL

LIST OF PARTICIPANTS [by ABC] - contd.

REJ Donald J., Dr.

Physics Division, Los Alamos National Laboratory, P.O. Box 1663 Mailstop D434, Los Alamos NM 87545
USA
Phone: 505 667 4117 **Fax:** 505 665 8520 or 3644
Email Address: drej@lanl.gov

ROSENBERG Avner, Mr.

RAFAEL,P.O. Box 2250, Dept. 23,Haifa, 31021, ISRAEL
Phone: 972 (4) 879 5018 **Fax:** 972 (4) 879 5315

ROSTOKER Norman , Prof.

University of California, Dept. of Physics, Irvine CA 92697-4575
USA
Phone: 714 824 6949 **Fax:** 714 824 2174
Email Address: nrostoke@ucl.edu

ROSTOV Vladislav V., Dr.

Institute of High Current Electronics , 4 Academichesky Avenue, Tomsk 634055
RUSSIA
Phone: 3822 259 652 **Fax:** 3822 259 134
Email Address: rostov@lfeup1.hcei.tomsk.su

ROTSHTEIN Vladimir P., Prof.

State Pedagogical University, 75 Komsomol'sky Avenue, Tomsk 634041
RUSSIA
Phone: 3822 258 695 **Fax:** 3822 259 410
Email Address: rvp@lve.hcei.tomsk.su

ROUDAKOV Leonid I., Prof.

Advanced Power Technologies, Inc. (APTI), 1250 24th Street, Suite 850, Washington D.C. 20037
USA
Phone: 202 223 8808 **Fax:** 202 223 1377
Email Address: rudakov@apti.com

ROYFE Ilia M., Prof.

D.V. Efremov Inst.,1 Sovetski PP, St. Petersburg 189631
RUSSIA
Phone: 812 462 7664 **Fax:** 812 464 4608
Email Address: rim@niiefa.spb.su

RULLHUSEN Pete , Prof.

JRC - Institute for Reference Materials and Measurements (IRMM), Retieseweg, B2440 Geel
BELGIUM
Phone: 14 571 476 **Fax:** 14 591 980
Email Address: rullhusen@irmm.jrc.be

RYASLOV Evgeny A, Dr.

Russian Federal Nuclear Center (VNIIEF), Pr. Mira 37, Sarov (Arzamas-16), Nizhnyi Novgorod Reg. 607 190, RUSSIA
Phone: 7 (83130) 54 638 **Fax:** 7 (83130) 54 565
Email Address: raslov_otd4@expd.rfnc.nnov.su

SALIMOV Rustam Abelievich, Prof.

The Budker Institute of Nuclear Physics, Acad. Lavrentiev av. 11, Novosibirsk 630090
RUSSIA
Phone: 3832 359740 **Fax:** 3832 352163
Email Address: golkovsk@inp.nsk.su

SAMSONOV Sergei V., Dr.

Institute of Applied Physics, RAS, 46, Ulyanov St., Nizhnyi Novgorod 603600,
RUSSIA
Phone: 8312 384 575 **Fax:** 7 8312 362 061
Email Address: bratman@appl.sci-nnov.ru

SANFORD Thomas W.L., Dr.

Intense Ion Beam Research Dept. 9531, Sandia National Laboratories, Org. 1231, P.O. Box 5800, Mail Stop 1196, Albuquerque NM 87185-1196
USA
Phone: (505) 845 7816 or 845 8864
Fax: (505) 845 7820
Email Address: twsanfo@sandia.gov

SARID Eli, Dr.

25 Eshel st., Omer 84965
ISRAEL

SAVELIEV Yuri M., Dr.

University of St. Andrews, School of Physics and Astronomy, North Haugh, St. Andrews, Fife, KY 16 9SS,
UK
Phone: (1334) 476 161 ext 3189 **Fax:** (1334) 463 104
Email Address: yms@st-and.ac.uk

SAWYER Adrian, Mr.

Dera Farnborough WX2, 1016A A2, Farnborough, Hants., GU140PX
UK

SCANNELL Edward, Dr.

Army Research Laboratory, AMSRL-SE-D, 2800 Powder Mill Rd., Adelphi MD 20783-1197
USA

SCHAMILOGLU Edl, Prof.

University of New Mexico, Department of EECE, 323C EECE Building, Albuquerque NM 87131
USA
Phone: (505) 277 4423 **Fax:** (505) 277 1439
Email Address: edl@eece.unm.edu

SCHERBININ Sergey, Mr.

Institute of Electropysics, Russian Academy of Sciences, 34 Komsomolskaya Str, Ekaterinburg 620219
RUSSIA
Phone: 3432 742038 **Fax:** 3432 745 051
Email Address: filatov@ief.intec.ru

SCHMIDT Jiri , Mr.

Institute of Plasma Physics , Department of Pulse Plasma Systems, 3 Za Slovankou P.O. Box 17, 18221 Prague
CZECH REPUBLIC

SCHNEIDER Ralph, Dr.

Simulation and Test Division, Defense Nuclear Agency,
EST, 6801 Telegraph Road, Alexandria VA 22310-3398
USA
Phone: 703 325 1142 **Fax:** 703 325 0249
Email Address: schneider@hqg.dswa.mil

SCHNITZER Itzhak, Dr.

Rafael
#23
P.O.Box 2250, Haifa
ISRAEL

SEGALOV Zvi, Dr.

RAFAEL, P.O. Box 2250, Haifa 31021
ISRAEL

SEMUSHIN Sergei, Dr.

Ecole Polytechnique, Laboratoire PMI, F-91128
Palaiseau
FRANCE
Phone: 1 6933 3248 **Fax:** 1 6933 3023
Email Address: sem@lpmi.polytechnique.fr

SENG Yeow Sing, Mr.

DSO National Laboratories, 20 Science Park Drive,
Singapore 118230
SINGAPORE
Phone: +65-373-2130 **Fax:** +65-775-9011
Email Address: syeowsin@dso.org.sg

SHILOH Joseph, Dr.

RAFAEL, Dept 23, P.O. Box 2250, Haifa 31021
ISRAEL
Email Address: jshiloh@rafael.co.il

SHLAPAKOVSKI Anatoli, Dr.

Institute of Nuclear Physics, Tomsk Polytechnical
University, P.O. Box 25, Tomsk 634050
RUSSIA
Phone: (3822) 440 726 **Fax:** 382 2440 812 / 242 3934
Email Address: shl@tsinph.tomsk.su

SHNEERSON G.A., Prof.

St. Petersburg State Technical University, 29
Polytechnicheskaya St., St Petersburg 195251
RUSSIA
Phone: 812-555-4286 **Fax:** 812-552-7954
Email Address: shne@phtf.stu.neva.ru

SHPITALNIK Reuven R., Dr.

Plasma Group, NRC Soreq, Dept. 27, Yavne 81 800,
ISRAEL
Phone: 08 434 760 **Fax:** 08 434 775
Email Address: reuven@ndc.soreq.gov.il

SHUKER Moshe, Mr.

Physics Departmant, Technion Haifa 32000
ISRAEL

SKLADNIK-SADOWSKA Elzbieta, Dr.

Soltan, Institute for Nuclear Studies, PL-05-400
Otwock-Swierk,
POLAND
Phone: 22 779 9673 **Fax:** 22 779 3481
Email Address: sadowski@cx1.cyt.gov.pl

SMILANSKI Israel

NRCL/Lasers, POBox 9001, Beer Sheva
ISRAEL

SMITH John R., Dr.

Los Alamos National Laboratory, CLS-7, MSE 525,
P.O. Box 1663, , Los Alamos NM 87544
USA
Phone: 505 665 3519 **Fax:** 505 665 6739

SOKOVNIN Sergei Yu., Dr.

Institute of Electrophysics, UD RAS, Komsomolskaya
34, Ekaterinburg 620 049,
RUSSIA
Phone: 343 493 320 **Fax:** 343 745 051 or
351 723 0979
Email Address: sokovnin@iep.uran.ru

SPASSOVSKY Ivan, Prof.

Sofia University
National Institute of Space Res. , Plasma Lab., Av.
Dos Astronautas , San Jose Dos Campus, San Jose
Campos SP
BRAZIL
Fax: 011-39694005607 physfac2@BGEA

SPRANGLE Phillip, Dr.

Code 6790, Naval research laboratory, 4555 Overlook
Avenue SW, WASHINGTON D.C. 20607
USA
Phone: 001 202 7673493 **Fax:** 001 202 767 0631
Email Address: sprangle@ppd.nrl.navy.mil.

SRINIVASAN-RAO Triveni, Dr.

Brookhaven National Laboratory, Instrumentation
Division, Bldg. 535B, Upton NY 11973
USA
Phone: 516-344-5072 **Fax:** 516-344-5773
Email Address: triveni@bnl.gov

STALLINGS Charles H., Dr.

Primex Physics International, Electromagnetic Systems,
2700 Merced St., P.O. Box 5010, San Leandro California
94577
USA
Phone: 510 577 7111 **Fax:** 510 577 7108
Email Address: chstallings@san.prmx.com

STERNLIEB Abraham, Dr.

MAFAT/R&D Directorate, Ministry of Defense, Hakirya,
Tel Aviv 61909,
ISRAEL
Phone: 972 (3) 697 7352 **Fax:** 972 (3) 697 6280

BEAMS'98

STEUKERS Catherine, Dr.

Royal Military Acadamy, Chaire OMRA, Renaissance Avenue, 30, B-1000 Brussels
BELGIUM

STRELKOV Pavel S. , Prof.

General Physics Institute, RAS, Vavilova Str.38, Moscow 117942,
RUSSIA
Phone:095 132 8216 **Fax:** 095 135 8011
Email Address: loza@fp7.gpi.msk.su

STRUVE Kenneth, Dr.

Mission Research Corporation, 1720 Randolph Road, S.E., Albuquerque, NM 87106,
USA
Phone: (505) 768 7720 **Fax:** (505) 768 7601
Email Address: kwstruv@sandia.gov

SWEGLE John, Dr.

Mail Stop L377, Lawrence Livermore National Laboratory, P.O. Box 808, Livermore, CA 94551,
USA
Phone: (505) 423 0548 **Fax:** (505) 423 0925
Email Address: swegle1@llnl.gov

TARAKANOV Vladimir P., Dr.

High Energy Density Research Center, Institute for High Temperatures, RAS (IVTAN), Izhorskaya 13/19, Moscow 127412,
RUSSIA
Phone: 095 183 8626 **Fax:** 095 4857 990
Email Address: tarak@sci.lpi.msk.su

TATSENKO Olga Mikhailovna, Dr.

Pr. Mira, 37, Sarov Nizhnii, Novgorod Region 607190
RUSSIA
Phone: 831 30 4 55 84
Email Address: bykov@ntc1.vniief.ru

THOMPSON John, Dr.

Maxwell Laboratories, Inc.
Balboa Division
Maxwell Technologies, Systems Division, 8888 Balboa Avenue, San Diego CA 92123-1504
USA
Phone: (619) 576-7799 **Fax:** (619) 576-7659
Email Address: thompson@maxwell.com

TOKUCHI Akira, Mr.

Tokki Branch, Nichicon Corporation , 2-3-1 Kusatsu,, Shiga 525-0053
JAPAN
Phone: 77-563 1184 **Fax:** 71 565 3818

TOULISOU Evgueni V., Dr.

Research Institute of Scientific Instruments, Turaevo-1, Lytkatina Moscow 140061
RUSSIA

TSIGUTKIN Konstantin, Mr.

Weizmann Institute of Science, Dept of Physics, Herzel Street, Rehovot 76100
ISRAEL
Phone: 08 934 2211 **Fax:** 08 934 3491
Email Address:tsigut@plasma-gate.weizmann.ac.il

TYDEMAN Andrew, Mr.

Electronic Measurements INC., 405 Essex Road, Neptune NJ OT153 07753
USA
Phone: 732-9229300+229 **Fax:** 732-9229334
Email Address: tudes@injersey.com

ULLSCHMIED Jiri, Dr.

Pulsed Plasma Systems Dept., Institute of Plasma Physics AS CR, Za Slovankou 3, P.O. Box 17, CZ-18200 Prague 8,
CZECH REPUBLIC
Phone: 2 6605-3233 **Fax:** 2 858-6389
Email Address: ullsch@ipp.cas.cz

URBANUS Wim, Dr.

FOM Institute of Plasma Physics, Rijnhuisen, P. O. Box 1207, NL-3430 BE Nieuwegein,
THE NETHERLANDS
Phone: 30 6096999 **Fax:** 30 6031204
Email Address:urbanus@huygens.rijnh.nl

VAISBURD David I., Prof.

High Current Electronics Institute, SD RAS, 4, Akademicheski Avenue, Tomsk 634055,
RUSSIA
Phone: 3822 258 611 **Fax:** 3822 259 410
Email Address: vaysburd@lnpspb.tomsk.su

VARIALE Vincenzo, Dr.

INFN - Se7.oli Bari, Via Amendola 173, I-70126 Bari
ITALY
Phone: 805 443 190 **Fax:** 805 443 185
Email Address: variale@axpba0.ba.infn.it

VENEZIA Abraham, Dr.

RAFAEL, P.O. Box 2250, Haifa 31021
ISRAEL

WEBER Bruce V., Dr.

Naval Research Laboratory, 4555 Overlook Ave., S.W., Washington, DC 20375-5320,
USA
Phone: (202) 767 8313 **Fax:** (202) 767 2012
Email Address: weber@suzie.nrl.navy.mil

WEINGARTEN Amit, Mr.

Department of Particle Physics, Weizmann Institute of Science, P.O. Box 26, Rehovot 76100,
ISRAEL
Fax: 972 (8) 466 966
Email Address: fnweing@wis.weizmann.ac.il

LIST OF PARTICIPANTS (by ABC order)

WEINSTEIN Meir, Dr.
Infrastructure Division, Mafat, Hakiria, Tel Aviv
ISRAEL

WEISMAN Efraim, Dr.
RAFAEL, P.O. Box 2250, Haifa 31021
ISRAEL

WESTERMANN Thomas, Prof.
FH Karlsruhe - University of Technology, Postfach
2440, 76012 Karlsruhe
GERMANY
Phone: 07247-82-3008 **Fax:** 7247-82-5070
Email Address: westermann@fh-karlsruhe.de

WHITE Roger, Dr.
Maxwell Technologies, Inc., Systems Division, 8888
Balboa Avenue, San Diego CA 92123
USA
Phone: 619 576 7716 **Fax:**619 637 7411
Email Address: rogerw@maxwell.com

WOOD Blake P., Dr.
Physics Div. Plasma Physics Group P-24, MS-E526,
Los Alamos National Laboratory, Los Alamos, NM
87545
USA
Phone: 505 665 6524 **Fax:** 505 665 3552
Email Address: bwood@lanl.gov

WURTELE Jonathan, Prof.
Dept. of physics UC Berkley, 366 Lecowte Hall, Berkley
CA 94720
USA

WURZBERG Eliezer, Dr.
23 REFAEL, POBox 2250, Haifa
ISRAEL
Phone: 04-8795018 **Fax:** 04-8795315

YAGHJIAN Arthur D., Dr.
115 Wright Road, Concord MA 01742
USA
Phone: 7813773961 **Fax:** 7813775040
Email Address:yaghjian@plh.af.mil

YAJUN Fan, Mr.
Northest Institute of Nuclear Technology, POBox 69-
13, xian shaan'xi 710024
CHINA

YAKIMOV Yurii M., Mr.
Rene-Uniief, 37 Nira, Shrov Nizhwii Novgord 607190
RUSSIA

YATSENKO Boris P., Dr.
D.V. Efremov Inst., 1 Sovetski PR., St. Petersburg
189631
RUSSIA
Phone: 812 464 4608 **Fax:** 812 464 4608

YATSUI Kiyoshi, Prof.
Laboratory of Beam Technology, Director, Nagaoka
University of Technology, Nagaoka Niigata 940-21
JAPAN
Phone: 258 47 9891 **Fax:** 258 47 9890/9500
Email Address: yatsui@nagaokaut.ac.jp

YONAS Gerold, Dr.
Sandia National Laboratories, P.O. Box 5800, Mailstop
0151, Albuquerque NM 87185
USA
Phone: 505 845-9820 **Fax:** 505-844-6307
Email Address: gyonas@sandia.gov

YOSHIDA Hiroaki, Dr.
Department of Physics , Faculty of Science , Kanazawa
University, Kakuma-Machi, Kanazawa 920-1192
JAPAN
Phone: 762 64 5917 **Fax:** 762 64 5739
Email Address: yoshida@plasma.s.kazazawa-u.ac.jp

YUSHKOV George Y., Dr.
High Current Electronics Institute, 4 Akademichesky
Ave, Tomsk 634055
RUSSIA
Phone: 3822 258 776 **Fax:** 3822 259 410
Email Address: gyushkov@hcei.tomsk.su

ZAGORULKO Oleg Z., Dr.
Institute of Nuclear Fusion RRC, Kurchatov Institute,
Ploshad Akademika Kurchatov 1, Moscow 123182
RUSSIA
Phone: 95 196 7334 **Fax:** 95 943 0073
Email Address: oleg@qq.nfi.kiae.su

ZAITSEV Nikolay I., Dr.
Institute of Applied Physics, RAS, 46, Ulyanov St.,
Nizhny Novgorod 603600,
RUSSIA
Phone: 8312 363562 **Fax:** 8312 362061
Email Address: zaitsev@appl.sa-nnov.zu

ZAITSEV Vladimir I., Dr.
TRINITI, Troitsk Inst. for Innov. & Thermonucl.
Investigation, Centralnaya St. 28-71, Troitsk Moscow
Region 142092
RUSSIA
Phone: 095 334 0493 **Fax:** 095 334 5614 or 5776
Email Address:zaitsev@fly.triniti.troitsk.ru

ZALMAN Aaron, Mr.
Rafael, P.O. Box 2250,
ISRAEL

ZAVJALOV Michael, Dr.
All-Russian Electrotechnical Institute (VEI),
Krasnokazarmennaya 12, Moscow 111250,
RUSSIA
Phone: 095 361 9766 **Fax:** 095 362 5114

LIST OF PARTICIPANTS (by ABC) - contd.

ZHANG Zhifu, Prof.

Chinese Academy of Physics , Institute of Applied Phys., POBox 527, Chengdu Sichuan 610003 CHINA

ZILBERMAN M.M., Dr.

Lenina Street 2/68, Apt 75, Ruasan 390023 RUSSIA
Phone: 912 442056

ZINAMON Zeev, Prof.

Dept. of Nuclear Physics, Weizmann Institute of Science, P.O. Box 26, Rehovot 76100 ISRAEL
Phone: 972-8-342083 **Fax:** 972-8-344106

ZINCHENKO Vladimir F., Dr.

Res. Inst. of Sci. Instruments, Min. of Atomic Energy, Turaevo, Lytkarino-1, Moscow Region 140 061, RUSSIA
Phone: 095 552 3911 **Fax:** 095 552 3911

ZOTOVA Irina V., Dr.

Institute of Applied Physics, RAS, 46, Ulyanov St., Nizhnyi Novgorod 603600, RUSSIA
Phone: (8312) 384 316 **Fax:** 8312) 362 061
Email Address: zotova@appl.sci-nnov.ru

BEAMS'98

12th INTERNATIONAL CONFERENCE ON HIGH-POWER PARTICLE BEAMS
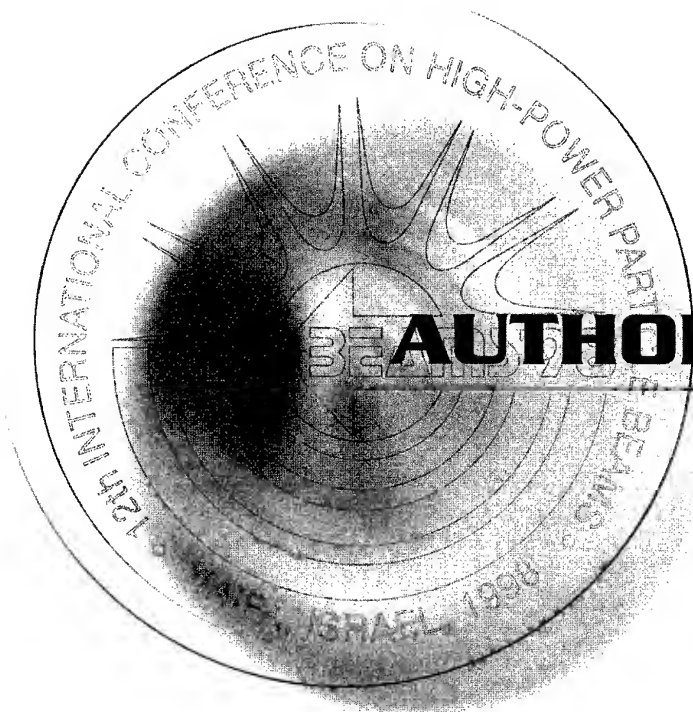
AUTHOR INDEX

Vol. II

	Proceedings
Toma, M.	257
Totmeninov, E.M.	849
Toyosugi, N.	816
Trischenko, T.V.	269
Trusilo, S.V.	585
Tsepilov, G.V.	581
Tsigutkin, K.	253
Tsuitsui, H.	153
Tsukuda, H.	816
Tulisov, E.V.	440
Tumanov, V.I.	623
Tur, Yu.D.	400, 784
Turtikov, V.	45

U

Ullschmied, J.	436, 619
Ulmaskulov, M.R.	55, 901
Urbanus, W.H.	**145**
Usenko, P.L.	585, 634
Ushakov, A.G.	591, 977, 981
Ushich, V.G.	1031

V

Vaisburd, D.I.	**21**
Vaisman, A.F.	1039
Van Der Geer, C.A.J.	145
Van Drie, A.	235
Varfolomeev, A.A.	145
Variale, V.	553
Vasilevskaya, Yu.A.	951
Vasilevsky, V.M.	330
Vath, W.	923
Veeser, L.R.	646
Velikhov, E.P.	71
Venediktov, N.P.	463, 736
Verhoeven, A.G.A.	145
Vesey, R.A.	9, 208
Vidoli, C.	5, 306
Vijazmenova, G.	404
Vikhrev, V.V.	615, 662, 666

	Proceedings
Vishnevskiy, A.	45
Vizir, A.V.	955
Vlasov, Yu.V.	83, 318, 588
Volkov, A.A.	585
Volkov, G.I.	634
Volkov, G.S.	49, 507, 599
Voss, U.	541

W

Waisman, E.	95
Walch, B.	487
Wang, P.	935
Watanabe, M.	927
Watanabe, T.	816
Watrous, J.J.	265
Weber, B.V.	**5**, 95, 265, 306, **342**
Weingarten, A.	**346**
Welch, D.R.	208
Wenger, D.F.	9, 208
Westermann, T.	513, **541**, **557**
Whitney, K.G.	229
Whitton, B.	95
Whyte, C.	857
Wiggins, S.M.	55, 901
Wolowski, J.	41
Woryna, E.	41
Wyndham, E.	240, 595

X

Xu, X.	788

Y

Yadlowsky, E.J.	95, 306, 338
Yakubov, V.B.	479, 585, 646
Yalandin, M.I.	55, 901
Yanenko, V.A.	588
Yankin, E.G.	951
Yanunkin, M.M.	961
Yatsui, K.	**111, 121**, 175, 222
	1048, **1052, 1056**

	Proceedings
Yermolovich, V.F.	83
Yonas, G.	**165**
Yoo, S.J.	203
Yoshida, H.	**889**
Yoshida, M.	927
Young, F.C.	31
Younger, S.M.	646
Yu, S.	380
Yulpatova, M.V.	463
Yushkov, G.Yu.	**955**

Z

Zabaidullin, O.	**350, 561**
Zaitsev, N.I.	820, **893**
Zaitsev, V.I.	**49**, 71, 507
Zakatov, L.P.	591, 977
Zakharov, S.V.	71, **567**, 603, **670**
Zakharov, V.S.	670
Zakutin, V.V.	400, 784
Zapevalov, V.E.	463, 736, 776, 780
Zasypkina, I.E.	463
Zavialov, M.	824, **897**
Zebrowski, J.	499
Zehnter, P.	507
Zemliansky, N.	756
Zerwekh, W.D.	646
Zhang, J.-D.	841
Zhdanov, V.S.	372
Zherlitsyn, A.G.	65
Zhong, H.-H.	841
Zhu, Q.	175
Zimmermann, F.	1008
Zinchenko, V.F.	**440**
Zinoviev, O.A.	977
Zoita, V.	257
Zolotikh, I.O.	642
Zotova, I.V.	55, **901**
Zurin, M.V.	599, 603, 607

13th International Conference on High-Power Particle Beams (BEAMS 2000)

Hotel New Otani Nagaoka Niigata, Japan

June 25 (Sun) - June 30 (Fri), 2000

First Call for Papers

Deadline of Abstracts;

December 20(Mon), 1999

Conference Information

Dates: June 25 (Sun) - June 30 (Fri), 2000
Location: Hotel New Otani Nagaoka, Niigata Japan (http://www.newotani.co.jp/en)

Main Topics

· Pulsed-Power Technology and Accelerators
electron and ion accelerators
beam drivers for fusion and fission
space charge dominated accelerators
industrial pulsed-power generators
emitters, plasmas and opening and closing switches
diagnostic methods

· Electron and Ion Beam Physics
-Experiment and Theory-
electron and ion beam generators and focusing
electron and ion beam interaction with matter
inertial confinement fusion
electron and ion rings
electron beam generation and transport
particle beams in astrophysics

· High-Power Radiation Sources
z-pinches, imploding liners, plasma focus
channeling radiation, strong turbulence
neutron sources
high power microwaves
hard and soft X-ray sources
FEMs, FELs and other beam-driven lasers

· Industrial Applications
material processing
environmental applications
medical applications
semiconductor applications

Conference Programs

Oral Sessions:
Authors will be allowed a total of 20 minutes for their oral presentations. Poster selection is the responsibility of the Technical Program Committee.

Poster Sessions:
Poster sessions will be offered all four days of the conference. The Technical Program Committee reserves the right to assign papers to their poster or oral sessions to ensure an optimum program.

Submission of Abstracts

Abstracts may be submitted by e-mail, or by mailing them in print to:

K.Yatsui: **beams@etigo.nagaokaut.ac.jp**
Conference Chair
13th International Conference on High-Power Particle Beams (BEAMS 2000)
Nagaoka, Niigata 940-2188, Japan
TEL: +81-258-47-9891,
FAX: +81-258-47-9890
December 20 (Mon), 2000 is the deadline for submitting abstracts of papers.

International Advisory Committee

A.Blaugrund   The Weizmann Institute of Science, Israel
H.Bluhm   Forschungszentrum Karlsruhe, Germany
T.Coffey   Naval Research Laboratory, USA
D.Cook   Sandia National Laboratories, USA
G.Cooperstein Naval Research Laboratory, USA
H.Doucet   C.E.A. Ecole Polytechnique, France
V.Fortov   Academy of Sciences, Russia
K.Jungwirth   Academy of Science, Czech Republic
G.Kessler   Forschungszentrum Karlsruhe, Germany
A.Kolb   Maxwell Technologies Inc., USA
G.Mesyats   Academy of Sciences, Russia
D.Rej   Los Alamos National Laboratories, USA
J.Shiloh   Rafael, Israel
V.Smirnov   Triniti Troitsk, Russia
C.Stallings   Primex Physics International, USA
R.Sudan   Cornell University, USA
R.White   Maxwell Technologies Inc., USA
K.Yatsui   Nagaoka University of Tech., Japan
G.Yonas   Sandia National Laboratories, USA

Important Date

Abstracts Due:	Dec. 20, 1999
Notification of Acceptance:	Jan. 31, 2000
Last day for Early Registration:	Mar.31, 2000
Submission of Full Paper:	Jun. 30, 2000
Conference:	Jun. 25-30, 2000